


2015

# Design and simulation of a distortion masking control algorithm for a pneumatic cylinder

Gabriel Fernando Bravo Palacios  
*Iowa State University*

Follow this and additional works at: <http://lib.dr.iastate.edu/etd>

 Part of the [Agriculture Commons](#), [Bioresource and Agricultural Engineering Commons](#), [Mechanical Engineering Commons](#), and the [Robotics Commons](#)

## Recommended Citation

Bravo Palacios, Gabriel Fernando, "Design and simulation of a distortion masking control algorithm for a pneumatic cylinder" (2015). *Graduate Theses and Dissertations*. 14769.  
<http://lib.dr.iastate.edu/etd/14769>

This Thesis is brought to you for free and open access by the Graduate College at Iowa State University Digital Repository. It has been accepted for inclusion in Graduate Theses and Dissertations by an authorized administrator of Iowa State University Digital Repository. For more information, please contact [digirep@iastate.edu](mailto:digirep@iastate.edu).

**Design and simulation of a distortion masking control algorithm for a pneumatic cylinder**

by

**Gabriel Bravo Palacios**

A thesis submitted to the graduate faculty  
in partial fulfillment of the requirements for the degree of

MASTER OF SCIENCE

Major: Mechanical Engineering

Program of Study Committee:  
Greg Luecke, Co-Major Professor  
Brian Steward, Co-Major Professor  
Sourabh Bhattacharya

Iowa State University

Ames, Iowa

2015

Copyright © Gabriel Bravo Palacios, 2015. All rights reserved.

## DEDICATION

To God

To my parents

To my brother

To my friends and teachers

## TABLE OF CONTENTS

	Page
DEDICATION .....	ii
LIST OF FIGURES .....	viii
LIST OF TABLES .....	xx
ACKNOWLEDGMENTS .....	xxii
ABSTRACT .....	xxiii
CHAPTER I. INTRODUCTION.....	1
System Dynamics and Control in Fluid Power Engineering.....	1
1.1.    Motivation .....	2
1.2.    Objectives.....	3
1.2.1. General objective.....	3
1.2.2. Specific Objectives.....	4
1.3.    Statement of Problem.....	4
1.4.    Background / Literature Review .....	8
1.4.1. Foundations of Thermodynamics.....	8
1.4.2. Foundations of Fluid Mechanics .....	11
1.4.3. Compressible flow.....	14
1.4.3.1. <i>The speed of sound</i> .....	14
1.4.3.2. <i>Classification of compressible flows</i> .....	15
1.4.4. Foundations of System Dynamics.....	18
1.4.4.1. <i>Classification of dynamic systems</i> .....	19
1.4.4.2. <i>System Analogs</i> .....	21
1.4.5. Control Theory .....	22
1.4.5.1. <i>Fundamental notions of control theory</i> .....	23
1.4.5.2. <i>Proportional, integral and derivative (PID) control</i> .....	25
1.4.5.3. <i>State-space feedback control</i> .....	27
1.4.5.4. <i>Optimal control</i> .....	31



1.4.5.5. <i>Non-linear compensation</i> .....	33
1.4.5.6. <i>Adaptive control</i> .....	36
1.4.5.7. <i>Robust control</i> .....	37
1.4.5.8. <i>Other control strategies applied in fluid power applications</i> .....	39
1.4.6. Energy efficiency analysis.....	41
1.4.6.1. <i>Energy efficiency of linear actuators</i> .....	41
1.4.6.2. <i>Energy efficiency of rotary actuators</i> .....	42
1.4.6.3. <i>Energy efficiency of control valves</i> .....	43
1.4.6.4. <i>Exergy efficiency of fluid power systems</i> .....	44
CHAPTER II. SYSTEM MODELING.....	48
Fluid Power System Dynamics .....	48
2.1. Modeling of the proportional control valves .....	49
2.1.1. Electromagnetic dynamics .....	50
2.1.2. Mechanical dynamics .....	51
2.1.3. Pneumatic dynamics.....	52
2.2. Modeling of pressure dynamics relative to the cylinder chambers .....	57
2.3. Modeling of force dynamics relative to the cylinder piston.....	61
2.4. Modeling of lengthy tube connecting the control valves and the cylinder.....	64
CHAPTER III. ANALYTIC DEVELOPMENT .....	71
Controller Design .....	71
3.1. Design Specifications .....	72
3.2. Delineation of control strategies.....	75
3.2.1. Design Alternative 1: Simplified representation .....	76
3.2.1.1. <i>Block Diagram Representation: Nonlinear and Linear Models</i> .....	80
3.2.1.2. <i>Further Simplification of the Reduced Model – Root Locus Analysis</i> .....	84
3.2.1.3. <i>Air Compliance – Length of Connective Tubing</i> .....	90
3.2.1.4. <i>Closed-Loop Control Design – P-Control</i> .....	98
3.2.1.5. <i>Response – Pole/Zero Cancellation</i> .....	101
3.2.1.6. <i>Discrete Time Analysis</i> .....	102

3.2.2. Design Alternative 2: State-space model representation.....	103
3.2.2.1. <i>Linearization of the system at an equilibrium point</i> .....	106
3.2.2.2. <i>Internal Stability and Input-Output Stability</i> .....	108
3.2.2.3. <i>Controllability and Observability</i> .....	109
3.2.2.4. <i>Linear Quadratic Regulator (LQR) Design</i> .....	110
3.2.2.5. <i>Tracking Control Design</i> .....	111
3.2.2.6. <i>System Discretization</i> .....	113
3.2.3. Design Alternative 3: Nonlinear Feedback Linearization .....	114
3.2.3.1. <i>Tracking control design</i> .....	117
3.3. Assessment of Design Alternatives .....	119
CHAPTER IV. EXPERIMENTAL METHODS .....	123
Technical Approach .....	123
4.1. Baseline Experimental Setup.....	123
4.2. Methodology .....	125
4.2.1. Data acquisition (DAQ).....	125
4.2.2. Validation of models and control strategies .....	130
4.2.3. Identification of transient profiles .....	133
4.3. Preliminary experimental results.....	136
4.3.1. Control valves.....	137
4.3.2. Connective tubing.....	143
4.3.3. Chambers of the pneumatic cylinder.....	149
4.4. Identification of system parameters and validation.....	154
4.4.1. Boundaries of the dead zone of the valves .....	155
4.4.2. Validation of flow equations .....	163
4.4.3. Dynamic constants – Block Diagrams Models .....	168
4.4.4. Flow and pressure gains .....	174
4.4.5. Discharge coefficients - Proportional control valves .....	180
4.4.6. Friction forces and friction coefficients .....	185
4.4.7. Summary – Parameters, gains and constants.....	189
4.5. Definitive Experimental Setup .....	192

CHAPTER V. SIMULATION RESULTS & PREDICTION .....	193
Simulation and Verification of Models .....	193
5.1. Block-Diagram Models .....	193
5.1.1. Nonlinear and Linear Models: Comparison and Verification of Simulation Responses .....	194
5.1.1.1. <i>Compressibility Models</i> .....	194
5.1.1.2. <i>Alternative Models – Hoses modeled as springs</i> .....	199
5.1.1.3. <i>Comparison of Reduced-linear Compressibility and Spring Models</i> .....	206
5.1.2. Simplified Reduced Models: Converting a Second-Order System into a First-Order System .....	212
5.1.3. P-Control: Finding Control Gains through Root Locus Analysis .....	221
5.1.4. Pole/Zero Cancellation: Attenuating the effect of air compressibility and the length of connective tubing .....	225
5.2. State-Space Models .....	231
5.2.1. Verification of Internal Stability and Input-Output Stability Conditions.....	231
5.2.2. Verification of Controllability and Observability Conditions.....	232
5.2.2.1. <i>Controllability</i> .....	232
5.2.2.2. <i>Observability</i> .....	232
5.2.3. Linear Quadratic Regulator (LQR) Design: Finding the Control Gain Matrix....	234
5.2.4. Tracking Control Design: Simulation Response .....	236
5.2.4.1. <i>Integral control</i> .....	236
5.2.4.2. <i>External reference gain tracking control</i> .....	238
5.2.5. System Discretization: Simulation Response.....	239
CHAPTER VI. EXPERIMENTAL RESULTS .....	242
Hypothesis Validation.....	242
6.1. Characterization of Pneumatic Attenuation in Lengthy Connective Tubing .....	242
6.2. Proportional Control.....	247
6.3. Pole/Zero Cancellation .....	264
6.4. Other Control Approaches.....	271
6.5. Performance and Efficiency Assessment .....	277

6.5.1. Performance.....	277
6.5.2. Efficiency .....	283
CHAPTER VI. CONCLUSIONS AND RECOMMENDATIONS.....	286
Overall Assessment.....	286
7.1. Conclusions .....	286
7.2. Recommendations for Future Work.....	289
BIBLIOGRAPHICAL REFERENCES .....	291

## LIST OF FIGURES

	Page
<b>CHAPTER I</b>	
Figure 1.1. Cost of energy delivery modes.....	3
Figure 1.2. (a) Three-way proportional control valve. (b) Five-way proportional control valve.....	6
Figure 1.3. Steady-flow adiabatic ellipse.....	16
Figure 1.4. Box representation of a dynamic system in terms of its inputs, outputs, and state variables .....	19
Figure 1.5. Block diagram of a closed-loop control system .....	24
Figure 1.6. Block diagram of a PID control scheme.....	25
Figure 1.7. Block diagram of modified PID control scheme .....	27
Figure 1.8. Block diagram of a state-space linear system.....	29
Figure 1.9. Block diagram of state-space feedback control system.....	29
Figure 1.10. Block diagrams for external reference gain tracking control .....	30
Figure 1.11. Block diagrams for integral tracking control.....	30
Figure 1.12. Modification of flow-pressure valve characteristic: (Left) Non-linear characteristic, (Right) Generated near-flat characteristic. ....	34
<b>CHAPTER II</b>	
Figure 2.1. Type SMC VEF 3121 pneumatic proportional valve.....	49
Figure 2.2. Free body diagram for the spool of the valve.....	51
Figure 2.3. Operating positions of the spool in relation to the orifices in the sleeve of the valve.....	54
Figure 2.4. Spool position at the lower boundary for input control.....	55
Figure 2.5. Effective area defined by the coupling between the spool and the sleeve of the valve at position 2 .....	55
Figure 2.6. Maximum effective are for one orifice in the sleeve of the valve.....	56
Figure 2.7. Schematic representation of the pneumatic system.....	58
Figure 2.8. Schematic representation of long pneumatic tube.....	64

### CHAPTER III

Figure 3.1. Step response specifications .....	72
Figure 3.2. Transient response specifications: Tracking control .....	73
Figure 3.3. Schematic Diagram of the Simplified System.....	76
Figure 3.4. Simulink model for the full, nonlinear simplified system.....	80
Figure 3.5. Simulink model for the full, linear simplified system.....	80
Figure 3.6. Simulink model for the reduced linear system.....	81
Figure 3.7. Block reduction steps: Step 1. ....	81
Figure 3.8. Feedback loop reduction.....	82
Figure 3.9. Block reduction steps: Step 2. ....	82
Figure 3.10. Block reduction steps: Step 3. ....	82
Figure 3.11. Normalized step response of a second-order system.....	83
Figure 3.12. Block reduction Step 2 – Feedback effect of the area of the piston.....	85
Figure 3.13. Further simplified reduced model .....	85
Figure 3.14. Further simplified reduced model - Block reduction Steps: Step 1.....	86
Figure 3.15. Further simplified reduced model - Block reduction Steps: Step 2.....	86
Figure 3.16. Simplification of the reduced model - Illustrative block diagrams .....	87
Figure 3.17. Simplification of the reduced model: Step response of illustrative first-order and second-order systems. ( $r_1 = 10$ ).....	87
Figure 3.18. Simplification of the reduced model: Root Locus for illustrative second-order system ( $r_1 = 10$ ). ....	88
Figure 3.19. Root Locus depending on the effective area of the piston .....	89
Figure 3.20. Impedance characterization: Free body diagram for the load of the piston .....	91
Figure 3.21. Impedance characterization: Global representation of the pneumatic system .....	92
Figure 3.22. Impedance characterization: Free-body diagram for the piston and the load .....	92
Figure 3.23. Impedance characterization: Simulink model for the full, nonlinear system.....	93
Figure 3.24. Impedance characterization: Simulink model for the full, linear system.....	94
Figure 3.25. Impedance characterization: Block reduction steps –Step1. ....	94
Figure 3.26. Impedance characterization: Block reduction steps –Step 2. ....	95
Figure 3.27. Impedance characterization: Block reduction steps –Step 3. ....	95
Figure 3.28. Impedance characterization: Block reduction steps –Step 4. ....	96

Figure 3.29. Impedance characterization: Block reduction steps –Resulting block diagram. ....	96
Figure 3.30. Impedance characterization: Block reduction steps –Resulting block diagram if the viscous friction is neglected. ....	96
Figure 3.31. (a) Spring-mass damper system, (b) Free body diagram for the mass. ....	97
Figure 3.32. Simulink model for the reduced closed-loop system .....	99
Figure 3.33. Simulation preliminary results: Closed-loop position response for a step input....	100
Figure 3.34. Structure of the controller by including Response-Pole/Zero Cancellation.....	101
Figure 3.35. Simulink model for the control system including response-pole/zero cancellation .....	101
<b>CHAPTER IV</b>	
Figure 4.1. Baseline Experimental Setup.....	124
Figure 4.2. National Instruments USB-6009 DAQ.....	126
Figure 4.3. MATLAB Data Acquisition graphical interface for data collection with National Instruments DAQ hardware.....	129
Figure 4.4. Dual full-bridge driver connected in half-bridge mode to the proportional valves..	131
Figure 4.5. (a) Arduino Uno Microcontroller Board, (b) MegaMoto ROBOT POWER Driver.....	131
Figure 4.6. Voltage divider circuit.....	134
Figure 4.7. Schematic of secondary experimental setup built to measure the pressure variation in pneumatic connective tubing .....	135
Figure 4.8. (a) Displacement and velocity of the piston in response to an open-loop 100% duty-cycle PWM step input. (b) Pressure at the ports of the valve connected to the cylinder cap end.....	138
Figure 4.9. (a) Displacement and velocity of the piston in response to an open-loop 70% duty-cycle PWM step input. (b) Pressure at the ports of the valve connected to the cylinder cap end.....	138
Figure 4.10. (a) Displacement and velocity of the piston in response to a closed-loop step input. (b) Pressure at the ports of the valve connected to the cylinder cap end. ....	140
Figure 4.11. (a) Displacement and velocity of the piston in response to a closed-loop 1-Hz sinusoidal input. (b) Pressure at the ports of the cylinder cap-end valve.....	141

Figure 4.12. (a) Displacement and velocity of the piston in response to a closed-loop 4.5-Hz sinusoidal input. (b) Pressure at the ports of the cylinder cap-end valve .....	142
Figure 4.13. (a) Displacement of the cylinder piston in response to a ramp input. (b) Pressure at the downstream side of the valve connected to the cylinder cap end. ..	143
Figure 4.14. Theoretical tube pressure wave damping ratio and natural frequency .....	145
Figure 4.15. Theoretical pressure-wave frequency response in pneumatic connective tubing ..	146
Figure 4.16. Three-meter tube pressure responses to: (a) Constant 2.5-Hz frequency sine wave input (b) Sinusoidal input with frequency swept between 0.0 and 2.5 Hz ....	147
Figure 4.17. Transient responses to a closed-loop 2.5-Hz frequency sinusoidal input command according to different tube lengths: (a) Cylinder piston displacement. (b) Tube inlet pressure. (c) Tube outlet pressure.....	148
Figure 4.18. (a) Piston displacement and velocity in response to an open-loop 100% duty-cycle PWM step input. (b) Cylinder chamber pressure (Tube length = 0.55 [m])..	150
Figure 4.19. (a) Piston displacement and velocity in response to an open-loop 70% duty-cycle PWM step input. (b) Cylinder chamber pressure (Tube length = 0.55 [m])..	150
Figure 4.20. (a) Piston displacement and velocity in response to a closed-loop step input. (b) Cylinder chamber pressure (Tube length = 0.55 [m]) .....	151
Figure 4.21. (a) Piston displacement and velocity in response to a closed-loop 1-Hz sinusoidal input. (b) Cylinder chamber pressure (Tube length = 0.55 [m]).....	152
Figure 4.22. (a) Piston displacement and velocity in response to a closed-loop 4.5-Hz sinusoidal input. (b) Cylinder chamber pressure (Tube length = 0.55 [m]).....	152
Figure 4.23. (a) Cylinder piston position in response to a ramp input. (b) Pressure at the cap-end cylinder chamber and valve (Tube length = 0.55 [m]).....	153
Figure 4.24. (a) Displacement of the cylinder piston in response to a ramp input. (b) Pressure at the rod-end cylinder chamber (Tube length = 0.55 [m]).....	154
Figure 4.25. Flow characteristic curves provided by the manufacturer of the proportional valves.....	155
Figure 4.26. Theoretical curves of the valve effective area as a function of analog control command .....	156
Figure 4.27. Control valves: Measurement of spool displacement vs. PWM input .....	157
Figure 4.28. Valve spool displacement as a function of PWM voltage applied.....	157



Figure 4.29. Experimental curves of the valve effective area as a function of analog control command .....	158
Figure 4.30. Schematic of the spool-sleeve coupling at the dead zone of the valve .....	159
Figure 4.31. (a) Fixed cylinder piston position and ramp input applied to the cylinder cap-end valve. (b) Supply pressure, atmospheric pressure, and pressure at the cap-end cylinder chamber and valve (Tube length = 0.55 [m]). .....	160
Figure 4.32. Closer views of figure 4.31b: (a) Interval of time between 40 and 44 seconds. (b) Interval of time between 45 and 47 seconds.....	160
Figure 4.33. (a) Fixed cylinder piston position and ramp inputs applied to the valves. (b) Supply pressure, atmospheric pressure, and pressure at the cap-end cylinder chamber and valve (Tube length = 0.55 [m])......	161
Figure 4.34. Closer views of figure 4.33b: (a) Interval of time between 1.0 and 1.4 seconds. (b) Interval of time between 2.6 and 3.0 seconds.....	162
Figure 4.35. System responses to an open-loop 100% duty-cycle PWM step input: (a) Cylinder piston displacement. (b) Cylinder cap-end pressure. (c) Cylinder rod-end pressure. (d) Cylinder cap-end volumetric flow. (e) Cylinder rod-end volumetric flow. ....	163
Figure 4.36. System responses to an open-loop 100% duty-cycle PWM step input: (a) Cylinder piston displacement. (b) Cylinder cap-end pressure. (c) Cylinder rod-end pressure. (d) Cylinder cap-end mass flow. (e) Cylinder rod-end mass flow. ...	164
Figure 4.37. System responses to a closed-loop 2.5-Hz sinusoidal input: (a) Cylinder piston actual and desired displacement. (b) Cylinder cap-end pressure. (c) Cylinder rod-end pressure. (d) Cylinder cap-end volumetric flow. (e) Cylinder rod-end volumetric flow. ....	165
Figure 4.38. System responses to a closed-loop 2.5-Hz sinusoidal input: (a) Cylinder piston actual and desired displacement. (b) Cylinder cap-end pressure. (c) Cylinder rod-end pressure. (d) Cylinder cap-end mass flow. (e) Cylinder rod-end mass flow.....	166
Figure 4.39. System responses to a closed-loop 2.5-Hz sinusoidal input: (a) Cylinder piston actual and desired displacement. (b) Cylinder cap-end flow and piston velocity. (e) Cylinder rod-end flow and piston velocity. ....	167

Figure 4.40. Simplified reduced model for the pneumatic system. ....	168
Figure 4.41. Simplified reduced model for the pneumatic system. ....	168
Figure 4.42. Transient response of the simplified reduced model for the pneumatic system.....	169
Figure 4.43. Identification of dynamic constants: 100%-PWM Step Response (Extension) .....	170
Figure 4.44. Identification of dynamic constants: 70%-PWM Step Response (Extension) .....	171
Figure 4.45. Identification of dynamic constants: 100%-PWM Step Response (Retraction) ....	172
Figure 4.46. Identification of dynamic constants: C vs. PWM Input.....	173
Figure 4.47. Identification of dynamic constants: C vs. PWM Input.....	174
Figure 4.48. Open-loop Step Response of the pneumatic cylinder to a 100% Duty-cycle PWM Input: (a) Piston displacement and velocity. (b) Pressure in the cylinder chambers.....	175
Figure 4.49. Identification of dynamic constants –Piston velocity vs. PWM Input .....	176
Figure 4.50. Identification of dynamic constants: Volumetric Flow vs. PWM Input .....	177
Figure 4.51. Identification of dynamic constants: Volumetric Flow vs. Differential Pressure of the Cylinder Chambers.....	179
Figure 4.52. Identification of dynamic constants: Volumetric Flow as a function of cylinder chamber differential pressure, and valve effective area .....	180
Figure 4.53. System responses to a closed-loop 2.5-Hz sinusoidal input: (a) Piston actual and desired displacement. (b) Cylinder cap-end valve pressure. (c) Cylinder cap-end chamber and valve volumetric flow (Eq. 4.18). (d) Cylinder cap-end chamber and valve mass flow (Eq. 4.18). ....	182
Figure 4.54. System responses to a closed-loop 2.5-Hz sinusoidal input: (a) Piston actual and desired displacement. (b) Cylinder cap-end valve pressure. (c) Cylinder cap-end chamber and valve volumetric flow (Eq. 4.19). ....	183
Figure 4.55. System responses to a closed-loop 2.5-Hz sinusoidal input: (a) Cylinder piston actual and desired displacement. (b) Cylinder cap-end valve pressure. (c) Cylinder cap-end chamber and valve volumetric flow (Eq. 4.20).....	184
Figure 4.56. System responses to an open-loop 1.0-Hz sinusoidal input: (a) Cylinder piston displacement. (b) Cylinder piston displacement and velocity (7.3 to 7.45 seconds). (c) Cylinder combined friction force (7.3 to 7.45 seconds) .....	187

Figure 4.57. Identification of dynamic friction coefficient and friction force: Combined Friction Force vs. Velocity (Time interval: 7.3 to 7.45 seconds).....	188
Figure 4.58. Definitive Experimental Setup .....	192
<b>CHAPTER V</b>	
Figure 5.1. Compressibility models: (a) Full-Nonlinear model.....	194
Figure 5.2. Compressibility models: (b) Full-Linear Model (c) Reduced-Linear Model.....	195
Figure 5.3. Simulated cylinder position step response of the three compressibility models .....	195
Figure 5.4. Simulated response of the three compressibility models to a step input: Cylinder piston velocity .....	196
Figure 5.5. Simulated response of the three compressibility models to a step input: Cylinder chambers differential pressure.....	196
Figure 5.6. Simulated cylinder position step response of the three compressibility models with and adjusted pressure gain: $G_D = 3.5E-09$ [ $m^5/Ns$ ].....	197
Figure 5.7. Simulated response of the three compressibility models to a step input: Cylinder piston velocity with an adjusted pressure gain ( $G_D = 3.5E-09$ [ $m^5/Ns$ ]).....	198
Figure 5.8. Simulated step response of the three compressibility models: Cylinder chamber differential pressure with an adjusted pressure gain ( $G_D = 3.5E-09$ [ $m^5/Ns$ ]) .....	198
Figure 5.9. Spring models: (a) Full-Nonlinear model, (b) Full-Linear Model .....	199
Figure 5.10. Spring models: (c) Reduced-Linear Model .....	200
Figure 5.11. Estimation of $k_x$ : 70%-PWM cylinder piston experimental step response .....	200
Figure 5.12. Simulated cylinder position step response of the three spring models: $k_x = 50$ [N/m] .....	201
Figure 5.13. Simulated response of the three spring models to a step input: Cylinder piston velocity ( $k_x = 50$ [N/m]) .....	201
Figure 5.14. Simulated response of the three spring models to a step input: Differential pressure in the cylinder chambers ( $k_x = 50$ [N/m]).....	202
Figure 5.15. Simulated cylinder position step response of the three spring models with an adjusted pressure gain: $G_D = 3.5E-09$ [ $m^5/Ns$ ] ( $k_x = 50$ [N/m]) .....	202
Figure 5.16. Simulated step response of the three spring models: Cylinder piston velocity with an adjusted pressure gain ( $G_D = 3.5E-09$ [ $m^5/Ns$ ], $k_x = 50$ [N/m]) .....	203

Figure 5.17. Simulated step response of the three spring models: Chamber differential pressure with an adjusted pressure gain ( $G_D = 3.5E-09$ [m <sup>5</sup> /Ns], $k_x = 50$ [N/m]) ..	204
Figure 5.18. Simulated position step response of the three spring models with an adjusted flow gain and increased spring constant: $G_f = 500$ [m/s], $k_x = 25000$ [N/m] .....	205
Figure 5.19. Simulated cylinder position step response of the compressibility and spring reduced-linear models ( $k_x = 25000$ [N/m], $G_f = 500$ [m/s]) .....	206
Figure 5.20. Simulated step response of the compressibility and spring models: Cylinder piston velocity ( $k_x = 25000$ [N/m], $G_f = 500$ [m/s]) .....	207
Figure 5.21. Simulated step response of the compressibility and spring models: Chamber differential pressure ( $k_x = 25000$ [N/m], $G_f = 500$ [m/s]).....	207
Figure 5.22. Simulated cylinder position step response of the compressibility and spring models with and adjusted effective bulk modulus: $\beta = 4.54E+06$ [Pa].....	208
Figure 5.23. Simulated step response of the compressibility and spring models: Cylinder piston velocity with and adjusted effective bulk modulus: $\beta = 4.54E+06$ [Pa].....	209
Figure 5.24. Simulated step response of the compressibility and spring models: Chamber differential pressure with and adjusted bulk modulus: $\beta = 4.54E+06$ [Pa] .....	209
Figure 5.25. Simulated cylinder position step response of the compressibility and spring reduced-linear models: $A_v = 3.5E-06$ [m <sup>2</sup> ].....	210
Figure 5.26. Simulated cylinder position step response of the compressibility and spring models with and adjusted flow gain ( $A_v = 3.5E-06$ [m <sup>2</sup> ], $G_f = 575$ [m/s]) .....	211
Figure 5.27. Simplification of the reduced models: Reduced-Linear model opposed to the simplified model.....	212
Figure 5.28. Simplification of reduced models: Identification of ignored block.....	212
Figure 5.29. Second-order block and equivalent first-order block step responses: (a) Y-axis scale between 0 and 1. (b) Y-axis scale between 0 and 1000. ....	213
Figure 5.30. Second-Order Transfer Function: Root Locus depending on the effective area of the piston: Increasing values .....	214
Figure 5.31. Second-Order Transfer Function: Root Locus depending on the effective area of the piston: Decreasing values.....	215
Figure 5.32. Ignoring a partial fraction of the second-order transfer function: Second-order block and equivalent first-order block step responses.....	217

Figure 5.33. Ignoring a partial fraction of the second-order transfer function: Second-order block and equivalent first-order block step responses ( $A_{p_{new}} = 0.5 \cdot A_{p_{old}}$ ).....	218
Figure 5.34. Ignoring a partial fraction of the second-order transfer function: Second-order block and equivalent first-order block step responses ( $G_D = 5.7e-08 [m^5/Ns]$ ) .....	219
Figure 5.35. Ignoring a partial fraction of the second-order transfer function: Second-order block and equivalent first-order block step responses (Adjusted values: $k_x = 250000 [N/m]$ ; $G_D = 5.44e-08 [m^5/Ns]$ ; $\beta = 4.54e+07 [Pa]$ ) .....	220
Figure 5.36. P-Control: Simulink model for the closed-loop system. ....	221
Figure 5.37. P-Control: Closed-loop simulation response for a step input and different proportional gains (Adjusted Pressure gain: $G_D = 5.6964e-08 [m^5/Ns]$ ) .....	221
Figure 5.38. P-Control: Simulated closed-loop step response for different proportional gains ( $k_x = 250000 [N/m]$ ; $G_D = 5.44e-08 [m^5/Ns]$ ; $\beta = 4.54e+07 [Pa]$ ) .....	222
Figure 5.39. P-Control: Simulated step response ( $K_P = 0.0001$ ): (a) $k_x = 25000 [N/m]$ , (b) $k_x = 250000 [N/m]$ .....	223
Figure 5.40. P-Control: Root locus for the reduced-linear model ( $G_D = 5.7e-08 [m^5/Ns]$ ).....	224
Figure 5.41. P-Control: Root locus for simplified reduced model ( $G_D = 5.7e-08 [m^5/Ns]$ ).....	224
Figure 5.42. Pole/Zero Cancellation: Reduced Simulink model .....	225
Figure 5.43. Pole/Zero Cancellation: Closed-loop simulation response to a step input.....	226
Figure 5.44. Pole/Zero Cancellation: Simulated step response (Adjusted values: $k_x = 250000 [N/m]$ , $G_D = 5.44e-08 [m^5/Ns]$ , $\beta = 4.54e+07 [Pa]$ ).....	227
Figure 5.45. Pole/Zero Cancellation: Air compliance associated with the canceled dynamics in the compressibility (a) and spring (b) models.....	228
Figure 5.46. Root Locus depending on the length of connective tubing .....	229
Figure 5.47. Continuous-time simulation: Open-loop step response.....	235
Figure 5.48. Continuous-time simulation: Closed-loop step response with LQR control law implemented .....	235
Figure 5.49. Continuous-time simulation: Step response with Integral control law implemented .....	237
Figure 5.50. Continuous-time simulation: Step response according to External reference gain tracking control scheme.....	238

Figure 5.51. Discrete-time simulation: Closed-loop step response with LQR control law implemented .....	239
Figure 5.52. Discrete-time simulation: Step response with Integral control law implemented..	240
Figure 5.53. Discrete-time simulation: Step response according to External reference gain tracking control scheme.....	241
<b>CHAPTER VI</b>	
Figure 6.1. Responses to a 3.0-Hz sinusoidal command input to the valves: (a) 31.5-meter tube upstream and downstream pressure. (b) Closer view of upper subplot a.....	243
Figure 6.2. Frequency response of pressure variation in 30.5-meter tubing.....	245
Figure 6.3. Frequency response of pressure variation in 30.5-meter tubing when the parameters of the theoretical model were adjusted .....	246
Figure 6.4. Block-diagram representation of the pneumatic system including a block accounting for pressure distortion in lengthy connective tubing .....	247
Figure 6.5. Block-diagrams: (a) Simulink model, (b) Schematic for actual implementation.....	248
Figure 6.6. Block-diagrams: Continuous-time Blocks vs. Discrete-Time Blocks.....	248
Figure 6.7. Operation of proportional control valves .....	249
Figure 6.8. Comparison of simulation and experimental results: Open-loop step response to a 75% duty-cycle PWM input (Length of connective tubing: 0.55 m) .....	252
Figure 6.9. Comparison of simulation and experimental results: Open-loop step response to a 88% duty-cycle PWM input (Length of connective tubing: 1.5 m) .....	252
Figure 6.10. Comparison of simulation and experimental results: Open-loop step response to a 94% duty-cycle PWM input (Length of connective tubing: 3.0 m) .....	253
Figure 6.11. Simplified reduced model for the pneumatic system .....	253
Figure 6.12. Open-loop guess: Root locus for system with 0.55-meter connective tubing.....	255
Figure 6.13. Open-loop guess: Root locus for system with 1.5-meter connective tubing.....	256
Figure 6.14. Open-loop guess: Root locus for system with 3.0-meter connective tubing.....	256
Figure 6.15. P-Control: Experimental step responses (Length of connective tubing: 0.55 m)...	257
Figure 6.16. P-Control: Experimental step responses (Length of connective tubing: 1.5 m).....	257
Figure 6.17. P-Control: Experimental step responses (Length of connective tubing: 3.0 m).....	258
Figure 6.18. Comparison of simulation and experimental step responses applying P-control: (a) $K_p = 0.5$ , (b) $K_p = 1.0$ , (c) $K_p = 2.5$ (Length of connective tubing: 0.55 m).....	260

Figure 6.19. Comparison of simulation and experimental step responses applying P-control: (a) $K_p = 0.5$ , (b) $K_p = 1.0$ , (c) $K_p = 2.0$ (Length of connective tubing: 1.5 m).....	260
Figure 6.20. Comparison of simulation and experimental step responses applying P-control: (a) $K_p = 0.5$ , (b) $K_p = 1.0$ , (c) $K_p = 1.5$ (Length of connective tubing: 3.0 m).....	261
Figure 6.21. Simulation and experimental responses to a sinusoidal input (light blue line) with P-control ( $K_p = 0.5$ ): (a) $f = 0.5$ Hz, (b) $f = 1.0$ Hz, (c) $f = 2.5$ Hz (Tube length: 0.55 m) .....	262
Figure 6.22. Simulation and experimental responses to a sinusoidal input (light blue line) with P-control ( $K_p = 0.5$ ): (a) $f = 0.5$ Hz, (b) $f = 1.0$ Hz, (c) $f = 2.5$ Hz (Tube length: 1.5 m) .....	262
Figure 6.23. Simulation and experimental responses to a sinusoidal input (light blue line) with P-control ( $K_p = 0.5$ ): (a) $f = 0.5$ Hz, (b) $f = 1.0$ Hz, (c) $f = 2.5$ Hz (Tube length: 3.0 m) .....	263
Figure 6.24. Pole/Zero Cancellation: Schematic for control implementation .....	264
Figure 6.25. Closed-loop guess: Root locus for system with 0.55-meter connective tubing .....	265
Figure 6.26. Closed-loop guess: Root locus for system with 1.5-meter connective tubing .....	266
Figure 6.27. Closed-loop guess: Root locus for system with 3.0-meter connective tubing .....	266
Figure 6.28. Comparison of experimental step responses applying P-control and Pole/Zero Cancellation: (a) $K_p = 0.3$ , (b) $K_p = 0.5$ , (c) $K_p = 1.0$ (Tube length: 0.55 m) .....	267
Figure 6.29. Comparison of experimental step responses applying P-control and Pole/Zero Cancellation: (a) $K_p = 0.25$ , (b) $K_p = 0.5$ , (c) $K_p = 1.0$ (Tube length: 1.5 m) .....	268
Figure 6.30. Comparison of experimental step responses applying P-control and Pole/Zero Cancellation: (a) $K_p = 0.3$ , (b) $K_p = 0.5$ , (c) $K_p = 1.0$ (Tube length: 3.0 m) .....	268
Figure 6.31. Experimental responses to a sinusoidal input (light blue line) with P-control and PZC ( $K_p = 0.5$ ): (a) 0.5 Hz, (b) 1.0 Hz, (c) 2.5 Hz (Tube length: 0.55 m).....	269
Figure 6.32. Experimental responses to a sinusoidal input (light blue line) with P-control and PZC ( $K_p = 0.5$ ): (a) 0.5 Hz, (b) 1.0 Hz, (c) 2.5 Hz (Tube length: 1.5 m).....	270
Figure 6.33. Experimental responses to a sinusoidal input (light blue line) with P-control and PZC ( $K_p = 0.5$ ): (a) 0.5 Hz, (b) 1.0 Hz, (c) 2.5 Hz (Tube length: 3.0 m).....	270
Figure 6.34. Alternative Approach 1: Proportional plus Derivative (PD) Control.....	272

Figure 6.35. Alternative Approach 2: Pole/Zero Cancellation plus Derivative (PZCD) Control.....	272
Figure 6.36. Actual responses to a sinusoidal input (light blue line) for P-control, PZC, PD-control and PZCD ( $K_p = 0.5$ , $K_d = 15.0$ ): (a) 0.5 Hz, (b) 1.0 Hz, (c) 2.5 Hz (Tube length: 0.55 m).....	273
Figure 6.37. Actual responses to a sinusoidal input (light blue line) for P-control, PZC, PD-control and PZCD ( $K_p = 0.5$ , $K_d = 15.0$ ): (a) 0.5 Hz, (b) 1.0 Hz, (c) 2.5 Hz (Tube length: 1.5 m).....	274
Figure 6.38. Actual responses to a sinusoidal input (light blue line) for P-control, PZC, PD-control and PZCD ( $K_p = 0.5$ , $K_d = 15.0$ ): (a) 0.5 Hz, (b) 1.0 Hz, (c) 2.5 Hz (Tube length: 3.0 m).....	274
Figure 6.39. Actual responses to a sinusoidal input (light blue line) for P-control, PZC, PD-control and PZCD ( $K_p = 1.0$ , $K_d = 25.0$ ): (a) 0.5 Hz, (b) 1.0 Hz, (c) 2.5 Hz (Tube length: 0.55 m).....	275
Figure 6.40. Actual responses to a sinusoidal input (light blue line) for P-control, PZC, PD-control and PZCD ( $K_p = 1.0$ , $K_d = 25.0$ ): (a) 0.5 Hz, (b) 1.0 Hz, (c) 2.5 Hz (Tube length: 1.5 m).....	276
Figure 6.41. Actual responses to a sinusoidal input (light blue line) for P-control, PZC, PD-control and PZCD ( $K_p = 1.0$ , $K_d = 25.0$ ): (a) 0.5 Hz, (b) 1.0 Hz, (c) 2.5 Hz (Tube length: 3.0 m).....	276
Figure 6.42. Performance Assessment: Tracking Error in sinusoidal responses.....	282
Figure 6.43. Overall Efficiency Assessment: Sinusoidal response.....	285



## LIST OF TABLES

	Page
<b>CHAPTER I</b>	
Table 1.1: Equations derived from the first and second law of thermodynamics.....	9
Table 1.2: Ideal thermodynamic processes applied to the modeling of pneumatic systems .....	10
Table 1.3: Equations derived from Fluid Mechanics.....	11
Table 1.4: Distributed parameter models – Fluid transmission lines.....	13
Table 1.5: Speed of sound.....	15
Table 1.6: Classification of dynamic systems.....	19
Table 1.7: Advantages and disadvantages of closed-loop and open-loop control systems. ....	24
Table 1.8: Effects of the proportional, integral, and derivative terms in a PID controller. ....	26
<b>CHAPTER III</b>	
Table 3.1: Controller Design Specifications.....	74
Table 3.2. Specific weight of the assessment criteria .....	120
Table 3.3. Specific weight of the alternatives according to the complexity criterion .....	120
Table 3.4. Specific weight of the alternatives according to the robustness criterion.....	121
Table 3.5. Specific weight of the alternatives according to the efficiency criterion .....	121
Table 3.6. Specific weight of the alternatives according to the accuracy criterion .....	121
Table 3.7. Specific weight of the alternatives according to the cost criterion .....	121
Table 3.8. Alternative assessment results .....	122
<b>CHAPTER IV</b>	
Table 4.1. Technical Specifications of the National Instruments USB-6009 DAQ .....	127
Table 4.2. Technical Specifications of the Arduino UNO Microcontroller Board.....	128
Table 4.3. Specifications of the Midori LP-300FJS linear transducer.....	130
Table 4.4. Specifications of the ROBOT POWER MegaMoto Dual full-bridge driver.....	132
Table 4.5. Specifications of the SMC VEF 3121 Flow Proportional control valves.....	132
Table 4.6. Specifications of the Danfoss AKS32 - 060G1889 pressure transducers.....	133
Table 4.7. Specifications of connective tubing tested.....	134
Table 4.8. Parameters to calculate the pressure-wave damping ratio and natural frequency .....	144
Table 4.9. Theoretical pressure-wave break frequencies as a function of tube length .....	146

Table 4.10. Boundaries of the dead zone of the valve .....	162
Table 4.11. Finding from the fitting procedure to find $C$ and $\tau$ .....	171
Table 4.12. Findings from the fitting procedure to find $G_f$ .....	178
Table 4.13. Findings from the fitting procedure to find $G_D$ .....	178
Table 4.14. Static Friction Force - Pressure in the chambers of the cylinder .....	186
Table 4.15. Dynamic Friction Coefficient and Friction Force.....	189
Table 4.16. Summary – Physical parameters: Pneumatic cylinder and connective tubing .....	189
Table 4.17. Summary – Physical parameters: Air Properties .....	190
Table 4.18. Summary – Physical parameters: Proportional Control Valves .....	190
Table 4.19. Summary – Friction Forces and Friction Coefficients.....	191
Table 4.20. Summary – Dynamic Constants and Gains .....	191

## CHAPTER V

Table 5.1. Simulation parameters: Compressibility Models (CM) and Spring Models (SM)....	211
Table 5.2. Simulation parameters: Prediction of the effect of the length of connective tubing .	230

## CHAPTER VI

Table 6.1. Threshold input values for control.....	250
Table 6.2. Summary – Simulation parameters: Compressibility (CM) and Spring Models (SM) – Open-Loop Control Scheme .....	251
Table 6.3. Summary – Normalized dynamic constants – Open-Loop Control Scheme .....	254
Table 6.4. Summary – Simulation parameters: Compressibility (CM) and Spring Models (SM) – Closed-Loop Control Scheme.....	259
Table 6.5. Pole/Zero Cancellation – Natural frequency and damping ratio values .....	267
Table 6.6. Performance Assessment: Step response – Length of connective tubing: 0.55 m ....	278
Table 6.7. Performance Assessment: Step response – Length of connective tubing: 1.5 m .....	278
Table 6.8. Performance Assessment: Step response – Length of connective tubing: 3.0 m .....	278
Table 6.9. Performance Assessment: Sinusoidal response – Tube length: 0.55 m.....	279
Table 6.10. Performance Assessment: Sinusoidal response – Tube length: 1.5 m.....	280
Table 6.11. Performance Assessment: Sinusoidal response – Tube length: 3.0 m.....	280

## ACKNOWLEDGMENTS

Always first, I thank God Almighty for the gift of life, the health, and the physical and intellectual capacity that He has granted me, and for having added to all the previously mentioned the strength and will force that enabled me to successfully complete this thesis.

I thank my parents for their love and unconditional support, for their daily effort to provide me with an integral education led by precepts of justice, honesty, and generosity.

I thank my brother, for being my friend and partner, for teaching me courage, determination and persistence to face the challenges of life.

I thank the Fulbright Commission for their support and the great opportunity to pursue a Master's degree at Iowa State University.

I thank Dr. Greg Luecke for letting me to join his research group, for all the knowledge transmitted, and for his support, advice and guidance throughout the course of this research.

I thank Dr. Brian Steward for his support, advice and guidance throughout the course of this research, for accepting to collaborate with Dr. Luecke and me in the development of this project, and for permitting me to develop my research using the equipment and installations of the Danfoss Fluid Power Lab and the Mechatronics Lab in the Agricultural and Biosystems Engineering Department at Iowa State University.

I thank Dr. Sourabh Bhattachraya for accepting to be part of my committee, and for reviewing my thesis.

I thank Danfoss Power Solutions and Wyatt Hall for providing the pressure transducers used for experimentation in this project.

I thank all my professors at Iowa State University, for the knowledge transmitted, and for their effort and commitment to prepare better professionals and human beings.

Lastly, I thank my friends, colleagues, and the university staff for making my time at Iowa State University a wonderful experience.

## ABSTRACT

Low energy efficiency is one of the main detractors of fluid power technology. To ensure the availability and sustainability of energy sources, fluid power technology needs to meet high energy-efficiency and cost standards. This study aims to design, simulate and test a control algorithm that attenuates the detrimental effects of air compressibility on the performance and efficiency of a pneumatic cylinder.

The transmission of power over long distances makes it more difficult for fluid power technology to meet energy-efficiency and cost requirements. Transmitting power over long distances represents a challenge particularly for pneumatics due to the compressibility of air. The compressibility of air transmitted through lengthy tubing decreases the performance and efficiency of pneumatic actuators, mainly affecting their time response and velocity.

The system under analysis was composed of a pneumatic cylinder, two proportional control valves, and connective tubing. The dynamics of the individual components were characterized through experimentation. Nonlinear and linear models for the system were validated through the comparison of simulated and experimental data. The models predicted the system behavior more accurately at 2.5 Hz, when friction effects became negligible, as compared to 1.0 and 0.5 Hz.

A controller was designed using pole/zero cancellation, a control strategy able to mask undesirable dynamics of the system being controlled. Pole/zero cancellation had superior performance in the attenuation of air compressibility effects in comparison to proportional and proportional-derivative (PD) control. System performance and efficiency were assessed in terms of the variation of the length of tubing connecting the pneumatic cylinder and the control valves.

Pole/zero cancellation enabled the cylinder to achieve similar levels of performance for long (3.0 m) tubing as with short (0.55 m) tubing. With a 1.0-Hz sinusoidal input and equal control gains, pole/zero cancellation reduced the tracking error by approximately 30% and 23% in comparison to proportional and PD control, respectively. In terms of efficiency, with the system tracking a 2.5-Hz sinusoidal command, and using equal control gains, pole/zero cancellation increased the cylinder efficiency by approximately 36% and 54% in comparison to proportional and PD control, respectively. In general, pole/zero cancellation increased the system performance and efficiency in comparison to the other control schemes applied.

# CHAPTER I

## INTRODUCTION

### **System Dynamics and Control in Fluid Power Engineering**

Many questions regarding the future of fluid power have arisen as result of social, economic, and political events related to the availability and sustainability of energy around the world. The most recent event to highlight is the so-called energy crisis of 2008, when the price of oil reached an astonishing cost of \$145.16 dollars per barrel ([U.S. Energy Information Administration, 2015](#)). At that time, many countries, including the United States, seriously questioned their energy policies and have sought to find a solution to the problems that their heavy dependency on fossil fuels had caused. The increasing reliance on fossil fuels, and the exacerbation of global warming effects are among the problems that have led to the emergence of clean-energy policies and energy reforms.

In that regard, much of the efforts to achieve energy independence from oil focused on the production of bio-renewable fuels to replace fossil fuels. Nevertheless, other potentially clean and efficient technologies, such as fluid power, regained attention as alternatives to transform the energy scenario in the world, by improving efficiency as an approach to conservation. Therefore, the main question lately posed regarding the future of fluid power has been: Is fluid power able to meet energy-efficiency and cost requirements to become a strong and competitive participant in the efforts to meet the growing global demand for energy?

The answer to this question depends on how fluid power competes with other power transmission and control technologies, such as electrical technologies. Advantages of fluid power systems, such as their high power, torque, and force densities are commonly emphasized in the literature, but disadvantages such as their low efficiency, imprecision, and high cost are also their main detractors. Accordingly, innovation in fluid power engineering is essential to overcoming the challenges that the global energy scenario poses. Accurate modeling and efficient control of fluid power systems are essential to achieving the required competitive advantage for fluid power systems.

Modeling and simulation techniques should enable the application of more sophisticated and robust control strategies. Moreover, the investigation of different control strategies should assist in the formulation of energy-saving control algorithms.

This thesis focuses on applying system dynamics and control theory to model and control a pneumatic system. The motivation and the objectives of this project are described in this chapter. In addition, the problem statement, and review of fundamental theory and research literature associated with the control of fluid power systems are also included in this section. The chapters that follow focus on the modeling, simulation, and design of a controller for the pneumatic system studied. At the end of this thesis, the results should demonstrate how pneumatic system performance improves with the application of specific control strategies.

## 1.1. Motivation

Uncertainty in fuel prices, detrimental effects of burning fossil fuels for the generation of energy, and increasing energy needs around the world have motivated research into alternative energy technologies. In this regard, the use of pressurized fluids for the transmission of power has emerged as a viable alternative for the replacement of nonrenewable energy transmission technologies. Fluid power is the technology of the application, control, and transmission of power using pressurized fluid. It is an important technology used in industry. Characteristic advantages are: high power density, small actuators dimensions, good time response, high torque at low speed, ability to transmit power over long distances or to inconvenient locations, and generation of constant force or torque (Backé, 1993; NFPA, 2014).

Nevertheless, the efficiency associated with fluid power systems is still a disadvantage in comparison to other means of power transmission. Losses in operation and control circuits lead to high-energy consumption by fluid power systems (Backé, 1993). Indeed, in relation to pneumatics, the sub-division of fluid power when the pressurized fluid is a gas (hydraulics uses a liquid as the pressurized fluid), studies demonstrate that up to 30% of the compressed air generated in a typical 1,000-CFM installation is wasted, generating a \$20,000 annual loss and an annual \$65,000 spent in electricity (Norgren, 2014).

Moreover, compressed air for the transmission of power could account for 70% to 90% of the total cost of electricity in common installations, placing itself as the most costly energy delivery mode in comparison to natural gas, steam and electricity (Saidur et al., 2010). For these reasons, the requirement to apply fluid power efficiently makes indispensable the identification and handling of circuit losses and the implementation of control strategies that permit fluid power systems to achieve higher levels of efficiency. Therefore, this thesis attempts to enhance the efficiency of pneumatic systems through the identification of losses related to the compressibility of air and the length of connective tubing, and by designing a control algorithm to mask the attenuation in performance of pneumatic cylinders due to the identified losses.

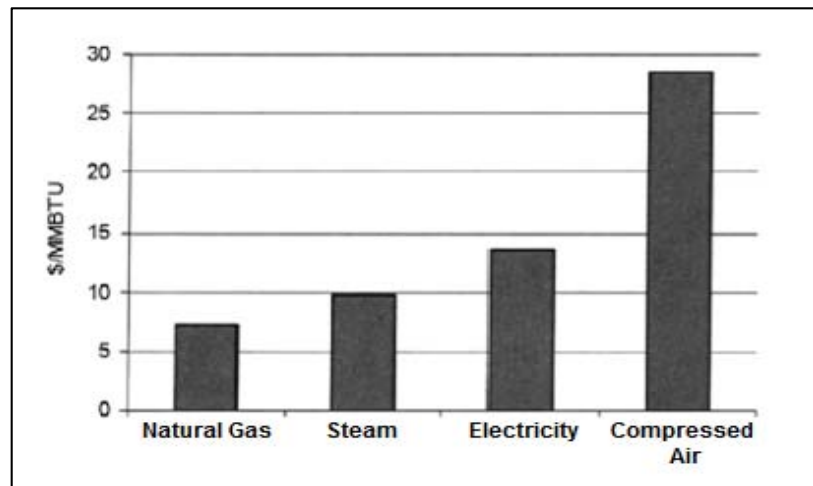


**Figure 1.1.** Cost of energy delivery modes [Source: Saidur et al., 2010]

## 1.2. Objectives

The development and completion of this thesis centers on the fulfillment of a general objective comprising the main motivation of this study. In addition, several specific objectives define the intent of the different sections in which this thesis is divided.

### 1.2.1. General objective

To investigate control algorithms that mask the distortion in performance of pneumatic cylinder motion control associated with the compressibility of air and the length of connective tubing.

### 1.2.2. Specific Objectives

- Characterize and simulate the transient response of elements composing a pneumatic system, such as, linear actuators, control valves, and connective tubing.
- Develop an experimental platform for identification of dynamic parameters associated with the compressibility of air and its effect on pneumatic systems.
- Investigate the effects of pneumatic tubing length on the control of pneumatic cylinder position using proportional flow control valves.
- Study the non-linear dynamics of a pneumatic system composed by proportional control valves, a linear actuator, and connective tubing.
- Assess control strategies for pneumatic cylinder position control with cancellation of air compressibility and connective tubing length effects.
- Measure the controller performance positioning pneumatic cylinders efficiently.
- Evaluate and validate control algorithms, from the comparison of experimental and simulated data, and the quantification of energy efficiency performance.

### 1.3. **Statement of Problem**

Although hydraulics and pneumatics share most of the advantages attributed to the application of fluid power in industry, pneumatics offers an additional benefit that hydraulics or electromechanical drives cannot provide. Pneumatics actuators can provide a gentle handling of materials due to their compliance and the cushioning effect inherent to compressed air. This ability of pneumatic actuators makes them suitable for applications that require controlled pressing or squeezing (NFPA, 2014), such as robotics. In fact, recent research focused on the development of mobile robotic applications has demonstrated a preference for pneumatics due to its larger power output, lighter weight, and lower cost in comparison to electric actuators (Granosik and Borenstein, 2004). Besides, many applications of pneumatics in robotics seek to resemble the performance of human muscles for actuation; nonetheless, the accuracy for control of pneumatic actuators depends on the appropriate treatment of the non-linear response attributed to the compressibility of air (Pearce, 2005).



Indeed, the high compressibility of air undermines one of the most important advantages of pneumatic systems, the ability to transmit power over long distances. Accordingly, the overall performance of pneumatic actuators might be reduced as the length of connective tubing increases. In particular, the accuracy for positioning and control could be affected the most. Special interest was given to the characterization of the effects of pneumatic tubing in the 1990's, as advances in aircraft control required the use of air pressure as a flight control feedback signal. Aircraft use air pressure sensors to collect unsteady pressure data, and the data collected needs to be of the highest fidelity and accuracy. For that reason, research was conducted to investigate the effects of high-frequency distortion in remotely located pneumatic pressure measurement systems (Whitmore et al., 1990). Furthermore, losses associated with the length of pneumatic tubing connecting linear actuators and directional control valves were identified in the literature; including pressure drops that decrease the steady-state air flow, and flow profile delays due to the acoustic wave diffusion along the tube (Richer and Hurmuzlu, 2000).

To account for the lower pneumatic actuation efficiency due to losses in lengthy air hoses, it is necessary to consider the dynamic behavior associated with the compressibility of air. In this regard, the bulk modulus, as the factor characterizing the compressibility of fluids, could be used as a reference parameter for the determination of the control gains necessary to achieve maximum system efficiency. Research should be conducted to identify the effects of air compressibility in relation to the length of pneumatic connective tubing. The results obtained will assist in the development of control algorithms that permit pneumatic cylinders to be positioned accurately with the minimum use of energy.

Additionally, the modeling of pneumatic control valves is crucial for the development of control algorithms aiming to produce accurate actuator positioning and minimum energy use. For this project, two three-way proportional solenoid valves were used to control the extension and retraction of a pneumatic cylinder. The valves used in this research (VEF 3121, SMC, Japan) have been already characterized in a previous study (Sorli et al., 2010). They focused on the modeling and experimental validation of this type of valves, with special emphasis on the study of the electrical behavior of the solenoid. The use of this type of valve might be justified by their relative low price and robust design; nonetheless, their use for the current study should demonstrate the validation of a new model for the valve and/or a novel control strategy.

In that regard, energy-saving control approaches have been applied to demonstrate the advantages of using two three-way valves instead of a single five-way valve for the control of pneumatic servo systems (Al-Dakkan et al., 2003). Likewise, other approaches compare the energy efficiency of the system in terms of the results obtained from linear and non-linear valve models (Ke et al., 2005). Thus, similar energy-based assessment methods could be developed in this project; for example, by comparing the accuracy for positioning and energy efficiency obtained from a new valve model and the models found in the literature.

Conversely, another alternative was to use and characterize a five-way proportional valve (e.g. LS-V15s, ENFIELD, USA). Although there is no reference to this valve in recent research publications, there exist numerous publications focused on the modeling and feedback control of similar valves. As described in the literature, the main advantages for the use and control of five-way proportional valves include: their quasi-linear flow characteristic, and their ability to control up-stream and backpressure with a single control signal (Richer and Hurmuzlu, 2000). Nevertheless, independently of the type of valve used, the design of the control algorithm for this thesis will depend on the modeling of the proportional valve selected.

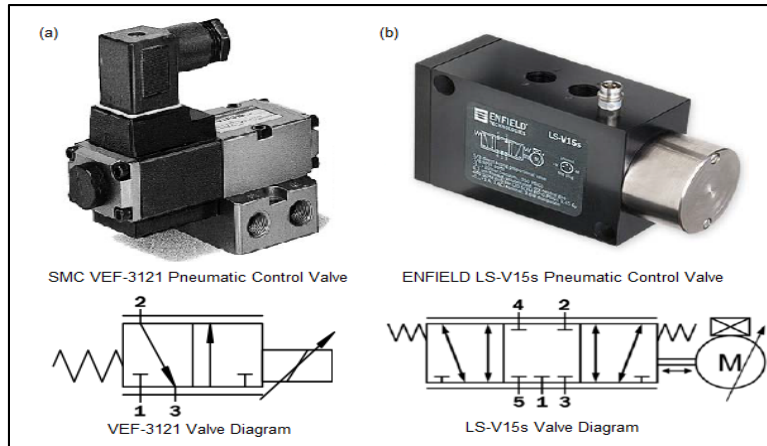


**Figure 1.2.** (a) Three-way proportional control valve. (b) Five-way proportional control valve

Furthermore, the control algorithm to be developed should minimize the error between the reference and actual position. Studies for minimizing specific control effects related to pneumatic proportional valves are common in the literature. To illustrate, models for minimizing the effect of hysteresis (Hamdan and Zhiqiang, 2000) seek to improve the response of pneumatic actuators to control inputs and provide greater bandwidth than conventional methods.

Likewise, other models seek to minimize the air consumption of pneumatic actuators to make them suitable for mobile robot applications ([Granosik and Borenstein, 2004](#)). For this project, in addition to minimizing the cylinder positioning error, the controller should minimize the effects of air compressibility on the system performance, by replicating conditions where the proportional valves are remotely located and the tube is longer than in normal applications.

By tracking the effects of air compressibility, it should be determined if further energy is required to achieve positioning accuracy when the connective tubing length increases. Increasing energy for positioning tracking should be measured by comparing air consumption depending on connective tubing length. Similarly, exergetic efficiency is another indicator commonly applied for the assessment of energy consumption in pneumatic systems ([Harris et al., 2013](#); [Petrilean et al., 2009](#)). The exergy of a system is defined as the maximum amount of theoretical work that could be obtained from a transformation that brings the system into equilibrium with a reference state ([Moran and Shapiro, 2008](#)).

The control strategy to be applied should define a unique control law to optimize the performance of the system. Optimal control strategies have been applied as part of energy efficiency analysis of pneumatic cylinders; nonetheless, the effect of air compressibility has not been associated with efforts to maximize efficiency. Hence, the control strategy applied could assess energy efficiency in relation to air compressibility as the performance criterion.

Ultimately, the efficiency increases in fluid power technology will depend on the identification and handling of parameters that usually restrict fluid power applications. In the case of pneumatics, air compressibility impedes further development of cost-effective technology for the replacement of nonrenewable energy technology. In fact, pressure drops at end-use points could account for up to 40% of the air pressure discharged by a compressor ([Saidur et al., 2010](#)); a fact that represents the high energy use in pneumatic systems.

Air compressibility jeopardizes the performance of pneumatic actuators, air sensors, and/or control valves interconnected through lengthy connective tubing. The impact of air compressibility on technology that transmits power or feedback information over long distances depends on the control strategies applied to overcome potential energy losses. To demonstrate the capability of pneumatics for power transmission and high-tech applications, such as robotics, this project seeks to overcome the negative effects of air compressibility on the consumption of energy and the positioning control accuracy of pneumatic cylinders.

## 1.4. Background / Literature Review

The following section provides a review of the fundamental theory and research literature associated with the modeling and control of fluid power systems. This section emphasizes topics related to the control of pneumatic systems. Some equations derived from the fundamental laws of thermodynamics and fluid mechanics are identified. A review of common assumptions and models applied to connective tubing in fluid power system is also included. Likewise, the basic concepts of system dynamics and control theory are highlighted. A review of control strategies applied to the control of fluid power systems complements the subsection covering control theory. Relevant research publications associated with the control of fluid power systems are also identified in this subsection. Finally, section 1.4 closes with an identification of different approaches for the measurement and quantification of efficiency in fluid power systems.

### 1.4.1. Foundations of Thermodynamics

Two fundamental thermodynamic principles are applied to study the compression and expansion of compressible fluids, such as air, in fluid power systems. The thermodynamic laws or principles that govern the behavior of compressible fluids in fluid power systems are:

- (i) The first law of thermodynamics, which states that energy is neither created nor destroyed, but it can be converted from one form to another.
- (ii) The second law of thermodynamics, which states that entropy of an isolated system always increases or remain constant over time.
- (iii) The law of conservation of energy, which is derived from the first and second laws of thermodynamics, and states that the total amount of energy of a system isolated from its surroundings remains constant.

In addition, four ideal thermodynamic processes can be used to describe the compression and expansion of air in a pneumatic cylinder. These ideal approximations derive from the application of the laws of thermodynamics to describe the variation of pressure, temperature, and volume in relation to the energy required to operate a particular system.

Table 1.1 summarizes the fundamental relationships derived from the first and second laws of thermodynamics applied to the analysis of compressible fluids.

**Table 1.1:** Equations derived from the first and second law of thermodynamics

Fundamental principle	Variants	Equations
First Law of Thermodynamics	Conservation of energy	$\delta Q - \delta W = dE$
		$\dot{Q} - \dot{W} = \frac{dE}{dt}\bigg _{system}$
	Total energy of a system	$E_{system} = \int_{m(system)} e dm = \int_{V(system)} e \rho dV$
		$e = u + \frac{v^2}{2} + gz$
Second Law of Thermodynamics	Change in entropy	$dS \geq \frac{\delta Q}{T}$
		$\frac{dS}{dt}\bigg _{system} \geq \frac{1}{T} \dot{Q}$
	Total entropy of a system	$E_{system} = \int_{m(system)} s dm = \int_{V(system)} s \rho dV$

[Source: Moran and Shapiro, 2010]

The nomenclature for the equations in Table 1.1 is:

$\rho$ = Density	$E, e$ = Energy, energy per unit of mass
$g$ = Acceleration of gravity	$Q, \dot{Q}$ = Heat transfer, heat transfer rate
$m$ = Mass	$S, s$ = Entropy, entropy per unit of mass
$t$ = Time	$U, u$ = Internal energy, internal energy per unit of mass
$T$ = Temperature	$V, v$ = Volume, volume per unit of mass
$\mathcal{V}$ = Velocity	$W, \dot{W}$ = Work, rate of work or power
$z$ = Elevation, position	

In the case of pneumatic systems, for the validation and assessment of simulation models, the ideal thermodynamic processes applied include:

- (i) Isochoric processes – Processes at constant volume.
- (ii) Isobaric processes – Processes at constant pressure.
- (iii) Isothermal processes – Processes at constant temperature.
- (iv) Isentropic processes – Reversible adiabatic processes, in which there is no heat transference between a system and its surroundings.

These four models describe the relation between temperature, pressure, and volume for an ideal gas under specific conditions. Air treated as an ideal gas obeys the equation of state, or gas law, given by:

$$PV = mRT \quad (1.1)$$

Where P is pressure, and R is the specific gas constant.

Considering the relationship between mass and volume in terms of the density ( $\rho$ ) of the gas, the gas law can also be expressed by:

$$P = \rho RT \quad (1.2)$$

Where:

$$\rho = m/V \quad (1.3)$$

Table 1.2 summarizes the main relationships for pressure, temperature and volume of an ideal gas according to the ideal thermodynamic process assumed.

**Table 1.2:** Ideal thermodynamic processes applied to the modeling of pneumatic systems

<b>Ideal Thermodynamic Process</b>	<b>Constant Property</b>	<b>Fundamental equation/relation</b>
Isochoric process	Volume	$\frac{P_1}{T_1} = \frac{P_2}{T_2} = \text{Constant}$
Isobaric process	Pressure	$\frac{T_1}{V_1} = \frac{T_2}{V_2} = \text{Constant}$
Isothermal process	Temperature	$P_1V_1 = P_2V_2 = \text{Constant}$
Isentropic process	Entropy	$P_1V_1^k = P_2V_2^k = \text{Constant}$

Nomenclature:  $k$  = Specific heat ratio

[Source: [Moran and Shapiro, 2010](#)]

The thermodynamic processes described above account for the variation of pressure, temperature and volume in closed systems. Nevertheless, the operation of most fluid power components is based on the transference of mass across their boundaries. Accordingly, to account for the transference of mass in pneumatic systems, the following section provides some fundamental relationships to model the mass flow rate of air in fluid power systems.

### 1.4.2. Foundations of Fluid Mechanics

Similar to the application of thermodynamics, fluid mechanics principles are essential to characterizing the behavior of compressible fluids in fluid power systems. To fully describe the dynamics of compressible fluids, two fundamental physical laws must be applied:

- (i) The law of conservation of mass, from which the continuity equation derives, and which states that in matter undergoing physical or chemical changes, the total mass remains always the same.
- (ii) The law of conservation of momentum, derived from the Newton's second law of motion, and mathematically described by the Navier-Stokes equations, indicates that the total momentum of a system is conserved if external forces do not affect the system.

Table 1.3 summarizes the fundamental relationships resulting from the continuity equation and the momentum conservation law applied to the analysis of compressible fluids.

**Table 1.3:** Equations derived from Fluid Mechanics.

Fundamental principle	Variant	Equations
Newton's Second Law	External force acting on a system	$\Sigma F_{x,y,z} = \frac{d}{dt}(m\mathcal{V}_{x,y,z})$
	Linear momentum of a system	$\mathcal{P}_{system} = \int_{m(system)} \mathcal{V} dm = \int_{V(system)} \mathcal{V} \rho dV$
Law of conservation of mass	Rate of change of mass	$\frac{\partial}{\partial t}(m_{c.v.}) = \int d\dot{m}_{in} - \int d\dot{m}_{out}$
	Continuity equation	$\int_{c.v} \frac{\partial \rho}{\partial t} dV = \int \rho \mathcal{V}_n dA_{in} - \int \rho \mathcal{V}_n dA_{out}$
Law of conservation of momentum	Momentum theorem	$\Sigma F_{x,y,z} = \frac{\partial(m\mathcal{V}_{x,y,z})_{c.v.}}{\partial t} + \int \mathcal{V}_{x,y,z} d\dot{m}_{out} - \int \mathcal{V}_{x,y,z} d\dot{m}_{in}$
	Working form of Momentum Theorem	$\Sigma F_{x,y,z} = \int_{c.v} \frac{\partial(\rho \mathcal{V}_{x,y,z})}{\partial t} dV + \int \rho \mathcal{V}_n \mathcal{V}_{x,y,z} dA_{out} - \int \rho \mathcal{V}_n \mathcal{V}_{x,y,z} dA_{in}$

[Source: Shapiro, 1953]

The nomenclature for the expressions included in Table 1.3 is:

A = Area

$\dot{m}$  = Mass flow rate

c.v. = Control volume

$\mathcal{P}$  = Linear momentum

F = Force

x, y, z = Coordinates of motion

In addition, the study of the dynamic characteristics of connective tubing is essential for the complete understanding and prediction of the behavior of fluid power systems under transient conditions. Different models have been proposed to account for the fluid velocity distribution, and the states of compressible fluids filling transmission lines in fluid power systems. The unknown quantities that these models seek to determine are: pressure, temperature, density, and velocity. In general, these unknown variables are functions of spatial coordinates and time, and they are found through the simultaneous solution of the equations derived from the thermodynamics and fluid mechanics laws identified above. In the literature reviewed, seven models for the analysis of the dynamic characteristics of compressible fluids in transmission lines were identified (Stecki and Davis, 1986). These models make different assumptions to simplify the analytic solution, and reduce the highly non-linear equations to linear relations. To illustrate, the most common assumptions made include (Stecki and Davis, 1986; Beater, 2007):

- Density and viscosity variations are negligible in comparison to their average values.
- The flow is axisymmetric and laminar.
- The fluid is incompressible, and it behaves as a Newtonian fluid.
- There is no radial pressure distribution.
- Thermal and heat transfer effects are negligible.

As the number of assumptions made increases, the accuracy of the model decreases. In contrast, higher order models most closely represent the behavior of compressible fluids transmitted through connective tubing in fluid power systems, but they are highly non-linear and difficult to solve, even numerically. The following table lists the seven models identified by Stecki and Davis (1986), and their most notable assumptions.



**Table 1.4:** Distributed parameter models – Fluid transmission lines

N	Model	Assumptions for the models
1	'Exact' First-order model	Coefficients function of pressure and temperature are treated as constants.
		Density variations are negligible.
		No radial pressure distribution and non-linear convective acceleration.
2	Two-dimensional thermal viscous compressible model	Density variations are negligible and the flow is axisymmetric.
		No radial pressure distribution and non-linear convective acceleration.
3	Two-dimensional viscous compressible model	No radial pressure distribution.
4	Two-dimensional viscous incompressible model	Incompressible fluid.
5	One-dimensional viscous compressible model	Plane wave propagation.
		Axial velocity is constant over the cross section of the tube.
6	One-dimensional linear resistance compressible model	Linear friction term account for viscous losses within the transmission line.
7	One-dimensional inviscid compressible model	Fluid viscosity is negligible.

[Adapted from: [Stecki and Davis, 1986](#)]

From the models listed in Table 1.4, the one commonly applied in the study and modeling of connective tubing in pneumatic systems is the one-dimensional linear resistance compressible model (number 6 in Table 1.4), for which the state equation, the continuity equation, and the momentum equation are respectively:

$$\frac{dp}{d\rho} = c^2 \quad (1.4)$$

$$\frac{\partial \rho}{\partial t} + \rho_o \frac{\partial v_x}{\partial x} = 0 \quad (1.5)$$

$$\rho_o \frac{\partial v_x}{\partial t} = -\frac{\partial p}{\partial x} + R_1 v_x \quad (1.6)$$

Where: t = Time

$\rho$  = Fluid density

c = Speed of sound

x = Axial coordinate

p = Instantaneous pressure

$v_x$  = Instantaneous axial velocity component

$\rho_o$  = Average dynamic density

$R_1$  = Resistance coefficient

Although the one-dimensional linear resistance compressible model is commonly applied, its application depends upon the selection of the resistance coefficient, which limits the accuracy of the frequency response obtained over specific ranges only. The resistance coefficient can be obtained experimentally, or by assuming that it is constant and that the instantaneous velocity profile in a fluid transmission line corresponds to the velocity profile for steady laminar flow (Stecki and Davis, 1986).

In addition to the distributed parameters models included in table 1.4, other models deal with the numerical and analytical approximation of the full solutions, or approximate the dynamic characteristic of full-distributed parameter models through lumped parameter schemes. For this thesis, as will be described in chapter 2, numerical and analytical approximations of the full solution will serve as foundations of the models adopted to simulate the dynamic effect of the length of connective tubing in the performance of pneumatic cylinders.

### 1.4.3. Compressible flow

In the study and modeling of pneumatic systems, due to the compressibility of air, different considerations must be made to describe pressure and flow profiles in pneumatic components. When dealing with compressible flow, variations in density throughout a field of flow relate to pressure changes, and to the speed of sound. The following section comprises a summary of concepts adopted from *The dynamics and thermodynamics of Compressible Fluid Flow* by Ascher Shapiro, 1953. Other general concepts come from the “*Introduction to Fluid Mechanics*” by Fox, Pritchard and McDonald, 2009.

#### 1.4.3.1. *The speed of sound*

The speed of sound represents a transitional boundary for the identification and classification of different types of compressible flows. Depending on the velocity of a fluid in relation to the speed of sound, the behavior of a compressible flow varies. Moreover, the importance of the speed of sound in fluid mechanics relates to the fact that, as an object travels through a medium, such as water or air, it generates disturbances in the form of infinitesimal pressure waves. These waves travel out at the speed of sound, and they define the behavior of the flow around a traveling object.

Depending upon the different assumptions or approximations made, the expressions utilized to calculate the speed of sound vary. The following table provides some general expressions to calculate the speed of sound.

**Table 1.5:** Speed of sound

Conditions	Relation / Equation	Assumptions/ Approximations
Speed of sound of a plane pressure pulse	$c^2 = \left(\frac{\partial p}{\partial \rho}\right)_{s=constant}$ $c = \sqrt{\left(\frac{\partial p}{\partial \rho}\right)_{s=constant}}$	Plane infinitesimal pressure wave travels along a pipe of uniform cross section.
		Shear forces are negligible compared with pressure forces.
		The process is nearly reversible and adiabatic - isentropic.
Speed of sound in a perfect gas	$c = \sqrt{\frac{kP}{\rho}} = \sqrt{kRT}$	Isentropic process.
Speed of sound in air	$c = 49.02\sqrt{T}$	Normal pressure (P = 101.325 kPa) and normal temperature (T = 293.15 K)
		Where c is in ft/sec, and T is in degrees R, or degrees F abs.

[Source: Shapiro, 1953]

From the definition of incompressible fluids, as fluids that do not experience changes in density; considering the relations in table 1.5, the speed of sound in an incompressible fluid would be infinite. Nevertheless, it must be noticed that no fluids are completely incompressible, and the reference to the incompressible flow of a fluid represents the fact that the fractional change in density is so small that it can be neglected.

#### 1.4.3.2. Classification of compressible flows

As it was stated before, the behavior of a compressible flow fluctuates depending on its velocity in comparison to the velocity of air. The ratio of the velocity of a fluid ( $\mathcal{V}$ ) to the speed of sound is designated as the Mach Number (M), which is represented by:

$$M = \mathcal{V}/c \quad (1.7)$$

Based on the value of the Mach number, the types of compressible flow are:

- Subsonic Flow: The velocity of the fluid is less than the speed of sound; accordingly, the Mach number is less than 1 ( $M < 1$ ).

- Supersonic Flow: The velocity of the fluid is greater than the speed of sound; accordingly, the Mach number is higher than 1 ( $M > 1$ ).
- Transonic Flow: The Mach number is comprehended between 0.9 and 1.2. Transonic flow fields have both subsonic and supersonic regions ( $M \approx 1$ ).
- Hypersonic Flow: The velocity of the fluid is very large in comparison to the speed of sound ( $M \geq 5$ ).

From the definition of the Mach number, it can be stated that the Mach number for an incompressible fluid is approximately zero ( $M \approx 0$ ). In fact, it is commonly assumed that for Mach numbers less than 0.3 ( $M < 0.3$ ), the flow can be considered incompressible.

Figure 1.3 represents the relation between the speed of sound and the velocity of an adiabatic, steady-state flow.

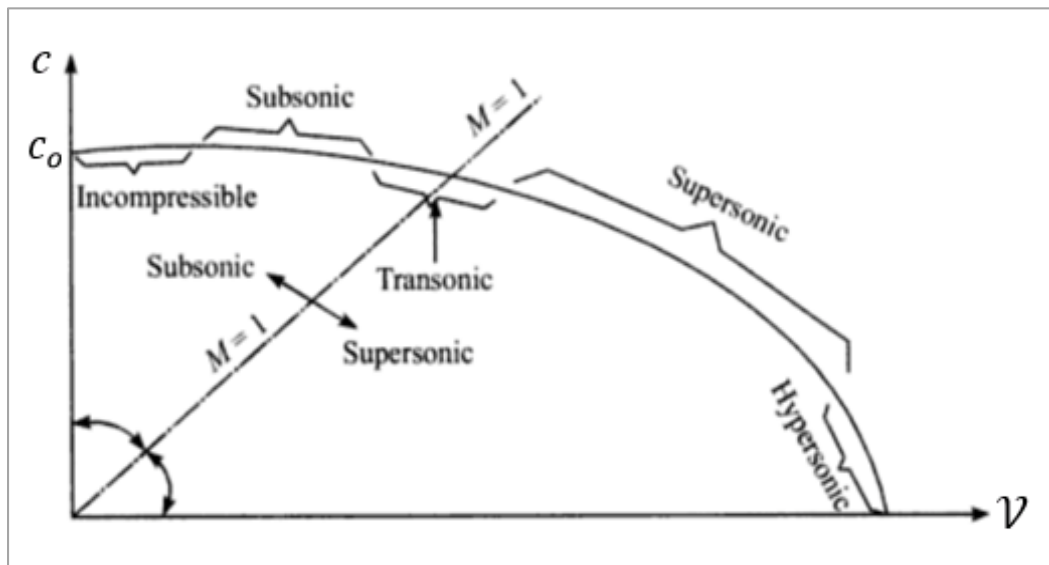


**Figure 1.3.** Steady-flow adiabatic ellipse

[Adapted from: [Balachandran, 2006](#)]

Figure 1.3 is derived from the adiabatic steady-flow energy equation given by:

$$\frac{v^2}{k-1} + \frac{v^2}{2} = \frac{c_0^2}{k-1} = \text{constant} \quad (1.8)$$

Where  $c_0$  is the speed of sound at the stagnation or static condition, which is the case when the flow velocity is zero.

Eq. 1.8 corresponds to the equation for an ellipse with coordinates  $c$  and  $\mathcal{V}$ . According to Eq. 1.8, by plotting the speed of sound,  $c$ , as a function of flow velocity,  $\mathcal{V}$ , a first quadrant ellipse is obtained. This ellipse is called Prandtl velocity ellipse or adiabatic steady-flow ellipse (Balachandran, 2006).

Moreover, in the analysis of the flow of air in pneumatic systems, it is commonly found the expressions “choked” and “unchoked” flow, which make reference to the relation of the flow of air to the supply pressure. Accordingly, unchoked and choked flow differ one from the other in the following characteristics:

- Unchoked flow: The flow is subsonic, and it depends non-linearly on the supply pressure ( $M < 1$ ).
- Choked flow: The flow attains sonic velocity, and it depends linearly on the supply pressure. The Mach number is equal to one ( $M = 1$ ), and beyond this point the flow does not increase.

As it will be acknowledged in following chapters, the distinction between choked and unchoked flow for the analysis of pneumatic systems is necessary if flow control valves are modeled as converging nozzles. For a converging nozzle, the choked flow is given by the following expression:

$$\dot{m}_{Choked} = A_{exit} p_{supply} \sqrt{\frac{k}{RT_{supply}}} \left( \frac{2}{k+1} \right)^{\frac{k+1}{2(k-1)}} \quad (1.9)$$

Where:  $A_{exit}$  = Exit area.

$p_{supply}$  = Supply pressure.

$T_{supply}$  = Temperature of supply air

Depending on the exit area of the nozzle, or the effective area of a pneumatic control valve, it will be experimentally verified that the choked flow region precedes to the unchoked flow region. Accordingly, the flow from a pneumatic valve should first attain sonic velocity; and later, it should become subsonic, which will be verified through experimental results in following chapters.

#### 1.4.4. Foundations of System Dynamics

System dynamics applied to the study of fluid power systems focuses on the modeling, simulation, and analysis of components interacting together to transmit power by means of compressed fluids. This section seeks to emphasize general concepts of system dynamics applied to the study of fluid power systems. Nevertheless, the purpose of this section is not to apply system dynamics theory for the analysis and modeling of specific components of the system under study. Chapter 2 will focus on the analysis and modeling of the pneumatic system under study, and it will present the mathematical models proposed for predicting the transient response of the system.

Applied to fluid power engineering, or any branch of engineering, fundamental concepts from the study of system dynamics include:

- System: A system is a combination of elements that interact together with a common purpose. Accordingly, a fluid power system could be defined as a collection of elements working together to transmit power by using compressed fluids. A system is static if its response does not depend on time, and it is dynamic if its response varies with time.
- Dynamic environment: A dynamic environment is the set of conditions, elements, and factors surrounding a system and influencing its behavior.
- Mathematical model: A mathematical model is a mathematical description of the behavior of a system, by using differential equations derived from fundamental laws.
- Input and output variables: Input variables are physical signals that cause acting on the system in reference to the environment. On the contrary, an output variable is a calculated or measured variable as result of the system action on the environment.
- State variables: State variables are variables that characterize the behavior of a system at any point in time. The state variables of a system have to be independent from each other, and they include one or more outputs. The use of state variables seeks to account for the behavior of a system independently of the output variables chosen.
- Parameters: Parameters of a system are generally constants included in its mathematical models. The parameters of a system usually comprise the coefficients of the equations describing the mathematical models for the system, and they represent measurable characteristics that define the system.

The following figure shows the general representation of a dynamic system, in terms of its inputs, outputs and state variables.

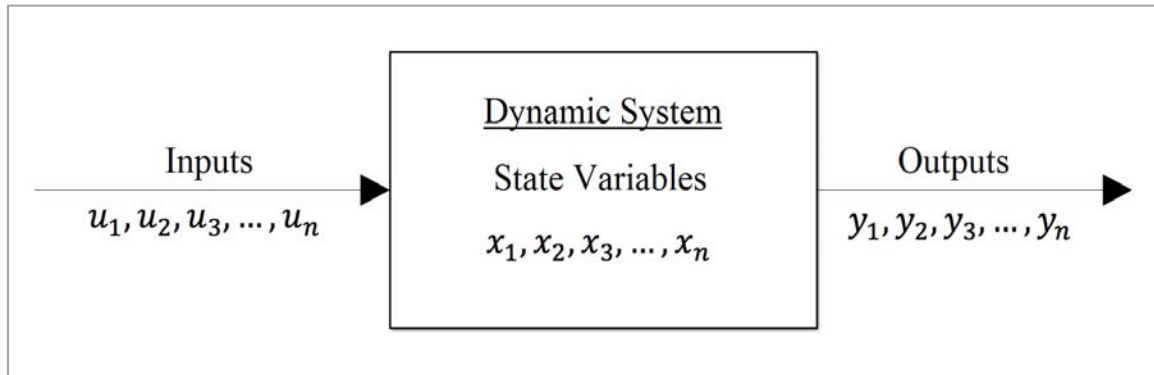


**Figure 1.4.** Box representation of a dynamic system in terms of its inputs, outputs, and state variables

#### 1.4.4.1. Classification of dynamic systems

Dynamic systems and their mathematical models can be classified according to different criteria. Based on the criteria defined in *Modeling and Analysis of Dynamic Systems* by [Close, Frederick, and Newell \(2009\)](#), dynamic systems can be divided in the following categories:

- Distributed and lumped systems.
- Continuous, discrete-time and hybrid systems.
- No quantized and quantized systems.
- Fixed and time-varying systems.
- Linear and nonlinear systems.

The following table summarizes the main characteristics of the different categories:

**Table 1.6:** Classification of dynamic systems.

Criterion	Category	Properties
Spatial characteristics	Distributed systems	State variables cannot be defined at a specific number of points.
		Models expressed in terms of partial differential equations.
	Lumped systems	Systems defined by a finite number of state variables.
		Models expressed in terms of ordinary differential equations.

Table 1.6 continued.

Criterion	Category	Properties
Continuity of the time variable	Continuous systems	Variables are defined over some continuous range of time.
		Models described by differential equations.
	Discrete-time systems	Variables are defined at different instants of time.
		Models described by difference equations.
Hybrid systems	Systems share continuous and discrete-time characteristics.	
Quantization of the dependent variable	Non-quantized systems	Variables may take on any value within some continuous range.
	Quantized systems	Continuous and no quantized variables are referred as analog variables.
		Variables may take on only a finite number of different values.
Discrete and quantized variables are referred as digital variables.		
Superposition property	Linear systems	Systems that satisfy the conditions for superposition.
	Nonlinear systems	Systems for which the superposition property does not hold.

[Adapted from: [Close et al., 2002](#)]

Note that most dynamic systems are inherently nonlinear; nonetheless, it is a common practice to approximate a nonlinear system with a linear system by obtaining solutions limited to small variations about an operating point. The advantages of dealing with linear systems relate to the simplification of the analytic solution of the mathematical models for a system. Based on the superposition property, a system is defined as a linear system if for every initial time ( $t_0$ ) and any  $n$  state-input - output pairs ([Chen, 1999](#)):

$$\left. \begin{array}{l} \text{States: } x_1(t_0), \dots, x_n(t_0) \\ \text{Inputs: } u_1(t), \dots, u_n(t) \end{array} \right\} \begin{array}{l} \text{Outputs: } y_1(t), \dots, y_n(t) \\ t \geq t_0 \end{array} \quad (1.10)$$

The following conditions hold:

- **Additivity condition:** Multiplying a state-input pair by any real constant  $\alpha$  results in the multiplication of the corresponding output by the same constant.

$$\left. \begin{array}{l} \text{State: } \alpha x_1(t_0) \\ \text{Input: } \alpha u_1(t) \end{array} \right\} \begin{array}{l} \text{Output: } \alpha y_1(t) \\ t \geq t_0 \end{array} \quad (1.11)$$



- Homogeneity condition: Adding multiple state-input pairs is equivalent to sum their corresponding outputs.

$$\left. \begin{array}{l} \text{States: } x_1(t_0) + \dots + x_n(t_0) \\ \text{Inputs: } u_1(t) + \dots + u_n(t) \end{array} \right\} \begin{array}{l} \text{Outputs: } y_1(t) + \dots + y_2(t) \\ t \geq t_0 \end{array} \quad (1.12)$$

The process of approximating a nonlinear system to a linear system by confining the inputs around an operating point is called linearization, and it will be further explained and applied in chapter 4.

#### 1.4.4.2. System Analogs

Systems characterized by mathematical models in which the equations have the same configuration, but the symbols used to represent the different variables and coefficients differ are called system analogs. According to the physical nature of a system analog, its dynamic variables can be generalized as:

- Effort variables: Effort variables, also called across variables or potential variables, represent the effort applied across a system element. In the case of fluid power systems, the differential pressure of the system corresponds to an effort variable.
- Flow variables: Flow variables represent the rate of change of a variable through a system element. For pneumatic systems, the mass flow rate of air corresponds to a flow variable.

Additionally, in the definition of system analogs, the different variables and coefficients found in equations applied to the modeling of dynamic systems can be expressed in term of three common quantities (Ogata, 1998):

- (i) Resistances: The resistance of a physical element is defined as the change in potential that produces a unit change of a flow variable.
- (ii) Capacitances: The capacitance of a physical element is defined as the change of a flow variable that causes a unit change in potential per second.
- (iii) Inductances: The inductance of a physical element is equivalent to the change in potential that causes a unit change of a flow variable per second.

Applied to pneumatic systems, the analog quantities defined before are respectively:

$$\text{Resistance } (R_1) = \frac{\text{differential pressure}}{\text{mass flow rate}} \left[ \frac{Ns}{kgm^2} \right] \quad (1.13)$$

$$\text{Capacitance } (C) = \frac{\text{mass flow rate}}{\text{time rate of change in pressure}} \left[ \frac{kgm^2}{N} \right] \quad (1.14)$$

$$\text{Inductance } (I) = \frac{\text{pressure}}{\text{time rate of change in mass flow rate}} \left[ \frac{Ns^2}{kgm^2} \right] \quad (1.15)$$

The identification of system analogs and variables applied in the study of pneumatic systems will be useful at the time of modeling and characterizing the system under study. As stated before, chapter 2 will entirely focus on the mathematical modeling of the pneumatic system subject of study in this thesis. Furthermore, chapter 4 will center on the design of the required controller; hence, the following sections of this chapter provide general guidelines in the application of control theory for the design and assessment of controllers for fluid power systems.

#### 1.4.5. Control Theory

The following section contains a review of research associated with the control of fluid power systems. Different control schemes are considered in terms of their suitability for implementation with fluid power systems, particularly with pneumatic systems. Moreover, due to the challenges in the use and control of fluid power systems for the transmission of power, the current trend line of research on the control of fluid power systems greatly focuses on the improvement of efficiency of these systems. Challenges in the control of fluid power systems include: the non-linear characteristics of control valves, the variation of stiffness of positioning cylinders, the compressibility of the fluid used, and the length of connecting tubing, among others.

Accordingly, despite of the challenges of fluid power systems, and given their great advantages for the transmission of power; such as their fast-response, and low-weight power ratio, control theory establishes as one of the most viable alternatives for the improvement of efficiency and sustainability of fluid power systems.

The following section will identify some of the advantages and disadvantages of control schemes commonly applied, and which are the target of current research into fluid power system control.

#### 1.4.5.1. *Fundamental notions of control theory*

This section defines the basic terminology used to describe control systems. In addition, an introduction to the feedback concept is made, by describing open-loop control and closed-loop control systems.

First, basic terminology for the description of control systems includes (Ogata, 1998; Stefani et al., 2002; Franklin et al., 2002):

- Plant: The plant comprises the process and the actuators that are going to be controlled. The output of the plant is a controlled variable.
- Actuator: An actuator is a device that influences the controlled variable of the process. An actuator produces an actuating signal.
- Controller: A controller is a device that generates desired input signals according to required or desired outputs. A controller produces a control signal.
- Disturbance: A disturbance is an uncontrolled signal that adversely affects the output of a system. It can be internal or external.
- Sensor: A sensor is a device that measures an output of the plant or process and produces a sensor signal, which is fed back to the controller for comparison with a reference signal.
- Comparator: A comparator or error detector computes the difference between a reference signal and the sensor signal. A comparator provides the system with an error signal.

Furthermore, feedback control is defined as an action that seeks to reduce the difference between a reference input and the output of a plant, through the input of this difference to the system. To understand the characteristics of a feedback system, open-loop control systems and closed-loop control systems have to be distinguished (Ogata, 1998):

- Open-loop control system: In an open-loop control system, the output has no effect on the control action. The output is neither measured nor fed back for comparison with the input.

- Closed-loop control system: In a closed-loop control system, the difference between a reference signal and a feedback signal is fed to the controller to reduce the error, and bring the system to a desired value.

The following table summarizes the advantages and disadvantages of open-loop control and closed-loop control systems.

**Table 1.7:** Advantages and disadvantages of closed-loop and open-loop control systems.

Type of Control	Advantages	Disadvantages
Open-Loop Control	Simple.	Inaccurate.
	Low cost.	Unreliable.
	Generally stable.	Unable to adapt to external disturbances.
	Easy to implement.	Requires exact estimates of parameters.
Closed-Loop Control	Improved accuracy.	Possibly unstable.
	Decreased sensitivity to disturbances.	Feedback may lead to oscillatory response.
	Less affected by noise.	More expensive than open-loop systems.
	More efficient than open-loop systems.	More complex than open-loop systems.

The following figure identifies the elements of a closed-loop control system:

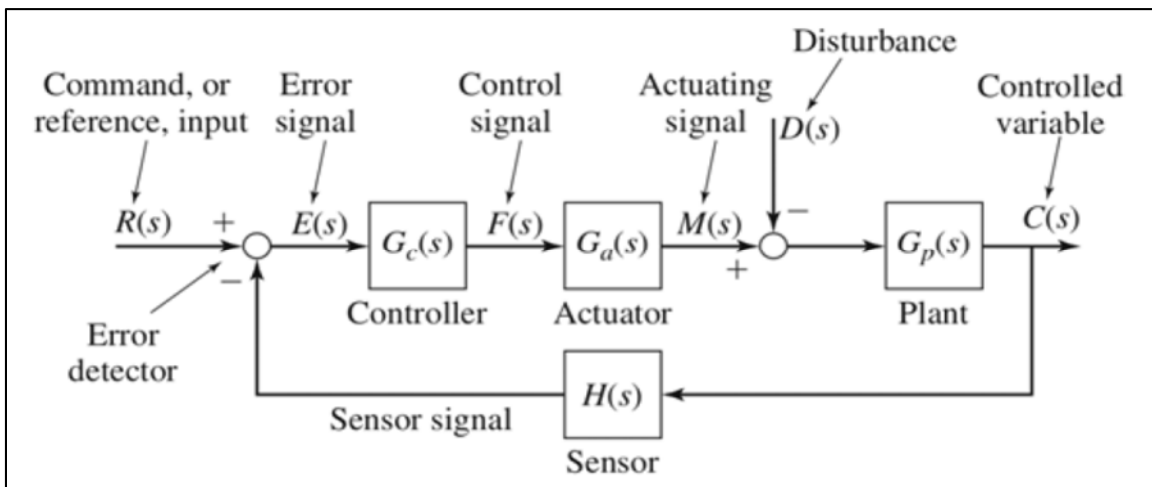


**Figure 1.5.** Block diagram of a closed-loop control system [Source: Palm, 2014]

Following sections describe control strategies in which closed-loop or feedback control is applied, particularly in relation to fluid power systems.

#### 1.4.5.2. Proportional, integral and derivative (PID) control

A PID configuration is one of the most commonly applied control schemes for industrial applications, including fluid power systems. As its name stands, a PID scheme establishes a proportional, derivative, and integral control action between the output of the controller and an actuating error signal. The proportional control action amplifies the error signal given by the difference between a desired value and a measured value. The derivative control action differentiates the error signal, and seeks to increase the natural frequency of the system in order to improve its transient response. In addition, the integral control action seeks to minimize the steady state error through low frequency compensation, by summing or accumulating the error signal.

The following figure shows the block diagram of a PID scheme for positioning control.

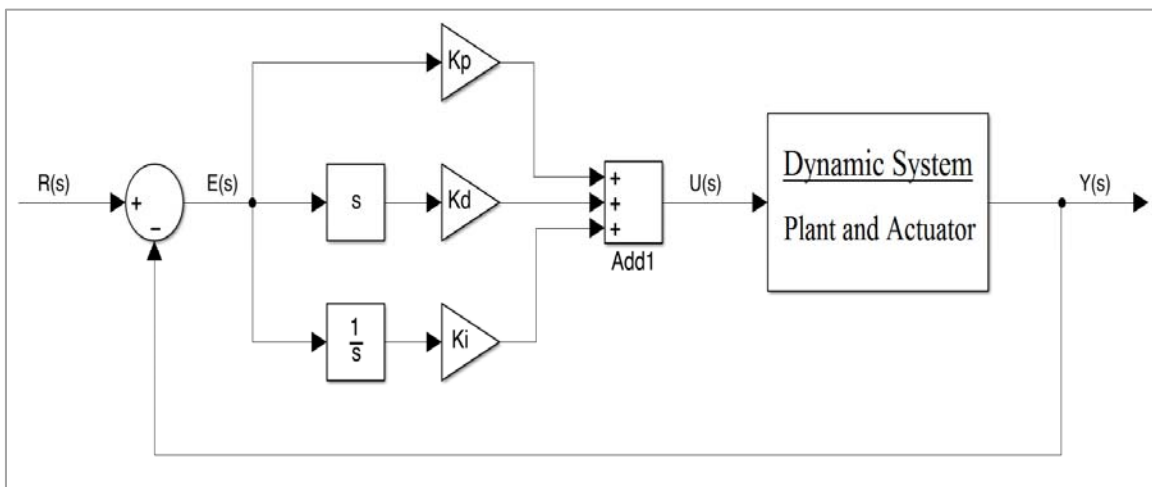


**Figure 1.6.** Block diagram of a PID control scheme

The overall control action of a PID scheme relates the output of the controller  $M(s)$  and the actuating error signal  $E(s)$  through a transfer function  $G_c(s)$  of the form:

$$\frac{M(s)}{E(s)} = G_c(s) = K_p \left( 1 + T_d s + \frac{1}{T_i s} \right) \quad (1.16)$$

$$G_c(s) = K_p + K_d s + \frac{K_i}{s}$$

Where:  $K_p, K_d, K_i$  = Proportional, derivative and integral gains, respectively.

$T_d, T_i$  = Derivative and integral time constant, respectively.

The following table summarizes the individual effects of the proportional, integral, and derivative terms in the performance of a PID controller.

**Table 1.8:** Effects of the proportional, integral, and derivative terms in a PID controller.

PID Gain Action	Effect on Performance Specifications				
	Rise Time	Overshoot	Settling time	Steady-state error	Stability
Increasing $K_P$	Decrease	Increase	Small increment	Decrease	Degrade
Increasing $K_I$	Small decrease	Increase	Increase	Large decrease	Degrade
Increasing $K_D$	Small decrease	Decrease	Decrease	Minor change	Improve

[Adapted from: [Heong Ang et al., 2005](#)]

As it can be acknowledged from table 1.7, the overall performance of a PID controller depends on the tuning of the proportional, derivative and integral gains, which represents the most challenging feature of a PID control design. Indeed, other marked disadvantages in the application of PID control schemes include: a prevalent steady-state error caused by the proportional action, the increase of the order of the system and the presence of oscillations and potential instability caused by the integral action, and the amplification of noise in measurement signals caused by the derivative action ([Palm, 2014](#)).

Moreover, difficulties in tuning the derivative term leads to it often being excluded, or that its action be modified in relation to the overall control scheme. For instance, in velocity PID control schemes, a pseudo-derivative term can be included to avoid differentiating the feedback signal, which in contrast to positioning strategies should improve the damping of the system ([Edge, 1996](#)).

Applied to the control of fluid power systems, [Wang et al. \(1999\)](#) reported the implementation of a modified PID controller for servo-pneumatic systems. The main objective of the study was to improve the stability of the system, and to compensate for the non-linearities inherent to pneumatic actuator systems. The modified PID control scheme incorporated acceleration feedback as an alternative to chamber pressure feedback, to improve the stability of the system. The results demonstrated performance improvement, but the comparison was made against fixed-gain PID configurations, which may be considered ineffective in high-performance applications.

The following figure shows the block diagram corresponding to the PID control scheme modified by Wang et al. (1999).

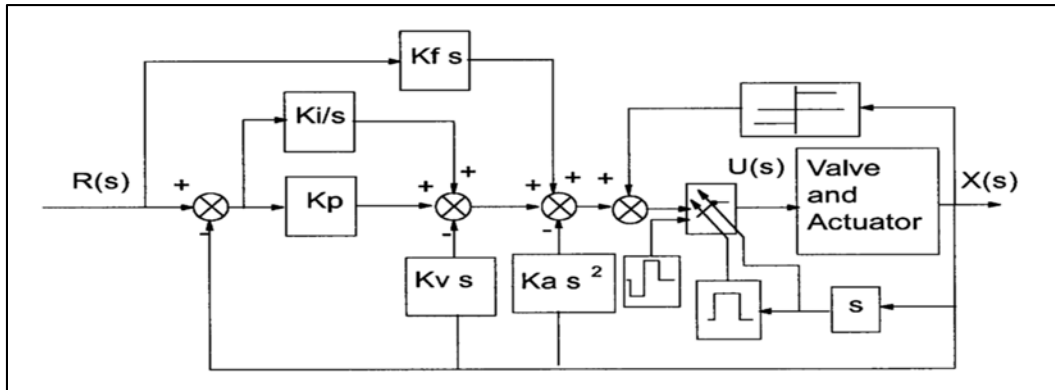


**Figure 1.7.** Block diagram of modified PID control scheme [Source: Wang et al., 1999]

Chillari et al. (2001), in their experimental comparison of several pneumatic position control methods, demonstrated that a PID control scheme produces the highest error, given by the standard deviation between the desired and the actual position. The comparison was made in accordance to different tracking trajectories, and reference signal frequency. Nevertheless, it was also demonstrated that in combination with other control schemes, or by including supplementary feedback signals, a PID control scheme still results a suitable approach for the control of fluid power systems, as will be acknowledged in the following sections.

#### 1.4.5.3. State-space feedback control

For the definition of state-space feedback control methods; first, it is necessary to distinguish between classical control and modern control theory. In that regard, classical control applies frequency-domain analysis to represent a process by its transfer function. In contrast, modern control theory deals with the characterization of a process using differential equations (Friedland, 2012).

Classic control theory applies techniques of root locus and frequency response in order to find a dynamic compensation that satisfies specific design requirements. The state-space method of modern control works with the state-variable description of a system, but it also aims to design a dynamic compensation.

In contrast, modern control methods, such as state-space feedback control, apply analytic results and tools from matrix linear algebra; therefore, they are well suited to be solved by using computer techniques. In addition, other advantages of state-space methods in comparison to classic control methods include (Franklin et al., 2002):

- The controlled systems do not have to be linear or time-invariant. State-space control methods are readily applied to non-linear and time-variant systems.
- State-space techniques of analysis and design extend to systems with multiple inputs and/or multiple outputs.
- While in classic control methods, the input relates to the output without interest in the internal behavior of the system, state-space methods are able to connect internal variables to the external inputs and to the sensor signals.

In state-space form, the differential state equations characterize the behavior of a dynamic system and are given by:

$$\begin{aligned} \dot{x}_1(t) &= \frac{dx_1}{dt} = a_{11}(t)x_1(t) + \dots + a_{1m}(t)x_m(t) + b_{11}(t)u_1(t) + \dots + b_{1n}(t)u_n(t) \\ &\vdots \\ \dot{x}_n(t) &= \frac{dx_n}{dt} = a_{n1}(t)x_1(t) + \dots + a_{nm}(t)x_m(t) + b_{n1}(t)u_1(t) + \dots + b_{nn}(t)u_n(t) \end{aligned} \quad (1.17)$$

Likewise, the algebraic output equations define the output of a dynamic system and are given by:

$$\begin{aligned} y_1(t) &= c_{11}(t)x_1(t) + \dots + c_{1m}(t)x_m(t) + d_{11}(t)u_1(t) + \dots + d_{1n}(t)u_n(t) \\ &\vdots \\ y_k(t) &= c_{k1}(t)x_1(t) + \dots + c_{km}(t)x_m(t) + b_{k1}(t)u_1(t) + \dots + b_{kn}(t)u_n(t) \end{aligned} \quad (1.18)$$

Hence, a linear time-varying system can be represented in terms of state-space variables as follows:

$$\begin{aligned} \dot{x}(t) &= A(t)x(t) + B(t)u(t) \\ y(t) &= C(t)x(t) + D(t)u(t) \end{aligned} \quad (1.19)$$

Where:  $x(t)$ ,  $u(t)$ ,  $y(t)$  = Vector of state variables, inputs, and outputs, respectively.

$A(t)$ ,  $B(t)$ ,  $C(t)$ ,  $D(t)$  = Matrices containing the coefficients of the differential equations.



Figure 1.8 shows the block diagram representation of a system in the form of Eq. 1.19.

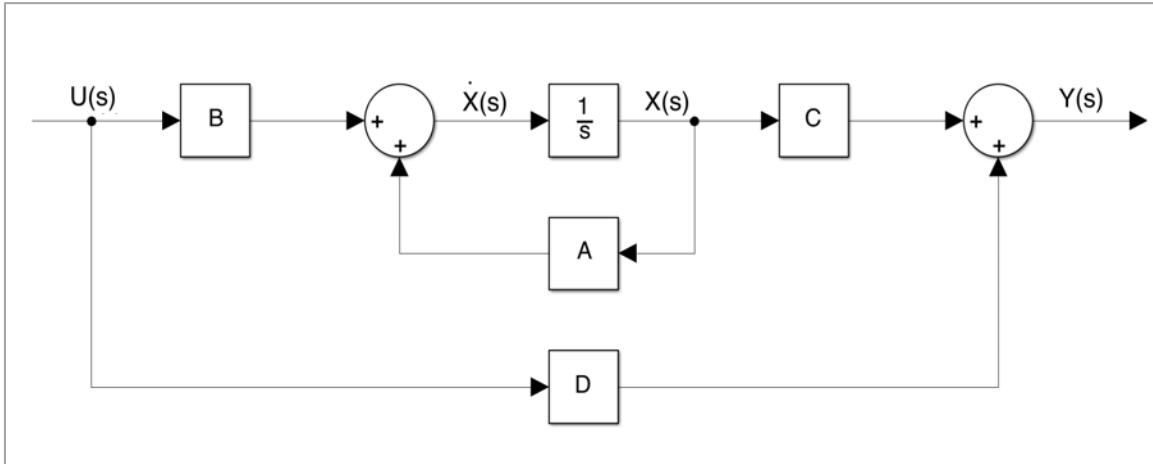


**Figure 1.8.** Block diagram of a state-space linear system

The control law, and the equivalent compensated system for Figure 1.8 are respectively:

$$\begin{aligned} u &= -Kx \\ \dot{x} &= (A - BK)x \end{aligned} \quad (1.20)$$

Where:  $K$  = Vector of feedback gains.

Assuming the matrix  $D$  in Figure 1.8 is zero, Figure 1.9 shows the block diagram representation of the compensated system defined by Eq. 1.20.

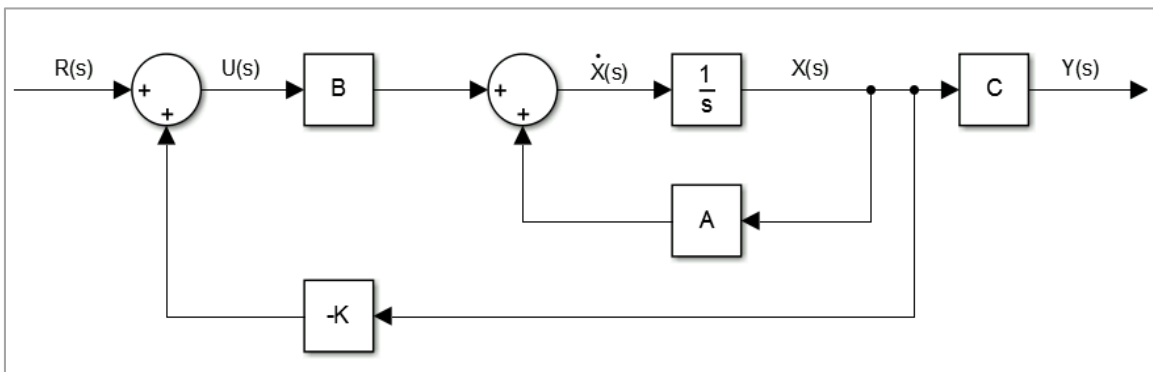


**Figure 1.9.** Block diagram of state-space feedback control system

In Figure 1.9, the complete system state vector is fed back to the control loop, which should ensure total control over the plant of the system. Nevertheless, the number of feedback gains would correspond to the number of state variables of the system, which gives more degrees of freedom in the design of the control system.

In addition, for tracking design, when a command or reference input is included, for a step input the control law can be given by:

$$u = -Kx + \bar{N}r \quad (1.21)$$

Where:  $r$  = Reference or command input.

$\bar{N}$  = Reference gain.

The main disadvantage of the control law given by Eq. 1.21 is that the reference gain is placed outside of the feedback loop, which increases the sensitivity of the system to external disturbances. To avoid this increase of sensitivity, an integrator can be placed in the forward path in series with the system (Stefani et al., 2002), which constitutes the basis of integral control.

Figures 1.10 and 1.11 show the block diagrams for state-space feedback control systems including an external reference gain, and an integrator placed in the forward path.

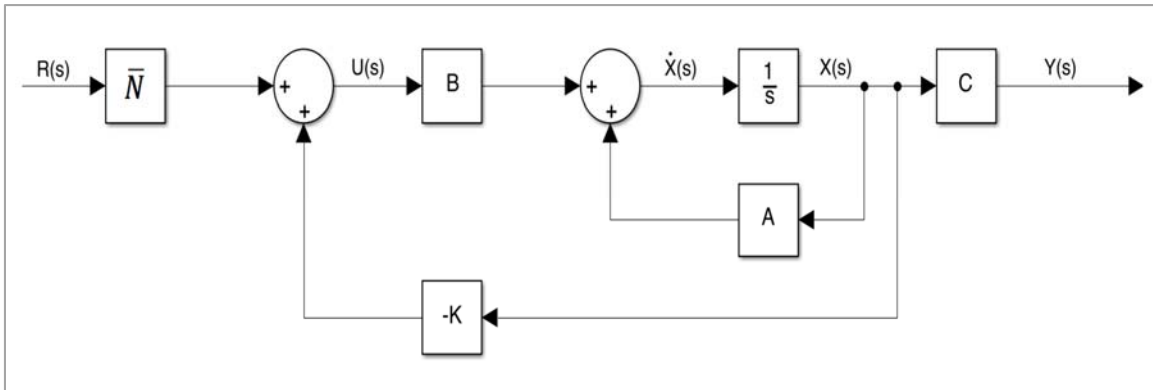


**Figure 1.10.** Block diagrams for external reference gain tracking control

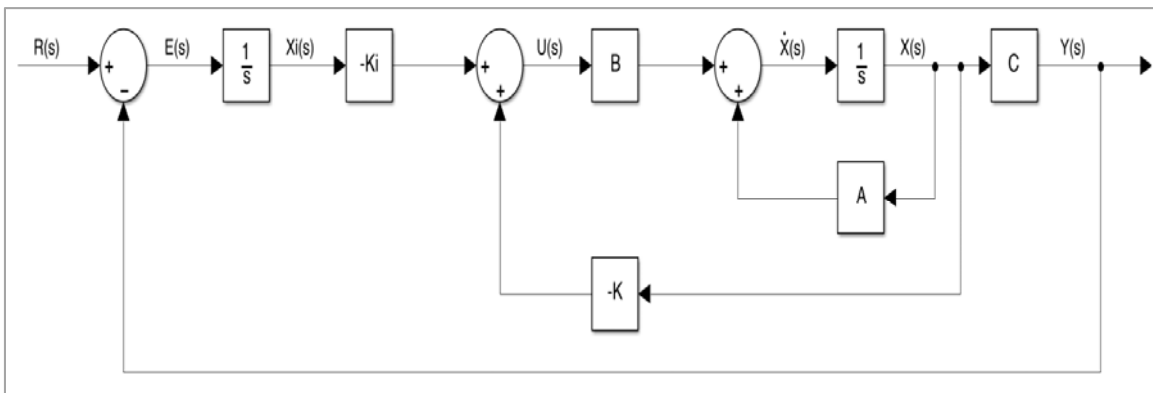


**Figure 1.11.** Block diagrams for integral tracking control [Source: Stefani et al., 2002]

Moreover, the design of feedback control schemes is based on finding the feedback gains. Different approaches have been applied to find the feedback gains for state-space control systems. Most methods derive from pole placement schemes, such as, time-domain analysis, and parameter sensitivity, among others (Edge, 1996). Nevertheless, the difficulty in determining feedback gains relates to physical restrictions of the plant. For example, in the case of fluid power systems, control valves operate within a certain range, which limits the power transmitted through the valve, and conditions the magnitude of the feedback gains (Beater, 2007).

Several authors have applied state-space feedback schemes for the control of pneumatic systems. Richard and Scavarda (1996) applied state-space feedback strategies to generate a non-linear control law for an electropneumatic servodrive. The study compared linear and nonlinear control schemes for electropneumatic servodrives. In comparison to a linearized third-order system, the results showed a limited improvement of the plant dynamics.

Likewise, Liu and Bobrow (1988) developed a state-space linearized model of a pneumatic servo system. Their main objective was to demonstrate that pneumatic systems are suitable for robotic applications. To determine the feedback gains, the authors used an on-line lookup table.

The success of state-space feedback control schemes depends on the definition of optimal gains, and on how a feedback scheme can be combined with other control strategies to compensate for nonlinearities of a plant. One of the most commonly applied techniques to find feedback gains derives from optimal control theory, which is treated in the following section.

#### 1.4.5.4. *Optimal control*

For a continuous-time system, optimal control schemes seek to find a control input  $u^*(t)$ , and a state solution  $x^*(t)$  that satisfy the state-space equations defined by Eq. 1.19, in addition to a set of initial conditions, terminal conditions, and control constraints, so that a performance index or “cost function”  $J$  is minimized (Lu, 2015). The performance index  $J$ , expressed as the integral of a quadratic form in the state  $x$  plus a second quadratic form in the control  $u$ , can be represented by:

$$J = \frac{1}{2} \int_{t_0}^T [x'(t)Q_J(t)x(t) + u'(t)R_Ju(t)]dt \quad (1.22)$$

Where  $Q_J$  and  $R_J$  are symmetric matrices.

The formulation of the performance index given by Eq. 1.22 is not unique. The definition of the performance index depends on the characteristics of the problem to be solved. For example, if the performance index represents the time, or the magnitude of the input, the performance index can take the form:

$$\begin{aligned} \text{Minimum time problem: } J &= \int_{t_0}^T dt \\ \text{Minimum fuel problem: } J &= \int_{t_0}^T |u(t)| dt \end{aligned} \quad (1.23)$$

Furthermore, for a closed-loop control system for which the control law is defined by Eq. 1.20 or 1.21, the gain matrix  $K$  can be found from the solution of the continuous-time algebraic Riccati equation given by:

$$0 = ZA + A'Z - ZBR_j^{-1}B'Z + Q_j \quad (1.24)$$

Where  $Z$  is an unknown symmetric matrix that represents the “optimal” state-space solution  $x^*(t)$ . Finding  $Z$  in Eq. 1.24, an “optimal” gain matrix can be derived by:

$$K = R_j^{-1}B'Z \quad (1.25)$$

Nevertheless, although multiple computational tools can assist to find the solution to the Riccati equation, this solution depends on the selection of the matrices  $Q_j$  and  $R_j$ , which makes the process highly iterative and time consuming. Moreover, the process to find a feedback gain matrix through the solution to the continuous-time algebraic Riccati equation applies to linear systems, only. Accordingly, in the case of fluid power systems, which are inherently nonlinear, the optimal solution derived from the solution to the continuous-time algebraic Riccati equation has to be found around an operating point.

Multiple authors have applied schemes derived from optimal control theory for the control of fluid power systems. Related to pneumatic systems, [Liu and Bobrow \(1988\)](#) applied root locus analysis, and optimal control theory to derive feedback gains for their control system. From the comparison of both techniques, it was demonstrated that the gains determined by applying optimal control methods provided better performance to the system. Nevertheless, physical limitations intrinsic to pneumatic systems constrain the magnitude of the gains found by using optimal control methods.

Similarly, [Surgenor et al. \(1991\)](#) applied optimal control theory to demonstrate the potential of pneumatic positioners in matching the performance of electro-pneumatic systems. The capability of pneumatic systems was demonstrated by designing a control scheme for an inverted pendulum. At the end, it was acknowledged that further improvement in the performance of pneumatic systems relies on theoretical robustness analysis of the control schemes that could be applied.

In addition, more advanced optimal control schemes have been applied to the control of complex pneumatic systems. For instance, [Grewal et al. \(2012\)](#) applied a linear quadratic Gaussian (LQG) scheme for the control of a pneumatic Stewart-Gough platform. The difficulty in controlling a Stewart-Gough platform is given by its six degrees of freedom. A LQG control scheme comprises the combination of a Kalman filter, and a linear quadratic regulator (LQR).

The performance index for a LQR corresponds to the one defined in Eq. 1.22. The results showed by [Grewal et al. \(2012\)](#) demonstrated that the overall control scheme successfully met the specifications required. It is important to observe that the differential equations that described the dynamics of the system were linearized around an operating point. In that regard, more advanced optimal control techniques are being investigated for the control of nonlinear systems, which will greatly benefit to the control of fluid power systems.

#### 1.4.5.5. *Non-linear compensation*

The application of non-linear compensation control strategies implies the design of algorithms able to virtually remove non-linearities associated with the operation of a system. In the case of fluid power systems, most of the non-linearities emerge from the synergism between flow and pressure. For example, in the case of control valves for hydraulic or pneumatic systems, non-linearities inherent to the interrelation between flow and pressure contribute to system damping ([Edge, 1996](#)). As the operation conditions change, the non-linearities in the control valves increase the damping of the load, which might severely affect the performance of fluid power systems. Some of the non-linearities that the application of non-linear compensation schemes seeks to attenuate in fluid power systems include:

- Control valve induced damping.
- Control valve underlap.

- Control valve overlap.
- Control valve dead zone.
- Cylinder area ratio.
- Cylinder friction.

In the case of control valve induced damping, one possibility to compensate for this nonlinearity is to add acceleration or pressure feedback, which helps to manage damping in a controlled manner (Wang et al., 1999). Furthermore, valve induced damping can be attenuated by creating modified flow pressure characteristics (Edge, 1996). For instance, a near-flat flow pressure characteristic can replace a non-linear valve characteristic, as it is shown in the following figure.

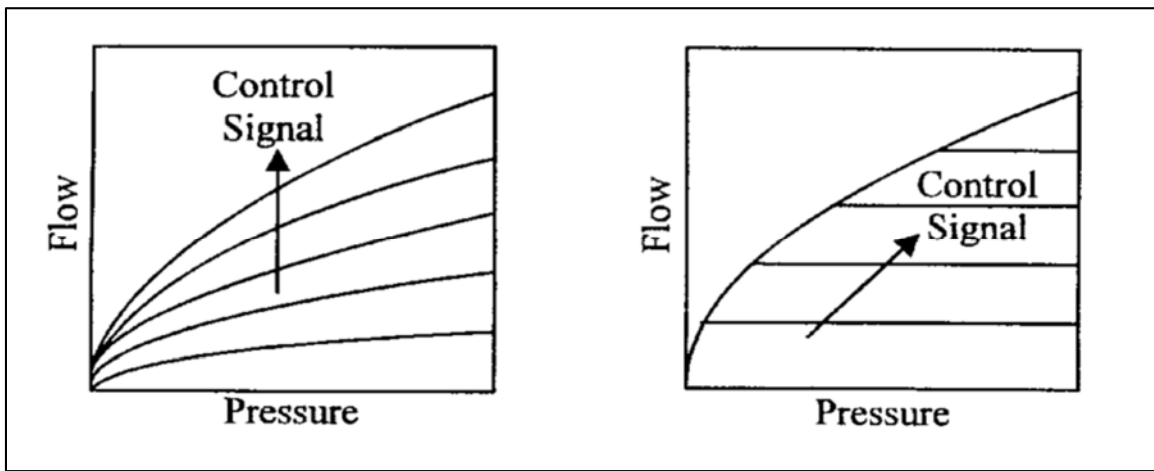


**Figure 1.12.** Modification of flow-pressure valve characteristic: (Left) Non-linear characteristic, (Right) Generated near-flat characteristic. [Source: Edge, 1996]

Moreover, the implementation of friction compensation for the control of fluid power systems is crucial in high-tech applications, such as robotics. In that regard, five friction compensation techniques are usually applied in robotic applications (Bona and Indri, 2005):

- (i) Friction parameters estimated off-line from a specific friction model are introduced as constants in general control schemes.
- (ii) The compensation action is tuned according to a specific friction parameter estimated on-line.

- (iii) Model-based adaptive algorithms generate static or dynamic parameters used for on-line friction compensation.
- (iv) Observers or control gains are introduced to counterbalance friction effects.
- (v) Friction parameters are reconstructed using so-called soft computing strategies, such as, fuzzy, neural and genetic algorithms.

Likewise, non-linear compensation can also be achieved through feedback linearization methods. Feedback linearization methods are non-linear control techniques applied to a specific class of non-linear systems. The nonlinear systems included in this class are denominated affine nonlinear systems, which are systems with state equations that are linear in the input controls.

A nonlinear affine system presents the following form:

$$\begin{aligned}\dot{x} &= f(x) + g(x)u \\ y &= h(x)\end{aligned}\tag{1.26}$$

Accordingly, feedback linearization techniques seek to find a control input  $u^*$  and a change of variables  $z^*$  that transform a nonlinear system into an equivalent linear system. The control input  $u^*$  and the change of variables  $z^*$  are expressed in the following form (Khalil, 2002):

$$\begin{aligned}u^* &= \alpha(x) + \beta(x)v \\ z^* &= \mathcal{T}(x)\end{aligned}\tag{1.27}$$

Where:  $\alpha, \beta$  = Vectors expressed in terms of the state variables of the system.

$v$  = Designed input.

$\mathcal{T}$  = Transformation matrix.

There exist two methods to linearize a system through nonlinear feedback linearization. The first one completely linearizes the state-space equation; and hence, it is called full-state feedback linearization. The second one might partially linearize the state-space equation, and it is called input-output map feedback linearization. Both methods comprehend complex non-linear compensation strategies that have been lately applied in the control of fluid power systems.

To illustrate, Wang et al. (2007) applied input-output map feedback linearization to develop a tracking control for a pneumatic actuator. Two different cases were discussed in the publication: first, the cylinder was controlled using a five-port proportional valve; and second, the cylinder was controlled using two three-port proportional valves. Nevertheless, there was no a comparison between the results obtained using one five-port valve, and two three-port valves. The results presented correspond to the response of the cylinder when it is controlled with a five-port proportional valve. In general, although the proposed control algorithms fulfilled the design requirements, they have to be simplified for on-line implementation, which reduces accuracy to the system.

#### 1.4.5.6. Adaptive control

Similarly to nonlinear compensation control strategies, adaptive control schemes seek to adjust the behavior of a plant according to established parameters. In contrast to nonlinear compensation methods, adaptive control strategies do not focus on correct or reduce nonlinearities inherent to a system. Adaptive control methods seek to adjust the performance of a system according to operating conditions. Two main adaptive control schemes are commonly applied for the control of fluid power systems:

- Gain scheduling: When applying gain-scheduling schemes, feedback gains are defined as continuous, or piecewise continuous, functions of parameters that affect the operation of a system. A previous knowledge of those parameters is required.
- Self-tuning control: When applying self-tuning control strategies, the controller adapts automatically to the variations in plant operation conditions. A priori knowledge of the parameters that could affect the system is not required.

Adaptive control methods have been commonly applied for the control of fluid power systems. For example, fluid power applications where adaptive control methods are applied include (Edge, 1996):

- Scheduling of tuning parameters as a function of motor displacement in hydrostatic transmissions.
- Scheduling of feedback gains as a function of stroke in positioning systems.



- Scheduling of observer parameters as a function of load position in electrohydraulic servo systems.
- Automatic pole placement for a servo-hydraulic positioning system in response to changes in supply pressure.
- Self-tuning speed control for pump-driven systems.
- Self-tuning of pressure for electropneumatic systems.

Most fluid power research publications where adaptive control schemes are implemented report improvement of the performance of the controlled system. Nevertheless, disadvantages to be considered in the application of adaptive control schemes include (Edge, 1996):

- A reference model might be required to acquire priori knowledge of the parameters that affect the behavior of a plant.
- For gain-scheduling methods, the reference parameters have to be measured, which might increase the cost of the controller, and difficult its implementation.
- Self-tuning controllers might exhibit degradation of performance due to sudden changes in operating conditions.
- Discretization of a system can lead to instability due to inappropriate placement of poles or zeros in discrete-time transfer functions.

Adaptive control schemes might appear as attractive strategies for the control of fluid power systems due to the general goal for which they are designed: to adjust the dynamic behavior of fluid power system in accordance to pre-known or not known operating conditions. Nonetheless, similarly to other control schemes described before, adaptive control strategies might produce the best results in collaboration with other control strategies.

#### 1.4.5.7. Robust control

In contrast to the control strategies described before, robust control methods explicitly manage the uncertainty associated with the fluctuation of operating conditions of a system. As defined by Edge (1996), a system is robust if it experiences acceptable changes in performance due to fluctuations of its operating conditions.

Likewise, a system is called robust when it operates within acceptable ranges in despite of imperfections of its reference models (Halbaoui et al., 2011). In relation to the control of fluid power systems, two robust control strategies are commonly applied: variable structure control (VSC) and H-infinity control.

#### Variable structure control (VSC)

VSC is a high-speed switching feedback control scheme derived from the relay and bang-bang theory. VSC bases on switching a control law according to a desired control trajectory, which is delineated on a surface in the state-space. This surface is called the sliding or switching surface, from which sliding mode control (SMC) takes its name. The design of a VSC scheme has two steps (DeCarlo et al., 1988): First, design the sliding or switching surface; and second, design the control law that forces the behavior of a plant to stick to a desired trajectory.

Nevertheless, although the application of VSC theory to a particular problem most likely ensures the robustness and high quality of the resulting control scheme, the required in-depth knowledge of the plant to be controlled complicates the design process.

#### H-infinity control:

H-infinity control schemes can be defined as robust optimal control methods. In applying H-infinity control schemes, the problem to be solved is specified as a minimum-maximum optimization problem. Resembling a zero-sum game, the controller is treated as a minimizing player, and the disturbance is modeled as a maximizing player (Başar and Bernhard, 2008). H-infinity control methods are described as frequency-domain control schemes, which in contrast to classical control methods are able to handle multivariable systems.

One of the main motivations to apply H-infinity methods is in attenuating disturbances by formulating a compensation problem as the solution to a well-defined optimization problem (Zames, 1981). Nevertheless, despite of the effectiveness of H-infinity control methods, similarly to other robust control schemes, their greatest challenge is in proving the existence of a suitable control configuration (Stoorvogel, 2000). Moreover, H-infinity control schemes are known for being difficult to implement due to their high-order and intricate structure.

Furthermore, most recent publications associated with the control of pneumatic systems apply state-space feedback schemes in collaboration with robust control strategies. To illustrate, [Richer and Hurmuzlu \(2000\)](#) developed a state-space model of a high performance pneumatic force actuator; and subsequently, they applied sliding mode control (SMC) theory to derive the control laws. The performance of a full order controller was compared against the performance of a reduced order controller. The reduced order controller showed to be suitable for low-performance applications.

Similarly, [Al-Dakkan et al. \(2003\)](#) applied bimodal SMC control to design an energy-saving control for pneumatic servo systems. The most remarkable part of their work is in the use of two three-port proportional valves to inflict dissipative forces on the load without using supply power. Accordingly, through robust control strategies, the two three-port valves are coupled together to behave as a single four-port valve, which considerably reduced the power consumption of the pneumatic servo system under study.

Also applied to the control of pneumatic servo systems, [Shen and Goldfarb \(2007\)](#) applied SMC control to develop an energy saving approach that reduced the energy consumption of a modified pneumatic system by 25 to 52% in comparison to a standard configuration. Therefore, based on similar approaches and applications, robust control schemes enable fluid power systems to operate in an energy-efficient manner, and with no sacrifice of performance.

#### *1.4.5.8. Other control strategies applied in fluid power applications*

The rapid evolution of computational tools in the last 50 years has led to the creation of novel and sophisticated control strategies for engineering applications. In relation to the control of fluid power systems, some novel control strategies lately applied include:

- Genetic algorithms (GA): GA are adaptive heuristic search algorithms that seek to minimize an objective function. Genetic algorithms base on the dynamics evidenced on evolutionary processes of natural selection and genetics transmission. Based on natural selection dynamics, the implementation of GA control schemes follows three basic steps: selection, crossover, and mutation. Accordingly, GA apply the principle of survival of the fittest, by directing the search of control parameters to a region of optimal performance.

- Fuzzy logic control: Fuzzy logic is an extension of multivalued logic. It converts a set of linguistic rules into mathematical equivalent expressions. Fuzzy logic avoids the need of a mathematical representation for the system to be controlled. Control algorithms created through fuzzy logic consist of an undefined number of linguistic conditional rules, according to which, control actions are prescribed to manipulate the behavior of a system.
- Neural control: Neural control schemes derive from theories that explain the functionality of the human brain and nervous system through neural networks. As defined by [Narendra \(1996\)](#), artificial neural networks are structures formed by massively parallel interconnection of simple processors. Accordingly, in neural control schemes, a plant is represented as an artificial neural network able to correlate the effect of one or several inputs to one or several outputs.

In relation to fluid power applications, for example, [Jeon et al. \(2003\)](#) used genetic algorithms to optimize the control of a pneumatic servo cylinder. Near-optimal position, velocity, and acceleration gains were found through the implementation of GA. The authors reported using minimum information relevant to the system to find the near-optimal gains, and it was emphasized the fact that optimal values of the velocity and acceleration gains increase as the mass of the load and the reference position of the cylinder increase. In the end, the authors concluded that GA strategies were suitable for finding the optimal values of gains in PID and state-space feedback configurations applied to the control of fluid power systems.

Likewise, [Schulte and Hahn \(2003\)](#) developed a fuzzy state feedback gain scheduling control of servo-pneumatic actuators. The main design specification for the controller was to maintain the accuracy of positioning control independent of the payload and position of the piston. Local linear models were used to design the controller, and fuzzy logic was applied to schedule state-space gains. The overall results showed satisfactory performance in relation to the closed-loop dynamics. Further improvements were recommended on the basis of the application of numerical optimization techniques to tune functions composing reference design models.

Illustrating the use of neural control schemes, [Hesselroth et al. \(1994\)](#) developed a neural network control for a pneumatic robot arm. The authors used a neural network algorithm to control the position and orientation of a robotic arm, and they reported to achieve a 3-mm positioning accuracy after 200 learning steps.

Hesselroth et al. (1994) justified the application of neural network control schemes due to the highly nonlinear and hysteretic behavior of the arm. They also reported that the time required to reach a desired target was around 30 seconds, which might be too long for pneumatic applications. Nevertheless, it is highlighted the importance of the results in relation to biological control applications that seek to resemble visual brain functions.

To conclude this section, it could be emphasized the fact that most of the novel control strategies lately applied for the control of fluid power system are implemented to supplement more basic and traditional control schemes. The main goal of these innovative techniques would be on compensating the nonlinear and hysteretic dynamic characteristics of fluid power systems.

#### 1.4.6. Energy efficiency analysis

The achievement of energy efficiency could be categorized as one of the most important challenges to overcome in fluid power systems. The efficiency of fluid power systems is commonly identified as one of their most prevalent disadvantages in comparison to other power transmission technologies.

Recently, high-energy efficiency has become a requirement for the application of fluid power systems in actual applications, especially high-tech applications such as robotics. To achieve a satisfactory level of energy efficiency, control theory appears to be a viable approach to manage and monitor energy expenditure in fluid power systems.

Energy efficiency in fluid power applications is usually measured in relation to specific elements composing a system. For instance, energy efficiency is frequently measured in relation to the type of control valves and actuators used for a specific application. The following subsection reviews different approaches to quantify energy efficiency in fluid power systems.

##### 1.4.6.1. *Energy efficiency of linear actuators*

Energy efficiency relative to a linear actuator is measured in terms of the inlet and outlet pressure and flow delivered to and expelled from a control volume enclosing the actuator. Accordingly, the overall efficiency of a linear actuator quantifies the ratio of output power to input power. The following equation provides a general expression for calculating the overall efficiency of a linear actuator ( $\eta_{la}$ ).

$$\eta_{la} = \left( \frac{F\mathcal{V}}{P_i Q_i} \right)_{la} \quad (1.28)$$

Where:  $F_{la}$  = Actuator force

$\mathcal{V}_{la}$  = Actuator velocity

$P_i$  = Inlet pressure

$Q_i$  = Inlet volumetric flow

It is common in fluid power applications to express the overall efficiency of a component in terms of the volumetric and mechanical efficiencies. Hence, Eq. 1.28 can be defined as:

$$\eta_{la} = (\eta_V \eta_M)_{la} \quad (1.29)$$

From Eq. 1.29, the volumetric efficiency  $\eta_V$ , and the mechanical efficiency  $\eta_M$  of a linear actuator are given by:

$$\eta_{V\_la} = \left( \frac{A_i \mathcal{V}}{Q_i} \right)_{la} ; \quad \eta_{M\_la} = \left( \frac{F}{P_i A_i} \right)_{la} \quad (1.30)$$

Where:  $A_i$  = Area of the piston at the inlet side.

In general, the efficiencies calculated relative to a linear actuator are less than unity. Fluid compressibility and leakage affect the volumetric efficiency, while friction and viscous shear impact the mechanical efficiency (Manning, 2005). Moreover, in relation to speed and pressure, the volumetric efficiency of a linear actuator increases with speed and decreases with pressure. On the other hand, the mechanical efficiency of a linear actuator decreases with speed and increases with pressure.

#### 1.4.6.2. Energy efficiency of rotary actuators

Similarly to the analysis for linear actuators, the overall efficiency of rotary actuators is given by the ratio of output power to input power. Different expressions result from the different characteristics of rotary actuators in terms of the type of input or output power used. For instance, hydraulic pumps and air compressors receive mechanical power and produce fluid power. Conversely, hydraulic and pneumatic motors receive fluid power and produce mechanical power. For hydraulic pumps, the volumetric and mechanical efficiencies are given by:

$$\eta_{V_p} = \frac{Q_A}{Q_T} = \frac{Q_A}{V_d \omega}; \quad \eta_{M_p} = \frac{T_T}{T_A} = \frac{V_d P_o}{T_A} \quad (1.31)$$

For hydraulic motors, the volumetric and mechanical efficiencies are given by:

$$\eta_{V_m} = \frac{Q_T}{Q_A} = \frac{V_d \omega}{Q_A}; \quad \eta_{M_m} = \frac{T_A}{T_T} = \frac{T_A}{V_d P_i} \quad (1.32)$$

Where:  $Q_{A/T}$  = Actual or theoretical (ideal) volumetric flow produced.

$T_{A/T}$  = Actual or theoretical (ideal) shaft torque.

$V_d$  = Volumetric displacement.

$P_o$  = Outlet pressure.

$\omega$  = Angular velocity of the pump shaft.

It must be noted that the efficiency equations for a hydraulic pump are the reciprocals of the efficiency equations for a hydraulic motor. Similar equations could be applied to pneumatic rotary actuators depending on their physical configuration; nevertheless, expressions derived from thermodynamic analysis are commonly applied in relation to pneumatic systems, as it will be described in following sections.

#### 1.4.6.3. Energy efficiency of control valves

The quantification of efficiency in control valves might strictly depend on their geometry. In general terms, the overall efficiency is also given by the ratio of the useful output power to the supplied input power. The overall efficiency of a control valve ( $\eta_{cv}$ ) can also be expressed in terms of two factors, a volumetric efficiency  $\eta_V$ , and a pressure efficiency  $\eta_P$ . Hence, the overall efficiency for a control valve is given by:

$$\eta_{cv} = (\eta_V \eta_P)_{cv} \quad (1.33)$$

In Eq.1.33, the volumetric efficiency and the pressure efficiency can be expressed as:

$$\eta_V = \frac{Q_d}{Q_u}; \quad \eta_P = \frac{P_d}{P_u} \quad (1.34)$$

Where:  $Q_{d/u}$  = Volumetric flow at the downstream/upstream side of the valve.

$P_{d/u}$  = Pressure at the downstream/upstream side of the valve.

A reference to a specific formula to calculate the efficiency of a valve depending on its geometry is not included in this section. Instead, a more general formula derived from thermodynamic precepts might be more practical. Hence, the following subsection, the last one of this chapter, defines some fundamental concepts related to exergy analysis, as an approach that could assist in assessing the efficiency of a pneumatic systems in a more practical way.

#### 1.4.6.4. *Exergy efficiency of fluid power systems*

As already defined in the statement of the problem, the exergy of a system is the maximum amount of theoretical work that could be obtained from a transformation that brings the system into equilibrium with a reference state (Moran and Shapiro, 2008). In more general terms, exergy could be understood as the potential of a system to be used in accomplishing a specific goal.

In contrast to the energy conservation law, which states that energy cannot be destroyed, the exergy concept bases on the fact that exergy is not conserved. Exergy is destroyed due to so-called irreversibilities, such as heat transfer, friction, and inelastic deformation, among others. Likewise, exergy is transferred to or from a system in the form of heat, work, or mass flow. Hence, the importance of the exergy concept in relation to fluid power systems centers on the identification of segments of a system where exergy destruction and losses occur. In that way, by identifying the most sensitive parts of a system, specific strategies could be applied to enhance its overall performance. Two main concepts have to be defined to carry out an exergy analysis:

- Exergy reference environment: An exergy reference environment comprehends a large portion of the surroundings of a system, unaffected by interactions of any kind between the system and its immediate surroundings. Intensive properties of an exergy reference environment, such as pressure and temperature, do not change as the system interacts with its immediate surroundings.
- Dead state: After a system reaches equilibrium with a reference environment, this system is called to be in the dead state. At the dead state, the exergy of a system is zero because there is no more potential to develop work by taking the system into equilibrium with its reference environment. Thus, the dead state of a system is the state of equilibrium with its reference environment.



Once the notions of reference environment and dead state are understood, the exergy of a system ( $\mathbb{E}$ ) at a specific state can be found by applying the following expression:

$$\mathbb{E} = (E - U_0) + p_0(V - V_0) - T_0(S - S_0) \quad (1.35)$$

Where:  $\mathbb{E}$  = Exergy

$E, V, S$  = Energy, volume and entropy of the system at a given state.

$U_0, V_0, S_0$  = Internal energy, volume and entropy of the system at the dead state.

$p_0, T_0$  = Pressure and temperature of the reference environment, respectively.

Moreover, for a closed system, the exergy balance is given by:

$$\mathbb{E}_2 - \mathbb{E}_1 = \int_1^2 \left(1 - \frac{T_0}{T_b}\right) \delta Q - [W - p_0(V_2 - V_1)] - T_0\sigma \quad (1.36)$$

Where:  $T_b$  = Temperature of the system boundary.

$\sigma$  = Entropy produced by internal irreversibilities.

Eq. 1.36 is fundamental for exergy analysis because it establishes the basis to understand the dynamic behavior of a system in terms of exergy not being conserved. Accordingly, Eq. 1.36 can be divided in three exergy forms: exergy transfer accompanying heat ( $\mathbb{E}_Q$ ), exergy transfer accompanying work ( $\mathbb{E}_W$ ), and exergy destroyed ( $\mathbb{E}_d$ ). These three forms of exergy are respectively represented by:

$$\begin{aligned} \mathbb{E}_{Q1-2} &= \int_1^2 \left(1 - \frac{T_0}{T_b}\right) \delta Q; & \mathbb{E}_{W1-2} &= [W - p_0(V_2 - V_1)] \\ \mathbb{E}_d &= T_0\sigma \end{aligned} \quad (1.37)$$

On the other hand, the exergy rate balance for a control volume is:

$$\frac{d\mathbb{E}_{c.v}}{dt} = \sum_j \left(1 - \frac{T_0}{T_j}\right) \dot{Q}_j - \left[\dot{W}_{c.v} - p_0 \frac{dV_{c.v}}{dt}\right] + \sum_i \dot{m}_i \mathbf{e}_{fi} - \sum_o \dot{m}_o \mathbf{e}_{fo} - \dot{\mathbb{E}}_d \quad (1.38)$$

Where:  $\mathbf{e}_{fi/o}$  = Specific flow exergy at an inlet (i) or outlet (o).

$\dot{\mathbb{E}}_d$  = Rate of exergy destruction.

Eq. 1.37 includes a new form of exergy, exergy accompanying mass flow. The time rate of exergy transfer accompanying mass flow ( $\dot{\mathbb{E}}_m$ ) is:

$$\dot{\mathbb{E}}_{m_{i-o}} = \sum_{i/o} \dot{m}_{i/o} e_{fi/o} \quad (1.39)$$

The specific flow exergy term, which accounts for exergy transfer accompanying mass flow across the boundaries of a control volume is defined by:

$$e_f = (e - u_0) + p_0(v - v_0) - T_0(s - s_0) + (pv - p_0v) \quad (1.40)$$

Where:  $e, v, s$  = Specific energy, volume and entropy at a given state, respectively.

$u_0, v_0, s_0$  = Specific internal energy, volume and entropy at the dead state.

Furthermore, an expression for the exergetic efficiency of fluid power systems can be derived from the application of exergy rate balances relative to the components included in a specific system. In general terms, by considering a control volume at steady state, and by assuming no heat transfer between a control volume and its surroundings, the exergy rate balance reduces to:

$$0 = -\dot{W}_{c.v.} + \sum_i \dot{m}_i e_{fi} - \sum_o \dot{m}_o e_{fo} - \dot{\mathbb{E}}_d \quad (1.41)$$

For a system of one input and one output, where exergy decreases as the system develop work, Eq. 1.41 becomes:

$$e_{f1} - e_{f2} = \frac{\dot{W}_{c.v.}}{\dot{m}} + \frac{\dot{\mathbb{E}}_d}{\dot{m}} \quad (1.42)$$

Applied to fluid power systems, Eq. 1.42 would apply to control valves of certain geometry, linear and rotary actuators, and connective tubing. Eq. 1.42 accounts for the decrease in flow exergy from the inlet to the exit of a specific component or system. Moreover, the physical meaning of Eq. 1.42 for fluid power systems centers on the fact that the flow of exergy might decrease as control valves and actuators develop work, and as exergy is destroyed due to irreversibilities, such as friction.

Hence, a parameter to measure how effectively the decrease of flow exergy contributes to produce a desired output is represented by an efficiency  $\varepsilon$  of the form:

$$\varepsilon = \frac{\dot{W}_{c.v.}/\dot{m}}{e_{f1} - e_{f2}} \quad (1.43)$$

The efficiency represented by Eq. 1.43 is an exergetic efficiency that can be applied to assess the effectiveness of the use of energy in certain fluid power applications. Nevertheless, in the case of pumps and compressors, for example, since the flow of exergy would increase with the exergy input to the pump, the exergetic efficiency would become:

$$\varepsilon = \frac{e_{f2} - e_{f1}}{(-\dot{W}_{c.v.}/\dot{m})} \quad (1.44)$$

Accordingly, as verified from Eq. 1.43 and 1.44, there is no a unique exergetic efficiency expression. It has to be found according to the characteristics of the system under analysis. In relation to fluid power systems, few authors have applied the exergy concept to assess the effectiveness of the expenditure of energy in relation to fluid power components.

[Harris et al. \(2013\)](#) applied exergy analysis to optimize the monitoring and quantification of energy expenditure in compressed air systems. They assert that the exergy approach is more suitable for air-compressed systems because the energy approach highly misrepresents the large amount of potential work available in pressurized air.

Moreover, [Petrilean et al. \(2009\)](#) also applied exergy analysis to determine the exergetic efficiency of a pneumatic installation. They treated air compression as a polytropic process, and exergy analysis was used to quantify the weight of energy losses. Besides, the exergetic efficiency of the pneumatic installation was calculated relative to a compressor and a pneumatic network, and it was used as a judgment parameter for technical and financial decisions.

Therefore, the potential of exergy analysis in relation to fluid power systems, especially pneumatic systems, might be represented by a more accurate identification of exergy losses. Indeed, in terms of the achievement of efficiency, the identification of energetically critical processes or components might be crucial for innovation in fluid power systems. The success of the strategies applied to control fluid power systems might ultimately also depend on the inclusion of energy-saving considerations for the design and implementation of control algorithms.

## CHAPTER II

### SYSTEM MODELING

#### Fluid Power System Dynamics

System dynamics focuses on the modeling, simulation, and analysis of complex systems for the understanding and manipulation of their behavior and performance over time. The study of system dynamics as a discipline embraces a diverse set of scientific fields. Indeed, system dynamics is broadly applied for the study and analysis of multifaceted problems in economics, logistics, law, and natural sciences among others. In relation to fluid power engineering, system dynamics examines the relationships between pressure, flow, and the translational, rotational or angular displacement of fluid power components.

This chapter centers on the identification and formulation of the differential equations necessary to characterize and influence the behavior of a pneumatic system. Due to the compressibility of air, the relationships between flow and pressure in pneumatic components are non-linear and highly influenced by the variation of the state variables of the system over time. Accordingly, thermodynamics and fluid mechanics relationships have to be combined to completely account for the response of pneumatic systems through time.

The mathematical models and formulations identified in this chapter cover the transient variation of flow and pressure in basic components of pneumatic systems. The system under analysis composes of a pneumatic cylinder, two proportional control valves, and connective tubing. Relationships affecting the displacement of the piston in relation to the pressure and flow in the cylinder chambers are crucial in the development of tracking and positioning control schemes. A model for the proportional control valves correlates the flow from the valves to a valve effective discharge area. In the modeling of lengthy connective tubing, the proposed formulation derives from the Navier-Stokes equations of momentum and continuity. As an alternative for avoiding intensive computation in the solution of the Navier-Stokes equations, this formulation includes an approximation based on a second-order linear filter.

The consideration of lengthy connective tubing aims to identify the effects of the pressure drop and time delay in the transmission of flow from pneumatic control valves to remotely positioned pneumatic actuators. The identification of such effects will influence the design of a control algorithm called to compensate and attenuate the fallouts of the compressibility of air in pneumatic systems.

### 2.1. Modeling of the proportional control valves

The characterization of the performance of pneumatic proportional control valves depends on the configuration of the components of a particular valve design. For the comprehensive description of the static and dynamic performance of a proportional valve, its model could be divided into three subsystems: the electromagnetic, the mechanical and the pneumatic subsystems. Sorli et al. (2010) applied this approach to produce a mechatronic model of a pneumatic proportional valve (model VEF-3121, SMC, Japan) similar to the ones used for the study and analysis reported in this thesis.

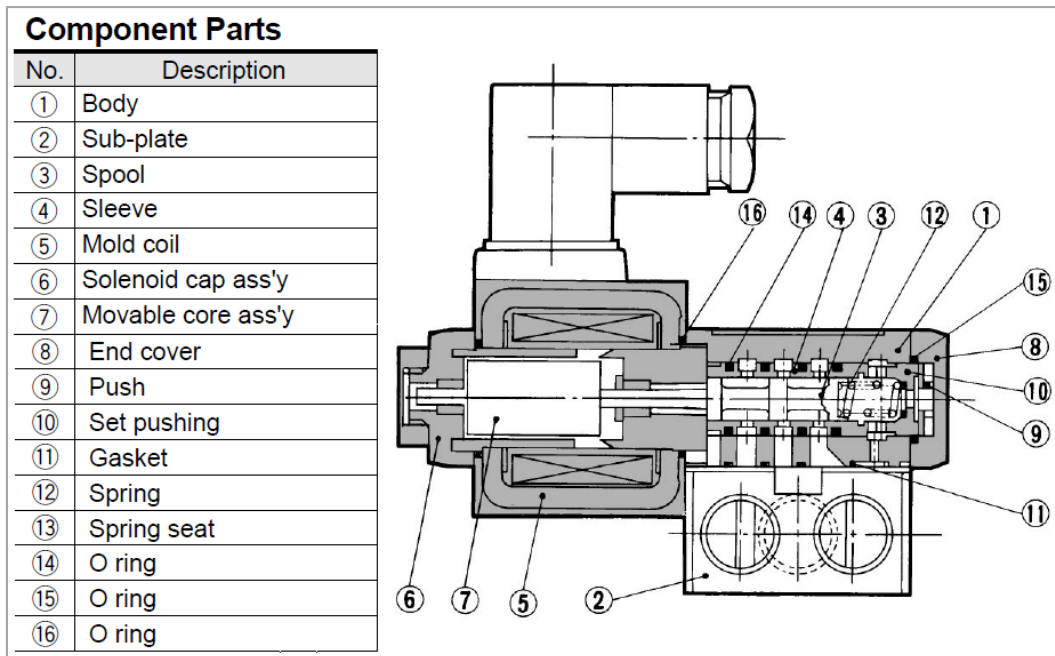


**Figure 2.1.** Type SMC VEF 3121 pneumatic proportional valve

[Source: <http://content2.smcetech.com/pdf/VEP.pdf>]

For controller design and position control of pneumatic actuators, the model of the valve could be limited to the characterization of the mechanical and pneumatic subsystems (Beater, 2007; Wang, et al. 2001). This thesis centers on the analysis and modeling of the mechanical and pneumatic subsystems of the valve; nonetheless, the model for the electromagnetic subsystem is included as reference for the analysis of the overall performance of proportional control valves.

### 2.1.1. Electromagnetic dynamics

Electromagnetic dynamics for a proportional flow control valve define the relationship between the voltage applied and the electromagnetic force generated. The electromagnetic subsystem of the valve studied consists of an electric coil, and a fixed and movable iron armatures separated by an air gap. Sorli et al. (2010) applied the following equation to define the electrodynamic equilibrium between the electric and magnetic parts composing the solenoid of the valve.

$$V_{PWM} = R_c i_c + \frac{d\psi(i_c, x_a)}{dt} \quad (2.1)$$

Where:  $V_{PWM}$  = Pulse width modulated input voltage.

$R_c$  = Coil resistance.

$i_c$  = Coil Current.

$x_a$  = Armature displacement.

$\psi(i_c, x_a)$  = Magnetic flux linkage.

According to Eq. 2.1, the input voltage applied at the connectors of the valve generates the current and the magnetic flux linkage responsible to generate the electromagnetic force required to move the spool of the valve. Sorli et al. (2010) defined the electromagnetic force as follows:

$$F_m(i, x_a) = \frac{\partial W'(i, x_a)}{\partial x_a}; \quad W'(i, x_a) = \int_0^i \psi(i, x_a) di \quad (2.2)$$

Where:  $F_m(i, x_a)$  = Electromagnetic force.

$W'(i, x_a)$  = Magnetic co-energy.

The magnetic co-energy is a non-physical quantity used to quantify the derivation of magnetic energy with respect to a virtual rigid displacement of the armature of the valve (Delfino et al., 2001). Nevertheless, for controller design purposes, the electromagnetic force can be expressed as the product of the coil current and a coil force coefficient, as Richer and Hurmuzlu (2010) reported.

### 2.1.2. Mechanical dynamics

From the free body diagram for the spool of the valve, as represented in figure 2.2, by applying Newton's second law in order to determine the dynamic equilibrium of the forces acting on the spool of the valve, the following equation is obtained:

$$M_s \ddot{x}_s + B_s \dot{x}_s + k_s(x_s - x_{0s}) + F_{Cf} = F_m \quad (2.3)$$

Where: $M_s$ = Coil and spool assembly mass.	$x_{0s}$ = Spring pre-compression displacement.
$B_s$ = Viscous friction coefficient.	$x_s$ = Spool displacement.
$k_s$ = Spring stiffness coefficient.	$\dot{x}_s$ = Spool velocity.
	$\ddot{x}_s$ = Spool acceleration.
	$F_{Cf}$ = Coulomb friction force.
	$F_m$ = Electromagnetic force.

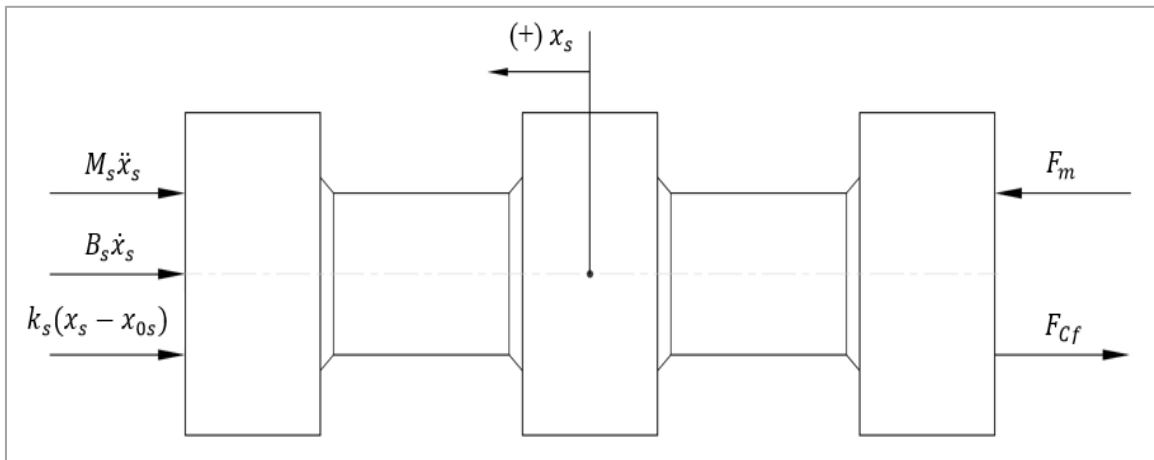


**Figure 2.2.** Free body diagram for the spool of the valve

By considering the equilibrium point at which the position, velocity and acceleration of the spool, and the electromagnetic force are zero, it is obtained:

$$k_s x_{0s} = F_{cf} \quad (2.4)$$

Indeed, the application of particular dither signals to the coil should minimize the Coulomb friction at the point that it could be neglected. Dither signals applied to minimize the Coulomb friction have small magnitude and frequency equivalent to the bandwidth of the valve (Richer and Hurmuzlu, 2000).

Accordingly, Eq. 2.3 becomes:

$$M_s \ddot{x}_s + B_s \dot{x}_s + k_s x_s = F_m \quad (2.5)$$

Eq. 2.5 is useful in expressing the overall model for the pneumatic systems in terms of the valve's coil current as the control command.

### 2.1.3. Pneumatic dynamics

The mathematical model describing the pneumatic dynamics of the valve correlates the air flow rate relative to the displacement of the spool of the valve, to the pressure profiles at the inlet and outlet ports of the valve. The standard equation describing the compressible mass flow rate ( $\dot{m}$ ) through a valve orifice is given by (Ben-Dov and Salcudean, 1995; Richer and Hurmuzlu, 2000; Wang et al., 2001; Al-Dakkan et al., 2003):

$$\dot{m} = \frac{C_D A_v P_{uv}}{\sqrt{RT}} \Phi_f \quad (2.6)$$

Where:  $A_v$  = Effective area of the valve orifice.

$C_D$  = Discharge coefficient.

$P_{uv}$  = Upstream Pressure.

$T$  = Fluid Temperature.

$R$  = Specific gas constant (For dry air,  $R = 287.058$  J/kgK).

$\Phi_f$  = Constant depending on the downstream ( $P_{dv}$ ) and upstream ( $P_{uv}$ ) pressures.



Then, from the ideal gas law and the relationship between the mass flow rate ( $\dot{m}$ ) and the volumetric flow rate (Q):

$$P = \rho RT; \quad \dot{m} = \rho Q \quad (2.7)$$

Where:  $\rho$  = Density of the fluid.

Assuming the temperature remains constant, by substituting Eq. 2.7 in Eq. 2.6, the compressible volumetric flow rate through a valve can be written as:

$$Q = \frac{C_D A_v \sqrt{RT}}{P_{rv}} \Phi_f \quad (2.8)$$

Where:  $P_{rv}$  = Downstream to upstream pressure ratio.

The constant  $\Phi_f$  accounts for the fact that the flow could depend linearly on the upstream pressure, or it could depend nonlinearly on the upstream and downstream pressures. If the flow attains sonic velocity, it will depend linearly on the upstream pressure; and the downstream to upstream pressure ratio will be smaller than a critical value represented by  $C_{cr}$ . In contrast, if the pressure ratio is larger than the critical value,  $C_{cr}$ , the flow will depend nonlinearly on both pressures, upstream and downstream pressures (Richer and Hurmuzlu, 2000). The flow that depends linearly on the upstream pressure is denominated choked flow, while the flow that depends non-linearly on upstream and downstream pressures is called unchoked flow.

The constant  $\Phi_f$  is defined by:

$$\Phi_f = \begin{cases} C_1 & \text{if } P_{rv} \leq C_{cr} \\ C_2 \sqrt{P_{rv}^{2/k} - P_{rv}^{(k+1)/k}} & \text{if } P_{rv} > C_{cr} \end{cases} \quad (2.9)$$

Where:  $k$  = Specific heat ratio (For air,  $k = 1.4$ )

The downstream to upstream pressure ratio,  $P_{rv}$ , and the critical value,  $C_{cr}$ , are given by:

$$P_{rv} = P_{dv}/P_{uv}; \quad C_{cr} = [2/(k + 1)]^{k/(k-1)} \quad (2.10)$$

Moreover, the no dimensional constants,  $C_1$  and  $C_2$ , are specific for the fluid used, and they are expressed as follows.

$$C_1 = \sqrt{k[2/(k+1)]^{(k+1)/(k-1)}}; \quad C_2 = \sqrt{2k/(k-1)} \quad (2.11)$$

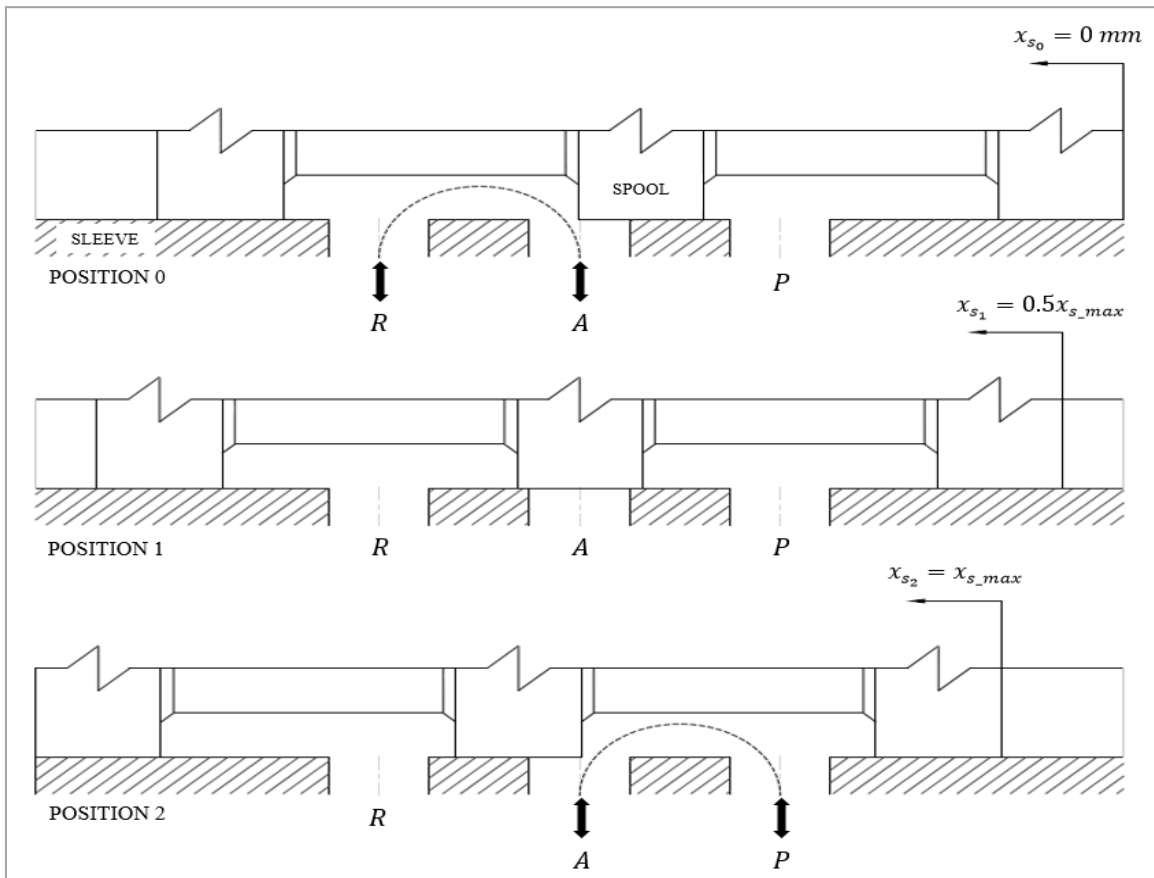
For air:  $C_1 = 0.68473$ ,  $C_2 = 2.64575$  and  $C_{cr} = 0.52828$

Then, the flow rate at the outlet of the valve (port A) can be expressed as the difference between the flows through the input ( $P \rightarrow A$ ) and exhaust ( $A \rightarrow R$ ) paths of the valve (Sorli et al., 2010); accordingly:

$$Q_{v-A} = Q_{P \rightarrow A} - Q_{A \rightarrow R} \quad (2.12)$$

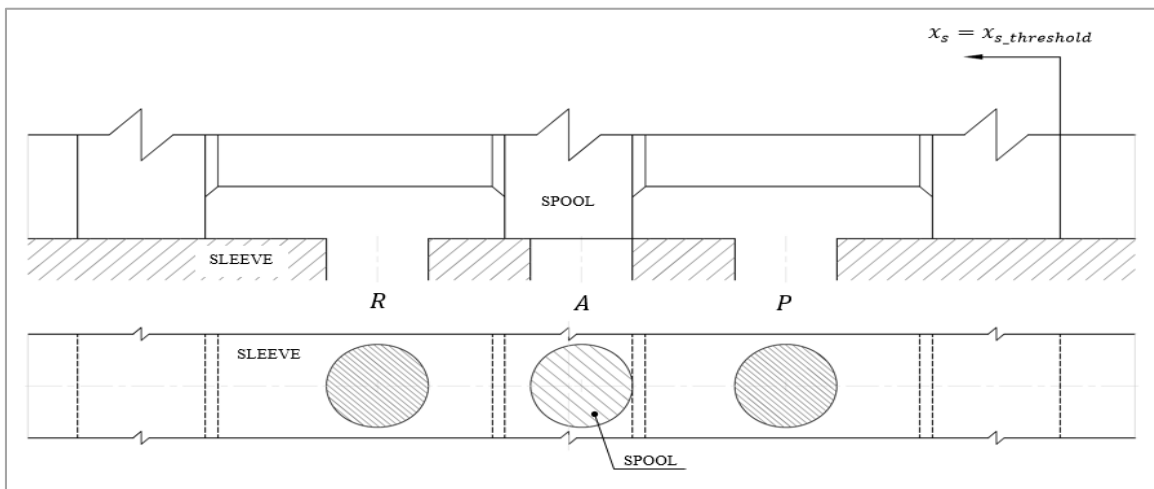
$$Q_{v-A} = \frac{C_D \sqrt{RT}}{P_R} [(A_v \phi_f)_{P \rightarrow A} - (A_v \phi_f)_{A \rightarrow R}] \quad (2.13)$$

Figure 2.3 illustrates the operating positions of the spool of the valve. The different positions are defined in terms of the maximum displacement of the spool,  $x_{s-max}$ .



**Figure 2.3.** Operating positions of the spool in relation to the orifices in the sleeve of the valve

From figure 2.3 it is verified that: at position 0 the output (A) and the exhaust (R) ports are connected, at position 1 the output port is completely closed, and at position 2 the output and supply (P) ports are connected. Hence, the input flow to the pneumatic system varies from zero at positions 0 and 1, to the maximum input flow at position 2. As it will be noticed later, it will be important to define the minimum signal required to position the spool of the valve at the point where the output flow becomes higher than zero ( $x_{s-threshold}$ ), as this point represents the lower boundary for input control.



**Figure 2.4.** Spool position at the lower boundary for input control

In their publication, [Sorli, et al. \(2010\)](#) showed that the orifices of the valve correspond to radial holes in the sleeve of the valve. Thus, the effective area of the valve is given by the position of the spool relative to the set of radial holes in the sleeve.

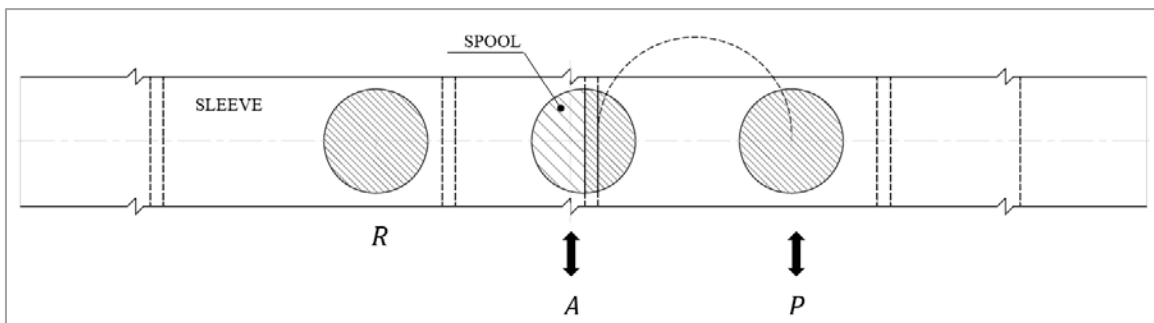


**Figure 2.5.** Effective area defined by the coupling between the spool and the sleeve of the valve at position 2

The effective area defined by the coupling between the spool and the sleeve of the valve corresponds to the area of a circular segment. In terms of the position of the spool ( $x_s$ ), the active effective area ( $A_{v-act}$ ) of the valve is expressed as:

$$A_{v-act} = N_{Ao} \left[ R_{Co}^2 \arccos \left( 1 - \frac{x_s}{R_{Co}} \right) - (R_{Co} - x_s) \sqrt{x_s(2R_{Co} - x_s)} \right] \quad (2.14)$$

Where:  $N_{Ao}$  = Number of active orifices in the sleeve of the valve.

$R_{Co}$  = Radius of the circumference of an orifice in the sleeve of the valve.

Figure 2.6 portrays the circular segment corresponding to the maximum effective area for one of the orifices in the spool of the valve.

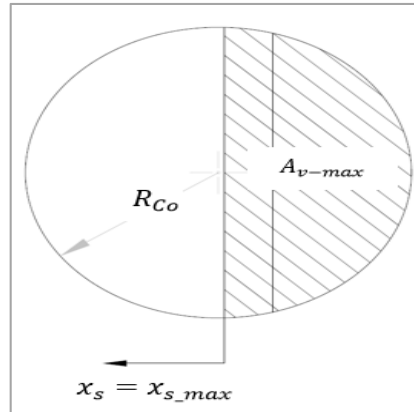


**Figure 2.6.** Maximum effective are for one orifice in the sleeve of the valve

Since Eq. 2.14 is highly non-linear, in order to find a linear expression for the effective area of the valve, the maximum effective area of each orifice might be approximated to the area of a rectangle. The width of this rectangle would correspond to the displacement of the spool, while the length ( $\ell_{Av}$ ) of the rectangle would be given by:

$$\ell_{Av} = \frac{A_{v-max}}{N_o(x_{s-max} - x_{s-threshold})} \quad (2.15)$$

Where:  $A_{v-max}$  = Maximum effective area of the valve ( $A_{v-max} = 12 \text{ mm}^2$ ).

$x_{s-max}$  = Maximum displacement of the spool of the valve.

$x_{s-threshold}$  = Lower boundary for input control.

From Eq. 2.15, the active effective area of the valve becomes:

$$A_{v-act} = x_s \ell_{Av} \quad (2.16)$$

Eq. 2.16 provides an approximation of the dynamic behavior of the valve, and it is suitable for linear control schemes; nevertheless, it reduces accuracy to the system and increases the tracking error. The effects of this approximation will be verified through simulation and validation of the models for the pneumatic system.

Independently of the expression relating the effective area to the displacement of the spool of the valve, an active and a passive region are identified for the input and exhaust paths. These regions are determined by:

$$A_{v-Input} = (A_v)_{P \rightarrow A} = \begin{cases} 0 & \text{if } 0 \leq x_s < x_{s-threshold} \\ A_{v-act} & \text{if } x_s \geq x_{s-threshold} \end{cases} \quad (2.17)$$

$$A_{v-Exhaust} = (A_v)_{A \rightarrow R} = \begin{cases} A_{v-act} & \text{if } 0 \leq x_s < (x_{s-max} - x_{s-threshold}) \\ 0 & \text{if } x_s \geq (x_{s-max} - x_{s-threshold}) \end{cases} \quad (2.18)$$

For the design of the controller, active and passive modes will be considered as an approach to find the optimum combination of control states. It might be expected that the maximum speed response will be achieved by switching the extension and retraction valves from an active to a passive mode alternatively. Further analysis and simulation should help to prove whether the independent control of the valves provides better stability than the use of a unique input to control both valves.

## 2.2. Modeling of pressure dynamics relative to the cylinder chambers

The development of the model describing the pressure dynamics relative to the cylinder chambers is based on the following assumptions:

- Air is a perfect gas.
- The temperature and pressure inside each chamber are homogeneous.
- Kinetic and potential energy of air are negligible.
- The process of pressure changes in the cylinder chambers is adiabatic because the pressure dynamics are fast relative to the heat transfer dynamics.

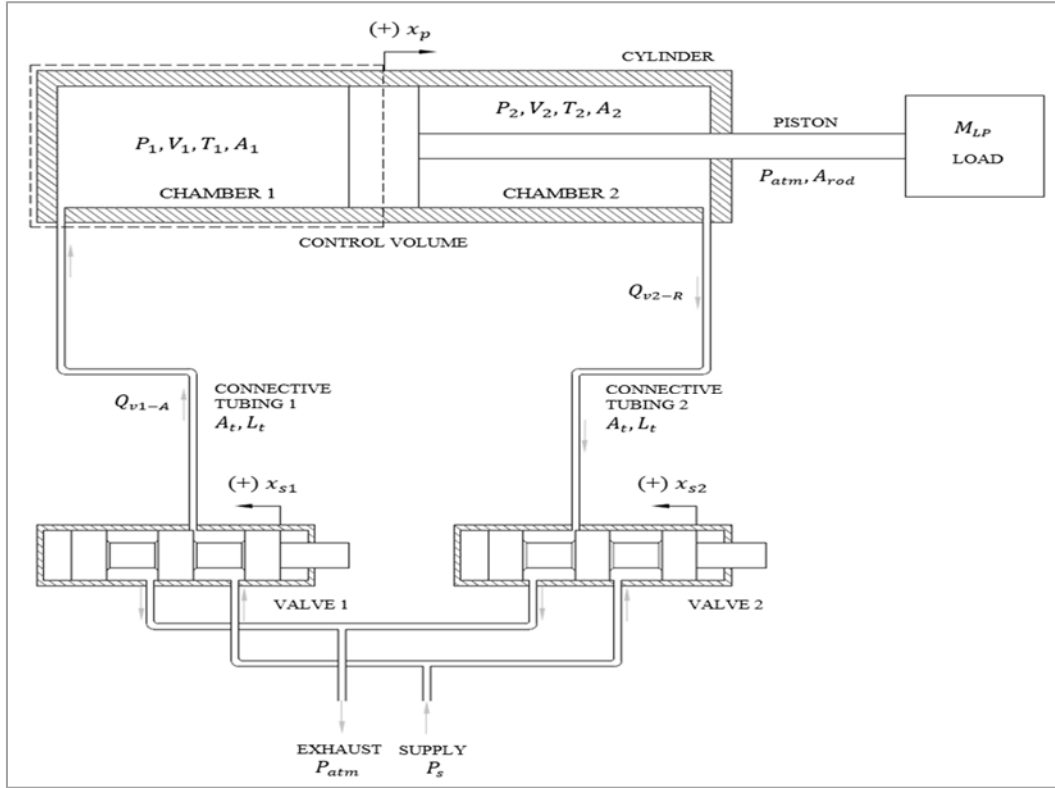


**Figure 2.7.** Schematic representation of the pneumatic system

Subsequently, based on figure 2.6, by defining any of the cylinder chambers as a control volume  $V$ , the conservation of mass is expressed applying the continuity equation as follows:

$$\dot{m} = \frac{d}{dt}(\rho V) \quad (2.19)$$

By solving the time derivative ( $d/dt$ ) in Eq. 2.19, it is obtained:

$$\dot{m} = \dot{\rho}V + \rho\dot{V} \quad (2.20)$$

Moreover, from the definition of the bulk modulus ( $\kappa$ ) as an indicator of the compressibility of air, the change of the volume of the fluid due to the change of pressure is defined by:

$$\kappa = \rho \frac{\dot{P}}{\dot{\rho}} \quad (2.21)$$

Where:  $\dot{P}$  = Rate of change of pressure.

$\dot{\rho}$  = Rate of change of density.

By substituting Eq. 2.21 in Eq. 2.20, and considering the relationship between the mass flow rate and the volumetric flow rate, it is obtained:

$$Q = \rho \dot{m}; \quad Q = \frac{V}{\kappa} \dot{P} + \dot{V} \quad (2.22)$$

Where:  $\dot{V}$  = Rate of change of volume.

In addition, since the continuity equation considers the mass flows entering and leaving the cylinder chamber, Eq. 2.22 can be expressed as:

$$Q_{in} - Q_{out} = Q_{v-A} = \frac{V}{\kappa} \dot{P} + \dot{V} \quad (2.23)$$

Where,  $Q_{v-A}$  would be the flow rate at the outlet of the valve, as defined in Eq. 2.14.

Furthermore, independently of the origin of the displacement of the piston ( $x_p$ ), the volume of each chamber can be expressed as:

$$V_i = V_{0i} \pm x_p A_i \quad (2.24)$$

Where:  $A_i$  = Piston active area for the chamber.

$V_{0i}$  = Initial volume in the cylinder chambers.

Hence, taking the derivative of Eq. 2.24 and substituting it in Eq. 2.23, it results:

$$Q_{v-A} = \frac{V_{0i} \pm x_p A_i}{\kappa} \dot{P} \pm \dot{x}_p A_i \quad (2.25)$$

Subsequently, by expressing Eq. 2.25 in terms of the time derivative of pressure, the equations describing the change of pressure in each cylinder chamber are given by:

$$\dot{P}_1 = \kappa_1 (Q_{v1-A} - \dot{x}_p A_1) / (V_{01} + x_p A_1) \quad (2.26)$$

$$\dot{P}_2 = \kappa_2 (Q_{v2-A} + \dot{x}_p A_2) / (V_{02} - x_p A_2) \quad (2.27)$$

Where subscript 1 and 2 correspond to the cylinder chambers connected to the valve 1 and 2, respectively. It has to be noted that these equations apply when the cylinder chamber 1 is the drive chamber. Nevertheless, in case of the chamber 2 being the drive chamber, the signs in Eq. 2.26 and 2.27 have to be switched, and the initial volume in the chamber has to be redefined.

Further simplification of Eq. 2.25 can be achieved, by considering an initial position for the cylinder where the initial volumes in the cylinder chambers are equal. This approach is commonly applied by definition of the origin of the piston displacement at the middle of the piston stroke (Richer and Hurmuzlu, 2000) (Wang et al., 2001).

It has to be noticed that the bulk modulus still depends on the variation of pressure and temperature; accordingly, from the first law of thermodynamics, and the fact that the internal energy of air, treated as an ideal gas, is a state variable that depends on temperature:

$$dU = dQ - PdV; \quad dU = nC_v dT \quad (2.28)$$

Where:  $U$  = Internal energy.

$Q$  = Heat.

$C_v$  = Molar heat capacity at constant volume.

Correlating the expressions for internal energy, and taking into consideration the assumption that the process is adiabatic ( $dQ = 0$ ), it is obtained:

$$dU = nC_v dT = -PdV; \quad (2.29)$$

Moreover, from the ideal gas law:

$$PV = nRT; \quad nRdT = (VdP + PdV) \quad (2.30)$$

Where:  $n$  = Number of moles.

Substituting Eq. 2.30 in Eq. 2.29, the resulting expression is:

$$C_v V dP = -(R + C_v) P dV \quad (2.31)$$

Additionally, from the relationship between the molar heat capacities at constant pressure and constant volume, and the definition of the specific heat ratio,  $k$ :

$$C_p = C_v + R; \quad k = \frac{C_p}{C_v} \quad (2.32)$$

Where:  $C_p$  = Molar heat capacity at constant pressure.



Combining Eq. 2.31 and Eq. 2.32, it is verified that the bulk modulus for an adiabatic process is directly proportional to the pressure by a factor corresponding to the specific heat ratio.

$$\kappa = -V \frac{dP}{dV} = kP \quad (2.33)$$

Hence, Eq. 2.26 and Eq. 2.27 become:

$$\dot{P}_1 = kP_1(Q_{v1-A} - \dot{x}_p A_1)/(V_{01} + x_p A_1) \quad (2.34)$$

$$\dot{P}_2 = kP_2(Q_{v2-A} + \dot{x}_p A_2)/(V_{02} - x_p A_2) \quad (2.35)$$

The expressions described by Eq. 2.34 and Eq. 2.35 would enable the model for the pneumatic system to describe different heat transfer characteristics during the extension and retraction of the cylinder. For instance, the idealization of an isothermal process for the expansion and compression of air inside the cylinder would be represented by a specific heat ratio equal to one,  $k = 1$ . Accordingly, for an isothermal process, the resulting bulk modulus would correspond to the pressure of the system,  $\kappa = P$ .

### 2.3. Modeling of force dynamics relative to the cylinder piston

From figure 2.7, by applying Newton's second law relative to the piston of the cylinder, the force dynamics are described by:

$$M_{PL}\ddot{x}_p + D_{vsc}\dot{x}_p + F_{sc} + F_{ex} = P_1 A_1 - P_2 A_2 - P_{atm} A_{rod} \quad (2.36)$$

Where:  $M_{PL}$  = Combined mass of the piston and rod assembly and the external load.

$D_{vsc}$  = Viscous friction coefficient.

$F_{sc}$  = Combined static and dynamic friction force.

$\dot{x}_p$  = Piston Velocity.

$\ddot{x}_p$  = Piston Acceleration.

$P_{atm}$  = Atmospheric pressure.

$A_{rod}$  = Piston rod area.

$F_{ex}$  = External force.

Assuming there is no external force, Eq. 2.36 becomes:

$$M_{PL}\ddot{x}_p + D_{vsc}\dot{x}_p + F_{sc} = P_1A_1 - P_2A_2 - P_{atm}A_{rod} \quad (2.37)$$

The external force is assumed to be negligible since it would correspond to the force required for the piston to overcome its own inertia and the inertia of the linear potentiometer to which the piston is connected for experimentation. Nevertheless, it might be necessary to assign a specific value to this parameter, which will be verified through experimentation.

Since the pressures  $P_1$  and  $P_2$  in Eq. 2.32 and Eq. 2.33 correspond to absolute values, from the relationship between absolute pressure and gauge pressure ( $P_g$ ), and the difference of the piston effective areas:

$$P = P_g + P_{atm}; \quad A_1 - A_2 = A_{rod} \quad (2.38)$$

Eq. 2.37 becomes:

$$M_{PL}\ddot{x}_p + D_{vsc}\dot{x}_p + F_{sc} = P_{g1}A_1 - P_{g2}A_2 \quad (2.39)$$

Furthermore, since  $F_{sc}$  represents the combination of static and dynamic friction forces, it is position and velocity dependent. This combined friction force can be expressed as:

$$F_{sc} = \begin{cases} F_{sc-Static} & \text{if } \dot{x}_p = 0 \\ F_{sc-Dynamic} & \text{if } \dot{x}_p \neq 0 \end{cases} \quad (2.40)$$

The static component of the friction force  $F_{sc-Static}$  plays its role when the velocity and acceleration of the piston are zero, it is when the piston reaches a steady state, or when it is about to move after an input is applied. Hence, the following expression derives from Eq. 2.40.

$$F_{sc-Static} = (P_{g1}A_1 - P_{g2}A_2)|_{Steady-State} \quad (2.41)$$

In Eq. 2.41, the pressure forces at steady-state would correspond to the pressure in the chambers of the cylinder exactly before the piston moves. Correlating this expression with the lower boundary for input control,  $x_{s-threshold}$  defined in section 2.1.3, Eq. 2.41 becomes:

$$F_{sc-Static} = (P_{g1}A_1 - P_{g2}A_2)|_{x_s-threshold} \quad (2.42)$$

It has to be noticed that the lower boundary for input control during extension of the cylinder differs from the lower boundary during retraction; accordingly, since the active area of the cylinder for retraction is smaller than the area for extension, the static component of the friction force during retraction is higher than the static component of the friction force during extension.

In addition, the dynamic component of the friction force can be defined according to the following expression (Richer and Hurmuzlu, 2000) (Wang et al., 2001):

$$F_{SC-Dynamic} = K_{SCD} \text{sign}(\dot{x}_p) \quad (2.43)$$

Where,  $K_{SCD}$  is the actual value of the dynamic component of the friction force, and  $\text{sign}(\dot{x}_p)$  is a function defined by:

$$\text{sign}(\dot{x}_p) = \begin{cases} -1 & \text{if } \dot{x}_p < 0 \\ 0 & \text{if } \dot{x}_p = 0 \\ +1 & \text{if } \dot{x}_p > 0 \end{cases} \quad (2.44)$$

Several authors have formulated friction models seeking to simplify the dynamic simulation of pneumatic cylinders. For example, Fleischer (1995) proposed the following expressions to calculate the static and dynamic component of the friction force:

$$F_{SC-Static} = 0.67D_{Bore} [N] \quad (2.45)$$

$$F_{SC-Dynamic} = 0.4D_{Bore} [N] \quad (2.46)$$

Where:  $D_{Bore}$  = Cylinder bore in millimeters.

Similar simplifications and more refined models can be found in the literature. Indeed, the assumption of ideal conditions would cancel the effect of friction forces. For the current study, friction forces are taking into account; hence, the models described by the equations presented above need to be validated through experimentation. As one of the overall goals of the project, the control law or algorithm generated for optimum control and performance of the cylinder should also provide a friction compensation effect.

## 2.4. Modeling of lengthy tube connecting the control valves and the cylinder

Two approaches can be applied for the modeling of lengthy tubes connecting the control valves and the cylinder. The first approach comprises the modeling in the time domain, while the second approach involves the modeling in the frequency domain. The use of one approach or another bases on the scope of the control applications. For the study of dynamic system in the state space form, it might result favorable to utilize time domain models. Nevertheless, frequency domain models are better suited for parameter identification, and they are easier to compute (Beater, 2007). For the current study, as it has been done until this point, time domain models will be used for the generation of a state space representation of the overall system, and frequency domain models will be applied for the identification of physical parameters.

Similarly to the modeling of the pressure chambers of the cylinder, the derivation of the differential equations characterizing the dynamic behavior of lengthy pneumatic tubing depends on the following postulations:

- Air is a perfect gas.
- Kinetic and potential energy of air are negligible.
- The process carried inside the pneumatic tube is adiabatic.
- The cross-sectional area of the pneumatic tube is constant.

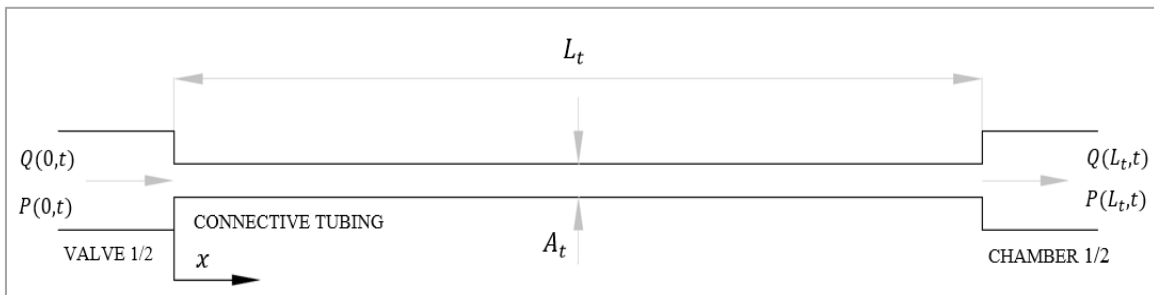


**Figure 2.8.** Schematic representation of long pneumatic tube

Zalmanzon (1965), in his study of components for pneumatic control instruments, derived the following differential equations for the transmission of air pressure changes in the tube axis coordinate  $x$  of long pneumatic lines:

$$\frac{\partial P(x, t)}{\partial x} + \frac{8\pi\mu}{A_t} Q(x, t) + \frac{\rho(x, t)}{A_t} \frac{\partial Q(x, t)}{\partial t} = 0 \quad (2.47)$$

$$\frac{\partial Q(x, t)}{\partial x} + \frac{A_t}{\rho(x, t)c^2} \frac{\partial P(x, t)}{\partial t} = 0 \quad (2.48)$$

Where:  $P$  = Pressure along the tube.

$Q$  = Volumetric flow.

$A_t$  = Cross-sectional area of the tube.

$\mu$  = Dynamic viscosity of air.

$c$  = Speed of sound.

$\rho$  = Density of air.

Eq. 2.47 assumes friction losses correspond to the case of laminar steady flow along the tube. In order to include the effect of turbulent flow, Eq. 2.47 is expressed in terms of a friction coefficient  $f_r$ :

$$\frac{\partial P(x, t)}{\partial x} + \frac{\pi\mu f_r}{8A_t^2} Q(x, t) + \frac{\rho(x, t)}{A_t} \frac{\partial Q(x, t)}{\partial t} = 0 \quad (2.49)$$

Where the friction coefficient depending on the characteristic of the flow is given by:

$$f_r = \begin{cases} 64 & \text{Laminar flow} \\ 0.316Re^{3/4} & \text{Turbulent flow} \end{cases} \quad (2.50)$$

$Re$  is the Reynolds number, and it can be evaluated from the average of input and output flow values (Beater, 2007). The Reynolds number in terms of the average velocity of the flow along the pneumatic tube is:

$$Re = \frac{D_t \bar{w} \rho}{\mu} \quad (2.51)$$

Where:  $D_t$  = Diameter of the tube.

$\bar{w}$  = Average velocity of the flow of air.

Moreover, it has to be remarked that Eq. 2.48 derives from the relationship between the bulk modulus and the coefficient of compressibility  $\epsilon$ .

The coefficient of compressibility is the reciprocal of the bulk modulus, and it accounts for the deformation of a differential element of air inside the pneumatic tube (Zalmanzon, 1965). The relationship between the bulk modulus and the coefficient of compressibility is given by:

$$\epsilon = \frac{1}{\kappa} = \frac{1}{\rho c^2} = -\frac{\dot{V}}{V \dot{P}} \quad (2.52)$$

The rate of change of pressure  $\dot{P}$  and the rate of change of the volume of air contained in the tube,  $\dot{V}$ , can be expressed as:

$$\dot{P} = \frac{dP}{dt} = \frac{\partial P}{\partial t}; \quad \dot{V} = \frac{dV}{dt} = A_t \frac{\partial w}{\partial x} dx \quad (2.53)$$

Then, Eq. 2.48 results from replacing Eq. 2.53 in Eq. 2.52, and from expressing the speed of the flow as the quotient between the volumetric flow and the area of the tube. Thus, by including Eq. 2.48 in the model for the pneumatic tube connecting the proportional valves and the cylinder, the overall solution should account for the effect of the compressibility of air in pneumatic control elements.

Eq. 2.48 and 2.49 represent the Navier-Stokes equations of continuity and momentum, respectively. The pressure and the density for an adiabatic process are related one to each other according to:

$$\frac{P}{\rho^k} = C_a \quad (2.54)$$

Where  $C_a$  is a constant.

Differentiating Eq. 2.48 with respect to time, and Eq. 2.49 with respect to  $x$ , and combining both equations, it is obtained the following nonlinear pressure wave equation:

$$\frac{\partial^2 P(x, t)}{\partial t^2} - c^2 \frac{\partial^2 P(x, t)}{\partial x^2} + \frac{\pi \mu f_r}{8 A_t \rho(t)} \frac{\partial P(x, t)}{\partial t} - \frac{1}{kP} \left[ \frac{\partial P(x, t)}{\partial t} \right]^2 = 0 \quad (2.55)$$

Likewise, differentiating Eq. 2.48 with respect to  $x$ , and Eq. 2.49 with respect to time, and combining both equations, it is obtained the following nonlinear volumetric flow wave equation:

$$\frac{\partial^2 Q(x, t)}{\partial t^2} - c^2 \frac{\partial^2 Q(x, t)}{\partial x^2} + \frac{\pi \mu f_r}{8 A_t \rho(t)} \frac{\partial Q(x, t)}{\partial t} - \frac{c^2 \rho(t)^{1-k}}{A_t k C_a} \frac{\partial}{\partial t} \left[ \frac{\partial Q(x, t)}{\partial x} \right] = 0 \quad (2.56)$$

Eq. 2.55 is similar to the one that [Whitmore \(1988\)](#) obtained in his formulation of a general technique for predicting pneumatic attenuation errors in airborne pressure sensing devices. Eq. 2.56 is similar to the equation formulated by [Richer and Hurmuzlu \(2000\)](#) in their nonlinear mathematical model of a high performance pneumatic force actuator. Eq. 2.55 and Eq. 2.56, as combinations of the Navier-Stokes equations, seek to account for the pressure drop and the delay of the flow profile at the outlet of lengthy pneumatic connective tube.

In addition, substituting Eq. 2.33 in Eq. 2.52, it is obtained:

$$P(x, t) = \frac{c^2}{k} \rho(x, t) \quad (2.57)$$

In Eq. 2.55 and Eq. 2.56, the resistance of the tube  $R_t$ , also denominated acoustic resistance, accounts for the damping effects of the viscosity of air, and it is given by the coefficient ([Zalmanzon, 1965](#); [Whitmore, 1988](#); [Richer and Hurmuzlu, 2000](#)):

$$R_t = \frac{\pi \mu f_r}{8 A_t} \quad (2.58)$$

Substituting Eq. 2.57 and Eq. 2.58 in Eq. 2.55, it is obtained:

$$\frac{\partial^2 P(x, t)}{\partial t^2} - c^2 \frac{\partial^2 P(x, t)}{\partial x^2} + \frac{1}{\rho} \left( R_t - \frac{1}{c^2} \frac{\partial P(x, t)}{\partial t} \right) \frac{\partial P(x, t)}{\partial t} = 0 \quad (2.59)$$

Assuming the resistance of the tube is considerably larger than the input pressure rates ([Whitmore, 1988](#)):

$$R_t \gg \frac{1}{c^2} \frac{\partial P(x, t)}{\partial t} \quad (2.60)$$

Eq. 2.55 becomes:

$$\frac{\partial^2 P(x, t)}{\partial t^2} + \frac{R_t}{\rho} \frac{\partial P(x, t)}{\partial t} - c^2 \frac{\partial^2 P(x, t)}{\partial x^2} = 0 \quad (2.61)$$

This equation is a linearized version of Eq. 2.55; and most importantly, it represents a generalization of a wave equation characterizing the propagation of longitudinal compression waves along lengthy pneumatic connective tube.

Eq. 2.61 can be solved in the form of a series solution (Zalmanzon, 1965; Whitmore, 1988), for which the initial and boundary conditions need to be defined. At time zero, the system would be at rest; hence, the initial conditions would be:

$$P(x, 0) = P_{t=0}; \quad Q(x, 0) = 0 \quad (2.62)$$

The boundary conditions at the inlet ( $x = 0$ ) and outlet ( $x = L_t$ ) of the tube are given by:

$$P(0, t) = P_{dv} = P_{ut}; \quad Q(0, t) = Q_{v-A}|_{x=0} \quad (2.63)$$

$$P(L_t, t) = P_{1/2} = P_{dt}; \quad Q(L_t, t) = Q_{v-A}|_{x=L_t} \quad (2.64)$$

Where:  $P_{t=0}$  = Initial pressure at any location after the control valve. ( $P_{t=0} \approx P_{atm}$ )

$P_{dv}$  = Pressure at the outlet of the control valve.

$P_{dt}$  = Pressure at the outlet of the connecting tube.

$P_{ut}$  = Pressure at the inlet of the connective tube.

$P_{1/2}$  = Pressure at the chamber 1 or 2 of the cylinder (Eq. 2.34, Eq. 2.35).

$Q_{v-A}$  = Volumetric flow from the control valve (Eq. 2.13).

Whitmore and Leondes (1991) approximated Eq. 2.61 to a second-order linear filter of the form:

$$\ddot{P}_{dt} + 2\xi_t \omega_{nt} \dot{P}_{dt} + \omega_{nt}^2 P_{dt} = \omega_{nt}^2 P_{ut} \quad (2.65)$$

Where:  $P_{dt}$  = Pressure at the outlet of the pneumatic tube – Downstream pressure.

$P_{ut}$  = Pressure at the inlet of the pneumatic tube – Upstream pressure.

$\omega_{nt}$  = Natural frequency of pressure waves in pneumatic tubing.

$\xi_t$  = Damping ratio of pressure waves in pneumatic tubing.

Whitmore and Leondes (1991) define the natural frequency and the damping ratio in Eq. 2.65 as follows:

$$\omega_{nt}^2 = \frac{c^2 A_t}{L_t V_e}; \quad \xi_t = \frac{R_t}{2\omega_{nt} \rho_0} \quad (2.66)$$

Where:  $\rho_0$  = Initial density.

$V_e$  = Effective sensor volume, which includes the volume of air in the tube and the enclosed transducer volume.



The effective sensor volume in Eq. 2.66 is given by:

$$V_e = V_s + \frac{A_t L_t}{2} \quad (2.67)$$

Where:  $V_s$  = Enclosed transducer volume.

In relation to the chambers of the pneumatic cylinder, Eq. 2.65 can be written as:

$$\ddot{P}_{1/2} + 2\xi_t \omega_{nt} \dot{P}_{1/2} + \omega_{nt}^2 P_{1/2} = \omega_{nt}^2 P_{rv} P_{sv} \quad (2.68)$$

Where:  $P_{rv}$  = Downstream to upstream pressure ratio for the valves.

$P_{sv}$  = Supply pressure to the valves.

As noticed by [Whitmore et al. \(1990\)](#), if the damping ratio and the natural frequency are properly selected, Eq. 2.65 can describe the wave behavior along lengthy pneumatic tubing up to the second harmonic. Accordingly, for the current study, in resemblance to the procedure developed by [Whitmore et al., \(1990\)](#), the natural frequency and the damping ratio could be determined experimentally as a function of the length of pneumatic connective tubing, and Eq. 2.68 could be included in the state-space model representing the overall pneumatic system.

In addition, [Richer and Hurmuzlu \(2000\)](#) proposed a model derived from the solution to a dispersive hyperbolic equation. The solution considers that a progressive wave propagates along a tube with a constant velocity not equal to the velocity of sound. The solution might only characterize the flow profile in connective tubing with a length in the range of 1 to 2 meters. For lengths higher than 2 meters, the proposed model would not account for dispersion phenomena, when waves do not propagate at the same velocity.

The solution proposed by [Richer and Hurmuzlu \(2000\)](#) includes an attenuation factor expressed as follows:

$$\phi = e^{-R_t RT / 2P_{sv} L_t / c} \quad (2.69)$$

Where:  $L_t$  = Length of the tube.

$P_{sv}$  = Supply pressure to the valves.

The attenuation factor presented in Eq. 2.69 seeks to account for the fact that the flow at the downstream side of the tube is attenuated in amplitude, and delayed in proportion to the length of the tube. Indeed, the flow at the downstream side of the tube is defined according to a delay time period ( $\tau_l$ ) of the form:

$$\tau_l = \frac{L_t}{c} \quad (2.70)$$

Accordingly, the mass flow ( $\dot{m}_t$ ) at the outlet of the tube is:

$$\dot{m}_t(t) = \begin{cases} 0 & \text{if } t < \tau_l \\ \phi \dot{m}_t(t - \tau_l) & \text{if } t > \tau_l \end{cases} \quad (2.71)$$

As noticed by [Richer and Hurmuzlu \(2000\)](#), Eq. 2.71 might be restricted to small frequencies. Nevertheless, it might be satisfactory for regular applications including pneumatic connective tubing. Simulation results should demonstrate that the mass flow calculated from Eq. 2.71 is equivalent to the solution obtained through numerical methods by integrating Eq. 2.55 and Eq. 2.56. In combination to Eq. 2.68, Eq. 2.71 should accurately describe the flow profile in pneumatic tubing connecting proportional control valves and pneumatic cylinders.

This chapter presented a series of mathematical models and equations that can be used to describe the dynamic behavior of the pneumatic system under study. To start with, mathematical models for the description of the electromagnetic, mechanical and pneumatic dynamics of the proportional valve were described. Emphasis was given to the mathematical expressions applied to represent the dynamics associated with the flow of air transmitted to the cylinder through the proportional valves. Moreover, the dynamics related to the variation of pressure in the cylinder chambers were modeled in terms of the compressibility of air. The compressibility of air, for an adiabatic process of pressure changes, was demonstrated to be proportional to the pressure of air by a factor corresponding to the air specific heat ratio. Then, the force dynamics relative to the cylinder piston were described. Especial attention was given to the modeling of the static and dynamic friction forces that oppose the motion of the piston. Finally, an entire section of this chapter focused on the modeling of lengthy pneumatic connective tubing. Several models from the literature were described and analyzed. The following chapter centers on the application of some of the models included in this chapter to generate an overall model for the pneumatic system under study.

## CHAPTER III

### ANALYTIC DEVELOPMENT

#### Controller Design

The design of a controller, or control system, comprises the derivation of control algorithms or control laws able to shape the dynamic response of the plant of a system according to certain specifications. In that regard, the design process seeks to transform the performance requirements of the plant of a system into a set of parameters that define the operation conditions of a controller. The operation conditions for a controller are defined in the basis of the different operation modes of the system. For instance, in the case of the pneumatic system under study, the operation conditions of the controller might change depending on whether the pneumatic cylinder is extending or retracting.

In addition, the performance specifications of the plant of a system vary depending upon the application for which the plant of a system is used. In the case of pneumatic systems; for example, the performance specifications for pneumatic cylinders used in robotic applications might exceed by far the specifications for pneumatic cylinders used in regular industrial applications, such as packing. High velocity, accuracy, power density, and efficiency are among the most common requirements that high-tech applications, such as robotics, include nowadays as a requisite. Indeed, new requirements associated with the sustainability of energy sources have strengthened the emphasis that the design of controllers applies on the pursuit of efficiency in pneumatic systems.

Therefore, this chapter focuses on the conceptual design of the control law necessary to operate the pneumatic system under study according to a set of pre-established specifications. In defining the design specifications for the controller, limiting requirements, critical functions, and critical parameters are identified through the analysis of the performance requirements for the controlled system. From the identification of the design specifications for the controller, several design alternatives can be presented and compared in terms of the dynamic response obtained through numerical simulations.

### 3.1. Design Specifications

The design specifications for the controller constitute the set of lineaments that guide the design process in terms of performance requirements for the pneumatic system. Particularly, the design specifications for the controller derive from the expected dynamic response of the system. In that regard, five factors are commonly used to characterize the quality of performance of a stable system in terms of its response to a step input. These factors are:

- **Rise time:** Rise time,  $T_r'$ , is the interval of time required for the step response of a system to go from 10% to 90% of its final value.
- **Peak time:** Peak time,  $T_p$ , is the time required for the step response of a system to reach the first peak of the overshoot.
- **Settling time:** Settling time,  $T_s$ , is the minimum time required before the system response remains within  $\pm 5\%$  of the final value.
- **Response Overshoot:** Overshoot is the percentage difference between the maximum and the steady state values of the response.
- **Steady-state error:** The steady-state error,  $e_{ss}$ , is the difference between a desired and actual magnitude of the system response, once the system attains a steady state.

Figure 3.1 shows the factors defined above in relation to the step response of a system:

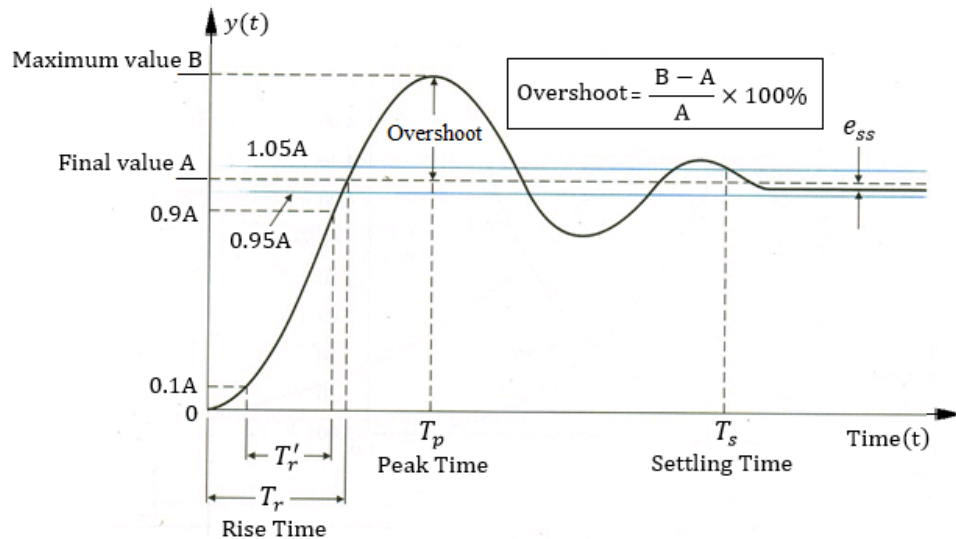


**Figure 3.1.** Step response specifications.

[Adapted from: [http://nptel.ac.in/courses/112104040/lecture23/23\\_7.htm](http://nptel.ac.in/courses/112104040/lecture23/23_7.htm)]

As it might be noticed from figure 3.1, an alternative rise time,  $T_r$ , could be defined as the interval of time required for the step response of a system to reach the final or desired value for the first time.

Additionally, in relation to a reference transient input, the following factors are commonly applied to assess the overall performance of a controller:

- **Tracking error:** In contrast to the steady-state error, the tracking error,  $e_{tr}$ , is a transient error. The tracking error is the difference between the desired and actual position for each point of a trajectory that fluctuates with time.
- **Phase shift:** Phase shift,  $\theta_{sh}$ , is a term that accounts for how displaced is the response of a system in relation to a reference signal. It is usually applied in the comparison of sinusoidal or wave signals, and it is expressed in terms of angular units.
- **Delay time:** In tracking control, the delay time,  $T_D$ , could be defined as the time that takes the plant of a system to respond to a reference command for the first time.

The following figure shows the assessment factors defined above in relation to a transient reference input:

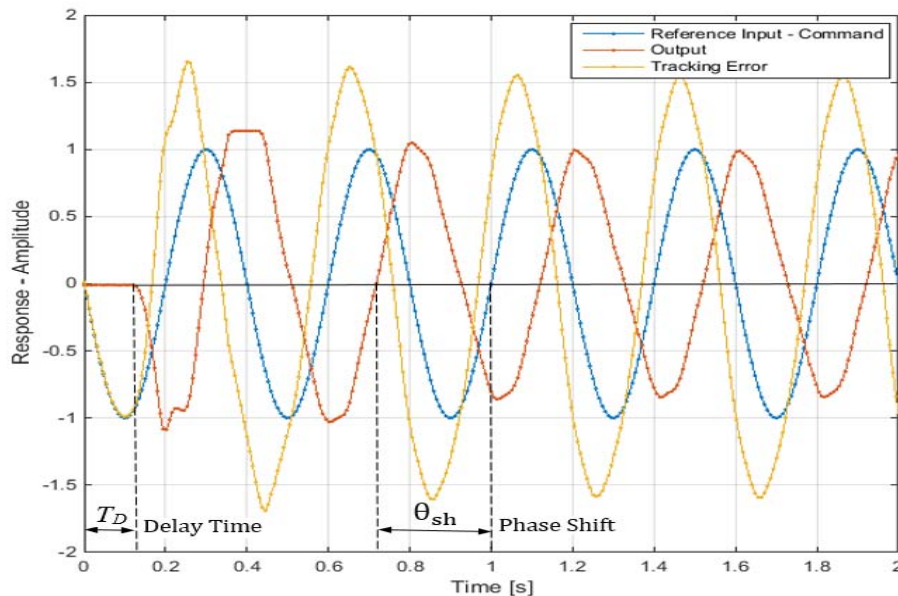


**Figure 3.2.** Transient response specifications: Tracking control

In the case of the pneumatic system under study, the delay time is described as the time required for the chambers of the cylinder to build up the differential pressure required to overcome static friction (Wang et al., 1999). Accordingly, the delay time for the pneumatic system would mark the time when the piston starts moving after the command input is applied.

After having identified the factors or parameters that could be used to assess the performance of the system, the design specifications for the controller were defined by using preliminary experimental data, and data found in the literature reviewed. Accordingly, the design specifications for the controller result from the delimitation of operation ranges for the pneumatic system. As described before, the design specifications are obtained in terms of two main operating conditions: when the input corresponds to a step signal, and when the input corresponds to a transient reference command, such as a sine wave. The following table contains the design specifications for the controller.

**Table 3.1:** Controller Design Specifications

<b>General Operating Conditions</b>		
<b>Operation Range Boundaries</b>	<b>Minimum</b>	<b>Maximum</b>
<i>Supply Pressure</i>	482.632 [kPa] (70 [psi])	620.527 [kPa] (90 [psi])
<i>Length of Connective Tubing</i>	0.55 [m] (1.81 [ft])	3.00 [m] (9.84 [ft])
<b>Operating Condition 1</b>		
<b>Input Command</b>	<u>Step Input</u>	
<b>Operation Range Boundaries</b>	<b>Maximum</b>	
<i>Rise Time</i>	0.075 [s]	
<i>Peak Time</i>	0.15 [s]	
<i>Settling Time</i>	0.25 [s]	
<i>Response Overshoot</i>	40 [%]	
<i>Position Steady-state Error</i>	±0.005 [m]	
<b>Operating Condition 2</b>		
<b>Input Command</b>	<u>Sinusoidal Reference Input</u>	
<b>Operation Range Boundaries</b>	<b>Maximum</b>	
<i>Tracking Frequency</i>	2.5 [Hz]	
<i>Delay Time</i>	0.3 [s]	
<i>Phase Shift</i>	10.0 [deg] ( $\pi/18$ [rad])	
<i>Position Tracking error</i>	±0.05 [m]	

In accordance to the design specifications presented in table 3.1, when the input corresponds to a step signal, the controller should enable the plant of the system to produce a well-damped and fast response, with a steady-state error tending to zero. Likewise, when the input is a tracking command, the plant of the system should be able to follow the reference command with a tracking error approaching zero, which implies that the delay time and the phase shift should be minimum.

Once the design specifications for the controller have been defined, the next step comprises the description and analysis of different design alternatives as an approach to find the one that produces the best response.

### **3.2. Delineation of control strategies**

The delineation of control strategies comprises the preliminary design of the control law or control algorithm to be developed for the pneumatic system. The goals of this preliminary design stage include:

- Map out how the control algorithm will fulfill the requirements for the pneumatic system: achievement of high positional tracking efficiency, and attenuation of negative effects associated with the length of connective tubing.
- Identify signals required to implement a specific control scheme.
- Identify constrains in the application of certain control strategies.
- Outline protocols for assessment of the control strategies to be implemented.

Through the independent or combined application of the control schemes identified in this section, the design alternative selected should demonstrate the complete fulfillment of the performance requirements for the pneumatic system. Three main control strategies will be described and analyzed:

- Proportional, derivative and integral feedback of the position error
- State feedback control
- Non-linear control through feedback linearization

### 3.2.1. Design Alternative 1: Simplified representation

The first controller design alternative centers on a simplified representation of the pneumatic system. The simplified model seeks to characterize the system as a single input single output (SISO) system, for which the controller would be designed by applying classical control techniques, such as root locus and frequency analysis. In order to simplify the model representation for the system, the following assumptions are made:

- The flow of air in the valves is incompressible, while the flow of air in the cylinder chamber is compressible.
- The piston is symmetric, as it would be a double rod piston; hence, the active areas of the piston are approximated to be equal.
- The two three-port valves operate as a one five-port valve.
- Friction in the cylinder is negligible.

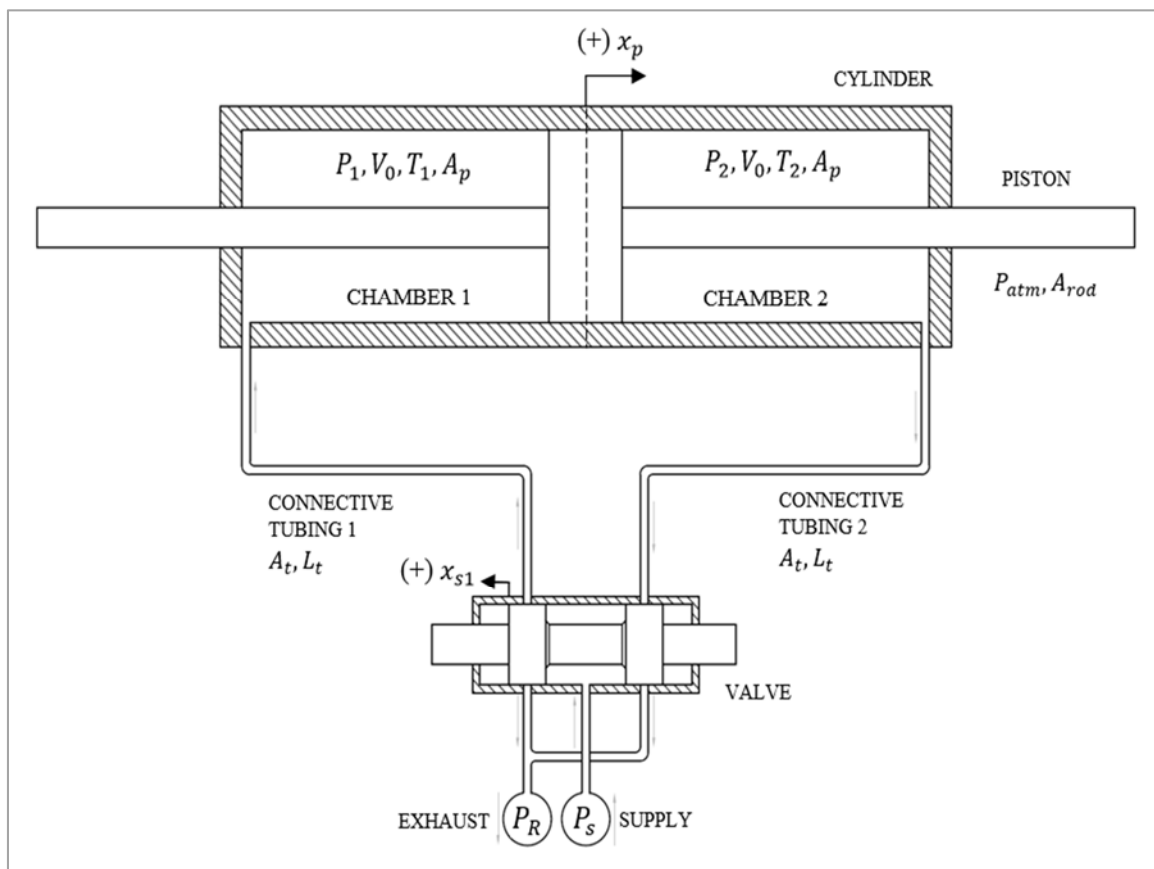


**Figure 3.3.** Schematic Diagram of the Simplified System



By considering that the flow in the valves is incompressible, it is assuming the air density remains constant; the flow from the valves can be modeled according to the equation of flow through thin, sharp edged orifices:

$$q_v = A_v C_d \sqrt{\frac{2(P_{uv} - P_{dv})}{\rho}} \quad (3.1)$$

Where:  $q_v$  = Volumetric flow.

$P_{uv}$  = Upstream pressure.

$A_v$  = Flow area.

$P_{dv}$  = Downstream pressure.

$C_d$  = Discharge coefficient.

$\rho$  = Density of the fluid (Constant).

Eq. 3.1 is commonly used for the modeling of flow in hydraulic control systems. For pneumatic systems, Eq. 3.1 might not be able to provide physical accuracy, but it could provide a useful approximation at the time of simulating the response of the system under specific conditions.

It has to be emphasized the fact that Eq. 3.1 is valid for steady, incompressible, and high-Reynolds-number flow through the orifice. When Eq. 3.1 is applied in the modeling of pneumatic systems, the fundamental assumptions on which this equation bases are substituted in order to embrace conditions of unsteady flow, compressible flow, or low-Reynolds-number flow (Manring, 2005). The main advantage of using Eq. 3.1 centers on the simplicity to carry out the calculation of the volumetric flow; nevertheless, major accuracy might be required in the case of pneumatic systems, especially if it is sought to achieve the most efficient operation profile.

Moreover, if the cylinder was symmetric, and the discharge coefficients were the same for the orifices in the valves, the inlet flow ( $q_1$ ) and the outlet flow ( $q_2$ ) from the cylinder should be equal. Accordingly, the volumetric flow could be modeled as:

$$q_1 = q_2 = Q = A_v C_d \sqrt{\frac{(P_S - P_R) - P_d}{\rho}} \quad (3.2)$$

Where:  $P_S$  = Supply Pressure.

$P_R$  = Return Pressure.

$P_d$  = Differential pressure in the chambers of the cylinder ( $P_1 - P_2$ ).

By expanding the right hand side of Eq. 3.2 through a first-order Taylor series expansion at an equilibrium point  $(A_v^*, P_d^*)$ , and by cancelling the higher-order terms, it is obtained:

$$\delta Q = Q - f(A_v^*, P_d^*, t) = \left. \frac{\partial f(A_v^*, P_d^*, t)}{\partial x} \right|_{(A_v^*, P_d^*)} \delta A_v + \left. \frac{\partial f(A_v^*, P_d^*, t)}{\partial u} \right|_{(A_v^*, P_d^*)} \delta P_d \quad (3.3)$$

$$Q = A_v^* C_{D'} \sqrt{(P_S - P_R) - P_d^*} + C_{D'} \sqrt{(P_S - P_R) - P_d^*} (\Delta A_v) - \frac{1}{2} \frac{A_v^* C_{D'}}{\sqrt{(P_S - P_R) - P_d^*}} (\Delta P_d)$$

Where  $C_{D'}$  is a combined discharge coefficient given by:

$$C_{D'} = \frac{C_d}{\sqrt{\rho}} \quad (3.4)$$

From Eq. 3.3, a flow gain ( $G_f$ ), and a pressure gain ( $G_D$ ) are defined by:

$$G_f = C_{D'} \sqrt{(P_S - P_R) - P_d^*}; \quad G_D = \frac{1}{2} \frac{A_v^* C_{D'}}{\sqrt{(P_S - P_R) - P_d^*}} \quad (3.5)$$

Hence, the volumetric flow could be expressed by:

$$Q = A_v^* C_{D'} \sqrt{(P_S - P_R) - P_d^*} + G_f (\Delta A_v) - G_D (\Delta P_d) \quad (3.6)$$

Where the steady-state volumetric flow,  $Q_0$ , would correspond to:

$$Q_0 = A_v^* C_{D'} \sqrt{(P_S - P_R) - P_d^*} \quad (3.7)$$

From the assumptions and simplifications made, the model for the pneumatic system can be reduce to three equations:

$$Q = Q_0 + G_f (\Delta A_v) - G_D (\Delta P_d) \quad (3.8)$$

$$\dot{P}_d = \frac{\beta}{V_0} (Q - \dot{x}_p A_p) \quad (3.9)$$

$$M_{PL} \ddot{x}_p = P_d A_p \quad (3.10)$$

In relation to the equations derived in chapter 2, Eq. 3.8 would replace Eq. 2.8, Eq. 3.9 would replace Eq. 2.34 and Eq. 2.35, and Eq. 3.10 would substitute Eq. 2.37. As it might be noticed, Eq. 3.8 is a linear equation expressed in terms of two constant coefficients or gains. The derivation of Eq. 3.9 follows the procedure developed in section 2.2, but considering the differential pressure in the chambers of the cylinder,  $P_d$ , and  $\beta$ ,  $V_0$ , and  $A_P$  as effective values for the bulk modulus, the volume of air, and the piston area, respectively. Finally, Eq. 3.10 represents the force dynamics of the piston by neglecting friction effects.

In addition, by considering the steady-state operating point for the system, and by setting to zero all the derivative terms in Eq. 3.9, it is found that the steady-state volumetric flow would be equal to zero; hence, Eq. 3.8 is further simplified as follows:

$$Q = G_f(\Delta A_v) - G_D(\Delta P_d) \quad (3.11)$$

By considering the expression for the steady-state volumetric flow, and by setting it to zero, two options to determine the equilibrium point ( $A_v^*$ ,  $P_d^*$ ), and the flow and pressure gains can be verified:

$$Q_0 = A_v^* C_{D'} \sqrt{(P_S - P_R) - P_d^*} = 0 \quad (3.12)$$

$$\left\{ \begin{array}{l} 1. A_v^* = 0 \rightarrow G_D = 0; \quad G_f = C_{D'} \sqrt{(P_S - P_R) - P_d^*} \\ 2. (P_S - P_R) = P_d^* \rightarrow G_D = \infty; \quad G_f = 0 \end{array} \right. \quad (3.13)$$

Accordingly, around the equilibrium points defined in Eq. 3.13, the volumetric flow would be respectively given by:

$$\left\{ \begin{array}{l} 1. Q = G_f A_v \\ 2. Q = \infty \end{array} \right. \quad (3.14)$$

Regarding the expressions in Eq. 3.13 and Eq. 3.14, the flow could be considered to tend to infinity just before the piston starts moving, when the flow depends merely on the supply pressure. In contrast, at the end of the stroke of the cylinder, when pressure in the cylinder becomes equal to the supply pressure and air has completely compressed in the cylinder chambers, the flow would become zero. Therefore, it is assumed that the equilibrium points are not in the vicinity of the origin of displacement of the piston, or of its maximum stroke, and that the volumetric flow is still defined in terms of a flow gain and a pressure gain.

### 3.2.1.1. Block Diagram Representation: Nonlinear and Linear Models

A Simulink block-diagram model for the full-nonlinear system was developed by using Eq. 3.2, Eq. 3.9, and Eq. 3.10. The simulation obtained from this nonlinear model should validate the overall response of the system in order to corroborate that the values and response of internal variables, such as the piston differential pressure, agree with the values and response expected. Figure 3.4 displays this model.

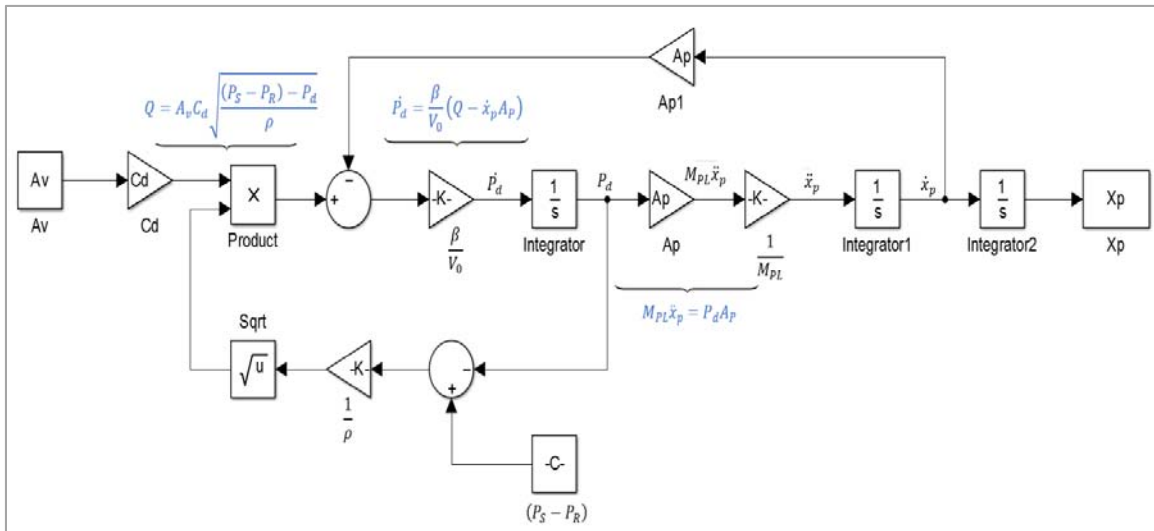


**Figure 3.4.** Simulink model for the full, nonlinear simplified system.

Moreover, a second Simulink model derived from Eq. 3.9 to Eq. 3.11 represents a linear model for the full simplified system. Figure 3.5 displays this model:

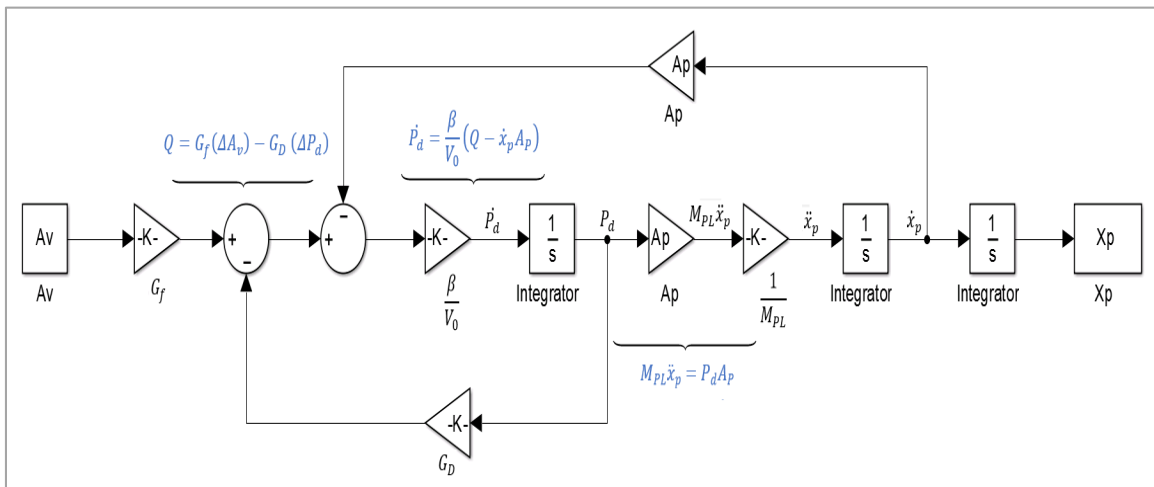


**Figure 3.5.** Simulink model for the full, linear simplified system.

Once that the full, linear simplified model is defined, block diagram algebra can be applied to reduce the model presented in figure 3.5 to a model of the form presented in the following figure:

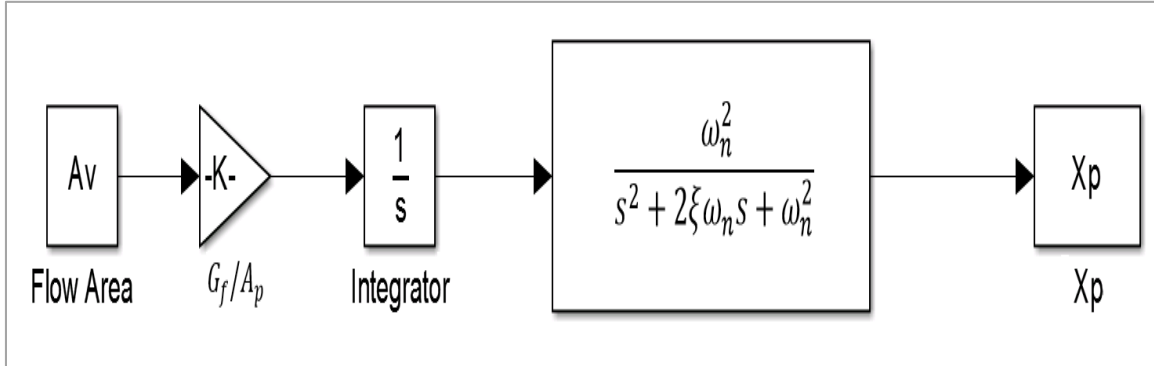


**Figure 3.6.** Simulink model for the reduced linear system

In order to reduce the linear model for the full-simplified system into a model of the form presented in figure 3.6, the following reduction steps are applied:

First, the two summing points in figure 3.5 are combined into one single summing point, as it is shown in the following figure.

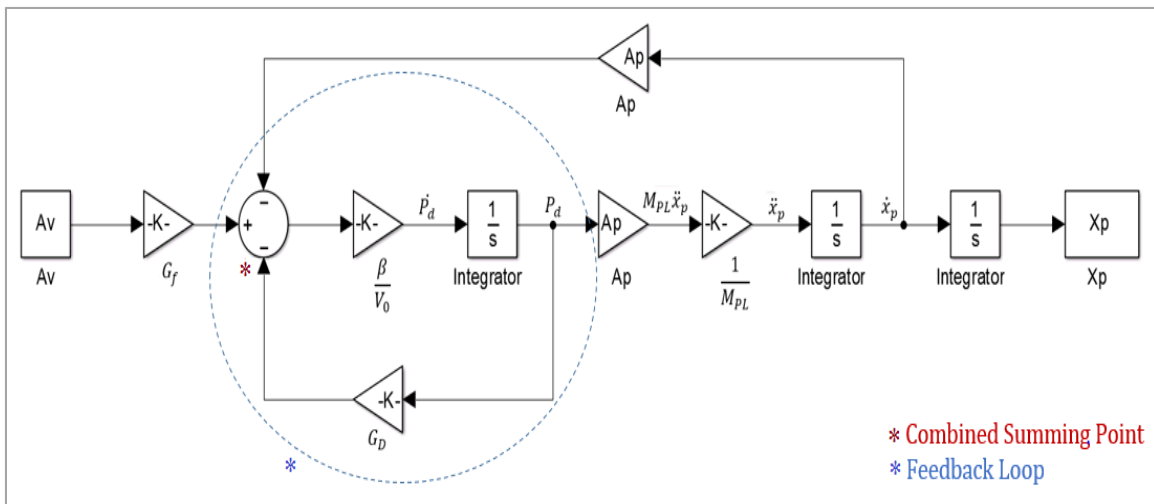


**Figure 3.7.** Block reduction steps: Step 1.

Secondly, the feedback loop circled in figure 3.7 is reduced by applying the block transformation described in the following scheme.

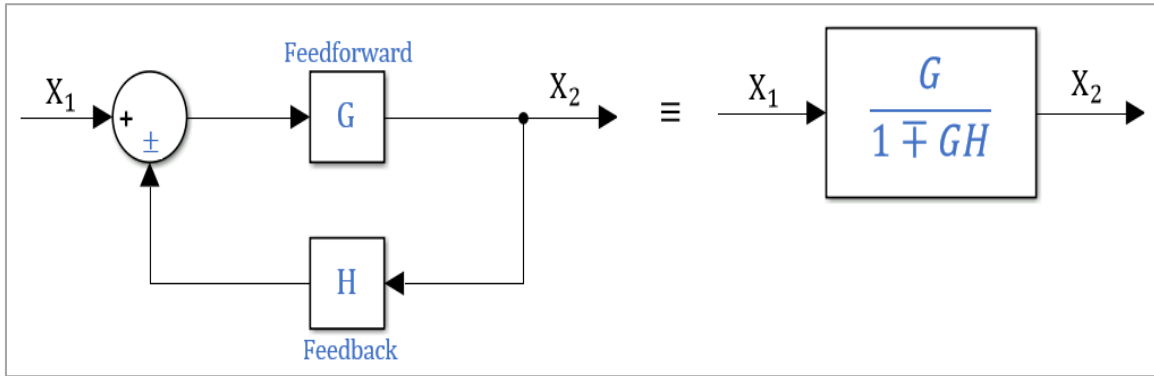


**Figure 3.8.** Feedback loop reduction

The result of this transformation is presented in figure 3.9.

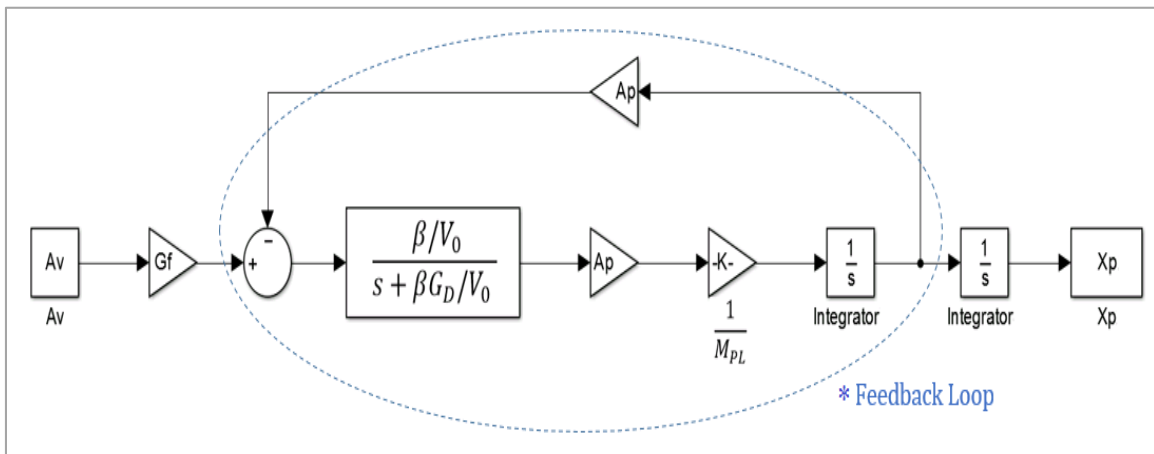


**Figure 3.9.** Block reduction steps: Step 2.

For the third step, the feedback loop circled in figure 3.9 is also reduced, which results in the block diagram presented in figure 3.10.

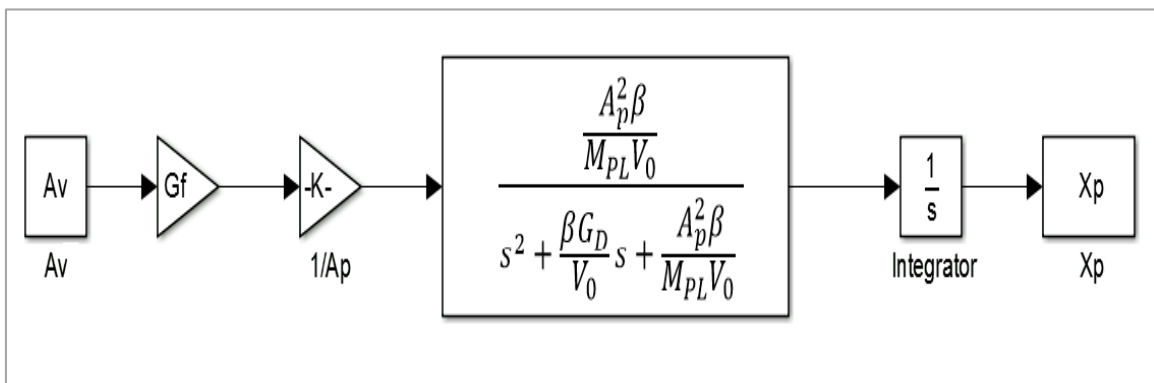


**Figure 3.10.** Block reduction steps: Step 3.

The block diagram presented in figure 3.10 is equivalent to the block diagram presented in figure 3.6, where the main block of the system has been expressed in the form of the transfer function for an underdamped second-order system. The following figure shows the normalized step response of a second-order underdamped system with constant transfer function numerator, and for different damping ratios.

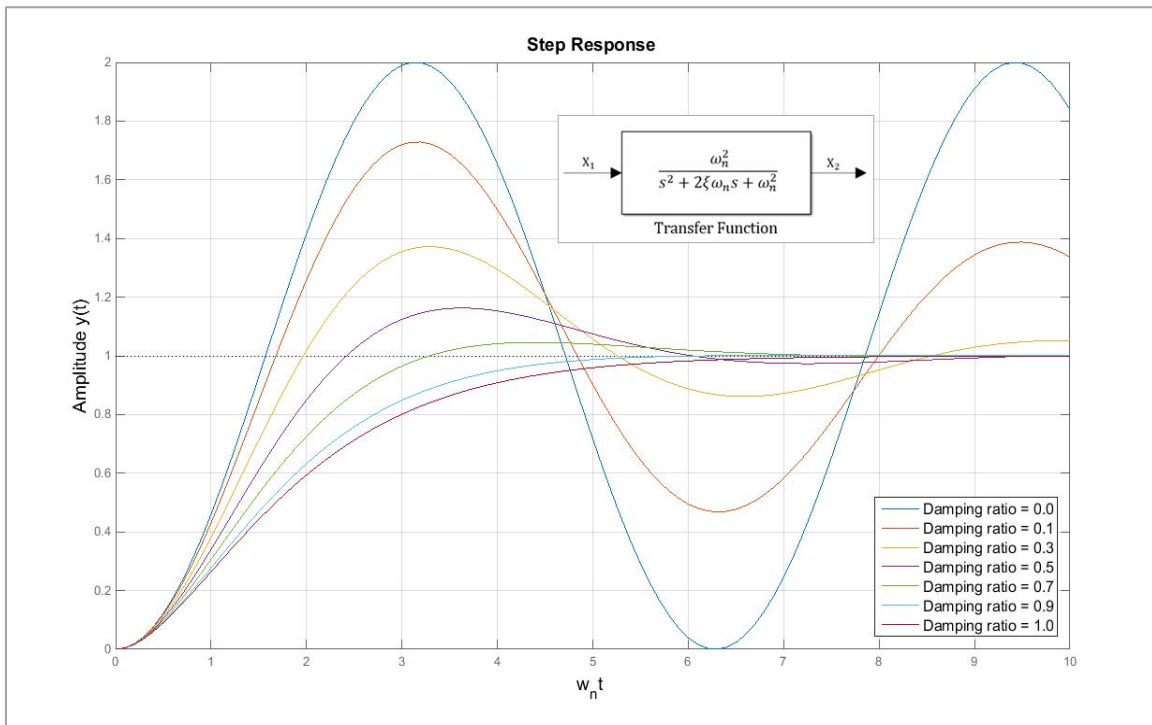


**Figure 3.11.** Normalized step response of a second-order system

From the comparison of figure 3.6 and figure 3.10, it can be demonstrated that the underdamped natural frequency,  $\omega_n$ , and the damping ratio,  $\xi$ , for the system would be given by:

$$\omega_n^2 = \frac{A_p^2 \beta}{M_{PL} V_0} \left\{ \begin{array}{l} \omega_n = \sqrt{\frac{A_p^2 \beta}{M_{PL} V_0}} \\ 2\xi \omega_n = \frac{\beta G_D}{V_0} \left\{ \xi = \frac{G_D}{2A_p} \sqrt{\frac{M_{PL} \beta}{V_0}} \right. \end{array} \right. \quad (3.15)$$

As it will be described in the following chapter, the values corresponding to the different parameters included in the block diagrams created to characterize the behavior of the system can be measured experimentally, or derived from test data.

### 3.2.1.2. Further Simplification of the Reduced Model – Root Locus Analysis

Further simplification of the reduced model displayed in figure 3.6 or 3.10 can be achieved by applying Root Locus Analysis. This method was developed by Walter Evans in the mid-1940s (Stefani et al., 2002), and it consists in sketching on the complex plane the path traced by the roots of the characteristic equation of a system as a parameter changes. In that regard, the transfer function of a system is a rational function in terms of the complex variable  $s$ , which can be expressed by:

$$G(s) = \frac{b_m s^m + b_{m-1} s^{m-1} + \dots + b_1 s + b_0}{a_n s^n + a_{n-1} s^{n-1} + \dots + a_1 s + a_0} \quad (3.16)$$

Where the numerator and denominator are expressed in the form of polynomials of order  $m$ , and  $n$ , with coefficients  $a$ , and  $b$ , respectively.

If the polynomials in the numerator,  $N(s)$ , and denominator,  $D(s)$ , are written in terms of their corresponding factors, the matrix function  $G(s)$  becomes:

$$G(s) = \frac{N(s)}{D(s)} = \frac{b_m (s - z_1)(s - z_2) \dots (s - z_{m-1})(s - z_m)}{a_n (s - p_1)(s - p_2) \dots (s - p_{n-1})(s - p_n)} \quad (3.17)$$

If  $N(s)$  and  $D(s)$  are individually set to zero, the roots of the corresponding equations are respectively the zeros and poles of the system. Accordingly, in Eq. 3.17, the  $z_i$ 's and the  $p_i$ 's are respectively the zeros and poles of the system. The polynomial that composes the denominator of the transfer function of the system is denominated the characteristic equation of the system. Hence, the roots of the characteristic equation of the system correspond to the poles of the system.

In figure 3.6, if the polynomial in the main block is decomposed in terms of irreducible factors, the transfer function for the pneumatic system can be expressed in the following form:

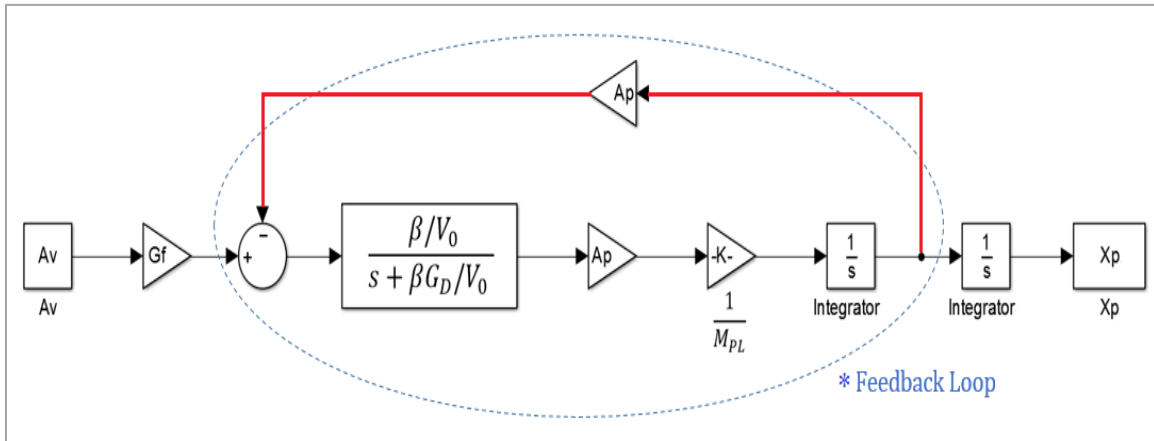
$$G(s) = \frac{G_f}{A_p s} \frac{\omega_n^2}{(s^2 + 2\xi\omega_n s + \omega_n^2)} = \frac{G_f}{A_p s} \frac{r_1 r_2}{(s + r_1)(s + r_2)} \quad (3.18)$$

Where  $r_1$  and  $r_2$  are roots of the polynomial, and also poles of the system.

By tracking back the block reduction steps, it is verified that the value of these roots,  $r_1$  and  $r_2$ , depends on the feedback effect of the effective area,  $A_p$ , on the response of the system.

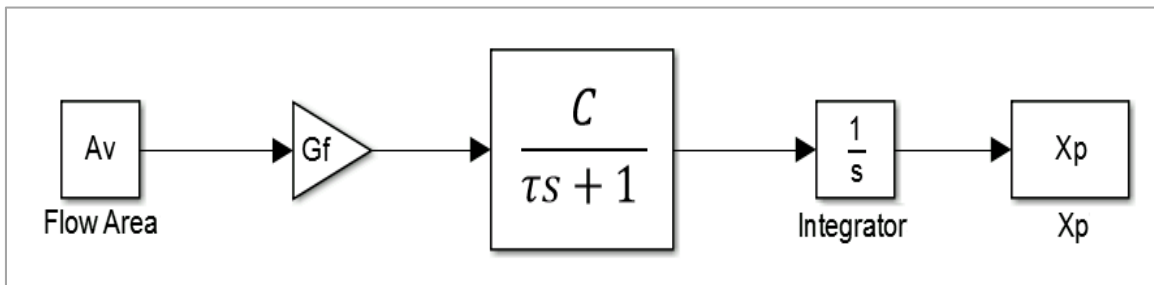


Figure 3.12 highlights in red the feedback effect of the effective area,  $A_p$ , on the final configuration of the system.



**Figure 3.12.** Block reduction Step 2 – Feedback effect of the area of the piston

Hence, it is in this instance that root locus analysis plays a fundamental role in order to verify the effect of  $A_p$  on the position of the poles of the system in the complex plane, and on the overall response of the system. In fact, the specific purpose of this analysis is to identify to what extent the second-order portion of the transfer function of the pneumatic system can be approximated to the form of a first-order system. Accordingly, for certain values of  $A_p$ , one of the roots of the characteristic equation,  $r_1$  or  $r_2$ , could be neglected with no or insignificant effect on the overall response of the system. By ignoring one of the roots of the characteristic equation, the block diagram presented in figure 3.6 can be further simplified to a block diagram of the form presented in figure 3.13.



**Figure 3.13.** Further simplified reduced model

Where  $C$  is a constant that depends on the properties of the systems, and  $\tau$  is a time constant.

In order to produce the block diagram presented in figure 3.13, the following reduction steps are applied: First, the block diagram presented in figure 3.12 is decomposed as follows:

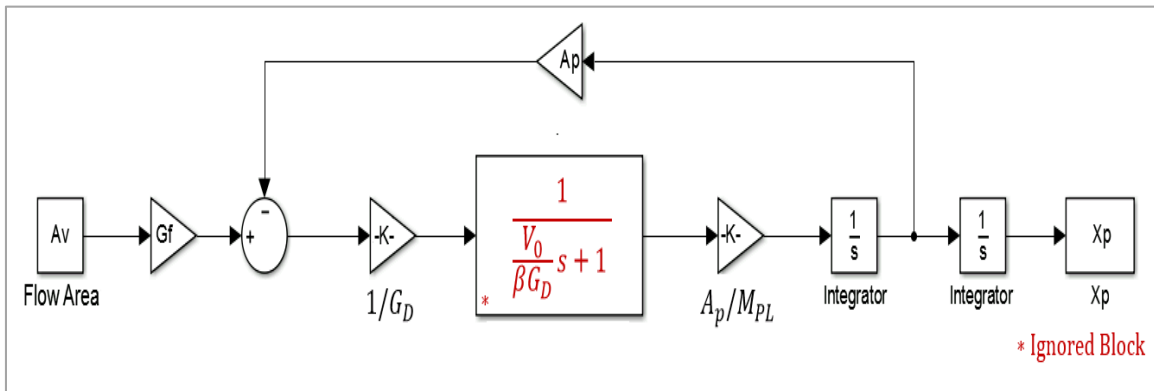


**Figure 3.14.** Further simplified reduced model - Block reduction Steps: Step 1.

Then, by ignoring the block marked in red in figure 3.14, the block diagram representation for the pneumatic system is the one presented in figure 3.15.

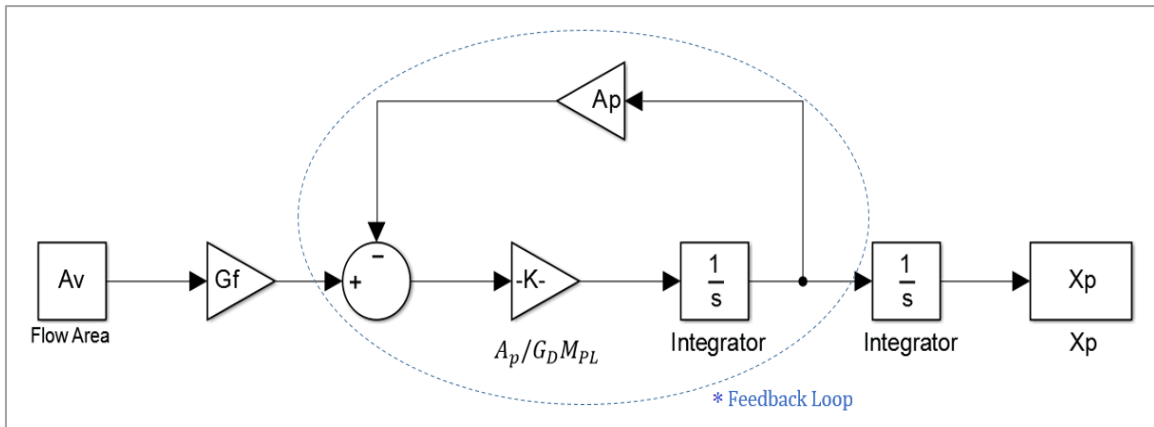


**Figure 3.15.** Further simplified reduced model - Block reduction Steps: Step 2.

Finally, by reducing the feedback loop circled in blue in figure 3.16, a block diagram of the form presented in figure 3.13 is obtained. From this last reduction step, it can be verified that the constants  $C$  and  $\tau$  correspond to the following expressions:

$$C = \frac{1}{A_p} \quad (3.19)$$

$$\tau = \frac{G_D M_{PL}}{A_p^2}$$

Based on root locus analysis, the block marked in red in figure 3.14 could be neglected if one of the roots of the characteristic equation,  $r_1$  or  $r_2$ , is considerably larger than the other, and accordingly; its effect on the response of the system is fast enough to be imperceptible and hence negligible in the characterization of the system. In order to illustrate this condition, for a first order system, and a second order system described by the following block diagrams:

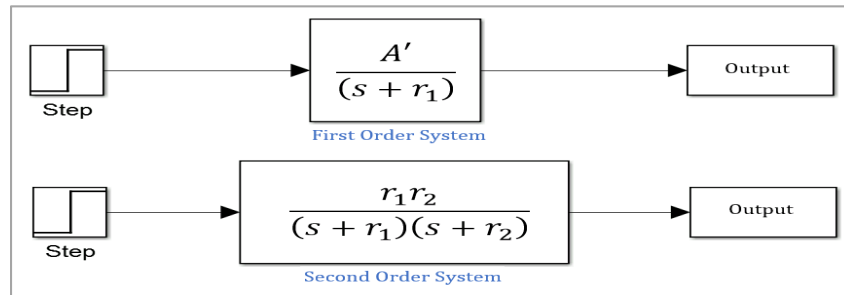


**Figure 3.16.** Simplification of the reduced model - Illustrative block diagrams

Where  $A'$  is a constant that results from the partial-fraction decomposition of the transfer function for the second-order system. The step responses of the systems for a constant value of  $r_1$ , and for different values of  $r_2$  are displayed in the following figure.

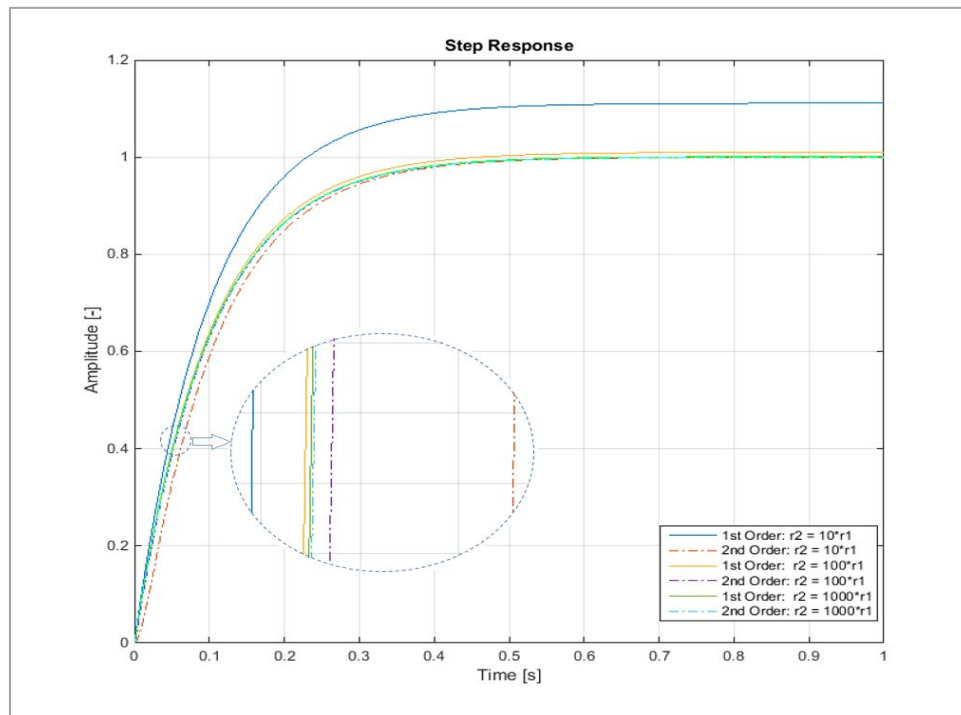


**Figure 3.17.** Simplification of the reduced model: Step response of illustrative first-order and second-order systems. ( $|r_1| = 10$ )

As it can be verified from figure 3.17, as the absolute value of  $r_2$  increases, and  $r_1$  remains constant, the step response of the second-order and first-order systems are close one to each other. Moreover, the effect of  $r_2$  in the response of a second order system is explicitly demonstrated through the root locus displayed in the following figure.

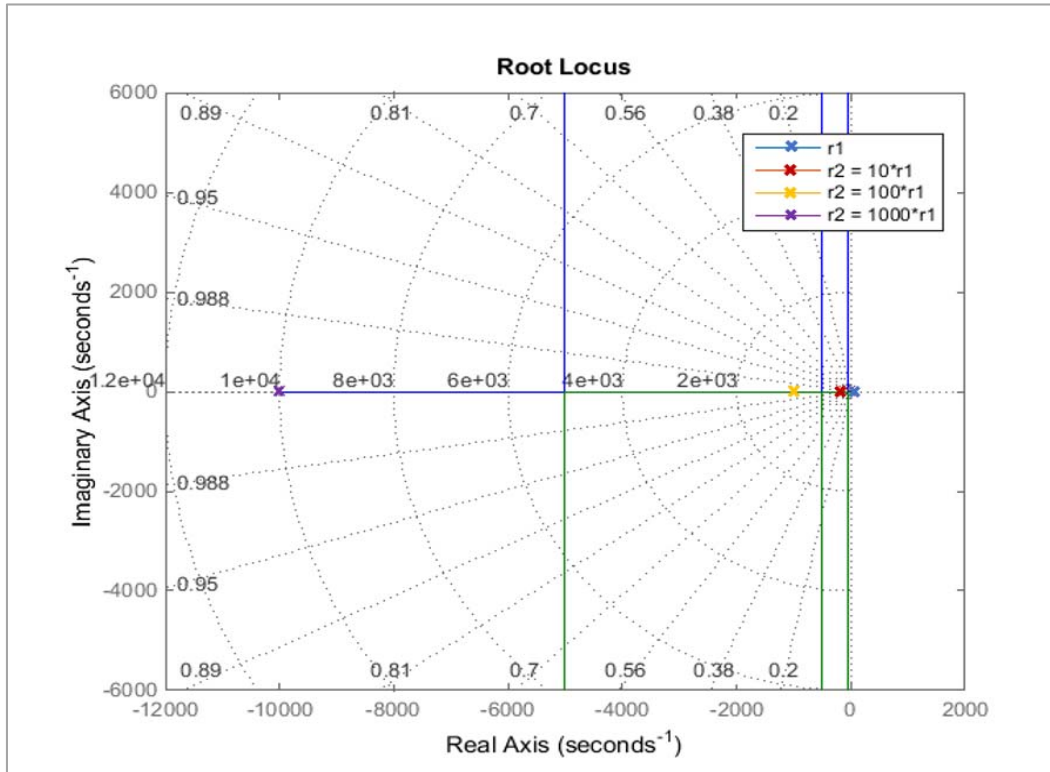


**Figure 3.18.** Simplification of the reduced model: Root Locus for illustrative second-order system ( $|r_1| = 10$ ).

As it is standard in control, the poles and zeros of a system are respectively denoted by “x” and “o” on the root locus. Due to the fact that the open loop roots of the characteristic equation for the second-order system correspond to its poles, the root locus on figure 3.18 shows the position of these poles on the complex plane and makes reference to the relation between  $r_1$  and  $r_2$ .

In addition, in order to further simplify the reduced model for the pneumatic system according to the considerations previously made, it would be necessary that the poles of the system remain in the real axis of the complex plane. If the poles of a second order system are complex numbers, they are conjugates of one another; hence, the simplification of the reduced model for the pneumatic system based on neglecting one of its poles could not be applied.

Root locus analysis can be used to corroborate the conditions under which the poles of the second-order portion of the reduced system become complex numbers, which as it was explained in previous sections, it could be associated with the feedback effect of the effective area of the piston. From the assumptions made to simplify the model for the pneumatic system, the effective area,  $A_p$ , would not correspond to the exact physical characteristics of the pneumatic piston. Hence, through root locus analysis, the path traced by the poles of the system according to the effective area  $A_p$  will have to be verified, which should provide a range of values for  $A_p$  that enable the system to be characterized as the model presented in figure 3.13. Schematically, what should be accomplished through root locus analysis in relation to the effective area of the piston is described in the following figure.

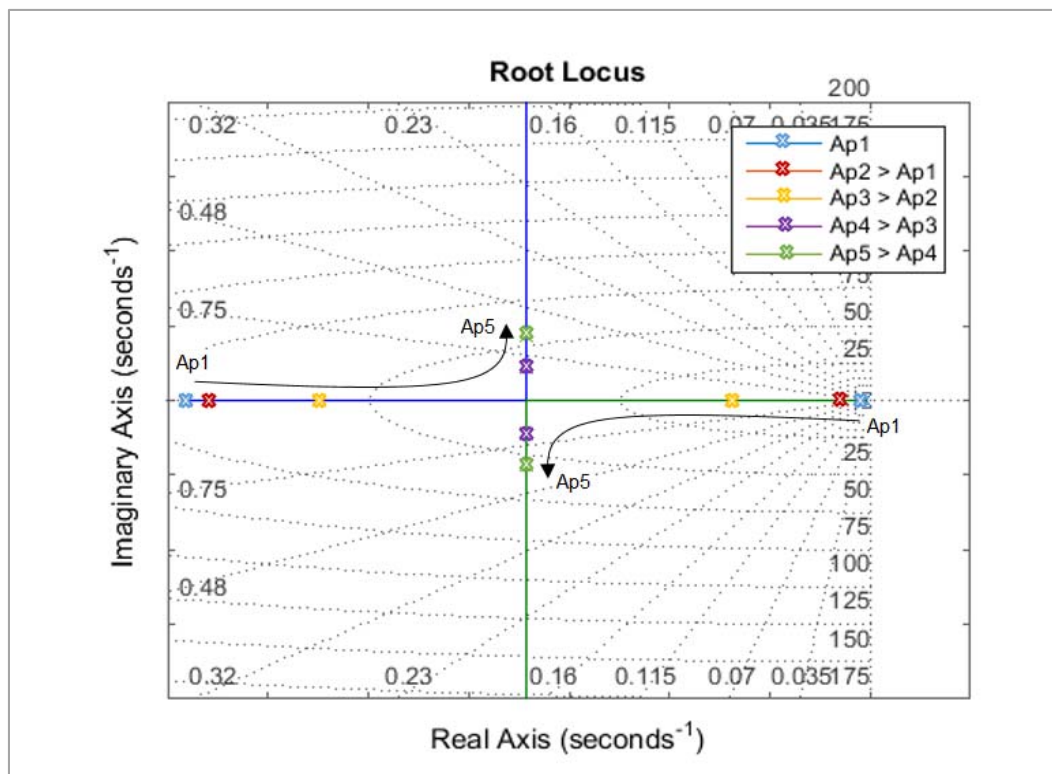


**Figure 3.19.** Root Locus depending on the effective area of the piston

Chapter 4 will describe how the parameters included in the models for the pneumatic system are obtained or assumed. Once these parameters are defined, chapter 5 will present the actual root locus for the pneumatic system, as part of the simulation results and prediction for the pneumatic system.

### 3.2.1.3. Air Compliance – Length of Connective Tubing

Compliance in pneumatic systems relates to the change in volume that air undergoes when it is subjected to pressure. Air compliance in the system under study can be described through the analysis of the expressions that characterize the rate of change of pressure in the chambers of the cylinder. From Eq. 2.22 in chapter 2, the rate of change of pressure in the cap-end and rod-end chamber of the cylinder can be written as follows:

$$\begin{aligned}\dot{P}_1 &= \frac{\kappa_1}{V_1} (Q_1 - \dot{V}_1); & V_1 &= V_{01} + x_p A_1 \\ \dot{P}_2 &= \frac{\kappa_2}{V_2} (Q_2 - \dot{V}_2); & V_2 &= V_{02} - x_p A_2\end{aligned}\quad (3.20)$$

The initial volumes in the chamber of the cylinders,  $V_{01}$  and  $V_{02}$ , depend on the origin of piston displacement. Setting the origin of displacement at the beginning of the stroke, the initial volumes in the chambers of the cylinder become:

$$V_{01} = V_{01t}; \quad V_{02} = V_{02t} + L_{Stroke} A_2 \quad (3.21)$$

Where  $V_{01t}$  and  $V_{02t}$  are the dead volumes in the hoses connecting the control valves and the pneumatic cylinder; accordingly:

$$V_{01t} = V_{02t} = L_t A_t \quad (3.22)$$

Taking the derivatives of the total fluid volumes in the chambers of the cylinder,  $V_1$  and  $V_2$ , and by substituting them in the expressions for the rate of change of pressure, it is obtained:

$$\begin{aligned}\dot{P}_1 &= \frac{\kappa_1}{L_t A_t + x_p A_1} (Q_1 - \dot{V}_{01t} - \dot{x}_p A_1); \\ \dot{P}_2 &= \frac{\kappa_2}{L_t A_t + (L_{Stroke} - x_p) A_2} (Q_2 - \dot{V}_{02t} + \dot{x}_p A_2);\end{aligned}\quad (3.23)$$

From Eq. 3.23, solving for the velocity of the piston, the outcome is:

$$\begin{aligned}\dot{x}_p &= \frac{Q_1}{A_1} - \frac{x_p \dot{P}_1}{\kappa_1} - \frac{L_t A_t \dot{P}_1}{A_1 \kappa_1} - \frac{\dot{V}_{01t}}{A_1}; \\ \dot{x}_p &= -\frac{Q_2}{A_2} + \frac{(L_{Stroke} - x_p) \dot{P}_2}{\kappa_2} + \frac{L_t A_t \dot{P}_2}{A_2 \kappa_2} + \frac{\dot{V}_{02t}}{A_2};\end{aligned}\quad (3.24)$$

Therefore, as verified from Eq. 3.24, air compliance associated with the variation of pressure in the chambers of the cylinder, and the dead volumes of air in lengthy connective tubing would affect the velocity profile of the piston. Although it is common in the design of controllers for pneumatic systems to disregard the dead volumes of air in connective tubing, particularly when the length of connective tubing is not significant ( $L_t < 0.5 [m]$ ), Eq. 3.24 demonstrates that the length of connective tubing is one of the main factors affecting the performance of pneumatic systems.

Moreover, due to the compressibility of air, pneumatic systems are considered natural impedances (Yu et al., 2008; Zhu et al., 2005). In electrical systems, impedance is the effective resistance of a circuit to alternating current when a voltage is applied. Pneumatic systems are considered natural impedances because compressed air changes its volume as pressure is applied, and this effect opposes the motion of pneumatic actuators. In that regard, because linear pneumatic actuators offer compliant actuation, the external force,  $F_{ex}$ , acting upon a linear pneumatic actuator can be modeled through an expression of the form:

$$F_{ex} = m\ddot{x}_m + B\dot{x}_m + k_x(x_m - x_{m0}) \quad (3.25)$$

Where:  $m$  = Mass of the external load.

$B$  = Viscous friction coefficient.

$k_x$  = Spring stiffness.

$x_{m0}$  = Reference load position.

$x_m$  = Load position.

Eq. 3.22 derives from the analysis of the free-body diagram for the load of the piston, as it is represented in the following figure.

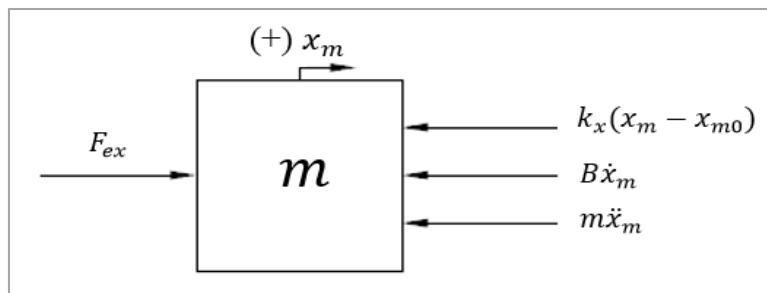


**Figure 3.20.** Impedance characterization: Free body diagram for the load of the piston

The free-body diagram presented in figure 3.20 comes from a global diagram representing the interaction between the external load, the pneumatic cylinder, and the control valves, as it is depicted in figure 3.21.

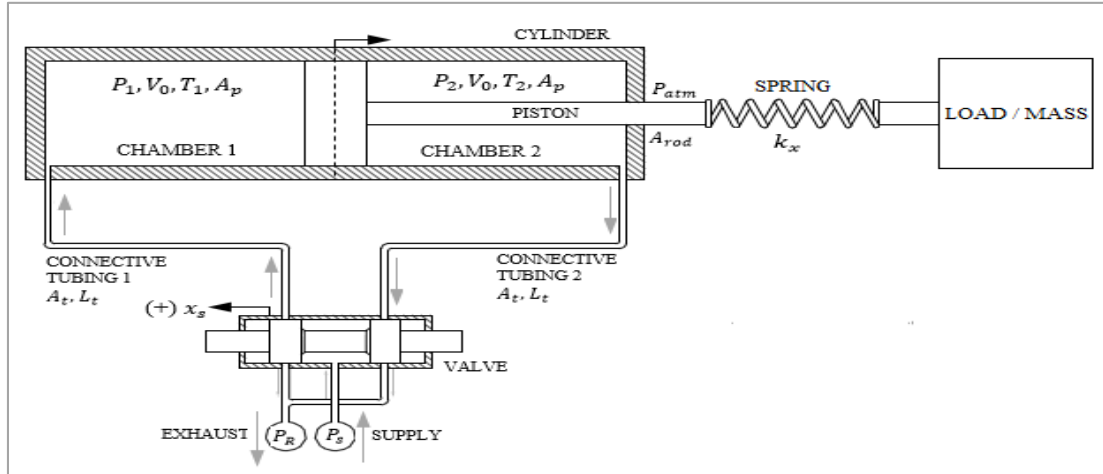


**Figure 3.21.** Impedance characterization: Global representation of the pneumatic system

Notice that a virtual spring has been included between the rod of the piston and the external load. The virtual spring would characterize the compliant actuation of the pneumatic actuator, and its description as a natural impedance. From figure 3.21, the free-body diagram for the piston and the load could be redefined as it is shown below.

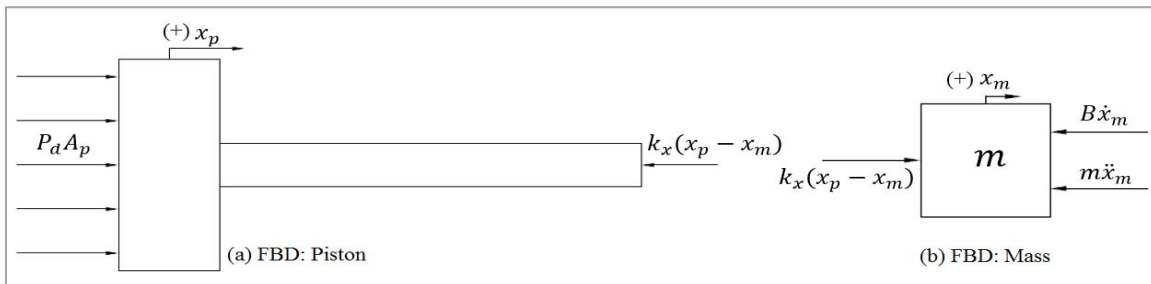


**Figure 3.22.** Impedance characterization: Free-body diagram for the piston and the load

In figure 3.22, the free body diagram for the piston disregards the inertia of the piston, and the friction forces that could act upon it. Nevertheless, the inertia of the load, the viscous friction acting upon it, and the stiffness of the virtual spring should compensate for the forces neglected in the case of the free-body diagram for the piston. In fact, if there is no an actual load acting against the piston, the inertia of the load, and the viscous friction depicted relative to the load would correspond to the inertia of the piston, and the viscous friction acting upon it.



Moreover, by modeling the volumetric flow provided by the valve as the product of the velocity and the effective area of the piston, the following expression can be derived.

$$Q = \dot{x}_p A_p = A_v C_d \sqrt{\frac{(P_S - P_R) - P_d}{\rho}} \quad (3.26)$$

Also, by considering the linearized equation for the flow, Eq. 3.26 becomes:

$$Q = \dot{x}_p A_p = G_f (\Delta A_v) - G_D (\Delta P_d) \quad (3.27)$$

Adding to Eq. 3.26 or Eq. 3.27, the equations derived from the free-body diagrams for the piston and the load, the model for the pneumatic system reduces to the three following equations:

$$Q = \dot{x}_p A_p \quad (3.28)$$

$$P_d A_p = k_x (x_p - x_m) \quad (3.29)$$

$$m \ddot{x}_m + B \dot{x}_m = k_x (x_p - x_m) \quad (3.30)$$

Then, as developed in section 3.2.1.1, a full-nonlinear model, a full-linear model, and a reduced model for the pneumatic system can be derived from the equations identified above.

The following figures show the Simulink models for the full-nonlinear and full-linear systems described in this section. Figure 3.23 shows the Simulink model for the full, nonlinear system, characterized by the use of Eq. 3.26 for describing the flow from the control valves.

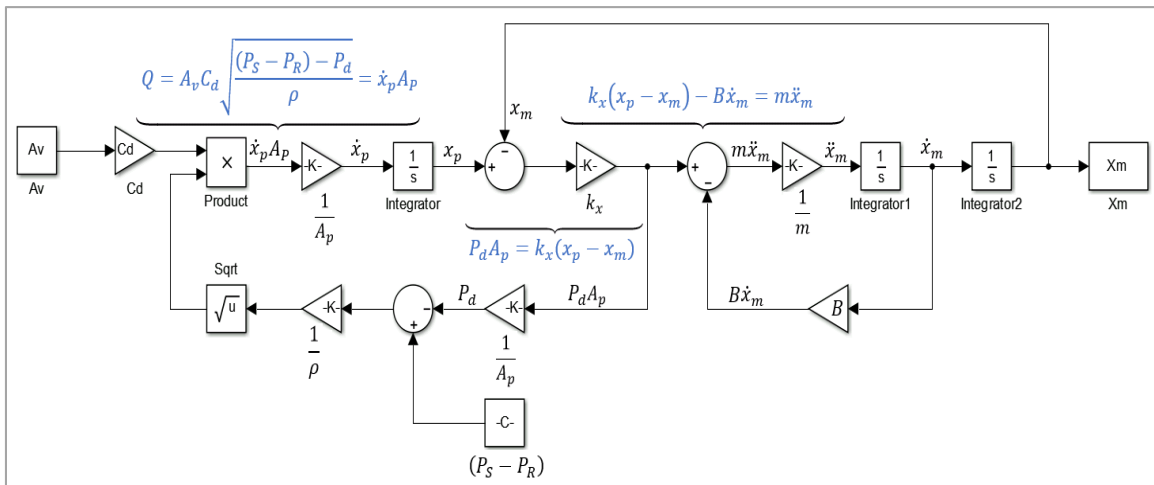


**Figure 3.23.** Impedance characterization: Simulink model for the full, nonlinear system

Figure 3.24 shows the Simulink model for the full, linear system, characterized by the use of Eq. 3.27 for describing the flow from the control valves.

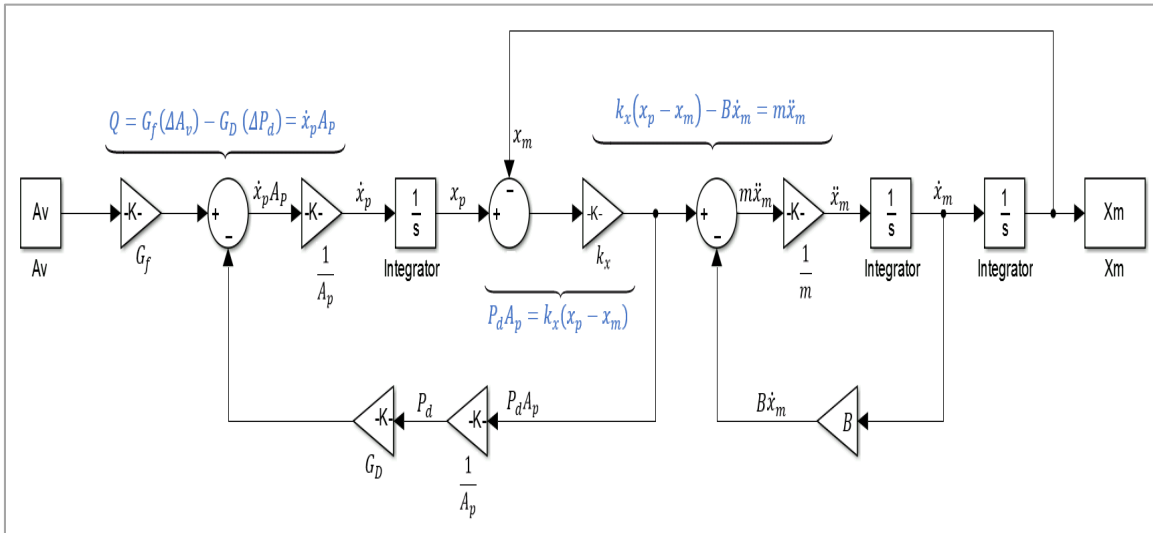


**Figure 3.24.** Impedance characterization: Simulink model for the full, linear system.

Then, to reduce the linear model presented in figure 3.24, the following reduction steps are applied:

First, the signal pick-off point to which the position of the load,  $x_m$ , is fed back in figure 3.24, is moved as shown in figure 3.25.

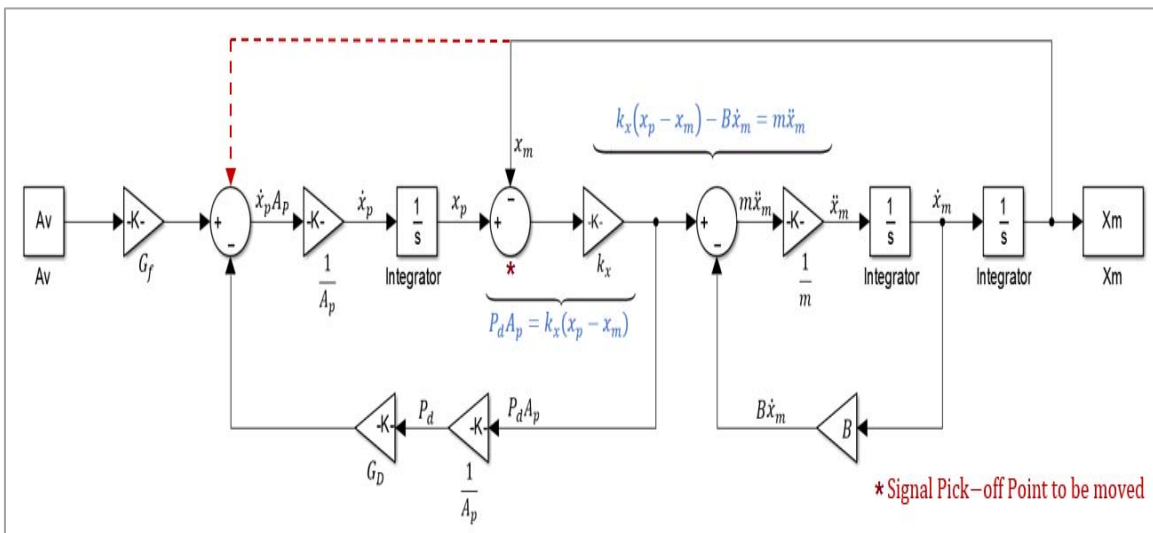


**Figure 3.25.** Impedance characterization: Block reduction steps –Step1.

Then, the block transformation described in figure 3.8 reduces the feedback loops circled in figure 3.26.

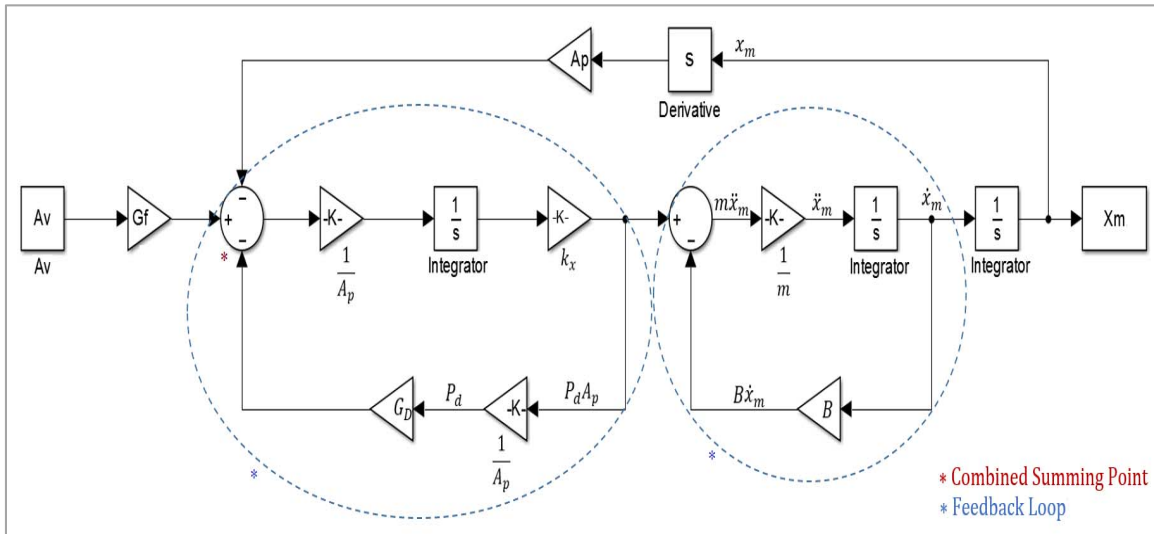


**Figure 3.26.** Impedance characterization: Block reduction steps –Step 2.

Thirdly, the signal pick-off point from which the position of the load,  $x_m$ , is fed back in figure 3.26, is moved as shown in figure 3.27.

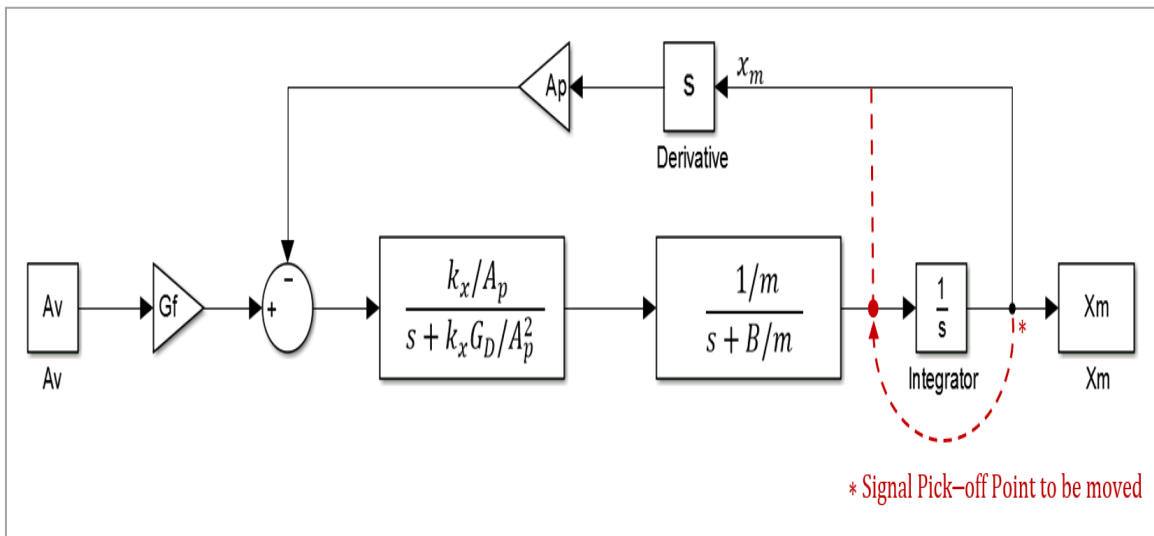


**Figure 3.27.** Impedance characterization: Block reduction steps –Step 3.

Finally, the feedback-loop circled in figure 3.28 is reduced, which results in the block diagram presented in figure 3.29.

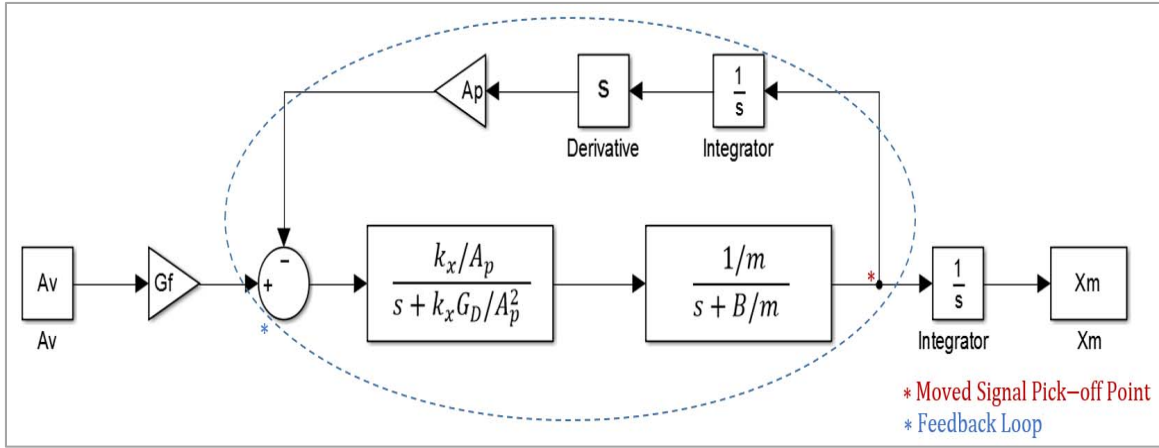


Figure 3.28. Impedance characterization: Block reduction steps –Step 4.

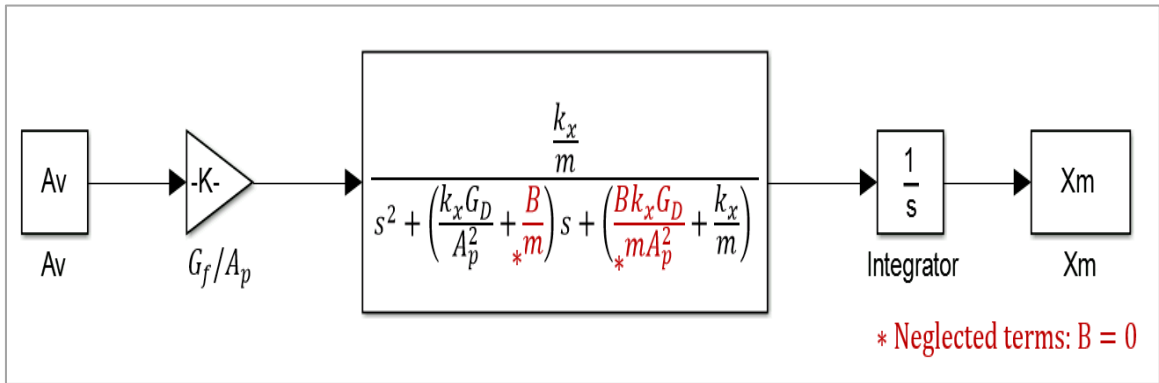


Figure 3.29. Impedance characterization: Block reduction steps –Resulting block diagram.

In figure 3.29, if the viscous friction coefficient,  $B$ , is set to zero, the terms highlighted in red would be neglected, and the resulting reduced block diagram would be represented by the following figure.

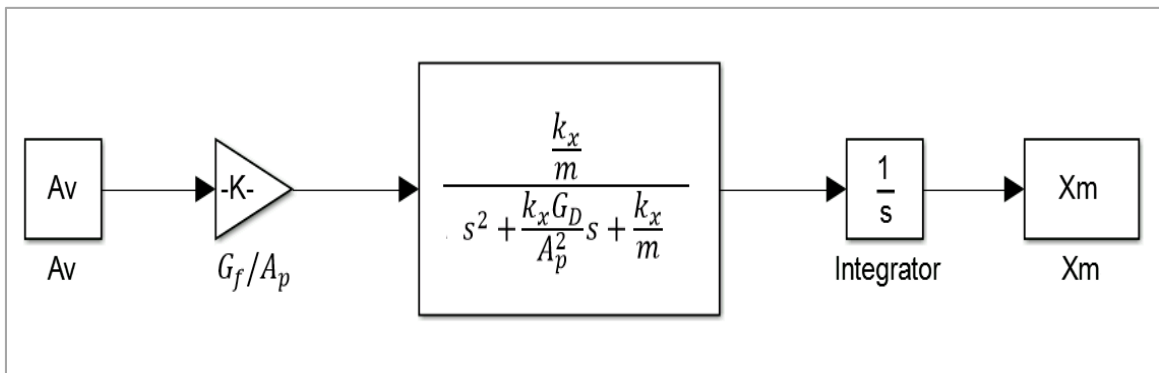
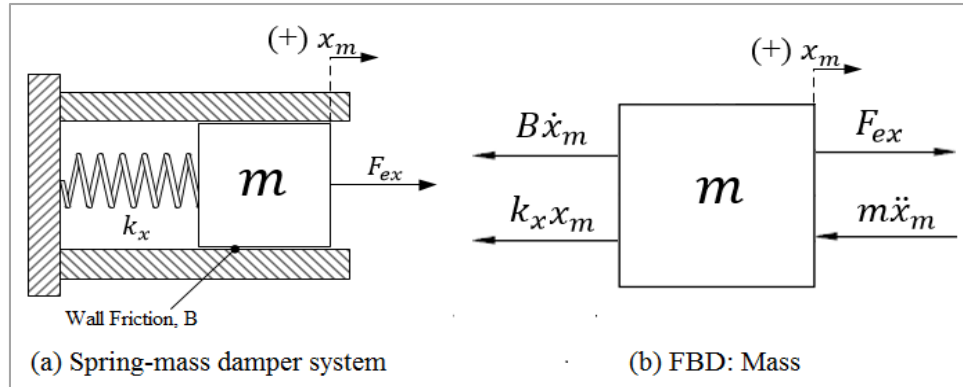


Figure 3.30. Impedance characterization: Block reduction steps –Resulting block diagram if the viscous friction is neglected.

The configuration of the block diagram in figure 3.30 is equal to the configuration for the block diagram in figure 3.6, where the transfer function for the main-larger block corresponds to the transfer function of a second-order underdamped system. Hence, it can be demonstrated that the underdamped natural frequency,  $\omega_n$ , and the damping ratio,  $\xi$ , for the system described in figure 3.30 would be given by:

$$\left. \begin{aligned} \omega_n^2 &= \frac{k_x}{m} \\ 2\xi\omega_n &= \frac{k_x G_D}{A_p^2} \end{aligned} \right\} \begin{aligned} \omega_n &= \sqrt{\frac{k_x}{m}} \\ \xi &= \frac{G_D}{2A_p^2} \sqrt{mk_x} \end{aligned} \quad (3.31)$$

Moreover, the second-order transfer function composing the block diagram in figure 3.30 resembles the transfer function of a simple spring-mass damper system, as the one shown in the following figure.



**Figure 3.31.** (a) Spring-mass damper system, (b) Free body diagram for the mass.

The transfer function for the spring-mass damper system from figure 3.31 is given by:

$$G(s) = \frac{\omega_n^2}{s^2 + 2\xi\omega_n s + \omega_n^2} = \frac{\frac{k_x}{m}}{s^2 + \frac{B}{m}s + \frac{k_x}{m}} \quad (3.32)$$

As noticed from Eq. 3.32, the natural frequency for the spring-mass damper system corresponds to the natural frequency derived in Eq. 3.31, which would validate the characterization of the pneumatic system as a natural impedance. Moreover, it is also verified that the pressure gain,  $G_D$ , would govern the effective damping of the system, as it is explicitly related to the damping ratio,  $\xi$ .

Furthermore, by comparing the natural frequency of the reduced model derived in section 3.2.1.1, with the natural frequency of the reduced model derived in this section.

$$\begin{array}{ccc} \text{Section 3.2.1.1} & \vdots & \text{Section 3.2.1.3} \\ \omega_n^2 = \frac{A_p^2 \beta}{M_{PL} V_0} & \vdots & \omega_n^2 = \frac{k_x}{m} \end{array} \quad (3.33)$$

If the mass of the load,  $m$ , corresponds to the mass of the piston-mass assembly,  $M_{PL}$ , the spring constant,  $k_x$ , would be equivalent to the following terms:

$$k_x \approx \frac{A_p^2 \beta}{V_0} \quad (3.34)$$

Where  $V_0$  is the effective volume in the chambers of the cylinder, including the dead volume in the hoses; and accordingly, it is the term associated with the compliance of air.

Therefore, if this last deduction is related to the deduction from Eq. 3.24, which asserts that the compliance of air in pneumatic systems originates mainly from the variation of pressure and the length of connective tubing, it could also be affirmed that the virtual spring included to characterize the pneumatic system as a natural impedance, primarily represents the effect of the length of pneumatic tubing in the response of the pneumatic system.

Further analysis of the correlation of the spring constant to the length of connective tubing and the effective volume of the cylinder will be presented in chapter 5, which includes the results from the simulation of the response of the pneumatic system characterized as a natural impedance.

#### 3.2.1.4. Closed-Loop Control Design – P-Control

The closed-loop control design proposed in this section corresponds to the design of a proportional controller. The control law for a proportional controller is expressed as follows:

$$A_v^* = K_p (x_{p\text{-desired}} - x_{p\text{-actual}}) \quad (3.35)$$

Where:  $K_p$  = Proportional gain.

$x_{p\text{-desired}}$  = Desired piston position.

$x_{p\text{-actual}}$  = Actual piston position.

Notice that the effective area of the valve,  $A_v$ , is the control input. Nevertheless, the effective area relates to the voltage or current applied to the solenoid of the valve; thus, one or more additional gains would have to be included in order to directly use the input voltage or current applied to the solenoid of the valve as the input for the system.

As it will be described in chapter 4, the relationship between the position of the solenoid, the position of the spool of the valve, and its effective area can be determined experimentally. Accordingly, at some point during the implementation of the controller, it will be necessary to express the control input in terms of the current or voltage applied to the solenoid. Nonetheless, in this section, in order to demonstrate the procedure applied to design a proportional closed-loop controller, the control input used corresponds to the effective area or flow area of the valve.

In addition, the main goal of the controller is to make the difference between the desired and actual position of the piston to become zero. The difference between the desired and actual position of the piston would become zero when the system attains the steady state. The difference between the desired and actual position, once the system attains the steady state is called the steady state error,  $e_{ss}$ , and it can be expressed by:

$$e_{ss} = (x_{p\text{-desired}} - x_{p\text{-actual}})_{ss} \quad (3.36)$$

Where the subscript, ss, denotes steady state.

By including the proportional gain,  $K_p$ , in the reduced model from figure 3.5, and by closing the control loop, the resulting control scheme is presented in the following figure:

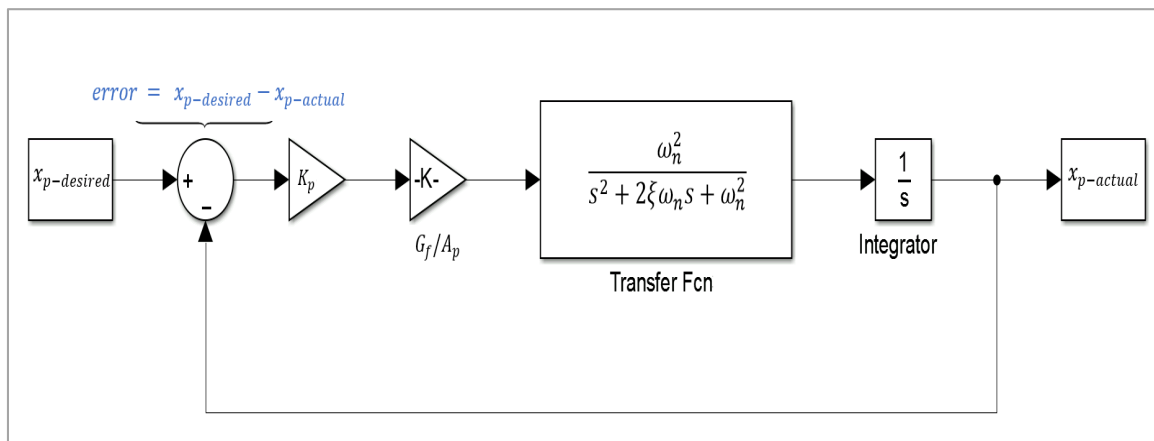


**Figure 3.32.** Simulink model for the reduced closed-loop system

Figure 3.33 shows the simulation response of the system according to the closed-loop model presented in figure 3.32, and by using a proportional gain equal to 0.000003.

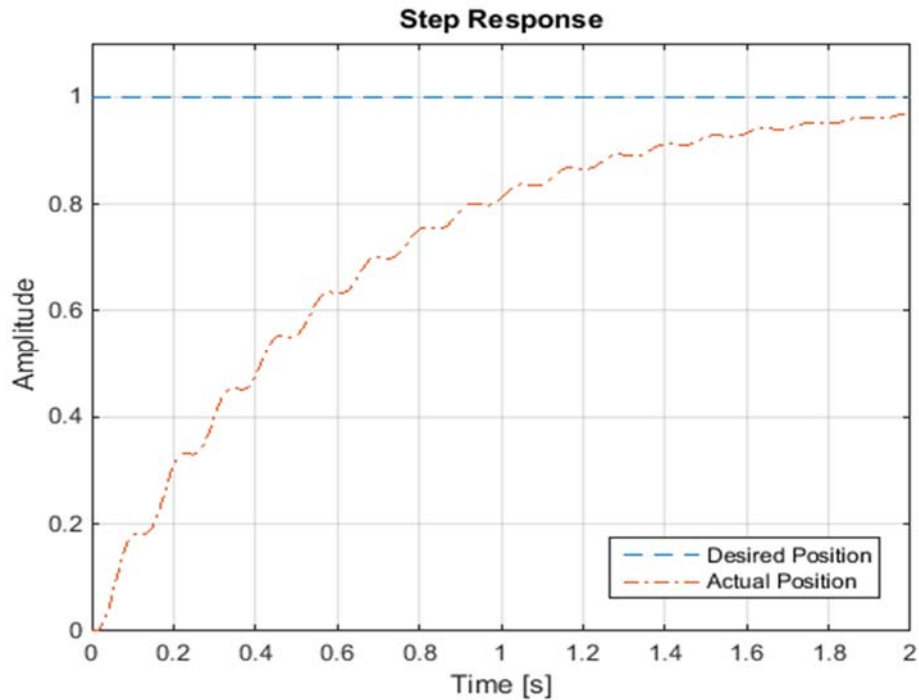


**Figure 3.33.** Preliminary simulation results: Closed-loop position response for a step input

The results displayed in figure 3.33 have been classified as preliminary simulation results because some of the values used for the parameters, gains and constants included in the block diagram were assumed, and not validated at this point. The definitive results from the simulation of the block diagram models derived in this chapter will be presented in chapter 5, after that all the parameters, dynamic gains and constants required be defined and validated in chapter 4.

As evidenced from figure 3.33, with the proportional gain used, the system would require more than 2 seconds in order to reach the desired position. Accordingly, with lower proportional gains than the one used to generate the response presented in figure 3.33, the system would require even more time to reach a steady-state value, which in some cases might not correspond to the desired position. Nevertheless, by increasing the proportional gain, the system might reach the desired position in less time, or it might become unstable. In finding the most appropriate proportional gain, a method commonly applied is root locus analysis, as it will be also demonstrated in chapter 5.



### 3.2.1.5. Response – Pole/Zero Cancellation

As an alternative approach to control the pneumatic system, response-pole/zero cancellation is a technique that seeks to cancel the open-loop poles of the plant of a system by including equivalent zeros in the controller. By placing controller zeros in order to cancel the open-loop poles of a system, what a controller aims to do is to completely or partially cancel dynamics associated with the operation of the plant.

A disadvantage of this control method is that the cancellation of the system open-loop poles can turn the system into a non-causal system. Therefore, in order to keep a system causal, a controller must include a set of poles specifically designed for the system being controlled. In general, the number of poles that have to be included in the controller would correspond to the number of zeros placed to cancel the dynamics of the plant. The following figure shows the structure of the controller including response-pole/zero cancellation.

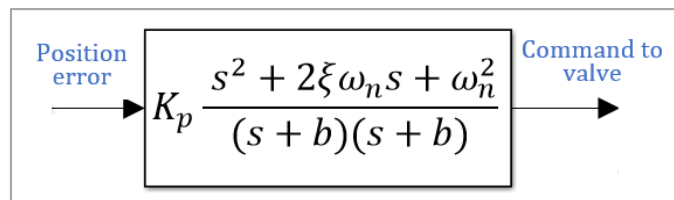


**Figure 3.34.** Structure of the controller by including Response-Pole/Zero Cancellation

As shown in figure 3.34, due to the implementation of response-pole/zero cancellation, the controller now constitutes an individual dynamic system. Figure 3.35 shows the structure of the closed-loop control system, including response-pole/zero cancellation. Marked in red, it can be recognized the effect of pole/zero cancellation in the dynamics of the plant.

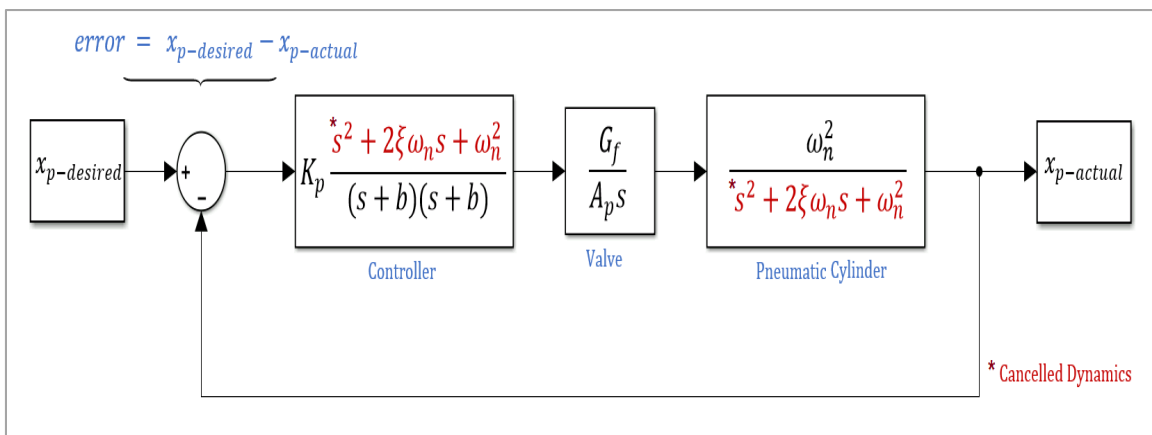


**Figure 3.35.** Simulink model for the control system including response-pole/zero cancellation

As it was emphasized before, the poles included in the controller have to be properly selected in order to keep the system casual. Nevertheless, these poles can also be selected in order to shape the response of the system according to the required design specifications.

Although it is not possible to completely cancel the dynamics of the plant of a system, a satisfactory approximation to the design requirements can be obtained through the implementation of response-pole/zero cancellation, which would be particularly important in order to attenuate the effect of the compressibility of air and the length of connective tubing in the overall response of the pneumatic system. The simulation response of the model described in figure 3.35 will be also included in chapter 5.

### 3.2.1.6. Discrete Time Analysis

Due to the fact that the controller derived in the previous sections has been produced in terms of a continuous-time dynamic system, in order to implement this controller using a digital-computer-based platform, such as the ARDUINO UNO board, it is necessary to convert the controller into a discrete dynamic system.

In order to discretize the controller, the added poles are ignored by considering that both are at infinity, and accordingly fast enough to be negligible. Hence, the control input corresponding to the flow area of the control valve can be expressed as follows:

$$A_v = K_p e(s^2 + 2\xi\omega_n s + \omega_n^2) \quad (3.37)$$

Since in the Laplace domain, multiplication by “s” represents the derivative of a term, by using a finite difference approximation of the derivative given by:

$$se \cong \frac{e - e_{old}}{\mathbb{T}} \quad (3.38)$$

Where the subscript “old” denotes that the value of the error corresponds to its immediate previous value, separated of the current value by a constant period of time  $\mathbb{T}$ .

It is verified that Eq. 3.37 becomes:

$$A_v = K_p \left[ \frac{e - e_{old}}{\mathbb{T}^2} - \frac{e_{old} - (e_{old})_{old}}{\mathbb{T}^2} + 2\xi\omega_n \left( \frac{e - e_{old}}{\mathbb{T}} \right) + e\omega_n^2 \right] \quad (3.39)$$

Finally, through mathematical manipulation, Eq. 3.39 can be converted into:

$$A_v = K_p \frac{[e(1 + 2\xi\omega_n T + \omega_n^2 T^2) - e_{old}(2 + 2\xi\omega_n T) + (e_{old})_{old}]}{T^2} \quad (3.40)$$

Eq. 3.40 would constitute the real-time expression that should be included in the code for the controller to be implemented. The results from the implementation of this controller will be presented in chapter 6.

### 3.2.2. Design Alternative 2: State-space model representation

The second controller design alternative bases on a state-space model representation of the pneumatic system. A state space model representation comprehends the set of differential equations that characterize the behavior of a system according to its response through time. Wang et al., (2001) demonstrated that a pneumatic system could be modeled as a fourth-order affine nonlinear system. An affine nonlinear system is a system whose state equations are linear in the input controls. The state-space model representation for an affine nonlinear system can be written as follows:

$$\begin{aligned} \dot{x} &= A(x(t), t) + B(x(t), t)u \\ y &= C(x(t), t) + D(x(t), t)u \\ x(t_0) &= x_0 \end{aligned} \quad (3.41)$$

Where A, B, C and D are matrices, the elements of which might be function of the states and time, u is the input control, and y is the output of the system. Moreover, the initial state at time  $t_0$  corresponds to  $x_0$ .

In the model of the pneumatic system described in Chapter 2, by ignoring the length of pneumatic tubing that connects the cylinder and the control valves, the resulting affine nonlinear system is of fourth. Defining the state variables, as follows:

$$x_1 = x_p; \quad x_2 = \dot{x}_p; \quad x_3 = P_1; \quad x_4 = P_2 \quad (3.42)$$

Where the notation corresponds to the nomenclature used in Chapter 2.

By taking the derivative of the state variables defined above, it results:

$$\dot{x}_1 = \dot{x}_p; \quad \dot{x}_2 = \ddot{x}_p; \quad \dot{x}_3 = \dot{P}_1; \quad \dot{x}_4 = \dot{P}_2 \quad (3.43)$$

From the differential equations identified and formulated in Chapter 2, the state variable equations for the pneumatic system under analysis are:

$$\dot{x}_1 = x_2 \quad (3.44)$$

$$\dot{x}_2 = \frac{1}{M_{LP}} [-D_{vsc}x_2 - F_{sc}(x_2, x_3, x_5) \pm A_1x_3 \mp A_2x_5 \mp P_{atm}A_{rod}] \quad (3.45)$$

$$\dot{x}_3 = kx_3 \left\{ \frac{C_D\sqrt{RT}}{P_{Rv1}} [(\Phi_f(x_3, P_{Rv1})u_1)_{P \rightarrow A} - (\Phi_f(x_3, P_{Rv1})u_1)_{A \rightarrow R}] \mp x_2A_1 \right\} / (V_{01} \pm x_1A_1) \quad (3.46)$$

$$\dot{x}_4 = kx_4 \left\{ \frac{C_D\sqrt{RT}}{P_{Rv2}} [(\Phi_f(x_4, P_{Rv2})u_2)_{P \rightarrow A} - (\Phi_f(x_4, P_{Rv2})u_2)_{A \rightarrow R}] \pm x_2A_2 \right\} / (V_{02} \mp x_1A_2) \quad (3.47)$$

Double signs in the state variable equations seek to account for the change of direction of displacement due to extension and retraction of the cylinder. The above and underneath signs apply respectively to the extension and retraction of the piston.

Likewise, Eq. 3.46 and Eq. 3.47 account for the change of direction of flow relative to each valve when the cylinder extends or retracts. It has to be noticed that the valves will never work under both regimes at the same time. Accordingly, different operation regimes require different combinations of input controls. For instance, during extension of the cylinder, Eq. 3.46 and Eq. 3.47 would become:

$$\dot{x}_3 = kx_3 \left\{ \frac{C_D\sqrt{RT}}{P_{Rv1}} [(\Phi_f(x_3, P_{Rv1})u_1)_{P \rightarrow A}] - x_2A_1 \right\} / (V_{01} + x_1A_1) \quad (3.48)$$

$$\dot{x}_4 = kx_4 \left\{ \frac{C_D\sqrt{RT}}{P_{Rv2}} [ -(\Phi_f(x_4, P_{Rv2})u_2)_{A \rightarrow R}] + x_2A_1 \right\} / (V_{02} - x_1A_2) \quad (3.49)$$

During retraction of the cylinder, Eq. 3.46 and Eq. 3.49 become:

$$\dot{x}_3 = kx_3 \left\{ \frac{C_D\sqrt{RT}}{P_{Rv1}} [ -(\Phi_f(x_3, P_{Rv1})u_1)_{A \rightarrow R}] + x_2A_1 \right\} / (V_{01} - x_1A_1) \quad (3.50)$$

$$\dot{x}_4 = kx_4 \left\{ \frac{C_D \sqrt{RT}}{P_{Rv2}} \left[ (\Phi_f(x_4, P_{Rv2})u_2)_{P \rightarrow A} \right] - x_2 A_1 \right\} / (V_{02} + x_1 A_2) \quad (3.51)$$

Around the desired positioning point, before the steady-state is reached, the cylinder might work alternately between the extension and retraction regimes. The identification of the most favorable combination of input controls might result from the application of optimal control schemes.

At this stage of the design of the controller, the input control corresponds to the effective area of the valve. Nevertheless, the effective area of the valve will have to be related to the displacement of the spool of the valve, according to Eq. 2.14 through Eq. 2.18; and ultimately, it will have to be correlated to the voltage and current applied to the solenoid of the valve.

In matrix form, the complete state-space representation for the system is given by:

$$\begin{bmatrix} \dot{x}_1 \\ \dot{x}_2 \\ \dot{x}_3 \\ \dot{x}_4 \end{bmatrix} = \begin{bmatrix} x_2 \\ \frac{1}{M_{LP}} [-D_{vsc}x_2 - F_{sc}(x_2, x_3, x_5) \pm A_1 x_3 \mp A_2 x_4 \mp P_{atm} A_{rod}] \\ kx_3 \left\{ \frac{C_D \sqrt{RT}}{P_{Rv1}} [(\Phi_f(x_3, P_{Rv1})u_1)_{P \rightarrow A} - (\Phi_f(x_3, P_{Rv1})u_1)_{A \rightarrow R}] \mp x_2 A_1 \right\} \\ (V_{01} \pm x_1 A_1) \\ kx_4 \left\{ \frac{C_D \sqrt{RT}}{P_{Rv2}} [(\Phi_f(x_4, P_{Rv2})u_2)_{P \rightarrow A} - (\Phi_f(x_4, P_{Rv2})u_2)_{A \rightarrow R}] \pm x_2 A_2 \right\} \\ (V_{02} \mp x_1 A_2) \end{bmatrix} \quad (3.52)$$

$$y = [1 \quad 0 \quad 0 \quad 0] \begin{bmatrix} x_1 \\ x_2 \\ x_3 \\ x_4 \end{bmatrix} = x_1$$

Where the output of the system,  $y$ , corresponds to the position of the cylinder.

Although Eq. 3.52 is a complete state-space representation of the system, in reference to the form given by Eq. 3.41, the matrixes  $A$  and  $B$  are not explicitly defined. They will be explicitly defined in the following section.

### 3.2.2.1. Linearization of the system at an equilibrium point

An equilibrium point analysis aims to find linear representations of non-linear systems when their states are close to an equilibrium point. At the equilibrium point, for the fourth-order system, the derivatives of the state variables become zero; hence:

$$\dot{x}_1 = 0; \quad \dot{x}_2 = 0; \quad \dot{x}_3 = 0; \quad \dot{x}_4 = 0; \quad (3.53)$$

$$\begin{bmatrix} \dot{x}_1 \\ \dot{x}_2 \\ \dot{x}_3 \\ \dot{x}_4 \end{bmatrix} = \begin{bmatrix} f_1(x_1, x_2, x_3, x_4, u_1, u_2, t) \\ f_2(x_1, x_2, x_3, x_4, u_1, u_2, t) \\ f_3(x_1, x_2, x_3, x_4, u_1, u_2, t) \\ f_4(x_1, x_2, x_3, x_4, u_1, u_2, t) \end{bmatrix} = \begin{bmatrix} 0 \\ 0 \\ 0 \\ 0 \end{bmatrix} \quad (3.54)$$

From Eq. 3.52 through Eq. 3.54, the equilibrium point is defined as follows:

$$x^* := (x_1^*, x_2^*, x_3^*, x_4^*) = (X_e, 0, P_{e1}, P_{e2}) \quad (3.55)$$

$$u_1^* := 0; \quad u_2^* := 0$$

Where  $X_e$  represents an arbitrary position of the cylinder between 0 and its maximum stroke, and  $P_{e1}$  and  $P_{e2}$  are equilibrium pressures in the extension and retraction chamber of the cylinder, respectively. These pressures have been determined experimentally according to the methodology presented in chapter 4. The values for these equilibrium pressures are:

$$P_{e1} \approx 1.2P_{atm}; \quad P_{e2} \approx P_{atm} \quad (3.56)$$

From Eq. 3.36, the static friction force,  $F_{SC-static}$ , can be found to be:

$$F_{SC-static} = \pm 1.2A_1P_{atm} \mp A_2P_{atm} \mp P_{atm}A_{rod} \approx P_{atm}(\pm 1.2A_1 \mp A_2 \mp A_{rod}) \quad (3.57)$$

Once the equilibrium point is determined, the next step is to verify the behavior of the system in the vicinity of this equilibrium point. From the knowledge of the equilibrium point, the behavior of a non-linear system can be approximated by linear dynamics of the form (Lu Ping, 2015):

$$\begin{aligned} \delta\dot{x} &= A(t)\delta x + B(t)\delta u \\ \delta y &= C(t)\delta x + D(t)\delta u \end{aligned} \quad (3.58)$$

$$\delta x(t) = x(t) - x^*(t)$$

$$\delta y(t) = y(t) - y^*(t)$$

$$\delta u(t) = u(t) - u^*(t)$$

In order to derive Eq. 3.58, it is acknowledged that:

$$\dot{x} = f(x, u, t) = f(x^* + \delta x, u^* + \delta u, t) \quad (3.45)$$

$$y = g(x, u, t) = g(x^* + \delta x, u^* + \delta u, t)$$

By expanding the right hand side of Eq. 3.59 through a first-order Taylor series expansion at the equilibrium point  $(x^*, u^*)$ , and by cancelling the higher-order terms, it is obtained:

$$\delta \dot{x} = \dot{x} - f(x^*, u^*, t) = \left. \frac{\partial f(x, u, t)}{\partial x} \right|_{(x^*, u^*)} \delta x + \left. \frac{\partial f(x, u, t)}{\partial u} \right|_{(x^*, u^*)} \delta u \quad (3.59)$$

$$\delta y = y - g(x^*, u^*, t) = \left. \frac{\partial g(x, u, t)}{\partial x} \right|_{(x^*, u^*)} \delta x + \left. \frac{\partial g(x, u, t)}{\partial u} \right|_{(x^*, u^*)} \delta u$$

The matrices A, B, C and D in Eq. 3.58 correspond to the Jacobian of the vector functions  $f(x, u, t)$  and  $g(x, u, t)$  respectively, with respect to the equilibrium point:

$$A(t) = \left. \frac{\partial f(x, u, t)}{\partial x} \right|_{(x^*, u^*)} ; \quad B(t) = \left. \frac{\partial f(x, u, t)}{\partial u} \right|_{(x^*, u^*)} \quad (3.60)$$

$$C(t) = \left. \frac{\partial g(x, u, t)}{\partial x} \right|_{(x^*, u^*)} ; \quad D(t) = \left. \frac{\partial g(x, u, t)}{\partial u} \right|_{(x^*, u^*)}$$

For the fourth-order system defined by Eq. 3.52, the A and B matrices result:

$$A = \begin{bmatrix} \frac{\partial f_1}{\partial x_1} & \dots & \frac{\partial f_1}{\partial x_4} \\ \vdots & \ddots & \vdots \\ \frac{\partial f_4}{\partial x_1} & \dots & \frac{\partial f_4}{\partial x_4} \end{bmatrix}_{(x^*, u^*)} = \begin{bmatrix} 0 & 1 & 0 & 0 \\ 0 & -D_{vsc}/M_{PL} & \pm A_1/M_{LP} & \mp A_2/M_{LP} \\ 0 & \mp A_1 k P_{e1}/(V_{01} \pm X_e A_1) & 0 & 0 \\ 0 & \pm A_2 k P_{e2}/(V_{02} \mp X_e A_2) & 0 & 0 \end{bmatrix}; \quad (3.61)$$

$$B = \begin{bmatrix} \frac{\partial f_1}{\partial u_1} & \frac{\partial f_1}{\partial u_2} \\ \vdots & \vdots \\ \frac{\partial f_4}{\partial u_1} & \frac{\partial f_4}{\partial u_2} \end{bmatrix}_{(x^*, u^*)} = \begin{bmatrix} 0 & 0 \\ 0 & 0 \\ \frac{kP_{e1}C_D\sqrt{RT}[\pm\phi_f(P_{e1}, P_{rv})]_{P \rightarrow A}}{(V_{01} \pm X_e A_1)} & \frac{kP_{e2}C_D\sqrt{RT}[\pm\phi_f(P_{e2}, P_{rv})]_{P \rightarrow A}}{(V_{02} \pm X_e A_2)} \\ 0 & 0 \end{bmatrix};$$

$$C = [1 \ 0 \ 0 \ 0]; \quad D = [0]$$

Once all the matrixes in Eq. 3.58 are defined, the next step comprises the simulation of the response obtained, by plugging the values corresponding to the different parameters, and by checking for stability of the system.

### 3.2.2.2. Internal Stability and Input-Output Stability

In general terms, a system is stable if its response goes to zero as time tends to infinity. In control jargon, a continuous-time system is stable if and only if all its poles lie in the left half complex plane. The stability of a system can be evaluated in relation to its internal and external behavior. In that regard, two different viewpoints can be applied:

- If the zero input response of a system decays to zero as time tends to infinity, independently of the initial conditions, the system has internal or asymptotic stability.
- If the zero-state response of a system is bounded (i.e. it does not grow to positive or negative infinity) as time approaches infinity, independently of the initial conditions, and for all bounded inputs, the system is said to be BIBO stable (bounded-input bounded-output stable).

The main condition for a system to be BIBO stable, and internally or asymptotically stable is that every pole of its transfer function must have a negative real part. Nevertheless, it has to be emphasized the fact that internal stability implies BIBO stability, and not contrariwise.

The case where a system is BIBO stable, but not asymptotically stable, occurs when all non-zero positive poles of the transfer function of a system are cancelled by its non-zero positive zeros. In that case, as time goes to infinity, at least one term in the zero-input response will go to infinity, while the zero-state response will decay to zero. Stability of the fourth-order state space system derived in this section will be verified in chapter 5.



In addition to the assessment of stability according to the criteria presented before, other conditions can be verified in order to ensure the fulfillment of the design requirements, as it will be demonstrated in the following section.

### 3.2.2.3. *Controllability and Observability*

In the design of a controller, the inspection of controllability and observability conditions provides a mean to determine at what extent the proposed control schemes satisfy the design requirements, and what additional measures should be taken to improve and monitor the performance of the controlled system.

#### 3.2.2.3.1. *Controllability*

First, a system is controllable if for any time different than zero, the system can be steered to a specific state, and kept at this condition by applying a specific control input. Controllability of a system ensures that the system is stabilizable, which is the main condition in order to solve a linear quadratic regulator (LQR) problem.

A practical way to verify whether or not a system is controllable is to define the controllability matrix  $CO$ , and to check if it is full row rank (i.e., the number of linearly independent rows of  $CO$  is equal to the order of the system). In that regard, the controllability matrix  $CO$  is given by:

$$CO = [B : AB : A^2B : \dots : A^{n-1}B] \quad (3.62)$$

Where  $n$  = Order of the system (i.e., the number of rows and columns of matrix  $A$ )

Hence, in order for the pneumatic system to be controllable, the controllability matrix for the fourth-order system defined by Eq. 3.58 must have a row rank equal to 4.

#### 3.2.2.3.2. *Observability*

Due to the fact that the optimal controller to be designed is of the state feedback form, it is important to know whether or not all the states would be available for feedback. The condition under which all the states are available for feedback is called observability. A system is completely observable if for a specific period of time, any initial state variable can be derived from the output of the system.

Similarly to the confirmation of controllability, in order to determine if a system is completely observable, an observability matrix OB is defined, and it is verified if it has full column rank (i.e., the number of linearly independent columns of OB is equal to the order of the system).

The observability matrix OB is defined by:

$$OB = [C : CA : CA^2 : \dots : CA^{n-1}]' \quad (3.63)$$

Where n = Order of the system (i.e., the number of rows and columns of matrix A)

In order for the system under study to be observable, the observability matrix for the fourth-order system defined by Eq. 3.58 must have a column rank equal to 4. MATLAB provides commands to calculate the controllability and observability matrix of a system expressed in state-space form, and to check its rank, as it will be shown in chapter 5.

#### 3.2.2.4. Linear Quadratic Regulator (LQR) Design

In Chapter 1, the LQR problem was referred as an optimal control problem for which the control function  $u^*$  seeks to minimize the following cost function J:

$$J = \frac{1}{2} \int_{t_0}^T [x'(t)Q_J(t)x(t) + u'(t)R_J u(t)] dt \quad (3.64)$$

Where  $Q_J$  and  $R_J$  are symmetric matrices. Moreover, the necessary and sufficient conditions to ensure the existence and uniqueness of an optimal control  $u^*$  able to asymptotically stabilize the system are:

- The system has to be controllable.
- $R_J$  must be positive definite (i.e., it is symmetric and has positive eigenvalues).
- $Q_J$  must be positive semidefinite (i.e., it is symmetric and has nonnegative eigenvalues).

Once it is verified that the system is completely controllable, the LQR design process continues with the definition of the matrices  $R_J$  and  $Q_J$  included in the cost function  $J$ . These matrices can be determined using frequency domain techniques in order to reach a certain bandwidth (Liu and Bobrow, 1988), or using MATLAB in order to interpolate several coefficient values until finding the most satisfactory response.

Although the method to find  $Q_J$  and  $R_J$  using MATLAB could become highly iterative and time consuming, this method is applied due to its versatility and efficacy.

Once the matrices  $Q_J$  and  $R_J$  are defined, from the solution to the steady continuous-time algebraic Riccati equation given by:

$$0 = ZA + A'Z - ZBR_J^{-1}B'Z + Q_J \quad (3.65)$$

The “optimal” gain matrix can be derived as follows:

$$K = R_J^{-1}B'Z \quad (3.66)$$

Subsequently, the LQR control law to be implemented would be of the form:

$$u^* = -Kx \quad (3.67)$$

At this point in the design of the controller, the implementation of the LQR control law would enable the system to stabilize around a desired position; nevertheless, a command reference input has not been included yet; and hence, it is not possible to measure the performance of the system in terms of the steady-state error, and the resulting steady-state accuracy. The next section deals with the design of a controller that depends on a command reference input, and the performance of which can be assessed in terms of its steady-state accuracy.

#### 3.2.2.5. Tracking Control Design

A controller that depends on a command reference input is known as a tracking controller. Several techniques can be applied to include the effect of a command reference input in the control of a system. Two techniques commonly applied in control are integral control, and external reference gain tracking control, which are applied and analyzed in this section.

##### 3.2.2.5.1. Integral control

As described in chapter 1, a technique that enables the system to achieve zero steady state error is integral control. Integral control bases on placing an integrator in the forward path in series with the system, by increasing the order of the system by one.

As described in Stefani, et al., 2002, in order to augment the order of the plant, the required new state variable is defined as:

$$x_i = \int error dt = \int (r - Cx) dt = \int (r - y) dt = \int (r - Cx) dt \quad (3.68)$$

Where: r = Command reference input

Accordingly, the derivative of the additional state variable would be given by:

$$\dot{x}_i = r - Cx \quad (3.69)$$

By including the additional state variable  $x_i$ , the state-space representation of the system is modified as follows:

$$\begin{bmatrix} \dot{x} \\ \dot{x}_i \end{bmatrix} = \begin{bmatrix} A & 0 \\ -C & 0 \end{bmatrix} \begin{bmatrix} x \\ x_i \end{bmatrix} + \begin{bmatrix} B \\ 0 \end{bmatrix} u + \begin{bmatrix} 0 \\ 1 \end{bmatrix} r \quad (3.70)$$

With a control law defined by:

$$u = -Kx - K_i x_i = -[K \quad K_i] \begin{bmatrix} x \\ x_i \end{bmatrix} \quad (3.71)$$

Where  $K$  and  $K_i$  are the matrix gains for the original and the augmented system, respectively.

#### 3.2.2.5.2. External reference gain tracking control

An external reference gain tracking controller, also called a feedforward compensator, places a reference gain,  $\bar{N}$ , outside the feedback loop, and incorporates the reference command input into the system through a control law of the form:

$$u = -Kx + \bar{N}r \quad (3.72)$$

For the case of state feedback, the control law defined above provides steady state accuracy to a system excited by a step input.

As described in Stefani, et al., 2002, by introducing the control law defined in Eq. 3.73, the state space representation of the system becomes:

$$\begin{aligned}\dot{x} &= (A - BK)x + B\bar{N}r \\ y &= Cx\end{aligned}\quad (3.73)$$

At steady state, the states and output must reach a constant value; accordingly:

$$\dot{x}_{ss} = 0 = (A - BK)x_{ss} + B\bar{N}r \quad (3.74)$$

Where the subscript “ss” denotes steady state.

From Eq. 3.74, at steady state, the states and the output are derived as follows:

$$x_{ss} = -(A - BK)^{-1}B\bar{N}r; \quad y_{ss} = -C(A - BK)^{-1}B\bar{N}r \quad (3.75)$$

Then, from the definition of steady state error,  $e_{ss}$ , as the difference between the input and the output:

$$e_{ss} = r - y_{ss} = r + C(A - BK)^{-1}B\bar{N}r = r[1 + C(A - BK)^{-1}B\bar{N}] \quad (3.76)$$

Since the steady state output must be equal to the input ( $e_{ss} = 0$ ), the reference gain,  $\bar{N}$ , is given by:

$$\bar{N} = -\frac{1}{C(A - BK)^{-1}B} \quad (3.77)$$

Where the inverse  $(A - BK)^{-1}$  exists only if  $(A - BK)$  is a stable matrix.

For the pneumatic system, in order to implement a feedforward compensator; first, the gain matrix,  $K$ , has to be determined following a pole placement method as the one described in section 3.2.2.4.

#### 3.2.2.6. System Discretization

As noted on section 3.2.1.6, in order to implement any control law designed through computer-aid methods, it is necessary to discretize the set of equations that characterize the dynamic system under analysis. Considering the continuous-time state equations presented in Eq. 3.41, the discrete counterpart of these equations is:

$$\begin{aligned}x[k + 1] &= A_d x[k] + B_d u[k] \\ y[k] &= C_d x[k] + D_d u[k]\end{aligned}\tag{3.78}$$

Where the subscript “d” denotes a discretized element.

In order to obtain Eq. 3.78, it is assumed that the value of the input changes only at a discrete time  $kT$ , with the response of the system being computed at the same discrete time that the input changes. A formal description of the discretization process for state-space systems can be found in [Chen, 1999](#).

In this section, it is emphasized that if the state-space design alternatives described in previous sections are applied, the state-space models used must be discretized before being implemented. In that regard, MATLAB also provides useful commands and functions for converting continuous-time state equations into discrete-time state equations, which will be covered in chapter 5.

### 3.2.3. Design Alternative 3: Nonlinear Feedback Linearization

The third controller design alternative centers on the application of nonlinear feedback linearization theory. Nonlinear feedback linearization is based on finding a state feedback control  $u^*$  and a change of variables  $z^*$  that linearize the state-space representation of a nonlinear system. Accordingly, for a non-linear affine system of the form:

$$\begin{aligned}\dot{x} &= f(x) + g(x)u \\ y &= h(x)\end{aligned}\tag{3.79}$$

There might exist a state feedback control  $u^*$ , and a change of variables  $z^*$ :

$$\begin{aligned}u^* &= \alpha(x) + \beta(x)v \\ z^* &= \mathcal{T}(x)\end{aligned}\tag{3.80}$$

Which transform the nonlinear system in Eq. 3.79 into an equivalent linear system. In Eq. 3.80,  $\alpha$  and  $\beta$  are vectors expressed in terms of the state variables of the system,  $v$  is a designed input, and  $\mathcal{T}$  is a transformation matrix.

The nonlinear feedback linearization procedure described in this section is similar to the procedure applied by Wang et al. (2007). This linearization method is summarized below according to the description found in Khalil and Grizzle (2002).

First, the Lie derivative of  $h$  with respect to  $f$  and  $g$  are defined as follows:

$$L_f h(x) = \frac{\partial h}{\partial x} f(x); \quad L_g h(x) = \frac{\partial h}{\partial x} g(x) \quad (3.81)$$

In general, for higher order derivatives the following notation applies:

$$L_f^k h(x) = L_f L_f^{k-1} h(x) = \frac{\partial (L_f^{k-1} h(x))}{\partial x} f(x) \quad (3.82)$$

Hence, by taking the first derivative of  $y$  in Eq. 3.79:

$$\dot{y} = \frac{\partial h}{\partial x} [f(x) + g(x)u] = L_f h(x) + L_g h(x)u \quad (3.83)$$

If  $L_g h(x) = 0$ , then the derivative of  $y$  does not depend on  $u$ . Similarly, by taking successive derivatives, denoted by  $y^{(2)}, y^{(3)}, \dots, y^{(q)}$ , if:

$$\begin{cases} L_g L_f^{i-1} h(x) = 0, & i = 1, 2, \dots, q-1; \\ L_g L_f^{q-1} h(x) \neq 0 \end{cases} \quad (3.84)$$

Then, the derivative  $y^{(q)}$  depends on  $u$ , as displayed below:

$$y^{(q)} = L_f^q h(x) + L_g L_f^{q-1} h(x)u \quad (3.85)$$

The integer  $q$  is called the relative degree of the system, and the state-feedback control can be expressed as follows:

$$u = \frac{1}{L_g L_f^{q-1} h(x)} [-L_f^q h(x) + v] \quad (3.86)$$

Therefore, by substituting Eq. 3.86 in Eq. 3.75, the input-output map would reduce to:

$$y^{(q)} = v \quad (3.87)$$

Following the procedure described above, for the fourth-order system defined in Eq. 3.52, it is verified that the relative degree of the system is equal to 3. Accordingly, the first three components of the coordinate transformation,  $z^*$ , can be defined as follows:

$$\begin{aligned}\phi_1(x) &= h(x) = x_1 \\ \phi_2(x) &= L_f h(x) = x_2 \\ \phi_3(x) &= L_f^2 h(x) = \frac{1}{M_{PL}} (-D_{vsc}x_2 + A_1x_3 - A_2x_4 - P_{atm}A_{rod})\end{aligned}\quad (3.88)$$

For the fourth component of  $z^*$ , no coordinate transformation is defined; thus, it is equal to the original fourth state variable previously defined.

In matrix form, the complete coordinate transformation  $z^*$ , would be given by:

$$z^* = \mathcal{J}(x) = \begin{bmatrix} 1 & 0 & 0 & 0 \\ 0 & 1 & 0 & 0 \\ 0 & \frac{-D_{vsc}}{M_{PL}} & \frac{A_1}{M_{PL}} & \frac{A_2}{M_{PL}} \\ 0 & 0 & 0 & 1 \end{bmatrix} \begin{bmatrix} x_1 \\ x_2 \\ x_3 \\ x_4 \end{bmatrix}\quad (3.89)$$

Hence, the change of variables made corresponds to:

$$z_1 = x_1; \quad z_2 = x_2; \quad z_3 = \frac{1}{M_{PL}} (-D_{vsc}x_2 + A_1x_3 - A_2x_4); \quad z_4 = x_4\quad (3.90)$$

And the system in Eq. 3.44 through Eq. 3.47 is transformed into:

$$\dot{z}_1 = z_2\quad (3.91)$$

$$\dot{z}_2 = z_3\quad (3.92)$$

$$\begin{aligned}\dot{z}_3 &= \frac{-D_{vsc}z_3}{M_{PL}} + \left( \frac{A_1}{M_{PL}} \right) \frac{kC_D\sqrt{RT}\phi_{f1}P_{Sv}u_1}{(V_{01} + z_1A_1)} \\ &\quad - \left( \frac{1}{M_{PL}} \right) \left[ \frac{kz_2A_1}{(V_{01} + z_1A_1)} (D_{vsc}z_2 + M_{PL}z_3 + A_2z_4) \right]\end{aligned}\quad (3.93)$$

$$\begin{aligned}&\quad - \left( \frac{A_2}{M_{PL}} \right) \left[ \frac{kC_D\sqrt{RT}\phi_{f2}P_{Sv}u_2}{(V_{02} + z_1A_2)} - \frac{kz_2z_4A_2}{(V_{02} + z_1A_2)} \right] \\ \dot{z}_4 &= \frac{kC_D\sqrt{RT}\phi_{f2}P_{Sv}u_2}{(V_{02} + z_1A_2)} - \frac{kz_2z_4A_2}{V_{02} - z_1A_2}\end{aligned}\quad (3.94)$$



By defining  $u_1$  and  $u_2$  as:

$$u_1 = \frac{M_{PL}(V_{01} + z_1 A_1)}{A_1 k C_D \sqrt{RT} \phi_{f1} P_{Sv}} \left[ \frac{k z_2 A_1}{M_{LP}(V_{01} + z_1 A_1)} (D_{vsc} z_2 + M_{LP} z_3 + A_2 z_4) + \left( \frac{A_2}{M_{PL}} \right) (-q z_4 + V_1) \right]; \quad (3.95)$$

$$u_2 = \frac{(V_{02} + z_1 A_1)}{k C_D \sqrt{RT} \phi_{f2} P_{Sv}} \left[ \frac{k z_2 z_4 A_2}{V_{02} + z_1 A_2} - q z_4 + v_2 \right];$$

After substituting Eq. 3.95 in Eq. 3.93 and Eq. 3.94, the resulting linearized system equations are:

$$\dot{z}_1 = z_2; \quad \dot{z}_2 = z_3; \quad \dot{z}_3 = \frac{-D_{vsc} z_3}{M_{PL}} + \frac{A_2}{M_{PL}} (v_1 - v_2); \quad \dot{z}_4 = -q z_4 + v_2 \quad (3.96)$$

Where  $q$  is a design parameter with a positive value.

It has be noticed that the signs used in developing the expressions shown in Eq. 3.88 through Eq. 3.96 were defined considering conditions where the piston extends while the extension and retraction valves supply flow to the system. Thus, both valves are active and connected to the extension and retraction chamber of the cylinder, respectively.

### 3.2.3.1. Tracking control design

As outlined by Wang et al. (2007), to provide tracking capability to a linearized system of the form defined above, it is possible to generate a system of trajectories with the same structure as the system defined by Eq. 3.89.

Accordingly, the linear system that defines the trajectories that the state variables should track could be given by:

$$\dot{\theta}_1 = \theta_2; \quad \dot{\theta}_2 = \theta_3; \quad \dot{\theta}_3 = \frac{-D_{vsc} \theta_3}{M_{PL}} + \frac{A_2}{M_{PL}} (w_1 - w_2); \quad \dot{\theta}_4 = -q \theta_4 + w_2 \quad (3.97)$$

Where  $w_1$  and  $w_2$  are external inputs designed to generate the desired trajectory.

By converting the tracking problem into an asymptotical stability problem, with the error defined by:

$$e(t) = \theta(t) - z(t) \quad (3.98)$$

A feedback controller that drives the error state,  $e(t)$ , to zero would have the following structure:

$$v = -ke + w \quad (3.99)$$

Where  $k$  is a set of gains that have to be defined by applying a pole-placement method or through experimentation.

Accordingly, after substituting Eq. 3.99 in Eq. 3.95, and by applying the coordinate transformation  $z^* = \mathcal{T}(x)$ , the control laws become:

$$u_1 = \frac{1}{A_1 C_D \sqrt{RT} \phi_{f1} P_{sv} k} [A_1^2 x_2 x_3 k + A_2 (V_{01} + x_1 A_1) (-q x_4 + w_1 - k_1 e)] \quad (3.100)$$

$$u_2 = \frac{(V_{02} + x_1 A_2)}{k C_D \sqrt{RT} \phi_{f2} P_{sv}} \left[ \frac{k x_2 x_4 A_2}{(V_{02} + x_1 A_2)} - q x_4 + w_2 - k_2 e \right]$$

The challenge in implementing the control laws defined above is in finding the design parameters  $q$ ,  $w_1$  and  $w_2$ . For example, by defining:

$$\theta_1 = -A_m \cos(\omega t) \quad (3.101)$$

Where:  $A_m$  = Half of the magnitude of the piston stroke.

$\omega$  = Frequency of motion,

From Eq. 3.97, it is found that:

$$\theta_2 = A_m \omega \sin(\omega t) \quad (3.102)$$

$$\theta_3 = A_m \omega^2 \cos(\omega t)$$

And by setting  $w_2$  equal to zero, it is found that:

$$\theta_4 = e^{-C_\theta q t} \quad (3.103)$$

$$w_1 = \frac{M_{PL}}{A_2} \left[ \frac{D_{vsc}}{M_{LP}} \theta_3 - A_m \omega^3 \sin(\omega t) \right]$$

Where  $C_\theta$  = Constant depending on initial conditions.

The definition of constants and parameters, such as  $q$ ,  $C_\theta$ , and  $w_2$  offers some level of versatility to the design process. Nevertheless, the challenge is still in finding the values that enable the system to reach the most efficient performance profiles. To find the most suitable parameters for implementation, numerical simulation should be applied.

### 3.3. Assessment of Design Alternatives

For the assessment of the design alternatives presented in previous sections, decision matrixes can be used to evaluate the alternatives proposed, and to pre-select the alternative that could fulfill the design requirements for the controller more extensively than the other options.

To generate selection matrices; first, selection criteria are defined as part of a decision model. Subsequently, each criterion is compared to the remaining criteria by assigning the following values in a table or matrix (Riba, 2002):

- 1 If the criterion of the rows is higher (or better;  $>$ ) than the criterion of the columns.
- 0.5 If the criterion of the rows is equivalent (equal;  $=$ ) to the criterion of the columns.
- 0 If the criterion of the rows is lower (or worse;  $<$ ) than the criterion of the columns.

For each criterion, the assigned values are added in relation to the remaining criteria, adding one unit to prevent that the less favored criteria have a null value. Another column calculates the weighted values for each criterion (or alternative); and finally, the sum of the products resulting from multiplying the specific weights for each alternative by the specific weight of a corresponding criterion provides the overall assessment of each alternative. Therefore, the total sum determines the order of priority for selection of an alternative.

The assessment criteria for the selection of the most suitable alternative for the design of the controller could include:

- Simplicity: The simplicity of a controller relates to the advantages in implementing a specific control algorithm, and the minimum instrumentation required to obtain the necessary input and output signals.
- Robustness: The robustness of a controller associates with its ability to adapt itself to the operation conditions of the plant of a system, and to manage the uncertainty associated with the fluctuation of those operation conditions within acceptable performance ranges.

- Efficiency: The efficiency of a controller can be measured in terms of the use of energetic resources, by quantifying the weight of energy losses, and by comparing the operation profiles that enable the plant of a system to produce the required outcomes within certain operation regimes.
- Accuracy: The accuracy of a controller is measured in terms of the steady-state error, or the tracking error that results from applying a specific input, and producing a desired outcome.
- Cost: The cost for implementing a controller can be evaluated in terms of the cost of instrumentation, hardware, and software required to implement a specific control law.

From the definition of the assessment criteria presented above, the specific weight of each criterion is determined in the following table.

**Table 3.2.** Specific weight of the assessment criteria

EFFICIENCY > ROBUSTNESS > ACCURACY = COST > SIMPLICITY								
<u>CRITERION</u>	<i>SIMPLICITY</i>	<i>ROBUSTNESS</i>	<i>EFFICIENCY</i>	<i>ACCURACY</i>	<i>COST</i>	$\Sigma+1$	<b>WEIGHT</b>	
<i>SIMPLICITY</i>		0	0	0	0.5	1.50	0.10	
<i>ROBUSTNESS</i>	1		0.5	0.5	0.5	3.50	0.23	
<i>EFFICIENCY</i>	1	0.5		1	0.5	4.00	0.27	
<i>ACCURACY</i>	1	0.5	0		0.5	3.00	0.20	
<i>COST</i>	0.5	0.5	0.5	0.5		3.00	0.20	
						<b>SUM</b>	15.00	1.00

Subsequently, it is determined the specific weights of the different alternatives (A1, A2, and A3) according to each criterion:

**Table 3.3.** Specific weight of the alternatives according to the complexity criterion

<i>A1 &gt; A2 &gt; A3</i>						
<u>SIMPLICITY</u>	<i>A1</i>	<i>A2</i>	<i>A3</i>	$\Sigma+1$	<b>WEIGHT</b>	
<i>A1</i>		1	1	3.00	0.50	
<i>A2</i>	0		1	2.00	0.33	
<i>A3</i>	0	0		1.00	0.17	
				<b>SUM</b>	6.00	1.00

**Table 3.4.** Specific weight of the alternatives according to the robustness criterion

$A3 > A1 = A2$					
<u>ROBUSTNESS</u>	<i>A1</i>	<i>A2</i>	<i>A3</i>	$\Sigma+1$	<b>WEIGHT</b>
<i>A1</i>		0.5	0	1.50	0.25
<i>A2</i>	0.5		0	1.50	0.25
<i>A3</i>	1	1		3.00	0.50
			<b>SUM</b>	6.00	1.00

**Table 3.5.** Specific weight of the alternatives according to the efficiency criterion

$A1 = A2 = A3$					
<u>EFFICIENCY</u>	<i>A1</i>	<i>A2</i>	<i>A3</i>	$\Sigma+1$	<b>WEIGHT</b>
<i>A1</i>		0.5	0.5	2.00	0.33
<i>A2</i>	0.5		0.5	2.00	0.33
<i>A3</i>	0.5	0.5		2.00	0.33
			<b>SUM</b>	6.00	1.00

**Table 3.6.** Specific weight of the alternatives according to the accuracy criterion

$A1 = A2 = A3$					
<u>ACCURACY</u>	<i>A1</i>	<i>A2</i>	<i>A3</i>	$\Sigma+1$	<b>WEIGHT</b>
<i>A1</i>		0.5	0.5	2.00	0.33
<i>A2</i>	0.5		0.5	2.00	0.33
<i>A3</i>	0.5	0.5		2.00	0.33
			<b>SUM</b>	6.00	1.00

**Table 3.7.** Specific weight of the alternatives according to the cost criterion

$A1 > A2 > A3$					
<u>COST</u>	<i>A1</i>	<i>A2</i>	<i>A3</i>	$\Sigma+1$	<b>WEIGHT</b>
<i>A1</i>		1	1	3.00	0.50
<i>A2</i>	0		1	2.00	0.33
<i>A3</i>	0	0		1.00	0.17
			<b>SUM</b>	6.00	1.00

Finally, the overall results are summarized in the following table.

**Table 3.8.** Alternative assessment results

<b>CONCLUSION</b>	<b>SIMPLICITY</b>	<b>ROBUSTNESS</b>	<b>EFFICIENCY</b>	<b>ACCURACY</b>	<b>COST</b>	<b><math>\Sigma</math></b>	<b>PRIORITY</b>
<i>A1</i>	<b>0.050</b>	<b>0.058</b>	<b>0.089</b>	<b>0.067</b>	<b>0.100</b>	<b>0.364</b>	<b>1</b>
<i>A2</i>	0.033	0.058	0.089	0.067	0.067	0.314	3
<i>A3</i>	0.017	0.117	0.089	0.067	0.033	0.322	2

As it can be acknowledged from Table 3.8, alternative 1, the results of which are highlighted in blue, would constitute the design option to be pre-selected for implementation of the controller. Nevertheless, it should be noted that the assessment process applied in this section is a qualitative process, and it constitutes a tool for preliminary design, and selection of the control strategy. Once that the control scheme based on alternative 1 is implemented, and depending on the experimental results obtained, the selection of alternative 1 should be confirmed, or reconsidered.

Likewise, it also has to be noticed that all alternatives have been equally rated in relation to the efficiency and accuracy criterion because the assessment of the design alternatives regarding these two criteria based on simulation results might result misleading for the design process. In contrast, for the other criteria, the comparison of the design alternatives can be qualitatively supported by engineering judgment, and the conclusions found in the literature reviewed.

At the end of the design process, as it will be shown in chapter 6, the structure of the definitive controller might combine some of the strongest features of all three, or at least two of the design alternatives presented in this chapter.

## CHAPTER IV

### EXPERIMENTAL METHODS

#### Technical Approach

The technical approach defines the scientific method applied in order to answer a specific research question. The research question is formulated as part of the hypothesis to be tested. The hypothesis for the project is:

*“If a control algorithm can attenuate the negative effects associated with the compressibility of air and the length of connective tubing in the performance of pneumatic actuators, the accuracy for positioning control, and the energetic efficiency of pneumatic systems could be improved.”*

From the formulated hypothesis, the required experimental setup was defined and the methodology was developed. The definition of the baseline and final experimental setups embraces the identification of parameters that govern the behavior of the system.

#### 4.1. Baseline Experimental Setup

The baseline experimental setup includes the instrumentation, methodology, and software used to establish the cause/effect relationships between independent and dependent variables of the system studied (<http://www.science-projects.com/SciMeth.htm>). Some cause/effect relationships relative to the hypothesis described above are:

- Position/velocity of the piston vs. time.
- Position/velocity of the piston vs. flow rate.
- Position/velocity of the piston vs. upstream/downstream cylinder/valve/tube's pressure.
- Effective area of the valve vs. valve's solenoid current.
- Flow rate vs. time.
- Flow rate vs. valve's solenoid current.
- Flow rate vs. upstream/downstream cylinder/valve/tube's pressure.

The baseline experimental setup for the project is represented in figure 4.1.

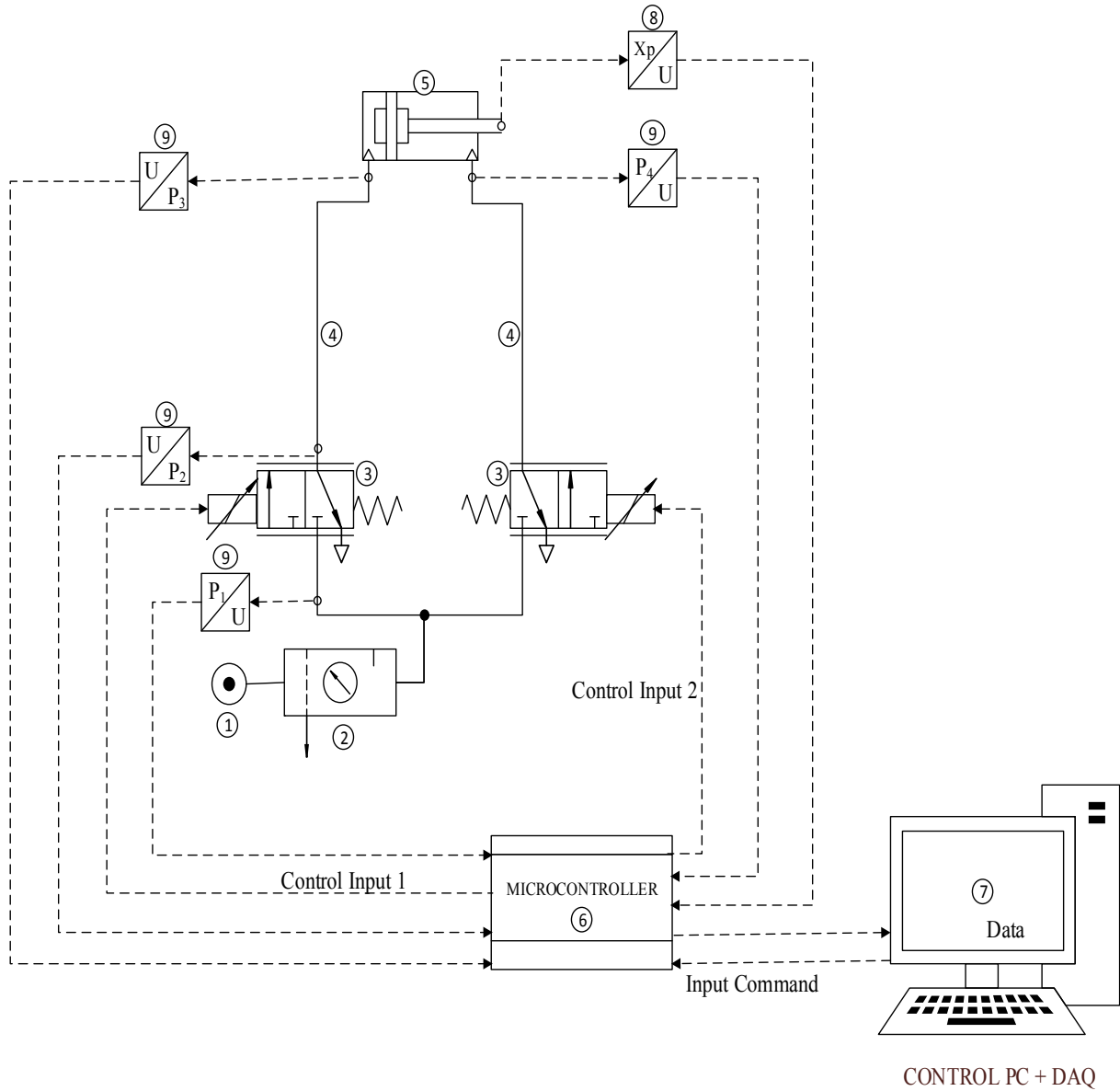


**Figure 4.1.** Baseline Experimental Setup

The elements identified by numbers in figure 4.1 include:

- |                                     |  |
|-------------------------------------|--|
| 1) Air source.                      | 6) Microcontroller board.                        |
| 2) Air conditioning unit.           | 7) Control PC and Data Acquisition System (DAQ). |
| 3) Proportional flow control valve. | 8) Position transducer.                          |
| 4) Pneumatic tube under test.       | 9) Pressure transducer.                          |
| 5) Pneumatic cylinder.              |  |



Based on figure 4.1, compressed air delivered to the control valves first passed through an air conditioning unit composed by a filter (model 14L10GA, Parker, USA) and a pressure regulator (model 14E11B13F8, Parker, USA). The maximum supply air pressure was 6.2 bar (90 psi). The pneumatic cylinder (model 1.50-CF2MAU18AC-12.00, Parker, USA) was connected to two 3-way proportional flow control valves (model VEF-3121, SMC, Japan) through a pair of rubber hoses (model 00447406400, Thermoid, USA) of equal length. Three different lengths of hoses connecting the valves and the cylinder were used in the experiments: 0.55, 1.5, and 3.0 meters. In addition, four gauge pressure transducers (model AKS32 - 060G1889, Danfoss, USA) were respectively connected to the cylinder chambers, and the inlet and outlet ports of the valve driving the cap end of the cylinder, and a linear transducer (model LP-300FJS, Midori, Japan) was attached to the end of the piston rod to measure its linear displacement. The signals from the transducers were collected through a data acquisition USB device (model USB-6009, National Instruments, USA), or directly by the microcontroller board (model UNO, Arduino, Italy). To drive the two proportional control valves, the microcontroller board was connected to a dual full-bridge driver (model MegaMoto, Robot Power, USA), which is a general-purpose power amplifier specifically designed to work with Arduino hardware.

Relevant parameters associated with some of the components of the experimental setup are described in the following sections along with the description of the methodology applied.

## 4.2. Methodology

Section 4.2 describes the methodology applied to test the hypothesis for the project. The methodology identifies: general concepts, general steps, dependent and independent variables, and the instrumentation used.

### 4.2.1. Data acquisition (DAQ)

Data acquisition (DAQ) entails the collection of measurements that represent a physical phenomenon, such as the pressure drop in connective tubing, or the displacement of the piston of a pneumatic cylinder, by using a computer. The process of data acquisition depends on three elements: the sensors used, the DAQ hardware, and the software or applications run by a computer.

Sensors, also called transducers, convert signals from a physical phenomenon in electric signals that can be measured and processed by DAQ devices. General characteristics of the different sensors used in this project will be specified in the following sections.

In collecting measurements or data from a sensor, DAQ hardware must fulfill two main functions: signal conditioning, and analog-to-digital conversion. Signal conditioning involves the manipulation of data collected from a sensor in order to make it suitable for analog-to-digital conversion. Accordingly, depending on their functionalities, DAQ devices might be able to: amplify, filter, isolate, linearize, and attenuate, among others, the electrical signal from a transducer. Once a signal is conditioned, it can be converted from analog to digital in order to be processed by a computer. Analog-to-digital conversion basically stands for the recording of periodic samples of an analog signal, so a computer can reconstruct the signal from the samples by using specialized software or computer applications.

For the project described in this thesis, as mentioned in section 4.1, two devices were utilized as DAQ hardware: a bus-powered multifunction National Instruments DAQ USB device, and an open source single-board microcontroller (Arduino UNO). Even though the microcontroller was primarily used for controlling the proportional valves, its DAQ functionality was useful at the time of comparing and processing data in a computer. Table 4.1 and Table 4.2 summarize the specifications of both devices. Figure 4.2 shows one of the DAQ devices used for the tests.



**Figure 4.2.** National Instruments USB-6009 DAQ

[Source: <http://sine.ni.com/nips/cds/view/p/lang/en/nid/201987>]

**Table 4.1.** Technical Specifications of the National Instruments USB-6009 DAQ

<b>GENERAL</b>	
Measurement Type	Voltage
On-Board Memory	512 B
<b>ANALOG INPUTS</b>	
Single-Ended Channels	8
Differential Channels	4
Resolution	14 bits
Maximum Voltage Range	[-10 10] V
Accuracy for maximum voltage range	7.73 mV
Minimum Voltage Range	[-1 1] V
Accuracy for minimum voltage range	1.53 mV
Maximum sample rate	48 kS/s
<b>ANALOG OUTPUTS</b>	
Number of channels	4
Resolution	12 bits
Maximum/Minimum Voltage Range	[0 5] V
Voltage range accuracy	7 mV
Update Rate	150 S/s
Current Drive Single	5 mA
Current Drive All	10 mA
<b>DIGITAL I / O</b>	
Bidirectional Channels	12
Input-Only / Output-Only Channels	0
Maximum Voltage Range	[0 5] V
Output - Current Drive Single	8.5 mA
Output - Current Drive All	102 mA
<b>COUNTERS / TIMERS</b>	
Counters	1
Maximum Source Frequency	5 MHz
Size	32 bits
Time-base Stability	50 ppm
Triggering	Digital

[Adapted from: <http://sine.ni.com/nips/cds/view/p/lang/en/nid/201987>]

As it will be acknowledged by comparing table 4.1 and table 4.2, the main advantages in using a device specifically designed for data acquisition might include: its higher resolution, and its higher sampling rate. A higher resolution and a higher sampling rate affect the accuracy with which a signal is reconstructed in a computer.

**Table 4.2.** Technical Specifications of the Arduino UNO Microcontroller Board

<b>GENERAL</b>	
Microcontroller	ATmega328P
Operating Voltage	5V
Input Voltage (recommended)	7-12V
DAQ Capability \ Measurement Type	Voltage
<b>ANALOG INPUT</b>	
Analog Input Pins	6
Resolution	10 bits
Default Voltage Range	[0 5] V
Maximum sample rate	9.7 KHz
<b>ANALOG OUTPUT</b>	
Analog Output Pins	1
Voltage generated	3.3 V
Current Drive Single	50 mA
<b>DIGITAL I / O</b>	
Bidirectional Pins	14
PWM Output Pins	6
Maximum Voltage Range	[0 5] V
DC Current per I/O Pin	20 mA
<b>MEMORY</b>	
Flash Memory	32 KB (ATmega328P)
<b>TIMER</b>	
Clock Speed	16 MHz

[Adapted from: <http://www.arduino.cc/en/Main/ArduinoBoardUno>]

The comparison of table 4.1 and table 4.2 confirms the fact that the resolution and sampling rate of the USB DAQ device surpass the specifications of the microcontroller board. Nevertheless, the overall functionality and cost of the microcontroller board might still make it more beneficial for some applications, such as applications in industry that do not require high accuracy for data collection. Moreover, the fact that the microcontroller board is programmed using open source software might provide it with the greatest advantage in comparison to other data acquisition boards.

In general terms, the use of both devices for data acquisition alternated depending on the following conditions:

- The accuracy and quality sought for data collection.
- The maximum output voltage of the sensors used.
- The number of signals to be measured from a test.

In fact, both devices might be used simultaneously, which should combine their strongest qualities. To combine the capabilities of both devices, it was necessary to find and use computer software able to communicate simultaneously with the two DAQ platforms. In that regard, MATLAB was used to interface with the USB DAQ device, and the microcontroller board. MATLAB provides the following packages and applications for handling the data collected by the DAQ devices described before:

- Data Acquisition Toolbox and Data Acquisition Application compatible with National Instruments hardware.
- MATLAB support package for ARDUINO hardware.
- Simulink support package for ARDUINO hardware.

Since for the project, the National Instruments and Arduino platforms were combined for data acquisition, it was necessary to use programming support packages and toolboxes in order to generate code able to communicate and acquire data from the DAQ devices used, independently or simultaneously. Figure 4.3 shows the graphical user interface for data acquisition using National Instruments hardware and MATLAB.

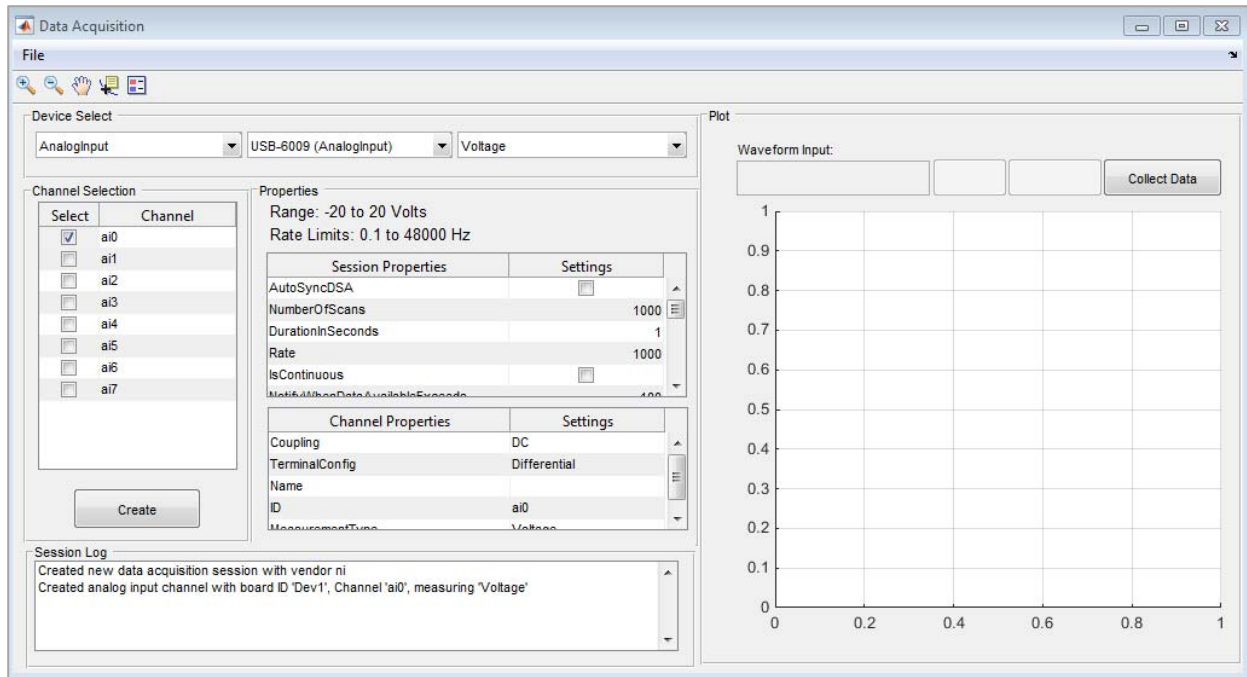


**Figure 4.3.** MATLAB Data Acquisition graphical interface for data collection with National Instruments DAQ hardware

#### 4.2.2. Validation of models and control strategies

Models and control strategies were validated by comparing experimental data and data produced through computer simulation or software commands. One of the main objectives of this process was to confirm the accuracy of dynamic computational models in reproducing the behavior of the pneumatic system within delimited bounds. In addition, the comparison between a desired output and the actual output obtained from the experimental setup validated the different control strategies proposed. In that regard, the sensors used in the experimental setup measured the output from the system in terms of the cylinder piston displacement, the pressure in the cylinder chambers, and the pressure drop in connective tubing and the control valves used.

Accordingly, two main approaches were implemented to validate the models and control strategies proposed.

- First, dynamical models for the pneumatic system and its individual components were validated by comparing simulation results with experimental data.
- Secondly, the performance of the controller was measured in terms of the efficacy and efficiency of the system to produce a desired output.

The position transducer identified in section 4.1 was used for most of the tests performed to validate the dynamical models and control strategies proposed. This transducer had a 300-millimeter effective electrical travel, and it was used to measure the linear position of the cylinder piston. Table 4.3 provides further technical specifications for the linear transducer.

**Table 4.3.** Specifications of the Midori LP-300FJS linear transducer

<b>GENERAL</b>	
Type	Conductive plastic linear sensor
Effective electrical travel	$300 \pm 1$ mm
Independent linearity	$\pm 0.3$ %
<b>ELECTRICAL SPECIFICATIONS</b>	
Total resistance	10 k $\Omega$
Total resistance tolerance	$\pm 20\%$
Maximum DC input voltage	36 V
<b>MECHANICAL SPECIFICATIONS</b>	
Maximum friction	4 N
Approximate mass	320 g
Mechanical stroke	$304 \pm 1$ mm

[Adapted from: <http://midoriamerica.com/products>]

Likewise, the microcontroller board was used to implement the control algorithms derived from the design of the controller. PWM voltage signals were generated by the microcontroller, and amplified by the dual full-bridge driver triggering the proportional valves. The dual full-bridge driver and the valves were connected in half-bridge mode (Figure 4.4).

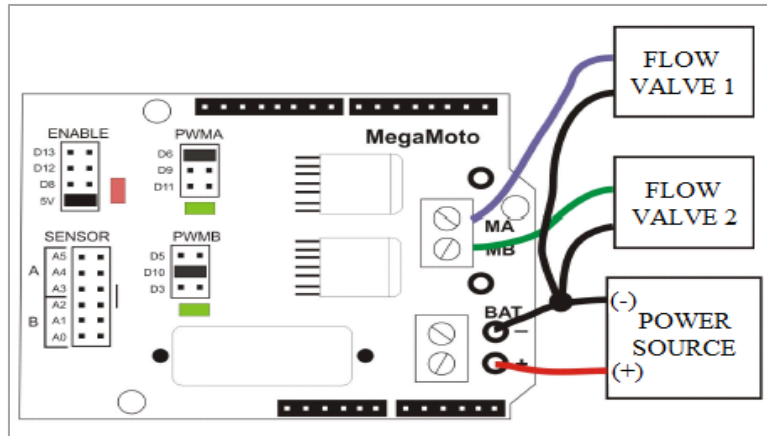


**Figure 4.4.** Dual full-bridge driver connected in half-bridge mode to the proportional valves

[Adapted from: [http://www.robotpower.com/products/MegaMoto\\_info.html](http://www.robotpower.com/products/MegaMoto_info.html)]

The flow proportional valves were connected to the driver in half-bridge mode because they constitute unidirectional loads; and accordingly, they had to be controlled independently. The driver used provides a maximum continuous current of 13 A, and the solenoid of the valves has a coil resistance of 13  $\Omega$  and admits a maximum current of 1 A. Further technical specifications for the driver and the flow proportional valves are provided in Table 4.4 and Table 4.5, respectively. Figure 4.5 shows pictures of the microcontroller board and bridge driver used.

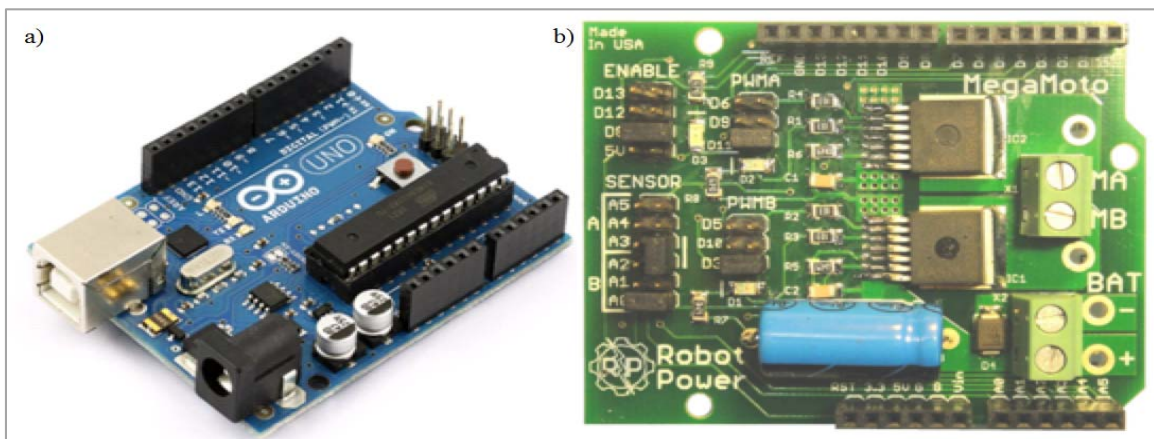


**Figure 4.5.** (a) Arduino Uno Microcontroller Board, (b) MegaMoto ROBOT POWER Driver



**Table 4.4.** Specifications of the ROBOT POWER MegaMoto Dual full-bridge driver

<b>GENERAL</b>	
Supply voltage	5V to 28V (24V max battery rating)
Power chips	2 ea. BTN7960B
Power Connectors	2 each screw terminals (14AWG wire)
<b>OUTPUT</b>	
Output Current (continuous)	13A
Output Current (surge)	30A \ 5 seconds
On Resistance	0.016 $\Omega$ max at 25C
PWM Frequency	DC to 20kHz
<b>SENSING CAPABILITY</b>	
Logic Interface	3V - 5V, minimum 1 pin required
Logic Inputs	Jumper select Enable and PWM source
Current Sense Outputs	0.0745 V/A - 2.98V at 40A
Current Sense Pins	Jumper select the analog input connected

[Adapted from: [http://www.robotpower.com/products/MegaMoto\\_info.html](http://www.robotpower.com/products/MegaMoto_info.html)]

**Table 4.5.** Specifications of the SMC VEF 3121 Flow Proportional control valves

<b>GENERAL</b>	
Style	Flow Style (VEF)
Fluid	Air (Inert gas)
Maximum operating pressure	1.0 MPa
Ambient and fluid temperature	[0 50] °C
<b>GEOMETRIC CHARACTERISTICS</b>	
Port size	9.525 mm (3/8 in)
Maximum effective area	12 mm <sup>2</sup>
<b>RESPONSE CHARACTERISTICS</b>	
Response time	0.03 s or less
Hysteresis	3% FS
Repeatability	3% FS
Sensibility	0.5% FS
<b>SOLENOID SPECIFICATIONS</b>	
Maximum current	1.0 A
Coil resistance	13 $\Omega$ (20 °C)
Rated power consumption	13 W (20 °C, at max. current)
Coil insurance	Class H or equivalent (180 °C)
Maximum temperature	140 °C (at max. current)

[Adapted from: <https://www.smc.eu/>]



#### 4.2.3. Identification of transient profiles

The identification of transient profiles involved the measurement and acquisition of data associated with the operation of the pneumatic system under specific conditions. A transient profile constitutes the outline of the progression of a variable measured within a range of time. In the delineation of transient profiles for the pneumatic system, three main variables were considered: the linear position of the cylinder piston, the pressure of air, and the electric input signal to the valves. The operating conditions for experimentation were defined in basis to the type of electrical signal generated through the microcontroller board and input to the valves. Three types of inputs were generated using the microcontroller board: step inputs, sinusoidal inputs, and ramp inputs. Accordingly, depending upon the input applied to the valves, the displacement of the cylinder piston was measured using the linear potentiometer, and the air pressure relative to the control valves, the connective tubing, and the chambers of the cylinder was measured using the pressure transducers identified in section 4.1. The pressure transducers used in the experimental setup work in a full span range of 0 to 100 psi gauge. Further specifications of the pressure transducers used are summarized in Table 4.6:

**Table 4.6.** Specifications of the Danfoss AKS32 - 060G1889 pressure transducers

<b>GENERAL</b>	
Pressure unit reference	Gauge (relative)
Pressure Range - Full Span (FS)	[0 100] psi
Maximum overload pressure	400 psi
Ambient temperature range	[-40 85] °C
<b>RESOLUTION</b>	
Accuracy - maximum +/- FS	0.80%
Accuracy - typical +/- FS	0.30%
Non-linearity best fit straight line +/- FS	0.20%
Maximum response time	4 ms
<b>ELECTRIC SIGNALS</b>	
Supply Voltage	[9 30] V DC
Output signal range	[1 6] V DC

[Adapted from: <http://products.danfoss.com/>]

The maximum output voltage of the pressure transducers used is 6 volts; hence, it was not possible to directly use the microcontroller board for pressure data acquisition. In that regard, the USB DAQ device was primarily used for pressure data acquisition.

Nevertheless, for control purposes, it was necessary to implement voltage divider circuits in order to use pressure data as feedback for control. Figure 4.6 shows the schematic of the voltage divider circuit employed.

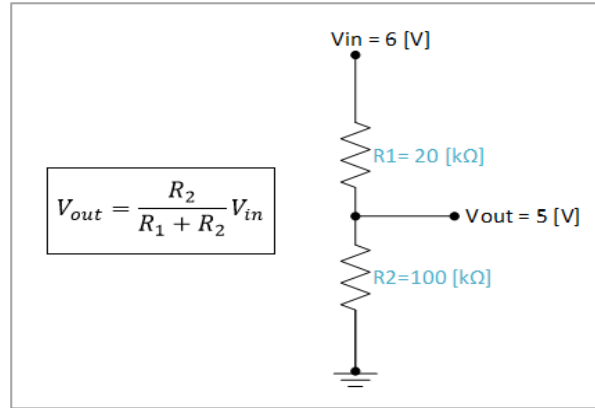


**Figure 4.6.** Voltage divider circuit

As depicted by figure 4.6, the voltage divider circuits were built using a resistor of 20 kΩ and a resistor of 100 kΩ, which enabled the voltage generated by the pressure transducers to be measured in a scale of 0 to 5 volts instead of 0 to 6 volts.

In addition, the definition of different experimental conditions also involved the variation of the length of the hoses connecting the proportional valves and the pneumatic cylinder. The hoses used tolerate a maximum pressure of 250 psi at 22 °C, which results sufficient for the pneumatic system studied. Table 4.7 provides further description of the hoses used in the experimental setup.

**Table 4.7.** Specifications of connective tubing tested.

<b>GENERAL</b>	
Type	Medium-Pressure oil resistant hose
Maximum Pressure @ 22 °C	1.723 MPa (250 psi)
Temperature Range	[-30 60] °C
<b>GEOMETRY</b>	
Length	[0.5 1.5 3.0] m
Internal Diameter	9.525 mm (3/8")
Outside Diameter	18.26 mm (23/32")
Bend Radius	57.15 mm (2 1/4")
<b>MATERIAL</b>	
Hose	Buna-N Rubber
Cover	Blended Rubber

[Adapted from: <http://www.mcmaster.com/#54765k22/=x0vp1d>]

In addition, a secondary experimental setup was built in order to measure the variation of pressure in lengthy connective tubing. Figure 4.7 shows the schematic of the secondary experimental setup built for the corresponding tests:

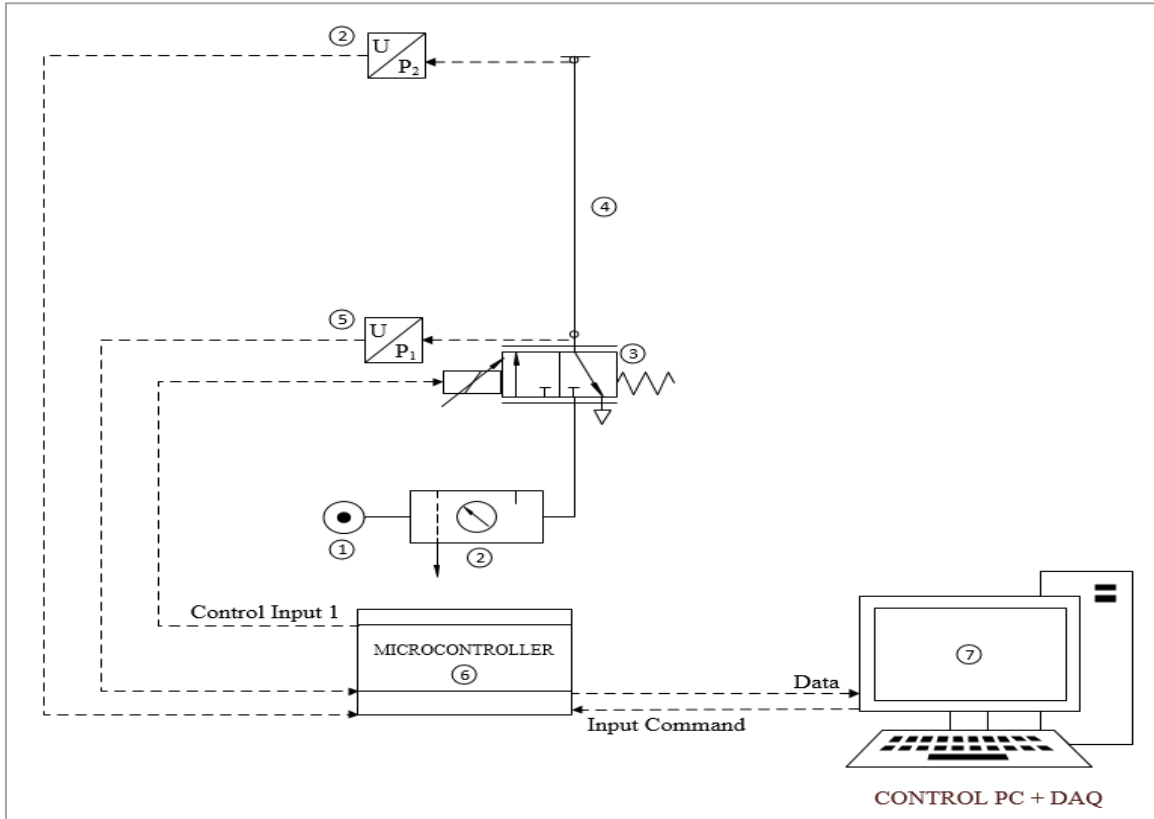


**Figure 4.7.** Schematic of secondary experimental setup built to measure the pressure variation in pneumatic connective tubing

The elements identified by numbers in figure 4.7 include:

- |                                     |  |
|-------------------------------------|--|
| 1) Air source.                      | 5) Position transducer.                          |
| 2) Air conditioning unit.           | 6) Microcontroller board.                        |
| 3) Proportional flow control valve. | 7) Control PC and Data Acquisition System (DAQ). |
| 4) Pneumatic tube under test.       |  |

In contrast to the experimental setup from figure 4.1, the pneumatic cylinder and the linear transducer were not included in the experimental setup depicted in figure 4.7. Moreover, just one proportional valve was used to generate the control signals required. The elements composing the setup from figure 4.7 correspond to the components identified in section 4.1

Figure 4.7 shows that the tube tested was not connected to the pneumatic cylinder, which prevented that the oscillations of the piston alter the pressure profile measured relative to the tube. A sinusoidal input was used to control the proportional valve to which the tube was connected. Two pressure transducers were connected relative to the upstream and downstream inlets of the tube tested, respectively. Several tests were run by keeping the frequency of the sinusoidal command input to the valves constant, and by sweeping the frequency within a specific range. Preliminary experimental results from the tests run to characterize the pressure variation in lengthy connective tubing are presented in the following section.

To conclude this section, as part of the experimental methodology described until this point, the identification of transient profiles sought to accomplish the following goals:

- Verify the non-linearities associated with the transient variation of pressure and cylinder piston position.
- Confirm assumptions made in the literature reviewed.
- Delimit regions where the relation between upstream and downstream pressure in a specific component establishes different conditions for the treatment of other variables.
- Validate assumptions that can be made in order to simplify the models for the system.
- Define limit values of transient response that can be achieved.

From the application of the methodology described in this and previous sections, preliminary experimental results were obtained to develop a better understanding of the dynamic behavior of the system and to identify parameters and constants required for the implementation of the controllers designed. The following section describes a series of preliminary results obtained through the methodology applied in this project.

### **4.3. Preliminary experimental results**

Section 4.2.4 describes a series of preliminary experimental results and deductions derived from the identification of transient profiles associated with the operation of the pneumatic system under different conditions. These preliminary results were categorized depending on the element of the experimental setup in reference to which the tests were performed. Accordingly, preliminary experimental results are presented in reference to the control valves, the connective tubing tested, and the chambers of the cylinder.

#### 4.3.1. Control valves

Relative to the control valves, experimental data was collected to identify the effect of the variation of pressure on the displacement of the pneumatic cylinder under specific control schemes. Specific objectives of the measurement of pressure relative to the proportional valves included:

- Verify to what extent the pressure at the air-inlet of the control valve, the supply pressure, can be assumed to be constant.
- Identify the operation conditions under which the supply pressure remains constant.
- Mark the regions where the flow attains special characteristics depending on pressure variation.
- Identify the threshold position value for the valves ( $x_{s-threshold}$ ).

Tests developed to measure the pressure variation in relation to the control valves included:

- Actuation of the pneumatic valves through step and sinusoidal inputs.
- Actuation of the pneumatic valves according to a periodic incremental input (ramp input).

In that regard, the microcontroller board commanded the actuation of the valves depending on two strategies: open loop control, and closed loop control. The electrical inputs generated by the microcontroller board correspond to PWM voltage signals, and their equivalent analog amplitudes are defined by a specific percentage duty cycle.

In the tests developed using open-loop control with a step input, the valve connected to the rod end of the cylinder remained inactive, which helped to identify the maximum values of pressure and transient response that can be achieved during extension of the cylinder piston. Figures 4.8 and 4.9 show the displacement and velocity of the cylinder piston in relation to the pressure variation at the inlet and outlet of the control valve connected to the cap end of the cylinder. The velocity of the piston was computed through a finite difference approximation of the form:

$$\dot{x}_p = \frac{x_p - x_{p_{old}}}{\Delta t} \quad (4.1)$$

Where the subscript “old” denotes that the value of the variable corresponds to an immediate previous value, separated of the current value by a period of time  $\Delta t$ .

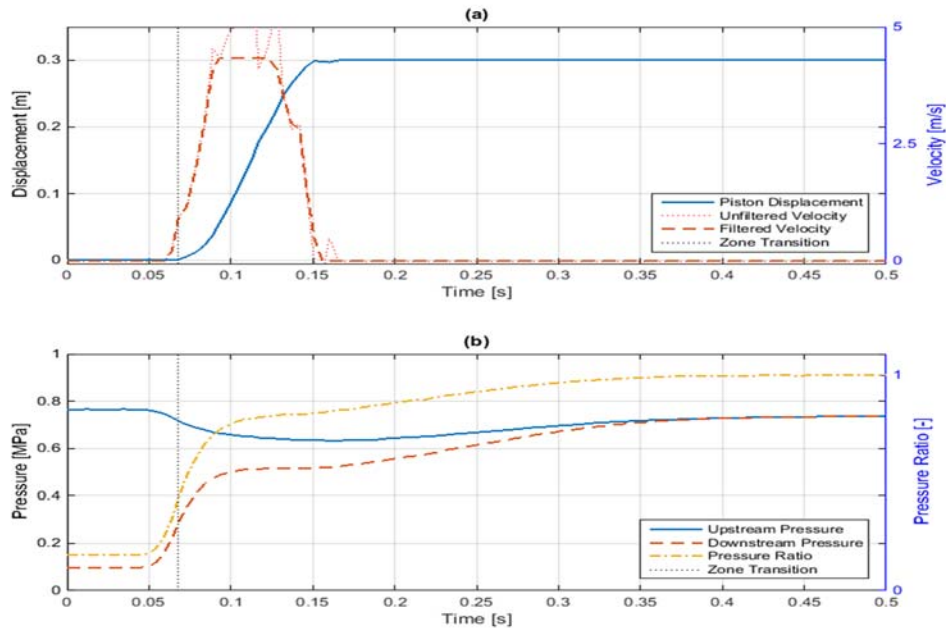


**Figure 4.8.** (a) Displacement and velocity of the piston in response to an open-loop 100% duty-cycle PWM step input. (b) Pressure at the ports of the valve connected to the cylinder cap end.

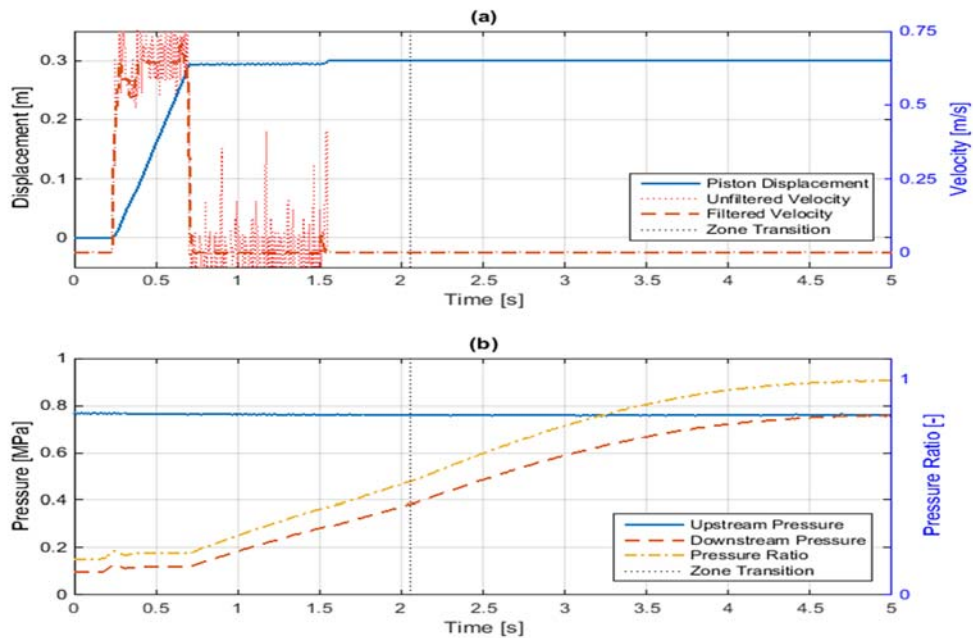


**Figure 4.9.** (a) Displacement and velocity of the piston in response to an open-loop 70% duty-cycle PWM step input. (b) Pressure at the ports of the valve connected to the cylinder cap end.

Figure 4.8 and figure 4.9 include the unfiltered and the filtered velocity. The filtered velocity was calculated using the MATLAB command “medfilt1”, which applies an order-n one-dimensional median filter to the input data. In this thesis, for all results calculated from experimental data, particularly results calculated through finite difference approximation, the unfiltered and filtered outputs are presented. Unfiltered outputs are depicted using dotted lines.

Moreover, from figure 4.8 and figure 4.9, it is verified that as the magnitude of the step input increases, the non-linearities in the pressure profiles become more evident, which restricts the assumption of a constant supply pressure. The fact that the supply pressure does not remain constant for high inputs may depend on the following factors:

- There exists an inherent pressure drop associated with the tubing and fittings used to connect the control valves to the compressed air source.
- As the magnitude of the step input increases, the transient response required from the compressed air source exceeds its nominal capability.
- The large distance between the air intake and the air compressor might increase the time required for the system to stabilize the supply pressure.

To compensate for the pressure drop at the upstream side of the control valves, several reservoirs were connected in series to the inlet ports of the valves. Nevertheless, independently of the volume of the reservoirs, the inherent pressure drop in some of the connective elements might not be avoided when high-magnitude step inputs trigger the valves.

By comparing the velocity profile of the piston with the pressure profiles for the valve, it can be identified an interval of time during which the velocity of the piston attains a constant value, as well as the upstream and downstream pressure of the valve. The development of the velocity and pressure profiles until attaining constant values might resemble a correlation between the pressure drop and the velocity of the piston.

In addition, in figures 4.8 and 4.9, a transition of zones were marked corresponding to the point in time when the downstream to upstream pressure ratio for the valve surpassed a critical value,  $C_{cr} = 0.52828$ , which was defined in chapter 2. The transition of zones marks the time from which the flow through the valves is no longer linear in relation to the downstream to upstream pressure ratio. The transition between zones demarcates the physical characteristics of the flow of air provided to the cylinder.

Furthermore, a delay between the point at which the controller produced the step input, and the point at which the piston started moving was identified (Figures 4.8 and 4.9). This delay would correspond to the time required for the cylinder piston to overcome static friction given specific input values. The delay time for a 100% duty cycle PWM step input was approximately 7 milliseconds.

Similarly, by implementing a closed-loop control scheme, it was possible to identify similar parameters and physical phenomena as the ones identified above. Figures 4.10, 4.11 and 4.12 show the displacement and velocity of the piston in relation to the pressure variation at the inlet and outlet of the control valve connected to the cylinder cap-end chamber, when a closed-loop control strategy was implemented. A proportional control scheme was applied to produce figures 4.10, 4.11 and 4.12. The inputs applied to the valves were defined so that the positive displacement of the spool of one valve was compensated by the negative displacement by the spool of the other. Figure 4.10 shows the dynamic response of the system to a step input generated from a proportional control scheme.

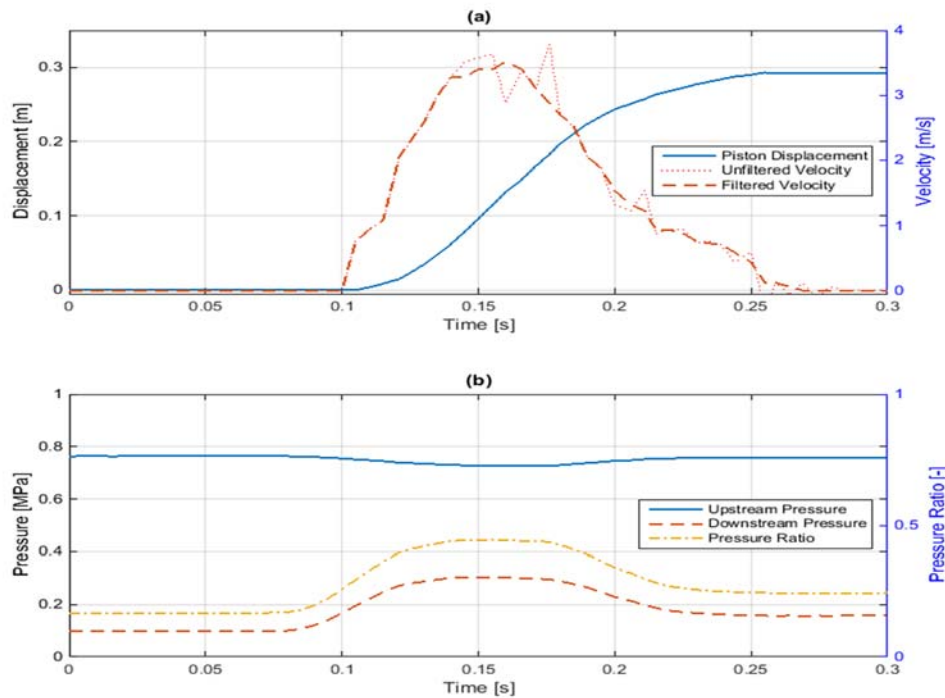


**Figure 4.10.** (a) Displacement and velocity of the piston in response to a closed-loop step input.  
(b) Pressure at the ports of the valve connected to the cylinder cap end.



For a closed-loop step input, in order for the piston to reach a specific position, both valves coordinated to achieve an equilibrium value of pressure at their corresponding outlet ports, which reduced the pressure drop caused by high-amplitude step inputs in the case of an open-loop control scheme. Accordingly, depending on the characteristics of the control strategy implemented, the pressure drop in the inlet of the valves can be reduced, and the assumption of constant supply pressure can be adopted.

Figures 4.11 and 4.12 respectively show the dynamic responses of the system to a 1-Hz and 4.5-Hz sinusoidal input generated through a proportional control scheme. In the case of a sinusoidal input, the frequency of the signal generated by the microcontroller board and input to the valves delimited until what extent the supply pressure could be considered constant. As the frequency decreased, the assumption of a constant supply pressure resulted more suitable. Likewise, the relation between upstream and downstream pressure relative to the valve defined the characteristics of the flow delivered to the pneumatic cylinder.

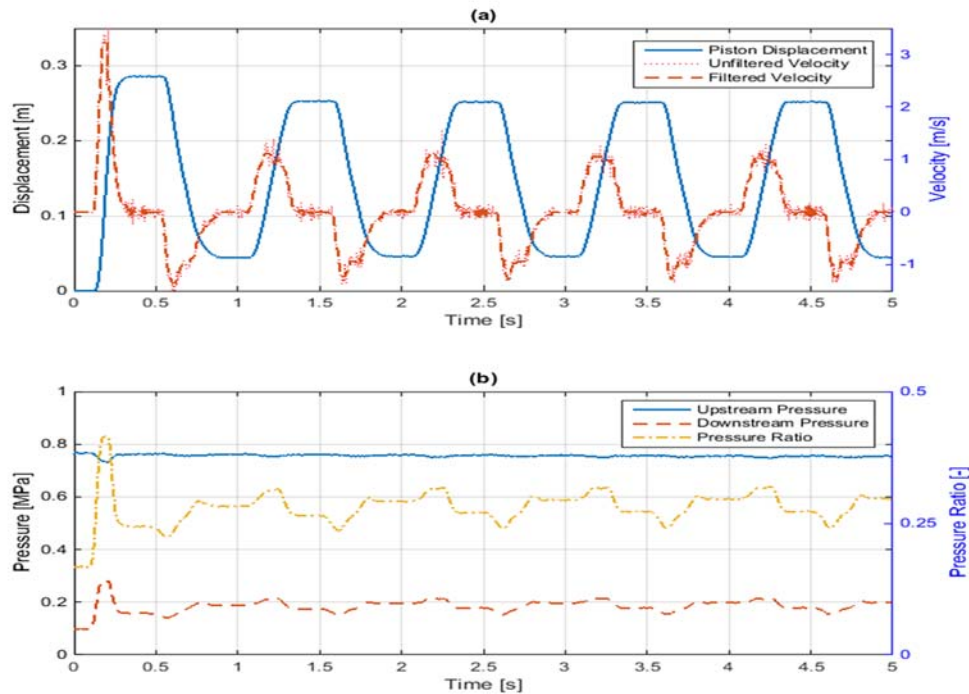


**Figure 4.11.** (a) Displacement and velocity of the piston in response to a closed-loop 1-Hz sinusoidal input. (b) Pressure at the ports of the cylinder cap-end valve

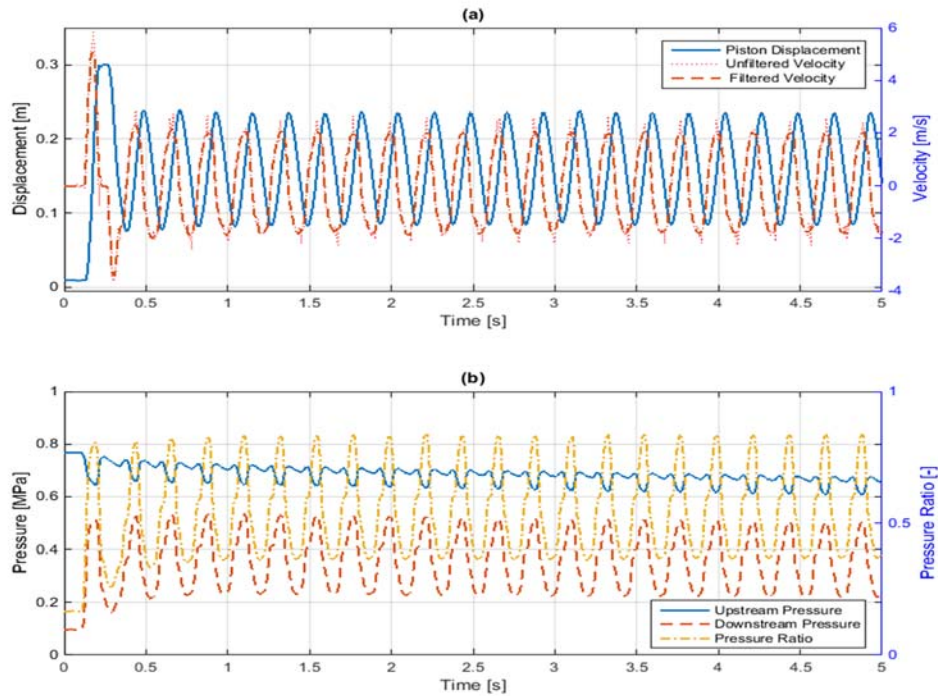


**Figure 4.12.** (a) Displacement and velocity of the piston in response to a closed-loop 4.5-Hz sinusoidal input. (b) Pressure at the ports of the cylinder cap-end valve

From the comparison of figure 4.11 and figure 4.12, it can be verified that for high-frequency sinusoidal inputs, the supply pressure cannot be accounted as a constant value. Also, in contrast to figure 4.11, in figure 4.12 the pressure ratio periodically exceeds the critical value  $C_{cr}$ , which might contribute to cause the pressure drop in the upstream port of the valve.

In the following section, to identify the threshold position value for the valves, periodic incremental inputs triggered the valves until the first increment of pressure in their downstream side was observed. The threshold position value for the valves would correspond to the signal required for positioning their spool at the last point where the output flow from the valve is still zero. Further displacement of the spool of the valves from this point would make the output flow to the cylinder to become higher than zero.

Figure 4.13 shows the incremental profile of the input signal for the valves, and it identifies the specific value required to cause the first increment of pressure in the downstream side of the valve.

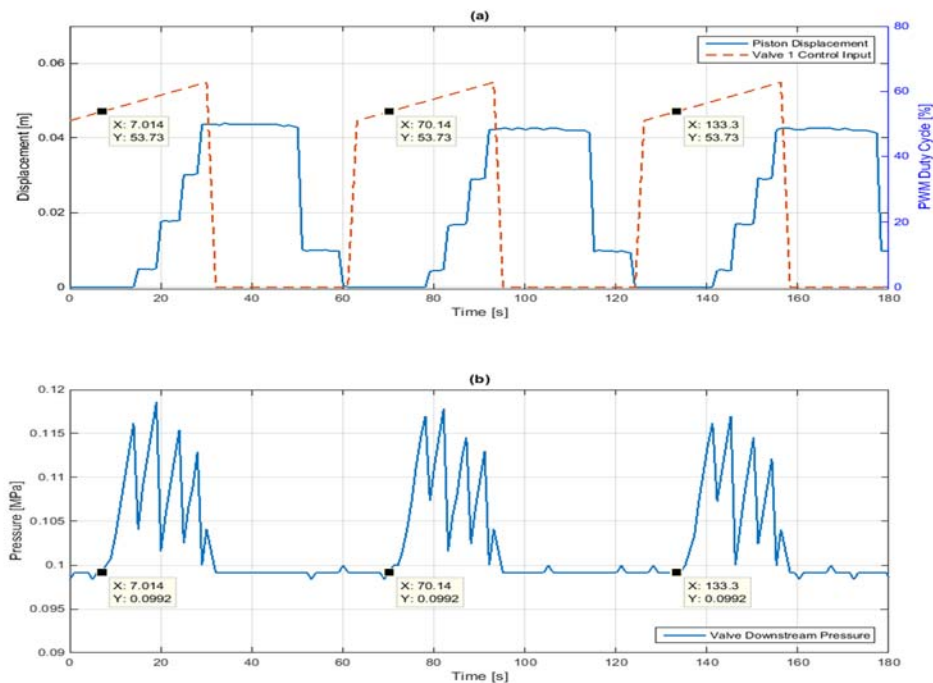


**Figure 4.13.** (a) Displacement of the cylinder piston in response to a ramp input. (b) Pressure at the downstream side of the valve connected to the cylinder cap end.

The control inputs applied to the valve were not high enough to cause the continuous displacement of the piston of the cylinder (Figure 4.13). Thus, the compressibility of air also might have contributed to the displacement of the piston for each periodically incremental input applied. Moreover, there is a clearance between the spool and sleeve of the valve, and so leakages in the valve combined with air compressibility of air might alter the identification of the threshold position values. Hence, several trials of the test were run in order to identify the final value. The threshold value identified corresponded to 54% of the valve PWM Duty Cycle.

#### 4.3.2. Connective tubing

Section 4.3.2 describes the deductions made to characterize the variation of pressure in lengthy connective tubing. Illustrating the methodology applied, experimental data collected under specific conditions is presented. At the end of this section, the dynamic behavior of the pneumatic cylinder is correlated to the variation of pressure in connective tubing of different length.

The pressure at the inlet and outlet of tubing that connects the control valves and the pneumatic cylinder was measured to accomplish the following:

- Characterize the effects of pressure drop in lengthy connective tubing, in relation to the dynamic performance of the pneumatic cylinder.
- Corroborate if the effects of pressure distortion in lengthy connective tubing can be described though a second-order linear filter model, as described in chapter 2.
- Identify feasible approaches for compensation of pressure distortion associated with the length of connective tubing,

Tests to verify the development of pressure in lengthy connective tubing included:

- Comparison of the frequency response of pressure transducers mounted at the input and output sections of connective tubing.
- Comparison of the transient response of the pneumatic cylinder in relation to the length of connective tubing.

With reference on the laboratory tests developed by [Whitmore et al. \(1990\)](#), the comparison of the frequency response of pressure transducers mounted at the input and output end of pneumatic tubing should demonstrate the distortion caused by air compressibility in relation to the length of tube tested. The secondary experimental setup described in section 4.2.3 (Figure 4.7) was utilized to replicate the tests performed by [Whitmore et al. \(1990\)](#).

In addition, by applying the equations identified in Chapter 2, section 2.4, the theoretical natural frequency and damping ratio associated with the wave behavior of pressure in connective tubing were computed as a function of tube length (Figure 4.14).

**Table 4.8.** Parameters used to calculate the pressure-wave damping ratio and natural frequency

PARAMETER	Value	Units	Equations	Consideration
Length of connective tubing	[0, ...,35]	[m]	2.66	Table 4.5
Internal diameter of the tube	0.0095	[m]	2.58	Table 4.5
Cross-sectional area of the tube	7.1256E-05	[m <sup>2</sup> ]	2.58	Table 4.5
Dynamic viscosity	1.8461E-05	[Pa.s]	2.58	Temperature: 295 K
Friction coefficient	64.00	[-]	2.50-2.58	Laminar Flow
Resistance of the tube	6.51	[Pa.s/m <sup>2</sup> ]	2.58	Laminar flow - 295K
Initial density	1.20	[kg/m <sup>3</sup> ]	2.66	Temperature: 295 K
Speed of sound	343.59	[m/s]	2.66	Table 1.5

Table 4.6 identifies the values of the parameters used to calculate the theoretical pressure-wave natural frequency and damping ratio as a function of the length of connective tubing (Figure 4.14). The equations where these parameters appear, and the considerations for their application are also included. Values for parameters such as the dynamic viscosity of air, the initial density of air, and the speed of sound are commonly found in the literature.

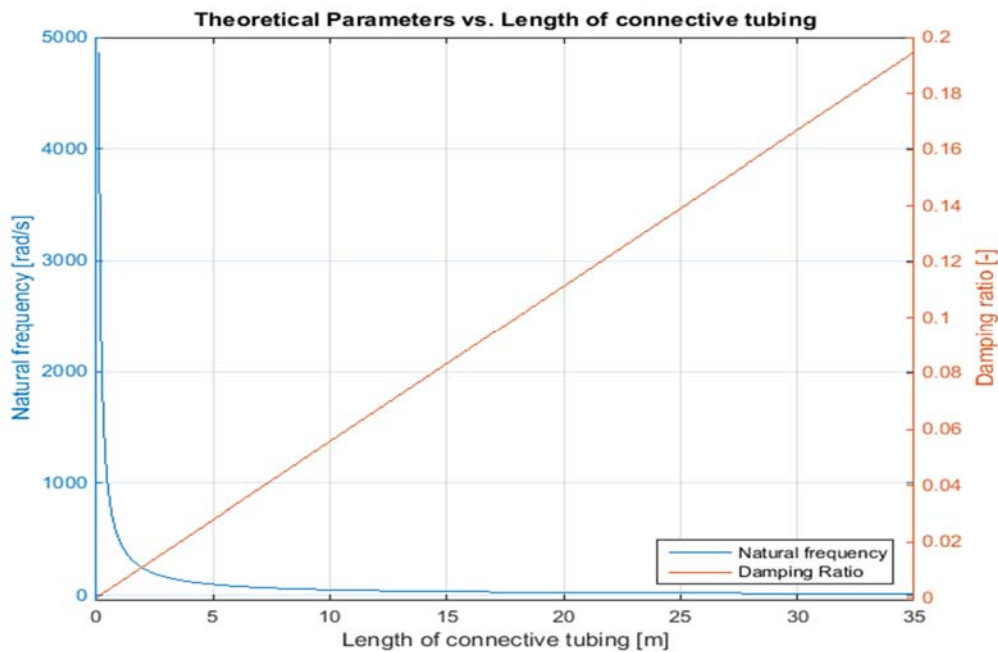


**Figure 4.14.** Theoretical tube pressure wave damping ratio and natural frequency

Moreover, by using the second-order linear-filter model from Eq. 2.65, the theoretical frequency response associated with the variation of pressure in pneumatic tubing was simulated for different tube lengths (Figure 4.15). The calculation of the theoretical pressure-wave natural frequency and damping ratio, and the simulation of the pressure frequency response in connective tubing served one primary goal: to determine the frequency of the sinusoidal input applied to the valve to measure the variation of pressure in lengthy pneumatic tubing.

As described by [Whitmore et al. \(1990\)](#), the second-order linear-filter model from Eq. 2.65 should be able to match the wave behavior of the pressure profile in pneumatic tubing until the second harmonic. Nevertheless, the accuracy of this correspondence depends on the frequency of the sinusoidal command input to the valve. Accordingly, for a specific tube length, the valve should be able to operate at a frequency at least equal or higher than the theoretical pressure-wave break frequencies (figure 4.15).

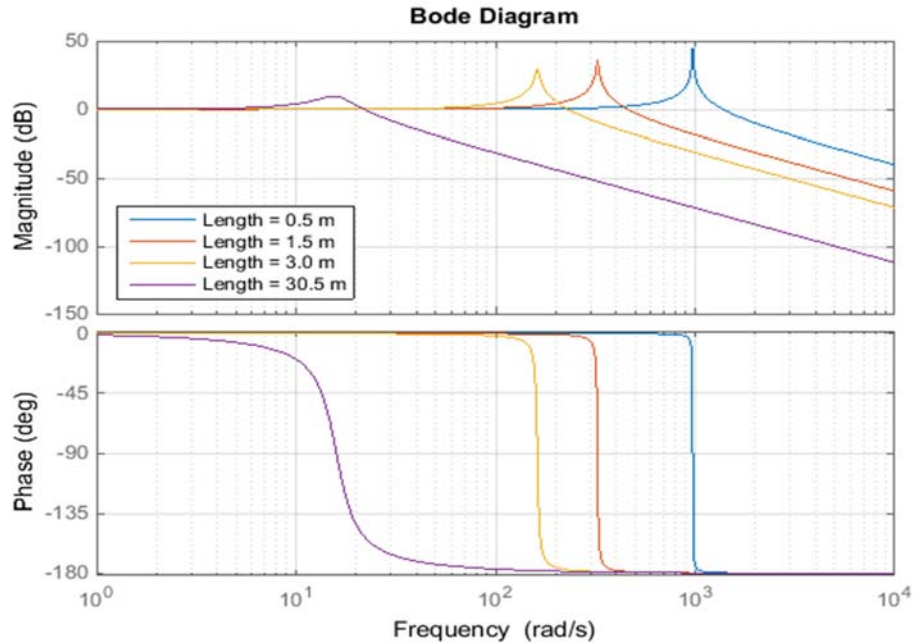


**Figure 4.15.** Theoretical pressure-wave frequency response in pneumatic connective tubing

Figure 4.14 and figure 4.15 demonstrate that as the length of connective tubing increases, the pressure-wave natural frequency decreases, while the damping ratio increases. Table 4.9 includes the break frequencies determined in accordance to the tube lengths for which the theoretical pressure-wave frequency response was simulated (figure 4.15).

**Table 4.9.** Theoretical pressure-wave break frequencies as a function of pneumatic tube length

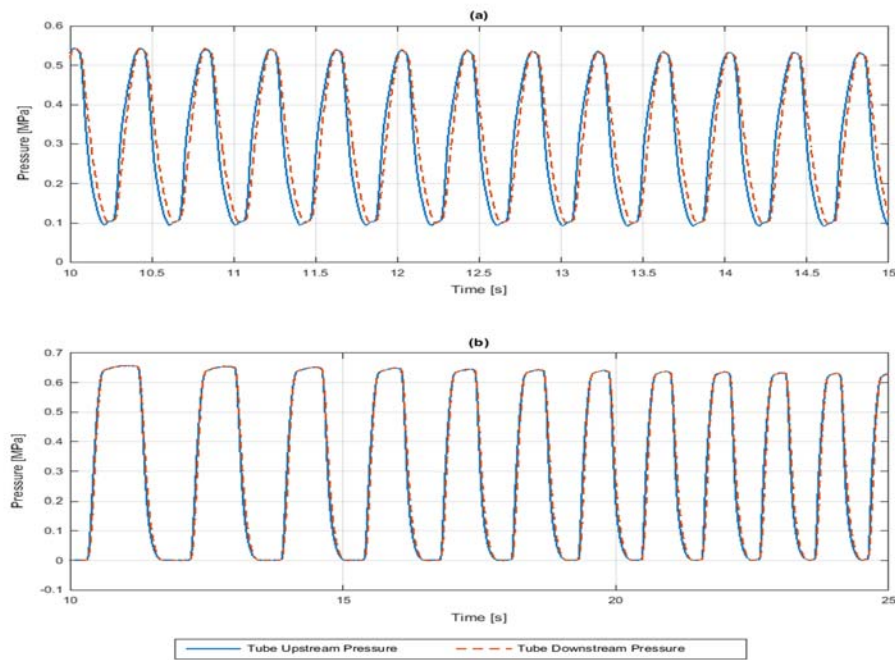
LENGTH [m]	BREAK FREQUENCY	
	[rad/s]	[Hz]
0.50	972	154.7
1.50	324	51.6
3.00	162	25.8
30.50	15.5	2.5

Using the secondary experimental setup from figure 4.7, it was verified that for frequencies higher than 10 Hz, the control valve did not respond fast enough in order to open and close according to a sinusoidal command. In fact, for constant frequencies higher than 5 Hz, the shape and amplitude of the pressure response obtained became less uniform than with lower frequencies, which affected the results obtained from frequency-response analysis.



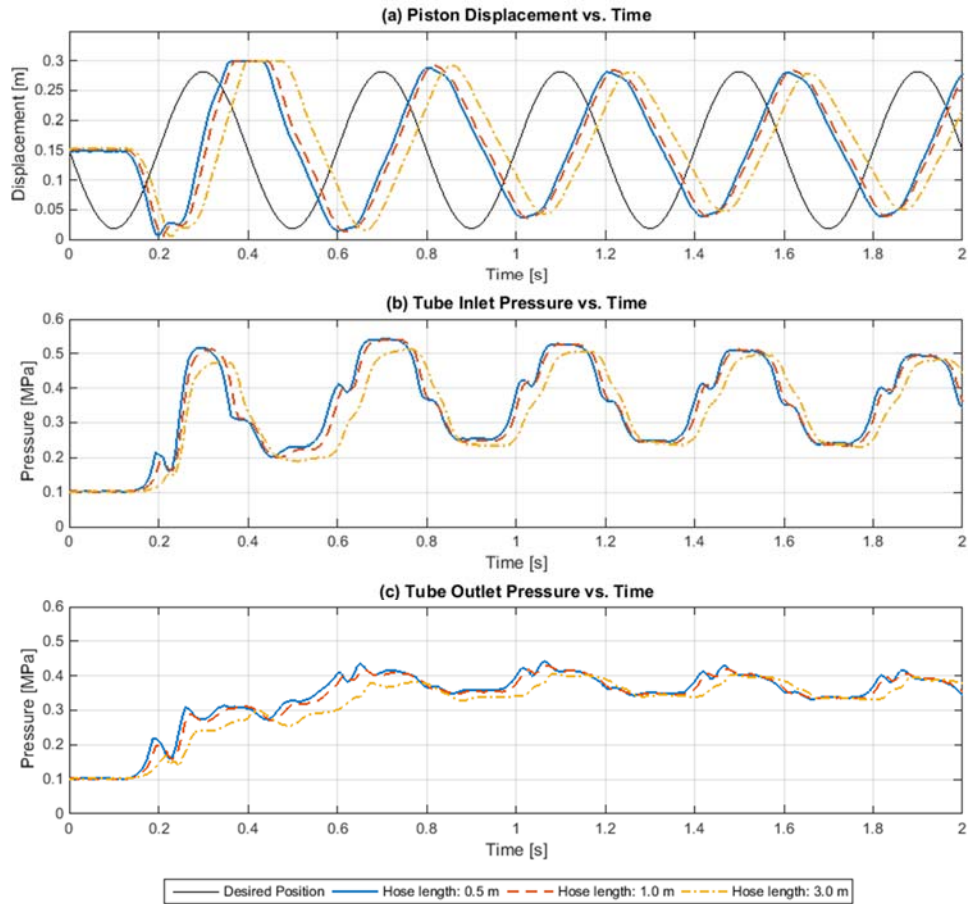
Hence, to validate the second-order linear-filter model from chapter 2, the length of tube tested should permit the proportional control valve to operate in a range of frequency that preserves most of the dynamic characteristics of the response obtained. The length of tube tested for validating the second-order linear-filter model described in chapter 2 was of 30.5 meters. Chapter 6 will report and analyze the final experimental results used to validate the second-order linear-filter model from Eq. 2.65.

Figure 4.16 shows experimental data corresponding to air pressure measured at the inlet and outlet of three-meter connective tubing using the experimental setup from figure 4.7.



**Figure 4.16.** Three-meter tube pressure responses to: (a) Constant 2.5-Hz frequency sine wave input. (b) Sinusoidal input with frequency swept between 0.0 and 2.5 Hz.

To conclude this section, figure 4.17 demonstrates the effects of the length of connective tubing on the transient response of the piston of the cylinder. A closed-loop proportional control scheme was adopted, and a 2.5-Hz sinusoidal input command was applied to the valves using the main experimental setup (figure 4.1). Two main effects of the length of connective tubing on the dynamic response of the pneumatic system were observed. The first effect relates to the pressure drop along the tube connecting the cylinder and the valves. As the length of connective tubing increased, the pressure drop along the tube increased.



**Figure 4.17.** Transient responses to a closed-loop 2.5-Hz frequency sinusoidal input command according to different tube lengths: (a) Cylinder piston displacement. (b) Tube inlet pressure. (c) Tube outlet pressure.

The second effect of the length of connective tubing observed through figure 4.17 relates to the time delay in the position profile of the cylinder piston. As the length of connective tubing increased, the time delay in the position profile of the cylinder piston increased. The phase shift of the piston displacement responses for the case of three-meter connective tubing was more pronounced than that for the cases of shorter connective tubing tested. In conclusion, figure 4.17 would represent the required effect of the control algorithm to be designed: to compensate for the pressure drop and time delay associated with the length of pneumatic connective tubing.



### 4.3.3. Chambers of the pneumatic cylinder

To corroborate the effects of the variation of pressure in the cylinder chambers in relation to the dynamic behavior of the pneumatic cylinder, the tests performed aimed the following:

- Verify whether the pressure at the cap-end and rod-end cylinder chambers develop according to a linear or non-linear profile.
- Associate the change of pressure in the cylinder chambers with other dynamic variables.
- Find coefficients and parameters of models that depend on the differential pressure between the cylinder chambers.
- Identify threshold-input control values corresponding to the first increment of pressure in the cylinder chambers.

Tests developed to verify the development of pressure in the chambers of the cylinder included:

- Actuation of the pneumatic valves through a step input.
- Actuation of the pneumatic valves according to a sinusoidal input.
- Periodic increment of the control command input to the valves until generating the raise of pressure in the cylinder chambers.

The tests to characterize the pressure profiles in the cylinder chambers were similar to the tests performed to measure the pressure at the upstream and downstream ports of the control valves (Section 4.3.1). However, depending on the length of connective tubing used, different pressure profiles were obtained. Figures 4.18 and 4.19 show the pressure profile at the cylinder chambers, for an open-loop step input.

A zone transition was marked to verify how the change in pressure in the cylinder chambers related to the physical characteristics of air entering or leaving the pneumatic cylinder. Moreover, the time required so that the air pressure in the cylinder chambers becomes equal to the supply pressure would correspond to the time required by air to compress inside the cylinder chambers (Figures 4.18 and 4.19). Therefore, for high-amplitude step inputs (Figure 4.18) the effects of air compressibility were noticed more rapidly than for low-amplitude step inputs (Figure 4.19).

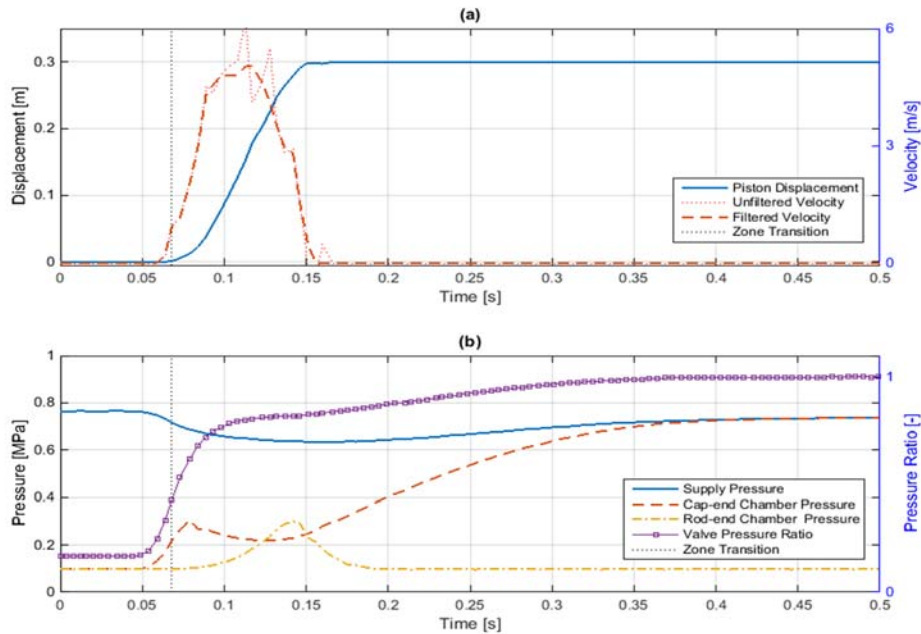


**Figure 4.18.** (a) Piston displacement and velocity in response to an open-loop 100% duty-cycle PWM step input. (b) Cylinder chamber pressure (Tube length = 0.55 [m])

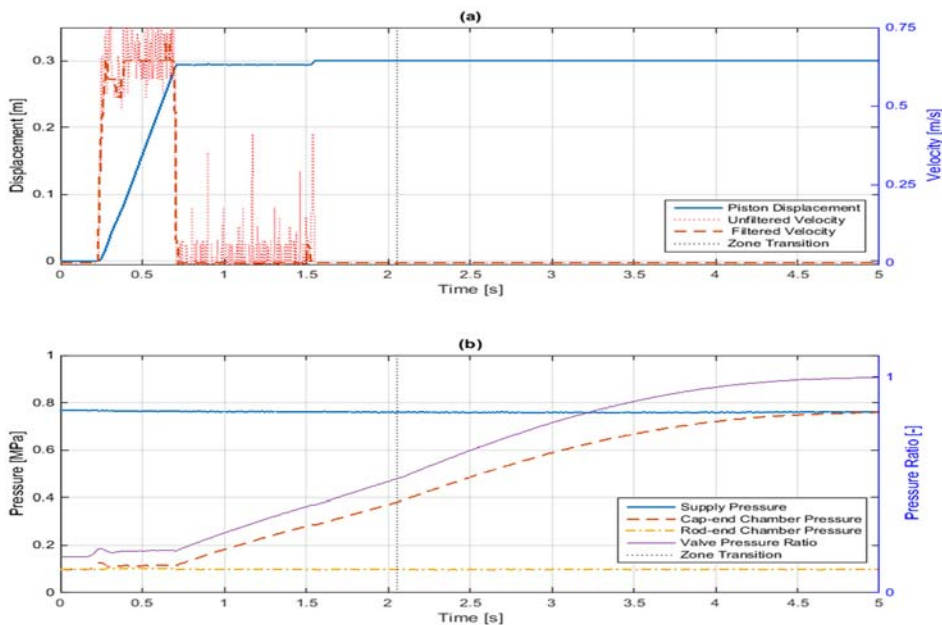


**Figure 4.19.** (a) Piston displacement and velocity in response to an open-loop 70% duty-cycle PWM step input. (b) Cylinder chamber pressure (Tube length = 0.55 [m])

The pressure profiles at the chambers of the cylinder were also measured according to a closed-loop control strategy (Figures 4.20 to 4.22). For a step input, in order for the piston to reach a specific position, the pressure in the extension and retraction chambers of the cylinder reached an equilibrium value (Figure 4.20).

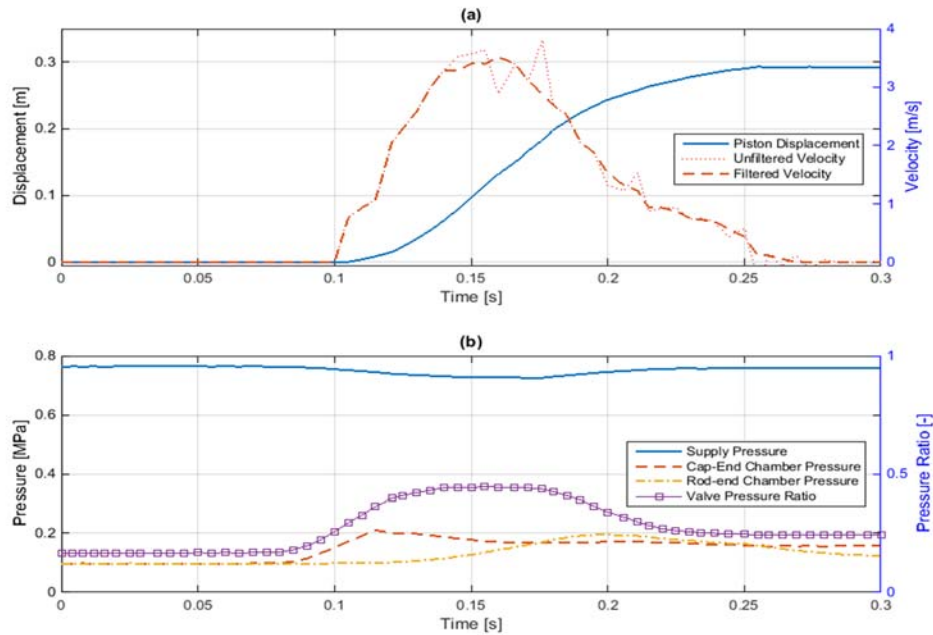


**Figure 4.20.** (a) Piston displacement and velocity in response to a closed-loop step input.  
(b) Cylinder chamber pressure (Tube length = 0.55 [m])

For a closed-loop step input, the pressure ratio of the valve remained below the critical value  $C_{cr}$  (Figure 4.20); consequently, based on Eq. 2.6 and Eq. 2.7, the volumetric flow would be inversely proportional to the pressure ratio of the control valve, and the mass flow would be proportional to the supply pressure.

Furthermore, when a closed-loop sinusoidal command was input to the valves, as the frequency of the command increased, the pressure profiles in the chambers of the cylinder adopted a more accurate sinusoidal shape (Figure 4.22). Nonetheless, in the case of a low-frequency sinusoidal control input (Figure 4.21), the pressure profiles in the chambers of the cylinder approximated a constant value.

Figures 4.21 and 4.22 respectively show the dynamic responses of the system to a 1-Hz and 4.5-Hz sinusoidal input generated through a proportional control scheme.

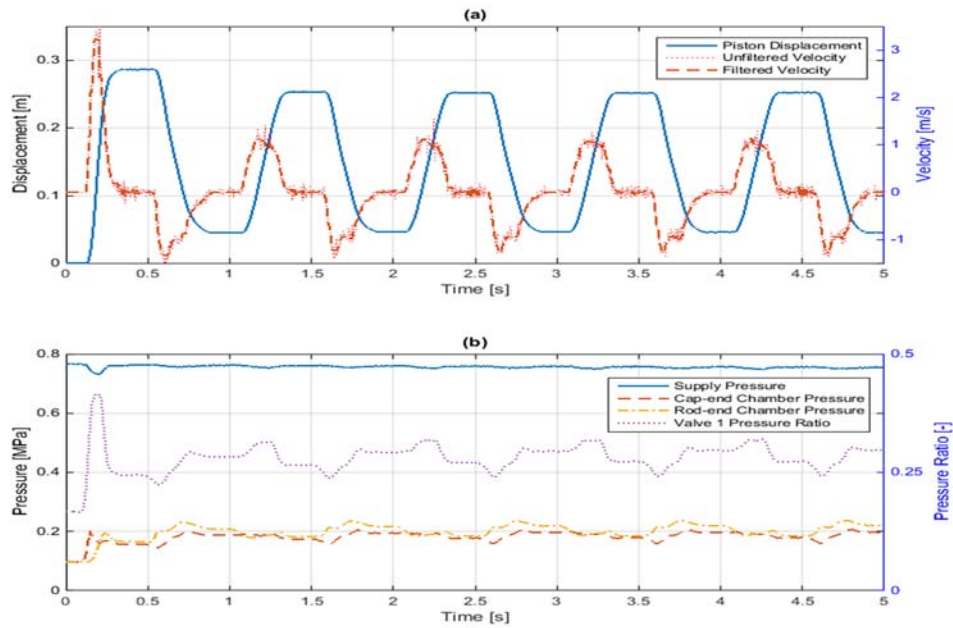


**Figure 4.21.** (a) Piston displacement and velocity in response to a closed-loop 1-Hz sinusoidal input. (b) Cylinder chamber pressure (Tube length = 0.55 [m]).

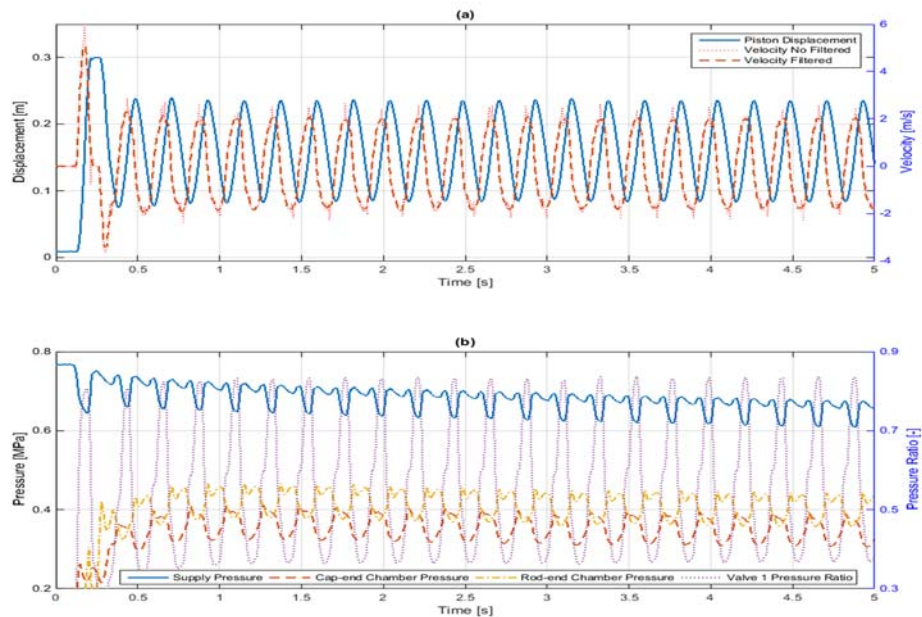


**Figure 4.22.** (a) Piston displacement and velocity in response to a closed-loop 4.5-Hz sinusoidal input. (b) Cylinder chamber pressure (Tube length = 0.55 [m]).

For low-frequency sinusoidal inputs (Figure 4.21), the pressure ratio of the valve remained below the critical value  $C_{cr}$ ; hence, the relation between the pressure and the flow profile could be assumed to be linear. Moreover, in figure 4.22, although a flow zone-transition line was not included, the downstream-to-upstream pressure ratio would mark the time when the choked flow became unchoked during piston extension, and the unchoked flow became choked during piston retraction.

Furthermore, following the procedure to identify the threshold position command for the valves (section 4.3.1), the minimum-value control commands needed to cause the first increment of pressure in the cylinder chambers were identified. Periodic incremental inputs triggered the valves until the first increment of pressure in the cylinder chambers was observed (Figures 4.23 and 4.24). The input values identified are the threshold input values required to overcome the static friction of the cylinder piston, by maintaining the opposite valve open to the atmosphere. Hence, an input control value higher than the threshold input value for one of the valves would cause the piston to move if the command input to the valve connected to the opposite side of the cylinder is lower than its corresponding threshold input value.

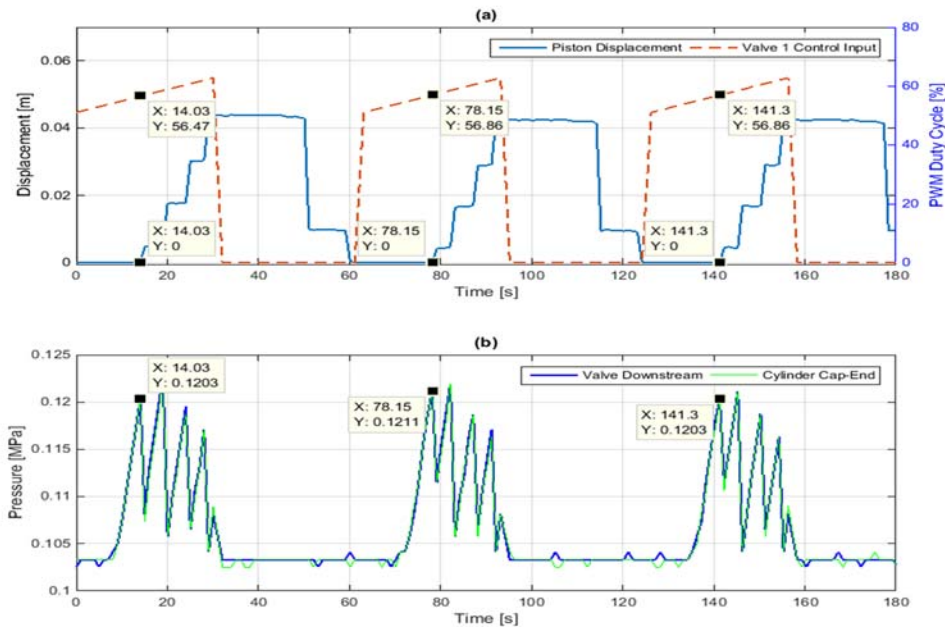


**Figure 4.23.** (a) Cylinder piston position in response to a ramp input. (b) Pressure at the cap-end cylinder chamber and valve (Tube length = 0.55 [m]).

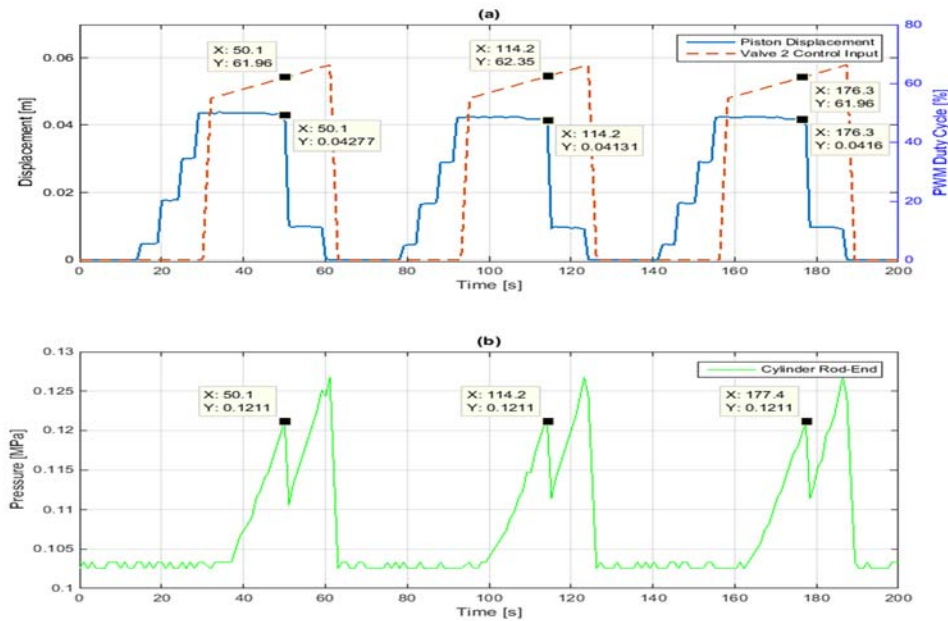


**Figure 4.24.** (a) Displacement of the cylinder piston in response to a ramp input. (b) Pressure at the rod-end cylinder chamber (Tube length = 0.55 [m]).

Due to the asymmetry of the active areas of the piston, the threshold value corresponding to the cylinder cap-end was lower than the value for the cylinder rod-end (Figures 4.23 and 4.24). The threshold input values for control at the cap-end and rod-end of the cylinder respectively corresponded to: 57% and 62% Duty Cycle PWM voltages. Moreover, for a specific threshold input control value, the pressure difference between the two chambers would correspond to the static friction force that the piston must overcome before it moves.

#### 4.4. Identification of system parameters and validation

Section 4.4 describes the experimental procedure followed to identify some of the constants, gains, and physical parameters included in the models for the pneumatic system. In addition, the mathematical equations describing the flow in the cylinder chambers and the control valves are validated. At the end of this section, several tables summarize the findings of this chapter.



#### 4.4.1. Boundaries of the dead zone of the valves

Since the flow from the valves depends on their effective area, it was necessary to correlate the input current and the corresponding analog value generated by the controller to the valve effective area. Based on flow characteristic charts provided by the manufacturer of the valves (figure 4.25), the input current corresponding to each analog control command generated by the controller was correlated to the effective area of each valve. Figure 4.25 shows the set of flow characteristic curves provided by the manufacturer of the control valves tested. The specific curve for the valves used is circled in red.

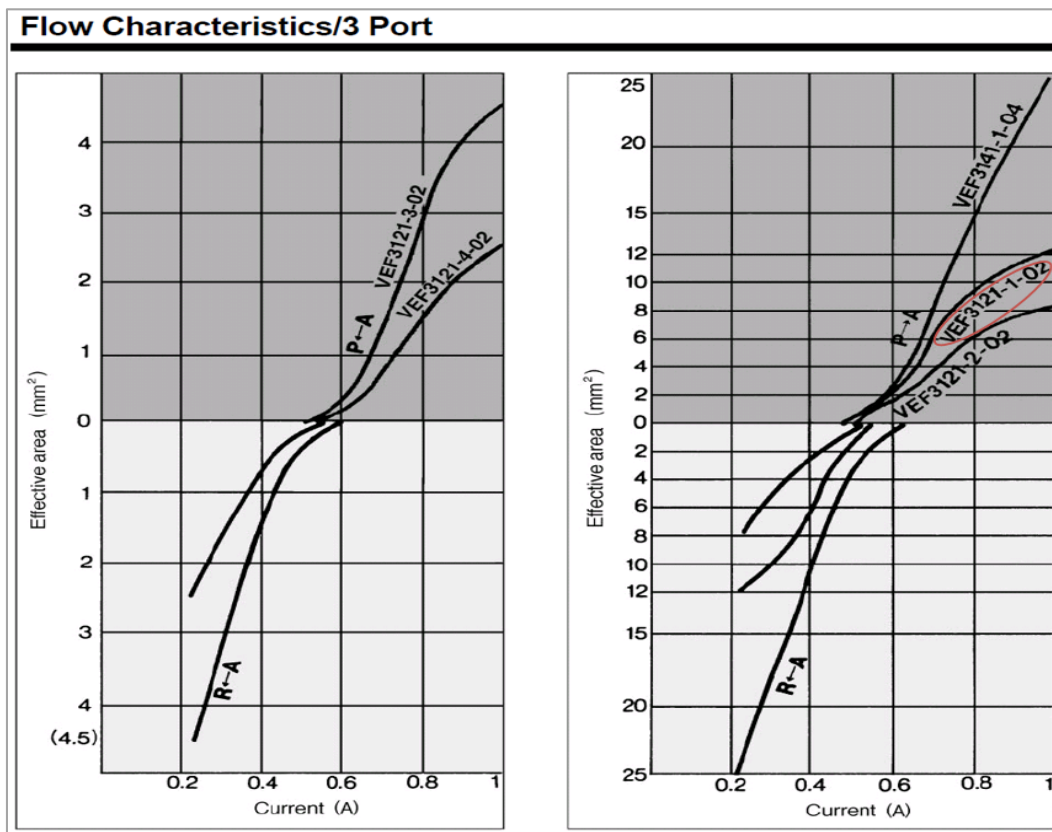


**Figure 4.25.** Flow characteristic curves provided by the manufacturer of the proportional valves

[Source: <http://content2.smcetech.com/pdf/VEP.pdf>]

Moreover, from Eq. 2.1, at steady state the PWM input voltage would be given by:

$$V_{PWM} = R_c i_c \quad (4.2)$$

Where  $R_c$  and  $i_c$  are respectively the coil resistance and the coil current for the valve.

The coil resistance of the proportional valves is 13  $\Omega$  (Table 4.5). Thus, using the flow curves provided by the manufacturer of the valves, and Eq. 4.2, the effective area of the valve was related to the analog control command generated by the controller (Figure 4.26).

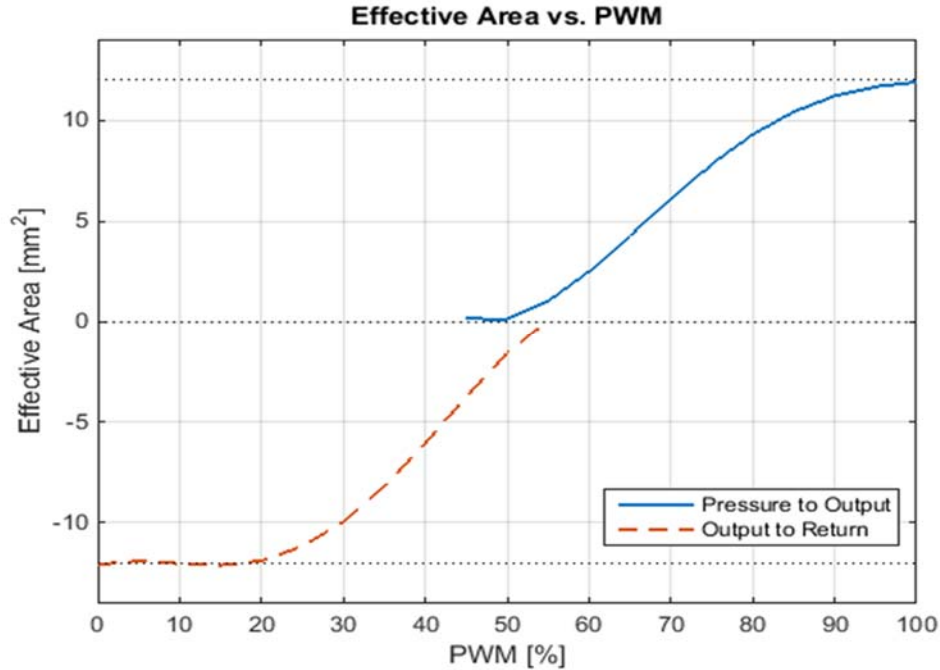


**Figure 4.26.** Theoretical curves of the valve effective area as a function of analog control command

To replicate and validate the theoretical curves (Figure 4.26), the displacement of the solenoid of the valve was measured in relation to the PWM voltage applied to the valves. For each PWM input voltage applied to the valve, the displacement of the solenoid was measured using the depth rod of a caliper pointing towards the backside of the armature of the valve (Figure 4.27). Subsequently, the effective area of the valve,  $A_{v-act}$ , was calculated using Eq. 2.14, which is shown again below:

$$A_{v-act} = N_{Ao} \left[ R_{Co}^2 \arccos \left( 1 - \frac{x_s}{R_{Co}} \right) - (R_{Co} - x_s) \sqrt{x_s (2R_{Co} - x_s)} \right] \quad (4.3)$$

Where:  $x_s$  is the position of the spool of the valve,  $N_{Ao}$  is the number of active orifices in the sleeve of the valve, and  $R_{Co}$  is the radius of the orifices of the sleeve of the valve.



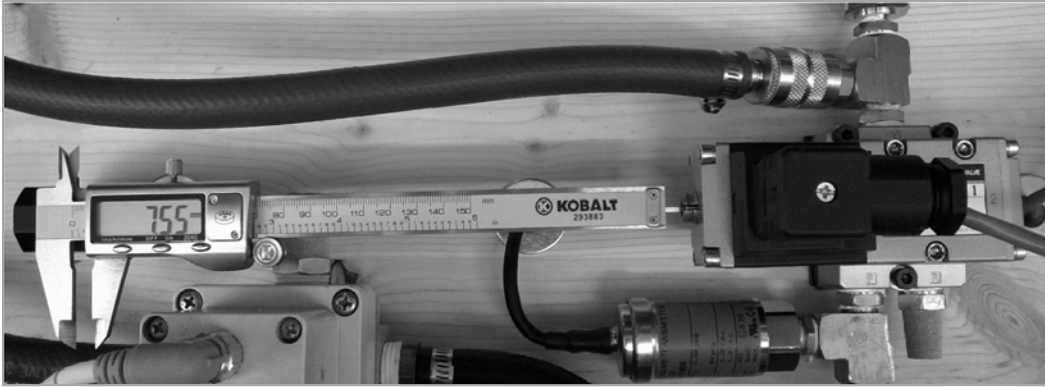


**Figure 4.27.** Control valves: Measurement of spool displacement vs. PWM input

Figure 4.28 shows the results obtained from measuring the displacement of the valve spool according to the PWM voltage applied to the valve. Each measurement was taken three times; and accordingly, the graph presented below also includes standard-deviation error bars.

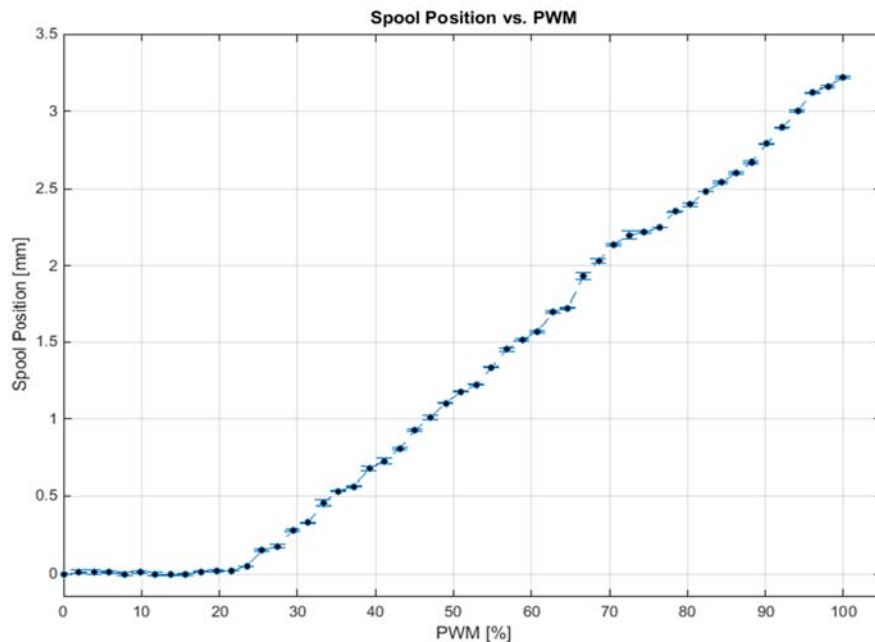


**Figure 4.28.** Valve spool displacement as a function of PWM voltage applied

The progress of the spool displacement curve was consistent (Figure 4.28). For PWM inputs lower than 20% of the duty cycle, the valve spool did not move. Besides, the maximum displacement of the spool of the valve was approximately 3.2 mm.

To calculate the effective area of the valve using Eq. 4.3, some of the geometric characteristics of the spool of the valve were needed. Sorli et al. (2010) provided a geometric detail of the spool-bushing coupling of a VEF SMC valve similar to the valves used in this thesis; nevertheless, the exact part number of the valve was not mentioned. Based on the fact that the maximum spool displacement measured value corresponded to the value reported by Sorli et al. (2010), it was assumed that the valves were the same. Hence, the orifices in the valve sleeve would have a radius of 1.25 millimeters.

As described in chapter 2, the effective area of the spool of the valve corresponds to the area of a circular segment. Based on the geometric detail provided by Sorli et al. (2010), the spool of the valve would displace 2.1 mm to position at the upper boundary for input control, which corresponds to the start of the circular segment enclosing the valve effective area. A 70% duty-cycle PWM input would be required for the valve spool to displace 2.1 mm (Figure 4.28). Figure 4.29 shows the experimental curve produced to correlate the valve effective area to the PWM voltage input to the valves.

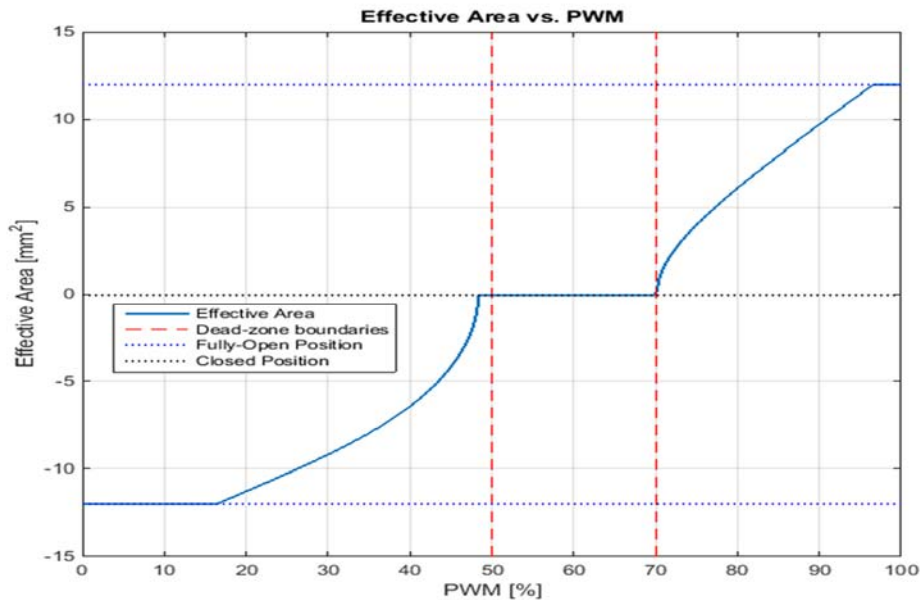


**Figure 4.29.** Experimental curves of the valve effective area as a function of analog control command

The number of orifices in the sleeve of the valve was defined from the knowledge of the maximum effective area of the valves (12 mm<sup>2</sup>). Hence, five orifices were determined to be required to match the maximum effective area on the pressure and exhaust sides of the valve.



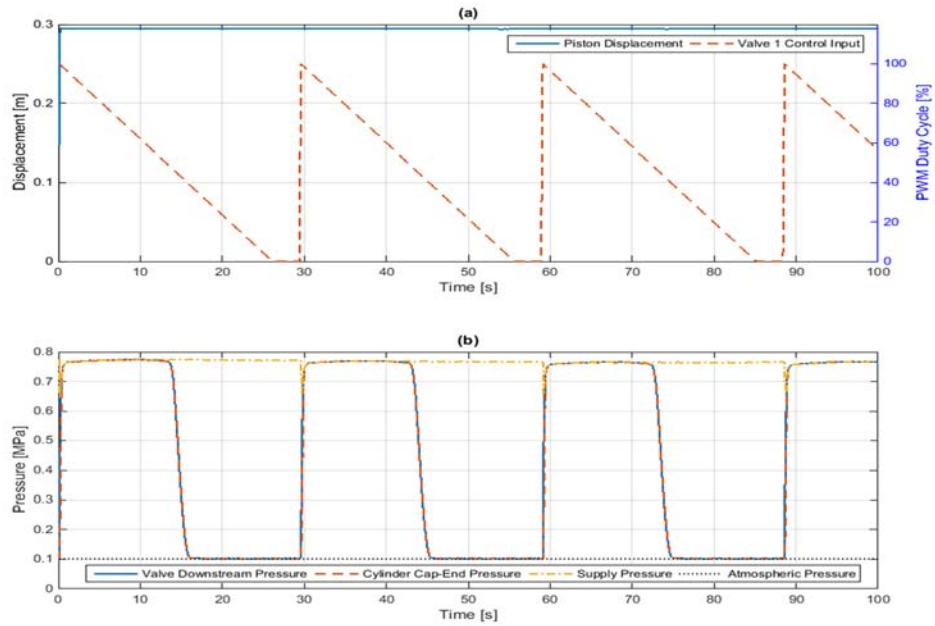


**Figure 4.31.** (a) Fixed cylinder piston position and ramp input applied to the cylinder cap-end valve. (b) Supply pressure, atmospheric pressure, and pressure at the cap-end cylinder chamber and valve (Tube length = 0.55 [m]).

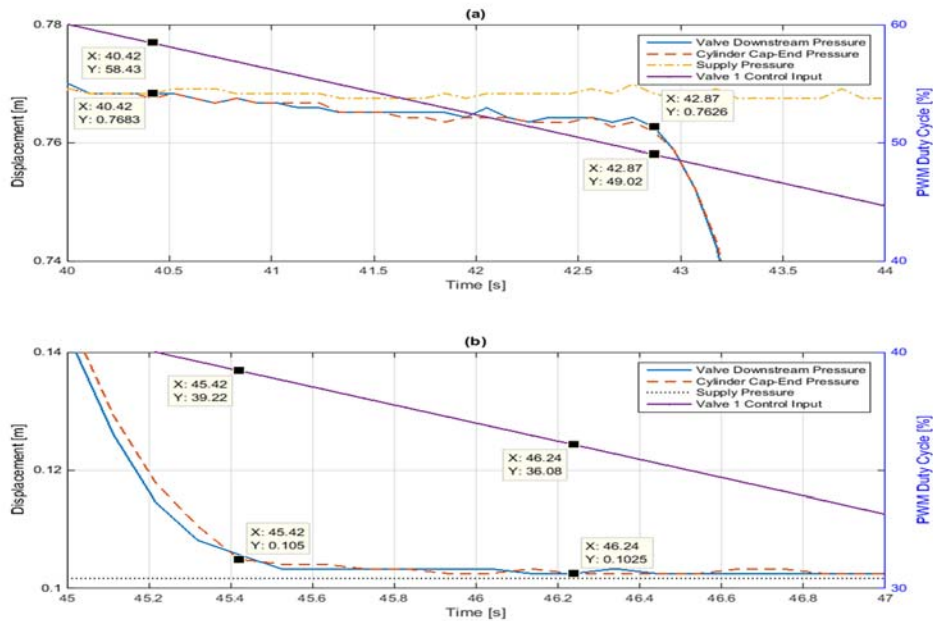


**Figure 4.32.** Closer views of figure 4.31b: (a) Interval of time between 40 and 44 seconds. (b) Interval of time between 45 and 47 seconds.

The dead-zone upper boundaries would have been identified when the valve downstream pressure and the cylinder cap-end pressure ceased to be equal to the supply pressure, and then started to decrease at a much faster rate (Figure 4.32a). In contrast, the dead-zone lower boundaries would correspond to the points at which the valve downstream pressure and the cylinder cap-end pressure started approximating the atmospheric pressure, and then became equal in value (Figure 4.32b).

A different approach to identify the limits of the valve dead-zone involved to progressively increase the input PWM voltage from zero to the maximum value (13 volts). Both valves were used to create the dynamic response required (Figure 4.33). A faster input rate than that of the results showed above (Figures 4.31 and 4.32) was applied. In this case, the lower dead-zone boundaries would correspond to the points at which the pressure at the cap-end cylinder chamber and valve approximated the atmospheric pressure, and became equal in value (Figure 4.34a). The upper boundaries of the dead zone would correspond to the points at which the pressure at the cap-end cylinder chamber and valve ceased to be equal, and started to rise rapidly (Figure 4.34b).

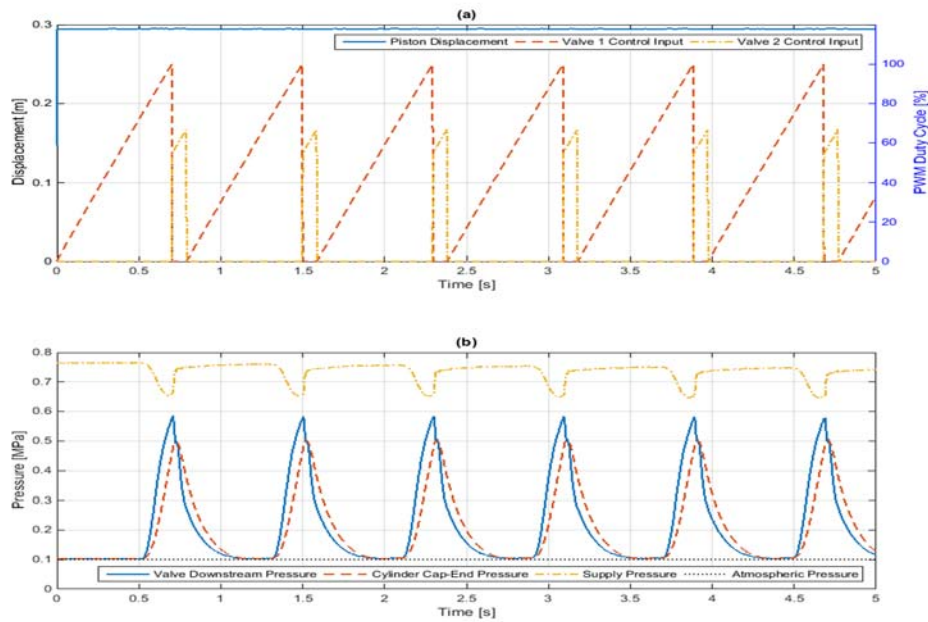


**Figure 4.33.** (a) Fixed cylinder piston position and ramp inputs applied to the valves. (b) Supply pressure, atmospheric pressure, and pressure at the cap-end cylinder chamber and valve (Tube length = 0.55 [m]).

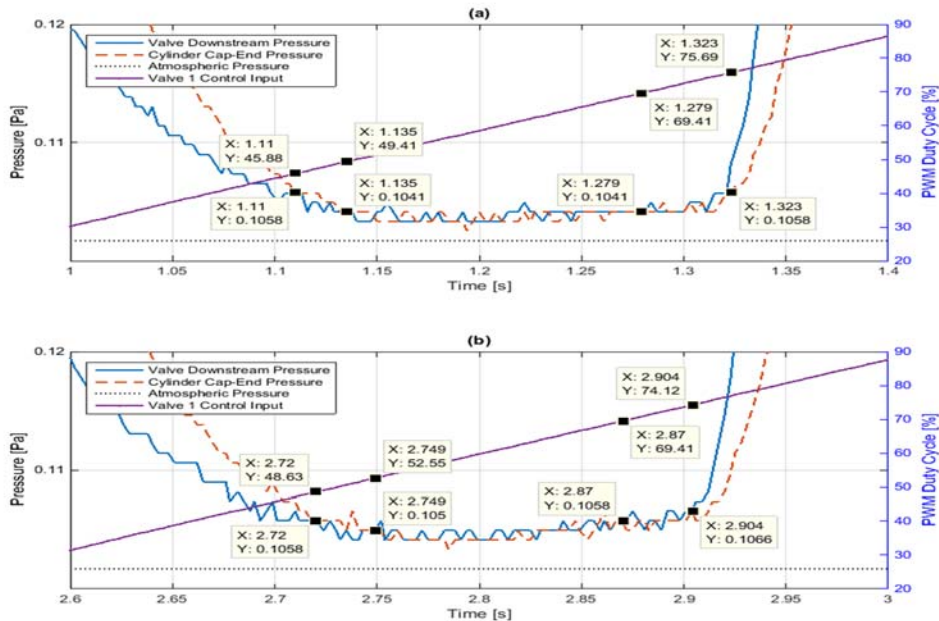


**Figure 4.34.** Closer views of figure 4.33b: (a) Interval of time between 1.0 and 1.4 seconds. (b) Interval of time between 2.6 and 3.0 seconds.

The boundaries of the dead zone of the valves are summarized in Table 4.10. The average of the values identified by following the experimental procedure previously detailed is included. The spool displacement is also included according to the results presented in Figure 4.28.

**Table 4.10.** Boundaries of the dead zone of the valve

Boundaries	PWM [%]					Average PWM [%]	Spool Displacement [mm]
	36.08	39.22	48.63	52.55	69.41		
Lower Boundary	36.08	39.22	48.63	52.55	69.41	49.178	0.9
Upper Boundary	49.02	58.43	69.41	74.12	75.69	65.334	1.9

The results presented in Table 4.10 validated the boundary values marked in Figure 4.29. A PWM input of approximately 50% and 70% of the valve voltage duty cycle would be required to position the valve spool at the lower and upper limits of the dead zone, respectively. Nevertheless, different values might be used in order to compensate negative dynamic effects that the transitional displacement of the valve spool through the dead zone might cause in the overall performance of the pneumatic system.



#### 4.4.2. Validation of flow equations

In this section, to provide a means of validation of the flow profile associated with the control valves, the flow profile in the chambers of the pneumatic cylinder was computed using Eq. 2.25 and Eq. 2.33. The combined resulting equation is expressed as follows:

$$Q = \frac{V_{0i} \pm x_p A_i}{kP} \dot{P} \pm \dot{x}_p A_i \quad (4.4)$$

Figure 4.36 shows the volumetric flow profiles relative to the chambers of the pneumatic cylinder for an open-loop step input, and for three different lengths of connective tubing.

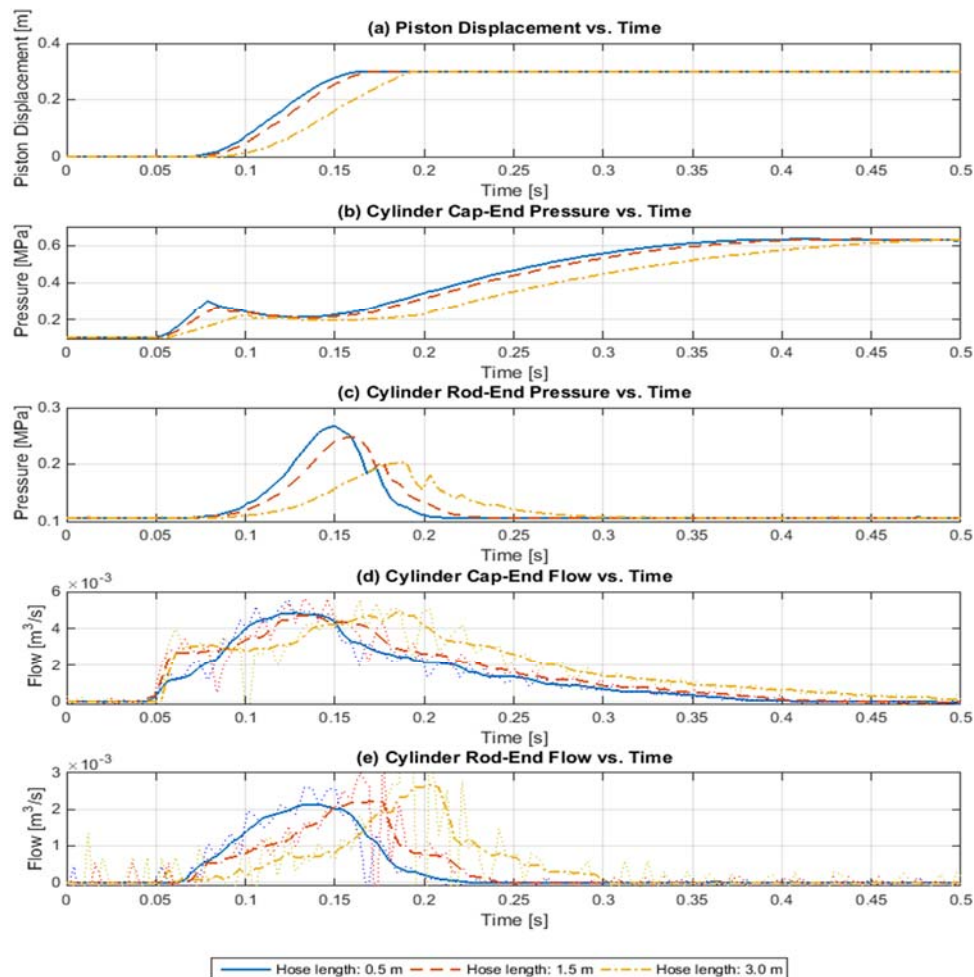


**Figure 4.35.** System responses to an open-loop 100% duty-cycle PWM step input: (a) Cylinder piston displacement. (b) Cylinder cap-end pressure. (c) Cylinder rod-end pressure. (d) Cylinder cap-end volumetric flow. (e) Cylinder rod-end volumetric flow.

Moreover, by following the procedure in Chapter 2, section 2.2, it can be verified that the equivalent mass-flow equation of Eq. 4.4 is given by:

$$\dot{m} = \frac{V_{0i} \pm x_p A_i}{kRT} \dot{p} \pm \frac{\dot{x}_p A_i}{RT} p \quad (4.5)$$

Where:  $\dot{m}$  = Mass flow rate of air enter and/or leaving the cylinder chamber.

Figure 4.37 shows the mass flow profiles relative to the chambers of the pneumatic cylinder for an open-loop step input, and for three different lengths of connective tubing.

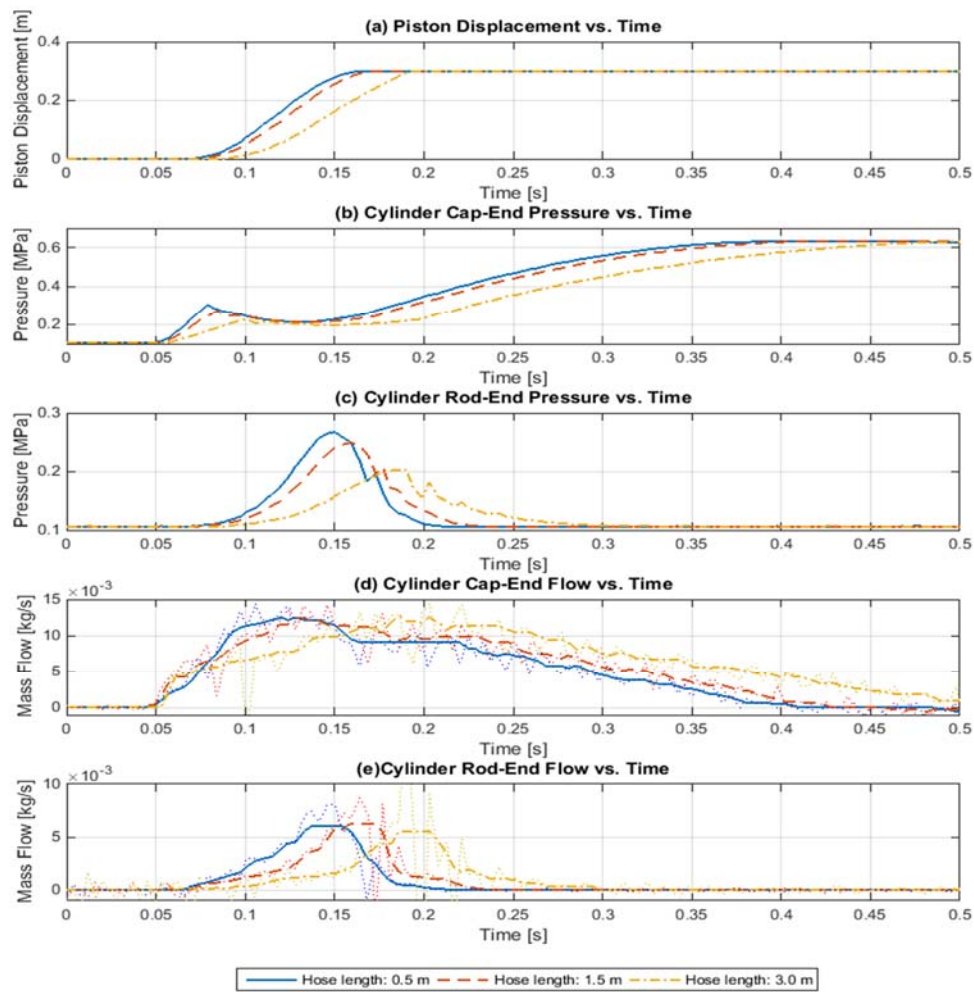


**Figure 4.36.** System responses to an open-loop 100% duty-cycle PWM step input: (a) Cylinder piston displacement. (b) Cylinder cap-end pressure. (c) Cylinder rod-end pressure. (d) Cylinder cap-end mass flow. (e) Cylinder rod-end mass flow.



Dotted lines on the background of the figures represent unfiltered values for the parameters depicted. The mass flow and the volumetric flow were calculated using the same experimental data (Figures 4.36 to 4.40).

As the length of connective tubing increased, more time was needed to compress the air in the chambers of the cylinder (Figures 4.36 and 4.37). Air was completely compressed when the flow in both chambers became zero, and the pressure at the cap-end and rod-end cylinder chambers attained a steady state. Therefore, as the length of connective tubing increases, pressure in the cylinder chambers takes more time to attain a steady state.

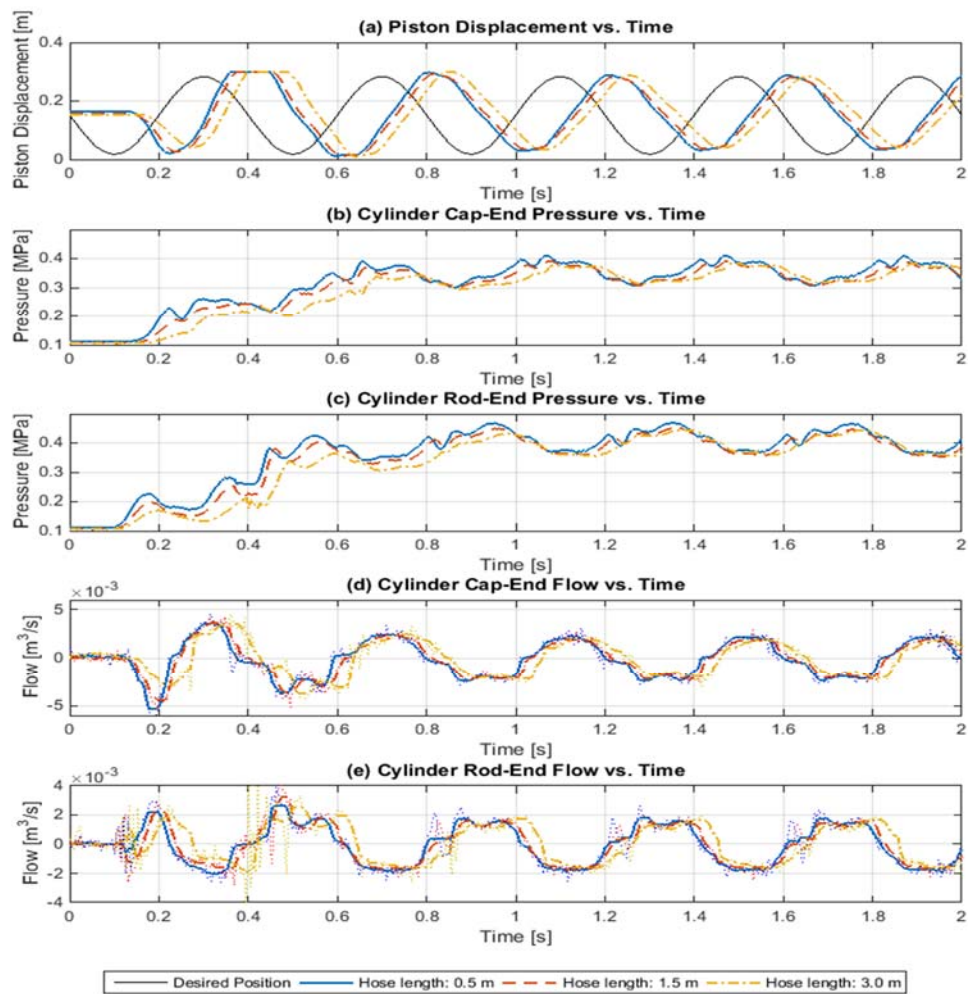


**Figure 4.37.** System responses to a closed-loop 2.5-Hz sinusoidal input: (a) Cylinder piston actual and desired displacement. (b) Cylinder cap-end pressure. (c) Cylinder rod-end pressure. (d) Cylinder cap-end volumetric flow. (e) Cylinder rod-end volumetric flow.

The volumetric flow and mass flow in the cylinder chambers were also calculated in relation to the response of the pneumatic system to a 2.5-Hz sinusoidal input command (Figures 4.38 and 4.39). A closed-loop proportional control scheme was implemented.

As in the case of a step input command, for a sinusoidal input command, the flow profiles in the cylinder chamber fluctuated according to the length of connective tubing tested. As the length of connective tubing increased, the flow profiles displaced further to the right in comparison to flow profiles observed for tubes of shorter length.

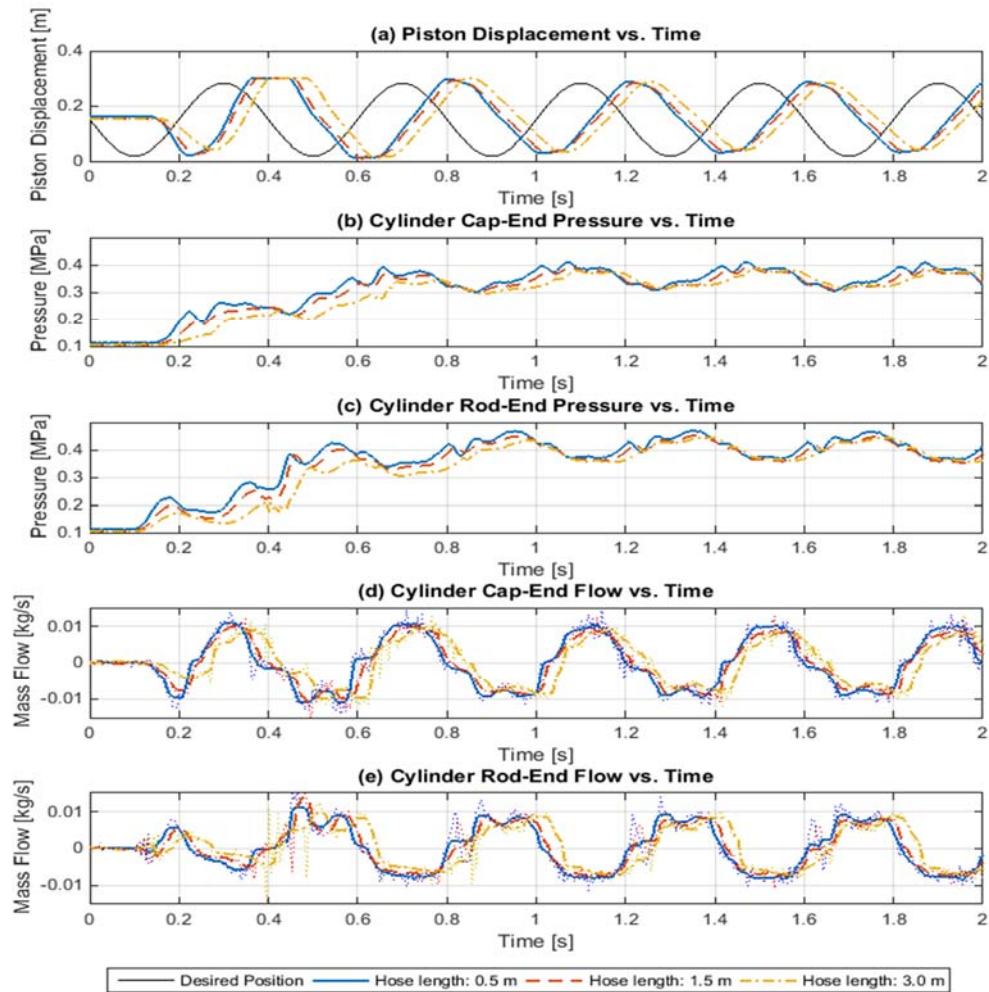


**Figure 4.38.** System responses to a closed-loop 2.5-Hz sinusoidal input: (a) Cylinder piston actual and desired displacement. (b) Cylinder cap-end pressure. (c) Cylinder rod-end pressure. (d) Cylinder cap-end mass flow. (e) Cylinder rod-end mass flow.

The development of the flow profile in the chambers of the cylinder depends on the time that the pressure waves need to travel throughout the entire length of connective tubing. Accordingly, as the length of connective tubing increased, the piston displacement profile was delayed by the extra time required for the flow profile to develop in the chambers of the cylinder. The piston displacement profile in the case of three-meter length connective tubing (Figure 4.38a and 4.39a) was shifted further to the right in comparison to the displacement profiles relative to connective tubing of shorter length.

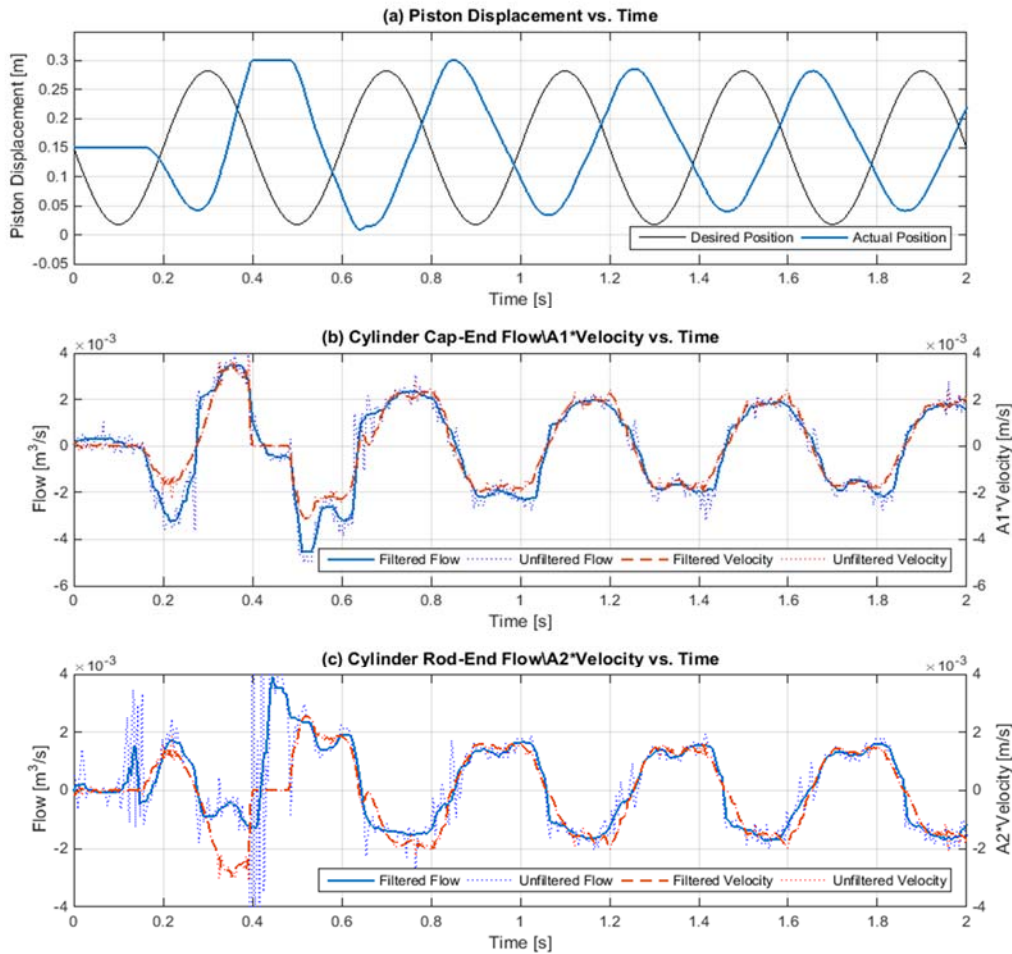


**Figure 4.39.** System responses to a closed-loop 2.5-Hz sinusoidal input: (a) Cylinder piston actual and desired displacement. (b) Cylinder cap-end flow and piston velocity. (e) Cylinder rod-end flow and piston velocity.

Figure 4.40 relates the volumetric flow in the chambers of the cylinder to the velocity and the areas of the piston. The active area of the piston respectively at the cylinder cap-end and rod-end was multiplied by the piston velocity. Once the piston attained steady state, after it overcame friction, the volumetric flow profiles in the chambers of the cylinder closely approximated the product of the velocity and the piston areas. This last deduction would help to further simplify the modeling and simulation of the pneumatic system, as a linear flow equation results from relating the volumetric flow to the velocity and areas of the cylinder piston.

#### 4.4.3. Dynamic constants – Block Diagrams Models

The block diagrams developed in chapter 3 included several constants and parameters that needed to be defined or determined to proceed with the simulation of the pneumatic system. This section describes how to determine the dynamic constants included in the simplified reduced model presented in chapter 3.

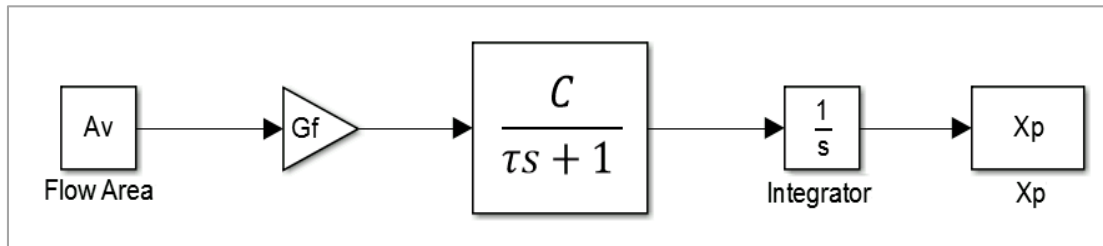


**Figure 4.40.** Simplified reduced model for the pneumatic system.

If a step input of amplitude  $A_m$  is applied to the system, and the constant  $C$  and the flow gain,  $G_f$ , are combined into a dynamic parameter  $C$ , figure 4.40 becomes figure 4.41.

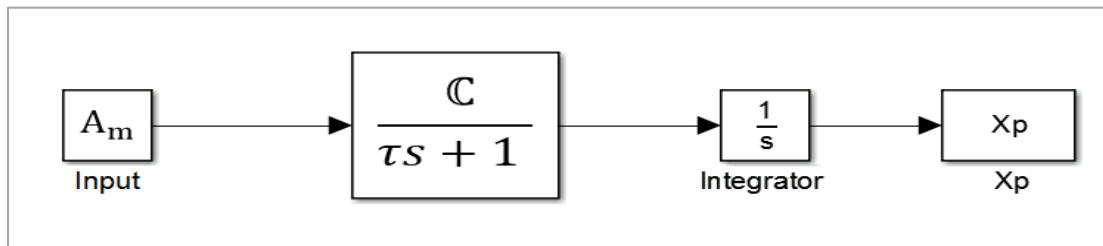


**Figure 4.41.** Simplified reduced model for the pneumatic system.

$C$  and  $\tau$  are dynamic parameters that can be found from experimental data. From convention in control, the constant  $\tau$  is called the time constant of the system.

The parameters  $\mathbb{C}$  and  $\tau$  were determined by fitting the simulation response obtained from the block-diagram model in figure 4.40, to the actual step response of the pneumatic system. Accordingly, the amplitude of the step input,  $A_m$ , would correspond to the amplitude of the PWM input applied to the control valves. The transfer function for the model presented in figure 4.41 is given by:

$$G(s) = \frac{\mathbb{C}}{s(\tau s + 1)} \quad (4.6)$$

The transient response of a system described by the transfer function presented in Eq. 4.6, to a step change of magnitude  $A_m$  is given by:

$$y(t) = \frac{\bar{\mathbb{C}}A_m}{a^2} e^{-at} + \frac{\bar{\mathbb{C}}A_m}{a} t - \frac{\bar{\mathbb{C}}A_m}{a^2} \quad (4.7)$$

Where:

$$a = \frac{1}{\tau}; \quad \bar{\mathbb{C}} = \frac{\mathbb{C}}{\tau} \quad (4.8)$$

Based on Eq. 4.7, figure 4.42 shows the transient response of the simplified reduced model for the pneumatic system to a step input of magnitude  $A_m$ .

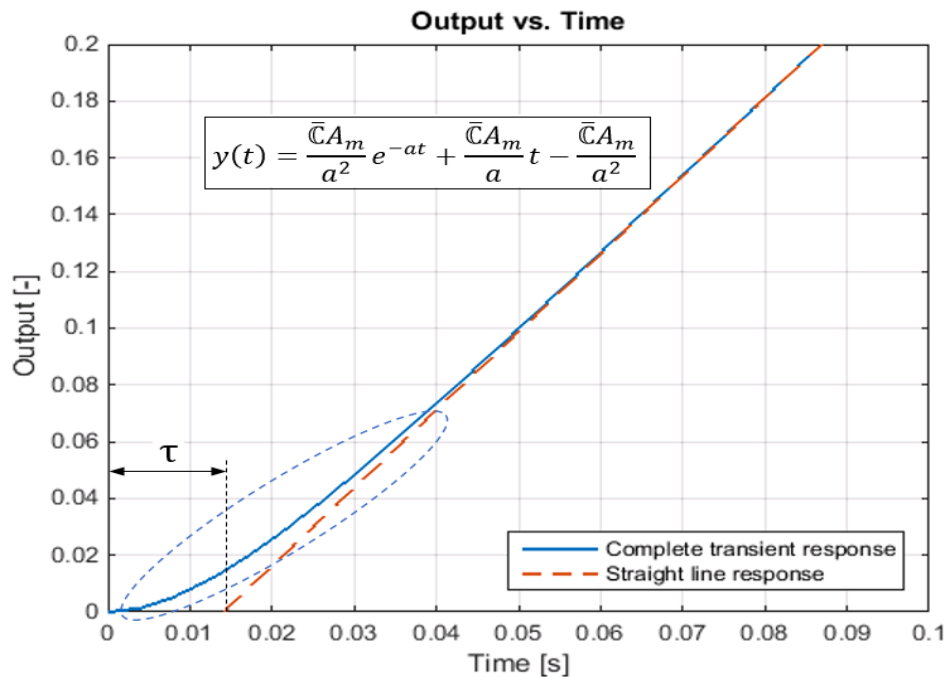


**Figure 4.42.** Transient response of the simplified reduced model for the pneumatic system.

Circled in blue in figure 4.42, it is the contribution of the exponential term (Eq. 4.7) to the complete response. If the exponential term is neglected, the remaining terms constitute the equation of a straight line. Figure 4.42 also includes the sole response of this straight line. The slope and y-intercept of this line would be given by:

$$\text{Slope} = \frac{\bar{C}A_m}{a}; \quad y_{\text{Intercept}} = \frac{\bar{C}A_m}{a^2} \quad (4.9)$$

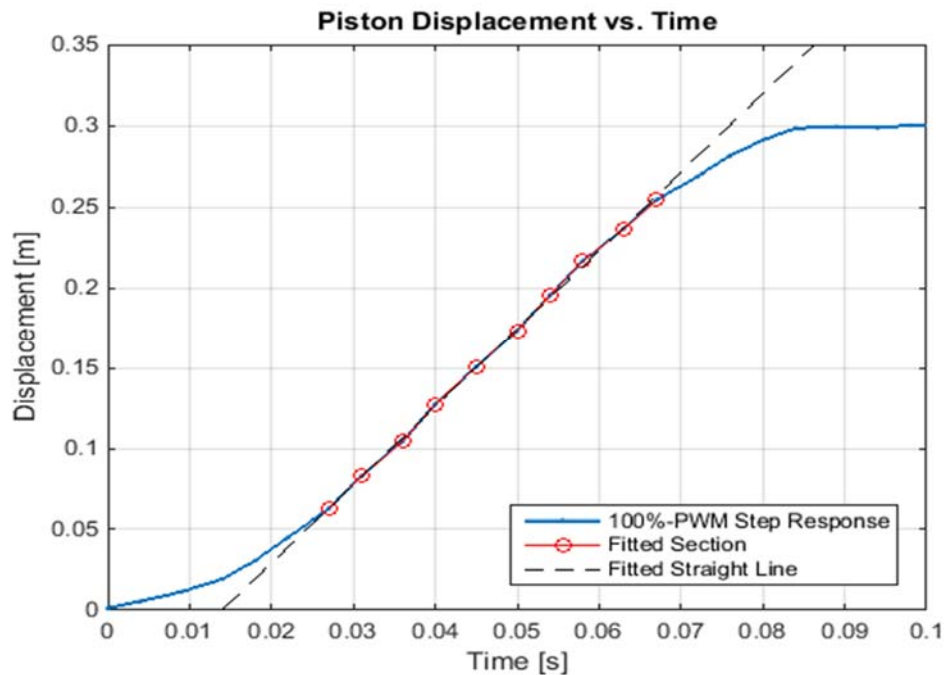
Moreover, the x-intercept of this straight line corresponds to the time constant of the system,  $\tau$  (Figure 4.42). The expressions included in Eq. 4.9 constitute a system of algebraic equations. Solving this system of equations for  $\bar{C}$  and  $a$ , it was obtained:

$$a = \frac{\text{Slope}}{y_{\text{Intercept}}}; \quad \bar{C} = \frac{1}{A_m} \left( \frac{\text{Slope}^2}{y_{\text{Intercept}}} \right) \quad (4.10)$$

Therefore, from Eq. 4.8:

$$\tau = \frac{y_{\text{Intercept}}}{\text{Slope}}; \quad C = \frac{\text{Slope}}{A_m} \quad (4.11)$$

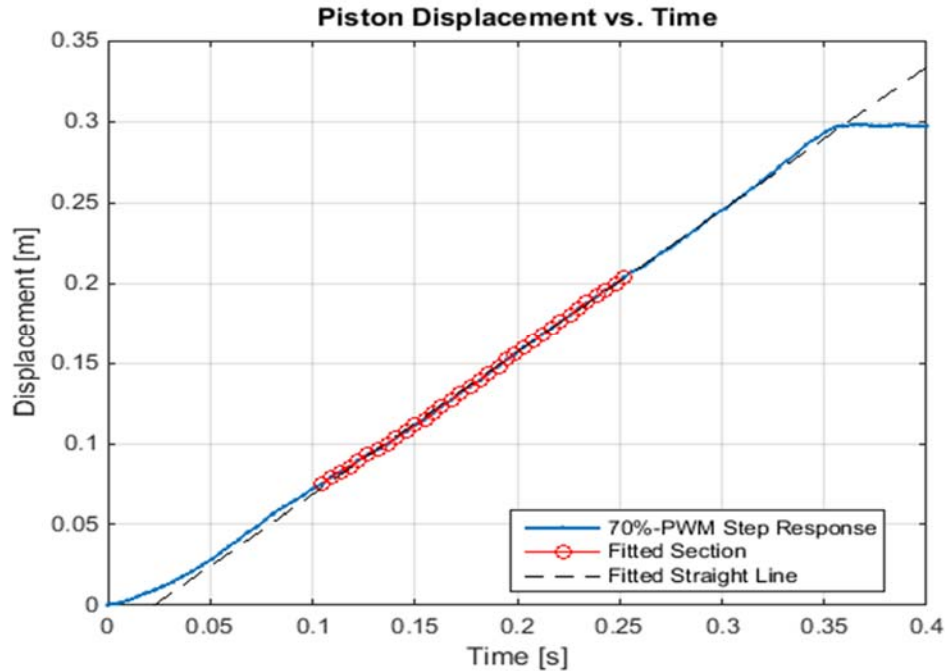
Figure 4.43 shows the outcome of the fitting procedure applied to find  $C$  and  $\tau$  relative to the open-loop response of the system to a 100-percent duty cycle PWM input.



**Figure 4.43.** Identification of dynamic constants: 100%-PWM Step Response (Extension)



A straight line fitted the actual step response of the pneumatic system (Figure 4.43). The straight line was fitted tangent to the steepest slope identified in the experimental response. Likewise, figure 4.44 shows the outcome of the fitting procedure relative to the system open-loop response to a 70-percent duty cycle PWM input.



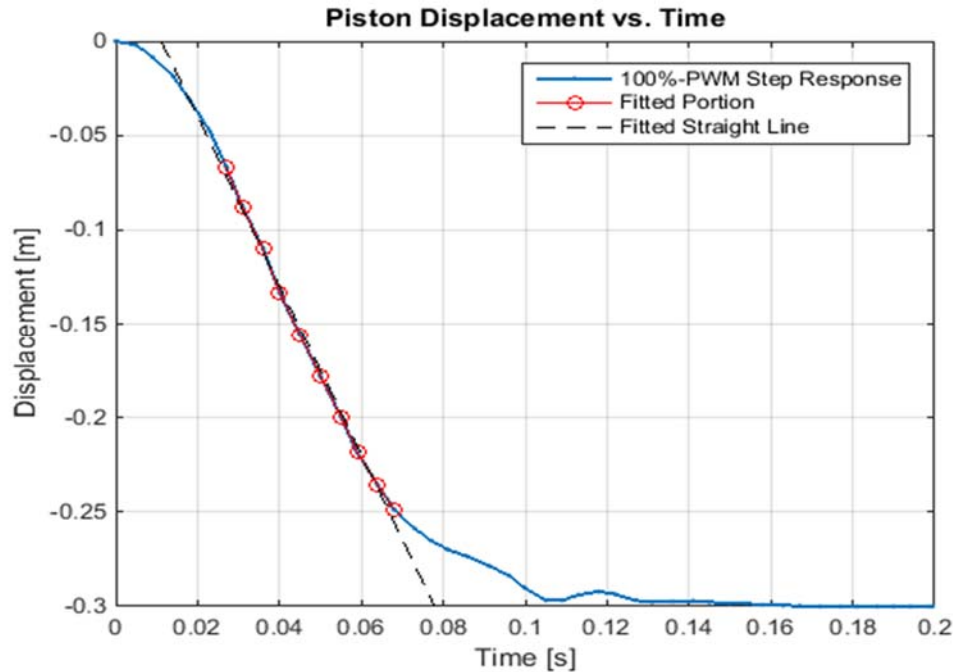
**Figure 4.44.** Identification of dynamic constants: 70%-PWM Step Response (Extension)

Table 4.11 presents the results from the fitting procedure to find the parameters  $\mathcal{C}$  and  $\tau$ .

**Table 4.11.** Finding from the fitting procedure to find  $\mathcal{C}$  and  $\tau$

EXTENSION						RETRACTION					
<i>PWM</i> [%]	$\tau$ [s]	$\mathcal{C}$ [m/s/bits]	<i>PWM</i> [%]	$\tau$ [s]	$\mathcal{C}$ [m/s/bits]	<i>PWM</i> [%]	$\tau$ [s]	$\mathcal{C}$ [m/s/bits]	<i>PWM</i> [%]	$\tau$ [s]	$\mathcal{C}$ [m/s/bits]
<u>67</u>	0.013	2.52E-04	<u>84</u>	0.016	1.65E-02	<u>67</u>	--	--	<u>84</u>	0.011	1.53E-02
<u>69</u>	0.015	2.16E-03	<u>86</u>	0.013	1.67E-02	<u>69</u>	--	--	<u>86</u>	0.011	1.57E-02
<u>71</u>	0.017	4.75E-03	<u>88</u>	0.013	1.73E-02	<u>71</u>	0.009	1.78E-03	<u>88</u>	0.013	1.66E-02
<u>73</u>	0.015	5.52E-03	<u>90</u>	0.013	1.85E-02	<u>73</u>	0.010	6.07E-03	<u>90</u>	0.013	1.77E-02
<u>75</u>	0.016	9.56E-03	<u>92</u>	0.015	1.81E-02	<u>75</u>	0.011	6.49E-03	<u>92</u>	0.013	1.80E-02
<u>76</u>	0.016	1.08E-02	<u>94</u>	0.013	1.82E-02	<u>76</u>	0.013	8.90E-03	<u>94</u>	0.012	1.78E-02
<u>78</u>	0.014	1.37E-02	<u>96</u>	0.014	1.72E-02	<u>78</u>	0.012	1.11E-02	<u>96</u>	0.012	1.80E-02
<u>80</u>	0.015	1.59E-02	<u>98</u>	0.015	1.88E-02	<u>80</u>	0.011	1.31E-02	<u>98</u>	0.013	1.79E-02
<u>82</u>	0.015	1.67E-02	<u>100</u>	0.014	1.90E-02	<u>82</u>	0.011	1.46E-02	<u>100</u>	0.011	1.76E-02

Due to the fact that the dynamic properties of the pneumatic system differ when the cylinder piston extends or retracts, mostly because of the difference between the active or driving area of the piston, the fitting procedure was applied to the step response of the cylinder for extension and retraction operation regimes. Figure 4.45 shows the outcome of the fitting procedure for a 100-percent duty cycle PWM input in retraction mode.



**Figure 4.45.** Identification of dynamic constants: 100%-PWM Step Response (Retraction)

The average time constant,  $\tau$ , for extension and retraction was respectively 0.015 seconds and 0.012 seconds (Table 4.11). These average values differed in no more than  $\pm 0.002$  seconds of the individual values for each PWM input; thus, they were used as the constant values to be included in the block diagram models for simulation. Nevertheless, in the case of the dynamic parameter  $\mathbb{C}$ , there was a considerable variation among the individual values for each PWM input applied to the valves; hence, a constant average value could not be used for simulation. To find a constant value, the data corresponding to the dynamic parameter  $\mathbb{C}$  was normalized, which implied to find a standard or canonical form of the dynamic parameter  $\mathbb{C}$ . Figure 4.46 shows the curves corresponding to the dynamic parameter  $\mathbb{C}$  as a function of the PWM input applied to the valves.



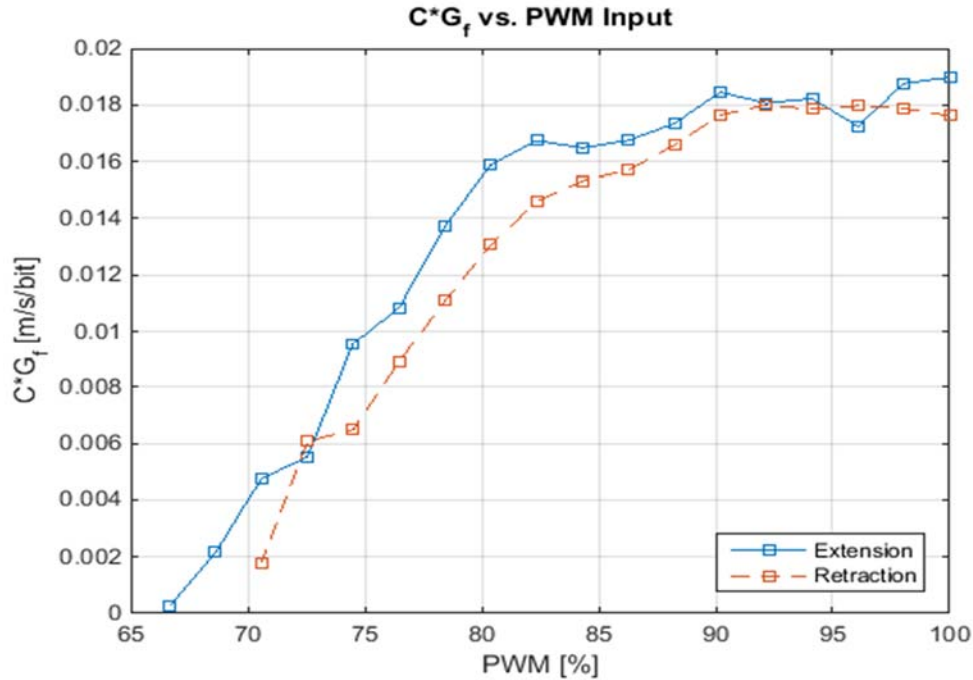


**Figure 4.46.** Identification of dynamic constants:  $\mathbb{C}$  vs. PWM Input

The minimum PWM inputs applied to the valves to extend and retract the cylinder piston corresponded to 67-percent and 71-percent duty cycle PWM inputs, respectively (Table 4.11). The minimum PWM input required to retract the cylinder was higher than the input required for extension because the rod-end piston area is smaller than the cap-end piston area. The units of  $\mathbb{C}$  were expressed in terms of “bits” because the commands in the controller are defined in a scale of 0 to  $2^8$  bits.

Subsequently, to normalize the dynamic parameter  $\mathbb{C}$ , the following expression derived through experimentation was applied:

$$\bar{\mathbb{C}} = \mathbb{C} \left( \frac{PWM - PWM_{Offset}}{PWM_{100\%} - PWM_{Offset}} \right)^{-1} \left( \frac{PWM}{PWM_{100\%}} \right)^2 \quad (4.12)$$

Where:  $\bar{\mathbb{C}}$  = Normalized  $\mathbb{C}$ .

$PWM$  = Input command applied in a scale of 0 to  $2^8$  bits.

$PWM_{Offset}$  = Minimum input applied in the operational range of the valve.

$PWM_{100\%}$  = Maximum PWM input ( $2^8 = 256$  bits).

Figure 4.45 shows the outcome of the normalization of the dynamic parameter  $\mathbb{C}$  for extension and retraction.

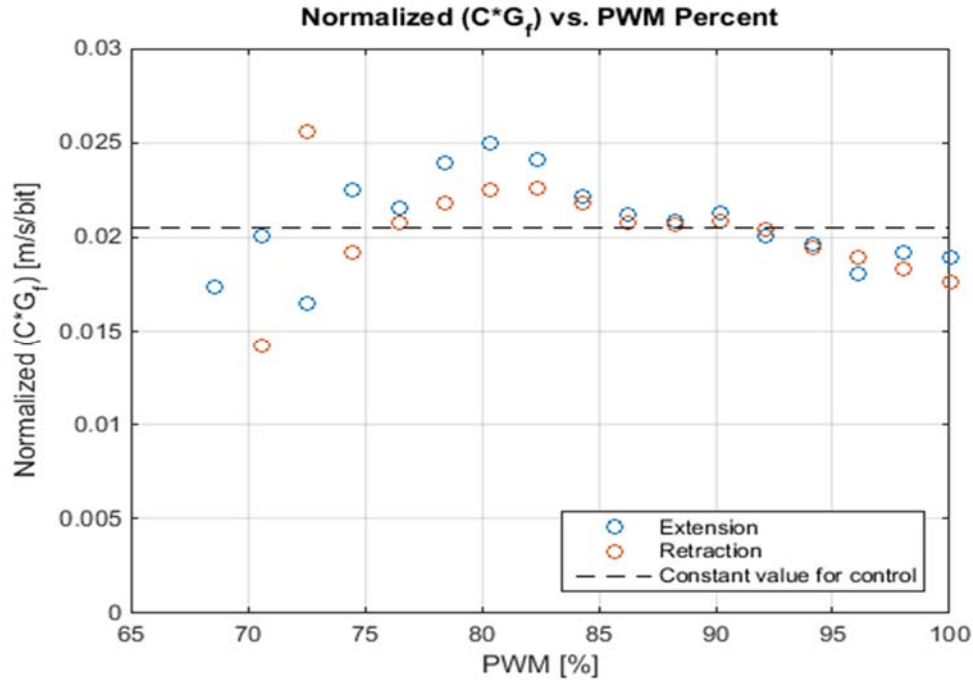


**Figure 4.47.** Identification of dynamic constants:  $\bar{C}$  vs. PWM Input

The offset values used to produce figure 4.47 corresponded to 67-percent and 69-percent duty-cycle PWM inputs for piston extension and retraction, respectively. Also, through the normalization method applied, a constant value for the normalized parameter  $\bar{C}$  could be used for implementation of the actual controller ( $\bar{C} \approx 5.3$  [m/s] according to the dashed line in figure 4.47). In addition, from the knowledge of  $C$  and  $\bar{C}$ , a normalized value for the flow gain,  $G_f$ , could be determined, as it will be demonstrated in the following chapters.

#### 4.4.4. Flow and pressure gains

Flow and pressure gains were defined in chapter 3, as coefficients through which the mathematical representation of the volumetric flow provided by the proportional valves can be linearized around an operating point. The linear expression to calculate the volumetric flow was defined as follows:

$$Q = G_f(\Delta A_v) - G_D(\Delta P_d) \quad (4.13)$$

In Eq. 4.13, the flow gain,  $G_f$ , and the pressure gain,  $G_D$ , are respectively related to the effective area of the valve and to the pressure in the chambers of the cylinder.

The flow gain and the pressure gain could be determined by associating the volumetric flow in the chambers of the cylinder with the effective area of the valves and with the pressure in the cylinder chambers. The dependence of the flow on the effective area of the valves and on the pressure in the cylinder chambers can be verified experimentally.

From experimental data relative to the open-loop step response of the pneumatic cylinder, it was verified that for a certain range of time, the rate of displacement of the piston became constant (Figure 4.48). Accordingly, during the interval of time at which the rate of displacement became constant, the velocity of the piston was constant as well.

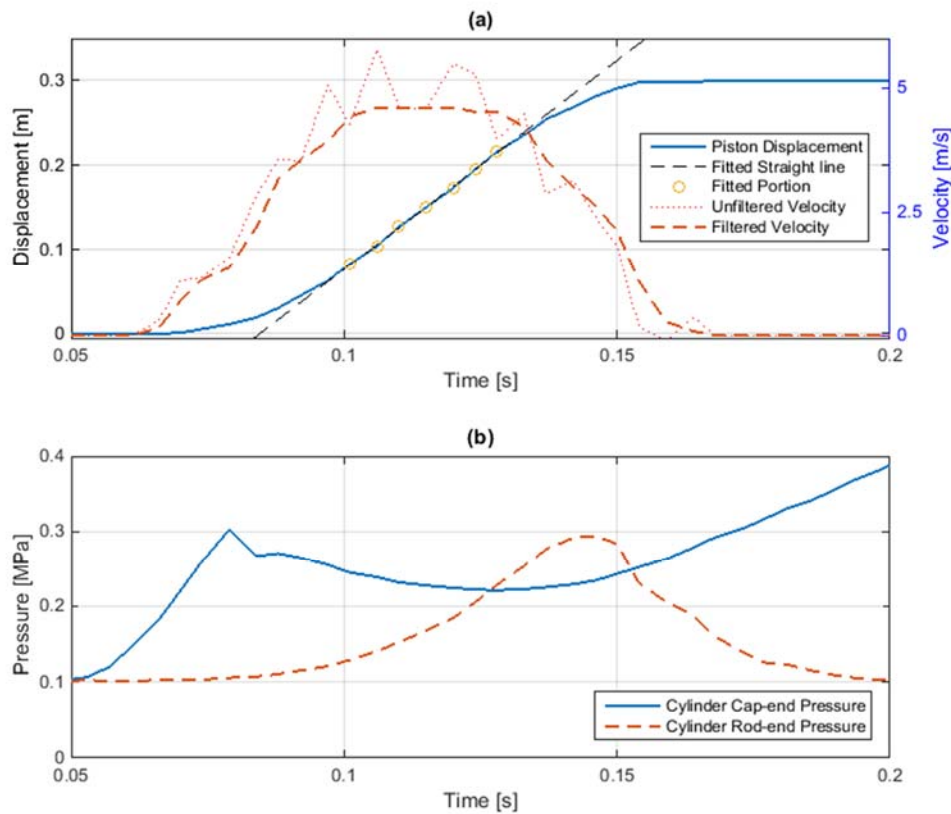


**Figure 4.48.** Open-loop Step Response of the pneumatic cylinder to a 100% Duty-cycle PWM Input: (a) Piston displacement and velocity. (b) Pressure in the cylinder chambers.

Moreover, from Eq. 3.9 expressed as follows:

$$\dot{P}_d \frac{V_0}{\beta} = (Q - \dot{x}_p A_p) = 0 \quad (4.14)$$

If the rate of change of pressure in the cylinder chambers tends to zero, the volumetric flow could be determined through the following equation:

$$Q = \dot{x}_p A_p \quad (4.15)$$

In fact, for the same interval of time during which the velocity of the piston was constant, the cylinder cap-end pressure approximated a constant value (Figure 4.48); thus, its rate of change would have approximated to zero, and Eq. 4.14 would be valid.

Therefore, the experimental procedure applied in this section correlates the volumetric flow determined through Eq. 4.15 to the effective area of the control valves, and to the differential pressure in the chambers of the pneumatic cylinder. To find the volumetric flow; first, the velocity of the piston was determined by taking the slope of a straight line fitted to the piston-displacement curve (Figure 4.48). This experimental procedure was applied for different step inputs in a range of 55 to 100-percent duty-cycle PWM voltages. Figure 4.49 shows the results obtained.

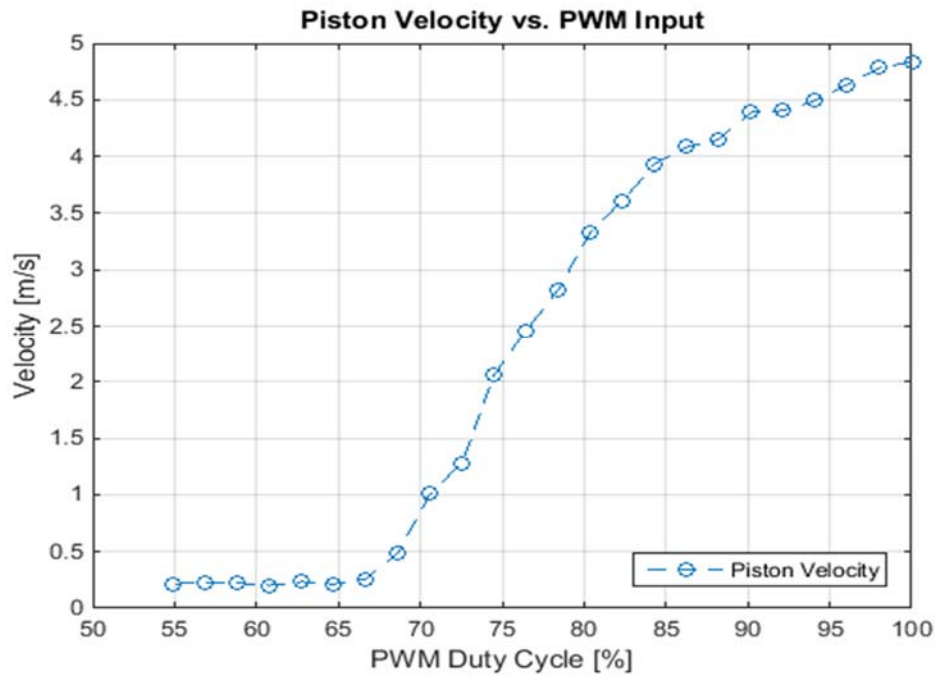


**Figure 4.49.** Identification of dynamic constants –Piston velocity vs. PWM Input

Then, to calculate the volumetric flow by applying Eq. 4.15, it was still necessary to define the value for the effective area of the piston,  $A_p$ .

The meaning of the piston effective area relates to the assumptions made in chapter 3 to simplify the mathematical representation of the pneumatic system. It was assumed that the piston was symmetric; and accordingly, its active areas were equal. Hence, in this section the effective area was defined as the average of the cap-end and rod-end areas of the piston.

$$A_p = \frac{A_1 + A_2}{2} \quad (4.16)$$

Where  $A_1$  and  $A_2$  correspond to the areas of the piston at the cap-end and rod-end of the cylinder, respectively. Figure 4.50 shows the volumetric flow calculated using Eq. 4.15 and Eq. 4.16, as a function of the PWM input applied to the proportional valves.

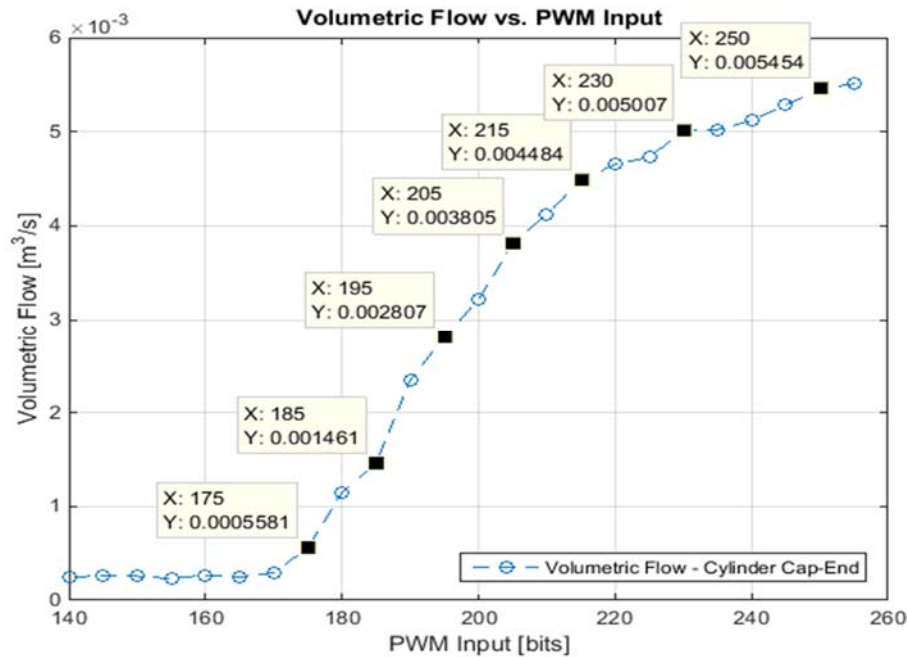


**Figure 4.50.** Identification of dynamic constants: Volumetric Flow vs. PWM Input

In figure 4.50, in contrast to figure 4.49, the PWM input was expressed in terms of the analog values introduced in the controller. Several points were identified in the graph, considering segments of the curve to which a straight line could fit. The slopes of the straight lines that fit to each consecutive segment were used as flow gains for simulation of the pneumatic system. Table 4.12 shows the results obtained.

**Table 4.12.** Findings from the fitting procedure to find  $G_f$ 

Pair	PWM [bits]	Effective Area [m <sup>2</sup> ]	Volumetric Flow [m <sup>3</sup> /s]	Flow Gain	
				[m <sup>3</sup> /s/bit]	[m/s]
1	175	0.00E+00	0.0005581	9.03E-05	3.54E+02
	185	2.55E-06	0.001461		
2	185	2.55E-06	0.001461	1.35E-04	7.33E+02
	195	4.39E-06	0.002807		
3	195	4.39E-06	0.002807	9.98E-05	6.64E+02
	205	5.89E-06	0.003805		
4	205	5.89E-06	0.003805	6.79E-05	4.89E+02
	215	7.28E-06	0.004484		
5	215	7.28E-06	0.004484	3.49E-05	2.63E+02
	230	9.28E-06	0.005007		
6	230	9.28E-06	0.005007	2.24E-05	1.72E+02
	250	1.19E-05	0.005454		
<b>Average</b>				<u>7.50E-05</u>	<u>4.46E+02</u>

In addition, to determine the pressure gain,  $G_D$ , the flow was related to the difference of pressure in the chambers of the cylinder. For the same interval of time at which the rate of piston-displacement became constant, by taking the mean of the values of pressure measured in the chambers of the cylinder, the following results were obtained.

**Table 4.13.** Findings from the fitting procedure to find  $G_D$ 

PWM [bits]	Chamber Pressure [MPa]		PWM [bits]	Chamber Pressure [MPa]	
	Cap-End	Rod-End		Cap-End	Rod-End
140	0.115	0.103	200	0.171	0.127
145	0.114	0.103	205	0.182	0.147
150	0.110	0.103	210	0.191	0.140
155	0.114	0.102	215	0.200	0.152
160	0.112	0.103	220	0.203	0.139
165	0.106	0.103	225	0.209	0.142
170	0.115	0.103	230	0.223	0.169
175	0.118	0.106	235	0.231	0.167
180	0.135	0.119	240	0.225	0.154
185	0.144	0.126	245	0.223	0.160
190	0.152	0.122	250	0.224	0.170
195	0.163	0.121	255	0.237	0.149

Then, the differential pressure in the chambers of the cylinder was calculated according to the following expression:

$$P_d = p_1 - p_2 \quad (4.17)$$

Where  $p_1$  and  $p_2$  are the pressure in the chambers of the cylinder at the cylinder cap-end and rod-end, respectively. By plotting the volumetric flow as a function of the differential pressure in the chambers of the cylinder, Figure 4.51 was obtained.

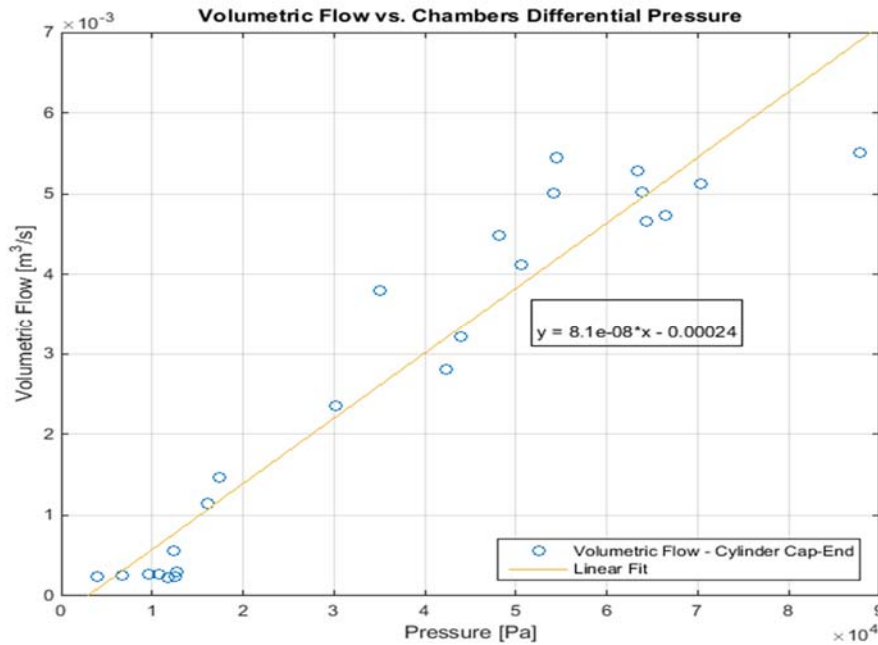


**Figure 4.51.** Identification of dynamic constants: Volumetric Flow vs. Differential Pressure of the Cylinder Chambers

A straight line fitted the resulting data dots (Figure 4.51). The slope of the equation that characterized the fitted straight line would correspond to the value of the pressure gain,  $G_D$ , which was used for simulation and implementation of the controller.

Figure 4.52 shows a 3-dimensional plot that relates the volumetric flow to the effective area of the valve, and to the differential pressure in the chambers of the cylinder. The plot was produced using interpolation methods in MATLAB. The plot would result useful at providing values for the flow and pressure gains required for simulation of the pneumatic system.

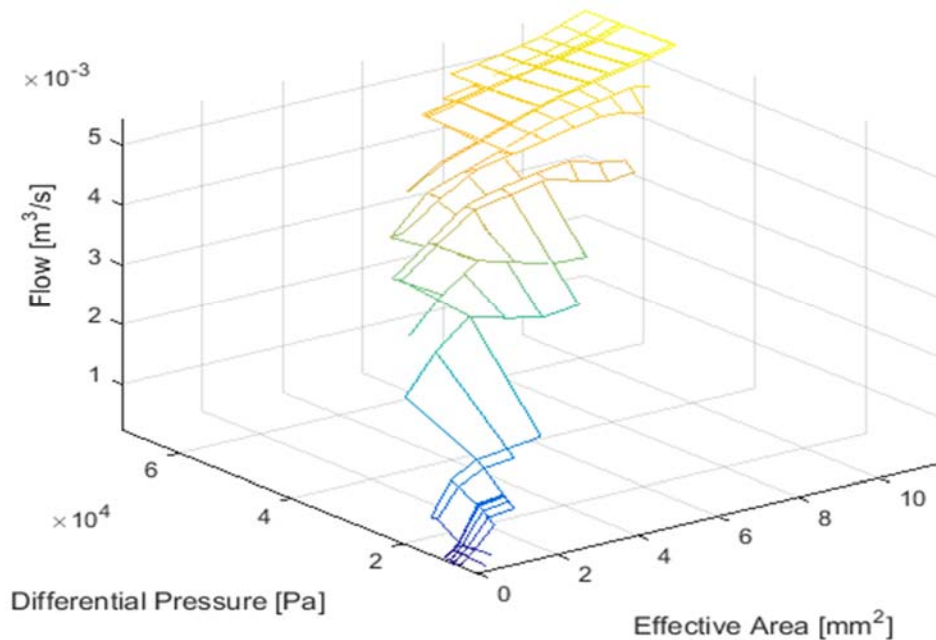


**Figure 4.52.** Volumetric Flow as a function of cylinder chamber differential pressure, and valve effective area

By fitting straight lines to the planes that compose the three-dimensional surface (Figure 4.52), values for the flow gain and pressure gain can be defined according to different operating conditions; and hence, different equilibrium points around which the expression for the volumetric flow could be linearized. As chapter 5 will demonstrate, with the simulation of the proposed models for the pneumatic system, some of the flow gains and pressure gains determined in this section matched the gain values required to compensate or modify the dynamic behavior of the pneumatic system according to the design requirements.

#### 4.4.5. Discharge coefficients - Proportional control valves

To identify the discharge coefficient of the control valves; first, the flow profile from the valves was calculated according to the equations identified in chapters 2 and 3. Experimental data was used to calculate the flow from the valves. This data corresponded to the pressure measured at the upstream and downstream sides of the control valves, in combination with the effective area of the valve derived from the PWM input applied to the valves under a specific control regime.



Once the flow profile from the valves was delineated, through comparison with the flow profile in the chambers of the cylinder, different values for the discharge coefficient were tested until the maximum amplitude of the flow from the valve matched the maximum amplitude of the flow in the chambers of the cylinder.

Due to the fact that the control valve connected to the cylinder rod-end did not count with pressure transducers connected to its supply and output ports, the flow was not calculated relative to this valve. The valve-flow profile was only calculated relative to the proportional control valve connected to the cylinder cap-end chamber.

The mass and volumetric flow equations described in section 2.3.1 are defined again underneath:

$$\dot{m} = \frac{C_D A_v P_{uv}}{\sqrt{RT}} \Phi_f; \quad Q = \frac{C_D A_v \sqrt{RT}}{P_{rv}} \Phi_f \quad (4.18)$$

These equations describe the compressible mass flow rate through a convergent nozzle.  $C_D$  is the discharge coefficient for the valve,  $A_v$  is the valve-effective area,  $P_{uv}$  is the valve-upstream pressure,  $T$  is the temperature of air ( $T = 295$  K),  $R$  is the specific gas constant (for dry air,  $R = 287.058$  J/kgK), and  $\Phi_f$  is a so-called flow constant, which depends on the downstream to upstream pressure ratio,  $P_{rv}$ , as defined in chapter 2 (section 2.3.1, Eq. 2.9). To calculate the flow constant,  $\Phi_f$ , adiabatic conditions were considered; thus, 1.4 was used as the value for the specific heat ratio for air,  $k$ .

The valve flow profile was calculated based on the response of the pneumatic cylinder to a closed-loop control sinusoidal input command (Figure 4.53). The length of connective tubing used was 0.55 meters. The phase of the flow profile in the cylinder cap-end displaced to the right in comparison to the flow profile in the valve. This phase displacement would be attributed to the delay effect caused by the length of connective tubing. The discharge coefficient used to match the maximum amplitude of the flow profiles was 0.7.

From the comparison of the volumetric flows (Figure 4.53c), it was observed that the amplitude of the flow profiles did not match in the negative side, which might have indicated that the discharge coefficient for the valve when the output port is connected to the exhaust was different. Nevertheless, the comparison of the mass flow profiles (Figure 4.53d) did not reveal a significant difference; accordingly, it was assumed that the discharge coefficient for the valve when it was connected to the supply pressure or to the exhaust was the same.

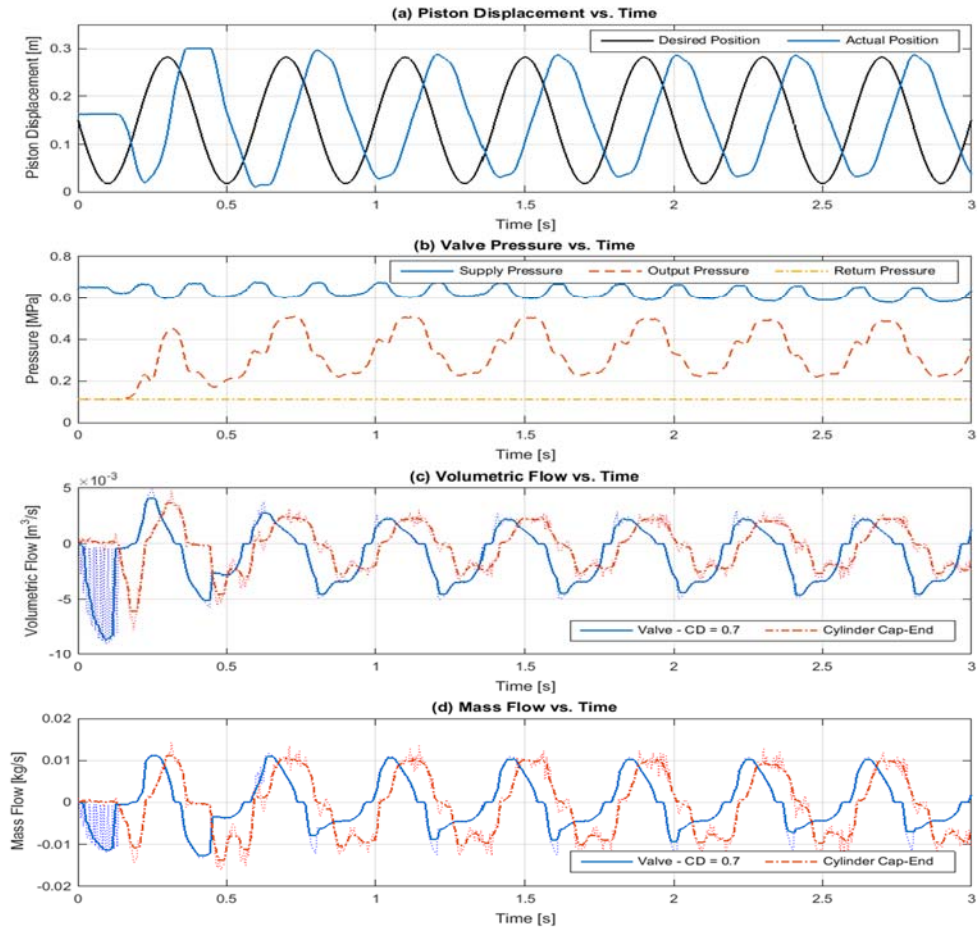


**Figure 4.53.** System responses to a closed-loop 2.5-Hz sinusoidal input: (a) Piston actual and desired displacement. (b) Cylinder cap-end valve pressure. (c) Cylinder cap-end chamber and valve volumetric flow (Eq. 4.18). (d) Cylinder cap-end chamber and valve mass flow (Eq. 4.18).

Furthermore, the equations described in section 3.2.1 correspond to equations for modeling flow,  $q_v$ , through thin, sharp edged orifices. The main equation from which other expressions derive is expressed again below:

$$q_v = A_v C_d \sqrt{\frac{2(P_{uv} - P_{dv})}{\rho}} \quad (4.19)$$

Where in contrast to Eq. 4.18,  $C_d$  is the discharge coefficient,  $\rho$  is the density of air, and  $P_{dv}$  is the valve-downstream pressure. The nomenclature for the remaining terms is the same.

In the case of applying Eq. 4.19 to calculate the flow profiles in the valves, the results obtained are presented in figure 4.54.

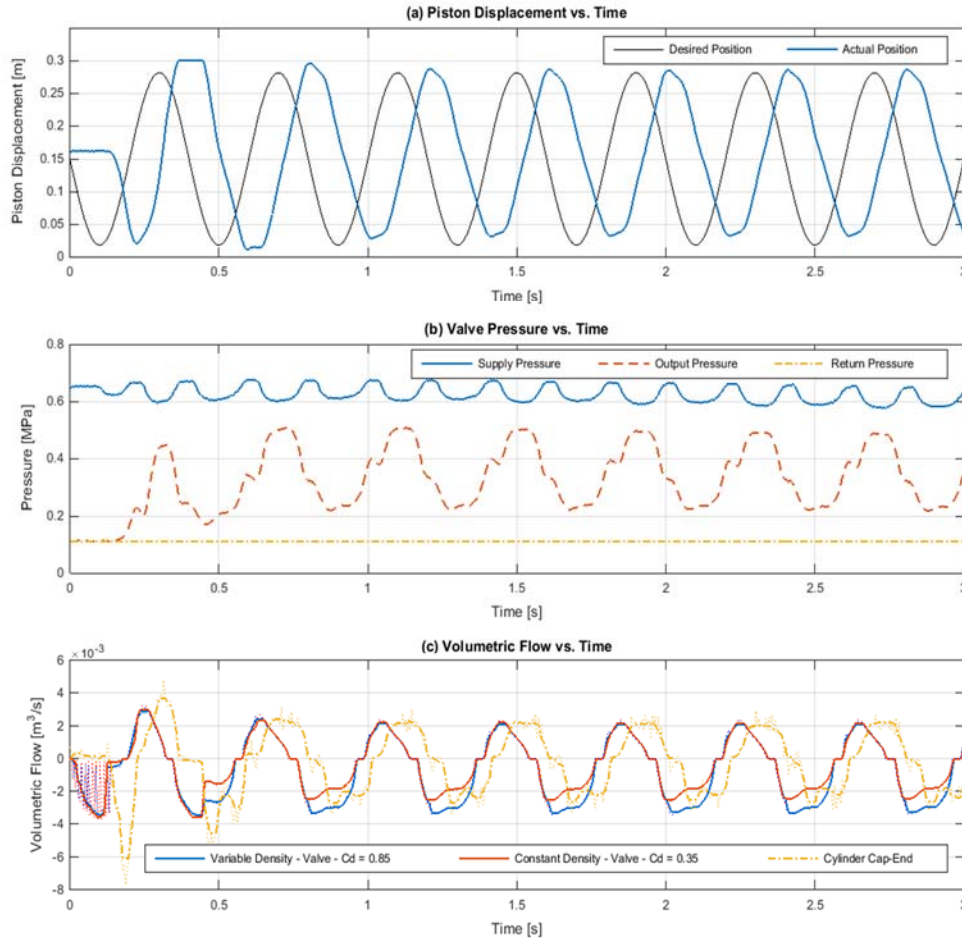


**Figure 4.54.** System responses to a closed-loop 2.5-Hz sinusoidal input: (a) Piston actual and desired displacement. (b) Cylinder cap-end valve pressure. (c) Cylinder cap-end chamber and valve volumetric flow (Eq. 4.19).

The volumetric flow was calculated according to two considerations (Figure 4.54): by keeping the density of air constant ( $\rho = 1.184 \text{ kg/m}^3$  for air at 295 K), or by expressing it as a function of pressure and temperature through the ideal gas law. The results demonstrated that in the case of maintaining the density of air constant, the discharge coefficient required to match the valve-flow profile to the chamber-flow profile was around 0.35. In contrast, if the density of air was calculated as a variable value, the discharge coefficient required was 0.8.

Then, because Eq. 4.19 was not directly applied in the models proposed for the pneumatic system, the discharge coefficient had to be determined in relation to the specific flow equations included in the models (Figure 4.55).

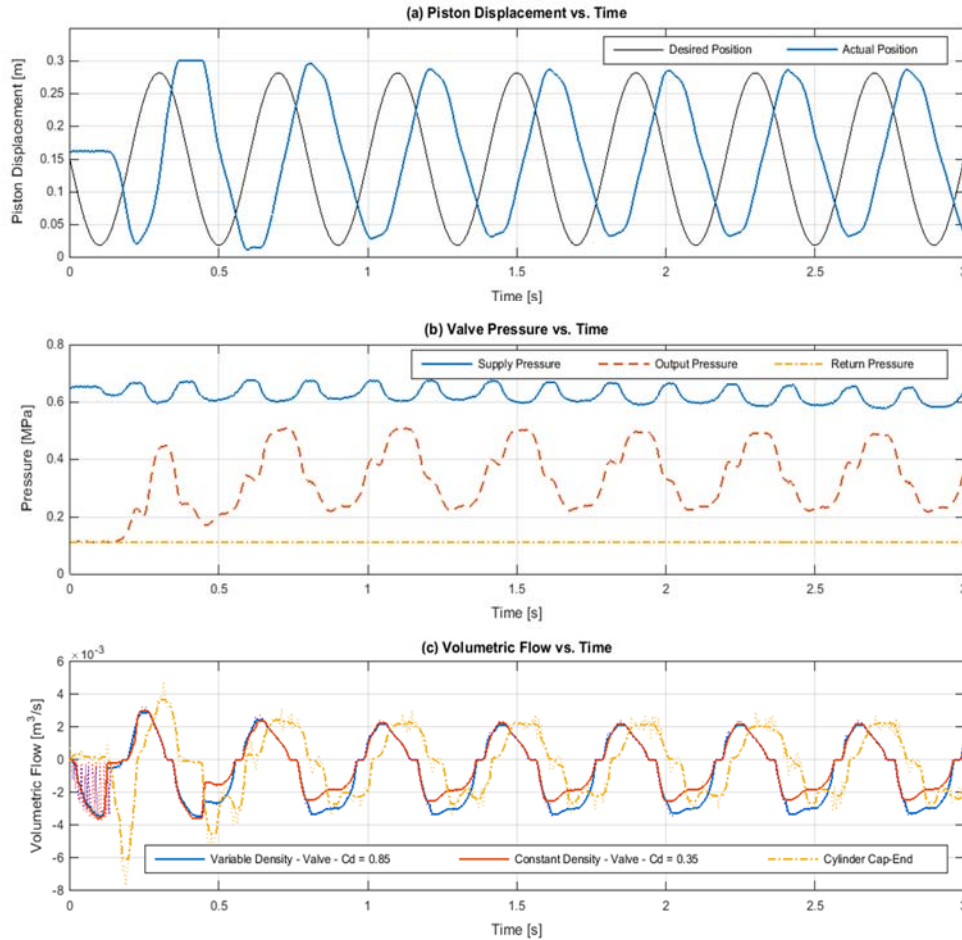


**Figure 4.55.** System responses to a closed-loop 2.5-Hz sinusoidal input: (a) Cylinder piston actual and desired displacement. (b) Cylinder cap-end valve pressure. (c) Cylinder cap-end chamber and valve volumetric flow (Eq. 4.20).

Figure 4.55 shows the results obtained from calculating the flow profile in the valves according to Eq. 3.2, which is the equation included in the models developed in chapter 3. This equation is presented again in this chapter below.

$$Q = A_v C_d \sqrt{\frac{(P_S - P_R) - P_d}{\rho}} \quad (4.20)$$

$P_S$  and  $P_R$  are respectively the supply pressure ( $P_S = 0.6212$  MPa) and the exhaust pressure ( $P_R = 0.1106$  MPa) for the pneumatic system.  $P_d$  is the difference of pressure in the cylinder chambers. Similarly to the results presented in figure 4.55, the flow profile relative to the valve was calculated by using a constant value for the density of air, and by applying the ideal gas law (Figure 4.55). When the density was defined as a variable depending on pressure and temperature, the discharge coefficient used to match the maximum amplitude of the flow profiles relative to the valve and the chamber of the cylinder was 0.55. In contrast, when the density was kept constant, the discharge coefficient used corresponded to a value of 0.25. Moreover, in section 3.2.1, a combined discharge coefficient was defined by the following expression.

$$C_{D'} = \frac{C_d}{\sqrt{\rho}} \quad (4.21)$$

Based on the assumption that the density remains constant, with a discharge coefficient of 0.25 (Figure 4.55), the value for the combined discharge coefficient,  $C_{D'}$ , would be:  $0.23 \text{ [m}^3/\text{kg}]^{1/2}$ . This combined discharge coefficient has units, in contrast to the others discharge coefficients determined above.

The identified discharge coefficients were used for the simulation and implementation of the controller for the pneumatic system. Section 4.3.5 provides a summary of the parameters identified throughout this chapter, and the conditions under which they could be applied.

#### 4.4.6. Friction forces and friction coefficients

In chapter 2, the force dynamics relative to the pneumatic piston were described using the following expression.

$$M_{PL}\ddot{x}_p + D_{vsc}\dot{x}_p + F_{sc} = P_1A_1 - P_2A_2 - P_{atm}A_{rod} \quad (4.22)$$

Where  $D_{vsc}$  is a viscous friction coefficient, and  $F_{sc}$  is a combined static and dynamic friction force. In that regard, this section provides numeric values for the friction forces and friction coefficients included in Eq. 4.22 and the models for the pneumatic system.

The combined static and dynamic friction force,  $F_{sc}$ , is defined by:

$$F_{SC} = \begin{cases} F_{SC-Static} = (\pm P_1A_1 \mp P_2A_2 \mp P_{atm}A_{rod})|_{x_s-threshold} & \text{if } \dot{x}_p = 0 \\ F_{SC-Dynamic} = K_{SCD} \text{sign}(\dot{x}_p) & \text{if } \dot{x}_p \neq 0 \end{cases} \quad (4.23)$$

Where  $P_1$  and  $P_2$  are respectively the absolute pressure in the cap-end and rod-end chambers of the pneumatic cylinder,  $P_{atm}$  is the atmospheric pressure ( $P_{atm} = 101720$  Pa),  $A_{rod}$  is the piston rod area ( $A_{rod} = A_1 - A_2$ ), and  $K_{SCD}$  is the magnitude of the dynamic component of the friction force.

Based on Eq. 4.23, the static component of the friction force was determined from the data collected in section 4.3.3 (Figures 4.23 and 4.24). The following table summarizes the information acquired in section 4.3.3, and shows the static friction force calculated.

**Table 4.14.** Static Friction Force - Pressure in the chambers of the cylinder

Cylinder Chamber	Extension		Retraction	
	Pressure [MPa]	PWM [%]	Pressure [MPa]	PWM [%]
Cap-End	0.1203	56.47	0.1033	0.00
	0.1211	56.86	0.1033	0.00
	0.1203	56.86	0.1033	0.00
<i>Average</i>	<u>0.12057</u>	<u>56.73</u>	<u>0.1033</u>	<u>0.00</u>
Rod-End	0.1033	0.00	0.1211	61.96
	0.1025	0.00	0.1211	62.35
	0.1025	0.00	0.1211	61.96
<i>Average</i>	<u>0.1028</u>	<u>0.00</u>	<u>0.1211</u>	<u>62.09</u>
<b>Static Friction Force [N]</b>	<b><u>20.50</u></b>		<b><u>16.42</u></b>	

The static friction force for retraction was smaller than the force for extension (Table 4.14); nevertheless, it had to be considered that for the experimental procedure described in section 4.3.3, the piston extended starting at the beginning of its stroke, where the fit of the cushion could have increased the force required to move the piston. In contrast, the retraction of the cylinder took place between the start and the end of the cylinder stroke, where it might have been easier for the piston to start moving. In fact, a higher magnitude of the static friction force would have been registered, if the piston had retracted starting at the end of its stroke. Accordingly, the static-friction force for extension was used as a maximum reference value for simulation of the pneumatic system.

Once the static-friction force was defined, it was necessary to generate some reference values for the viscous friction coefficient,  $D_{vsc}$ , and the magnitude of the dynamic friction force,  $K_{SCD}$ .



To determine reference values for the viscous friction coefficient,  $D_{vsc}$ , and the magnitude of the dynamic friction force,  $K_{SCD}$ , Eq. 4.22 was expressed as follows.

$$D_{vsc}\dot{x}_p + K_{SCD}sign(\dot{x}_p) = P_1A_1 - P_2A_2 - P_{atm}A_{rod} - M_{PL}\ddot{x}_p \quad (4.24)$$

The left-hand side of Eq. 4.24 is a function of piston velocity, and its structure corresponds to the equation of a straight line. The terms on the right-hand side of Eq. 2.24 can be measured and/or derived from experimental data. Consequently, by plotting the outcome of the right-hand side of Eq. 4.24 as a function of the velocity of the piston, the dynamic coefficient and force associated with friction acting on the pneumatic cylinder were determined.

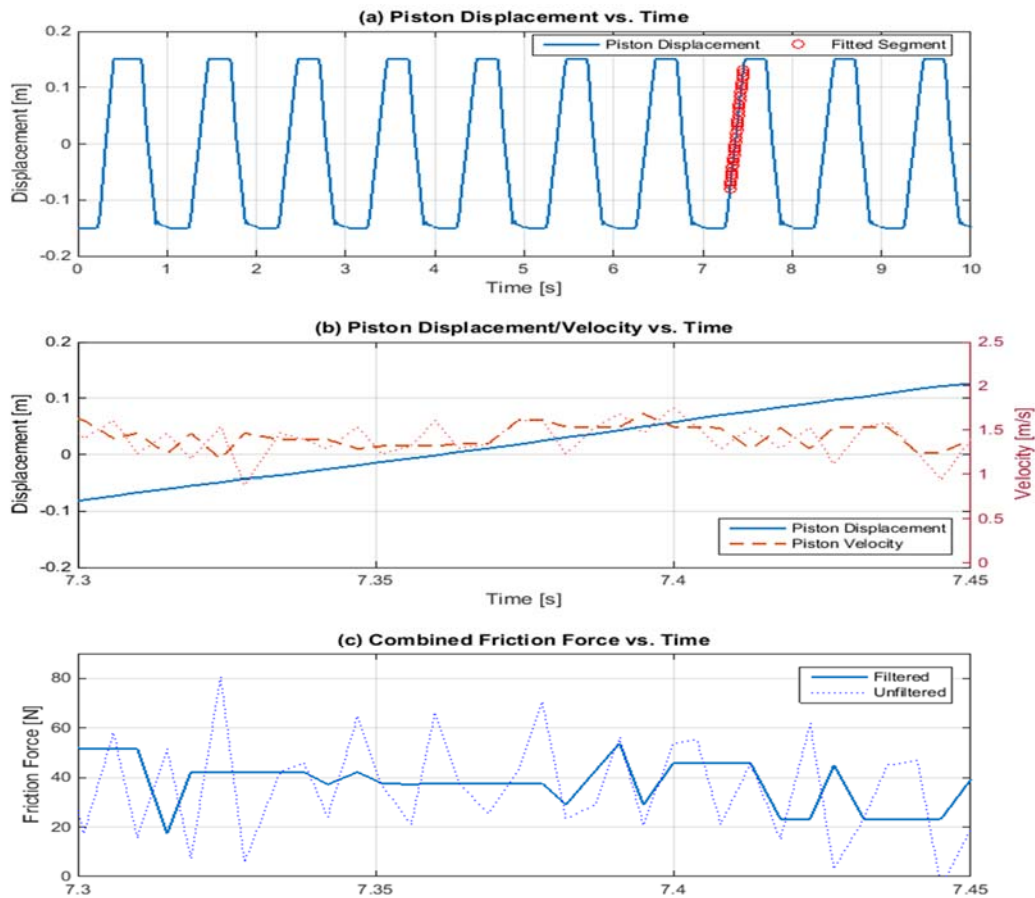


**Figure 4.56.** System responses to an open-loop 1.0-Hz sinusoidal input: (a) Cylinder piston displacement. (b) Cylinder piston displacement and velocity (7.3 to 7.45 seconds). (c) Cylinder combined friction force (7.3 to 7.45 seconds)

Figure 4.56 shows the results from the experimental procedure applied to find the viscous friction coefficient,  $D_{vsc}$ , and the magnitude of the dynamic friction force,  $K_{SCD}$ . An open-loop sinusoidal input command was applied to move the piston. Then, for time intervals in which the piston purely extended, it is after and before it reached the peaks of its trajectory, the outcome of the right-hand side of Eq. 4.42 was calculated, which was identified as a combined friction force. Figure 4.56 shows one of the time intervals for which this combined friction force was calculated.

By plotting the combined friction force as a function of the velocity of the piston for a specific interval of time, the results obtained are of the type presented in Figure 4.57.

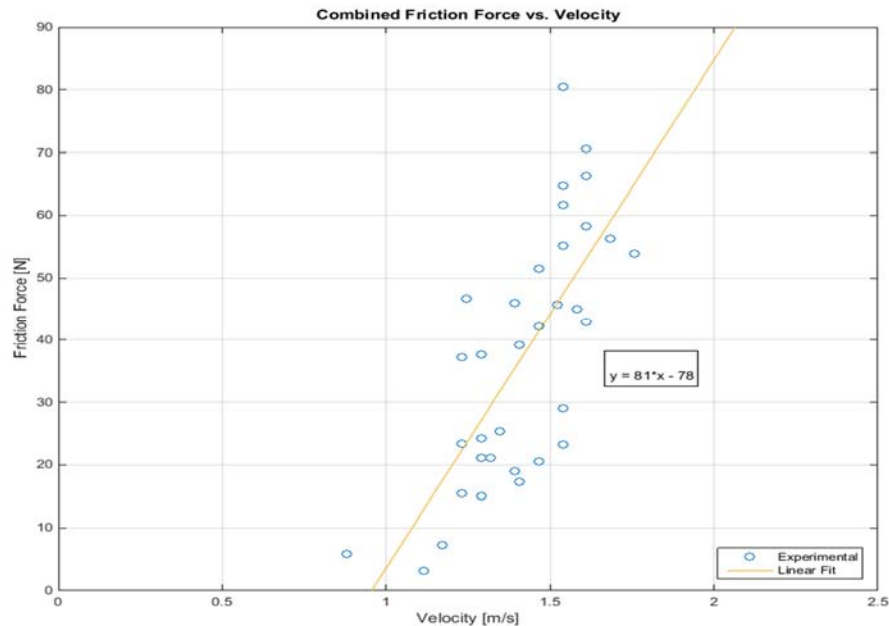


**Figure 4.57.** Identification of dynamic friction coefficient and friction force: Combined Friction Force vs. Velocity (Time interval: 7.3 to 7.45 seconds)

Subsequently, by fitting a straight line to the experimental data dots plotted in figure 4.57, the viscous friction coefficient,  $D_{vsc}$ , and the magnitude of the dynamic friction force,  $K_{SCD}$ , were identified as the slope and the intercept of the straight line, respectively. The experimental procedure described above was applied for parameter identification during extension and retraction of the piston. Table 4.15 shows the result obtained for four different intervals of time in which the piston extended and retracted.



**Table 4.15.** Dynamic Friction Coefficient and Friction Force

Extension			Retraction		
Time Interval [s]	$D_{vsc}$ [Ns/m]	$K_{SCD}$ [N]	Time Interval [s]	$D_{vsc}$ [Ns/m]	$K_{SCD}$ [N]
1.3:1.5	72.0	62.0	4.7:4.8	73.0	84.0
7.3:7.5	81.0	78.0	9.7:9.8	68.0	77.0
14.3:14.5	82.0	76.0	14.7:14.8	58.0	52.0
17.3:17.5	87.0	83.0	17.7:17.8	67.0	67.0
<i>Average</i>	<i>80.5</i>	<i>74.8</i>	<i>Average</i>	<i>66.5</i>	<i>70.0</i>

The average values for the viscous friction coefficient,  $D_{vsc}$ , and the magnitude of the dynamic friction force,  $K_{SCD}$  (Table 4.15), were used for simulation of the pneumatic system.

#### 4.4.7. Summary – Parameters, gains and constants

The following tables comprise a summary of the findings of this chapter, including: physical parameters of the components of the pneumatic system, and dynamic gains and constants incorporated in the models proposed for simulation of the pneumatic system.

**Table 4.16.** Summary – Physical parameters: Pneumatic cylinder and connective tubing

Pneumatic Cylinder			
Parameter	Nomenclature	Value	[Units]
Piston Mass	$M_{PL}$	0.30	[kg]
Bore Diameter	$\Phi_{Bore}$	38.10	[mm]
Rod Diameter	$\Phi_{Rod}$	15.88	[mm]
Cap-End Area	$A_1$	0.0014	[m <sup>2</sup> ]
Rod-End Area	$A_2$	0.0009	[m <sup>2</sup> ]
Rod Section Area	$A_{rod}$	0.0005	[m <sup>2</sup> ]
Area ratio	$A_1/A_2$	1.5	[-]
Piston Stroke	$L_{Stroke}$	0.3048	[m]
Connective Tubing			
Parameter	Nomenclature	Value	[Units]
Length	$L_t$	[0.55,1.5,3.0]	[m]
Internal Diameter	$\Phi_{t-int}$	9.525	[m]
External Diameter	$\Phi_{t-ext}$	18.256	[mm]
Transversal flow area	$A_t$	7.13E-05	[m <sup>2</sup> ]

**Table 4.17.** Summary – Physical parameters: Air Properties

Air Properties				
Parameter	Nomenclature	Value	[Units]	Condition
Supply Pressure	$P_S$	764000.0	[Pa]	NA
Atmospheric Pressure	$P_{atm} \setminus P_R$	101720.0	[Pa]	NA
Temperature	$T$	293.15	[K]	NA
Air Constant	$R$	287.06	[J/kg/K]	Dry air
Ratio of specific heats	$k$	1.4	[-]	Adiabatic conditions
Density	$\rho$	1.184	[kg/m <sup>3</sup> ]	T = 295 K
Bulk Modulus	$\kappa \setminus \beta$	1.42E+05	[Pa]	Adiabatic conditions
Flow function	$\Phi_f$	0.6	[-]	Assumed constant value (Chapter 5)

[\* NA = Not Applicable]

**Table 4.18.** Summary – Physical parameters: Proportional Control Valves

Proportional Control Valves				
Parameter	Nomenclature	Value	[Units]	Condition
Effective Area	$A_{v-max}$	12.00	[mm <sup>2</sup> ]	Maximum value
Sleeve orifice radius	$R_{Co}$	1.25	[mm]	NA
Sleeve active orifices	$N_{Ao}$	5.00	[-]	Approximated value
Spool displacement	$x_{s-max}$	3.20	[mm]	Maximum value
Dead zone - Lower Boundary	$LB_{Dead\ zone}$	0.9-1.1	[mm]	Spool displacement
		50	[%]	PWM duty cycle
		130	[bits]	PWM analog value
Dead zone - Upper Boundary	$UB_{Dead\ zone}$	1.9-2.1	[mm]	Spool displacement
		70	[%]	PWM duty cycle
		180	[bits]	PWM analog value
Threshold Input Command Extension	$PWM_{0-Extension}$	57	[%]	Cap-end valve \ No Opposite pressure force
		145	[bits]	
Threshold Input Command Retraction	$PWM_{0-Retraction}$	62	[%]	Rod-end valve \ No Opposite pressure force
		158	[bits]	
Discharge coefficient Equation convergent nozzle	$C_D$	0.7	[-]	Compressible flow
Discharge coefficient Equation thin, sharp edged orifice	$C_d$	0.85	[-]	Compressible flow
		0.35	[-]	Incompressible flow
Discharge coefficient Modified flow equation	$C_d$	0.55	[-]	Compressible flow
		0.25	[-]	Incompressible flow
Simplified model	$C_D'$	0.23	[m <sup>3</sup> /kg] <sup>1/2</sup>	Combined coefficient

[\* NA = Not Applicable]

**Table 4.19.** Summary – Friction Forces and Friction Coefficients

Friction Forces and Friction coefficients				
Parameter	Nomenclature	Value	[Units]	Condition
Static friction force	$F_{SC}$	20.50	[N]	Extension (Table 4.13)
		16.42	[N]	Retraction (Table 4.13)
Viscous friction coefficient	$D_{vsc}$	80.50	[Ns/m]	Extension (Table 4.14)
		66.50	[Ns/m]	Retraction (Table 4.14)
Dynamic friction force	$K_{SCD}$	74.80	[N]	Extension (Table 4.14)
		70.00	[N]	Retraction (Table 4.14)

**Table 4.20.** Summary – Dynamic Constants and Gains

Dynamic Constants and Gains				
Parameter	Nomenclature	Value	[Units]	Condition
Time constant	$\tau$	0.015	[s]	Extension
		0.012	[s]	Retraction
Numerator Transfer function First order system	$\bar{C}$	0.021	[m/s/bit]	Normalized value
Flow Gain	$G_f$	4.46E+02	[m/s]	Average value
		7.50E-05	[m <sup>3</sup> /s/bit]	Average value
Pressure Gain	$G_D$	8.10E-08	[m <sup>3</sup> /s/Pa]	Figure 4.50
Piston Effective Area	$A_P$	0.0012	[m <sup>2</sup> ]	Eq. 4.16
Effective Volume of the chambers	$V_0$	1.9E-04	[m <sup>3</sup> ]	$x_{p0} = 0.14 [m]$

In table 4.20, the effective volume of the chambers,  $V_0$ , is defined as the volume in the chambers of the cylinder when the origin of the piston displacement is approximately at 0.14 meters from the beginning of the stroke. At this point, the volume in the chambers is equal, as it is described through the following expression.

$$V_1 = V_2 = V_0$$

$$V_0 = x_{p0}A_1 = (L_{stroke} - x_{p0})A_2 \quad (4.25)$$

Once the physical parameters, dynamic constants and gains were defined, the next step embraced the simulation of the response of the pneumatic system. Some of values for the parameters, dynamic constants, and gains defined in this section might vary depending upon the results from the simulation, which will be appropriately justified whenever it is the case.

#### 4.5. Definitive Experimental Setup

In contrast to the baseline experimental setup (Figure 4.1), the definitive experimental setup included several air reservoirs (Figure 4.58-11) and a pressure regulator (Figure 4.58-12). The pressure regulator (model ITV3050-31N4L4, SMC, Japan) and the air reservoirs (model AVT-PP-35, Clippard, USA; model 15200, Craftsman, USA) were installed for compensating the pressure drop at the upstream side of the control valves; nevertheless, they were not included in the simulation models or in the analysis for designing the controller. Moreover, a triple output DC power supply (Figure 4.58-1) was used in all the experiments (model 1760, B&K PRECISION, USA), which provided two supplies with a 0-30 volt dc output and one with a 4-6.5 volt dc output. Some of the numbers used to identify the setup elements (Figure 4.58) correspond to the numbers used in Figure 4.1.

Using the definitive experimental setup, the research hypothesis was tested by comparing simulation results with data acquired through experimentation, which was addressed in chapter 6.

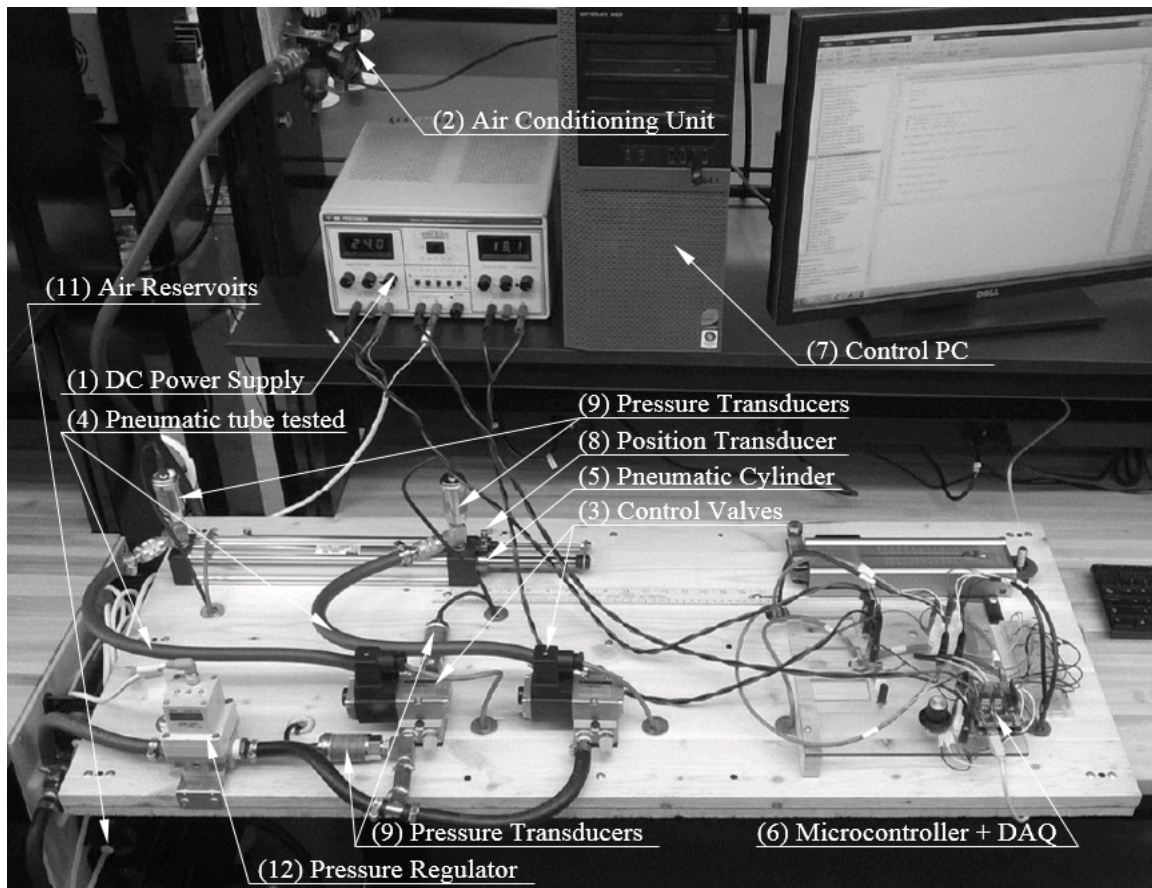


Figure 4.58. Definitive Experimental Setup

## CHAPTER V

### SIMULATION RESULTS & PREDICTION

#### Simulation and Verification of Models

The simulation and verification of the models created to describe the transient response of the pneumatic system primarily aims to assess to what extent, or under what conditions, it would be feasible to approximate the simulation response obtained to the actual response of the system. Moreover, the simulation of the response of the actual system attempts to corroborate or refute hypothesis made throughout the design of the control strategies proposed.

From the results of the simulations, dynamic parameters found through experimentation were adjusted or confirmed, as well as the proposed control strategies were sharpened for implementation. At the end of the simulation process, predictions based on assumptions about the incidence of certain parameters on the overall performance of the pneumatic system were made, which provided a means to assess the accuracy of the simulation models in relation to the actual response of the pneumatic system in the following chapter.

#### 5.1. Block-Diagram Models

Section 5.1 deals with the simulation of the response of the pneumatic system modeled according to the block-diagram schemes described in Chapter 3. The simulation results from the full-nonlinear, full-linear, and reduced-linear models are presented, analyzed and compared one to each other. The simplified reduced model derived from the reduced-order transfer function of the reduced-linear model was also assessed. The original and simplified reduced models were used later to simulate the closed-loop response of the pneumatic system according to a P-control and a Pole/Zero cancellation control strategies. Root locus analysis was applied to trace the path of the closed-loop system poles, which varied based on the control strategy. Finally, root locus analysis was used to predict the behavior of the system and the controller in relation to the length of connective tubing.

### 5.1.1.1. Nonlinear and Linear Models: Comparison and Verification of Simulation Responses

This section analyzes the results from the simulation of the open-loop responses of the full-nonlinear, full-linear, and reduced-linear models proposed for the pneumatic system. The responses of two sets of models are included. The first set was labeled the compressibility models because the air bulk modulus was included in the models as a referent of air compressibility. The second set was called the spring models since air compliance and the effect of air compressibility were modeled as a natural impedance. At the end of this section, estimated parameters, dynamic gains and constants composing the different models were reported.

#### 5.1.1.1.1. *Compressibility Models*

The following figures show the full-nonlinear, full-linear, and reduced-linear models composing the set of compressibility models. As it can be verified, the effective bulk modulus,  $\beta$ , appears in each of the models. The values for the parameters included in the models correspond to the values determined and reported in chapter 4.

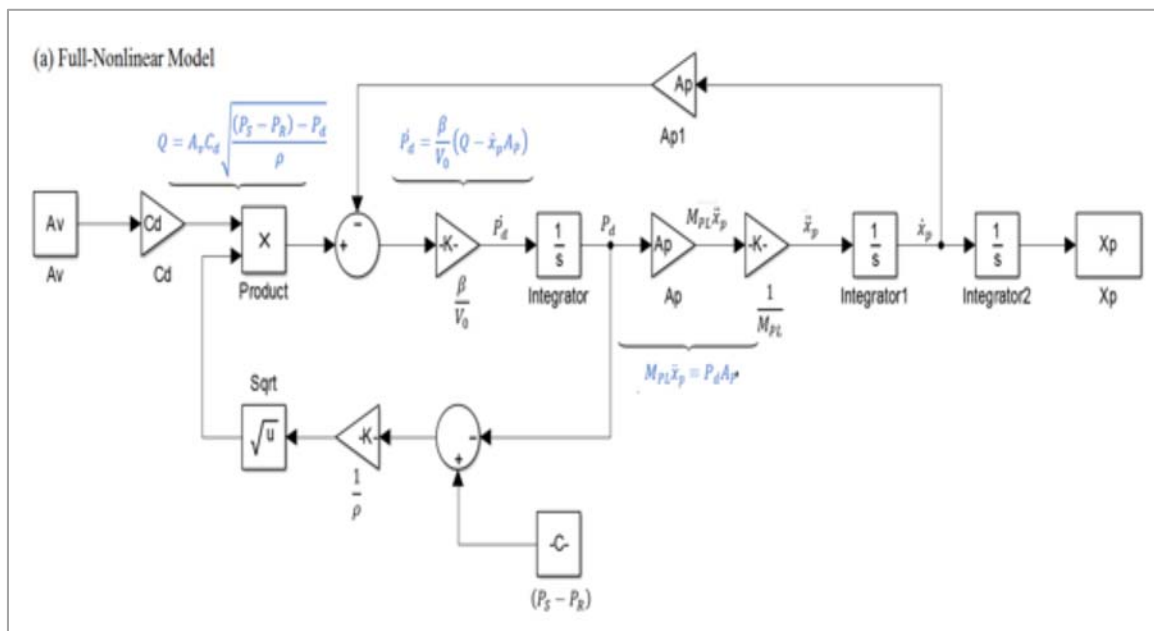


**Figure 5.1.** Compressibility models: (a) Full-Nonlinear model



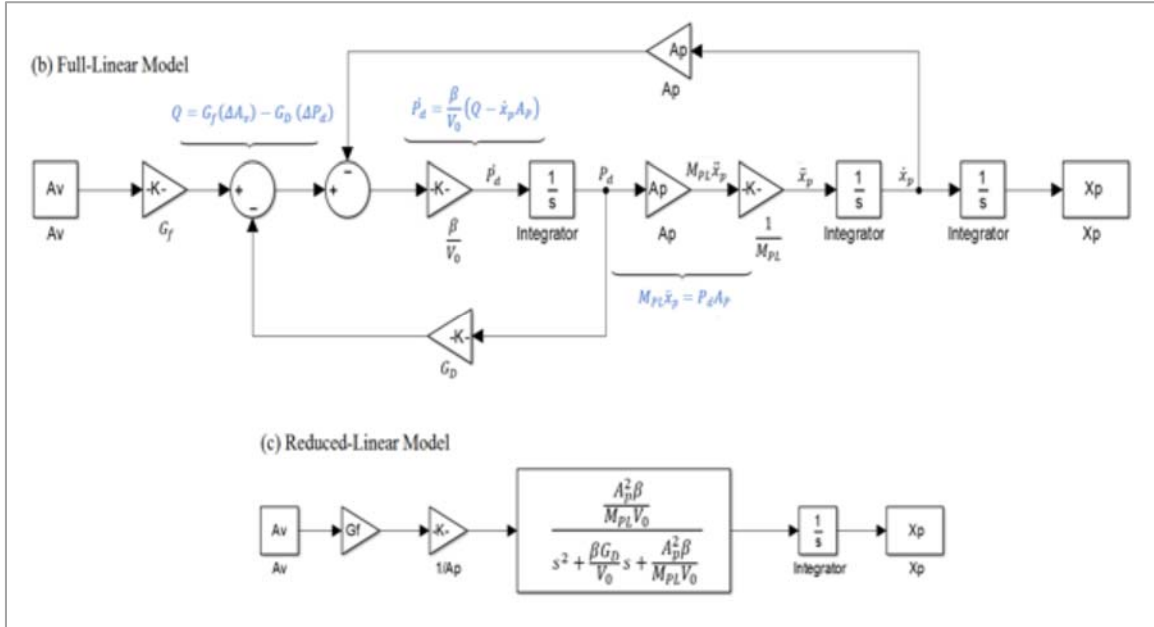


**Figure 5.2.** Compressibility models: (b) Full-Linear Model (c) Reduced-Linear Model

Based on the response to a step input, the following figures show the simulation response of the models in regard to the displacement and velocity of the piston, and the differential pressure in the chambers of the pneumatic cylinder.

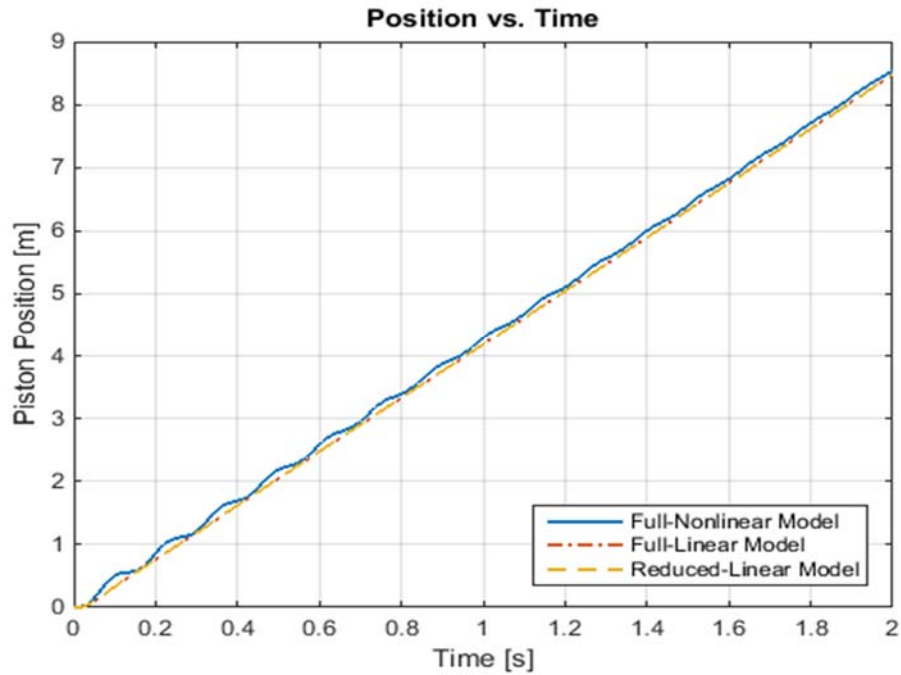


**Figure 5.3.** Simulated cylinder position step response of the three compressibility models

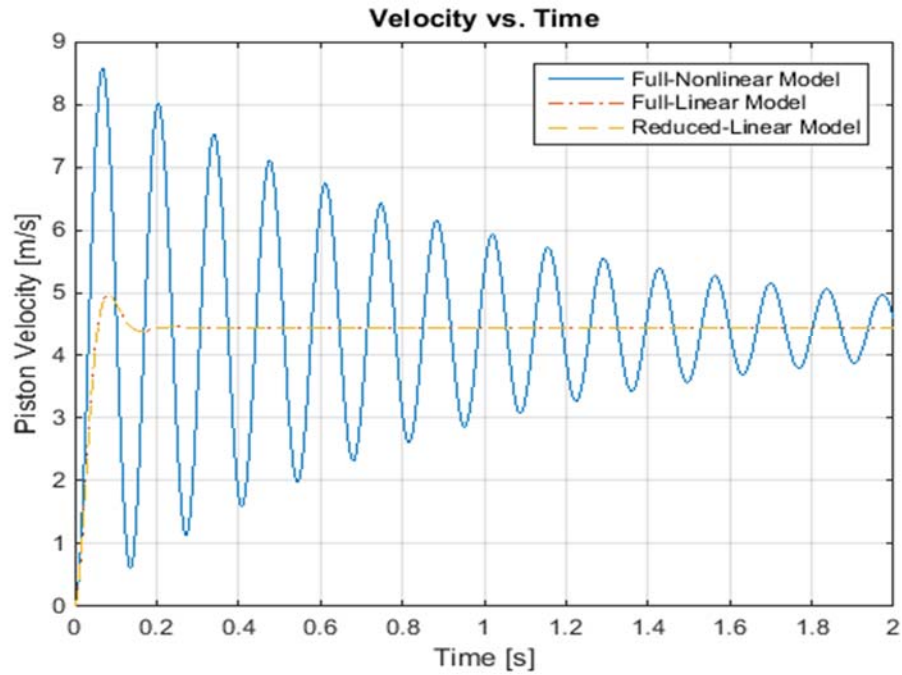


**Figure 5.4.** Simulated response of the three compressibility models to a step input: Cylinder piston velocity

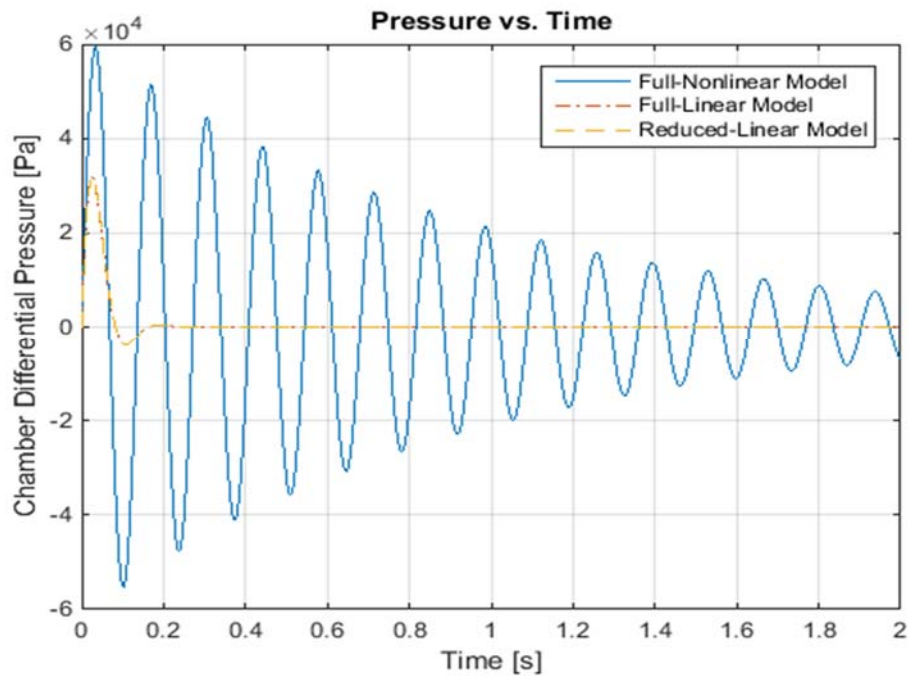


**Figure 5.5.** Simulated response of the three compressibility models to a step input: Cylinder chambers differential pressure



The amplitude of the step input used to simulate the response of the system should be within the admissible input values for the proportional control valves. The input in the models corresponds to the effective area of the proportional control valves, for which the operational range is between  $0.0 \text{ m}^2$  and  $1.2\text{E-}05 \text{ m}^2$ . The amplitude of the step input applied to generate the responses shown in the above figures was:  $1.0\text{E-}05 \text{ m}^2$ .

A divergence existed among the responses for the nonlinear and linear models (Figures 5.3 to 5.5). This divergence would come from differences in the damping ratios,  $\xi$ , across the different models. The damping ratio for the nonlinear model was lower than that of the linear models, as can be observed from the longer decay time of the full-nonlinear model response, in contrast to that of the linearized models. In that regard, the block diagrams for the reduced-linear model show that the value of the damping ratio depends on the pressure gain,  $G_D$ . Hence, in order for the responses obtained from the linearized models to match the responses from the nonlinear model, the pressure gain could be adjusted. The following figures show the simulation responses obtained by adjusting the value of the pressure gain,  $G_D$ , in the linear models.

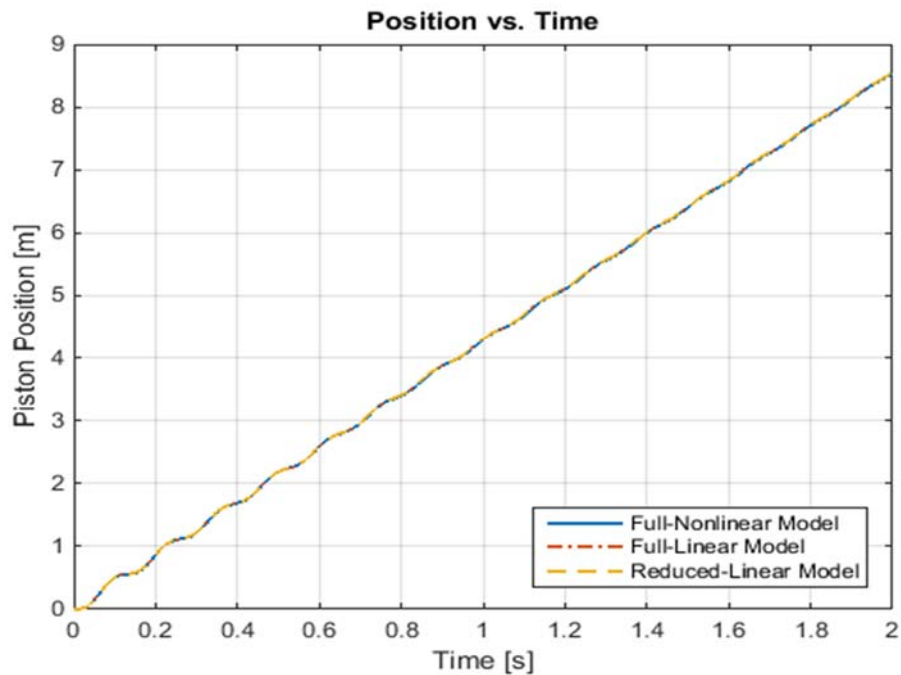


**Figure 5.6.** Simulated cylinder position step response of the three compressibility models with adjusted pressure gain:  $G_D = 3.5\text{E-}09 \text{ [m}^5/\text{Ns]}$

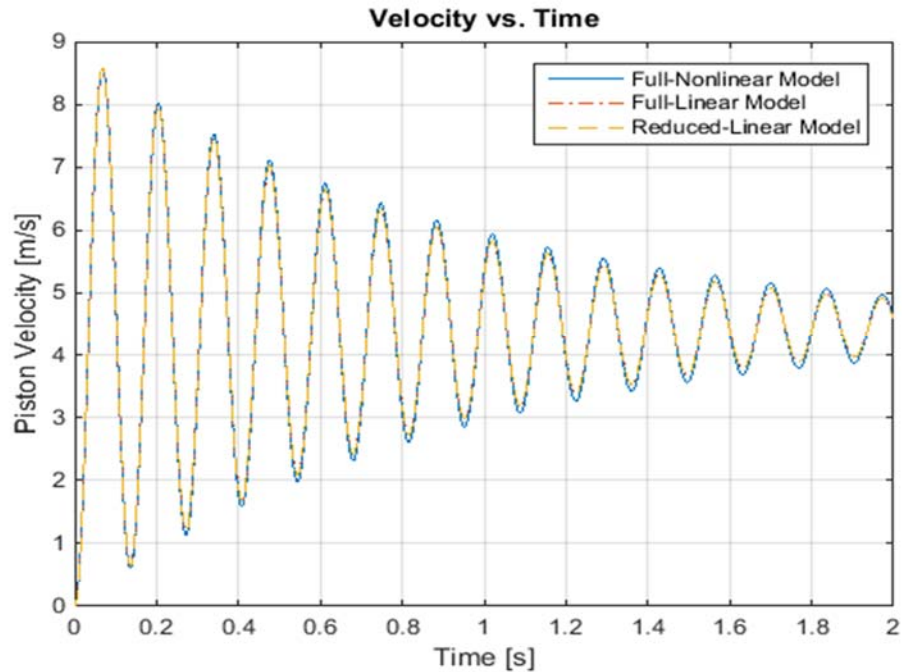


**Figure 5.7.** Simulated response of the three compressibility models to a step input: Cylinder piston velocity with an adjusted pressure gain ( $G_D = 3.5E-09$  [m<sup>5</sup>/Ns])

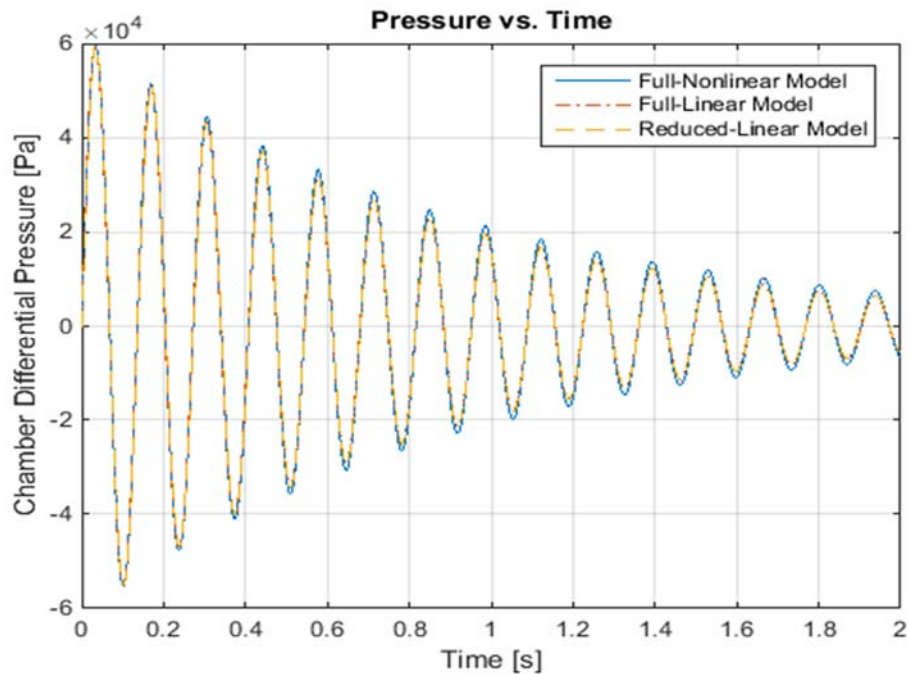


**Figure 5.8.** Simulated step response of the three compressibility models: Cylinder chamber differential pressure with an adjusted pressure gain ( $G_D = 3.5E-09$  [m<sup>5</sup>/Ns])

An adjusted value of the pressure gain,  $G_D$ , enabled the simulation responses from the nonlinear model to match the responses from the linear models (Figures 5.6 to 5.8). Nevertheless, the adjusted value for the pressure gain,  $G_D$ , could not be taken as a definitive value because the responses displayed in the figures presented above were not being corroborated with actual data. Moreover, the velocity and pressure responses obtained initially from the linearized models would be more desirable in terms of the required performance, and the expected responses of the pneumatic system. Hence, the value for the pressure gain obtained experimentally, as described in chapter 4, was maintained.

5.1.1.2. *Alternative Models – Hoses modeled as springs*

Full-nonlinear, full-linear, and reduced-linear models were developed with a spring modeling approach (Figures 5.9 and 5.10). The spring constant,  $k_x$ , appears in each of the spring models. The value for this spring constant was not determined in chapter 4; accordingly, a value for  $k_x$  had to be defined before simulating the response of the pneumatic system in basis to the spring models.

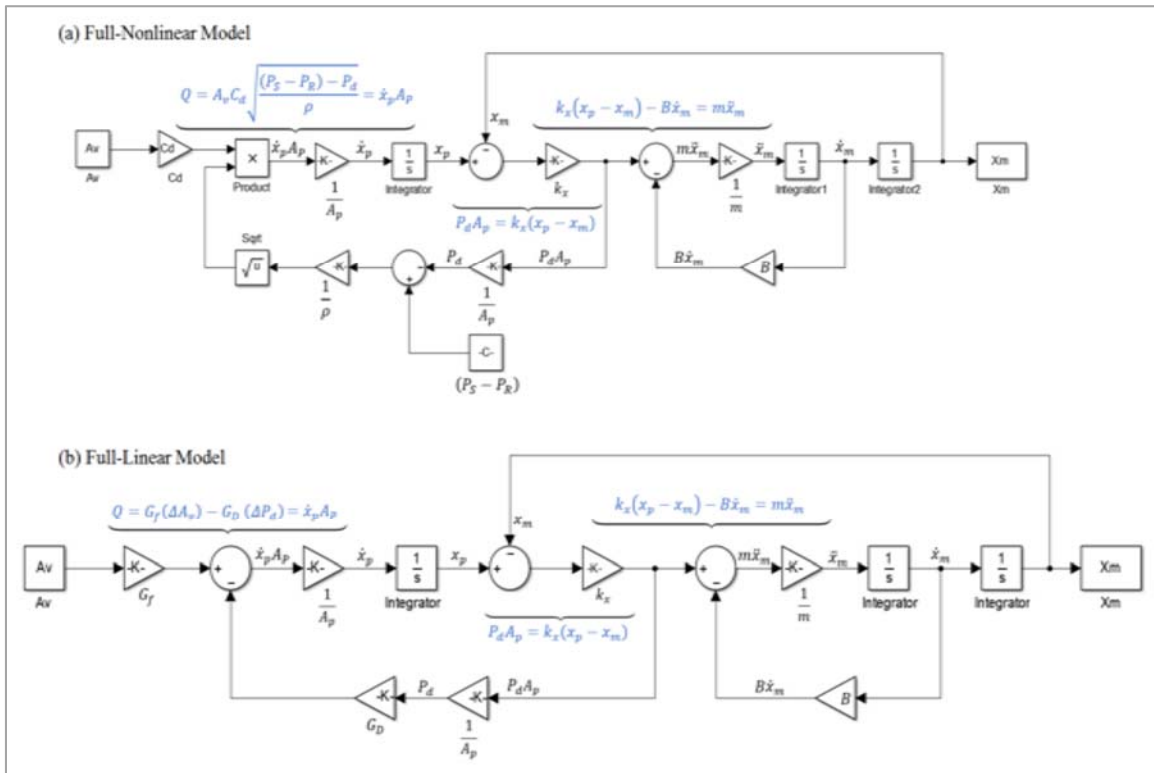
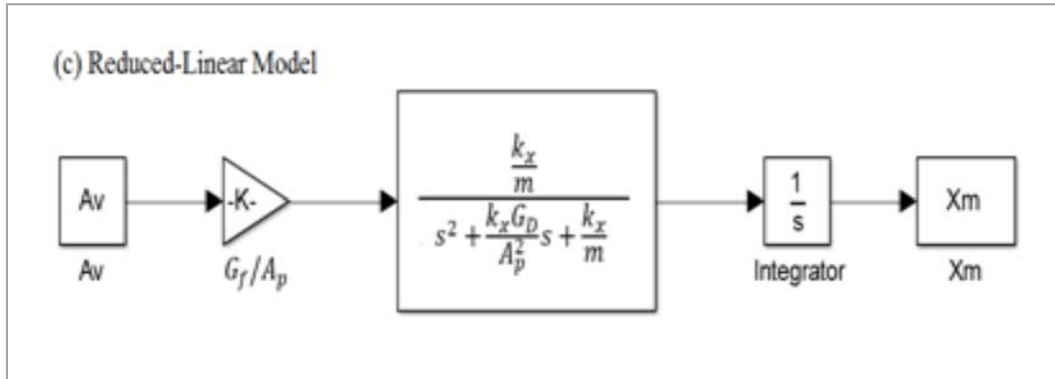
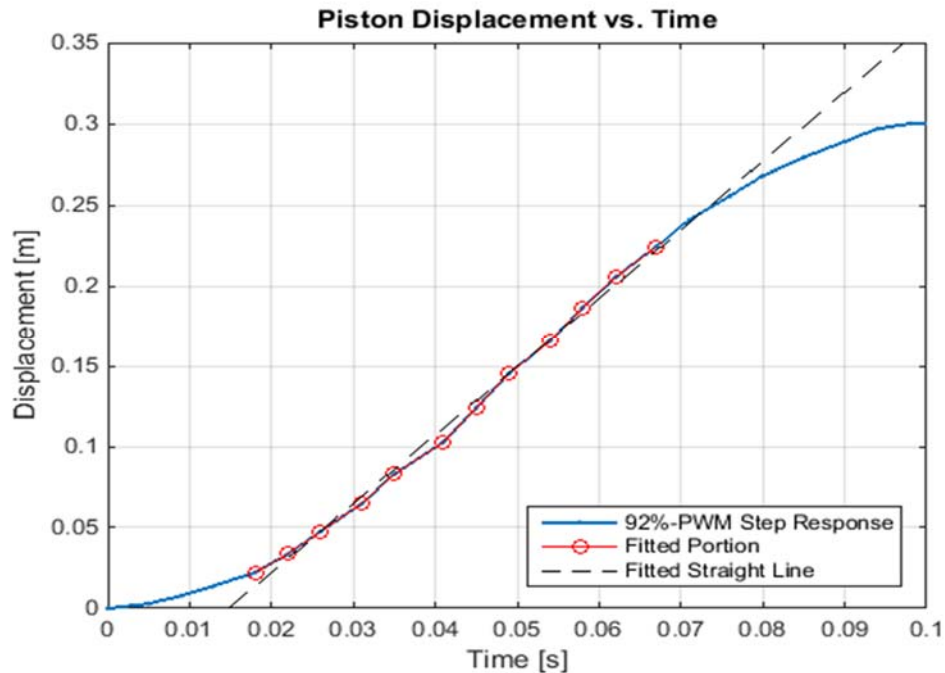


Figure 5.9. Spring models: (a) Full-Nonlinear model, (b) Full-Linear Model



**Figure 5.10.** Spring models: (c) Reduced-Linear Model

To estimate the spring constant,  $k_x$ , several values were tested in the models until the displacement response matched an experimental step response of the pneumatic system. The actual response from the piston was obtained by triggering the valves with a PWM step input equivalent to the input entered for simulation. According to the findings from chapter 4, a 92-percent duty cycle PWM input would correspond to an effective area of  $1.0\text{E-}05 \text{ m}^2$ , which is the input introduced for simulation. The following figure shows the actual step response and the straight line fit. The linear fit was used for identification of dynamic constants, as described in chapter 4, section 4.4.3.



**Figure 5.11.** Estimation of  $k_x$ : 70%-PWM cylinder piston experimental step response

The following figures show the simulation responses obtained from the spring models by entering a spring constant value of 50 [N/m].

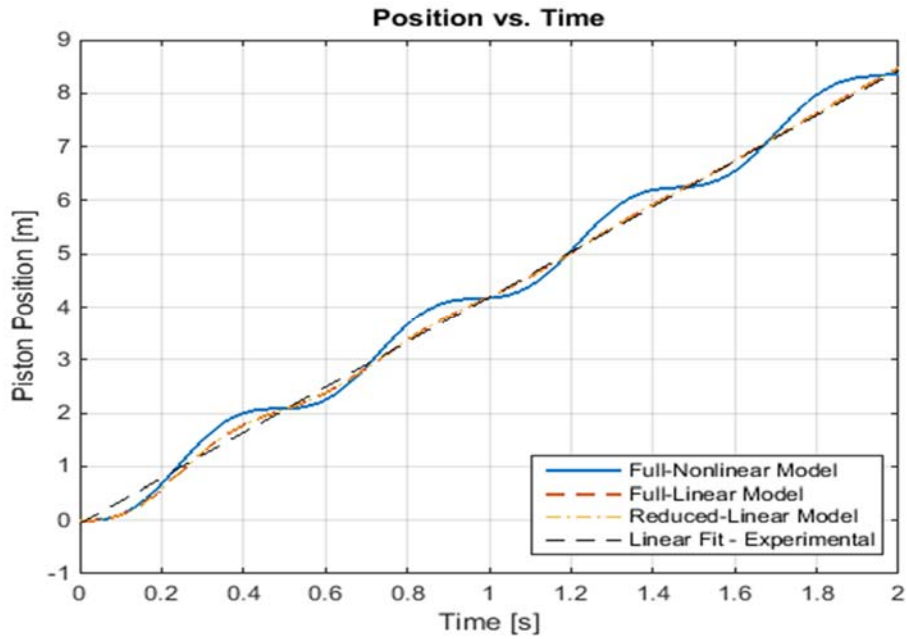


**Figure 5.12.** Simulated cylinder position step response of the three spring models:  $k_x = 50$  [N/m]

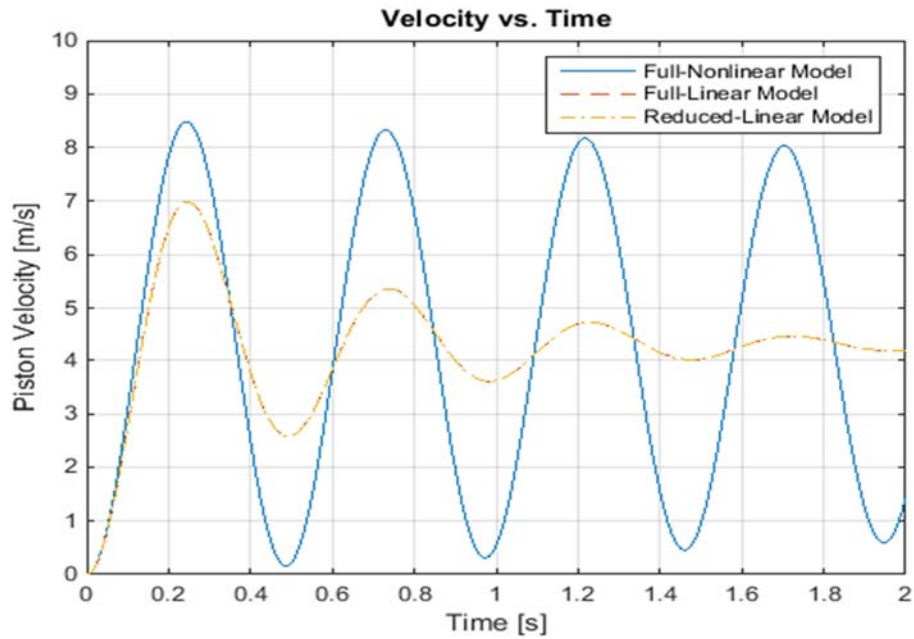


**Figure 5.13.** Simulated response of the three spring models to a step input: Cylinder piston velocity ( $k_x = 50$  [N/m])

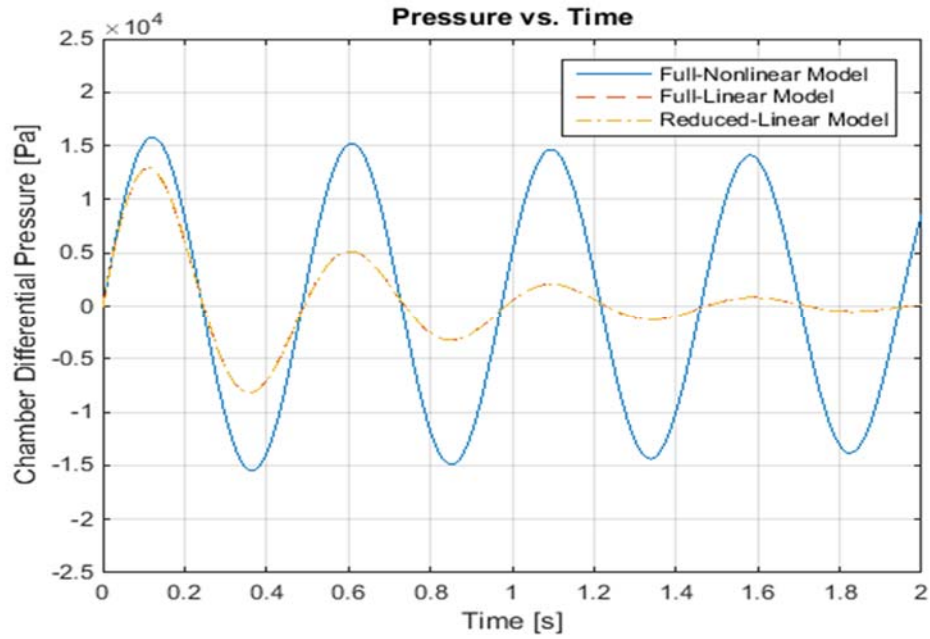


**Figure 5.14.** Simulated response of the three spring models to a step input: Differential pressure in the cylinder chambers ( $k_x = 50$  [N/m])

The following figure shows the displacement responses from the spring models once the pressure gain was adjusted.

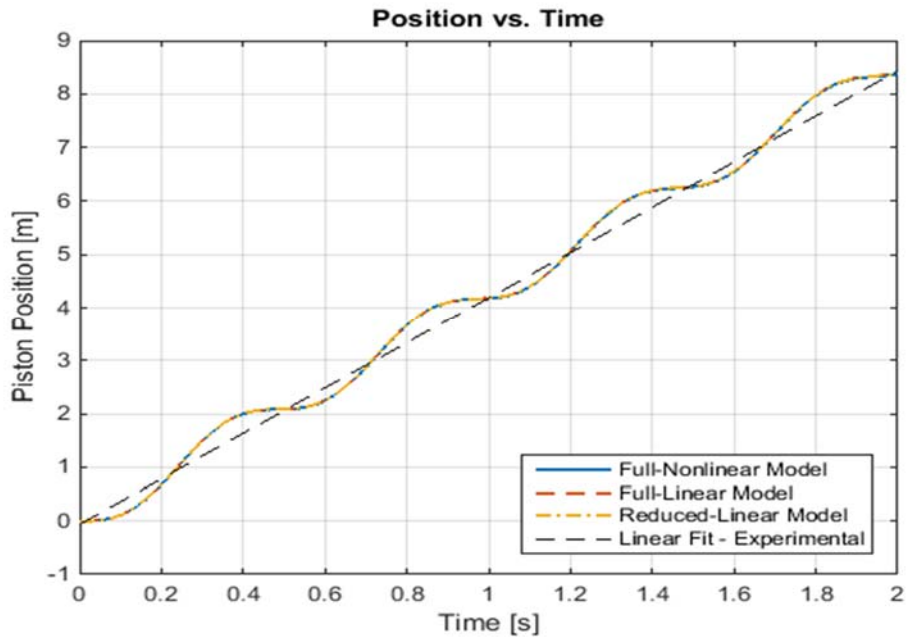


**Figure 5.15.** Simulated cylinder position step response of the three spring models with an adjusted pressure gain:  $G_D = 3.5E-09$  [ $m^5/Ns$ ] ( $k_x = 50$  [N/m])

The simulation responses from the nonlinear model did not match the responses from the linear models (Figure 5.12 to 5.14). Accordingly, like in the case of the compressibility models, in order for the nonlinear and linear responses to match, the pressure gain had to be adjusted.

The simulated displacement responses did not exactly fit the straight lines included as reference (Figure 5.12 and 5.15). Moreover, although the displacement simulation responses followed the trajectory traced by the straight line, it was necessary to infringe a more accurate fitting of the simulation response with the linear fit during the interval of time in which the piston attains its maximum actual displacement; it is the interval of time in which the piston reaches the end of its stroke. Further adjustment of the flow gain and the spring constant would have required to accomplish a more accurate fitting between the simulation response and the linear experimental fit. Nevertheless, by adjusting the pressure gain,  $G_D$ , the simulation responses from the nonlinear models matched the responses from the linear models under specific operating conditions, which represented the operating points around which the nonlinear models were linearized.

The following figures show the velocity and pressure simulated responses obtained from the spring models by adjusting the pressure gain,  $G_D$ .

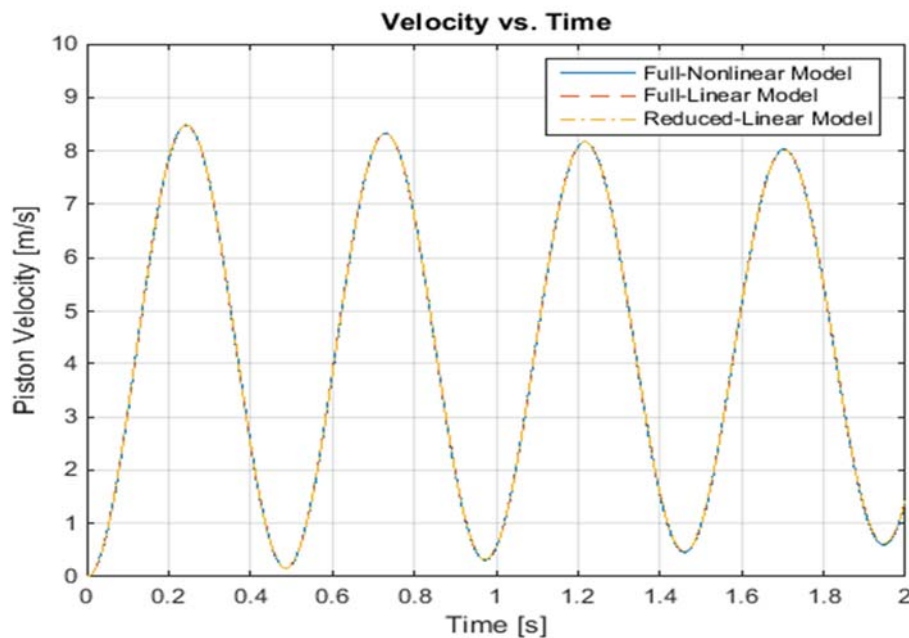


**Figure 5.16.** Simulated step response of the three spring models: Cylinder piston velocity with an adjusted pressure gain ( $G_D = 3.5E-09$  [m<sup>5</sup>/Ns],  $k_x = 50$  [N/m])



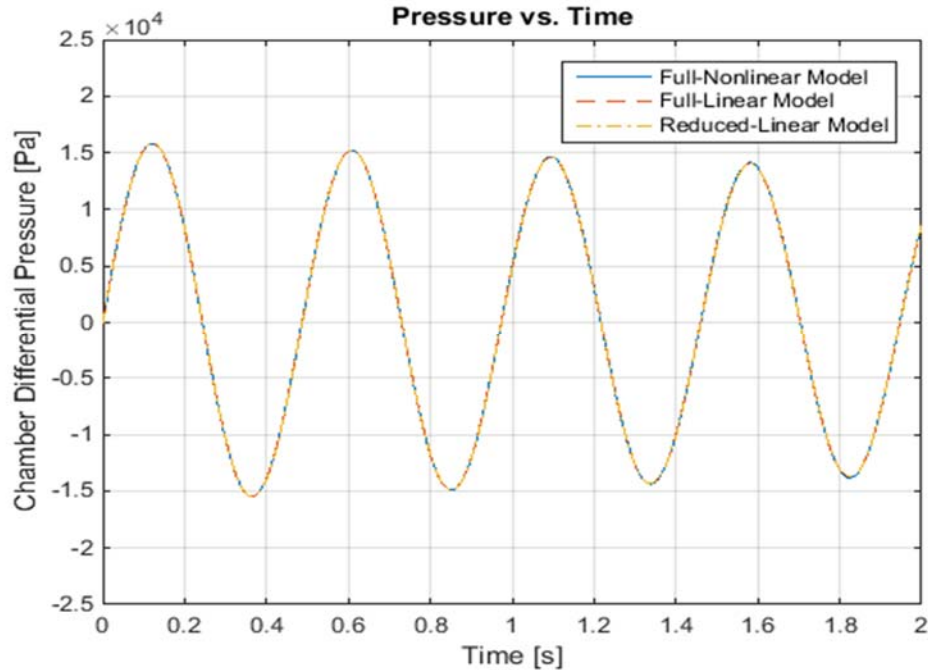


**Figure 5.17.** Simulated step response of the three spring models: Chamber differential pressure with an adjusted pressure gain ( $G_D = 3.5E-09$  [ $m^5/Ns$ ],  $k_x = 50$  [ $N/m$ ])

The adjusted value of the pressure gain for the spring models corresponded to the adjusted value for the compressibility models, which validated the operating point around which the nonlinear models were linearized. This operating point could be traced back by verifying the slopes of the consecutive points obtained from plotting the volumetric flow as a function of the differential pressure in the cylinder chambers, as described in chapter 4, section 4.4.4.

Furthermore, for the interval of time in which the pneumatic piston would reach the end of its stroke, by maintaining the value of the pressure gain found in chapter 4, but adjusting the gain flow, and substantially increasing the value of the spring constant, the responses of the linear models in some extent adjusted themselves to the experimental linear fit included as reference. Nevertheless, it was not possible to make the response of the nonlinear model to approximate closer to the experimental linear fit (Figure 5.17).

When the spring constant was increased by a factor of 500, the natural frequency and the damping ratio of the system increased, as observed in the oscillatory behavior of the response (Figure 5.17).



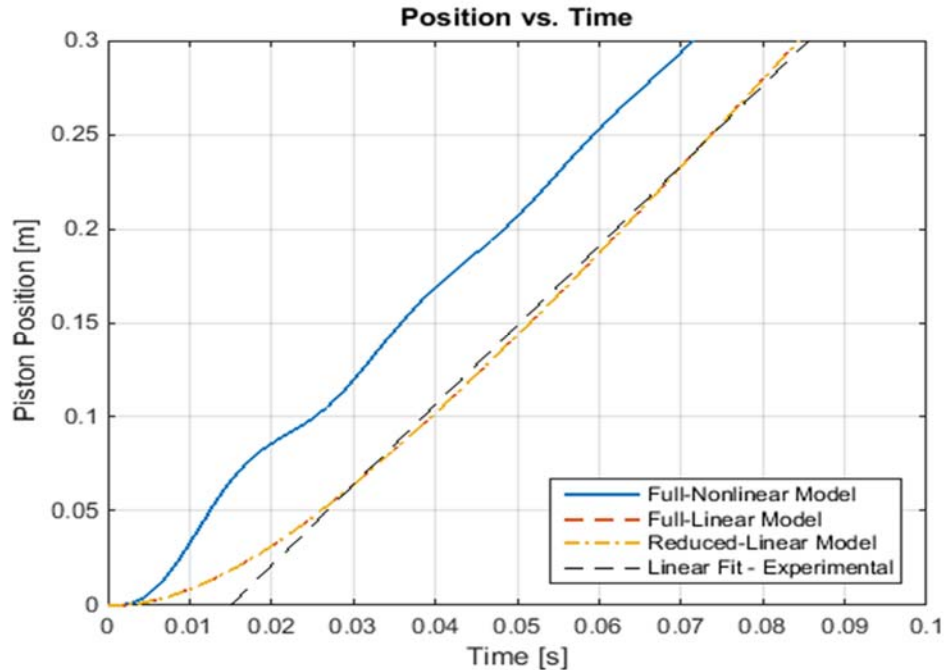


**Figure 5.18.** Simulated cylinder position step response of the three spring models with an adjusted flow gain and increased spring constant:  $G_f = 500$  [m/s],  $k_x = 25000$  [N/m]

The difference between the adjusted and the experimental values of the flow gain could be disregarded. As it was explained in chapter 4, from the 3-D plot relating the volumetric flow to the effective area of the valves, and to the differential pressure in the chambers of the cylinder, different values for the flow gain and the pressure gain can be defined by fitting straight lines to the planes that compose the three-dimensional surface, which would represent the linearization of the nonlinear models for the pneumatic system around different operating points.

Moreover, due to the fact that the reduced linear models will be used for the analysis and implementation of the control strategies for the pneumatic system, it could be also ignored the fact that the nonlinear model for the pneumatic system was not able to match the required response under the established operating conditions. Hence, the subsequent simulation responses shown correspond to the responses obtained from the reduced linear-models, only. In that regard, the next section in this chapter compares the simulation results obtained from the reduced-linear compressibility model and the reduced-linear spring model, as an approach to match the outcome of both models under specific operation conditions.

### 5.1.1.3. Comparison of Reduced-linear Compressibility and Spring Models

The results from the preceding sections showed that a step input applied to the pneumatic system would cause motion at a constant rate. After the initial dynamic oscillations, the rate of change of the position of the piston was constant, and equivalent to the slope of the curve. Moreover, the transient responses observed might correspond to the responses of an underdamped system, although for the cases where the spring of the constant significantly increased, the transient responses would resemble the responses of an overdamped system.

This section compares the responses from the reduced-linear models for the interval of time in which the pneumatic cylinder remains operational; it is the interval of time in which the piston would be able to reach the end of its stroke for a specific input. The following figure shows the displacement response produced by the reduced-linear compressibility model and the reduced-linear spring model in reference to the experimental linear fit used for parameter identification in chapter 4.

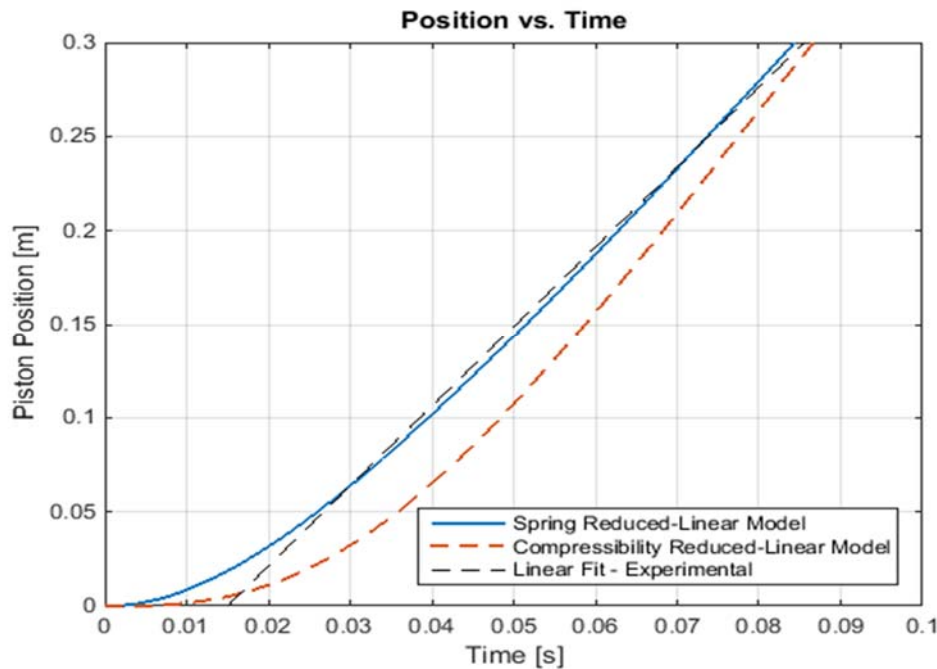


**Figure 5.19.** Simulated cylinder position step response of the compressibility and spring reduced-linear models ( $k_x = 25000$  [N/m],  $G_f = 500$  [m/s])

The displacement response from the reduce-linear compressibility model did not adjust to the trajectory traced by the experimental linear fit (Figure 5.19).

Likewise, the velocity and pressure responses from the compressibility model did not match the responses from the spring model (Figure 5.20 and 5.21).

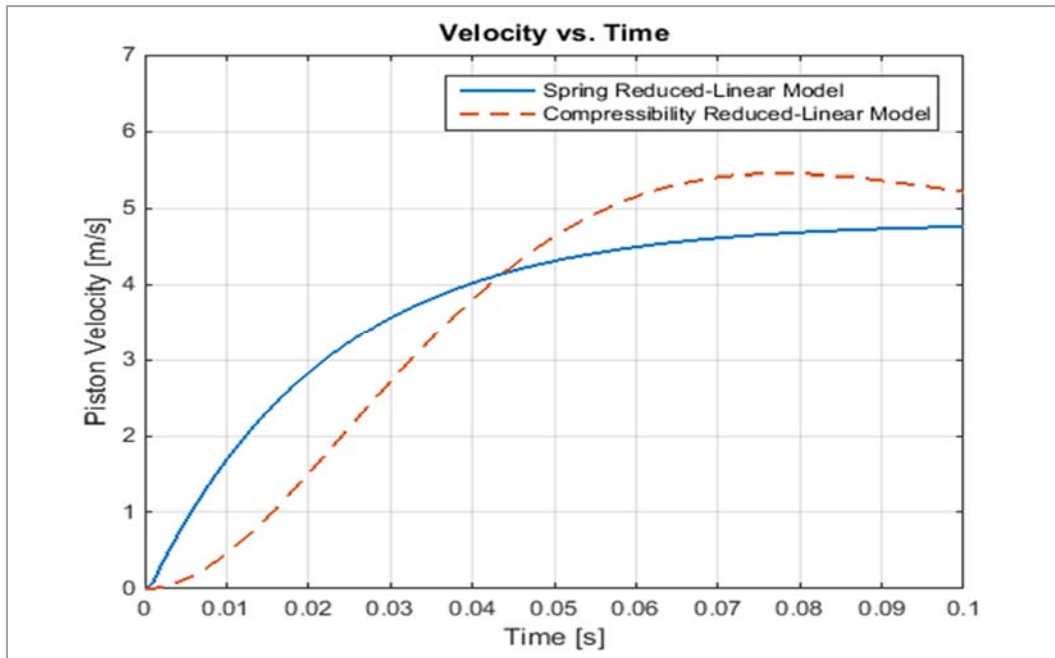


**Figure 5.20.** Simulated step response of the compressibility and spring models: Cylinder piston velocity ( $k_x = 25000$  [N/m],  $G_f = 500$  [m/s])

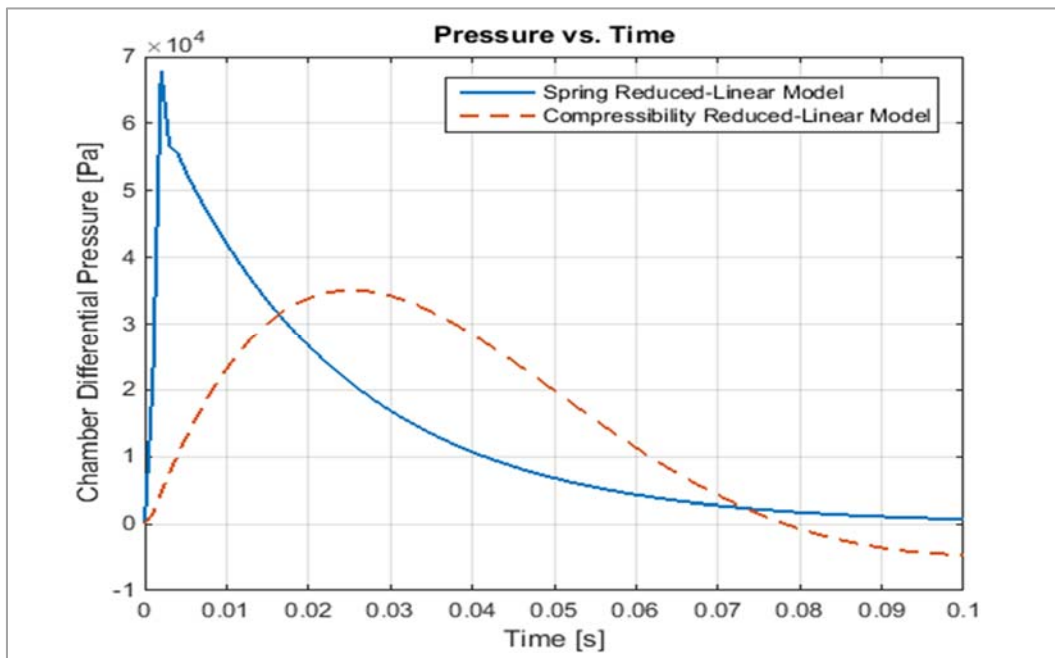


**Figure 5.21.** Simulated step response of the compressibility and spring models: Chamber differential pressure ( $k_x = 25000$  [N/m],  $G_f = 500$  [m/s])

To make the dynamic responses produced by the compressibility model to match the responses from the spring model, the coefficients of the denominator of the second-order transfer functions included in the block diagrams for the reduced-linear models should be equal. These coefficients are compared below.

$$\begin{array}{lcl}
 \text{Compressibility} & & \text{Spring} \\
 \text{Model} & \vdots & \text{Model} \\
 \omega_n^2 = \frac{A_p^2 \beta}{M_{PL} V_0} & \vdots & \omega_n^2 = \frac{k_x}{m} \\
 2\xi \omega_n = \frac{\beta G_D}{V_0} & \vdots & 2\xi \omega_n = \frac{k_x G_D}{A_p^2}
 \end{array} \quad (5.1)$$

By equating the natural frequency,  $\omega_n$ , or the damping ratio terms,  $\xi$ , the results showed that the equivalent air bulk modulus,  $\beta$ , would be defined by the following expression.

$$\beta = \frac{k_x V_0}{A_p^2} \quad (5.2)$$

This last deduction denotes the fact that in order for the compressibility reduced-linear model to match the spring model, the effective value of the air bulk modulus used for simulation needed to be adjusted (Figures 5.22 to 5.24).

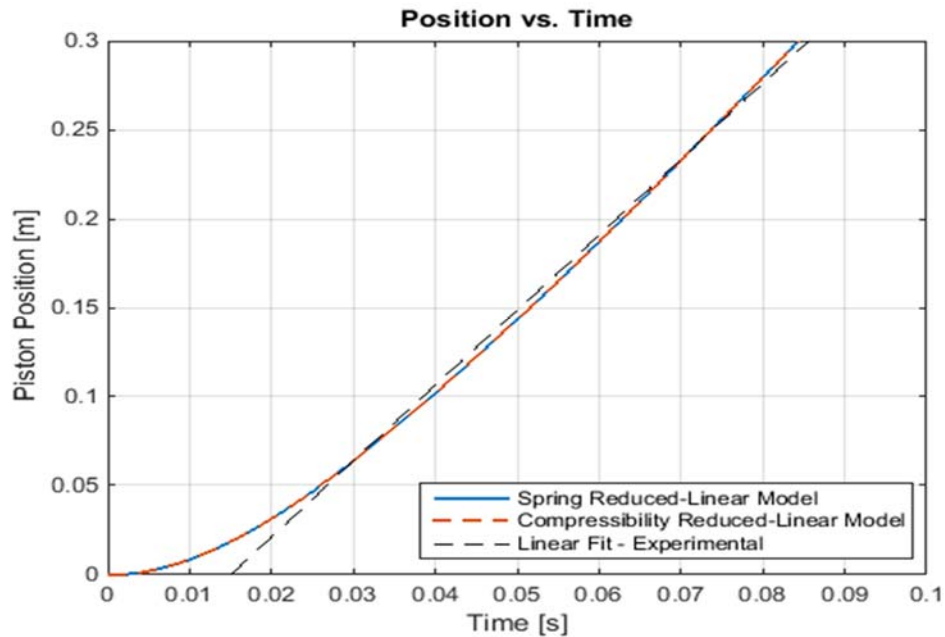


**Figure 5.22.** Simulated cylinder position step response of the compressibility and spring models with and adjusted effective bulk modulus:  $\beta = 4.54\text{E}+06$  [Pa]

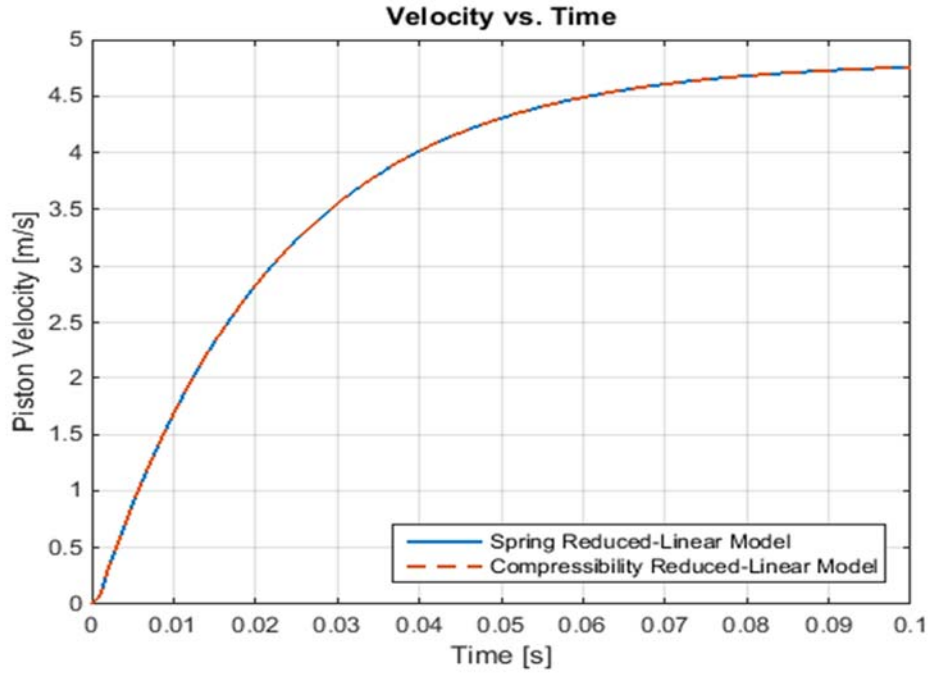


**Figure 5.23.** Simulated step response of the compressibility and spring models: Cylinder piston velocity with and adjusted effective bulk modulus:  $\beta = 4.54\text{E}+06$  [Pa]

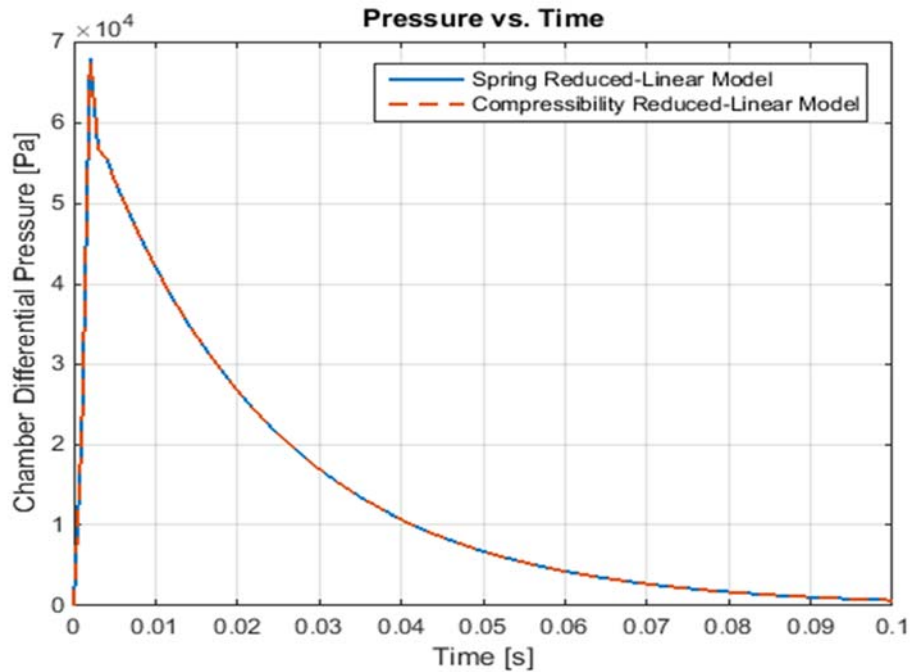


**Figure 5.24.** Simulated step response of the compressibility and spring models: Chamber differential pressure with and adjusted bulk modulus:  $\beta = 4.54\text{E}+06$  [Pa]

Based on the results from figures 5.22 to 5.24, the dynamic responses produced by the compressibility and spring reduced-linear models matched once the value of the effective bulk modulus was adjusted. Moreover, the dynamic responses from the compressibility and spring models should be able to adjust to the actual response of the pneumatic system, for any input within the admissible values for triggering the control valves. To illustrate, figure 5.25 shows the displacement responses produced by the simulation models for a low-amplitude step input of  $3.5\text{E-}06 \text{ m}^2$ .

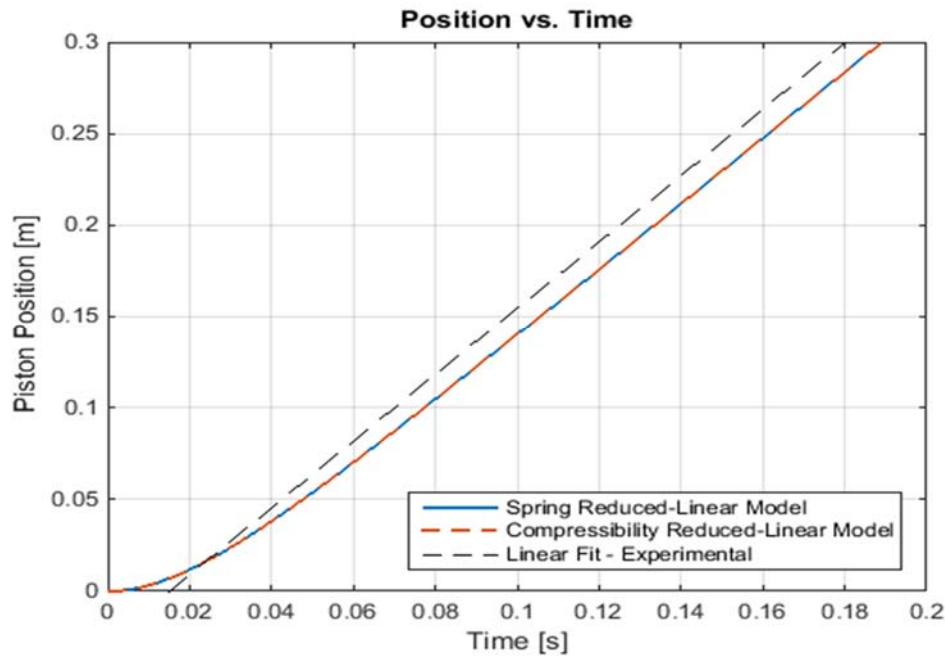


**Figure 5.25.** Simulated cylinder position step response of the compressibility and spring reduced-linear models:  $A_v = 3.5\text{E-}06 \text{ [m}^2\text{]}$

Figure 5.25 shows that the displacement response produced by the compressibility and spring models approximate the experimental linear fit used for parameter identification in chapter 4. A 75-percent duty cycle PWM input is equivalent to the effective area used as input for simulation. In order to produce a more accurate fitting between the actual trajectory and the responses produced by the simulation models, the flow gain,  $G_f$ , was increased. The increase of the flow gain for low-amplitude step inputs would be justified by the results found in chapter 4, table 4.12: As the amplitude of the step input increases, the rate of change of volumetric flow per change of effective area decreases. In figure 5.26, the gain flow was adjusted, which enabled the simulation responses to more accurately adjust to the actual trajectory.

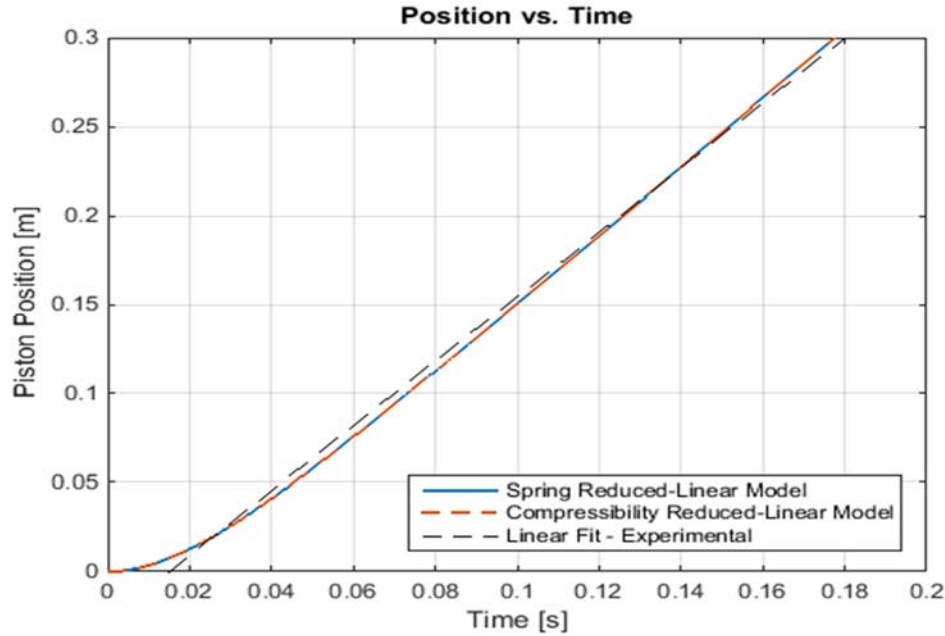


**Figure 5.26.** Simulated cylinder position step response of the compressibility and spring models with and adjusted flow gain ( $A_v = 3.5E-06$  [m<sup>2</sup>],  $G_f = 575$  [m/s])

Finally, table 5.1 comprises a summary of the parameters entered in the simulation models.

**Table 5.1.** Simulation parameters: Compressibility Models (CM) and Spring Models (SM)

Parameter	Symbol	OV	AV	Units	Conditions
Piston Mass	$M_{PL}$	0.30	NA	[kg]	Piston-rod assembly + Load (CM - SM)
Supply Pressure	$P_S$	764000.0	NA	[Pa]	(CM - SM)
Atmospheric Pressure	$P_{atm} \setminus P_R$	101720.0	NA	[Pa]	(CM - SM)
Density	$\rho$	1.184	NA	[kg/m <sup>3</sup> ]	T = 295 K (CM - SM)
Effective Bulk Modulus	$\beta$	1.42E+05	4.54E+06	[Pa]	OV: Adiabatic conditions (CM)
Effective Volume of the chambers	$V_0$	1.57E-04	1.96E-04	[m <sup>3</sup> ]	AV= OV + Dead volume in 0.55-meter hoses (CM - SM)
Piston Effective Area	$A_P$	0.0012	NA	[m <sup>2</sup> ]	Eq. 4.16 (CM - SM)
Discharge Coefficient	$C_d$	0.60	NA	[-]	(CM - SM)
Viscous Friction Coefficient	$B$	NA	0.00	[Ns/m]	(SM)
Spring Constant	$k_x$	NA	25000.00	[N/m]	(SM)
Flow Gain	$G_f$	446.00	150 -750	[m/s]	(CM - SM)
Pressure Gain	$G_D$	8.1E-08	NA	[m <sup>3</sup> /s/Pa]	(CM - SM)

[\* OV = Original Value, AV = Adjusted Value, NA = Not Applicable]

### 5.1.2. Simplified Reduced Models: Converting a Second-Order System into a First-Order System

Chapter 3, section 3.2.1.2 approached the simplification of the reduced linear model for the pneumatic system by reducing the order of its transfer function. In order to reduce the order of the transfer function of the system, it was predicted that by ignoring one of the roots of the characteristic equation corresponding to the second-order block, the response from the second-order block could be approximated to the response produced by a first-order system. The following figure shows the reduced-linear block diagram opposed to the simplified block diagram.

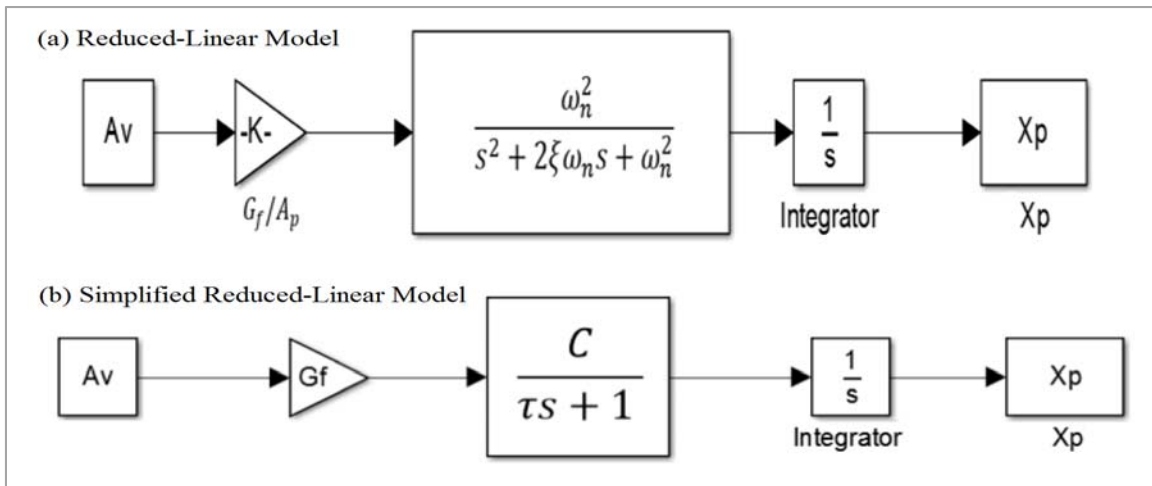


**Figure 5.27.** Simplification of the reduced models: Reduced-Linear model opposed to the simplified model.

First, as an approach to simplify the reduced-linear model, it was assumed that the block marked in red in the following figure could be neglected.

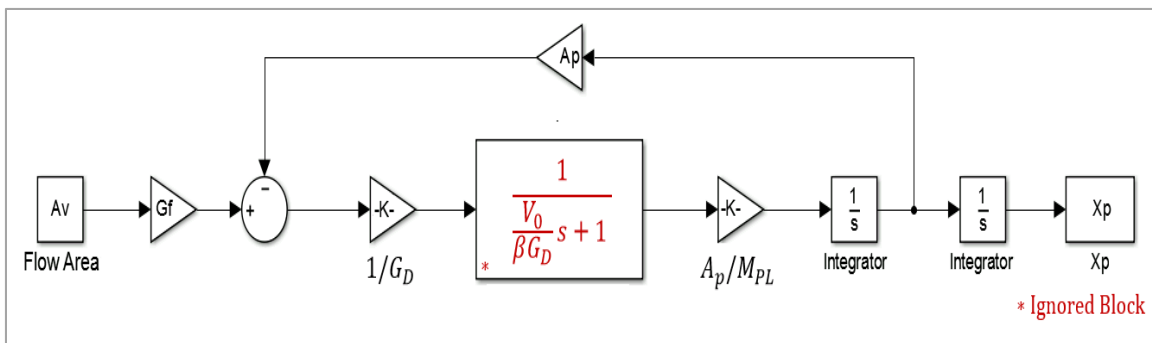


**Figure 5.28.** Simplification of reduced models: Identification of ignored block.



By ignoring the block marked in red in figure 5.28, and by following the block reduction steps as described in chapter 3, it was found that the constants  $C$  and  $\tau$  for the resulting first-order block would be defined by:

$$C = \frac{1}{A_p}; \quad \tau = \frac{G_D M_{PL}}{A_p^2} \quad (5.3)$$

Then, using the parameters included in table 5.1, the simulation and comparison of the step responses from the second-order block and the equivalent first-order block produced the following results.

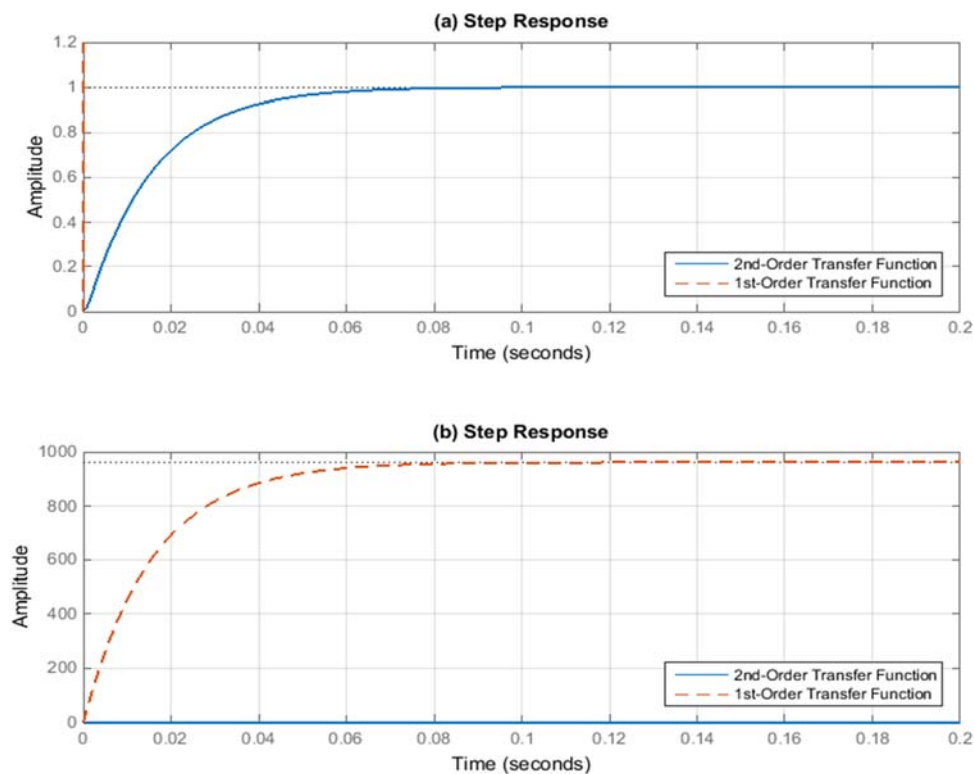


**Figure 5.29.** Second-order block and equivalent first-order block step responses: (a) Y-axis scale between 0 and 1. (b) Y-axis scale between 0 and 1000.

The amplitude of the step response produced by the first-order block was approximately 1000 times bigger than the response produced by the second order block (Figure 5.29). Hence, neglecting the block marked in red in figure 5.28 to reduce the order of the system might not be a feasible approach.

Nevertheless, as it was described in chapter 3, in neglecting one of the roots of the characteristic equation of the second-order block of the reduced-linear model, the effective area of the piston plays an important role acting as a feedback gain. Accordingly, root locus analysis was applied to verify the path traced by the poles of the system according to the value of the effective area of the piston. The following figures show the root locus for the second-order transfer function composing the reduced-linear model, according to different values for the effective area of the piston,  $A_p$ .

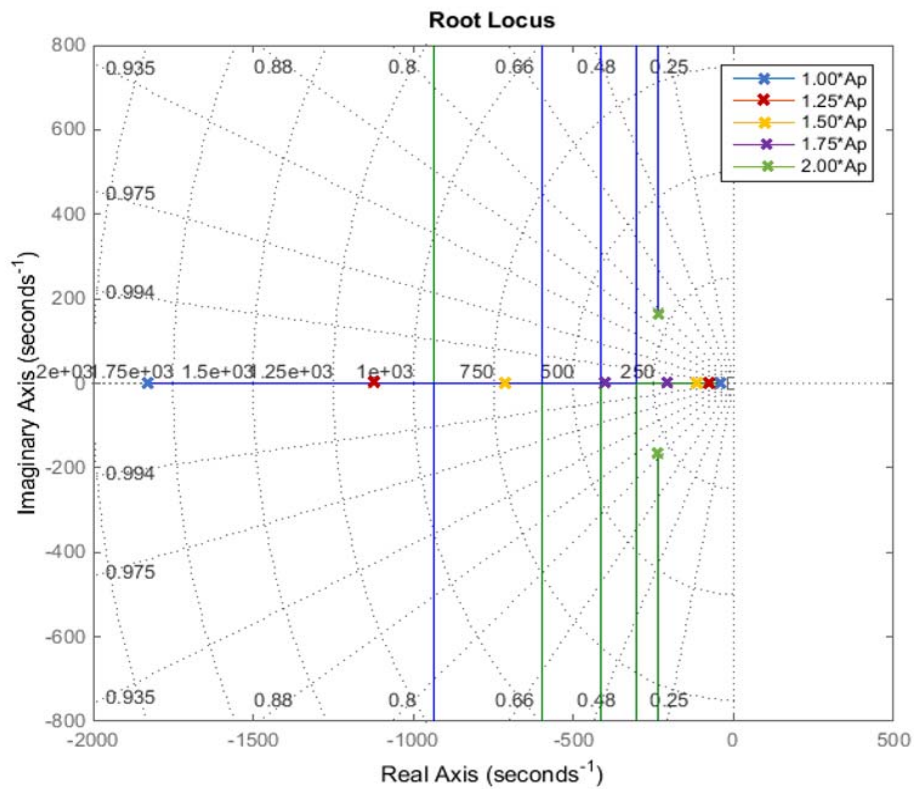


**Figure 5.30.** Second-Order Transfer Function: Root Locus depending on the effective area of the piston: Increasing values

In figure 5.30, the value of the effective area was increased in relation to the value defined in chapter 4. In this case, the root locus demonstrates that as the effective area of the piston increases, the roots of the characteristic equation approximate closer one to each other, until they become conjugates of one another.

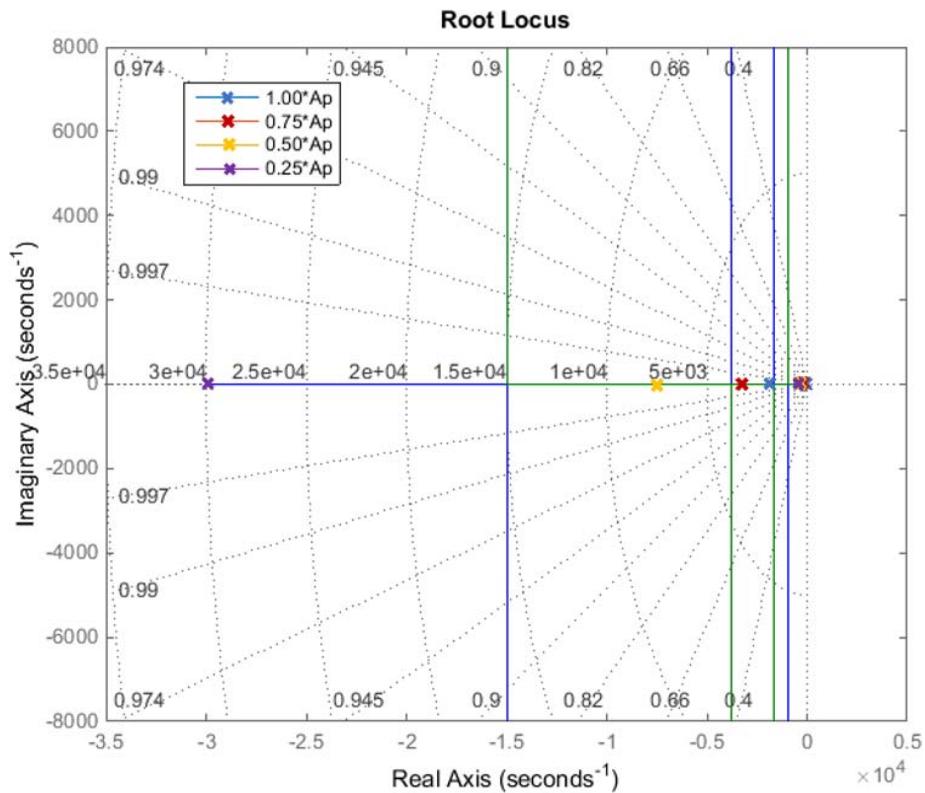


**Figure 5.31.** Second-Order Transfer Function: Root Locus depending on the effective area of the piston: Decreasing values

In contrast to figure 5.30, in figure 5.31 the value of the effective area is decreased in relation to the value defined in chapter 4. In this case, the root locus demonstrates that as the effective area of the piston decreases, the roots of the characteristic equation draw further away one from each other. Accordingly, to successfully neglect the effect of the larger root of the characteristic equation, the effective area of the piston should be decreased.

In the case of the simplified reduced-linear model derived from neglecting one of the blocks while performing block-reduction steps, in order for its response to match the response of the original reduced-linear model, the effective area of the piston should be increased over the maximum value that would keep the roots of the characteristic equation as real dissimilar values. Therefore, roots locus analysis confirmed the fact that neglecting the block marked in red in figure 5.28 to reduce the order of the system would not be a feasible approach. In looking for a practical approach to simplify the reduced linear model, a second approach was proposed.

The second approach proposed to simplify the reduced-linear models involved two steps: First, the second-order transfer function that composes the reduced-linear models was decomposed in partial fractions. Then, the partial fraction corresponding to the fastest pole of the system was neglected. The partial fraction decomposition of the second-order transfer function was accomplished as follows:

$$G(s) = \frac{\omega_n^2}{(s^2 + 2\xi\omega_n s + \omega_n^2)} = \frac{r_1 r_2}{(s + r_1)(s + r_2)} = \frac{A'}{(s + r_1)} + \frac{B'}{(s + r_2)} \quad (5.4)$$

Where  $r_1$  and  $r_2$  are roots of the characteristic equation, and also poles of the system. In addition,  $A'$  and  $B'$  are coefficients that result from the partial-fraction decomposition of the overall transfer function.

Assuming that  $r_2$  corresponds to the fastest pole of the system; it is the pole that is located further away from the complex axis in the root locus diagram, by neglecting the partial fraction corresponding to  $r_2$ , the simplified transfer function for the system would be defined by:

$$G(s) = \frac{C}{\tau s + 1} = \frac{A'}{(s + r_1)} \begin{cases} C = \frac{A'}{r_1} \\ \tau = \frac{1}{r_1} \end{cases} \quad (5.5)$$

For which, it can be demonstrated that:

$$r_1 = \frac{2\xi\omega_n - \sqrt{(2\xi\omega_n)^2 - 4\omega_n^2}}{2}; \quad r_2 = \frac{2\xi\omega_n + \sqrt{(2\xi\omega_n)^2 - 4\omega_n^2}}{2}; \quad (5.6)$$

$$A' = \frac{r_1 r_2}{r_2 - r_1} = \frac{\omega_n^2 \sqrt{(2\xi\omega_n)^2 - 4\omega_n^2}}{(2\xi\omega_n)^2 - 4\omega_n^2};$$

From these last deductions, indistinctly for the compressibility or spring reduced-linear models, by simulating and comparing the step responses of the second-order transfer function and its equivalent first-order transfer function; the results obtained are depicted in the following figure. The natural frequency,  $\omega_n$ , and the damping ratio,  $\xi$ , were determined according to the dynamic parameters defined for the compressibility and spring linear-reduced models, respectively (Eq. 5.1).

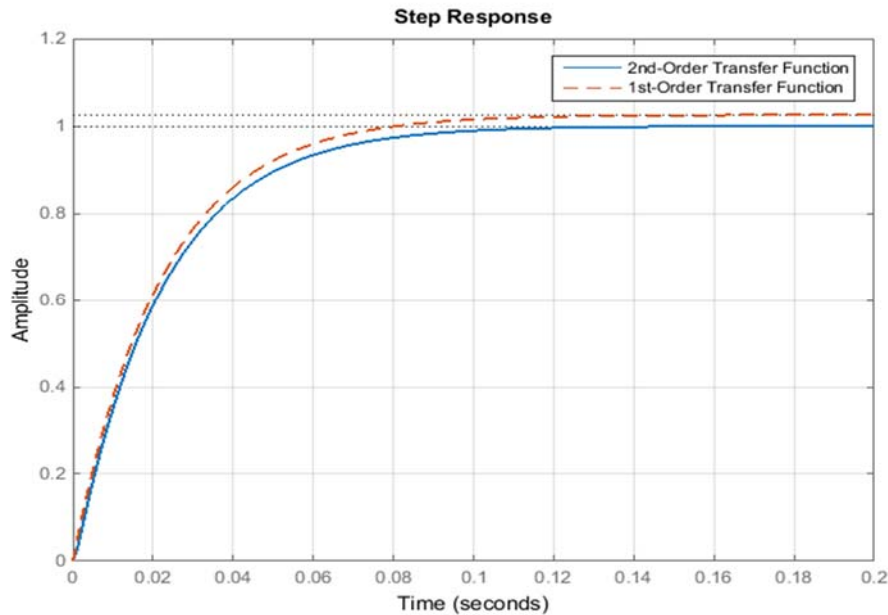


**Figure 5.32.** Ignoring a partial fraction of the second-order transfer function: Second-order block and equivalent first-order block step responses

By neglecting the partial fraction that corresponds to the fastest pole of the system, the response of the first-order block of the simplified reduced-linear model approximated the response of the second-order block of the reduced-linear model (Figure 5.32). However, a small divergence among the amplitude of the step responses was still noted. In addition, the values of the time constant,  $\tau$ , in the simplified reduced-linear model should be equal to the experimental value found in chapter 4, which was approximately equal to 0.015 seconds. For the response from the first-order block in figure 5.32, the time constant,  $\tau$ , was approximately equal to 0.022 seconds. Hence, to match more accurately the response produced by the second-order block of the reduced-linear model, and to match the experimental time constant, some of the dynamic parameters had to be adjusted.

As a first approach to compensate for the divergence between the amplitudes of the responses from the simplified and original reduced-linear models, the effective area of the piston was reduced. A lower value for the effective area of the piston should draw further away the root of the second-order characteristic equation corresponding to the fastest pole of the system, by decreasing its effect on the system dynamic response.

The following figure shows the results from reducing the effective area of the piston to half of its predetermined value.

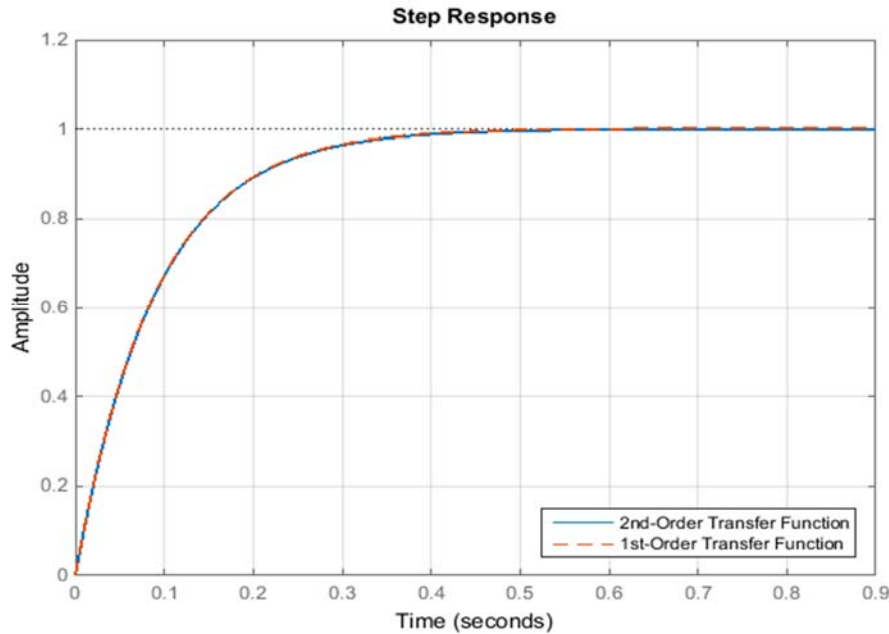


**Figure 5.33.** Ignoring a partial fraction of the second-order transfer function: Second-order block and equivalent first-order block step responses ( $A_{p-new} = 0.5 * A_{p-old}$ )

The reduction of the effective value of the area of the piston was successful in accomplishing that the response of the simplified reduced model matches the response of the original model (Figure 5.33). Nevertheless, there was a disadvantage associated with this procedure: the time constant,  $\tau$ , increased considerably. For the case in which the effective area of the piston was decreased to half of its original value, the resulting time constant was found to be approximately 0.09 seconds, which was significantly larger than the value required.

Then, to fix the inconsistency between the time constant for the simulation models, and the time constant found experimentally, the pressure gain was adjusted. Considering the definition of the time constant in Eq. 5.5, and the definition of the first root of the characteristic equation,  $r_1$ , the adjusted value for the pressure gain,  $G_D$ , was derived respectively for the compressibility and the spring models.

The corresponding expressions for the pressure gain,  $G_D$ , according to the compressibility and spring models, are respectively the following:

$$\begin{aligned} \text{Compressibility Model} \left\{ G_D = \frac{V_0 \tau}{\beta} \left( \frac{1}{\tau^2} + \frac{A_p^2 \beta}{M_{PL} V_0} \right) \right. \\ \left. \text{Spring Model} \left\{ G_D = \frac{A_p^2 \tau}{k_x} \left( \frac{1}{\tau^2} + \frac{k_x}{M_{PL}} \right) \right. \right. \end{aligned} \quad (5.7)$$

It should be noted that by comparing the pressure gain for the compressibility and the spring models, the spring constant could be defined by the following expression:

$$k_x = \frac{A_p^2 \beta}{V_0} \quad (5.8)$$

This last deduction was already inexplicitly derived in Eq. 5.2

Accordingly, by adjusting the value of the pressure gain according to Eq. 5.7, the resulting step responses are displayed in figure 5.34.

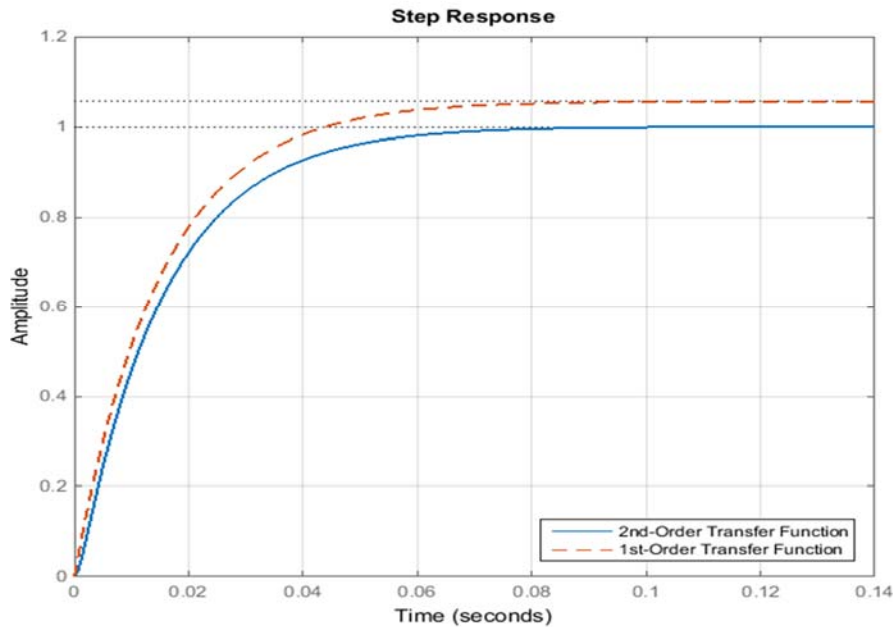


**Figure 5.34.** Ignoring a partial fraction of the second-order transfer function: Second-order block and equivalent first-order block step responses ( $G_D = 5.7\text{e-}08$  [m<sup>5</sup>/Ns])

Although now it was guaranteed that the value of the time constant corresponded to the experimental value, there was still a difference between the amplitude of the responses produced by the second-order and first-order blocks of the simplified and original reduced-linear models, respectively. Therefore, the last option to reduce this difference was to adjust the value of the spring constant, which according to Eq. 5.2, Eq. 5.7 and Eq. 5.8, would also modify the value of the pressure gain,  $G_D$ , and the effective bulk modulus,  $\beta$ . Figure 5.35 shows the results obtained by adjusting the value of the spring constant.

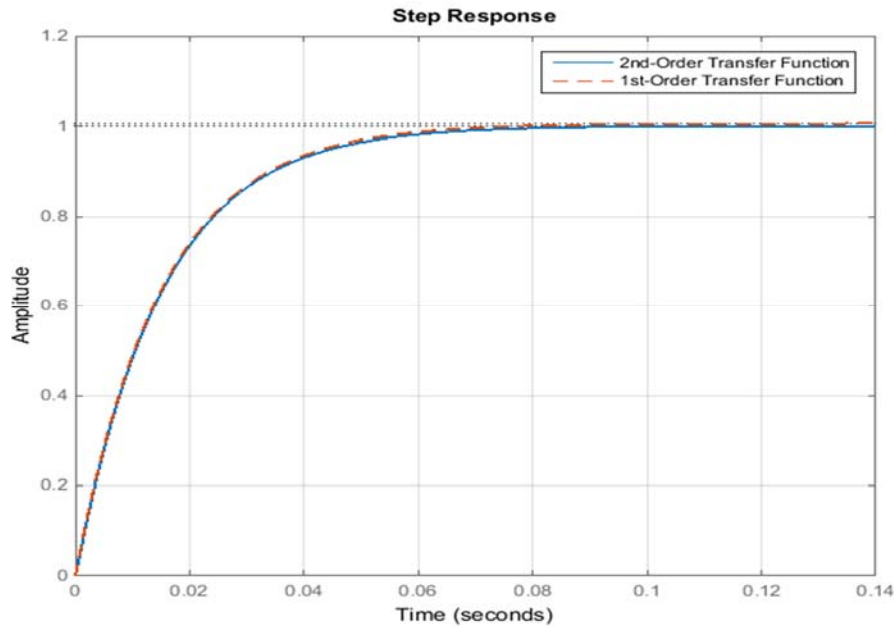


**Figure 5.35.** Ignoring a partial fraction of the second-order transfer function: Second-order block and equivalent first-order block step responses (Adjusted values:  $k_x = 250000$  [N/m];

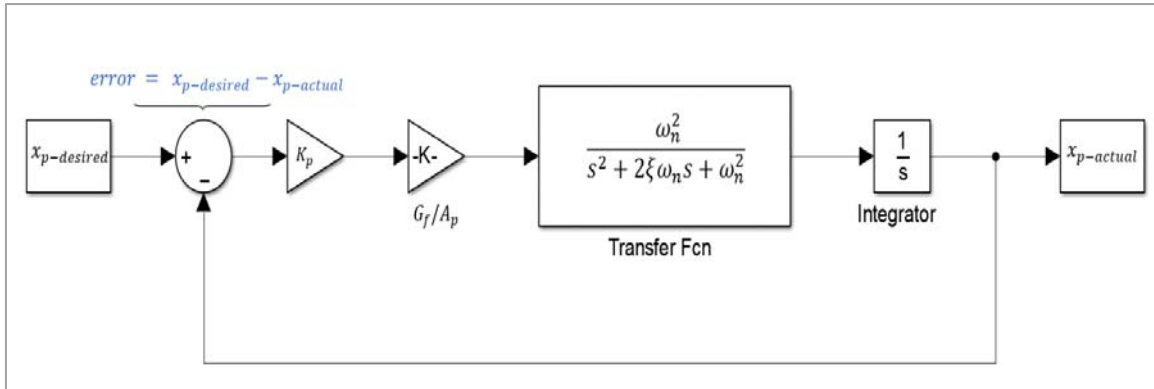
$$G_D = 5.44e-08 \text{ [m}^5\text{/Ns]}; \beta = 4.54e+07 \text{ [Pa]})$$

By adjusting the spring constant, the amplitude of the response from the first-order block matched more accurately the response from the second-order block (Figure 5.35). Nevertheless, a minimum difference between the amplitudes of the responses was still noted. Moreover, the value of the spring constant had to be increased by a factor of 10, which might not be necessary depending on the control strategy applied, and will be analyzed in the following sections of this chapter.



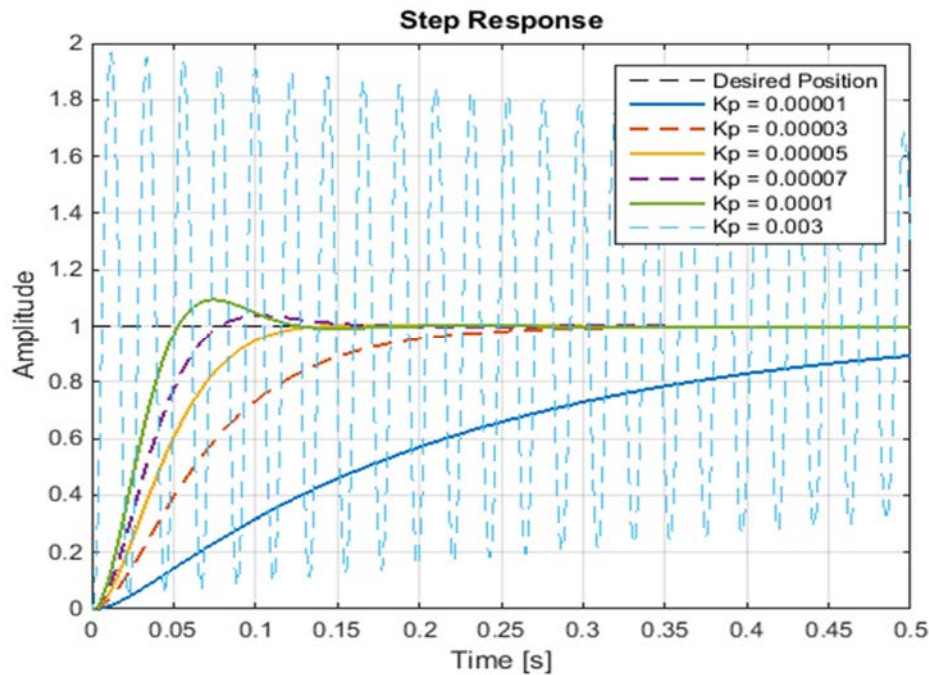
### 5.1.3. P-Control: Finding Control Gains through Root Locus Analysis

As described in chapter 3, by implementing a proportional control scheme relative to the reduced linear models for the pneumatic system, the resulting block diagram is the one displayed in figure 5.36.



**Figure 5.36.** P-Control: Simulink model for the closed-loop system.

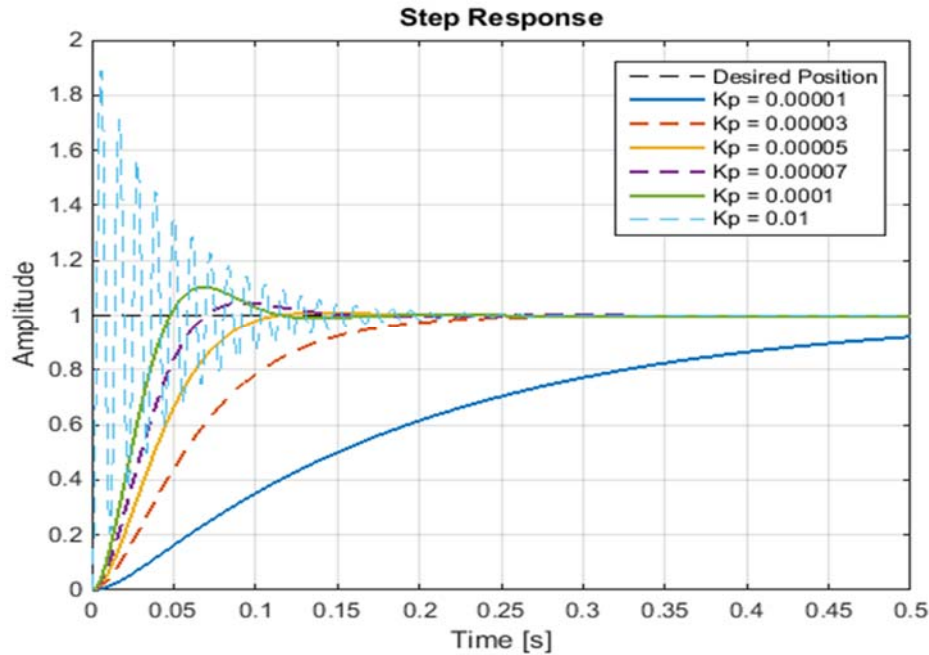
Figure 5.37 shows the closed-loop response of the pneumatic system, modeled according to the reduced-linear schemes described in section 5.1.



**Figure 5.37.** P-Control: Simulated closed-loop step response for different proportional gains  
(Adjusted Pressure gain:  $G_D = 5.6964e-08$  [ $m^5/Ns$ ])

To produce figure 5.37, the pressure gain was adjusted according to the results from figure 5.34. For proportional gains as low as 0.00001 the system would require more than 0.5 seconds to reach the desired position (Figure 5.37). Nevertheless, for proportional gains over 0.003 the system would become unstable.

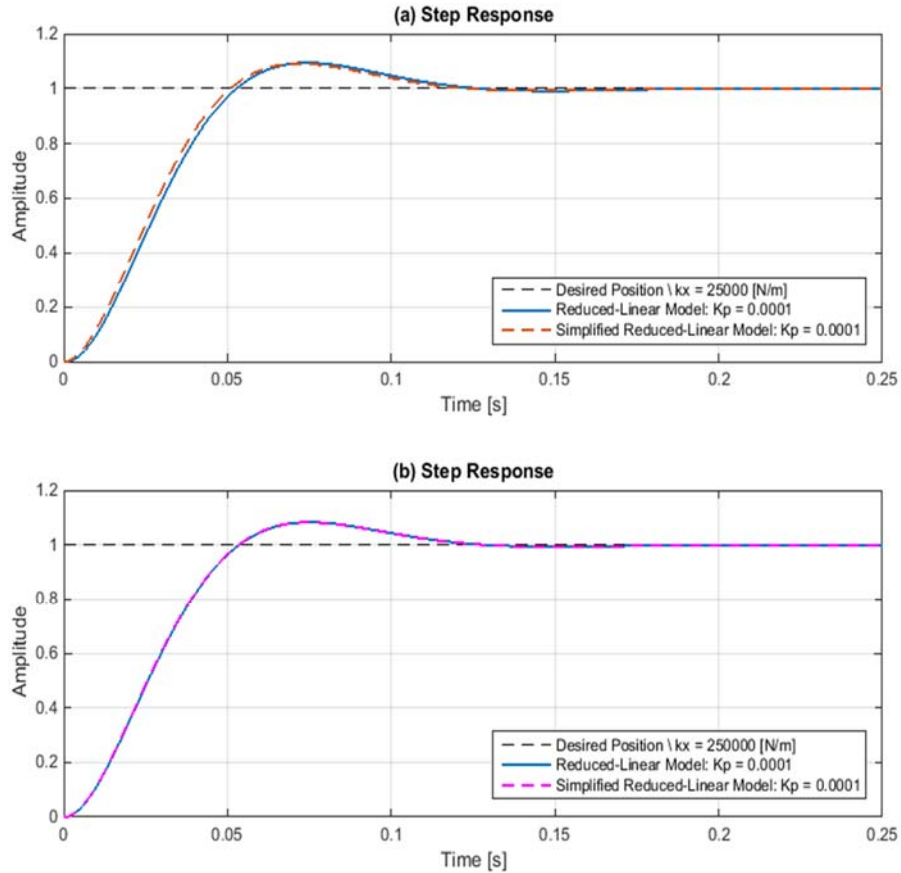
Figure 5.38 shows the closed loop response of the system according to the parameters adjusted to obtain the results presented in figure 5.35.



**Figure 5.38.** P-Control: Simulated closed-loop step response for different proportional gains ( $k_x = 250000$  [N/m];  $G_D = 5.4368e-08$  [m<sup>5</sup>/Ns];  $\beta = 4.5354e+07$  [Pa])

The increase of the value of the spring constant (Figure 5.38) augmented the amplitude of the minimum proportional gain required to turn the closed-loop system into an unstable system. In this case, for proportional gains over 0.029 the system would become unstable. This last finding was verified through root locus analysis, as described in the next pages. Moreover, independently of the response, the magnitude of the proportional gains used was relatively low, which depended on the magnitude of the parameter defined as input in the open-loop models. In the case of the model from which figure 5.36 was derived, the variable defined as input in the corresponding open-loop models was the effective area of the valve, which has operation limits between 0.0 and 1.2E-5 m<sup>2</sup>.

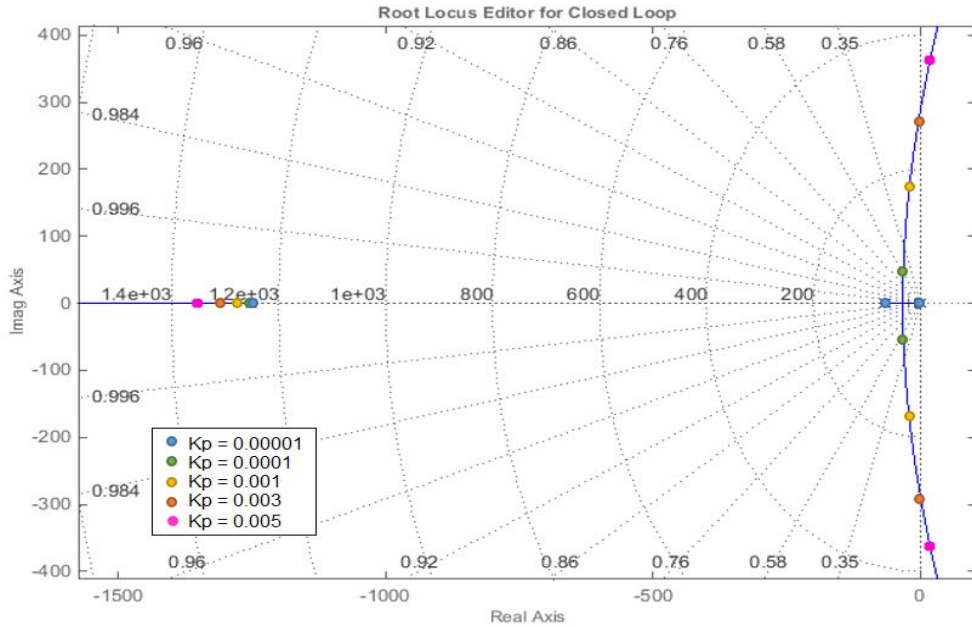
Moreover, from the simulation results of the preceding section, it was important to verify if the increase of the value of the spring constant was strictly necessary. Figure 5.39 accomplished that goal.



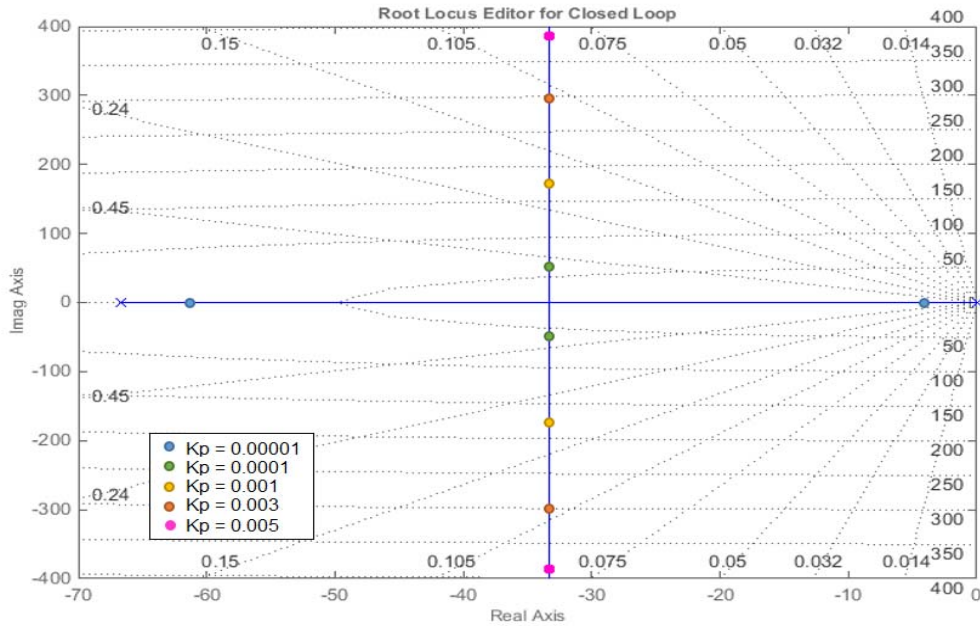
**Figure 5.39.** P-Control: Simulated step response ( $K_P = 0.0001$ ): (a)  $k_x = 25000$  [N/m],  
(b)  $k_x = 250000$  [N/m]

Figure 5.39 shows the closed-loop responses produced by the simplified reduced model and by the original reduced model for a specific proportional gain. The upper plot shows the responses obtained by keeping the spring constant equal to 25000 [N/m]; in contrast, in the lower plot the spring constant has been increased to a value of 250000 [N/m]. In both cases, the response from the simplified reduced-linear model would be satisfactory in relation to the response from the original reduced model. Although by maintaining the predetermined value of the spring constant the response of the simplified model did not exactly match the response of the original reduced model, the resulting approximation was sufficient for control purposes.

Figures 5.40 and 5.41 respectively depict the root locus for the original and simplified reduced-linear models, for the case in which only the pressure gain was adjusted. According to the proportional gains used, the closed-loop poles were identified with filled-color dots.



**Figure 5.40.** P-Control: Root Locus for the reduced-linear model ( $G_D = 5.7e-08$  [m<sup>5</sup>/Ns])



**Figure 5.41.** P-Control: Root Locus for the simplified reduced model ( $G_D = 5.7e-08$  [m<sup>5</sup>/Ns])

The root locus diagrams presented in figure 5.40 and figure 5.41 were obtained by using the SISO Design Tool of MATLAB, which is a graphical user interface for the design of single-input single-output (SISO) control systems.

As verified through figure 5.40, in the case of the original reduced-linear model, as the magnitude of the proportional gain increases, the system turns unstable because the closed-loop poles of the system pass to locate in the right-half plane of the plot. Contrariwise, in the case of the simplified reduced-linear model (Figure 5.41), as the value of the proportional gain increases the closed-loop poles of the system remain in the left-half plane of the plot. In fact, for the simplified-reduced linear system, the proportional gain may be varied from zero to an infinitely large positive value without turning the system into an unstable system. Therefore, as the proportional gain increases, for a specific set of simulation parameters, the simplified reduced model would leave to be equivalent to the original reduced-linear system.

Section 5.1.3 traced the path of the closed-loop poles of the system depending on the value of the proportional gain used, and according to the simulation models applied. Root locus analysis was fundamental in identifying that by increasing the value of the spring constant for the simulation models, the range of proportional gains for which the simplified reduced model remains equivalent to the original reduced model expands as well. Nevertheless, in validating the original or simplified reduced-linear models for a specific set of simulation parameters, the comparison with experimental results will provide the definitive verdict in chapter 6.

#### 5.1.4. Pole/Zero Cancellation: Attenuating the effect of air compressibility and the length of connective tubing

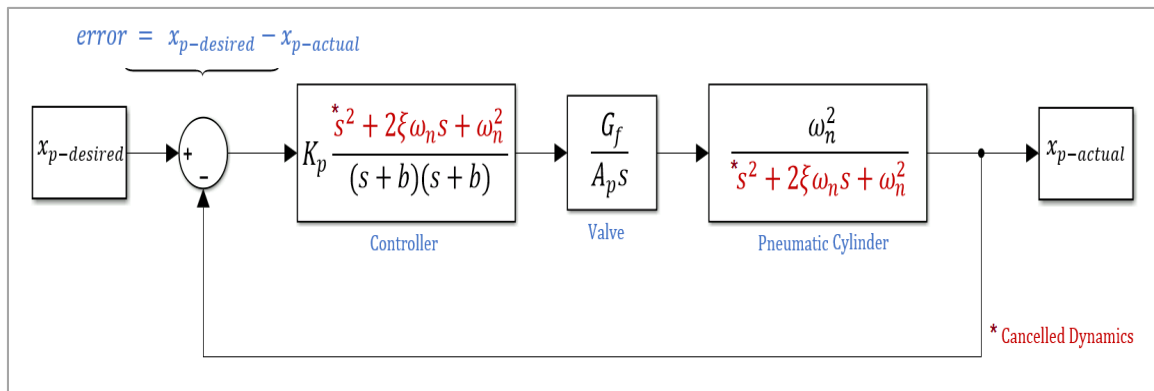


**Figure 5.42.** Pole/Zero Cancellation: Reduced Simulink model

Chapter 3 described the implementation of Pole/Zero cancellation according to the block diagram included in figure 5.42. In this section of chapter 5, pole/zero cancellation will be evaluated as a control strategy to attenuate the effect of air compressibility and the length of connective tubing in the performance of the pneumatic system.

In section 5.1.3, it was not possible to completely rule out the use of a large-amplitude spring constant in the simplified and original reduced-linear models. It was found that a large value of the spring constant enabled the simplified model to match the response of the original reduced model under the effect of proportional gains of higher value. Nevertheless, running the models, without increasing the value of the spring constant and by just adjusting the pressure gain, would also produce satisfactory results under a reduced range of proportional gains. Hence, in which remains of section 5.1, the simulation results for the reduced models are presented according to both conditions: (1) The spring constant remains equal to 25000 [N/m] and the pressure gain is adjusted to a value of  $5.6964e-08$  [ $m^5/Ns$ ]. (2) The spring constant is increased to 250000 [N/m], with the consequent variation of the pressure gain and the effective bulk modulus.

The following figures show the results from the simulation of the response of the pneumatic system for a step input, including pole/zero cancellation, and according to both cases.

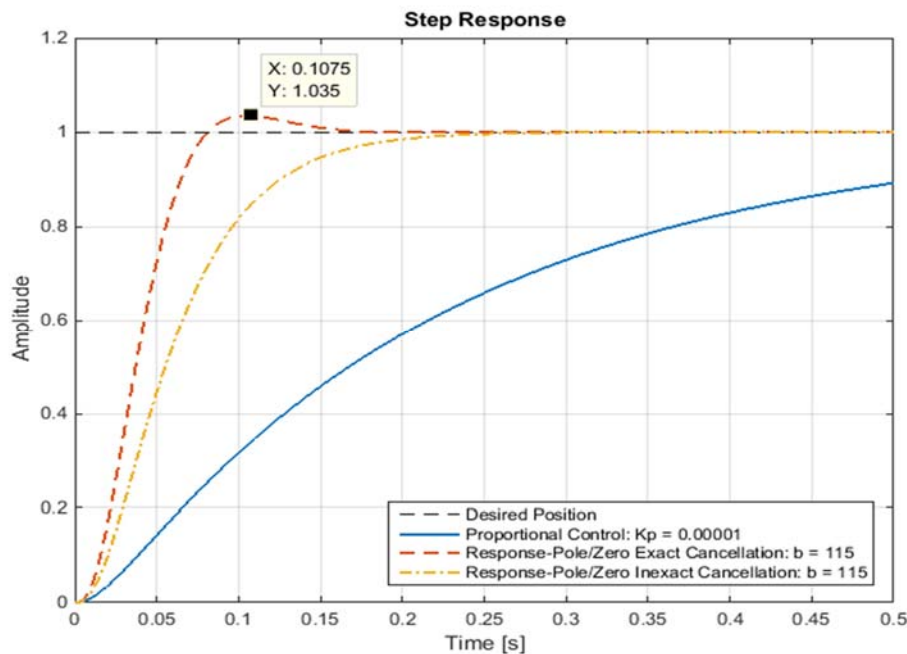


**Figure 5.43.** Pole/Zero Cancellation: Closed-loop simulation response to a step input

$$(G_D = 5.6964e-08 \text{ [m}^5/\text{Ns]})$$



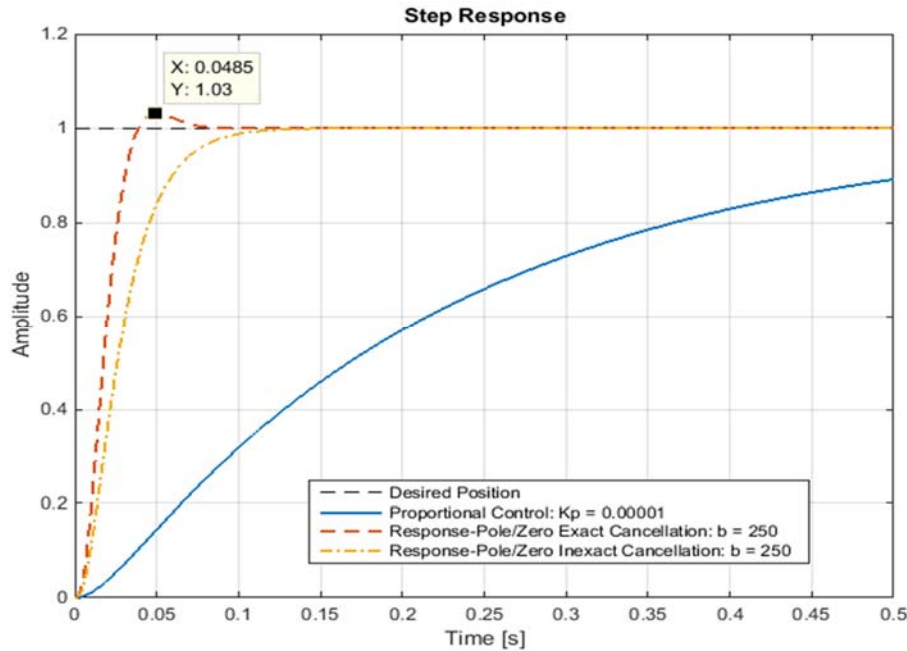


**Figure 5.44.** Pole/Zero Cancellation: Simulated step response (Adjusted values:  $k_x = 250000$  [N/m],  $G_D = 5.4368e-08$  [m<sup>5</sup>/Ns],  $\beta = 4.5354e+07$  [Pa])

Although it is not possible to completely cancel the dynamics of the plant of a system, a satisfactory approximation to the design requirements can be obtained through the implementation of response-pole/zero cancellation. As demonstrated in Figure 5.43 and Figure 5.44, response-pole/zero cancellation would produce a better response than a proportional controller, even when the zeros included in the controller are not exactly equivalent to the open-loop poles of the plant of the system (responses drawn in yellow). In contrast, the responses drawn in red would correspond to an ideal case, when the zeros included in the controller are exactly equivalent to the open-loop poles of the plant of the system.

The differences between the responses shown in Figure 5.43 and Figure 5.44 lie on the magnitude of the poles included in the denominator of the transfer function corresponding to the controller. For the case in which the spring constant remained equal to 25000 [N/m], the magnitude of these poles was lower than the magnitude of the poles included in the case where the spring constant was increased to 250000 [N/m]. In both cases, to simulate the inexact cancellation response, the natural frequency and the damping ratio included in the numerator of the transfer function of the controller were set equal to 75 percent of the actual values.

Moreover, when the dynamics of the plant were completely cancelled (Figures 5.43 and 5.44), in both cases the responses presented an approximately equal overshoot; nevertheless, in the case where the spring constant was increased, the settling time was lower than in the first case. In any case, the benefit of applying pole/zero cancellation was obvious when the responses produced by applying this control strategy are compared with the response produced by solely applying proportional control: the performance of the system was increased even for the instance where the dynamics of the plant were not exactly cancelled. This last deduction would make of pole/zero cancellation a crucial strategy to be applied in the attenuation of the effect of air compressibility and the length of connective tubing on the performance of the pneumatic system being studied. In fact, the plant dynamics that pole/zero cancellation aims to attenuate in accordance to Figure 5.42 would be particularly related to the effect of air compliance and the length of connective tubing in the performance of the pneumatic system. In other words, the poles of the system depend on the variables associated with air compliance and the length of connective tubing, as the Figure 5.45 seeks to highlight.

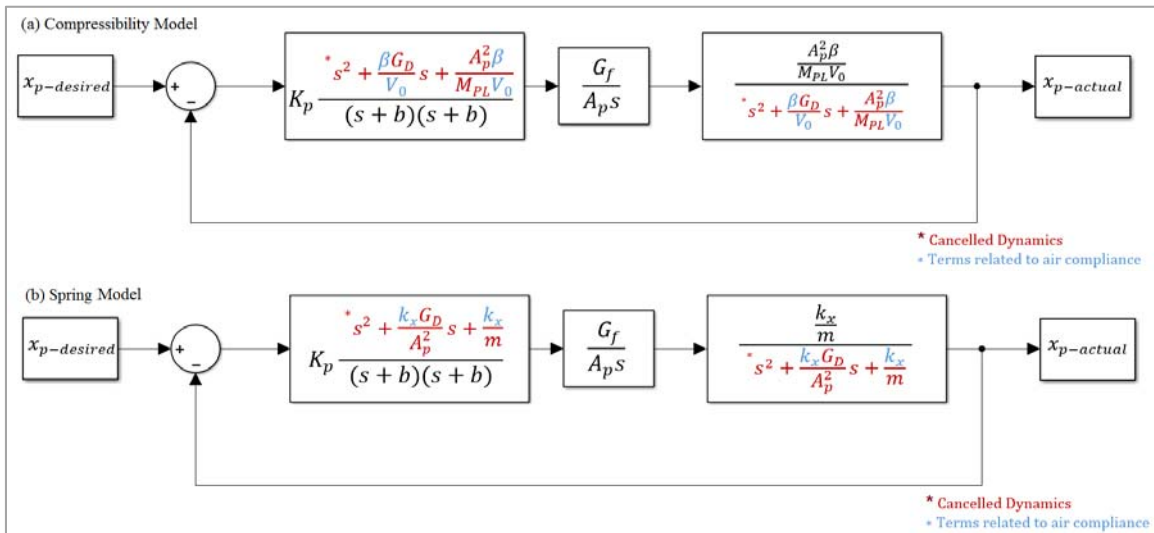


**Figure 5.45.** Pole/Zero Cancellation: Air compliance associated with the canceled dynamics in the compressibility (a) and spring (b) models.

Hence, pole/zero cancellation would annul the effect of air compliance caused by the bulk modulus of air,  $\beta$ , the volume of air in connective tubing,  $V_0$ , and the spring constant,  $k_x$ , respectively in the compressibility models and the spring models.



In that regard, a prediction of the location of the poles of the system according to the length of connective tubing was made (Figure 5.46).

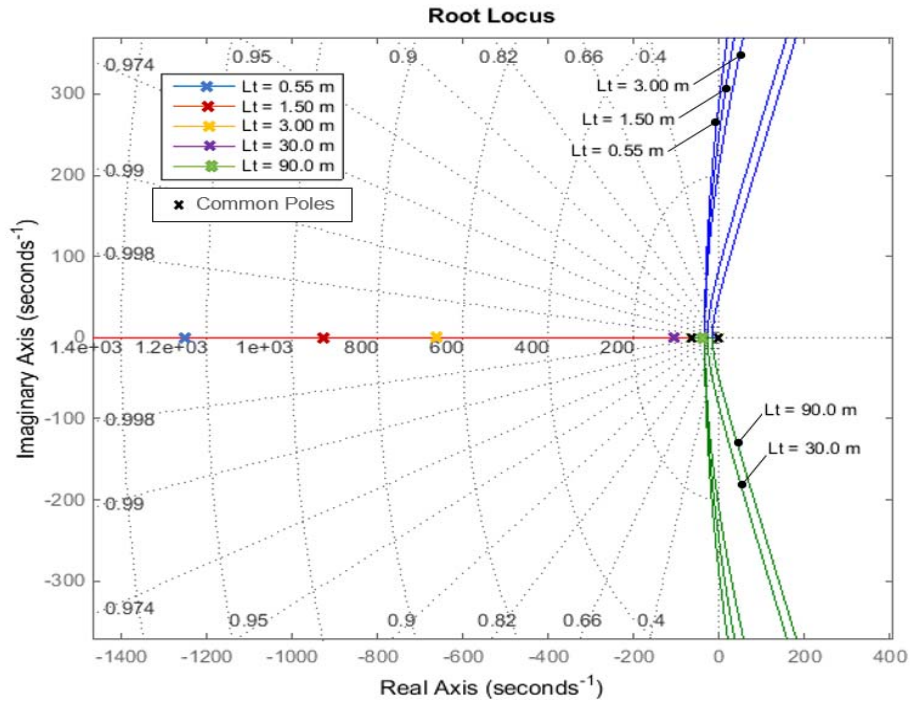


**Figure 5.46.** Root Locus depending on the length of connective tubing

In order to generate Figure 5.46, it was assumed that, if the order of the system was reduced by one as described in section 5.1.2, the time constant of the system for every different length of connective tubing was equal to the experimental time constant determined in chapter 4. This assumption was not accurate, as it was known that the increase of the length of connective tubing delays the displacement response of the pneumatic system. Nevertheless, the approximation resulted useful for the analysis of the behavior of the poles of the system according to the length of connective tubing. Based on the assumption of a unique time constant, the pressure gain and the spring constants were determined according to Eq. 5.7 and Eq. 5.8, respectively. Nonetheless, the reduction of the order of the system by one, as described in section 5.1.2 would be also compromised by the increase of the length of connective tubing. As depicted in figure 5.46, as the length of connective tubing increases, the pole neglected in order to reduce the order of the system approximates closer to the others, which would preclude the simplification of the system by reducing the order of its transfer function.

Table 5.2 summarizes the parameters used for simulation in order to generate figure 5.46.

**Table 5.2.** Simulation parameters: Prediction of the effect of the length of connective tubing

Length [m]	$\tau$ [s]	$\beta$ [Pa]	$V_0$ [m <sup>3</sup> ]	$k_x$ [N/m]	$G_D$ [Pa]	$\omega_n$ [rad/s]	$\xi$
0.55	0.015	4.54E+06	1.96E-04	25000.00	5.70E-08	288.68	2.28
1.50	0.015	4.54E+06	2.64E-04	18588.00	5.80E-08	248.92	2.00
3.00	0.015	4.54E+06	3.71E-04	13230.00	5.95E-08	210.00	1.73
30.0	0.015	4.54E+06	0.0023	2137.80	8.78E-08	84.41	1.03
90.0	0.015	4.54E+06	0.0066	746.65	1.51E-07	49.89	1.04
90.0	0.15	4.54E+06	0.0066	746.65	5.50E-07	49.89	3.81

As noticed from table 5.2, the effective value for the bulk modulus was also defined as a constant value, and it corresponds to the value defined in section 5.1.1.3, which enabled the compressibility models to match the response of the spring models and the expected response trajectory defined from experimental data. Furthermore, according to table 5.2, it could be predicted that as the length of connective tubing increases, the natural frequency and the damping ratio of the system decrease. Nevertheless, by increasing the value of the time constant, as it will occur in the actual system, the damping ratio might increase, which was corroborated by setting a random higher time constant for the case in which the length of connective tubing was equal to 90 meters, marked in blue in table 5.2. Also, from table 5.2, it is verified that the value of the spring constant and the pressure gain required to simulate the response of the system should have to be decreased and increased, respectively, as the length of connective tubing increases. The predictions made in this section should be validated through experimentation, which will be approached in the following chapter.

In conclusion for this last section, by increasing the length of connective tubing (Figure 5.46) the curvature ratio of the path of the poles in the root locus diagram decreases, which would increase the sensitivity of the system to become unstable because the poles would approximate faster to the complex axis in response to a predetermined control gain. Hence, it is justified again the application of pole/zero cancellation to annul the dynamics of the system associated with the compressibility of air and the length of connective tubing. In that regard, chapter six will present the results from the application of pole/zero cancellation as the strategy to control the pneumatic system and mask the effects of air compliance in the performance of the pneumatic system.

## 5.2. State-Space Models

Section 5.2 deals with the simulation of the response of the pneumatic system according to the state-space models derived in Chapter 3. The simulation results from the continuous-time models and the discrete-time models are presented in reference to the tracking control strategies identified in chapter 3: integral control and external reference gain tracking control. In addition, gain matrices depending on the control strategy applied are reported and recommended for implementation.

### 5.2.1. Verification of Internal Stability and Input-Output Stability Conditions

For the fourth-order system defined in chapter 3, its corresponding transfer functions are presented below. Both transfer functions are respectively associated with the inputs of the system, it is; with the input to each proportional control valve.

$$G(s)_{4^{th}-Input1} = \frac{1.264e10 s}{s^4 + 268.3 s^3 + 1.973e04 s^2} \quad (5.9)$$

$$G(s)_{4^{th}-Input2} = \frac{-1.669e08 s}{s^4 + 268.3 s^3 + 1.973e04 s^2}$$

The transfer functions defined above were determined using MATLAB. In the same way, the poles of the system were determined to be:

$$Poles_{4^{th}} = [0, -1.3417 + 0.4155i, -1.3417 - 0.4155i, 0] \quad (5.10)$$

From the values of the poles determined above, it was verified that the proposed fourth-order system was unstable because two of its poles lied on the imaginary axis. Nonetheless, although the system resulted to be unstable, it could be stabilized if the condition of controllability held for it. Therefore, in addition to the assessment of stability based on the criteria presented before, the controllability and observability conditions are tested in the following section. The proposed fourth-order state-space model should be at least controllable in order to ensure the complete or partial fulfillment of the design requirements. That the system be observable is also desirable, as the fulfillment of this condition might facilitate the implementation of the controller according to state-space control schemes.

## 5.2.2. Verification of Controllability and Observability Conditions

As stated in the previous section, section 5.2.2 embraces the verification of the controllability and observability conditions for the fourth-order state-space model derived in chapter 3.

### 5.2.2.1. *Controllability*

The software package MATLAB provides useful commands to determine the controllability matrix  $CO$ , and to verify its rank. Thus, for the equilibrium points defined in section 3.2.2.1, by using the commands “ctrb” and “rank” it was found that the fourth-order system was completely controllable. As described in chapter 3, the row rank of the controllability matrix  $CO$  had to be equal to 4 in order for the system to be completely controllable.

Moreover, due to the fact that, according to the results from section 5.2.1, the system was unstable, the confirmation of the controllability condition made the system stabilizable as well. The fact that a state-space system could not be completely controllable implies that the system was not appropriately defined, or some of the states are not directly affected by the inputs or through the controllable states.

### 5.2.2.2. *Observability*

MATLAB also provides commands to calculate the observability matrix of a system, and to check its rank. By using the commands “obsv” and “rank”, it was found that for the equilibrium points defined in section 4.3.1, the fourth-order system used to describe the pneumatic system under study was not observable. Therefore, for certain state variables of the system, it may not be possible to reconstruct their initial values from the resulting output. In that regard, the fact that one or more states are not observable would add complexity and cost to the implementation of a controller, since additional sensors might have to be included in order to acquire the feedback signals required.

To ensure that the condition of observability held for the state-space system defined in chapter 3, one option was to redefine the matrices  $A$  and  $B$  by selecting a different equilibrium point, as it is described below.

From the condition for which at the equilibrium point the derivatives of the state variables become zero, for the state variable representing the pressure in the rod-end chamber of the cylinder ( $\dot{x}_4 = 0$ ), the following expression has to be true:

$$\phi_f(x_4, P_{Rv2})u_2 \cong 0 \quad (5.11)$$

Accordingly, the input  $u_2$  must be equal to zero, which was the choice for defining the equilibrium points before, or the flow function,  $\phi_f$ , must be equal to zero. The flow function,  $\phi_f$ , is zero when the downstream to upstream pressure ratio  $P_{Rv}$  is equal to 1. Nevertheless, by setting the value of the flow function to zero, the resulting system was still not observable. In that case, another option was to approximate Eq. 5.11 to zero, by determining what minimum value of  $\phi_f$  kept the system controllable and observable. The minimum value found was 0.00015, which provided a good approximation of Eq. 5.11.

In the case of the flow function associated with the pressure variation in the cap-end cylinder chamber, the flow function was set equal to 0.6. This value was deducted from experimental data in relation to the computation of the flow provided by the control valves, as described in chapter 4. A constant value for the flow function facilitates the computation relative to the state-space models. In actual conditions, the flow function varies between 0.6843, when the flow is choked, to zero once the flow becomes unchoked. In that regard, through experimental data it was verified that the flow function normally fluctuates between 0.6843 and approximately 0.5, reason for which a median value of 0.6 was assumed in table 4.16.

In the case of setting the flow function approximately equal to zero, the operating condition under which the pressure ratio  $P_{Rv}$  in the second valve approximates to a value of 1 would correspond to a valve-opening area equivalent to the maximum effective area for the valve. Accordingly, the alternative equilibrium points to ensure controllability and observability of the system proposed would be:

$$\begin{aligned} x^* &:= (x_1^*, x_2^*, x_3^*, x_4^*) = (X_e, 0, P_{e1}, P_{e2}) \\ u_1^* &:= 0; \quad u_2^* := 1.2 \times 10^{-5} \end{aligned} \quad (5.12)$$

As it can be noticed, the state-variable equilibrium points would remain the same, as the only change is in the equilibrium point for the input to the second valve. The equilibrium position,  $X_e$ , was defined as the middle of the stroke of the piston.

Based on the equilibrium points defined in Eq. 5.12 and according to the criteria applied in section 5.2.1, it was found that the system was still unstable; however, now the system was completely controllable and observable. Hence, it was decided to continue the design process with the state-space matrix defined according to the equilibrium points reported in Eq. 5.12.

### 5.2.3. Linear Quadratic Regulator (LQR) Design: Finding the Control Gain Matrix

Once it was confirmed that the fourth-order model proposed was completely controllable, it was feasible to continue with the design of the controller based on a LQR scheme. The next step in the design procedure involved finding the weighting matrices  $Q_J$  and  $R_J$ , as described in chapter 3, section 3.2.2.4. The weighting matrices  $Q_J$  and  $R_J$  found are:

$$Q_J = \begin{bmatrix} 1000 & 0 & 0 & 0 \\ 0 & 1 & 0 & 0 \\ 0 & 0 & 0 & 0 \\ 0 & 0 & 0 & 0 \end{bmatrix}; \quad R_J = \begin{bmatrix} 1000 & 0 \\ 0 & 1000 \end{bmatrix} \quad (5.13)$$

A satisfactory response was obtained by increasing the value of the term in  $Q_J$  that corresponded to the position state. Also, it was verified that as the value of the term corresponding to the velocity state tended to zero, the response settling time decreased. Likewise, the terms relative to the error from the pressure in the cylinder chambers were set to zero, which enabled the system to produce a satisfactory response. Accordingly, by using MATLAB the gain matrix found is:

$$K = \begin{bmatrix} 1.000 & 0.0300 & 2.5924e-08 & -2.1376e-08 \\ 2.5423e-04 & 7.6310e-06 & 6.5908e-12 & -5.4345e-12 \end{bmatrix} \quad (5.14)$$

According to the gain matrix presented above, the coefficients associated with the pressure in the cylinder chambers could be approximated to zero. Nevertheless, it might be appropriate to check the order of magnitude of the error from the pressure in the chambers, since as the pressure is expressed in Pascals, the resulting error for certain operation conditions could be relatively high, and for that instance the gains might produce a considerable effect in the response of the system.

From the implementation of the solutions presented above, the system computer-simulated step responses are presented in the following figures (Figures 5.47 and 5.48).

Figure 5.47 describes the open-loop response of the system, while figure 5.48 describes the closed loop response according to the LQR control law from Eq. 4.68.

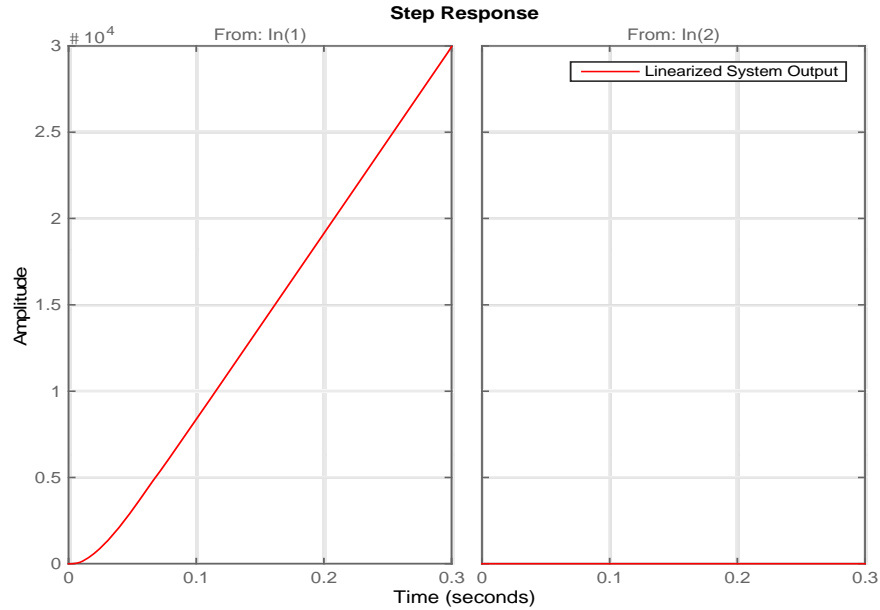


**Figure 5.47.** Continuous-time simulation: Open-loop step response

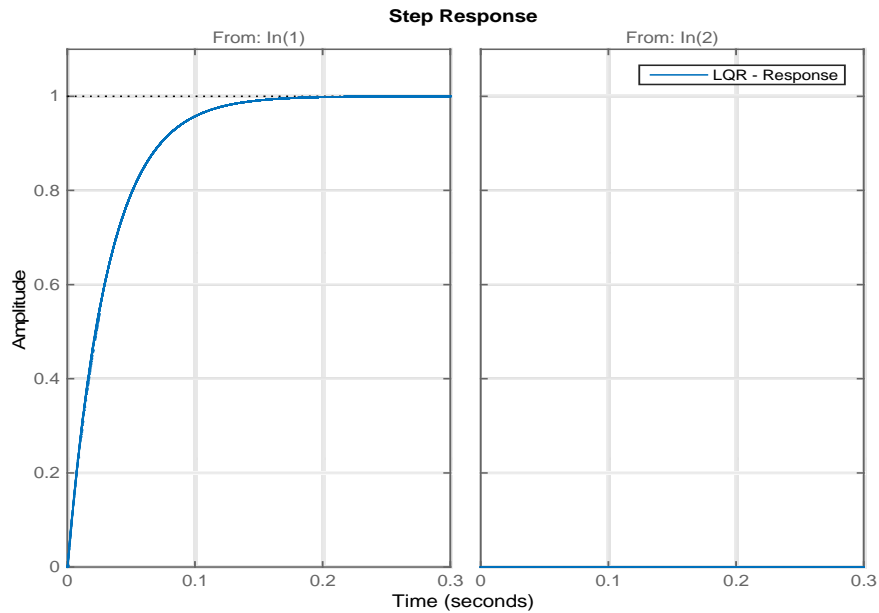


**Figure 5.48.** Continuous-time simulation: Closed-loop step response with LQR control law implemented

As shown in figures 5.47 and 5.48, the implementation of the LQR control law would enable the system to stabilize around a desired position; nevertheless, a command reference input still has not been included. The next section deals with the design of a controller that depends on a command reference input, and the performance of which can be assessed in terms of its steady-state accuracy.

#### 5.2.4. Tracking Control Design: Simulation Response

As stated before, this section includes the simulation response of the pneumatic system according to a command reference input. In that regard, the results from the simulation of the response of the system relative to an integral tracking control scheme, and an external reference gain control scheme are reported.

##### 5.2.4.1. *Integral control*

As described in chapter 3, by applying integral control the state-space representation of the system is modified as follows:

$$\begin{bmatrix} \dot{x} \\ \dot{x}_i \end{bmatrix} = \begin{bmatrix} A & 0 \\ -C & 0 \end{bmatrix} \begin{bmatrix} x \\ x_i \end{bmatrix} + \begin{bmatrix} B \\ 0 \end{bmatrix} u + \begin{bmatrix} 0 \\ 1 \end{bmatrix} r \quad (5.15)$$

With a control law defined by:

$$u = -Kx - K_i x_i = -\begin{bmatrix} K & K_i \end{bmatrix} \begin{bmatrix} x \\ x_i \end{bmatrix} \quad (5.16)$$

Where  $K$  and  $K_i$  are the matrix gains for the original and the augmented system, respectively.

By defining the state-space model according to Eq. 5.18, and by following the procedure described in section 5.2.3 to find the matrix gains, the  $Q_J$ ,  $R_J$ ,  $K$ , and  $K_i$  matrices found are:

$$Q_{J-Integral} = \begin{bmatrix} 0.01 & 0 & 0 & 0 & 0 \\ 0 & 0 & 0 & 0 & 0 \\ 0 & 0 & 0 & 0 & 0 \\ 0 & 0 & 0 & 0 & 0 \\ 0 & 0 & 0 & 0 & 50 \end{bmatrix}; \quad R_{J-Integral} = \begin{bmatrix} 1 & 0 \\ 0 & 1 \end{bmatrix}; \quad (5.17)$$



$$K_{Integral} = \begin{bmatrix} 0.1284 & 2.7464e-04 & 2.4798e-09 & -2.0447e-09 \\ 3.2634e-05 & 6.9822e-08 & 6.3042e-13 & -5.1981e-13 \end{bmatrix};$$

$$K_{iIntegral} = \begin{bmatrix} -7.0711 \\ -0.0018 \end{bmatrix};$$

From the definition of  $Q_J$  and  $R_J$ , it was verified that as the term of  $Q_J$  associated with the feedback error, or the error from the additional state increased, and the term associated with the position error decreased, the settling time decreased. Also, it was found that the coefficients of  $R_J$  did not cause major impact in the response of the system. Indeed, the coefficients of  $Q_J$  associated with the velocity error, and the error relative to the pressure in the chamber were all set to zero, which enabled the system to reach the desired position.

Figure 5.49 shows the system computer-simulated response to a step input, with an integral control law implemented. The simulation was run in MATLAB.

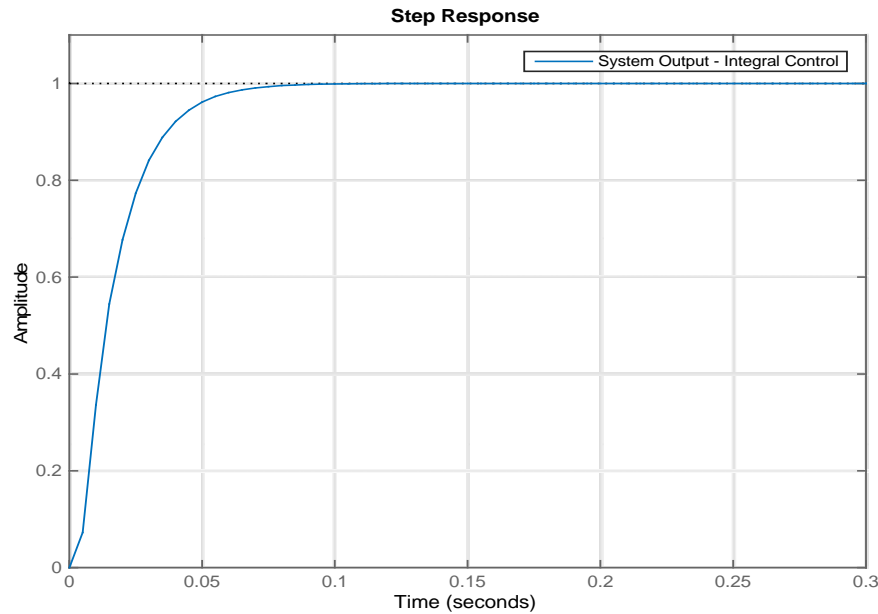


**Figure 5.49.** Continuous-time simulation: Step response with Integral control law implemented

Figure 5.4 shows a single response, in contrast to the case where a LQR scheme was implemented, as verified in figures 5.48, where the output from each input constituted the global response of the system.

#### 5.2.4.2. External reference gain tracking control

External reference gain tracking control characterizes for placing a reference gain,  $\bar{N}$ , outside the feedback loop. In chapter 3, this reference gain was defined according to the following expression.

$$\bar{N} = -\frac{1}{C(A - BK)^{-1}B} \quad (5.18)$$

According to Eq. 5.18, to implement a feedforward compensator; first, a gain matrix,  $K$ , should be determined following a pole placement method. Thus, by following the procedure for the design of a Linear Quadratic Regulator, the weighting matrices  $Q_J$  and  $R_J$ , and the gain matrix  $K$  corresponded to the same matrices determined in section 5.2.3. Then, in basis to Eq. 5.18, the reference gain found was:

$$\bar{N} = [1.0003 \quad 1.0003] \quad (5.19)$$

The continuous-time simulation response obtained through MATLAB is presented below.

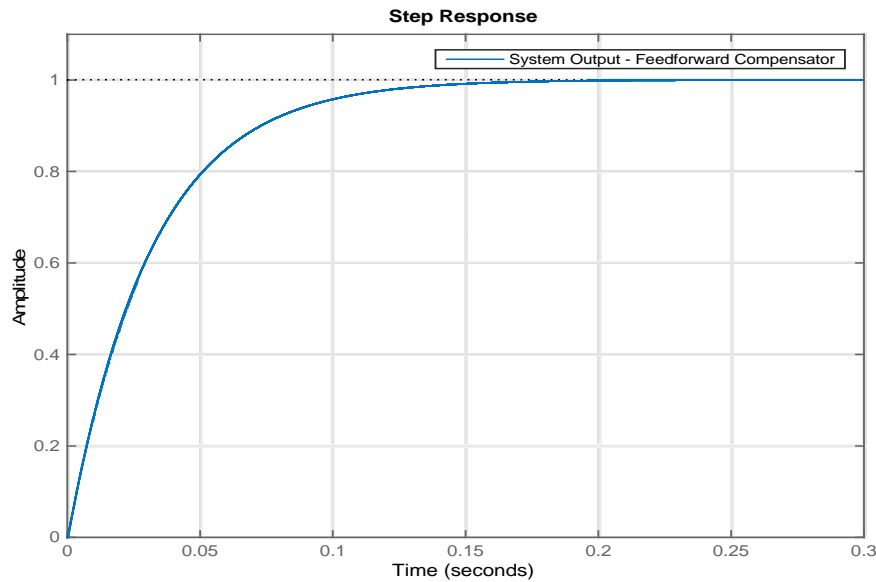


**Figure 5.50.** Continuous-time simulation: Step response according to External reference gain tracking control scheme

Based on the methodologies applied in this section, the following section determines the gain matrices for the discretized system according to the different control strategies proposed.

### 5.2.5. System Discretization: Simulation Response

From applying the commands that MATLAB provides for discretizing continuous-time state-space systems, the discrete gain matrices, and the corresponding simulated responses were obtained by defining a constant sampling time of 6.0 milliseconds. This sampling time was found experimentally for the ARDUINO UNO board used.

Without including a tracking control scheme, from the design of a linear quadratic regulator for the discretized system, the weighting matrices  $Q_{JD}$  and  $R_{JD}$ , and the gain matrix  $K_D$  found are:

$$Q_{JD} = \begin{bmatrix} 1 & 0 & 0 & 0 \\ 0 & 0 & 0 & 0 \\ 0 & 0 & 0 & 0 \\ 0 & 0 & 0 & 0 \end{bmatrix}; \quad R_{JD} = \begin{bmatrix} 1 & 0 \\ 0 & 1 \end{bmatrix} \quad (5.20)$$

$$K_D = \begin{bmatrix} 1.0384 & 8.5564e-05 & 1.2860e-09 & -3.4459e-09 \\ 10.2855 & 1.0217e-06 & 6.8914e-13 & -3.1848e-06 \end{bmatrix}$$

Where the subscript “D” denotes discrete time. The following figure shows the simulated response of the discretized system, by including the control law corresponding to a LQR scheme.

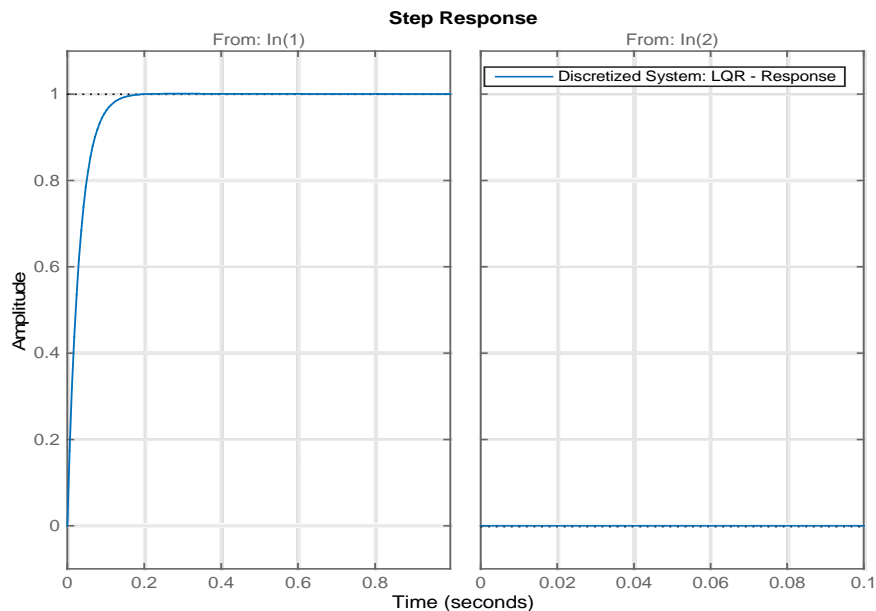


**Figure 5.51.** Discrete-time simulation: Closed-loop step response with LQR control law implemented

Likewise, by implementing an integral tracking control scheme, the weighting matrices, and the corresponding gain matrices for the discretized system result to be:

$$Q_{JD-Integral} = \begin{bmatrix} 0 & 0 & 0 & 0 & 0 \\ 0 & 0.00005 & 0 & 0 & 0 \\ 0 & 0 & 0 & 0 & 0 \\ 0 & 0 & 0 & 0 & 0 \\ 0 & 0 & 0 & 0 & 20000 \end{bmatrix};$$

$$R_{JD-Integral} = \begin{bmatrix} 0.00001 & 0 \\ 0 & 0.1 \end{bmatrix}; \quad (5.21)$$

$$K_{DIntegral} = \begin{bmatrix} 973.4382 & 0.0131 & 1.5554e-07 & -1.2753e-07 \\ 10.2926 & -1.2127e-05 & 6.6886e-11 & -3.1866e-06 \end{bmatrix};$$

$$K_{iDIntegral} = \begin{bmatrix} -4.4721e+04 \\ 0.0034 \end{bmatrix};$$

The following figure shows the simulated step response of the discretized system when an integral tracking control scheme was implemented.

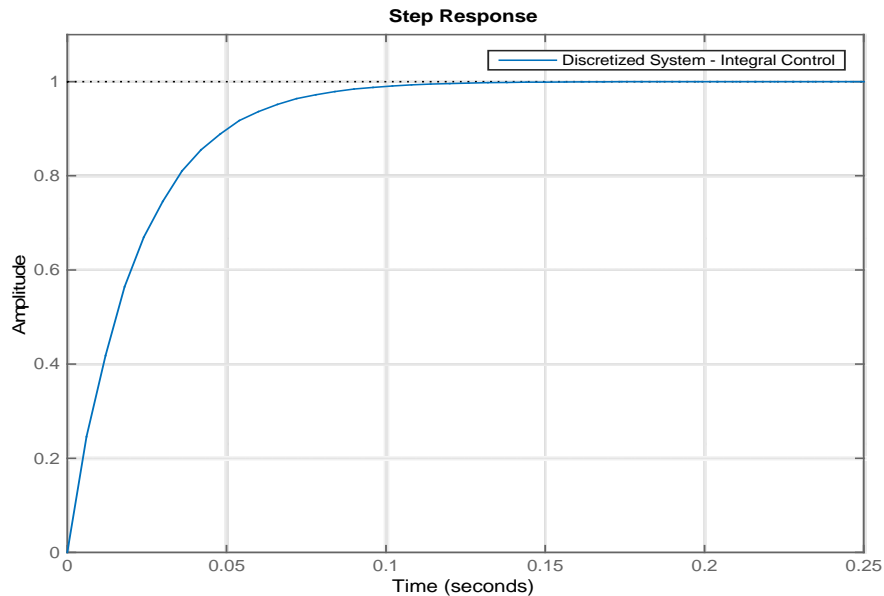


**Figure 5.52.** Discrete-time simulation: Step response with Integral control law implemented

Finally, in the case that a feedforward compensator is designed for the discretized system, the weighting matrices  $Q_{JD}$  and  $R_{JD}$ , the gain matrix  $K_D$ , and the reference gain,  $\bar{N}_D$ , result to be:

$$\begin{aligned}
 Q_{JD-External} &= \begin{bmatrix} 1 & 0 & 0 & 0 \\ 0 & 0 & 0 & 0 \\ 0 & 0 & 0 & 0 \\ 0 & 0 & 0 & 0 \end{bmatrix}; \quad R_{JD-External} = \begin{bmatrix} 0.5 & 0 \\ 0 & 0.05 \end{bmatrix} \\
 K_{D_{External}} &= \begin{bmatrix} 1.4432 & 8.6083e-05 & 1.2900e-09 & -4.8187e-10 \\ 10.2889 & 1.2182e-06 & 1.3910e-12 & -3.1848e-06 \end{bmatrix} \\
 \bar{N}_D &= [1.4148 \quad 1.4148]
 \end{aligned} \tag{5.22}$$

The simulated response of the discretized system including an external reference gain is presented in the following figure:

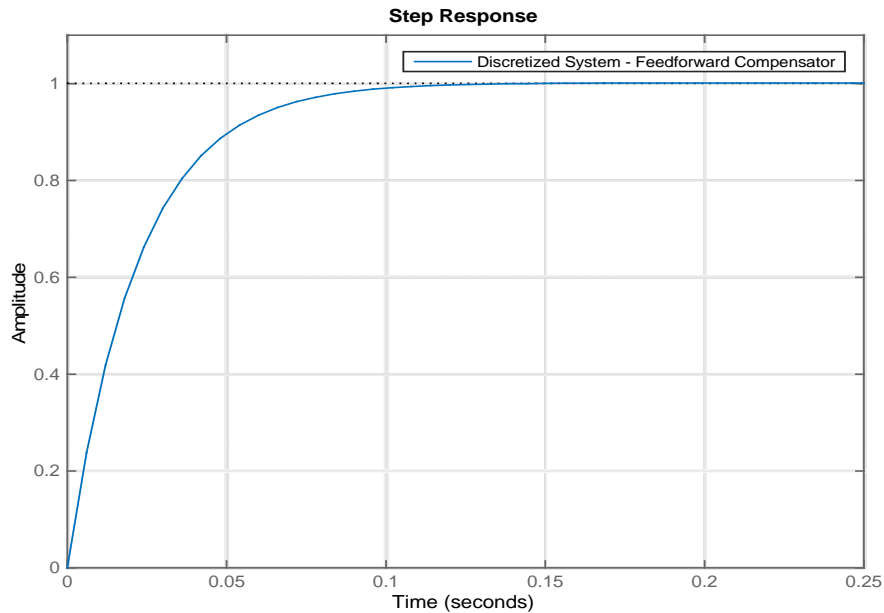


**Figure 5.53.** Discrete-time simulation: Step response according to External reference gain tracking control scheme

The weighting matrices, and the gain matrices found for the discretized system differed from the matrices determined for the continuous-time system, which constitutes the main factor to be considered for implementation of the controller: the results obtained through simulation cannot be directly implemented in real control applications. In that regard, chapter 6 describes the implementation of different control strategies in reference to simulation models developed throughout this thesis.

## CHAPTER VI

### EXPERIMENTAL RESULTS

#### Hypothesis Validation

The validation of the project hypothesis assesses to what extent the goals of this thesis have been accomplished. The validation process centers on the comparison of results obtained through simulation and actual implementation of the control strategies proposed. The main purpose of this chapter is to answer the research question encompassed in the hypothesis:

*“Is a control algorithm able to attenuate the detrimental effects of air compliance and the length of connective tubing on the performance of pneumatic cylinders?”*

From the comparison of experimental and simulation results, analytical models applied, and assumptions made in this thesis will have to be confirmed, complemented, or annulled. Moreover, from the validation of the hypothesis, guidelines for correction, improvement and/or modification of the scientific method applied will be identified and discussed.

#### 6.1. Characterization of Pneumatic Attenuation in Lengthy Connective Tubing

To analytically describe the attenuation of pressure and flow in lengthy connective tubing mounted relative to pneumatic cylinders and remotely positioned control valves, a model proposed by [Whitemore and Leondes \(1991\)](#) was validated. This model describes the propagation of pressure variations through connective tubing as a combination of frictional attenuation and wave reflection. Considering that pressure variations propagate in the form of longitudinal waves through connective tubing, the model seeks to account for the attenuation caused by friction along the walls of the tubing, and the amplification or damping caused by pressure waves reflected from the downstream end of connective tubing.

The proposed model constitutes an approximation of an original model ([Whitemore, 1988](#)) derived from the application of the Navier-Stokes equations of continuity and momentum. The original model is approximated through a second-order linear filter, which was described in chapter 2, section 2.4.

This second-order model is supposed to be able to match the pressure wave behavior up to the second harmonic if the natural frequency,  $\omega_{nt}$ , and the damping ratio,  $\xi_t$ , of the pressure waves in pneumatic tubing are appropriately selected.

Hence, as part of the identification of pressure profiles in pneumatic connective tubing; as described in chapter 4, section 4.3.2, it was verified if the second-order linear filter model adjusts to experimental frequency-response data.

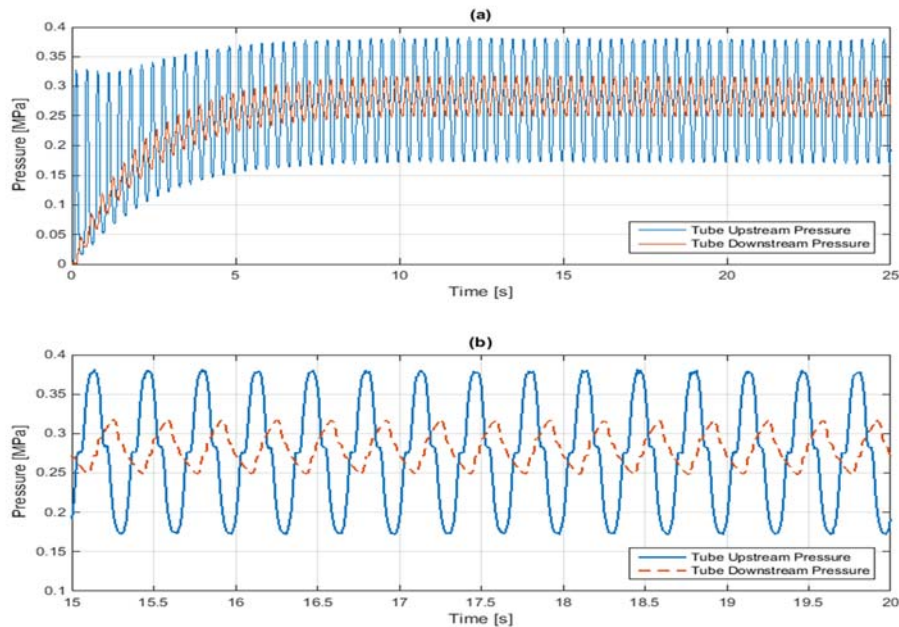


**Figure 6.1.** Responses to a 3.0-Hz sinusoidal command input to the valves: (a) 31.5-meter tube upstream and downstream pressure. (b) Closer view of upper subplot (a).

According to the experimental procedure described in chapter 4, a sinusoidal pressure input was generated using one of the proportional control valves included in the experimental setup. From the transient data collected (Figure 6.1), the frequency response corresponding to the pressure profile was obtained by computing the Fast Fourier transform of the input and output pressure signals at the inlet and outlet of the tube. The Fast Fourier transform converts the time-domain data collected into frequency-domain data, so that the magnitude and the phase of the response can be calculated and visualized in a Bode plot diagram. The Fast Fourier (FFT) transform of the data collected was computed using the command “fft” in MATLAB, which returns the discrete Fourier transform of an input vector according to a FFT algorithm.

Using the data converted into the frequency domain, a transfer function estimate,  $H$ , can be computed using the following expression (Broersen, 1995):

$$H(e^{j\omega}) = \frac{\frac{1}{S} \sum_{i=1}^S Y_N^{(i)}(\omega) U_N^{(i)}(\omega)^*}{\frac{1}{S} \sum_{i=1}^S U_N^{(i)}(\omega) U_N^{(i)}(\omega)^*} \quad (6.1)$$

Where  $U_N^{(i)}(\omega)$  and  $Y_N^{(i)}(\omega)$  are the Fourier transforms of subframe  $i$  of length  $N$  corresponding to the transient input and output respectively defined for a specific case, and  $S$  is the total number of observations.

In this case, the input and output vector corresponded to the pressure at the inlet and outlet of the pneumatic tube tested. Eq. 6.1 would provide a smoothed estimate of the transfer function associated with the frequency response of the input and output data collected. From the results of Eq. 6.1, the magnitude and phase of the frequency response were computed using the following expressions:

$$\begin{aligned} \text{MAGNITUDE}_H &= 20 \log(|H(e^{j\omega})|) \\ \text{PHASE}_H &= \tan^{-1} \left[ \frac{\text{Im}\{H(e^{j\omega})\}}{\text{Re}\{H(e^{j\omega})\}} \right] \end{aligned} \quad (6.2)$$

Where  $Im$  and  $Re$  represent the imaginary and real part of  $H$ , respectively. Moreover, the magnitude and phase of  $H$  would be expressed in units of decibels and radians, correspondingly.

In addition, from Eq. 2.65, the theoretical transfer function would be given by:

$$G(s) = \frac{P_{dt}(s)}{P_{ut}(s)} = \frac{\omega_{nt}^2}{s^2 + 2\xi_t \omega_{nt} s + \omega_{nt}^2} \quad (6.3)$$

Hence, the Bode diagrams corresponding to the experimental and theoretical frequency response associated with the pressure profile in pneumatic connective tubing were generated using Eq. 6.2 and Eq. 6.3, respectively. From the first estimate of the theoretical natural frequency,  $\omega_{nt}$ , and damping ratio,  $\xi_t$ , using Eq. 2.66, the theoretical results did not fit the experimental results perfectly (Fig. 6.2). Reasons for the divergence between the theoretical and experimental results might include: inappropriate experimental setting and equipment, the assumptions for the theoretical model might not fit actual conditions, and the data-processing approach might be inappropriate or inaccurate.



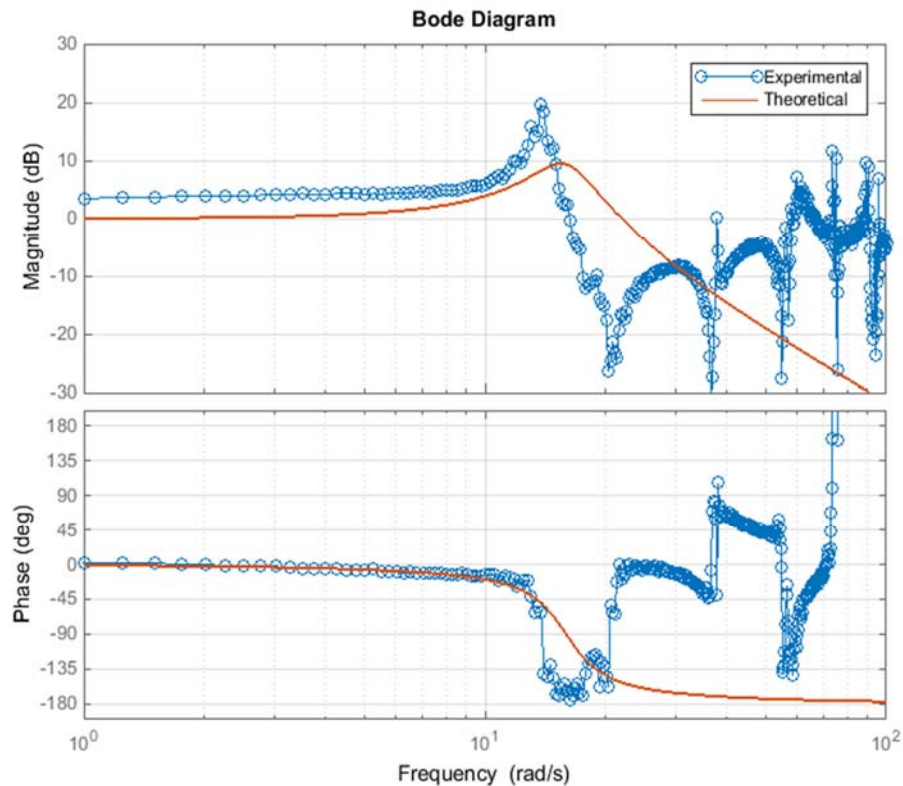


**Figure 6.2.** Frequency response of pressure variation in 30.5-meter tubing

Nevertheless, there might be a close correlation between the theoretical and experimental results (Figure 6.2). The main difference would be caused by the natural frequency and damping ratio entered in the theoretical model. Moreover, the second-order linear filter model would be valid for matching the pressure wave behavior up to the second harmonic of the wave pattern. In that regard, [Bergh and Tijdeman \(1972\)](#) reported that the magnitude of the second harmonic of pressure waves that propagate in pneumatic tubing would be negligible in comparison to the first harmonic, with exception of tubing of large section area and short length.

The magnitude peak that occurs at the break frequency would reveal the first harmonic of the pressure wave pattern; hence, the model would be accomplishing its goal. In fact, as noticed by [Whitemore \(1988\)](#), because of the difference of magnitude between the first and second harmonic of the wave pattern, the second-order linear filter would not be greatly restricted. In the case of 30.5-meter connective tubing, the second harmonic occurred at a frequency approximately equal to 30 rad/s, which is twice the frequency at which the first harmonic was identified (Figure 6.2).

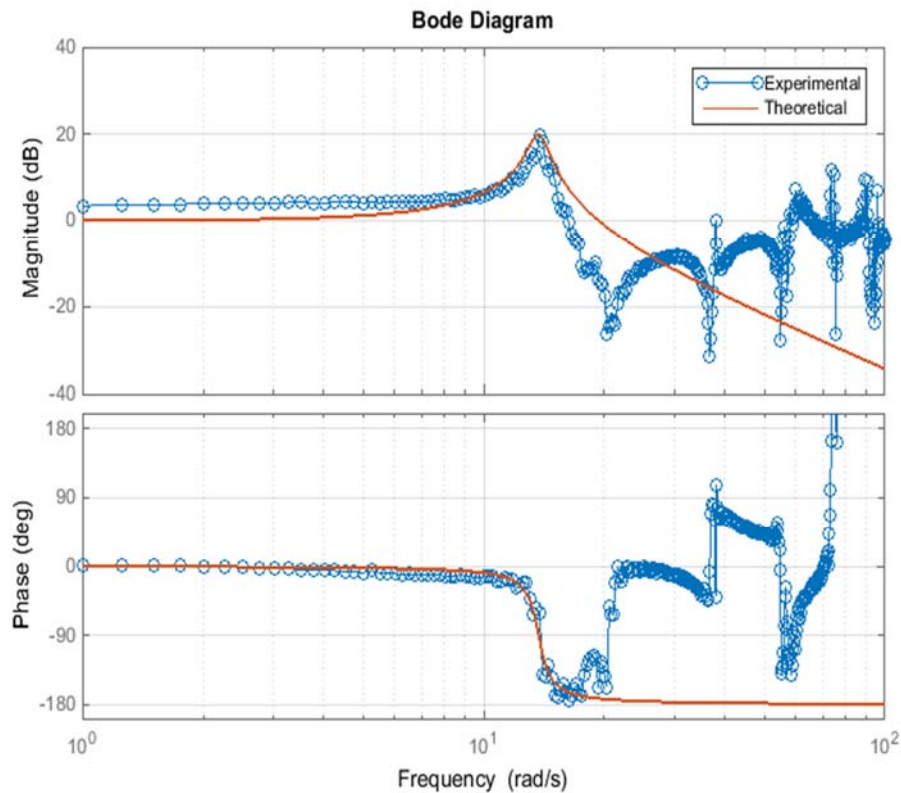


**Figure 6.3.** Frequency response of pressure variation in 30.5-meter tubing when the parameters of the theoretical model were adjusted

The adjustment of the values for the theoretical natural frequency and damping ratio produced a closer correlation between the theoretical and experimental frequency responses (Figure 6.3). The first and second wave harmonics observed correspond to the dominant pressure wave harmonics within the tube; while above 20 rad/s, the magnitude and phase frequency response correspond to the reflected pressure wave harmonics.

Therefore, by making the second-order linear filter model to match the actual pressure wave behavior at least up to its second harmonic, an effective model to account for the effect of pneumatic distortion in lengthy hoses connecting the control valves and the pneumatic cylinder could be implemented (Figure 6.4). The main advantage of the theoretical model would be represented by its capability to estimate the natural frequency and damping ratio associated with the pressure distortion in pneumatic connective tubing.

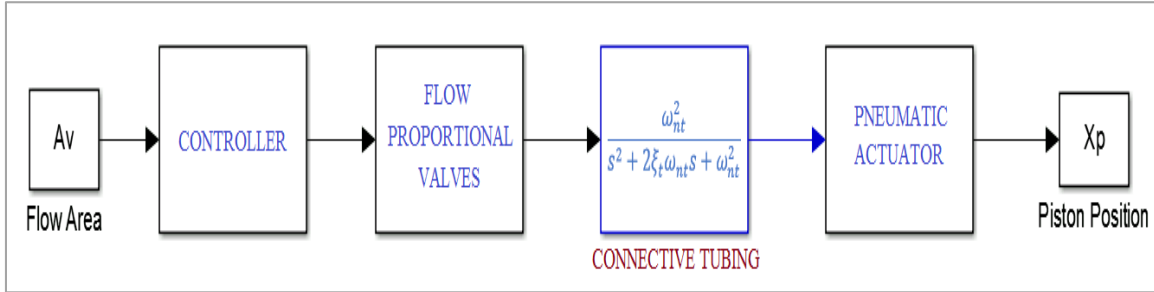


**Figure 6.4.** Block-diagram representation of the pneumatic system including a block accounting for pressure distortion in lengthy connective tubing

As it was explained in chapter 4, the experimental method applied was restricted by the operational frequency of the proportional valve used, which precluded the identification of the frequency response for tubes of length shorter than 30.5 meters.

In addition, by including the second-order linear filter model in the overall simulation model for the pneumatic system (Figure 6.4), several aspects should be considered; for example, the order of the transfer functions in the block diagrams described in chapter 3 would increase, as well as the order of the matrixes in the state-space models. This and other considerations would increase the complexity of analysis, computation, and implementation of the control strategies proposed. Therefore, the implementation of the model validated in this section is recommended as future work, as a means to increase the effectiveness of the simulation models used to describe the behavior of the pneumatic system under study.

## 6.2. Proportional Control

Chapter 5 described and analyzed the simulation response of the pneumatic system in accordance to a proportional control (P-Control) scheme. This chapter compares the simulation results with results obtained from the actual implementation of a P-Control algorithm. Figure 6.5 shows the block-diagram used for simulation in Simulink, and a schematic that describes the implementation of proportional control relative to the actual pneumatic system.

Some of the blocks in the simulation diagram look different to the blocks included in schemes shown in previous chapters. For example, the block circled in a dashed-red line in figure 6.5 is an integrator block, but it looks different because it is the discrete equivalent of the continuous-time integrator blocks included in prior schematics (Figure 6.6).

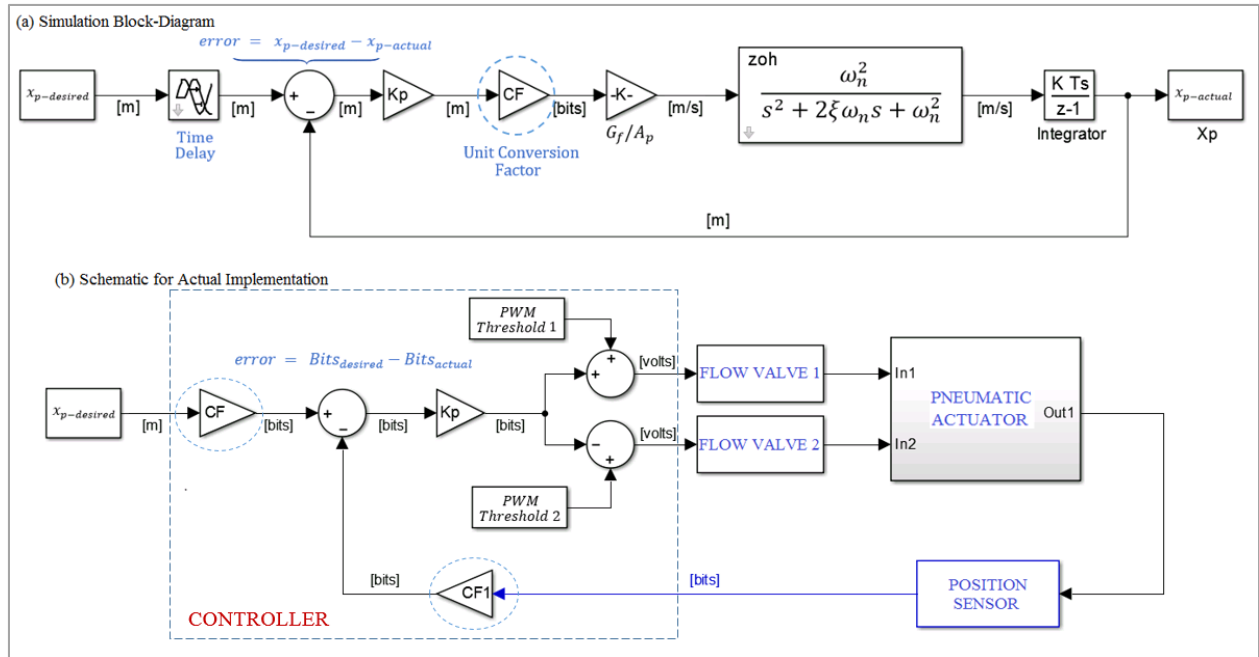


**Figure 6.5.** Block-diagrams: (a) Simulink model, (b) Schematic for actual implementation

The continuous-time models shown in previous chapters have been discretized using the Model Discretizer tool provided by Simulink. The transform technique applied corresponds to the Zero-Order Hold method (ZOH), which converts continuous-time input signals into staircase inputs. Hence, the discretization process takes place by sampling a continuous-time input signal, and by holding each sample value constant during a specific period of time.

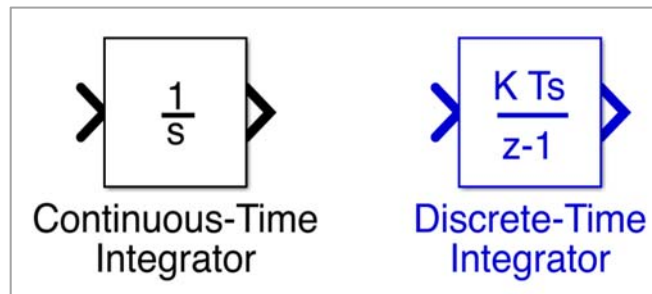


**Figure 6.6.** Block-diagrams: Continuous-time Blocks vs. Discrete-Time Blocks

The sample time entered for simulation of closed-loop control schemes was equal to 6.0 milliseconds. In the simulation of open-loop schemes, the sample time was reduced to 4.4 milliseconds. The sampling times were identified from experimental data. The reduction of the sampling time for open-loop schemes was caused by the simplification of the control algorithm entered in the controller.

Additionally, a time-delay block was included in the simulation block-diagram (Figure 6.5), which accounted for the time required for the controller to process the control algorithm, for the time that took to the electrical subsystem in the control valves to produce the commanded input, as well as for the time necessary to build up pressure in the cylinder chambers in order to overcome static friction. The initial delay time was not modeled as an internal delay of the system, and accordingly; the time-delay block adopted the value of the delay time from experimental data. The time-delay block was included only for the cases in which the models simulated the response of the system to a step input. In the case of sinusoidal inputs, the initial time delay was not included because it resulted beneficial for the analysis to visualize the actual delay of the system in comparison to the simulation response.

Regarding to the schematic for actual implementation in figure 6.5, the single input generated according to the P-control algorithm was distributed equally to the two control valves. Nevertheless, for each valve the single input was added to or subtracted from a PWM threshold value. The single input was added to a threshold value in the case of the valve connected to the cap-end of the cylinder, while the input was subtracted from a threshold value for the valve connected to the rod-end of the cylinder.

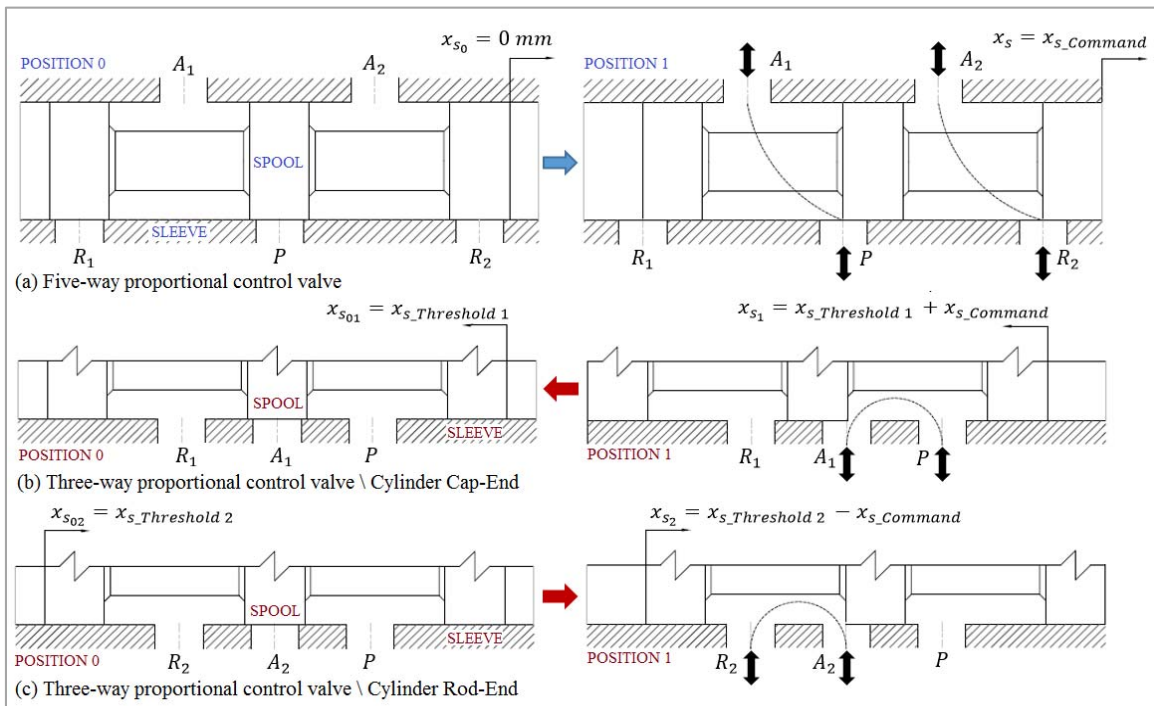


Figure 6.7. Operation of proportional control valves

Adding or subtracting an input to or from a threshold value emulated the operation of the two three-way valves as a single five-way proportional control valve (Figure 6.7). Hence, when the P-control algorithm generated a positive input, the valve connected to the cylinder cap-end opened by providing flow and pressure to the cylinder, while the valve connected to the cylinder rod-end closed by expelling the air in the rod-end chamber to the atmosphere, and vice versa. The definition of a PWM threshold value for each valve accomplished two important goals: to compensate for the discontinuity caused by the dead zone of the control valves, and to compensate for the difference between the active areas of the pneumatic piston.

In chapter 4, threshold input values for the valves were defined as the input values required to overcome static friction if no pressure force was applied on the side of the piston opposed to the direction of displacement. Accordingly, because of the asymmetry of the piston active areas, it was confirmed that the threshold input value for the rod-end valve was higher than the threshold value for the opposite valve. Nevertheless, these threshold values caused an improper synchronization between both valves: the displacement of the piston turned erratic during extension or retraction. Hence, a new set of threshold values was determined experimentally (Table 6.1).

**Table 6.1.** Threshold input values for control

Threshold Input Control Values				
Parameter	Symbol	Value	[Units]	Condition
Threshold Input Command Extension	$PWM_{0_{Cap-End}}$	57	[%]	Cap-end valve
		145	[bits]	
Threshold Input Command Retraction	$PWM_{0_{Rod-End}}$	55	[%]	Rod-end valve
		140	[bits]	

The threshold input values (Table 6.1) ensured the synchronized operation of the control valves in emulation to the operation of a sole five-way proportional valve, for most of the control gains and control schemes tested. By setting the threshold value for each valve inside the boundaries of the dead zone, the initial position of the valve spool was set closer to the upper boundary of the dead zone, from which the flow of air to the cylinder is theoretically always positive. Hence, the travel of the spool of each valve in switching from being connected to the chamber of the cylinder or to the atmosphere through the exhaust port was reduced, which would have diminished the discontinuity caused by the dead zone of the valve.

Similarly, by keeping the threshold value for the valve connected to the cylinder rod-end chamber higher than that for the opposite valve, the asymmetry of the piston active areas would have been counterweighed, which supposed to balance the pressure and flow provided to each chamber of the cylinder.

Besides, in resembling the action of the actual controller, the flow gains used in the simulations corresponded to values expressed in units of [m<sup>3</sup>/s/bit], which implied that the input applied corresponded to the PWM voltage generated by the ARDUINO UNO board. By using the flow gains expressed in units of volumetric flow per bit, which were determined in chapter 4, section 4.4.4, it was important to corroborate one more time that the open-loop responses from the simulation models matched the experimental responses from the pneumatic system (Figures 6.8 to 6.10). Table 6.2 summarizes the simulation parameters determined through the process applied to adjust the response of the simulation models to the actual response of the pneumatic system. Since chapter 4 and chapter 5 mostly considered the case of 0.55-meter connective tubing, in this section the parameters are reported according to the three different lengths of connective tubing tested experimentally: 0.55, 1.5, and 3.0 meters.

**Table 6.2.** Summary – Simulation parameters: Compressibility (CM) and Spring Models (SM) – Open-Loop Control Scheme

Parameter	Symbol	Length of Connective Tubing			[Units]	Condition
		0.5 [m]	1.5 [m]	3.0 [m]		
Piston Mass	$M_{PL}$	0.30	0.30	0.30	[kg]	(CM - SM)
Supply Pressure	$P_S$	764000	764000	764000	[Pa]	(CM - SM)
Atmospheric Pressure	$P_R$	101720	101720	101720	[Pa]	(CM - SM)
Air Density	$\rho$	1.18	1.18	1.18	[kg/m <sup>3</sup> ]	T = 295 K (CM - SM)
Air Bulk Modulus	$\beta$	4.54E+06	3.66E+06	3.60E+06	[Pa]	Effective value (CM)
Cylinder Volume	$V_0$	1.96E-04	2.64E-04	3.71E-04	[m <sup>3</sup> ]	Effective value (CM - SM)
Piston Effective Area	$A_P$	1.04E-03	1.04E-03	1.04E-03	[m <sup>2</sup> ]	Eq. 4.16 (CM - SM)
Discharge Coefficient	$C_d$	0.60	0.60	0.60	[-]	(CM - SM)
Viscous Friction Coefficient	$B$	0.00	0.00	0.00	[Ns/m]	(SM)
Spring Constant	$k_x$	25000	15000	10500	[N/m]	(SM)
Flow Gain	$G_f$	7.5E-05	7.5E-05	7.5E-05	[m <sup>3</sup> /s/bit]	Average value – Table 4.11 (CM - SM)
Pressure Gain	$G_D$	5.70E-08	7.57E-08	9.43E-08	[m <sup>3</sup> /s/Pa]	(CM - SM)
Time Constant	$\tau$	0.015	0.020	0.025	[s]	Simplified reduced model
Transfer-function numerator	$\bar{C}$	0.021	0.019	0.018	[m/s/bit]	Simplified reduced model – Normalized value



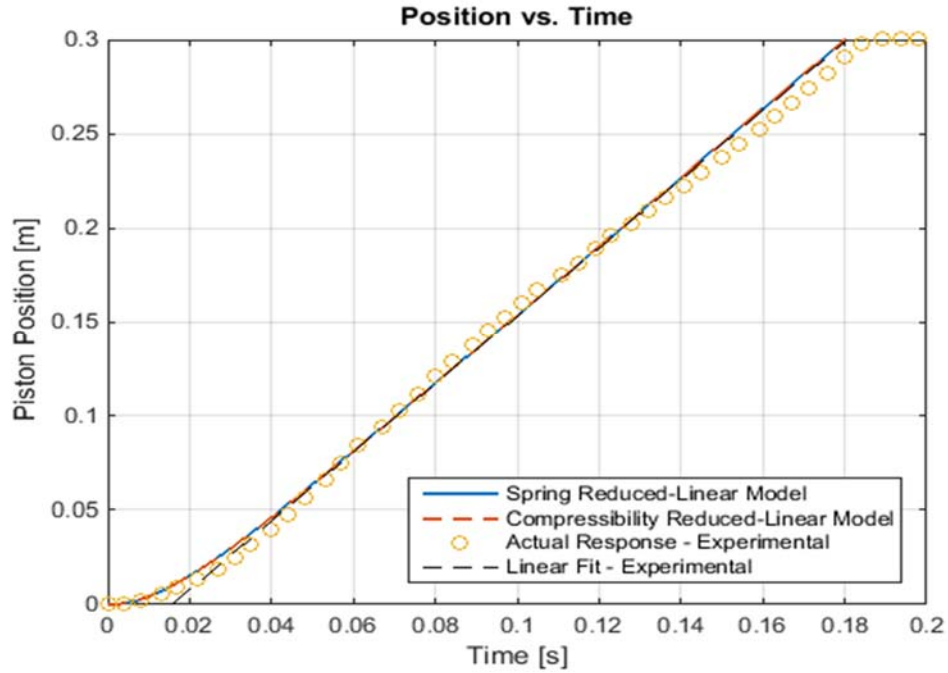


**Figure 6.8.** Comparison of simulation and experimental results: Open-loop step response to a 75% duty-cycle PWM input (Length of connective tubing: 0.55 m)

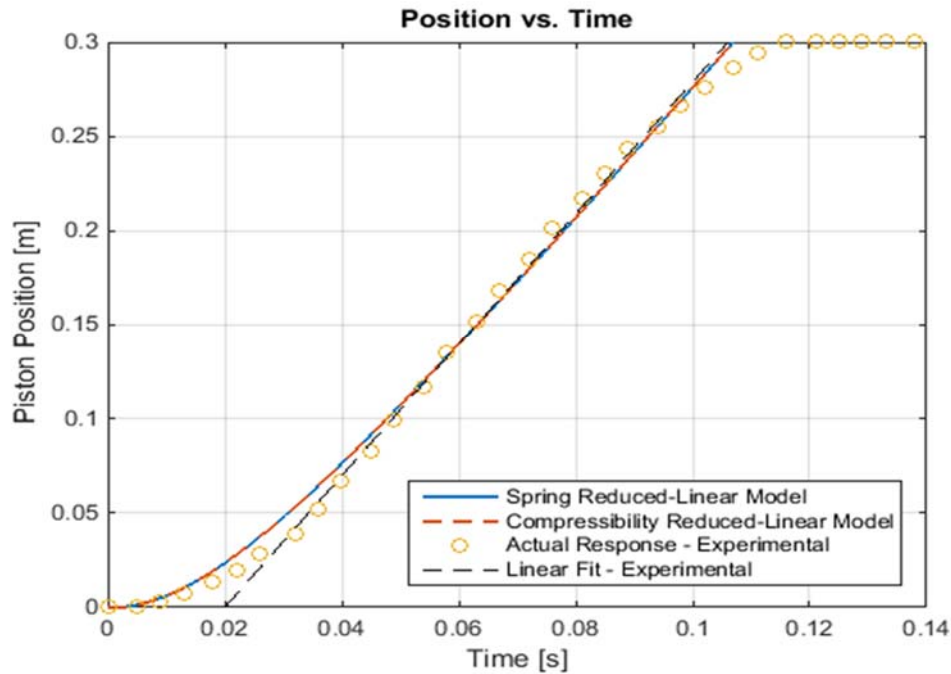


**Figure 6.9.** Comparison of simulation and experimental results: Open-loop step response to a 88% duty-cycle PWM input (Length of connective tubing: 1.5 m)



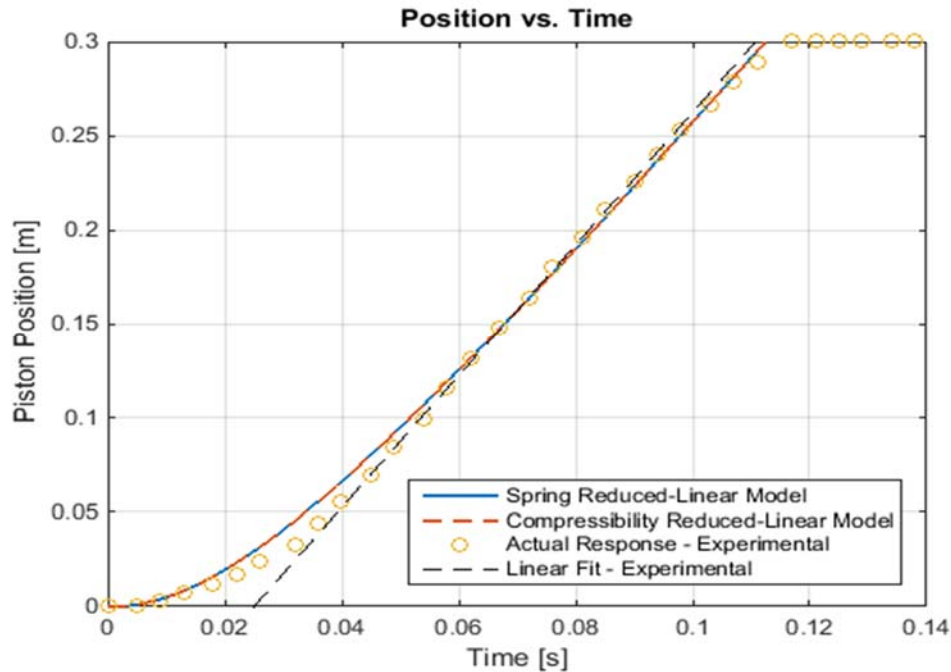


**Figure 6.10.** Comparison of simulation and experimental results: Open-loop step response to a 94% duty-cycle PWM input (Length of connective tubing: 3.0 m)

A close correlation between the simulation and actual responses of the pneumatic system to an open-loop step input was observed (Figures 6.8 to 6.10). The end and start of the piston stroke revealed a slight deviation between the simulation and experimental responses, which was attributed to the effect of the cushions in both ends of the cylinder. Depending on the amplitude of the input applied, the flow gain was different, as it was verified in chapter 4, section 4.4.4. Nevertheless, for the simulation of the response of the system in basis to a closed-loop control strategy, a constant flow gain had to be entered for simulation. In that regard, a normalized value for the flow gain was calculated from the normalized coefficient  $\mathcal{C}$  derived in relation to the simplified reduced-linear model for the system (Figure 6.11).

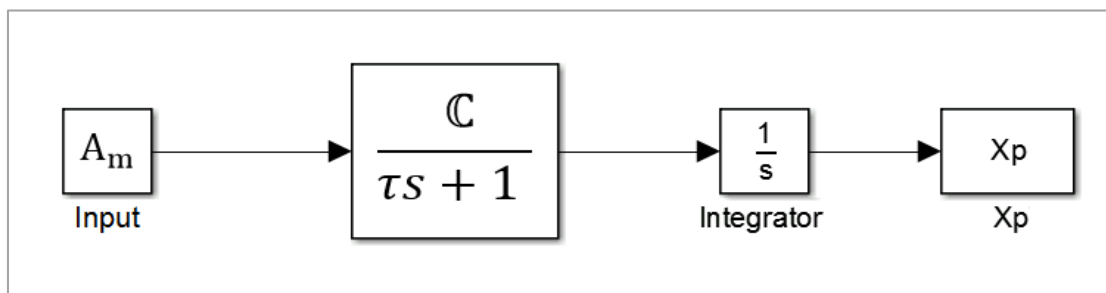


**Figure 6.11.** Simplified reduced model for the pneumatic system

The normalized value of  $\mathbb{C}$ , denoted as  $\overline{\mathbb{C}}$  in chapter 4, would be expressed as follows.

$$\overline{\mathbb{C}} = \frac{\overline{G_f} C}{A_p} \quad (6.4)$$

Denoting  $\overline{G_f}$  as the normalized value of the flow gain. The coefficient  $C$  can be determined from the expressions derived in chapter 5 through the partial-fraction decomposition of the second-order transfer function composing the reduced-linear models for the pneumatic system (Eq. 5.5, Section 5.1.2).

$$C = \frac{A'}{r_1} \quad (6.5)$$

Since the coefficient  $A'$  and the root  $r_1$  were defined in terms of the damping ratio and the natural frequency of the system (Eq. 5.6, Section 5.1.2), the value of  $C$  would be different depending upon the length of connective tubing considered in the models. Nonetheless, from the simulation results obtained in chapter 5, by making the response of the simplified reduced-linear model to match the response of the original reduced-linear model, it was verified that the value of the coefficient  $C$  tends to one for all the cases. Accordingly, the normalized flow gain,  $\overline{G_f}$ , would be given by:

$$\overline{G_f} \approx \overline{\mathbb{C}} A_p \quad (6.6)$$

Table 6.3 shows the values corresponding to the normalized gain flow,  $\overline{G_f}$ , and the coefficient  $C$  depending upon the length of connective tubing tested.

**Table 6.3.** Summary – Normalized dynamic constants – Open-Loop Control Scheme

Parameter	Symbol	Length of Connective Tubing			[Units]	Condition
		0.5 [m]	1.5 [m]	3.0 [m]		
Time Constant	$\tau$	0.015	0.020	0.025	[s]	Simplified reduced model
Transfer-function numerator	$\overline{\mathbb{C}}$	0.021	0.019	0.018	[m/s/bit]	Simplified reduced model
Transfer-function numerator	$C$	1.056	1.053	1.048	[-]	Simplified reduced model
Flow Gain	$\overline{G_f}$	2.07E-05	1.88E-05	1.79E-05	[m <sup>3</sup> /s/bit]	Normalized Value
		2.18E-05	1.98E-05	1.87E-05	[m <sup>3</sup> /s/bit]	Normalized Value $C \approx 1$

As it was predicted in chapter 5, the value of the time constant increased as the length of connective tubing increased. Likewise, the approximation of  $C$  to a value of one was valid (Table 6.3). Moreover, the normalized values for the flow gain approximated the gain values determined in chapter 4, section 4.4.4.

After defining all the simulation parameters, it was necessary to establish the range of proportional gains that could be implemented for simulation and implementation of the actual controller. The range of proportional gains was defined through root locus analysis, as described in chapter 5 for the case of 0.55-meter hoses. In that regard, by entering in the controller the gains identified through root locus for the simulation models, the actual responses from the pneumatic system should follow a pattern similar to the simulation responses. It is, for example; if a gain that causes the response of the simulation models to become unstable is entered in the actual controller, the same gain, within a reasonable range, should cause the actual response to become unstable in a parallel range of frequency and damping. Figures 6.12 to 6.14 show the root locus for the pneumatic system described by the reduced-linear model, and depending on the length of connective tubing tested.

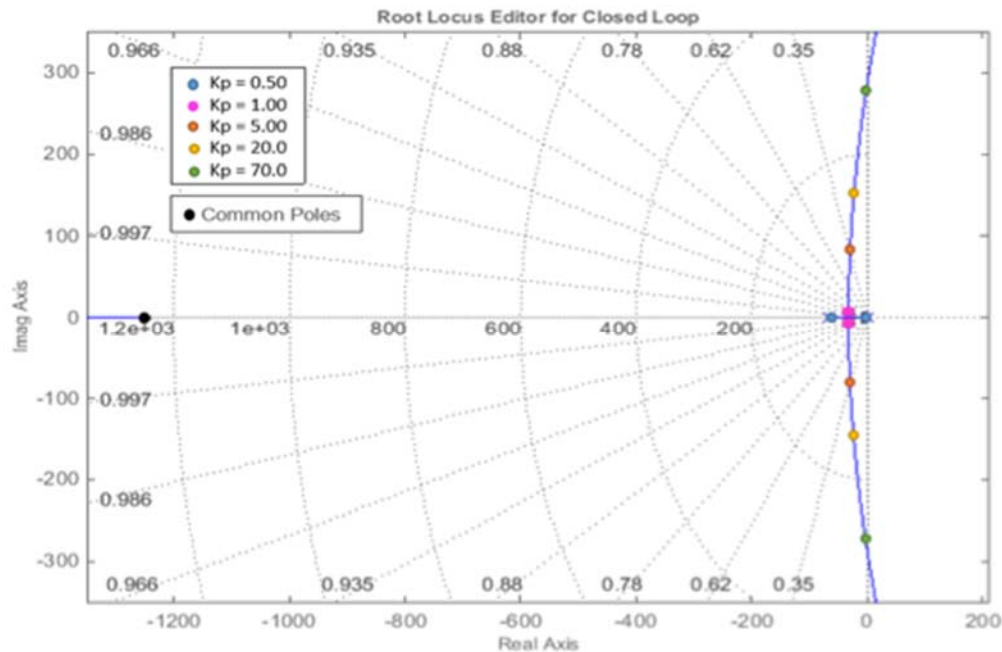


**Figure 6.12.** Open-loop guess: Root locus for system with 0.55-meter connective tubing

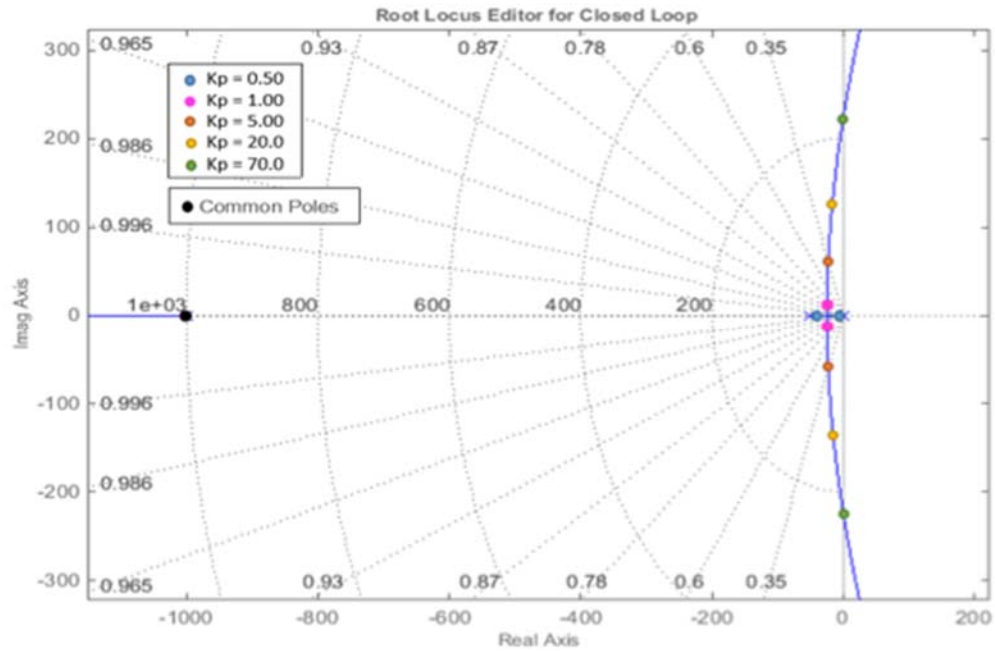


Figure 6.13. Open-loop guess: Root locus for system with 1.5-meter connective tubing

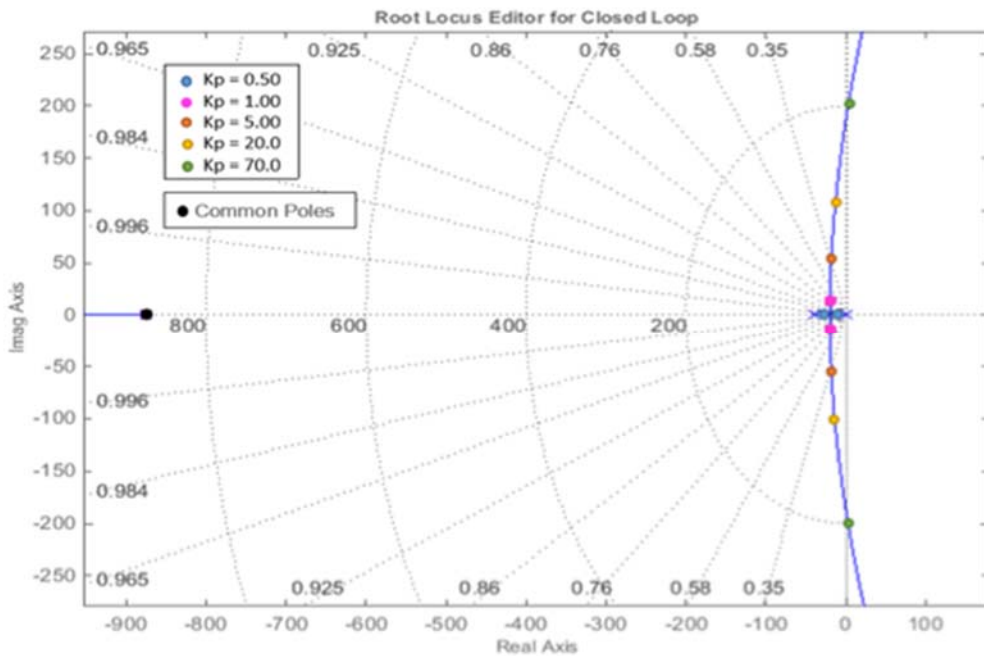
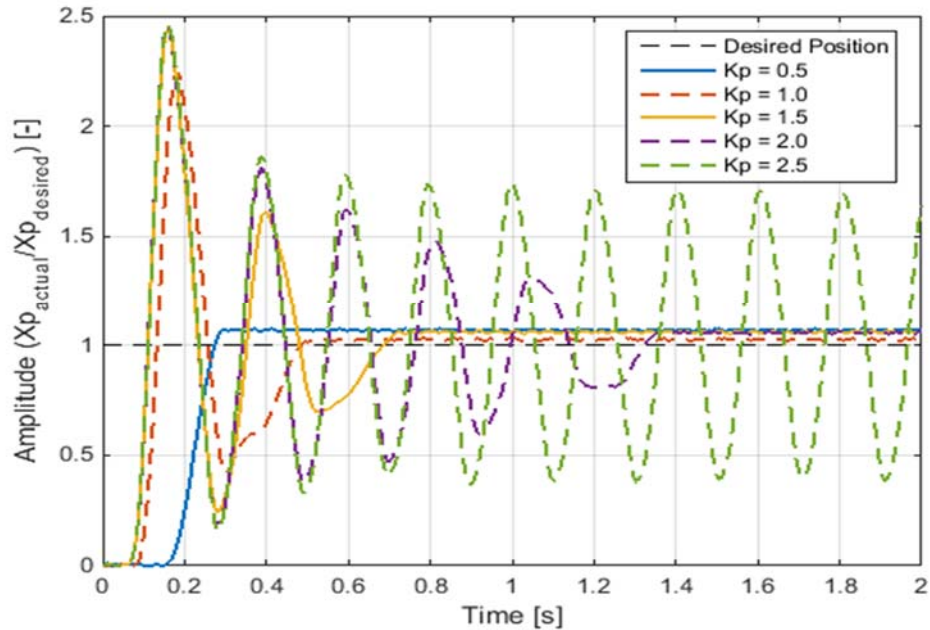
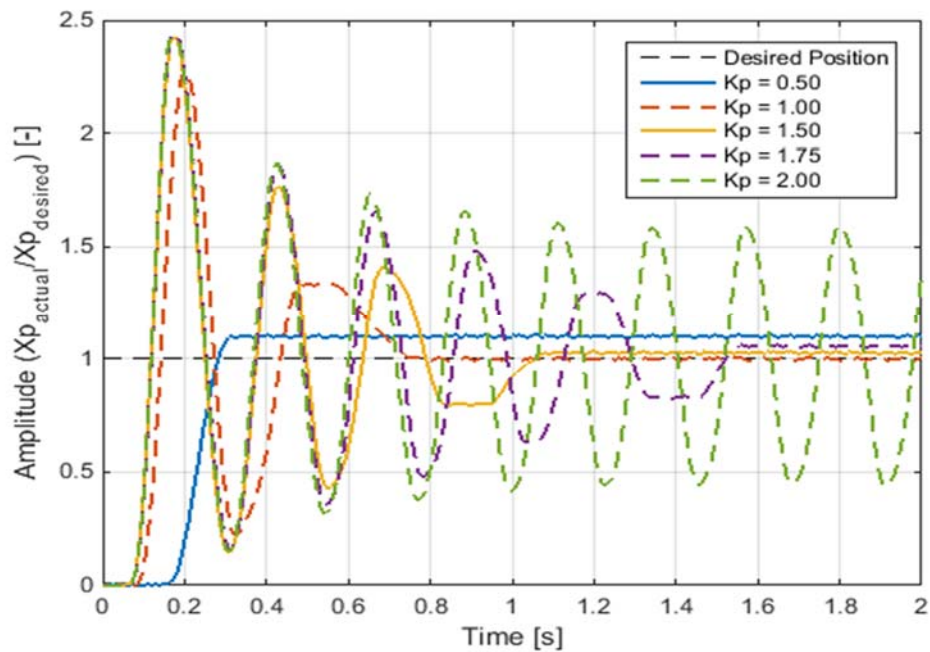


Figure 6.14. Open-loop guess: Root locus for system with 3.0-meter connective tubing

Then, to corroborate the root path traced by the root locus (Figures 6.12 to 6.14), the experimental step responses from the pneumatic system according to different proportional gains were obtained (Figures 6.15 to 6.17).



**Figure 6.15.** P-Control: Experimental step responses (Length of connective tubing: 0.55 m)



**Figure 6.16.** P-Control: Experimental step responses (Length of connective tubing: 1.5 m)

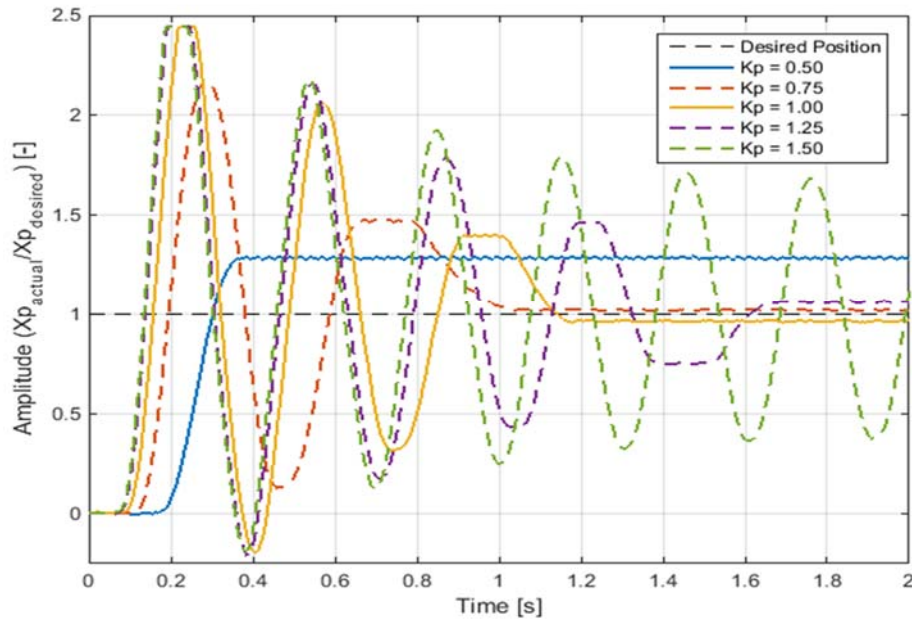


**Figure 6.17.** P-Control: Experimental step responses (Length of connective tubing: 3.0 m)

Based on the root locus plots and the experimental responses (Figures 6.12 to 6.17), it was not likely that the simulation responses match the experimental responses, as the gains that caused the pneumatic system to become unstable were much smaller than the gains identified through the root locus for the simulation models. Hence, the simulation parameters identified in table 6.2 and table 6.3 would not have permitted the simulation models to match the closed-loop response of the pneumatic system. In order to make the simulation models to match the closed-loop response of the pneumatic system, the simulation parameters were adjusted one more time.

Table 6.4 includes the simulation parameters and dynamic constants that enabled the simulation models to approximate the actual response of the pneumatic system for a closed-loop P-control scheme. In particular, the main adjusted parameters corresponded to the spring constant,  $k_x$ , and the normalized gain flow,  $\overline{G_f}$ . Due to the fact that in chapter 5 the spring constant was related to the bulk modulus,  $\beta$ , and the pressure gain,  $G_D$ , in order to generate the values included in table 6.4, the correlation between those values was preserved. Accordingly, the values for the bulk modulus and the pressure gain also result adjusted in comparison to the values presented in table 6.2 and table 6.3. Nevertheless, values for parameters such as the piston effective area and the effective volume of air in the cylinder chambers, among others, remained the same.



**Table 6.4.** Summary – Simulation parameters: Compressibility (CM) and Spring Models (SM) – Closed-Loop Control Scheme

Parameter	Symbol	Length of Connective Tubing			[Units]	Condition
		0.5 [m]	1.5 [m]	3.0 [m]		
Piston Mass	$M_{PL}$	0.30	0.30	0.30	[kg]	(CM - SM)
Supply Pressure	$P_S$	764000	764000	764000	[Pa]	(CM - SM)
Atmospheric Pressure	$P_R$	101720	101720	101720	[Pa]	(CM - SM)
Air Density	$\rho$	1.18	1.18	1.18	[kg/m <sup>3</sup> ]	T = 295 K (CM - SM)
Air Bulk Modulus	$\beta$	8.25E+04	6.95E+04	5.79E+04	[Pa]	Effective value (CM)
Cylinder Volume	$V_0$	1.96E-04	2.64E-04	3.71E-04	[m <sup>3</sup> ]	Effective value (CM - SM)
Piston Effective Area	$A_P$	1.04E-03	1.04E-03	1.04E-03	[m <sup>2</sup> ]	Eq. 4.16 (CM - SM)
Discharge Coefficient	$C_d$	0.60	0.60	0.60	[-]	(CM - SM)
Viscous Friction Coefficient	$B$	0.00	0.00	0.00	[Ns/m]	(SM)
Spring Constant	$k_x$	455.00	285.00	169.00	[N/m]	(SM)
Flow Gain	$\overline{G}_f$	2.88E-05	3.00E-05	3.34E-05	[m <sup>3</sup> /s/bit]	Normalized – (CM - SM)
Pressure Gain	$G_D$	2.13E-07	2.62E-07	3.46E-07	[m <sup>3</sup> /s/Pa]	(CM - SM)
Time Constant	$\tau$	0.015	0.020	0.025	[s]	Simplified reduced model
Transfer-function numerator	$\overline{C}$	0.021	0.019	0.018	[m/s/bit]	Simplified reduced model – Normalized value

Highlighted in blue in table 6.4 are the parameters that were adjusted in contrast to the values included in table 6.2 and table 6.3. The values for the experimental time constants included in the simplified reduced models remained the same, and they intervened in finding new values for the pressure gains by applying Eq. 5.7.

In comparison to the values included in table 6.1, and table 6.2, the value for the spring constant,  $k_x$ , was significantly reduced, which consequently increased and decreased the values of the effective air bulk modulus,  $\beta$ , and the pressure gain,  $G_D$ , respectively. On the other hand, the value for the normalized flow gain was increased. In that regard, it was remarkable that the range of adjusted values for the flow and pressure gains were within the range of gain values determined in chapter 4. In fact, even the effective value of the bulk modulus,  $\beta$ , approximated relatively closer to the adiabatic bulk modulus used as reference in chapter 5 ( $\beta = 1.42E + 05$ ). In fact, the simulation parameters included in table 6.2 and 6.3 could also be associated with the range of experimental values defined in chapter 4. Hence, the no correspondence between the open-loop and the closed-loop simulation parameters would be justified by the different effective operating points around which the simulation models resulted linearized.

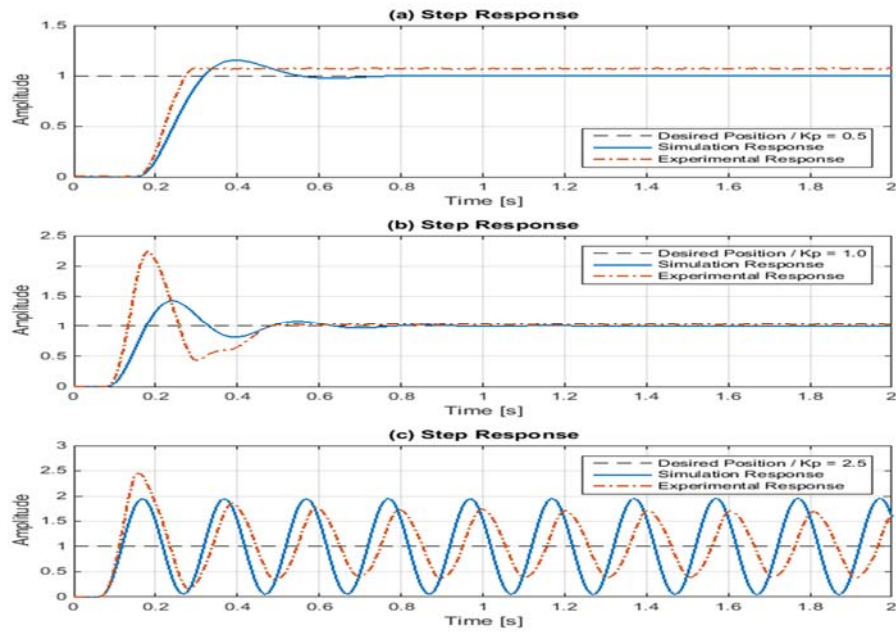


**Figure 6.18.** Comparison of simulation and experimental step responses applying P-control:  
 (a)  $K_p = 0.5$ , (b)  $K_p = 1.0$ , (c)  $K_p = 2.5$  (Length of connective tubing: 0.55 m)

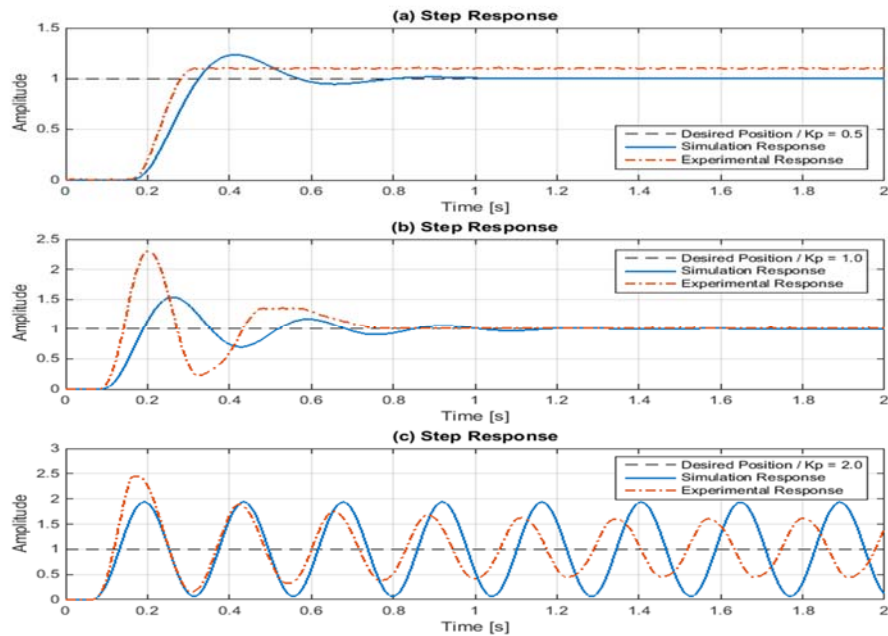


**Figure 6.19.** Comparison of simulation and experimental step responses applying P-control:  
 (a)  $K_p = 0.5$ , (b)  $K_p = 1.0$ , (c)  $K_p = 2.0$  (Length of connective tubing: 1.5 m)



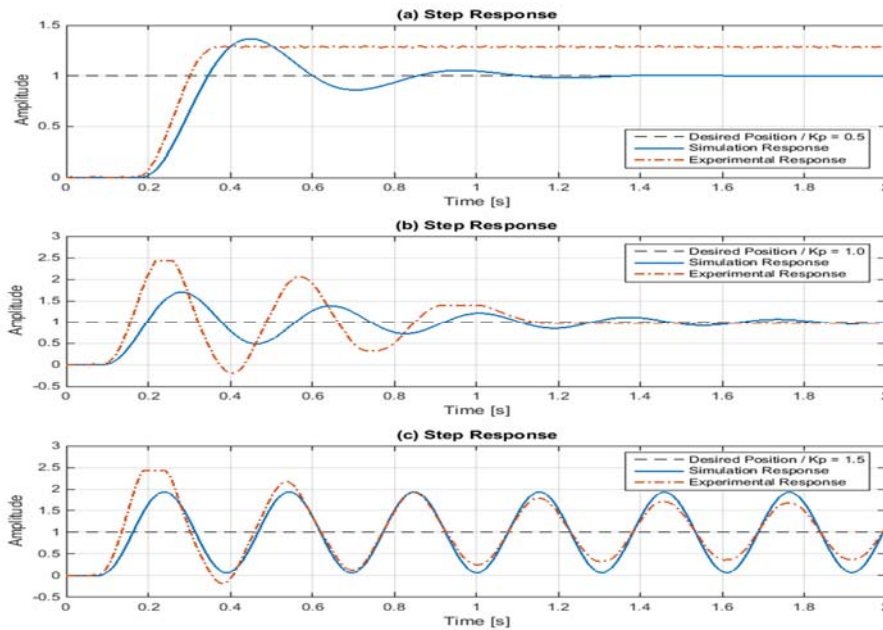


**Figure 6.20.** Comparison of simulation and experimental step responses applying P-control:  
(a)  $K_p = 0.5$ , (b)  $K_p = 1.0$ , (c)  $K_p = 1.5$  (Length of connective tubing: 3.0 m)

The comparison of simulation and experimental responses of the pneumatic system triggered by a step input under proportional control (Figure 6.18 to 6.20) demonstrated a not accurate correspondence. The approximation of the simulation responses to the experimental results might constitute the nearest estimate that could be achieved through the simulation models proposed. In fact, the nature of the experimental results might describe a much more complex dynamic behavior than the one produced by the simulation models, which would stem from the characteristic nonlinearity of the pneumatic system. Nevertheless, the approximation obtained through the simulation models resulted useful at the time of implementing pole/zero cancellation, as projected values for the damping ratio and natural frequency of the pneumatic system were computed from the simulation parameters defined in table 6.2 through table 6.4.

Furthermore, figures 6.21 to 6.23 show the simulation and experimental responses to a sinusoidal input command, for different frequencies, and depending on the length of connective tubing tested. In order to compare the results obtained, the value of the proportional gain used remained constant. A proportional gain equal to 0.5 was selected for all the cases because, according to the step simulation results, this gain was able to produce the best dynamic response; that is a fast and well-damped response.

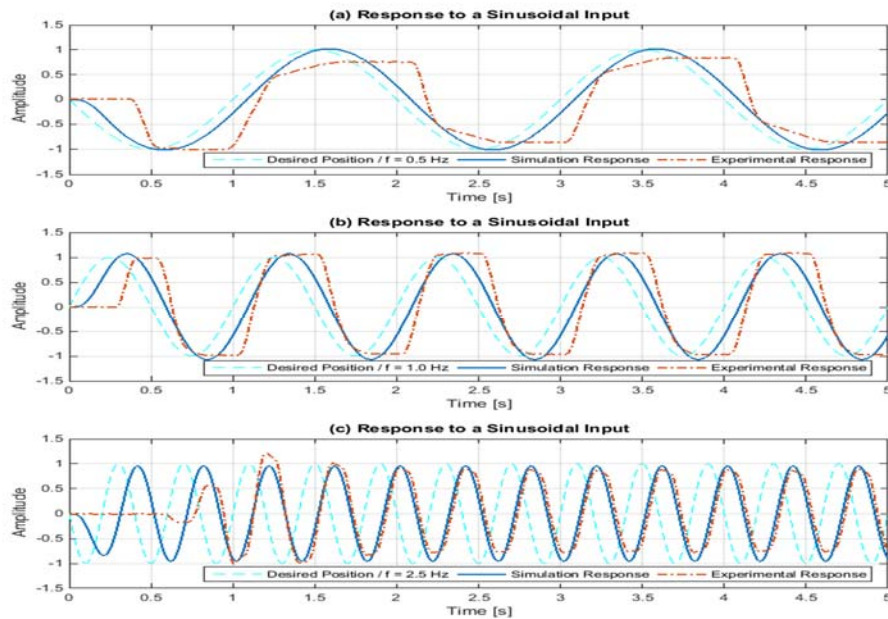


**Figure 6.21.** Simulation and experimental responses to a sinusoidal input (light blue line) with P-control ( $K_p = 0.5$ ): (a)  $f = 0.5$  Hz, (b)  $f = 1.0$  Hz, (c)  $f = 2.5$  Hz (Tube length: 0.55 m)

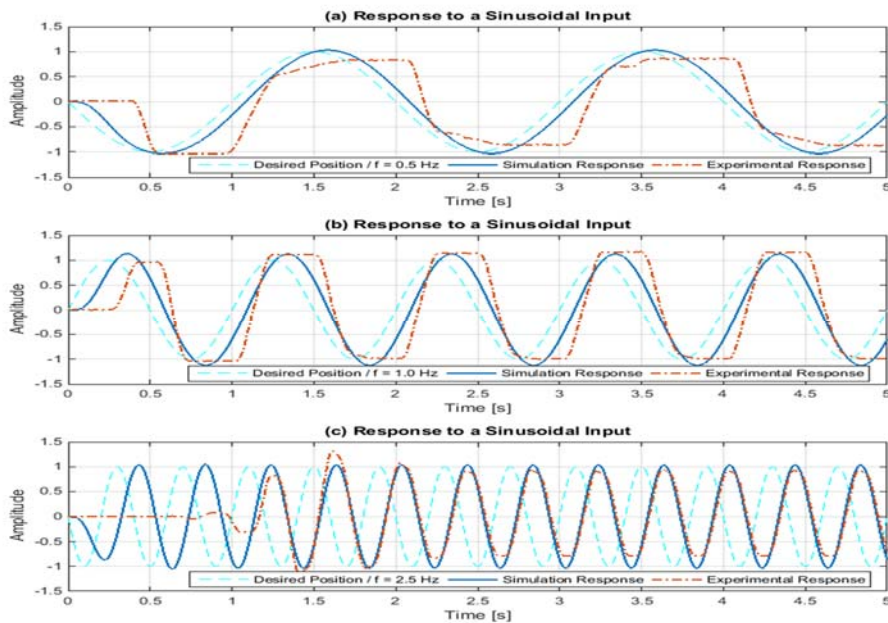


**Figure 6.22.** Simulation and experimental responses to a sinusoidal input (light blue line) with P-control ( $K_p = 0.5$ ): (a)  $f = 0.5$  Hz, (b)  $f = 1.0$  Hz, (c)  $f = 2.5$  Hz (Tube length: 1.5 m)

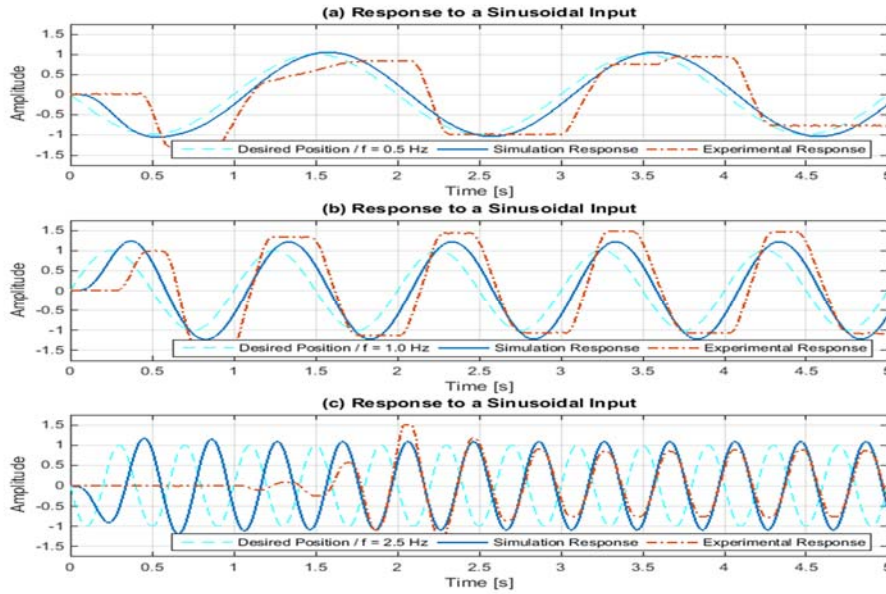


**Figure 6.23.** Simulation and experimental responses to a sinusoidal input (light blue line) with P-control ( $K_p = 0.5$ ): (a)  $f = 0.5$  Hz, (b)  $f = 1.0$  Hz, (c)  $f = 2.5$  Hz (Tube length: 3.0 m)

The simulation responses adjusted better to the actual responses of the pneumatic system when the frequency of the sinusoidal input command increased (Figures 6.21 to 6.23). Nevertheless, for none of the cases considered – short or lengthy hoses and slow or fast frequency – the simulation models were able to replicate the start of the process. In fact, for low-frequency input commands (Figures 6.21a to 6.23a), the shape of the actual response resulted considerably distorted in respect to the expected sinusoidal profile, while the simulation response maintained its sinusoidal outline. This effect was observed because the simulation models did not account for static and/or dynamic friction in the cylinder. Viscous friction and Coulomb friction were disregarded from the simulation models. However, independently of the response at the start time of the plots, the frequency of the simulation response and the actual response were the same, as the high-frequency results demonstrated (Figures 6.21c to 6.23c).

In the following section, the results from the implementation of pole/zero cancellation are compared to the responses obtained from the application of proportional control. The comparison is made in reference to the improvement or deterioration of the dynamic response of the system when a control algorithm derived from a pole/zero cancellation scheme was introduced in the controller.

### 6.3. Pole/Zero Cancellation

Section 6.3 reports the findings from the implementation of a pole/zero cancellation strategy for control of the pneumatic system. As it was explained in chapter 3, because of the implementation of a pole/zero cancellation scheme, the controller becomes an individual dynamic system. The following expression was derived from the discretization of the continuous-time model for the controller in chapter 5.

$$A_v = K_p \frac{[e(1 + 2\xi\omega_n T + \omega_n^2 T^2) - e_{old}(2 + 2\xi\omega_n T) + (e_{old})_{old}]}{T^2} \quad (6.7)$$

Eq. 6.7 is further simplified by combining the proportional gain,  $K_p$ , and the square of the sampling time,  $T$ , in a sole gain  $K_{pT}$ . Hence, the real-time expression used for implementation of pole/zero cancellation results to be:

$$A_v = K_{pT}[e(1 + 2\xi\omega_n T + \omega_n^2 T^2) - e_{old}(2 + 2\xi\omega_n T) + (e_{old})_{old}] \quad (6.8)$$

Where  $A_v$  would correspond to the input applied to the control valves; it is to the PWM voltage generated by the ARDUINO UNO board. The sampling time in the ARDUINO UNO board was verified to be approximately 6.0 milliseconds; and accordingly, this value was entered as a constant in the code for the controller. Figure 6.24 shows a schematic for implementation of the pole/zero cancellation control strategy proposed

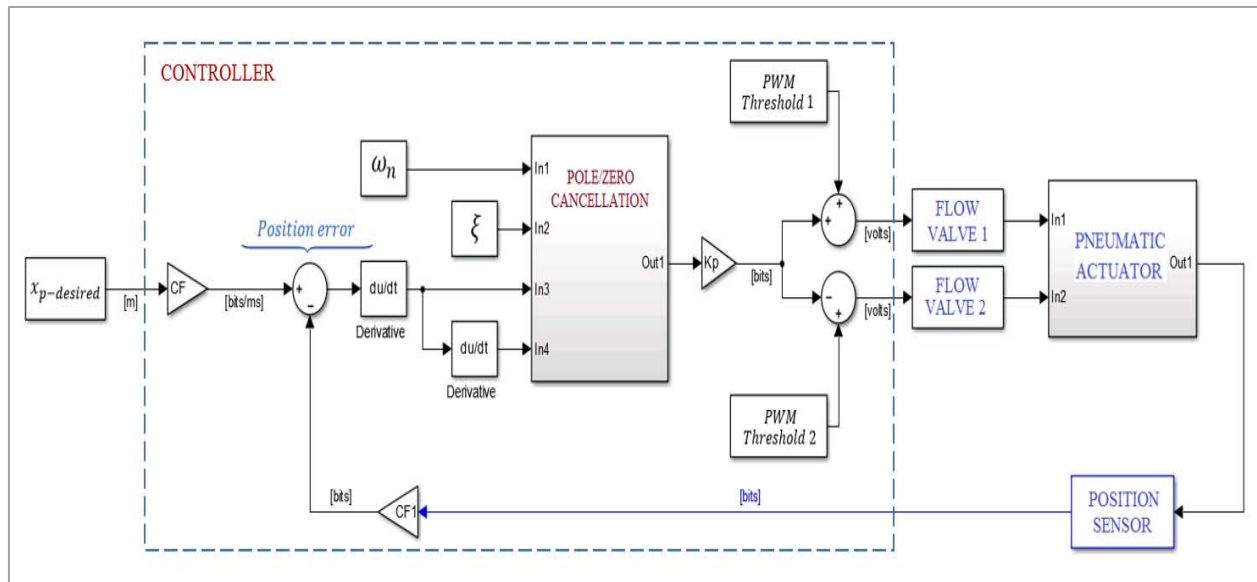


**Figure 6.24.** Pole/Zero Cancellation: Schematic for control implementation

Eq. 6.8 and figure 6.24 include the natural frequency,  $\omega_n$ , and damping ratio,  $\xi$ , describing the dynamics of the pneumatic system according to the simulation models proposed in previous sections. The values for these dynamic constants were determined from the simulation parameters defined in table 6.2 through table 6.4. Therefore, two sets of values for the natural frequency,  $\omega_n$ , and damping ratio,  $\xi$ , were obtained: one derived from the open-loop estimate of the response of the system, and a second one resulting from the closed-loop approximation.

The root locus sketched according to the simulation parameters included in table 6.4. (Figures 6.25 to 6.27) could be considered the most accurate estimate for the actual poles of the system according to the simulation models proposed. As it was predicted in chapter 5, as the length of connective tubing increased, the curvature ratio of the root path in the left-half plane decreased, which made the system more sensitive to the increase of the amplitude of the proportional gains. Moreover, the magnitude of the gains for which the closed-loop poles were marked in color in figures 6.25 to 6.27 was closer in agreement with the gains applied to obtain the experimental responses shown in figures 6.15 to 6.17, in section 6.2.

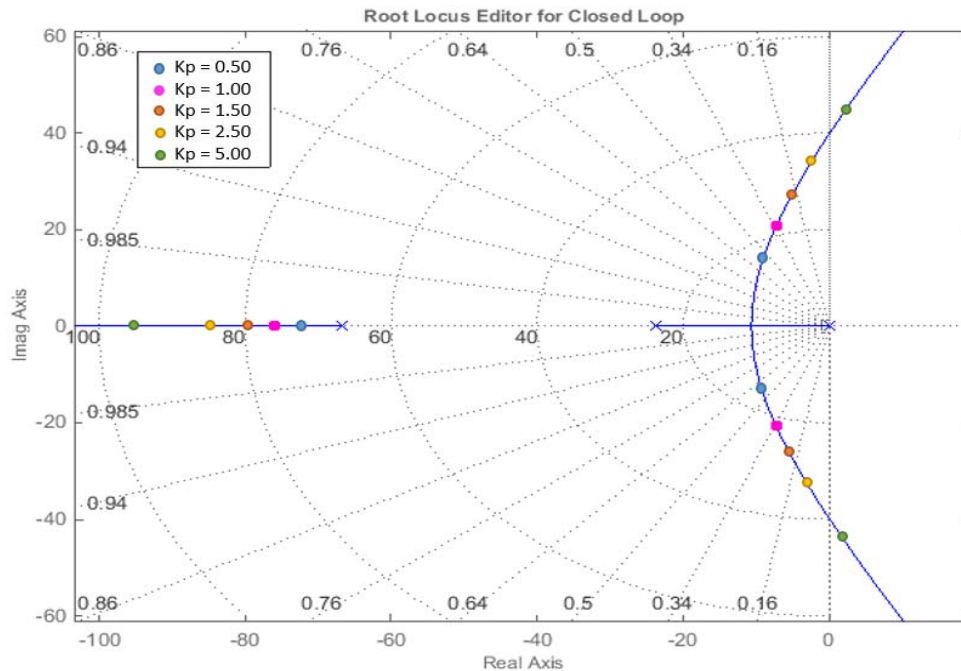


**Figure 6.25.** Closed-loop guess: Root locus for system with 0.55-meter connective tubing



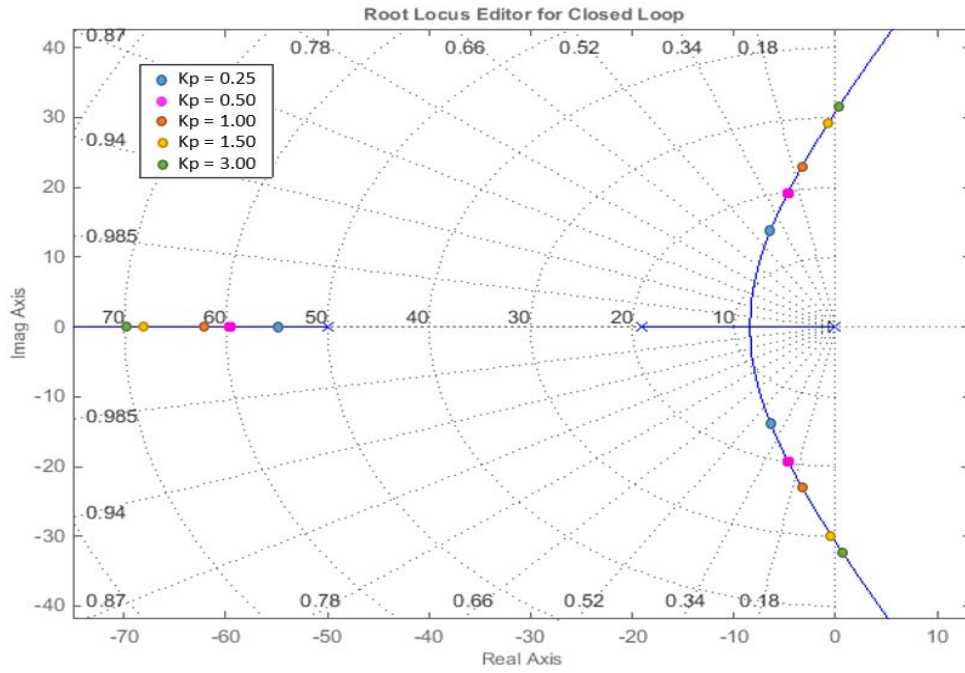


Figure 6.26. Closed-loop guess: Root locus for system with 1.5-meter connective tubing

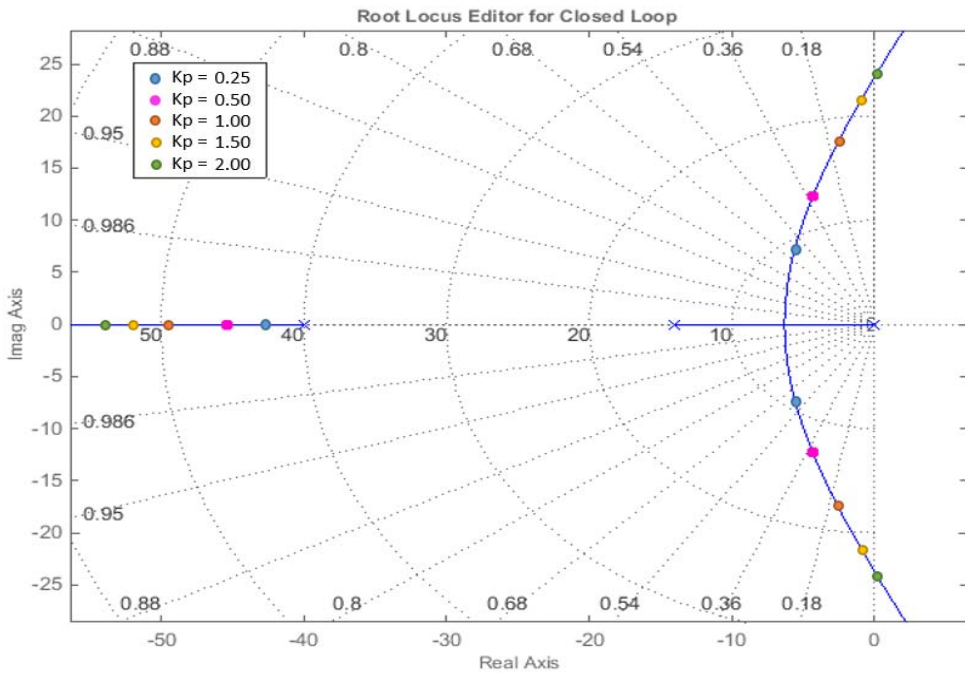


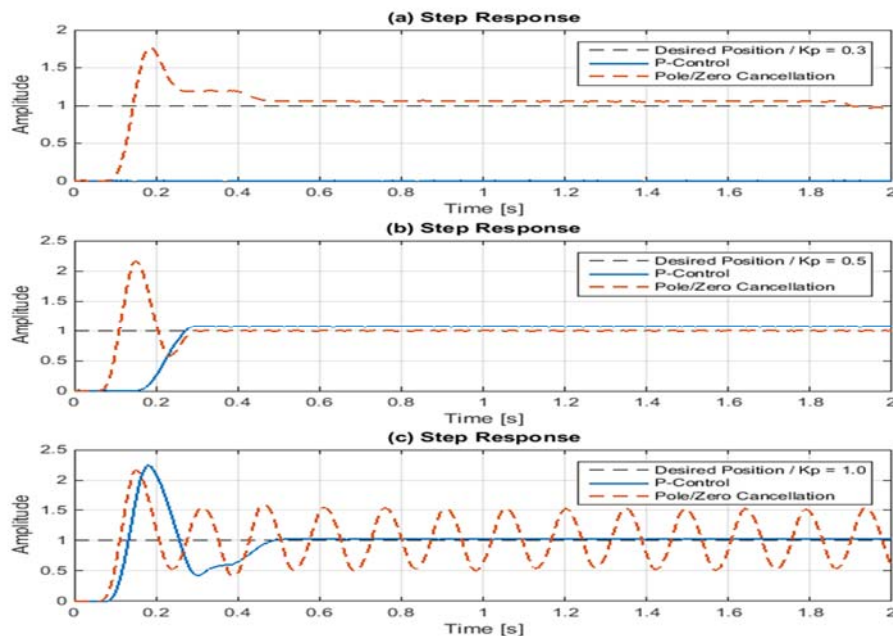
Figure 6.27. Closed-loop guess: Root locus for system with 3.0-meter connective tubing

Table 6.5 summarizes the natural frequency and damping ratio values generated according to the simulation models for an open-loop and a closed-loop control scheme.

**Table 6.5.** Pole/Zero Cancellation – Natural frequency and damping ratio values

Parameter	Symbol	Length of Connective Tubing			[Units]	Condition
		0.5 [m]	1.5 [m]	3.0 [m]		
Natural Frequency	$\omega_n$	288.68	223.61	187.08	[rad/s]	Open-Loop Estimate
		38.94	30.82	23.73	[rad/s]	Closed-Loop Estimate
Damping Ratio	$\xi$	2.28	2.35	2.45	[-]	Open-Loop Estimate
		1.15	1.12	1.14	[-]	Closed-Loop Estimate

The natural frequency and damping ratio values obtained from the open-loop estimate were larger than the values from the closed-loop estimate (Table 6.5). In that regard, when implemented according to Eq. 6.8, the values obtained from the closed-loop estimate did not produce any response in relation to the gains applied in basis to the P-control scheme. However, reasonable responses resulted from entering the natural frequency and damping ratio values corresponding to the open-loop estimate.



**Figure 6.28.** Comparison of experimental step responses applying P-control and Pole/Zero Cancellation: (a)  $K_p = 0.3$ , (b)  $K_p = 0.5$ , (c)  $K_p = 1.0$  (Tube length: 0.55 m)

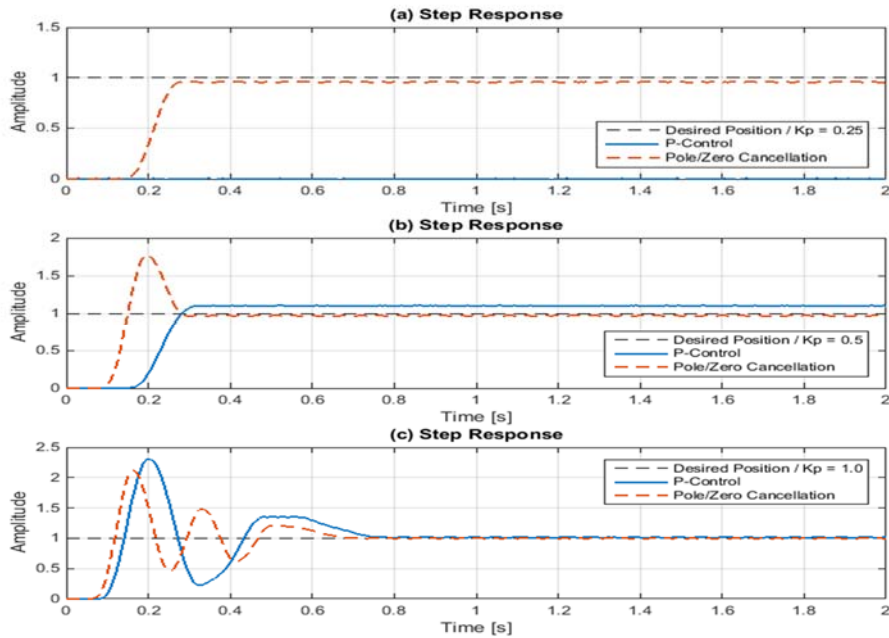


**Figure 6.29.** Comparison of experimental step responses applying P-control and Pole/Zero Cancellation: (a)  $K_p = 0.25$ , (b)  $K_p = 0.5$ , (c)  $K_p = 1.0$  (Tube length: 1.5 m)

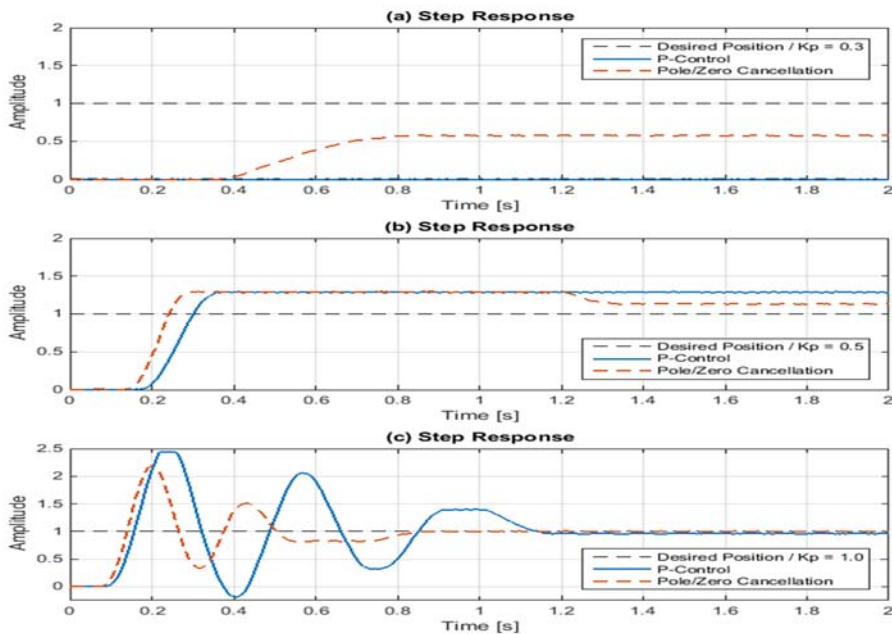


**Figure 6.30.** Comparison of experimental step responses applying P-control and Pole/Zero Cancellation: (a)  $K_p = 0.3$ , (b)  $K_p = 0.5$ , (c)  $K_p = 1.0$  (Tube length: 3.0 m)



The implementation of pole/zero cancellation caused the expected outcome in relation to the results from proportional control (Figures 6.28 to 6.30): in most of the cases, the step response of the system improved thanks to the implementation of pole-zero cancellation. In order to compare the results, equal gain values were applied relative to the P-control and pole/zero cancellation control schemes. In general, the implementation of pole/zero cancellation reduced the steady-state error and the settling time. Likewise, the response overshoot and the peak time also decreased thanks to pole/zero cancellation.

Pole/zero cancellation (PZC) responses resembled an outline more accurately described by a second-order system (Figures 6.28 to 6.30), as it was expected based on the analysis from section 3.2.1 in chapter 3. For this reason, the natural frequency and damping ratio values determined through the open-loop approximation enabled the actual system to operate under the pole/zero cancellation scheme proposed. In the case of the closed-loop approximation relative to a P-control scheme, the simulation models would have been forced to approximate a response of different nature than the response produced by a second-order system. In order to further corroborate this deduction, the experimental responses obtained according to a sinusoidal input command, for P-control and pole/zero cancellation, were compared.

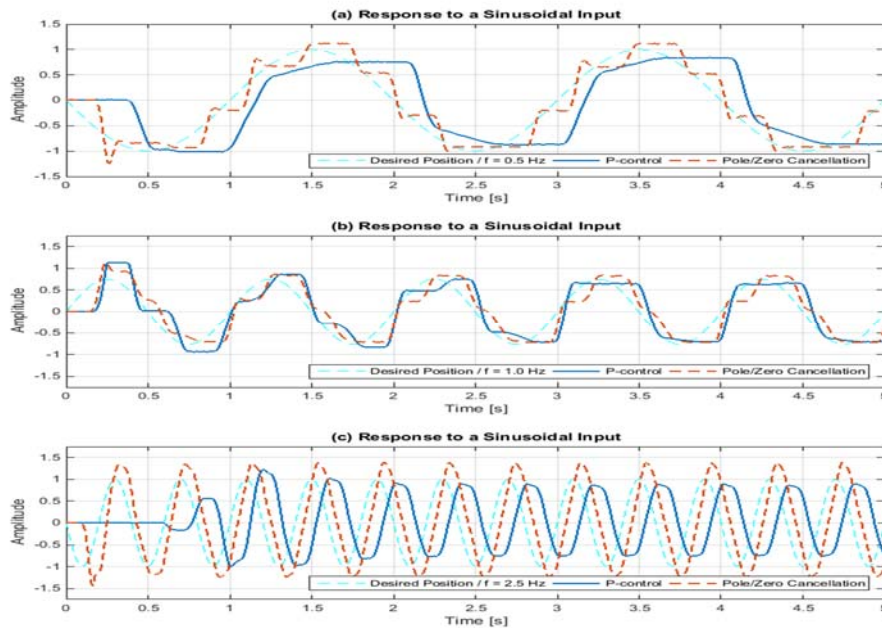


**Figure 6.31.** Experimental responses to a sinusoidal input (light blue line) with P-control and PZC ( $K_p = 0.5$ ): (a)  $f = 0.5$  Hz, (b)  $f = 1.0$  Hz, (c)  $f = 2.5$  Hz (Tube length: 0.55 m)

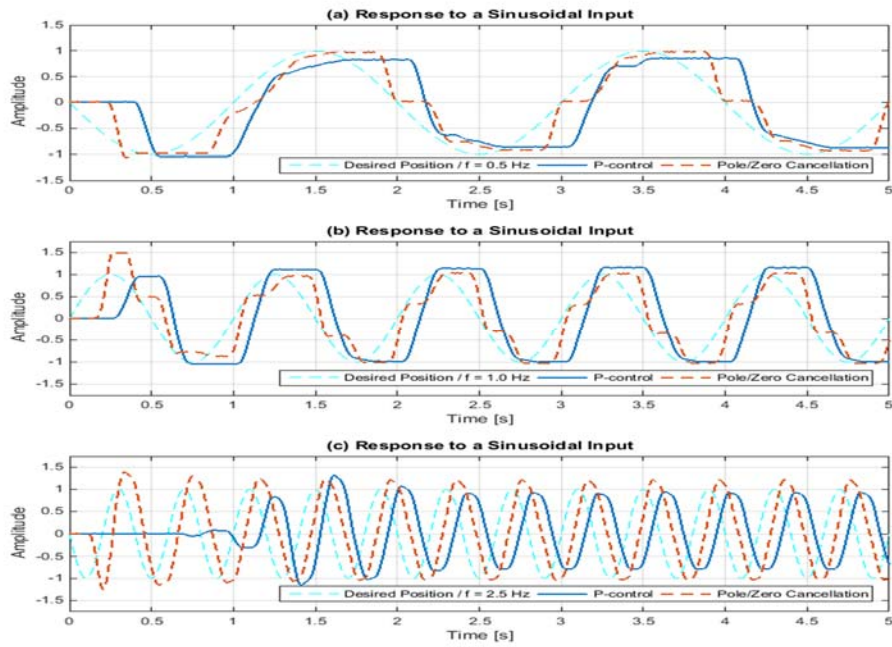


**Figure 6.32.** Experimental responses to a sinusoidal input (light blue line) with P-control and PZC ( $K_p = 0.5$ ): (a)  $f = 0.5$  Hz, (b)  $f = 1.0$  Hz, (c)  $f = 2.5$  Hz (Tube length: 1.5 m)

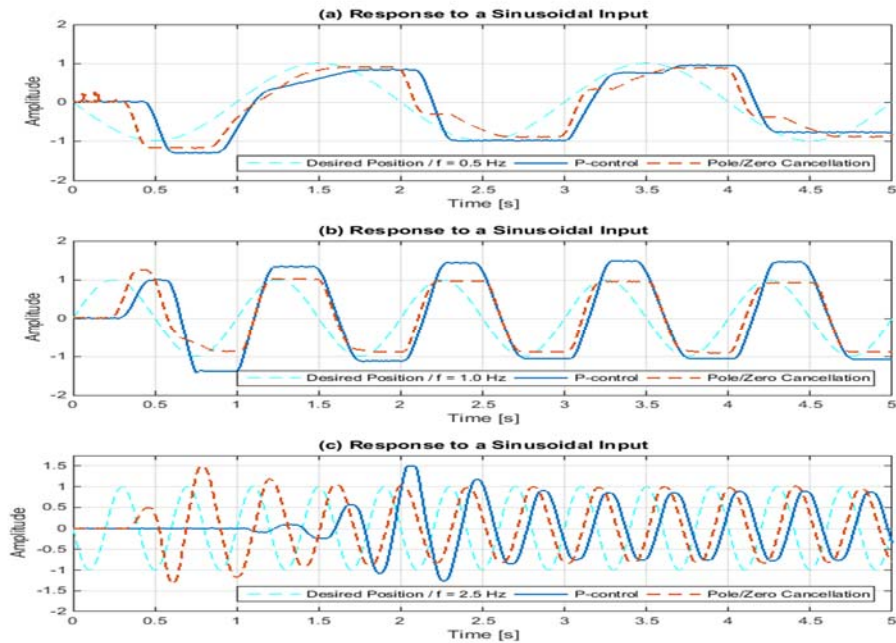


**Figure 6.33.** Experimental responses to a sinusoidal input (light blue line) with P-control and PZC ( $K_p = 0.5$ ): (a)  $f = 0.5$  Hz, (b)  $f = 1.0$  Hz, (c)  $f = 2.5$  Hz (Tube length: 3.0 m)

The benefits of implementing pole/zero cancellation in comparison to P-control were confirmed through the comparison of experimental responses according to a sinusoidal input (Figures 6.31 to 6.33). Although for certain frequencies, and depending on the length of connective tubing tested, the shape of the experimental responses became irregular, the tracking error and the phase shift were reduced. That the shape of the response became irregular depended on the magnitude of the gain used, as it is known that for gains of larger magnitude the experimental responses will tend to be unstable around the desired position. Accordingly, for certain combinations of frequency and lengths of connective tubing tested, a gain of magnitude equal to 0.5 caused that the physical system makes more effort in tracking the desired position, by deforming the outline of the response produced.

Nevertheless, mostly in relation to responses generated at the highest frequency tested (Figures 6.31c to 6.33c), pole/zero cancellation significantly reduced the phase shift in relation to the desired position profile. Another positive outcome associated with the application of pole/zero cancellation was observed from the decrease of the initial time delay, in particular for the case of three-meter hoses (Figure 6.33). In that regard, it was important to verify in following sections whether or not the efficiency of the system also increased thanks to the implementation of pole/zero cancellation, as the use of a gain of equal value did not imply that the magnitude of the input applied was the same. This and other considerations were taken into account in section 6.5, where the efficiency of the system depending on the control strategy applied was assessed. The following section proposes other control approaches as a means to further improve the performance of the system by reducing the steady-state error, the delay time, and the phase shift among others.

#### **6.4. Other Control Approaches**

This section centers on complementing or modifying the control strategies presented before to enhance the performance of the pneumatic system. Special emphasis is applied to the reduction of the tracking error relative to the response of the pneumatic system to a sinusoidal input. Moreover, the effect of increasing or decreasing the magnitude of the control gains on the response of the system is also verified.

Based on experimental results, the control schemes presented before were modified by including the feedback of the piston velocity, which was expected to improve the stability of the system and reduce the steady-state error.

Figures 6.34 and 6.35 show the schematics for implementation of the control strategies proposed by including the feedback of the piston velocity. The velocity feedback was included relative to the proportional control and the pole/zero cancellation schemes presented before.

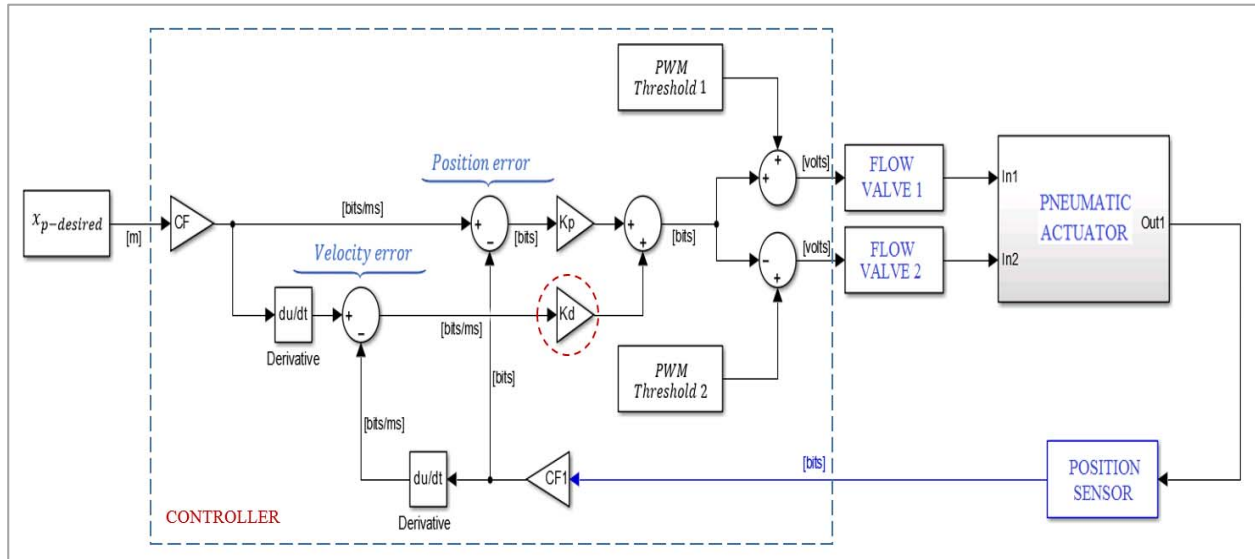


**Figure 6.34.** Alternative Approach 1: Proportional plus Derivative (PD) Control

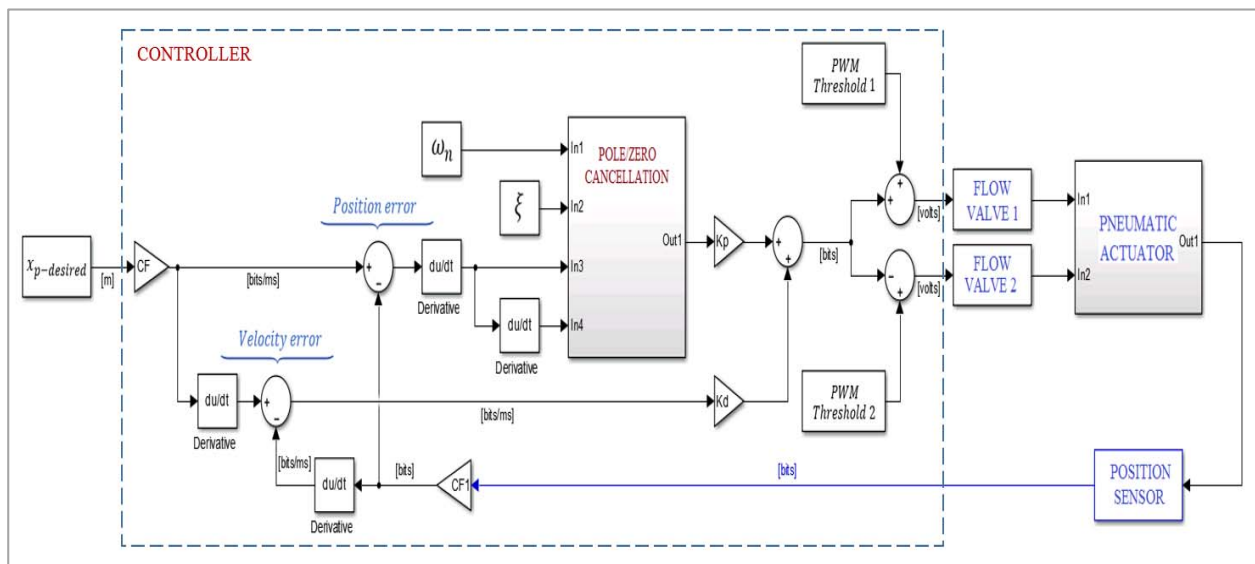


**Figure 6.35.** Alternative Approach 2: Pole/Zero Cancellation plus Derivative (PZCD) Control

The alternative control strategies (Figures 6.34 and 6.35) were denominated “plus derivative” control schemes because adding the velocity feedback is equivalent to differentiating the position error, which characterizes the application of derivative control. Similarly to P-control, a derivative gain  $K_d$ , circled in red in figure 6.34, was included in both cases.

PD control improved the response of the system only in comparison to proportional control (Figures 6.36 to 6.38). In comparison to pole/zero cancellation and its derivative variant, PD control might not have produced any improvement, which will be verified in the following section when the overall performance of the system is assessed. The main effect of the application of a PD control strategy in relation to P-Control was verified relative to the 2.5-Hz responses (Figures 6.36c to 6.38c): the addition of the feedback of the velocity reduced the phase shift and the tracking error. Nevertheless, depending on the frequency of the command signal and the length of connective tubing tested, the reduction of the phase shift of the response was accompanied by a significant reduction of its amplitude, which would not contribute to reduce the steady-state error and would be undesirable.

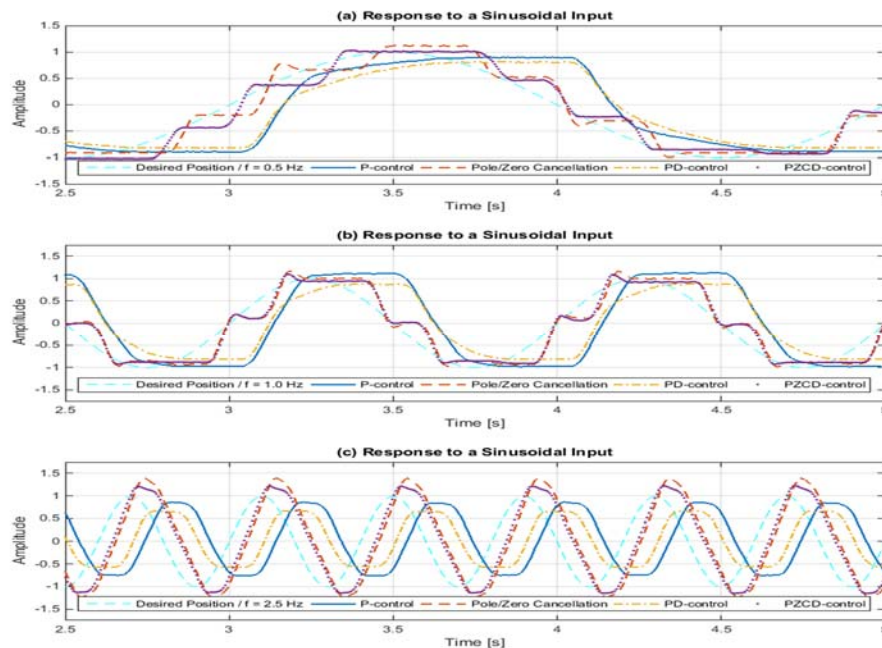


**Figure 6.36.** Actual responses to a sinusoidal input (light blue line) for P-control, PZC, PD-control and PZCD ( $K_p = 0.5$ ,  $K_d = 15.0$ ): (a) 0.5 Hz, (b) 1.0 Hz, (c) 2.5 Hz (Tube length: 0.55 m)



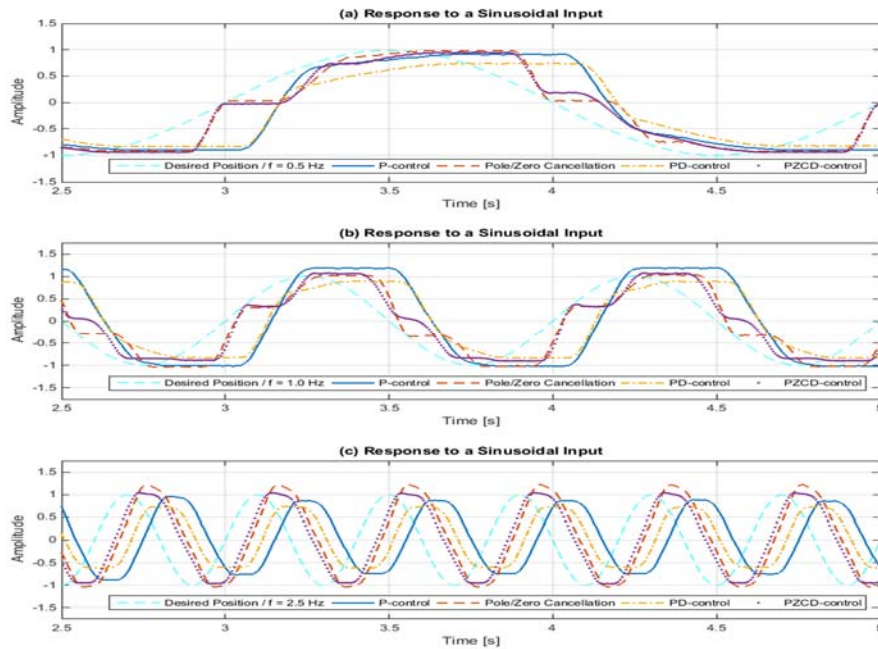


**Figure 6.37.** Actual responses to a sinusoidal input (light blue line) for P-control, PZC, PD-control and PZCD ( $K_p = 0.5$ ,  $K_d = 15.0$ ): (a) 0.5 Hz, (b) 1.0 Hz, (c) 2.5 Hz (Tube length: 1.5 m)

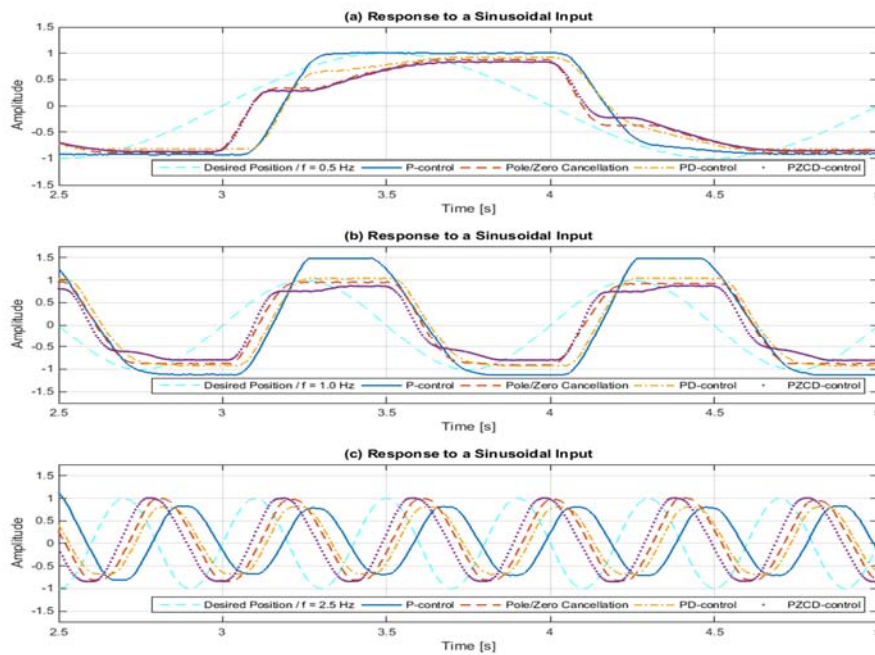


**Figure 6.38.** Actual responses to a sinusoidal input (light blue line) for P-control, PZC, PD-control and PZCD ( $K_p = 0.5$ ,  $K_d = 15.0$ ): (a) 0.5 Hz, (b) 1.0 Hz, (c) 2.5 Hz (Tube length: 3.0 m)

Furthermore, from comparing the responses obtained by applying pole/zero cancellation, and its variant including velocity feedback, no significant improvement was observed, with exception of the 2.5-Hz frequency cases (Figures 6.36c to 6.38c), where the velocity feedback in addition to the pole/zero cancellation effect reduced the phase shift of the response, and for some cases, corrected its amplitude in accordance to the command input signal.

In contrast to figures 6.36 to 6.38, figures 6.39 to 6.41 were obtained by increasing the magnitude of the proportional and derivative gains entered in the controller. The increase of the magnitude of the proportional and derivative gains causes two main outcomes: the phase shift decreased, which implied the reduction of the tracking error; and for some cases, the response turned unstable, which was caused by the increase of the magnitude of the proportional gain.

From comparing the results of applying a proportional control and a PD control scheme (Figures 6.39 to 6.41), it was verified again that the velocity feedback reduced the tracking error by decreasing the phase shift of the response in relation to the command input. In fact, in relation to the response obtained through P-control, a PD control scheme provided an additional stabilizing effect, particularly in the case of a 0.5-Hz frequency command and 3-meter connective tubing (Figures 6.41a).

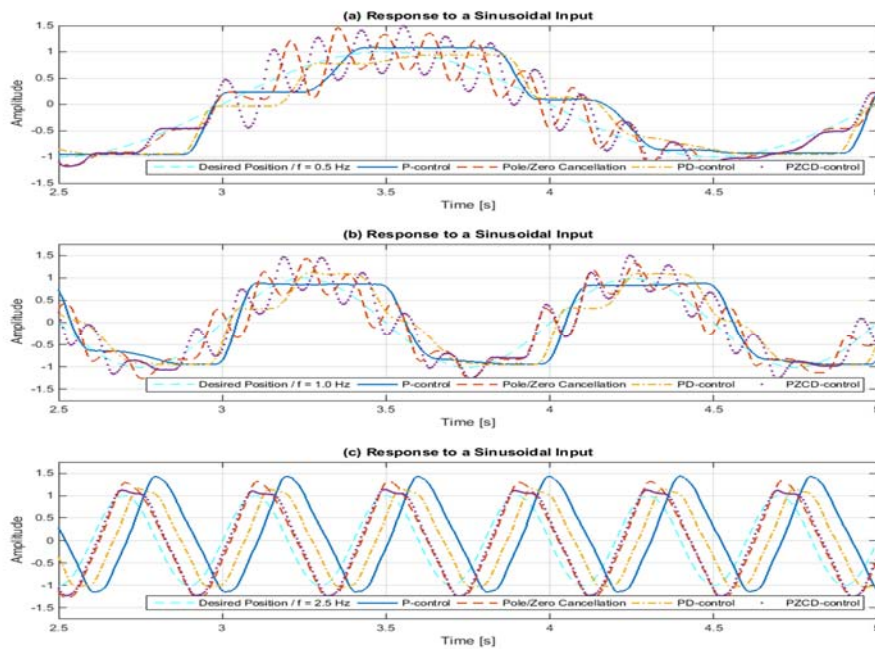


**Figure 6.39.** Actual responses to a sinusoidal input (light blue line) for P-control, PZC, PD-control and PZCD ( $K_p = 1.0$ ,  $K_d = 25.0$ ): (a) 0.5 Hz, (b) 1.0 Hz, (c) 2.5 Hz (Tube length: 0.55 m)

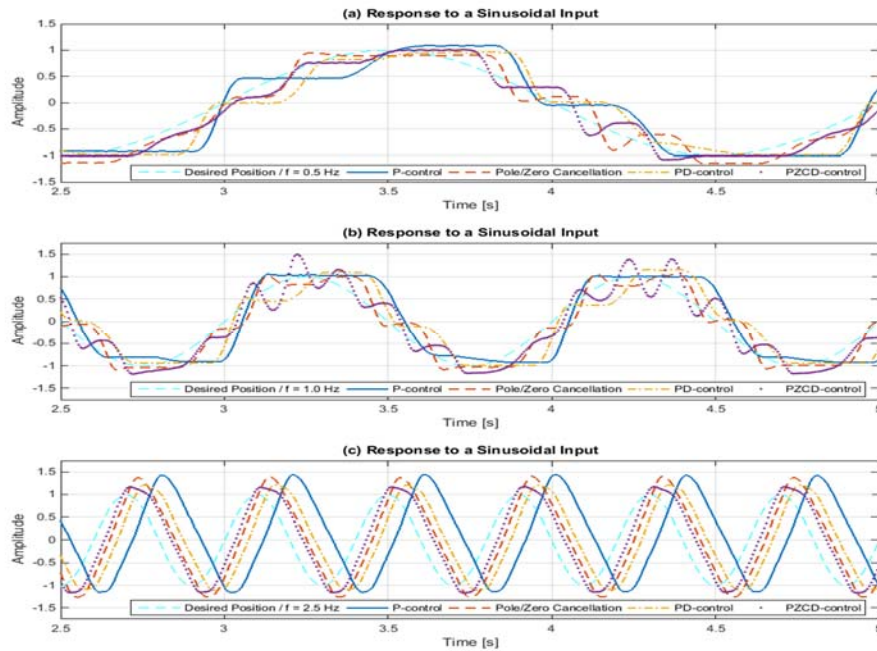


**Figure 6.40.** Actual responses to a sinusoidal input (light blue line) for P-control, PZC, PD-control and PZCD ( $K_p = 1.0$ ,  $K_d = 25.0$ ): (a) 0.5 Hz, (b) 1.0 Hz, (c) 2.5 Hz (Tube length: 1.5 m)

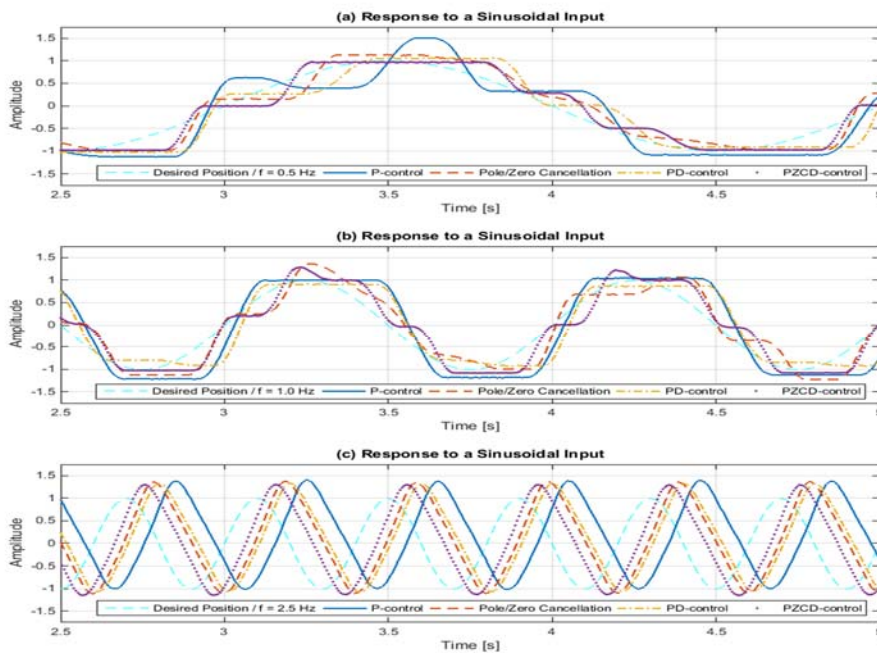


**Figure 6.41.** Actual responses to a sinusoidal input (light blue line) for P-control, PZC, PD-control and PZCD ( $K_p = 1.0$ ,  $K_d = 25.0$ ): (a) 0.5 Hz, (b) 1.0 Hz, (c) 2.5 Hz (Tube length: 3.0 m)



Moreover, by comparing the responses produced by pole/zero cancellation and its derivative variant (Figures 6.39 to 6.41), the improvement caused due to the insertion of the velocity feedback was more evident as the frequency of the input command and the length of connective tubing increased. For instance, in figure 6.41, for the 2.5-Hz subplot the improvement in the response of the system due to the application of a PZCD scheme was notorious in relation to the other control strategies applied.

The next section deals with the overall assessment of the performance and efficiency of the system according to the control schemes proposed, and the different conditions tested.

## 6.5. Performance and Efficiency Assessment

As stated before, section 6.5, the final section of this thesis, evaluates the overall performance of the pneumatic system according to the different control strategies applied, and the different operating conditions tested. This section provides the final verdict regarding the validation of the hypothesis of this thesis. It is demonstrated whether or not a specific control algorithm is able to mask the effects of air compliance and the length of connective tubing in relation to the control of a pneumatic cylinder.

Two main assessment criteria are considered: a performance criterion and an efficiency criterion. The performance criterion focuses on the fulfillment of the design specifications, while the efficiency criterion concentrates on the expenditure of energy.

### 6.5.1. Performance

Chapter 3 defined the design specification for the controller according to different assessment factors associated with the type of command input applied. In the case of a step input, five factors were identified and described: rise time, peak time, settling time, response overshoot, and steady-state error.

Tables 6.6 to 6.8 comprise the results from the quantitative assessment of the system step response according to different operating conditions. The system step responses were evaluated in relation to the control strategy implemented, the magnitude of gains entered in the controller, and the length of connective tubing tested. The numeric values included in the following tables correspond to the step responses shown in figure 6.28 through figure 6.30.

**Table 6.6.** Performance Assessment: Step response – Length of connective tubing: 0.55 m

<b>Control Strategy</b>	<b>Proportional Control</b>			<b>Pole/Zero Cancellation</b>		
	<b><u>0.3</u></b>	<b><u>0.5</u></b>	<b><u>1.0</u></b>	<b><u>0.3</u></b>	<b><u>0.5</u></b>	<b><u>1.0</u></b>
<b>Gain (<math>K_p</math>)</b>						
<i>Rise Time [s]</i>	>30.0	0.12	0.04	0.06	0.04	0.04
<i>Peak Time [s]</i>	NA	NA	0.10	0.10	0.08	0.08
<i>Settling Time [s]</i>	>30.0	0.15	0.42	0.38	0.23	NA
<i>Response Overshoot [%]</i>	NA	0.0	124.8	77.5	116.2	116.1
<i>Steady-state Error [m]</i>	NA	0.0071	0.0017	0.0071	0.0003	NA

[\*NA = Not applicable]

**Table 6.7.** Performance Assessment: Step response – Length of connective tubing: 1.5 m

<b>Control Strategy</b>	<b>Proportional Control</b>			<b>Pole/Zero Cancellation</b>		
	<b><u>0.3</u></b>	<b><u>0.5</u></b>	<b><u>1.0</u></b>	<b><u>0.3</u></b>	<b><u>0.5</u></b>	<b><u>1.0</u></b>
<b>Gain (<math>K_p</math>)</b>						
<i>Rise Time [s]</i>	>30.0	0.12	0.05	0.13	0.06	0.04
<i>Peak Time [s]</i>	NA	NA	0.11	NA	0.10	0.09
<i>Settling Time [s]</i>	>30.0	0.15	0.71	6.83	0.21	0.66
<i>Response Overshoot [%]</i>	NA	0.0	130.5	0.0	77.5	111.3
<i>Steady-state Error [m]</i>	NA	0.0096	0.0011	0.0091	0.0034	0.0003

[\*NA = Not applicable]

**Table 6.8.** Performance Assessment: Step response – Length of connective tubing: 3.0 m

<b>Control Strategy</b>	<b>Proportional Control</b>			<b>Pole/Zero Cancellation</b>		
	<b><u>0.3</u></b>	<b><u>0.5</u></b>	<b><u>1.0</u></b>	<b><u>0.3</u></b>	<b><u>0.5</u></b>	<b><u>1.0</u></b>
<b>Gain (<math>K_p</math>)</b>						
<i>Rise Time [s]</i>	>30.0	0.12	0.06	25.47	0.12	0.06
<i>Peak Time [s]</i>	NA	NA	0.15	NA	0.19	0.12
<i>Settling Time [s]</i>	>30.0	10.55	1.09	25.63	2.24	0.78
<i>Response Overshoot [%]</i>	NA	0.0	143.5	0.0	29.6	118.6
<i>Steady-state Error [m]</i>	NA	0.0042	0.0042	0.0071	0.0003	0.0006

[\*NA = Not applicable]

Tables 6.6 to 6.8 compare the results obtained through the quantitative assessment of the step response of the system chiefly in accordance to the control strategy applied. In general, as it was verified from the graphical delineation of the step responses, the implementation of pole zero cancellation improved the step response of the system in comparison to the response produced when proportional control was implemented. The improvement caused by the implementation of pole/zero cancellation was primarily observed through the reduction of the steady-state error.

Other assessment factors that corroborated the enhancement of the step response of the system due to the implementation of pole/zero cancellation were the rise time and the settling time. In fact, it was verified that the increase of the magnitude of the proportional gain caused the reduction of the rise time and the settling time, for most of the cases.

Other factors such as the peak time and the overshoot percentage were also reduced due to the implementation of pole/zero cancellation. Nevertheless, as the proportional gain increased, the overshoot increased, and for most of the cases it was higher than the maximum operation boundaries established for the design specifications in chapter 3. In that regard, by increasing the length of connecting tubing tested, the overshoot decreased or remained almost the same when pole/zero cancellation was applied.

Moreover, for certain gains, pole/zero cancellation enabled the system to fulfill most of the design specifications independently of the length of connective tubing tested. The most problematic parameters for the system to completely remain under specification were the settling time and the overshoot percentage. In fact, the most unfavorable effect caused by the increase of the length of connective tubing was the increase of the settling time. However, the application of a pole/zero cancellation scheme accomplished its goal: to reduce the effects of air compliance associated with the length of connective tubing by reducing the steady-state error and the settling time. To further corroborate this deduction, tables 6.9 to 6.11 include numeric values from the assessment of the response of the system to a sinusoidal input.

**Table 6.9.** Performance Assessment: Sinusoidal response – Length of connective tubing: 0.55 m

Parameters	Delay Time [s]			Phase Shift [deg]			Gains
	<u>0.5</u>	<u>1.0</u>	<u>2.5</u>	<u>0.5</u>	<u>1.0</u>	<u>2.5</u>	
<b>Frequency [Hz]</b>	<b>0.5</b>	<b>1.0</b>	<b>2.5</b>	<b>0.5</b>	<b>1.0</b>	<b>2.5</b>	<b><math>K_p \setminus K_d</math></b>
<i>Proportional Control</i>	0.41	0.27	0.62	29.3	50.0	126.9	0.5 \ -
	0.24	0.18	0.13	25.6	15.5	96.3	1.0 \ -
<i>Pole/Zero Cancellation</i>	0.17	0.12	0.09	17.5	15.8	49.5	0.5 \ -
	0.12	0.09	0.08	0.0	0.0	27.0	1.0 \ -
<i>PD Control</i>	0.35	0.22	0.34	29.3	45.0	98.1	0.5 \ 15.0
	0.21	0.15	0.10	25.6	7.2	61.2	1.0 \ 25.0
<i>PZCD Control</i>	0.17	0.12	0.09	7.0	15.8	41.4	0.5 \ 15.0
	0.12	0.09	0.08	0.0	0.0	19.8	1.0 \ 25.0

**Table 6.10.** Performance Assessment: Sinusoidal response – Length of connective tubing: 1.5 m

Parameters	Delay Time [s]			Phase Shift [deg]			Gains
	<u>0.5</u>	<u>1.0</u>	<u>2.5</u>	<u>0.5</u>	<u>1.0</u>	<u>2.5</u>	
Frequency [Hz]							$K_p \setminus K_d$
Proportional Control	0.41	0.28	1.37	29.9	46.4	137.7	0.5 \ -
	0.25	0.17	0.13	28.7	20.5	109.8	1.0 \ -
Pole/Zero Cancellation	0.23	0.15	0.11	13.7	41.8	67.5	0.5 \ -
	0.15	0.10	0.09	5.4	0.0	44.1	1.0 \ -
PD Control	0.41	0.24	0.37	29.9	46.4	103.5	0.5 \ 15.0
	0.23	0.15	0.11	15.5	9.0	69.3	1.0 \ 25.0
PZCD Control	0.23	0.15	0.11	13.7	41.8	54.9	0.5 \ 15.0
	0.15	0.10	0.09	5.4	0.0	32.4	1.0 \ 25.0

**Table 6.11.** Performance Assessment: Sinusoidal response – Length of connective tubing: 3.0 m

Parameters	Delay Time [s]			Phase Shift [deg]			Gains
	<u>0.5</u>	<u>1.0</u>	<u>2.5</u>	<u>0.5</u>	<u>1.0</u>	<u>2.5</u>	
Frequency [Hz]							$K_p \setminus K_d$
Proportional Control	0.47	0.32	1.22	32.4	55.8	167.4	0.5 \ -
	0.28	0.18	0.14	28.3	11.5	138.6	1.0 \ -
Pole/Zero Cancellation	0.31	0.23	0.33	15.1	40.0	105.3	0.5 \ -
	0.18	0.12	0.10	18.7	22.3	86.4	1.0 \ -
PD Control	0.41	0.27	0.57	32.4	55.8	120.6	0.5 \ 15.0
	0.25	0.18	0.12	28.3	19.8	97.2	1.0 \ 25.0
PZCD Control	0.31	0.19	0.15	15.1	35.3	75.6	0.5 \ 15.0
	0.18	0.12	0.10	15.8	22.3	61.2	1.0 \ 25.0

The numeric values in tables 6.9 to 6.11 correspond to the responses depicted in figures 6.36 to 6.41. In addition to the comparison of the results obtained through the application of proportional control and pole/zero cancellation, the results were compared according to the application of the control schemes including velocity feedback: proportional plus derivative (PD) control and pole/zero cancellation plus derivative (PZCD) control.

In general, independently of the gains applied and the frequency of the input command, the implementation of pole/zero cancellation reduced the delay time and the phase shift of the responses in relation to proportional control and PD control. In relation to its derivative variant, pole/zero cancellation was inferior in performance, although for some cases the delay time measured was the same. The major improvement caused by the implementation of a PZCD control scheme manifested on the reduction of the phase shift of the actual response.

As the frequency of the sinusoidal input command increased, the phase shift of the actual response increased (Tables 6.9 to 6.11). However, when the magnitude of the control gains increased, the frequency increment also caused the reduction of the delay time. In relation to the control gains applied, the increase of the magnitude of the control gains reduced the time delay and the phase shift of the response, independently of the control scheme, the length of connective tubing, and the frequency of the input command.

In addition, perhaps the most important parameter to measure relative to the response of the system to a sinusoidal input was the tracking error, which would include the effect of the delay time and the phase shift in a single parameter. The tracking error describes how closely the actual response of the system follows the input command or desired response. It might be most appropriately described by the standard deviation of the difference between the desired and actual responses, as it is a common practice in economics in order to quantify the difference between the price behavior of a portfolio and a benchmark index. Accordingly, the tracking error was computed according to the following expression.

$$\text{Tracking Error} = \sqrt{\frac{\sum_{i=1}^N (x_{desired_i} - x_{actual_i})^2}{N - 1}} \quad (6.9)$$

Where N is the total number of samples.

By applying Eq. 6.11, the tracking error relative to the sinusoidal response of the system is computed and graphically represented in figure 6.42.

Figure 6.42 compares the tracking error relative to the sinusoidal responses of the system, for different frequencies, different control gains, and different lengths of connective tubing. The most noticeable result from figure 6.42 was the increase of the tracking error when a 2.5-Hz sinusoidal input command was applied.

The increase of the tracking error results unfavorable in the overall assessment of the performance of the pneumatic system; nevertheless, according to the control strategy applied, the tracking error can be reduced to levels where the performance of the system under the use of short or lengthy connective tubing can be considered equivalent. For example, by comparing the tracking error associated with the responses obtained using 0.55-meter and 3.0-meter connective tubing, for a 1.0-Hz sinusoidal input command, the tracking error levels measured depending on the control scheme applied were approximately the same.

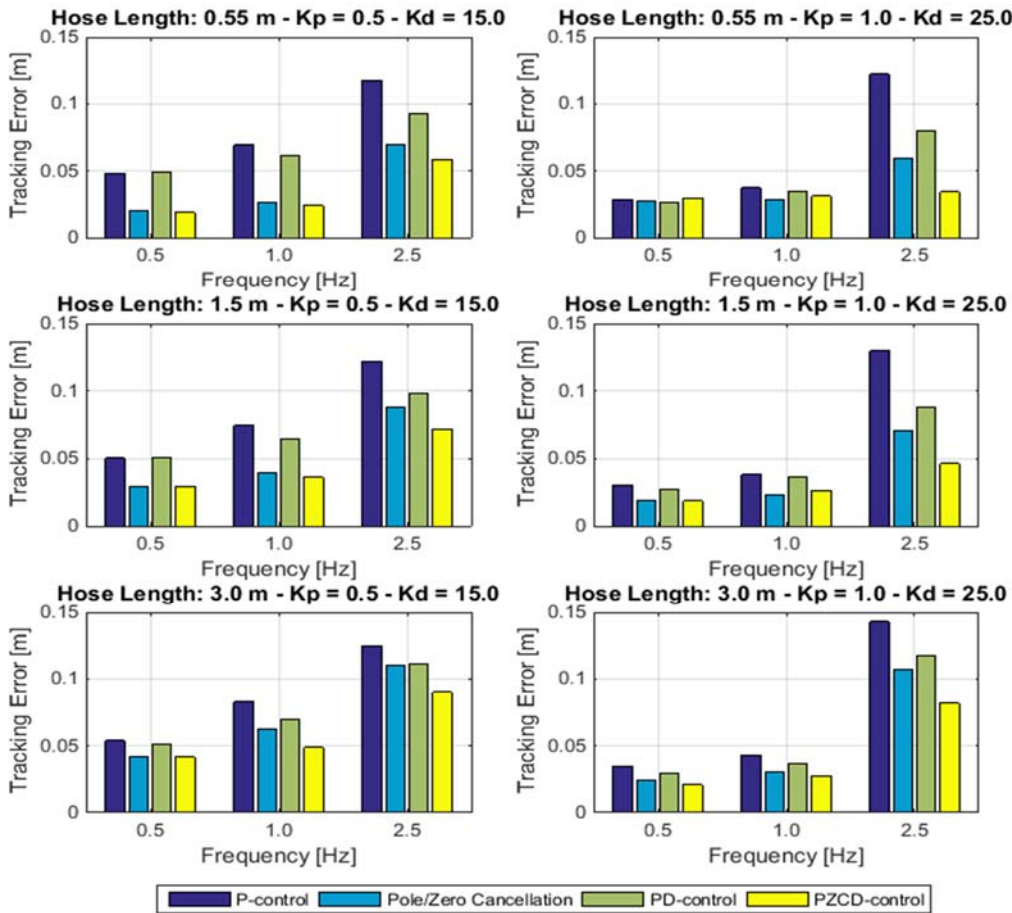


**Figure 6.42.** Performance Assessment: Tracking Error in sinusoidal responses

In relation to the control strategy applied, the implementation of proportional control caused the maximum tracking error for most of the operating conditions tested (Figure 6.42). The application of PD control in relation to proportional control generally reduced the tracking error. Likewise, the application of a pole/zero cancellation scheme reduced the tracking error of the responses in relation to the implementation of proportional control and PD control. Overall, the application of the derivative variant of pole/zero cancellation (PZCD) produced the best results in terms of the lowest tracking error measured for all the operating condition tested.

Regarding the effect of the magnitude of the control gains, the increase of the magnitude of the gains had a positive effect on the performance of the system by decreasing the tracking error, with exception of the cases where proportional control was applied in combination to a 2.5-Hz sinusoidal input command. For those cases, the tracking error increased significantly.

In conclusion for this section, it can be asserted that the application of certain control strategies, under specific operating conditions, is capable of attenuating the negative effects of air compliance and the length of connective tubing on the performance of the pneumatic system. Specifically, pole/zero cancellation and its derivative variant demonstrated to be successful on reducing the steady-state error, tracking error, time delay and settling time of the response of the pneumatic system, by making its performance under short or lengthy connective tubing approximately equivalent.

### 6.5.2. Efficiency

In section 6.5.1, the performance of the system was measured in terms of its efficacy to reach certain levels of accuracy and speed in response to specific inputs and under diverse operating conditions. In this section, the response of the system was evaluated in terms of the use of energetic resources; specifically in the case of pneumatic cylinders, the use of compressed air.

In chapter 1, the energetic efficiency of linear actuators was defined in terms of the ratio of the output power to the input power, as described by the following expression already defined in chapter 1, section 1.4.6.

$$\eta_{la} = \left( \frac{F \dot{x}_p}{P_i Q_i} \right)_{la} \quad (6.10)$$

Where the input power corresponds to the product of the inlet pressure,  $P_i$ , and the inlet volumetric flow,  $Q_i$ ; and the output power corresponds to the product of the actuator force,  $F$ , and the actuator velocity,  $\dot{x}_p$ .

Due to the asymmetry of the piston areas, the dominating forces during piston extension and retraction are different, and they correspond to the force generated by pressure relative to the piston active area in the cylinder cap-end and rod-end, respectively. The following expressions define the dominating forces during extension and retraction of the pneumatic piston.

$$\begin{aligned} F_1 &= P_1 A_1 \\ F_2 &= P_2 A_2 \end{aligned} \quad (6.11)$$

Where the subscript 1 and 2 have been respectively included in reference to the pressure force on the cap-end of the cylinder during piston extension, and the pressure force on the rod-end of the cylinder during piston retraction.

Likewise, the volumetric inlet flow during extension and retraction of the piston relative to the cap-end and rod-end cylinder chambers were defined according to Eq. 2.25.

$$\begin{aligned} Q_{i1} &= \frac{V_{01} + x_p A_1}{k P_1} \dot{P}_1 + \dot{x}_p A_1 \\ Q_{i2} &= \frac{V_{02} + x_p A_2}{k P_2} \dot{P}_2 + \dot{x}_p A_2 \end{aligned} \quad (6.12)$$

Therefore, an overall energetic efficient for the pneumatic system could be given by:

$$\begin{aligned} \eta_{Overall_{la}} &= \eta_{Extension} \eta_{Retraction} \\ \eta_{Overall_{la}} &= \left( \frac{F_1 \dot{x}_{p1}}{P_1 Q_{i1}} \right) \left( \frac{F_2 \dot{x}_{p2}}{P_2 Q_{i2}} \right) \end{aligned} \quad (6.13)$$

Based on Eq. 6.15, figure 6.43 graphically represents the efficiency of the pneumatic actuator relative to its response to a sinusoidal input, and in reference to the control strategy applied, the length of connective tubing tested, the magnitude of the control gains, and the frequency of the command input applied. The results in figure 6.43 correspond to the sinusoidal responses depicted in figures 6.36 to 6.41

Among the efficiency patterns identified, the most consistent was the one associated with the implementation of the derivative variant of pole-zero cancellation (PZCD). In general, figure 6.43 demonstrates that the implementation of a PZCD control scheme enabled the pneumatic actuator to operate more efficiently in contrast to the other control schemes applied. Nevertheless, it was also important to recognize the efficiency pattern associated with the implementation of proportional control. For most of the cases, the overall efficiency of the pneumatic actuator operating under a proportional control scheme equaled or even surpassed the efficiency associated with the implementation of PD control and pole/zero cancellation.

Moreover, as the length of connective tubing increased, the overall efficiency of the pneumatic actuator decreased. Likewise, the increase of the magnitude of the control gains decreased the efficiency of the system, primarily in relation to the responses obtained by applying a 0.5-Hz and a 1.0-Hz sinusoidal input command. Nevertheless, when a 2.5-Hz input command was applied, the efficiency of the system tended to increase, which would be caused by the reduction of friction when the piston works at higher speed.



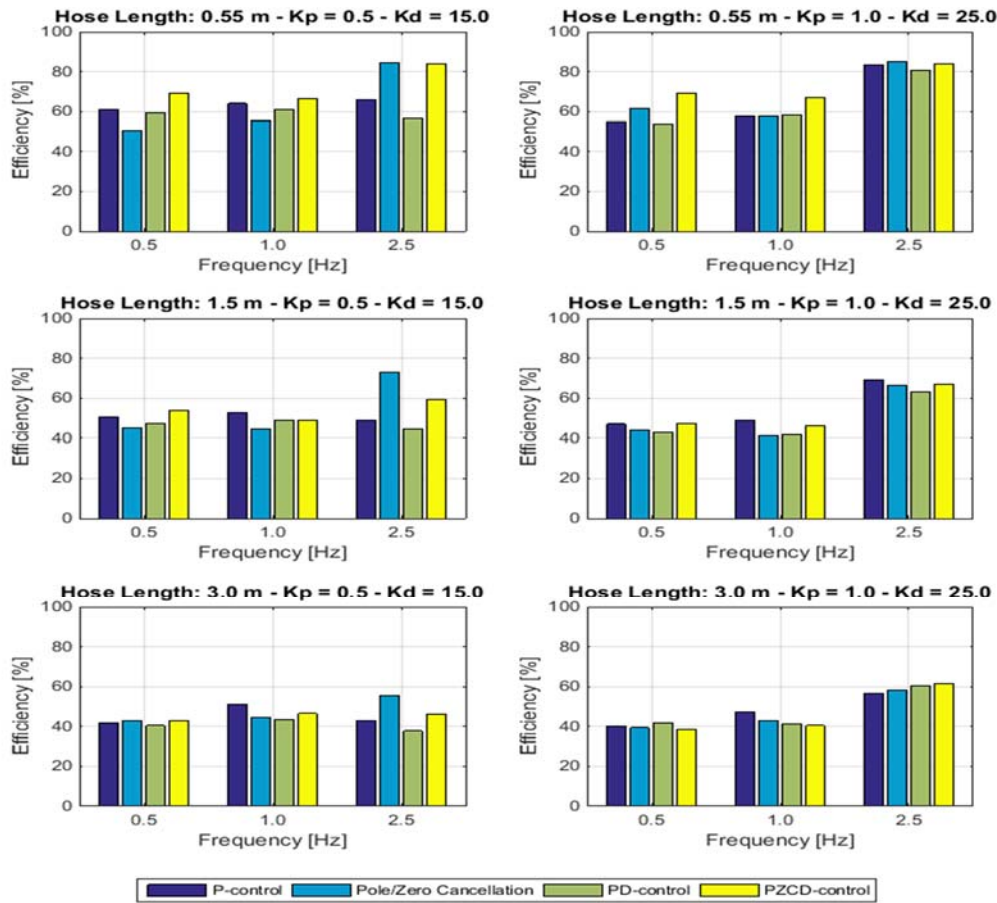


**Figure 6.43.** Overall Efficiency Assessment: Sinusoidal response

Regarding the implementation of pole/zero cancellation, the levels of efficiency achieved were not consistent, although a significant improvement was still observed in some cases, such as for the three different lengths of connecting tubing tested, when a 2.5-Hz input was applied.

Similar levels of efficiency could be reached by applying pole/zero cancellation or its derivative variant, PZCD, in combination to the use of 1.5-meter and 3-meter connective tubing. However, it would not be feasible to approximate the levels of efficiency calculated in relation to the use of 0.55-meter connective tubing. The levels of efficiency for those cases exceed in approximately 10 to 20 percent the levels of efficiency achieved with lengthier hoses.

Summarizing, the implementation of pole/zero cancellation and its derivative variant accomplished its goal in masking the effects of air compliance and the length of connective tubing when the efficiency associated with the use of 3-meter connective tubing could be approximated to the efficiency of the pneumatic system including 1.5-meter connective tubing.

## CHAPTER VII

### CONCLUSIONS AND RECOMMENDATIONS

#### Overall Assessment

This chapter provides the overall assessment of the project for this thesis. The assessment of the project is made in relation to the fulfillment of the research objectives. The main research question is explicitly answered, and the research contributions are summarized as part of the conclusions of this thesis.

Based on the research contributions from this project, recommendations for future work are made, mainly considering the potential of the application of control theory to improve the performance and efficiency of pneumatic systems, and fluid power technology in general.

#### 7.1. Conclusions

The answer to the main research question for this project reduces to the confirmation of the improvement of performance and efficiency of the system studied due to the implementation of the controller designed. The overall results of this study demonstrated the potential of control theory to increase the performance and efficiency of a pneumatic cylinder under specific conditions. One of the main research goals was to correlate the measurement of performance and efficiency of the pneumatic cylinder to the length of connective tubing tested. The control algorithm implemented demonstrated to match the performance and efficiency of the pneumatic cylinder when lengthy connective tubing was tested, to the performance and efficiency achieved using shorter hoses. Therefore, based on the results obtained and answering the main research question, the control algorithm designed did attenuate the detrimental effects of air compliance and the length of connective tubing on the performance and efficiency of the pneumatic cylinder.

In the first stage of this study, several deductions were made based on preliminary experimental results. The dynamic behavior of the individual components of the system was corroborated through experimentation, which provided a better understanding of the overall system.

Equations, models, and assumptions derived from the literature reviewed were validated. The first two chapters centered on presenting relevant findings from research developed in relation to the modeling and control of pneumatic systems. Particularly, the equations and models describing the transitory flow progression relative to the cylinder chambers and the control valves were applied and validated. The increase of the length of tubing connecting the control valves and the pneumatic cylinder caused a more prominent delay on the flow entering the cylinder chambers in relation to the flow immediately produced by the control valves. As the length of connective tubing increased, the cylinder piston required more time to reach a specific position, as well as the compression of air in the cylinder chambers took more time. The delay of the flow in the cylinder chambers would come from the time required by the pressure waves to travel along the connective tubing tested. In that regard, the measurement of pressure relative to the system components was important for the verification and deduction of assumptions.

Preliminary experimental results demonstrated that the consideration of constant pressure supplied to the valves is dependent on the magnitude of the valve control commands. As the control gains and frequency of the valve control commands increased, the assumption of a constant supply pressure was no longer valid. In addition, the measurement of pressure in relation to the control valves and the cylinder chamber enabled the identification of valve operational control values. The boundaries of the valve dead zone were identified, from which compensation strategies were applied for synchronizing the two three-way proportional valves included in the experimental setup. By defining a higher threshold control value for the valve connected to the cylinder rod-end chamber, the flow provided to both cylinder chambers was balanced, as well as the operational distortion caused by the transitional displacement of the valve spool through the valve dead zone was reduced.

In addition, through the acquisition and analysis of preliminary experimental data, the dynamic parameters, constants, and control gains included in the models for the pneumatic system were determined. The volumetric flow transmitted to the cylinder was related to the PWM input voltage applied to the valves, and to the differential pressure relative to the cylinder chambers. From these correlations, the flow and pressure gains derived from the linearization of the flow equations included in the models were determined. A graphical method for the identification of the flow and pressure gains was applied, which implied the selection of the operational points around which the flow equations were linearized.

In Chapter 3, nonlinear and linear models for the pneumatic system were derived and implemented for simulation using Simulink and MATLAB. Block full-nonlinear models and full-linear models were derived. To generate the block full-linear models, the flow equations were linearized applying a Taylor series expansion. The block full-linear models were reduced using block-reduction algebra. The reduced-linear models constituted the definitive models for simulation and controller design. Further simplification of the reduced linear models was achieved by decreasing the order of their transfer function. The variation of the piston effective area and the pressure gain enabled the simplified reduced models to match the responses from the original reduced models. Root locus analysis supported the simplification of the models and the design of the controller.

Two sets of block non-linear and linear models were derived. One set explicitly included the compressibility of air represented by the air bulk modulus, and for that was labeled the compressibility models. An alternative set, for which air compliance and air compressibility were modeled in basis to a virtual spring, was labeled the spring models. The responses from both sets of models were matched based on the association of their dynamic parameters. The virtual spring constant was associated with the air bulk modulus, the cylinder effective volume, and the piston effective area. Because the length of connective tubing relates to the cylinder effective volume and the air bulk modulus, the virtual spring would represent the hoses connecting the cylinder chambers and the control valves. As the length of connective tubing increased, the value of the spring constant and the air bulk modulus decreased, which represented an accentuated effect of air compressibility and air compliance on the dynamic behavior of the system. In that regard, root locus analysis demonstrated that as the length of connective tubing increases, the sensitivity of the system increases: the use of lengthier connective tubing reduces the margin available to turn the system into an unstable system under the application of a control scheme.

Regarding the design of the controller, a proportional control scheme was first designed and implemented in relation to the simulation models and the actual system. Subsequently, pole/zero cancellation was applied as an alternative to mask the dynamics associated with air compressibility, air compliance, and the length of connective tubing. In fact, theoretically, pole/zero cancellation specifically targeted the dynamics represented by the air bulk modulus, the cylinder effective volume, and the virtual spring constant, all directly related to the length of connective tubing.

Pole/zero cancellation demonstrated to be superior to proportional control in maintaining the performance of the system at a certain desired level when lengthier connective tubing was used. Pole/zero cancellation was also compared to PD control. PD control improved the accuracy and performance of the system in comparison to sole proportional control. Pole/zero cancellation was also superior to PD control in reducing the steady state and tracking error of the system. Nevertheless, in terms of efficiency assessment, pole/zero cancellation did not show improvement in comparison to sole proportional control and PD control. In fact, proportional control demonstrated to be relatively high efficient in comparison to PD control and sole pole/zero cancellation. With proportional control, the cylinder operated under lower regimes of pressure and flow than PD control and sole pole/zero cancellation, which traduced into a minor effort to fulfill the design specifications; and hence, in a lower system performance but higher efficiency. Pole/zero cancellation demonstrated a complete superiority, in terms of performance and efficiency, when it was implemented in combination with derivative control.

Therefore, in terms of performance, the implementation of pole/zero cancellation and its derivative variant enabled the cylinder to achieve similar levels of performance when short (0.55 m) and lengthy hoses (3.0 m) were used. In terms of energetic efficiency, the implementation of pole/zero cancellation schemes enabled the cylinder to achieve similar levels of efficiency when 3.0-meter and 1.5-meter hoses were used. Nevertheless, under any control scheme, by using 3.0-meter and 1.5-meter hoses, the cylinder was able to match the efficiency achieved using 0.55-meter hoses. Overall, the implementation of pole/zero cancellation and its derivative variant enabled the project to accomplish its ultimate research goal: to investigate the effects of the length of connective tubing on the performance and efficiency of pneumatic cylinders, and to produce a control algorithm able to mask those effects.

## 7.2. Recommendations for Future Work

Further work in the modeling and control of pneumatic cylinders should include a more accurate representation of the dynamics associated with pressure and flow variation in lengthy connective tubing. As an alternative, the second-order linear filter model proposed by [Whitemore and Leondes \(1991\)](#) could be implemented or merged into the models already proposed.

The friction dynamics associated with the motion of the cylinder piston should not be neglected. As the simulation results demonstrated, friction severely affects the system performance under low-frequency control schemes. The simulation results presented would constitute a representation of ideal performance when friction is not considered. In that regard, the use of two three-way valves could provide a means to compensate for the friction dynamics of the cylinder piston, which should be further investigated. Likewise, additional methods for compensation of friction in pneumatic cylinders should be explored and applied.

The use of two three-way valves might have enabled the pneumatic system to achieve higher levels of efficiency, which should be confirmed through the comparison of experimental results produced by using a sole five-way proportional valve. In that regard, a more accurate representation of the dynamics of the control valve is also need. The incorporation of a flow sensor in the experimental setup would permit the flow equations included in the valve models to be completely validated.

Relative to the design of the controller, different control strategies derived from modern control theory should be explored. The state-space models proposed in Chapter 3 should be implemented and assessed in terms of performance and efficiency. Similarly, their simulation responses (Chapter 5, section 5.2) should be validated with experimental data. The application of optimal control theory would enable the pneumatic system to achieve higher performance and efficiency, for which further study of nonlinear control theory is required.

Furthermore, the use of the Arduino UNO microcontroller board demonstrated the potential of low-cost open-source electronics platforms in control application. In that regard, the results obtained could be compared with results produced through more advanced electronics platforms. The implementation of more advanced electronic platforms would increase the resolution of the signals produced, as well as the accuracy with which a signal is reconstructed in the computer. Likewise, the use of more advanced techniques for the processing and analysis of data could enable the results obtained to more accurately match the theoretical models.

Finally, research for the improvement of performance and efficiency of fluid power systems should be continued. Energy-saving actuators and control valves should be designed and tested. Novel control strategies should be implemented and validated. Simplified models that enable the use of open-source control platforms should be created, all with the ultimate goal of producing clean and sustainable technology for the transmission and generation of power.

## BIBLIOGRAPHICAL REFERENCES

- Al-Dakkan, K. A., Goldfarb, M., & Barth, E. J. (2003, July). Energy saving control for pneumatic servo systems. In *Advanced Intelligent Mechatronics, 2003. AIM 2003. Proceedings. 2003 IEEE/ASME International Conference on (Vol. 1, pp. 284-289)*. IEEE.
- Ang, K. H., Chong, G., & Li, Y. (2005). PID control system analysis, design, and technology. *Control Systems Technology, IEEE Transactions on*, 13(4), 559-576.
- Balachandran, P. (2006). *Fundamentals of compressible fluid dynamics*. PHI Learning Pvt. Ltd.
- Başar, T., & Bernhard, P. (2008). *H-infinity optimal control and related minimax design problems: a dynamic game approach*. Springer Science & Business Media
- Backé, W. (1993). The present and future of fluid power. *Proceedings of the Institution of Mechanical Engineers, Part I: Journal of Systems and Control Engineering*, 207(4), 193-212.
- Beater, P. (2007). *Pneumatic drives*. Springer-Verlag Berlin Heidelberg.
- Ben-Dov, D., & Salcudean, S. E. (1995). A force-controlled pneumatic actuator. *IEEE Transactions on Robotics and Automation*, 11(6), 906-911.
- Bergh, H. & Tjrdeman, H. (1972). The influence of the main flow on the transfer function of tube-transducer systems used for unsteady pressure measurements. *Nationaal Lucht-en Ruimtevaartlaboratorium*.
- Bona, B., & Indri, M. (2005, December). Friction compensation in robotics: an overview. In *Decision and Control, 2005 and 2005 European Control Conference. CDC-ECC'05. 44th IEEE Conference on (pp. 4360-4367)*. IEEE.
- Broersen, P. M. (1994, May). A comparison of transfer function estimators. In *Instrumentation and Measurement Technology Conference, 1994. IMTC/94. Conference Proceedings. 10th Anniversary. Advanced Technologies in I & M, 1994 IEEE (pp. 1377-1380)*. IEEE.
- Close, C. M., Newell, J. C., & Frederick, D. K. (2002). *Modeling and analysis of dynamic systems*. Wiley.
- Chillari, S., Guccione, S., & Muscato, G. (2001). An experimental comparison between several pneumatic position control methods. In *Decision and Control, 2001. Proceedings of the 40th IEEE Conference on (Vol. 2, pp. 1168-1173)*. IEEE.
- Chi-Tsong, C. (1999). *Linear system theory and design*. Oxford Univ. Press, Oxford, England, UK, 121-140.



- DeCarlo, R., Zak, S. H., & Matthews, G. P. (1988). Variable structure control of nonlinear multivariable systems: a tutorial. *Proceedings of the IEEE*, 76(3), 212-232.
- Delfino, F., Procopio, R., & Rossi, M. (2002). Evaluation of forces in magnetic materials by means of energy and co-energy methods. *The European Physical Journal B-Condensed Matter and Complex Systems*, 25(1), 31-38.
- Edge, K. A. (1996). The control of fluid power systems-responding to the challenges. *Proceedings of the Institution of Mechanical Engineers, Part I: Journal of Systems and Control Engineering*, 211(2), 91-110.
- Fleischer, H. (1995). *Manual of pneumatic systems optimization*. McGraw-Hill.
- Fox, R. W., McDonald, A. T., & Pritchard, P. J. (1985). *Introduction to fluid mechanics (Vol. 7)*. New York: John Wiley & Sons.
- Franklin, G. F., Powell, J. D., & Emami-Naeini, A. (2002). *Feedback control of dynamics systems*. Addison-Wesley, Reading, MA.
- Friedland, B. (2012). *Control system design: an introduction to state-space methods*. Courier Corporation.
- Granosik, G., & Borenstein, J. (2004). Minimizing air consumption of pneumatic actuators in mobile robots. *IEEE International Conference on Robotics and Automation, 2004. Proceedings. ICRA '04. 2004, 4*, 3634–3639.
- Grewal, K. S., Dixon, R., & Pearson, J. (2012). LQG controller design applied to a pneumatic Stewart-Gough platform. *International Journal of Automation and Computing*, 9(1), 45-53.
- Halbaoui, K., Boukhetala, D., & Boudjema, F. (2011). *Introduction to Robust Control Techniques*. INTECH Open Access Publisher.
- Hamdan, M., & Gao, Z. G. Z. (2000). A novel PID controller for pneumatic proportional valves with hysteresis. *Conference Record of the 2000 IEEE Industry Applications Conference. Thirty-Fifth IAS Annual Meeting and World Conference on Industrial Applications of Electrical Energy (Cat. No.00CH37129)*, 2, 1198–1201.
- Harris, P., Nolan, S., O'Donnell, G., & Meskell, C. (2013). Optimizing Compressed Air System Energy Efficiency-The Role of Flow Metering and Exergy Analysis. *20th CIRP International Conference on Life Cycle Engineering*. Retrieved from [http://link.springer.com/chapter/10.1007/978-981-4451-48-2\\_21](http://link.springer.com/chapter/10.1007/978-981-4451-48-2_21) [Accessed February 2014]
- Hesselroth, T., Sarkar, K., van der Smagt, P. P., & Schulten, K. (1994). Neural network control of a pneumatic robot arm. *Systems, Man and Cybernetics, IEEE Transactions on*, 24(1), 28-38.



- Jeon, Y. S., Lee, C. O., & Hong, Y. S. (1998). Optimization of the control parameters of a pneumatic servo cylinder drive using genetic algorithms. *Control Engineering Practice*, 6(7), 847-853.
- Ke, J., Wang, J., Jia, N., Yang, L., & Wu, Q. H. (2005, August). Energy efficiency analysis and optimal control of servo pneumatic cylinders. In *Control Applications, 2005. CCA 2005. Proceedings of 2005 IEEE Conference on* (pp. 541-546). IEEE.
- Khalil, H. K., & Grizzle, J. W. (2002). *Nonlinear systems* (Vol. 3). New Jersey: Prentice hall.
- Liu, S., & Bobrow, J. E. (1988). An analysis of a pneumatic servo system and its application to a computer-controlled robot. *Journal of Dynamic Systems, Measurement, and Control*, 110(3), 228-235.
- Lu, P. (2015). *Optimal Control. Course Notes*. Iowa State University.
- Manring, N. (2005). *Hydraulic control systems*. Wiley.
- Moran, M. J., Shapiro, H. N., Boettner, D. D., & Bailey, M. B. (2010). *Fundamentals of engineering thermodynamics*. John Wiley & Sons.
- Narendra, K. S. (1996). Neural networks for control theory and practice. *Proceedings of the IEEE*, 84(10), 1385-1406.
- NFPA (2014). *Fluid Power Advantages*. Retrieved from: <http://www.nfpa.com/fluidpower/fluidpoweradvantages.aspx> [Accessed December 2014]
- Norgren (2014). *Saving energy with compressed air systems*. Retrieved from: <http://www.norgren.com/us/savingenergy> [Accessed December 2014]
- Ogata, K. (1998). *System dynamics* (Vol. 3). New Jersey: Prentice Hall.
- Palm, W. J. (2014). *System dynamics*. McGraw-Hill Higher Education.
- Pearce, M. (2005). Is there an alternative to fluid power? *Computing & Control Engineering Journal*, (May). Retrieved from: [http://ieeexplore.ieee.org/xpls/abs\\_all.jsp?arnumber=1454278](http://ieeexplore.ieee.org/xpls/abs_all.jsp?arnumber=1454278) [Accessed December 2014]
- Petrilean, D., Jitea, P., & Suci, A. (2009). Exergetic efficiency of pneumatic installation with polytropic compression. *Upet.ro*, 11, 183–190. Retrieved from: <http://upet.ro/annals/mechanical/pdf/2009/Annals-Mechanical-Engineering-2009-a23.pdf> [Accessed May 2015]
- Richer, E., & Hurmuzlu, Y. (2000). A high performance pneumatic force actuator system: part II—nonlinear controller design. *Journal of dynamic systems, measurement, and control*, 122(3), 426-434.

- Richer, E., & Hurmuzlu, Y. (2000). A high performance pneumatic force actuator system: Part I—nonlinear mathematical model. *Journal of dynamic systems, measurement, and control*, 122(3), 416-425.
- Saidur, R., Rahim, N. a., & Hasanuzzaman, M. (2010). A review on compressed-air energy use and energy savings. *Renewable and Sustainable Energy Reviews*, 14(4), 1135–1153. doi:10.1016/j.rser.2009.11.013
- Schulte, H., & Hahn, H. (2004). Fuzzy state feedback gain scheduling control of servo-pneumatic actuators. *Control Engineering Practice*, 12(5), 639-650.
- Shapiro, A. H. (1953). *The dynamics and thermodynamics of compressible fluid flow*. New York: Ronald Press, 1953-54, 1.
- Shen, X., & Goldfarb, M. (2007). Energy saving in pneumatic servo control utilizing interchamber cross-flow. *Journal of dynamic systems, measurement, and control*, 129(3), 303-310.
- Sorli, M., Figliolini, G., & Almondo, A. (2010). Mechatronic Model and Experimental Validation of a Pneumatic Servo-Solenoid Valve. *Journal of Dynamic Systems, Measurement, and Control*, 132(5), 054503. doi:10.1115/1.4002065
- Stecki, J. S., & Davis, D. C. (1986). Fluid transmission lines—distributed parameter models part 1: A review of the state of the art. *Proceedings of the Institution of Mechanical Engineers, Part A: Journal of Power and Energy*, 200(4), 215-228.
- Stefani, R. T., Savant, C. J., Shahian, B., & Hostetter, G. H. (2002). *Design of feedback control systems*. Oxford University Press, Inc.
- Stoorvogel, A. A. (1992). *The  $H_\infty$  Control Problem: A State Space Approach*. Prentice Hall.
- Surgenor, B. W., Pieper, J. K., & Wijesuriya, E. T. (1991, March). On the control of pneumatic positioners and the case of the inverted pendulum. In *Control 1991. Control'91., International Conference on* (pp. 1117-1122). IET.
- U.S. Energy Information Administration (2015). Spot prices for crude oil and petroleum products. Retrieved from: <https://www.eia.gov/dnav/pet/hist/LeafHandler.ashx?n=pet&s=rwtc&f=d> [Accessed July 2015]
- Wang, J., Pu, J., & Moore, P. (1999). A practical control strategy for servo-pneumatic actuator systems. *Control Engineering Practice*, 7(12), 1483–1488. Retrieved from: [http://doi.org/10.1016/S0967-0661\(99\)00115-X](http://doi.org/10.1016/S0967-0661(99)00115-X) [Accessed May 2015]

- Wang, J., Wang, D. J. D., Moore, P. R., & Pu, J. (2001). Modelling study, analysis and robust servocontrol of pneumatic cylinder actuator systems. *IEE Proceedings-Control Theory and Applications*, 148(1), 35-42.
- Wang, J., Kotta, Ü., & Ke, J. (2007, March). Tracking control of nonlinear pneumatic actuator systems using static state feedback linearization of the input-output map. In *PROCEEDINGS-ESTONIAN ACADEMY OF SCIENCES PHYSICS MATHEMATICS* (Vol. 56, No. 1, p. 47). Estonian Academy Publishers; 1999.
- Whitmore, S. A. (1988). Formulation of a general technique for predicting pneumatic attenuation errors in airborne pressure sensing devices. National Aeronautics and Space Administration, Ames Research Center, Dryden Flight Research Facility.
- Whitmore, S., Lindsey, W., Curry, R., & Gilyard, G. (1990). Experimental Characterization of the Effects of Pneumatic Tubing on Unsteady Pressure Measurements. *NASA Technical Memorandum*, 4171. Retrieved from <http://ntrs.nasa.gov/search.jsp?R=19900018387> [Accessed January 2015]
- Whitmore, S. A., & Leondes, C. T. (1991). Pneumatic distortion compensation for aircraft surface pressure sensing devices. *Journal of Aircraft*, 28(12), 828-836.
- Yu, N., Hollnagel, C., Blickenstorfer, A., Kollias, S. S., & Riener, R. (2008). Comparison of MRI-compatible mechatronic systems with hydrodynamic and pneumatic actuation. *Mechatronics, IEEE/ASME Transactions on*, 13(3), 268-277.
- Zalmanzon, L. A. (1965). Components for pneumatic control instruments: the static and dynamic characteristics of pneumatic resistances, capacitances and transmission lines. Elsevier.
- Zames, G. (1981). Feedback and optimal sensitivity: Model reference transformations, multiplicative seminorms, and approximate inverses. *Automatic Control, IEEE Transactions on*, 26(2), 301-320.
- Zhu, Y., & Barth, E. J. (2005, April). Impedance control of a pneumatic actuator for contact tasks. In *Robotics and Automation, 2005. ICRA 2005. Proceedings of the 2005 IEEE International Conference on* (pp. 987-992). IEEE.